IMPROVEMENT AND VALIDATION OF A THERMODYNAMIC S.I. ENGINE SIMULATION CODE

By:
Ebrahim Abdi Aghdam

BSc, MSc

Submitted in accordance with the requirements for the degree of
Doctor of Philosophy

The University of Leeds
School of Mechanical Engineering

August 2003

The candidate confirms that the work submitted is his own and appropriate credit has been given where reference has been made to the work of others.

Abstract

This study was concerned with improvement and validation of a thermodynamic spark ignition engine simulation code developed in Leeds.

Experimental validation data were generated using a central ignition, disc-shaped combustion chamber variant of a ported single-cylinder research engine with full-bore overhead optical access. These data included simultaneous measurement of cylinder pressure and flame position at different operating conditions. The engine was skip fired (fired once every five cycles), to remove residuals and ensure well defined in-cylinder fuel-air mixture for simulation. Flames were imaged using a digital camera capturing the light emitted from the flame ("natural light").

New methods were developed to process the pressure and film data. Flame pictures were processed to determine enflamed area, mean flame radius and flame centroid. Parameters were also developed to describe flame "circularity" ("shape factor") and to describe asymmetry of flame approach to the cylinder walls ("active perimeter fraction", APF). Time-base crank angle records allowed evaluation of engine speed variation within a cycle and mean engine speed for a cycle.

Although generated principally for model validation, the experimental results proved interesting in their own right. Middle, slow and fast cycles were defined for each condition. Analysis of these cycles suggested that there was no correlation between the initial flame centroid displacement, its locus over the flame propagation period or the flame "shape factor" and the speed of combustion and pressure development. As the flame approached the wall, the active perimeter fraction fell in a similar manner for all the middle cycles.

Substantial modifications were made to a pre-existing thermodynamic engine cycle code. Deficiencies in the blowby, heat transfer and thermodynamic aspects were corrected. An additional ("Zimont") turbulent burning velocity sub-model and a new routine for the influence of engine speed variation within a cycle were incorporated into the code. The active perimeter fraction parameter function determined in the experiments was encoded to allow for the effects of flame-wall contact on entrainment rate during the late flame propagation. A radial stratified charge model was also developed. Burned gas expansion over the flame propagation period was shown to significantly change the unburned gas charge stratification from the initial variation. Two types of initial stratification (linear and parabolic distributions, rich of the centre and lean close to the wall) were imposed. Faster combustion development was observed in both cases, c.f. that for equivalent homogeneous charge.

Good agreement was observed between experimental results and "Zimont model" predictions at different equivalence ratios and engine speeds. Other computations using the pre-existing Leeds K and KLe correlations gave reasonable predictions at the various engine speeds and at rich conditions; however, they yielded slower results than experimentally observed for lean conditions.

Acknowledgements

I would like first of all to acknowledge my indebtedness to my supervisor, Professor Chris Sheppard, for his unfailing assistance in broadening my entire perspective on research, and for his thoughtful comments on my innumerable documents and queries. Certainly, without his support, the writing of this thesis would have been neither possible, nor enjoyable. I would also like to sincerely thank Dr. R. Woolley for his interesting advice.

I am also very grateful to technicians John Groves, Brian Leach, Mark Batchelor, and Jonathan Stephenson for their assistance in the laboratory. In addition, I would like to thank Pam Harron and Pat Richardson for their help with university procedures and administration.

I would also like to take this opportunity to thank all of my colleagues in the combustion group at Leeds; especially A. Murad for his valuable assistance in my data collection, A. Melbourne and C. Wu for their helps.

I wish to thank the Iranian Ministry of Science, Research and Technology for granting me the scholarship, and Mohaghegh Ardebili University for the study leave which enabled me to follow up my studies at Leeds University.

Finally, as a token of my deepest gratitude, I dedicate this thesis to my wife, Laili Saied Hatami, for all her kindness and my lovely sons, Ali and Ata.

Contents

Abstract ii

Acknowledgements iii

Contents iv

Nomenclature viii

1 Introduction 1

1.1 General background 1
1.2 Thesis outline 3

2 Combustion and Modelling of Spark Ignition Engine 5

2.1 Introduction 5
2.2 Spark ignition engine models 6
2.2.1 Multi-dimensional models 7
2.2.2 Thermodynamic models 7
2.3 Turbulence features of in-cylinder flow 9
2.4 Flame detection techniques 13
2.5 Cyclic variations 15
2.6 Stratified charge spark ignition engines 17
2.6.1 Mixture formation 17
2.6.2 Flow field in DISC engines 20

3 Experimental Engine and Instrumentation 27

3.1 Introduction 27
3.2 LUPOE1 engine 27
3.3 Heating and temperature measurement systems 29
3.4 Fuel-air supply and control 30
3.4.1 Air supply system 30
3.4.2 Fuel supply system 31
3.5 Engine ignition and measurement systems 31
3.5.1 Ignition system 31
3.5.2 Pressure measurement 33
3.5.3 Crank angle measurement 33
3.5.4 Flame filming system 34
3.5.5 Data acquisition system 34
3.6 Test procedure 35
3.7 LUPOE2 engine 36

4 Data Processing and Analysis Techniques 45

4.1 Introduction 45
4.2 Cylinder pressure data processing 46
4.2.1 Developing the digitised binary data with FAMOS sequences 46
4.2.2 Resampling and arranging the digitised pressure data versus crank angle 47

4.2.2.1 Uniform engine speed assumption 47
4.2.2.2 Relative to external clock 47
4.2.3 In-cylinder pressure referencing 48
4.2.4 Estimation of cycle engine speed 49
4.2.5 Fortran program for pressure data processing 51
4.3 Film processing 51
4.3.1 Converting raw image to black and white 52
4.3.2 Converting binarised image to ASCII format 53
4.3.3 Flame edge processing 54
4.3.4 Enflamed cross-sectional area and centroid 56
4.3.5 Flame radius and edge perimeter 56
4.3.6 Fortran program for film processing 58
4.4 Synchronisation between film data and crank position 59
4.4.1 Synchronising by set engine speed 60
4.4.2 Synchronisation using average engine speed for the cycle concerned 60
4.4.3 Synchronisation using external clock data 60
4.5 Discussion 61

5 Experimental Results 77

5.1 Introduction 77
5.2 Reference condition 78
5.2.1 Cyclic variation 78
5.2.2 Typical cycles 80
5.2.3 Analysis of representative middle, fast and slow cycles (at reference condition) 82
5.3 Effect of engine speed 87
5.3.1 Higher engine speed (2000 *rpm*) 87
5.3.2 Lower engine speed (750 *rpm*) 88
5.3.3 Variation of (middle cycle) behaviour with engine speed 89
5.4 Effect of equivalence ratio 90
5.4.1 Rich mixture (ϕ=1.1) 90
5.4.2 Lean mixture (ϕ=0.8) 91
5.4.3 Variation of (middle cycle) behaviour with equivalence ratio 92
5.5 Effect of compression ratio 93
5.5.1 Medium compression ratio (CR=10.2) 93
5.5.2 High compression ratio (CR=12.4) 94
5.5.3 Variation of (middle cycle) behaviour with compression ratio 95
5.6 Engine speed variation within a cycle 96
5.6.1 LUPOE1 97
5.6.2 Engine speed variations in single and multi-cylinder four-stroke engines 98
5.7 Summary and conclusions 98

6 Leeds University Spark Ignition Engine Code and Modifications Made in the Code 145

6.1 Introduction 145
6.2 Pre-existing LUSIE 146

6.2.1 Compression 147
6.2.2 Ignition 148
6.2.3 Combustion 148
6.2.4 Expansion 154
6.2.5 Exhaust and intake 154
6.3 Blowby modelling 154
6.3.1 Piston-ring-cylinder pack crevices 156
6.3.2 Mass flow through crevices and ring gaps 156
6.3.3 Volume and orifice blowby theory 157
6.3.4 Blowby geometric parameters 160
6.3.5 Numerical aspects of the blowby model 161
6.4 Pressure equalisation subroutine 162
6.4.1 Governing equations 162
6.4.2 Revised pressure equalisation routine 164
6.4.3 Comparison of original and revised subroutines 165
6.5 Combustion modelling 167
6.5.1 Burning velocity and flame propagation 167
6.5.1.1 Laminar burning velocity 168
6.5.1.2 Turbulent burning velocity 170
6.5.2 Leeds *K* and *KLe* correlations 172
6.5.3 Zimont model 173
6.5.4 Numerical solution of burn-up equation in the entrainment model 175
6.5.5 Application of engine speed variation within a cycle 176
6.5.6 Non-circularity of flame propagation 178
6.6 Other modifications 179
6.6.1 Compression stroke 179
6.6.2 Ignition period 180
6.6.3 Effect of cylinder mass loss on unburned gas zone 180
6.6.4 Cylinder charge heat transfer 181
6.6.4.1 Annand equation 181
6.6.4.2 Woschni equation 181
6.6.4.3 Modification to the heat transfer routines 182
6.6.5 Thermodynamic properties 183
6.6.6 Structure of the combustion routine 185
6.6.7 Expansion stroke 185
6.7 Radial stratified charge 186
6.7.1 Burned gas expansion and unburned gas stratification 187
6.7.2 Evaluating average equivalence ratio 188
6.7.3 Successive incremental burned gas expansions and unburned gas stratification 190
6.7.4 Flame development in radial stratified charge 192
6.8 Summary 196

7 Validation 222

7.1 Introduction 222
7.2 Blowby model setting for motoring condition 223
7.2.1 Comparison with experimental motoring 224
7.2.2 Additional motoring predictions 225
7.3 Model constant setting at the reference condition 226

7.3.1 Comparison between model output and experiment 226
7.3.2 Sensitivity analysis of the combustion model 227
7.3.3 Additional information from model 228
7.4 Validation at other conditions 230
7.4.1 Engine speed 230
7.4.2 Mixture strength 231
7.4.3 Compression ratio 233
7.5 Zimont model, Leeds K and KLe correlations 235
7.5.1 Homogeneous case 236
7.5.2 Stratified charge case 238
7.6 Conclusions 239

8 Summary, Conclusions and Recommendations for Future Work 266

8.1 Summary of principal findings 266
8.1.1 Experimental study 266
8.1.2 Modelling studies 269
8.1.3 Model validation 272
8.2 General conclusions and discussion 273
8.3 Recommendations for future work 277

References 279

Nomenclature

A	mm^2 / -	Area / constant
a	-	Constant
A_e	mm^2	Entrainment flame front area
$(A/F)_{st}$	-	Stoichiometric air/fuel ratio by mass
b	-	Constant
c	-	Constant
C_d	-	Discharge coefficient
c_p	kJ kg^{-1} K^{-1}	Specific heat capacity (constant pressure)
D	mm	Cylinder bore diameter
Da	-	Damköhler number
$\overline{F}$	-	Dimensionless frequency
f	- / Hz	Diluent mass fraction / frequency
H	kJ	Enthalpy
h	kJ kg^{-1} / mm	Specific enthalpy / combustion chamber height
K	- / -	Karlovitz stretch factor / constant
K_l	-	Laminar Karlovitz stretch factor
K	kJ kg^{-1} / kW m^{-1} K^{-1}	Turbulent kinetic energy / thermal conductivity
k_τ	-	Burning time constant of proportionality
L	-	Markstein length
Le	-	Lewis number
l	-	Integral length scale
m	kg	Mass
Ma	-	Markstein number
N_c	-	Number of cycles for averaging
$N_{D.P.}$	-	Number of data points
n_f	fps	Filming speed
n_{set}	rpm	Set engine speed
$\overline{n}$	rpm	Average engine speed
Nu	-	Nusselt number
P	mm / bar / -	Flame perimeter length / pressure / constant
p	bar	Pressure

p_f	bar	Final pressure
p_m	bar	Motoring pressure
p_{max}	bar	Cylinder peak pressure
$\bar{p}_{\max}$	bar	Average peak pressure
Q	kJ	Heat transfer from system
q	kW m^{-2}	Heat flux
R	kJ kg^{-1} K^{-1} / mm	Particular gas constant / cylinder radius
R_a	kJ kg^{-1} K^{-1}	Particular gas constant for air
R_h	-	Reynolds number defined by chamber height
R_l	-	Reynolds number defined by integral length scale
Re	-	Reynolds number
r	mm	Radius
$\bar{r}_e$	mm	Mean entrainment flame radius
S_e	m s^{-1}	Entrainment flame speed
S_r	m s^{-1}	Reacting flame speed
$\bar{S}$	-	Dimensionless power spectrum
T	K	Temperature
T_w	K	Wall temperature
t	s	Time
t_k	s	Elapsed time from ignition
$\bar{t}_k$	-	Dimensionless elapsed time from ignition
U	m s^{-1} / kJ	Velocity / internal energy
$\bar{U}$	m s^{-1}	Mean velocity
u	m s^{-1} / kJ kg^{-1}	Velocity / specific internal energy
u_l	m s^{-1}	Laminar burning velocity
u_n	m s^{-1}	Stretched laminar burning velocity
u_t	m s^{-1}	Turbulent burning velocity
u_{te}	m s^{-1}	Turbulent burning (entrainment) velocity
u_{tr}	m s^{-1}	Turbulent burning (reacting) velocity
u'	m s^{-1}	Root mean square (rms) turbulent velocity
u'_k	m s^{-1}	Effective "rms" turbulent velocity
V	m^3	Volume
V_s	m^3	Displacement volume

$\overline{V}_p$	m s^{-1}	Mean piston speed
W	kJ	Work transfer from system
w	m s^{-1}	Mean velocity
x_f	-	Mass fraction
$\widetilde{x}_f$	-	Mole fraction

Greek symbols

α	- / m^2 s^{-1}	Constant / thermal diffusivity
β	-	Constant
γ	-	Specific heat ratio
δ_l	mm	Laminar flame thickness
ε	m^2 s^{-3}	Turbulent kinetic energy dissipation rate
η	mm	Kolmogrov length scale
θ	-	Crank angle
$\theta_{p_{\max}}$	-	Crank angle position of peak pressure
λ	mm	Taylor microscale
μ	-	Mean value
ν	m^2 s^{-1}	Kinematic viscosity
ρ	kg m^{-3}	Density
$\sigma_{p_{\max}}$	bar	Peak pressure variance
τ_t	s	Eddy lifetime
τ_a	s	Integral time scale
τ'	s	Turbulent time scale
ϕ	-	Equivalence ratio by mass

Subscripts, superscripts and notation

a	Air
av	Average
b	Burned

EA	Ensemble averaged value
e	Entrained / entrainment
f	Fuel / flame
g	Guessed / gas
ig	Ignition
t	Total / turbulent
Δ	Difference
°	Degrees
~	Molar base

Abbreviations

ADC	Analogue to Digital Converter
APF	Active Perimeter Fraction
aTDC	After Top Dead Centre
B/W	Black/white
BDC	Bottom Dead Centre
BS	Back Scatter
bTDC	Before Top Dead Centre
CA	Crank Angle
CFD	Computational Fluid Dynamic
COIE	Constant Overall Internal Energy
COV	Coefficient Of Variation
CR	Compression Ratio
CVAC	Constant Volume Adiabatic Combustion
DISC	Direct Injection Stratified Charge
EPC	Exhaust Port Closure
EPO	Exhaust Port Opening
F, M and S	Fast, Middle and Slow
FAMOS	Fast Analysis and Monitoring Of Signals
FFT	Fast Fourier Transform
FMBF	Fuel Mass Fraction Burned
FS	Forward Scatter

FSD	Full-Scale Deflection
GDI	Gasoline Direct Injection
HCR	High Compression Ratio
IsC	Isentropic Compression
IsE	Isentropic Expansion
LDV	Laser Doppler Velocimetry
LUPOE	Leeds University Ported Optical Engine
LUPOE1-D	LUPOE1 Disc-shaped version
LUSIE	Leeds University Spark Ignition Engine (code)
MFB	Mass Fraction Burned
PC	Personal Computer
PFI	Port Fuel Injection
PLIF	Planer Laser Induced Fluorescence
RMS/rms	Root Mean Square
SF	Shape Factor
TDC	Top Dead Centre
TLC	Top Land Crevice
UES	Uniform Engine Speed
VES	Variable Engine Speed
2D	Two-dimension
3D	Three-dimension

Chapter1

Introduction

1.1 Background

Ever tightening emissions regulations, depletion of fossil fuel reserves and global warming considerations continue to stimulate spark ignition engine development. This is resulting in many new concepts, such as: variable valve timing, gasoline direct injection, variable compression ratio, exhaust gas recirculation (EGR), turbo-charged downsized engines, homogeneous charge compression ignition (HCCI), hybrid engines, etc. These technologies and combinations of them are leading to engines of ever greater complexity, with the greater number of variables involved requiring ever more extensive control systems. At the same time, there are marketing and production pressures to reduce lead times in the delivery of new powertrains and vehicles. Hence, to improve design and minimise development testing, manufacturers are employing more modelling methods to simulate engine and vehicle behaviour – to the point of having "virtual vehicles" of close to "real time" operation.

For simulation of engines, a number of commercial "packages" exist and are widely used as development tools by motor companies; e.g. Ricardo's WAVE, Gamma Technology's "GT-Power" and others. For simulation of the in-cylinder processes in such codes, "thermodynamic" models (Heywood, 1988; Stone, 1991) are usually invoked; these often include some empirical expression to govern the burn rate (e.g. Weibe function). Such software is relatively simple to use, does not make excessive computer hardware demands and can produce results fast enough for incorporation into complete powertrain/vehicle simulation programs. The codes are effective where engines already exist (or of very similar design to existing motors) to produce the necessary experimental in-cylinder pressure data to set the controlling parameters of the Weibe (or similar) empirical burn rate parameter. They can also be very useful in 'reverse mode', applied to experimental data to generate information (e.g. mass fraction of fuel burned or unburned gas temperature at any instant) which would be

difficult to measure. However, the codes prove less useful for engine designs of radically new geometry or for operating conditions departing from those adopted in traditional/conventional designs where the burn rate parameters cannot be pre-determined. To overcome such restrictions, a number of alternative "turbulent entrainment/burn-up" or "quasi-dimensional" modelling concepts based on the ideas of Blizard and Keck (1974) have sometimes been incorporated into commercial thermodynamic codes; these ideas are reviewed more thoroughly in Chapter 6. Nevertheless, to date, the experience of many companies of such codes has not proved entirely satisfactory.

More complex Computational Fluid Dynamic (CFD) programs (e.g. "CD-Star", "VECTIS", "FIRE" etc.) have also been developed for engines. Although these codes are very computer intensive, making heavy hardware and run-time demands, they are now very widely used by engine development engineers. These softwares are particularly useful for study of (intake, exhaust and in-cylinder) flow and fuel/air/residual mixing etc., although still not entirely proven for unsteady/transient flows. Recent years have also seen good progress in the combustion routines within the codes. However, inclusion of combustion raises (already very large) hardware requirements and run times – without commensurate improvement (vis-à-vis "thermodynamic" codes) in predictive accuracy or universal application to different engine designs. The computing requirements of such codes are too extensive to allow incorporation into complete engine or "virtual vehicle" simulations. Arguably, the most effective way to use CFD codes for engines is to apply them for the study of detailed flow and mixing features; using the output to provide turbulence data input to simpler thermodynamic models for the combustion process, possibly using the output from these to drive even simpler models for virtual vehicle simulations.

The School of Mechanical Engineering at Leeds has, over a number of years [Hynes, (1986); Bradley et al. (1988); Merdjani and Sheppard (1993); Langridge (1995); Merdjani (1996) and Cairns (2001)], evolved a research computer program (Leeds University Spark Ignition Engine – LUSIE) for in-house study of the fundamentals of flame propagation, autoignition and knock in its optically accessed research engines. The objectives of the work reported in the current thesis were with the development of LUSIE into a reliable, accurate and robust vehicle for the implementation,

development and testing of turbulent entrainment and end gas autoignition sub-models and its possible extension to the stratified combustion inherent in direct injection engines. An essential pre-requisite of this was the generation of a very extensive, accurate and consistent experimental database for validation purposes. These data were gathered (by the current author) for a somewhat idealised, "disc-shaped", single cylinder, ported, "skip-fired" research engine of exceptional optical access. This represented the first stage in a much wider on-going Leeds programme of work encompassing idealised "pent roof" cylinder head optical and production engines, including a gasoline direct injection variant. This includes incorporation of the version of LUSIE developed in the current study as an "external cylinder" in Ricardo's WAVE code, to take advantage of the latter's proven engine "breathing" routines, to permit testing of the various combustion and autoignition models available within LUSIE against real production engine performance.

1.2 Thesis outline

Following this introductory chapter, presented in Chapter 2 is a literature review covering spark ignition engine modelling. This also encompasses engine in-cylinder flame imaging, cyclic variation and stratified charge concepts.

Described in Chapter 3 are the full bore optical access research spark ignition engine and supplementary apparatus used in this work. Chapter 4 is concerned with the revised methods developed in this study to process and analyse the simultaneous film and pressure data captured from the research engine to provide the required model validation information; in particular, the various methods developed to permit accurate synchronisation of the image and in-cylinder pressure data are outlined. The experimental results and subsequent analysis of them, for a range of engine speeds, mixture strengths and compression ratios, are presented in Chapter 5.

The modelling work is presented in Chapter 6, starting with a review of the pre-existing version of the LUSIE thermodynamic spark ignition engine code inherited from previous researchers at Leeds and moving on to description of the various major and minor modifications made to the code by the current author in the course of the study (highlighting the effects of each correction/modification in turn). In particular,

critical corrections to the code's "pressure equalisation" routines and extensive alterations made to the three-ring "blowby" sub-model (vital to effective simulation of the ported optical research engine) are described; the results are critically compared to those obtaining with earlier variants of the code. Also described in this chapter is a new sub-model devised and coded for flame development in radial stratified charge within a disc-shaped combustion chamber.

The experimental and theoretical work are brought together in Chapter 7, setting out the manner in which the model constants were set at an experimental "reference" condition and how the code was subsequently validated by comparing "predictions" with experimental data at other conditions.

Finally, in Chapter 8, the findings of the study are summarised, conclusions are drawn and recommendations for future work are made.

Chapter 2
Combustion and Modelling of Spark Ignition Engine

2.1 Introduction

In commercial spark ignition engines, the cylinder mixture is ignited by a spark in a complex turbulent flow field late in the compression stroke. The electrical discharge of the spark creates a burned flame kernel. This kernel propagates as a result of combustion of unburned charge and heat and turbulent diffusion between burned and unburned gases. During the flame propagation, pressure, temperature and the flow field of the unburned mixture vary because of burning gas expansion, piston motion and turbulence decay. Moreover, during the combustion process, the cylinder charge experiences complex chemical reactions, heat transfer (with the chamber wall) and work transfer (with the piston). The situation can be further complicated by interaction between the gases and the chamber geometry, mass flow to/from crevices, auto-ignition and mixture stratification.

A basic understanding of the physics and chemistry of the phenomena can be obtained through experimental studies conducted in simplified circumstances. Therefore, much fundamental research has been conducted in constant volume bombs and Bunsen burners under laminar conditions to understand the effects of pressure, temperature, fuel type, equivalence ratio and diluents on laminar burning velocity (described in Section 6.5.1.1). Also, investigations have been performed to characterise the turbulent flow field in well-stirred bombs and motored engines in the absence of a combustion event (Hall and Bracco, 1987; Atashkari, 1997; Jakubík, 2002). Heat exchange between the cylinder charge and chamber walls has been the subject of research for many investigators (Annand, 1963; Woschni, 1967; Morel et al., 1985). A number of investigations have been concerned with ring-piston-cylinder pack crevice flow, because of its importance for engine efficiency, unburned hydrocarbon emissions and engine simulation and design (detailed in Section 6.3). A lot of researches have been conducted to understand auto-ignition phenomena, utilising

simple chamber shape engines such as disc-shaped chamber with side and central ignition modes (Langridge, 1995; Tindal, 1997; Mahmud, 1999). Several correlations, semi-emperical and theoretical models have been presented to characterise turbulent burning velocity or flame speed in homogenous charge in terms of various fundamental parameters e.g. laminar burning velocity, turbulent intensity, length scale, Lewis number, effective turbulent intensity and flame radius (reviewed and discussed by Lipatnikov and Chomiak 2002).

Engine combustion processes can be modelled using equations expressing the physics and chemistry of the phenomena. However, various simplifications and assumptions are usually required. Modelling can make a valuable contribution here; providing an understanding of the processes, identifying key controlling variables for providing guidelines for experimental work and predicting engine behaviour over a wide range of operating conditions. If the model is satisfactorily accurate, it can be used as a tool to optimise engine design and control. Chow and Wyszynski (1999) defined an engine system as a collection of elements (such as cylinder, intake and exhaust manifolds, three way catalytic converter/reformer (TWC), junctions and turbocharger) operating together to provide an improved power output for meeting a particular purpose. They reviewed the available thermodynamic and gas flow process models for the system elements; then they concluded that the future expectations from engine systems required a further comprehensive model including the development of composition tracking, TWC and fuel reformer models to predict engine performance in transient conditions in addition to steady state operating conditions. Since the currently reported study was concerned only with modelling of in-cylinder thermodynamic phenomena in spark ignition engines, only in-cylinder models are described in the sections below.

2.2 Spark ignition engine models

On the basis of temporal and temporal-spatial resolution of the flow field, mathematical in-cylinder models of spark ignition engines can be divided into two main groups: *multi-dimensional* (based on fluid dynamics) and *thermodynamic* (based on the First and Second Laws of Thermodynamics). These models are briefly described below.

2.2.1 Multi-dimensional models

In multi-dimensional models the spatial and temporal variations of the velocity and temperature fields are considered together. Two or three dimensions are taken into account using instantaneous time-dependent conservation equations of mass, momentum, species and energy in conjunction with some simplifying assumptions. Much effort has been spent towards the development of comprehensive 3-D models, describing all the relevant phenomena relating to engine operation and emission formation. They can be used to predict the effect of geometrical and operating parameters on the complex fluid dynamics and thermo-chemical phenomena involved in engine operation; nevertheless, they do not as yet represent the ultimate solution for all applications in the internal combustion engine area. As these models require very high computing power, they are not very suitable for those uses which involve many repeated computations (as in design applications). Some researchers prefer just to use such models principally for motoring conditions, to obtain the flow field history in complex engine geometries. Moreover, the quantitative precision of these models, requiring an appropriate "balanced precision" in all their sub-models, could prove inadequate for applications which need high accuracy (Arsie et al., 1998). In the currently reported work, only thermodynamic models are considered.

2.2.2 Thermodynamic models

In thermodynamic models, the First Law of Thermodynamics provides the key equation in the incremental procedure used. In these models, the cylinder charge is divided into a number of zones; in which each zone has uniform temperature, pressure and composition. These models have been developed for *forward* and *reverse* analysis of engine cycles. The *forward* mode is employed to predict engine behaviour at different conditions and could be used for improvement of engine design. The *reverse* operation is applied to experimental engine data to extract information additional to those directly measured. According to the number of zones used, these models can be subdivided into two categories: single-zone (zero-dimensional) and multi-zone (quasi-dimensional) models which are described in the following sub-sections.

- ***Single zone models***

In single-zone models of SI engines the cylinder pressure, temperature, and composition are assumed uniform throughout the combustion chamber and the flame propagation process is neglected. They may include expressions for heat losses to the cylinder walls and heat addition as functions of time. In the *reverse* form of these models, the heat release rate of engine cycle can be extracted using pressure-crank angle data (Brunt et al., 1998; Chun et al., 1987; Gatowski et al., 1984).

- ***Multi-zone models***

In multi-zone models, the charge in the chamber is divided into more than one zone; usually two zones, burned and unburned. The two zones are separated from each other by a discontinuity surface (flame front). In such models flame propagation is usually governed by a turbulent burning velocity expression. Uniform temperature and pressure are assumed in the burned and unburned regions without allowance of heat transfer between the two zones. The unburned gases are generally assumed to be of "frozen" composition and the burned gases are considered to be in thermochemical equilibrium.

Blizard and Keck (1974) introduced an eddy entrainment model assuming a spatially homogeneous volume of eddies. They supposed that entrained eddies were burned by diffusive transport of radicals between neighbouring eddies, at a laminar burning velocity over a characteristic time. Such models, usually termed "entrainment models", have the advantage of linking with experimental flame visualisation techniques; e.g. natural light and Schlieren photography. The models usually incorporate two differential equations, for the mass entrained and mass burned (described in Chapter 6). Using the turbulent entrainment and eddy burn-up model, several thermodynamic models have been constructed and developed [Liu et al., 1999; Zhao et al., 1999; Reid and Douglas, 1994; Wahiduzzaman et al., 1993; Chen et al., 1992; Hynes, 1986]. In the currently reported work, a *forward* thermodynamic SI engine simulation developed in Leeds was used (detailed in Chapter 6).

Two-zone *reverse* thermodynamic models based on pressure time history (measured during combustion) have been developed to derive the temperature and the volume of burned and unburned gases as well as heat release and mass fraction burned [Krieger and Borman (1966) and Guezennec (1999)]. Assuming the crevice volume as a third zone, Jensen et al. (2000) developed a three-zone heat release model to investigate the effects of crevices and cyclic variations on unburned hydrocarbon emissions (ignoring blowby phenomenon). In Leeds parallel to development of the *forward* simulation (Hynes, 1986; Merdjani and Sheppard, 1993; Langridge, 1995; Merdjani, 1996; Cairns, 2001), two two-zone *reversed* models, termed LUSIEDA and THERMO, have been developed [König (1993), Lee (1995) and Mahmud (1999)]; both models were developed employing the routines used in the *forward* model.

2.3 Turbulence features of in-cylinder flow

Engine cylinder flows generally feature strong bulk motions with turbulence. In turbulent flow (a statistical phenomenon) rates of mixing, heat and mass transfers are much greater than those of laminar flows (where the heat and mass transfers and mixing are molecular processes). Although the same overall flow events occur every cycle, there are considerable cyclic variations in bulk motion and corresponding turbulent fluctuations. For this reason, an ensemble-averaging or phase-averaging approach is used for the quasi-periodic in-cylinder flows. An instantaneous velocity in the i th cycle at crank angle θ is described as (Heywood, 1988):

$$U(\theta,i)=\overline{U}(\theta,i)+u(\theta,i) \tag{2.1}$$

where $\overline{U}(\theta,i)$ and $u(\theta,i)$ are the mean and fluctuating components of the instantaneous velocity. The ensemble-averaged velocity is defined as:

$$\overline{U}_{EA}(\theta)=\frac{1}{N_c}\sum_{i=1}^{N_c}U(\theta,i) \tag{2.2}$$

where N_c is the number of cycles for the averaging. In reality, the mean velocity of an individual cycle can be different from the ensemble-averaged value, hence:

$$\hat{U}(\theta,i) = \overline{U}(\theta,i) - \overline{U}_{EA}(\theta) \tag{2.3}$$

where $\hat{U}(\theta,i)$ denotes deviation of the mean velocity of the individual cycle (i th) at θ from the ensemble-average. Using Equations (2.1) and (2.3), the instantaneous velocity becomes:

$$U(\theta,i) = \hat{U}(\theta,i) + \overline{U}_{EA}(\theta) + u(\theta,i) \tag{2.4}$$

Due to the crucial effects of both the bulk motion and turbulence on burning velocity (or flame propagation) and even emissions, a lot of attention has been paid to engine flow fields in the last three decades. Hall and Bracco (1987) found that the ensemble-averaged velocity increased approximately linearly with intake velocity at a fixed engine speed; also the mean velocity increased with engine speed at a fixed flow rate.

The root mean square (*rms*) turbulent velocity (u') is defined from the instantaneous fluctuation of velocity (u) about the mean velocity as:

$$u' = \underset{\tau\to\infty}{Lim}\left(\frac{1}{\tau}\int_{t_0}^{t_0+\tau} u^2 dt\right)^{1/2} \tag{2.5}$$

which is normally referred to as the "turbulent intensity" in literature and occasionally in this thesis (although the turbulent intensity is properly defined by the ratio of the *rms* turbulent velocity to the mean velocity).

In spark ignition engines, u' is dependent on inlet flow, piston speed and combustion chamber shape (Hall and Bracco, 1987; Arcoumanis et al., 1994; Atashkari, 1997; Liu et al., 1999; Kim and co-workers, 2002). In a disc-shaped chamber engine, Hall and Bracco (1987) observed approximately linear behaviour between turbulent intensity at TDC and mean piston speed. From their LDV results in firing and non-firing conditions, they observed little difference in turbulence intensity ahead of flame. They recorded an increased turbulent intensity across the flame zone; however, they argued that the measurement in the flame region could be unpredictable due to low data rate.

In Leeds Atashkari (1997) conducted LDV measurements in the LUPOE1 engine (disc-shaped chamber, CR=7.6) used in the currently reported study. He measured turbulent intensity at the mid-plane of clearance volume and found the turbulence to be both isotropic and homogenous. Shown in Figure 2.1(a) and (b) are his two-dimensional measurements of turbulent intensity and mean velocity at the mid-plane at TDC (1500 rpm engine speed). From measurements conducted at different engine speeds, he observed a linear correlation between turbulent intensity at TDC and mean piston speed as shown in Figure 2.2(a). He also noted a consistent linear decrease of turbulent intensity within the range of $40^{\circ} bTDC$ to $40^{\circ} aTDC$ at 1500 *rpm* engine speed as illustrated in Figure 2.2(b). These data were used in the modelling part of this study at the "reference" condition.

Using the similar technique, Jakubík (2002) extended the turbulent intensity data for LUPOE1 engine for different conditions. He found very similar results to those of Atashkari at 1500 *rpm*. Shown in Figure 2.3 are his observed turbulent intensity data, versus crank angle, at different engine speeds (CR=7.6); these data were employed in modelling part of this work at 7.6 compression ratio. For the high compression ratio (HCR) variant of the engine (CR=12.4), he had to use back scatter (BS) due to the lack of side windows on the cylinder head. For this compression ratio, he observed lower turbulent intensity and a substantial reduction in the number of samples over the range of interest ($10^{\circ} bTDC$ - $20^{\circ} aTDC$); the mid-plane of the clearance volume was only ~2.3 *mm* from the top window. Shown in Figure 2.4(a) are his obtained turbulent intensity data for the HCR together with corresponding back scatter and forward scatter (FS) data for 7.6 compression ratio at 1500 rpm; the related numbers of sampled data versus crank angle are displayed in Figure 2.4(b).

Three length scales are commonly used to characterise turbulent flows: integral length scale, Taylor microscale and Kolmogorov microscale.

Integral length scale (l) is a measure of the large scale eddies (Reynolds, 1980) – although eddies much larger than this scale exist in the chamber. Integral length scale is usually determined from autocorrelation of two-point spatial velocity measurements. Fraser et al. (1986) evaluated the integral length scale in a disc-shaped

ported engine employing two-point LDV measurements. They concluded that the integral length scale was proportional to instantaneous clearance height, with a proportionality of 0.2 at TDC position as illustrated in Figure 2.5. Kern et al. (1996) evaluated the integral length scale using single point LDV measurement and the expression proposed by Tabaczynski (1983).

Taylor microscale (λ) is defined by the ratio of the velocity gradient of a turbulent flow field to its turbulent intensity. Various expressions have been given for the ratio of the microscale to integral length scale in the literature. Heywood (1988) quoted the following expression from Tennekes et al. (1972):

$$\frac{\lambda}{l} = \sqrt{\frac{15}{A}} R_l^{-0.5} \tag{2.6a}$$

where A is a constant of order unit and R_l denotes Reynolds number defined as $R_l = {l.u'}/{\nu}$. Abdel-Gayed et al. (1984) proposed the following expression:

$$\frac{\lambda}{l} = \sqrt{40.4} R_l^{-0.5} \tag{2.6b}$$

In their investigation, Ting et al. (1997) used an alternative expression [from Kido et al. (1983)]:

$$\frac{\lambda}{l} = \frac{\sqrt{15}}{c^{0.4}} R_l^{-0.2} \tag{2.6c}$$

where c is a constant of order 11. Mann et al. (2000) noted that the integral length scale could be evaluated directly from measurement while Taylor microscale derived from measurements and Equation (2.6c) introduced some uncertainty. For this reason, they preferred to use integral length scale in their semi-empirical model of turbulent flame.

In a turbulent flow field, the smallest eddies dissipate due to the viscosity of the fluid. Assuming that ε is the kinetic energy dissipation rate per unit mass and ν is kinematic viscosity, Kolmogorov microscale (η) is defined in terms of ν and ε using dimensional analysis as:

$$\eta = \left(\frac{\nu^3}{\varepsilon} \right)^{1/4} \tag{2.7}$$

Turbulent kinetic energy per unit mass is proportional to u'^2. During one eddy lifetime ($\tau_l = l/u'$), considerable fraction of the energy dissipates and transforms to thermal energy. Application of an equilibrium condition between the energy dissipation rate and rate of kinetic lost leads to the following expression for η:

$$\eta = l \cdot R_l^{-3/4} \tag{2.8a}$$

From simplification of the Ramos (1989) definition, the following expression can be derived:

$$\eta = 0.51 l R_l^{-0.6} \tag{2.8b}$$

The various expressions of Taylor and Kolmogorov microscales from different sources may produce some uncertainty in application of the scales in comparison with the integral length scale. Therefore, integral length scale is generally considered the most reliable for use in correlations and models, rather than the other scales.

2.4 Flame detection techniques

To detect the development of flame position, most researchers use one or more of three common ciné optical techniques: (i) natural light, (ii) shadowgraph or Schlieren or (iii) laser sheet Mie scatter imaging. In the natural light technique, the emitted light from flame species is the only light source for detection. This method presents no special problems except that, for short exposure times, the luminosity is not always

sufficient to detect; particularly in the case of lean flames (Lewis, 1987). However, the method has the advantages of being simple to perform and ease of processing to a binary image.

Shadowgraph and Schlieren techniques both require a light source and optical lens to generate a parallel beam of light, which is guided into the combustion chamber. The techniques rely on density gradients in the combustion mixture to change refractive index and generate an image on screen. Due to substantial difference between burned and unburned gas densities, the entrainment flame front can be derived from the image. In full-bore optical access, this method needs a mirror on piston to reflect the affected light from the chamber. Any rocking motion of piston crown surface may displace the image on the screen.

Mie-scatter laser sheet imaging requires a thin sheet of laser light and a tracer added to the fuel-air mixture. The tracer should either be consumed or change scattering characteristics in the high temperature of the flame, such that it no longer scatters light and, as a result, generates an image which can be captured by a camera placed at right angle to the laser sheet. This technique results in very good information about the flame in the light plane; however, no information can be derived for the third dimension.

Schlieren and natural light methods are commonly used to define the entrainment flame front. The Schlieren technique offers better flame front definition; however, it is difficult technique to apply because of piston mirror fragility and involves considerable processing time. Modern high speed digital cameras are extremely light sensitive and are capable of using just natural light to detect the flame positions with exposure times shorter than $50\,\mu\text{sec}$. Hence the simpler natural light technique was used in the currently reported work to generate a very extensive database. At lean engine operating conditions, to compensate the lower level of natural light a small quantity of Sodium Ethylate was dissolved into the fuel to create a more intense yellow light (following Hynes, 1986).

2.5 Cyclic variations

Cyclic variation in SI engines may be defined as non-repeatability of the combustion process on a cycle-resolved basis (Ball et al., 1998). The topic has been the subject of studies for many researchers. Cyclic variation can result from combination of: variation in mixture motion, variation in air/fuel ratio and in mixing of fresh mixture and residual gases (especially in the vicinity of the spark plug, Heywood, 1988). These effects determine the mixture adjacent to the plug at ignition, convection of the spark kernel away from the electrodes and kernel heat loss to the electrodes.

Cyclic variation can be characterised in terms of the related parameters of in-cylinder pressure, combustion, flame and exhaust gas as detailed by Ozdor et al. (1994). Changes in in-cylinder motion can result in variation in turbulence intensity, u', and mean flow velocity in the vicinity of spark gap. In the initial flame kernel development, the mean velocity can convect the flame kernel away from the spark electrodes; so reducing heat losses to them (Pischinger and Heywood, 1990). In the worst case, it can push the flame towards metal surfaces such as electrodes and the cylinder head and cause substantial increase in the early flame heat loss.

From analysing results of experiments conducted on a square cross section engine, Keck et al. (1987) concluded that cycle-by-cycle variation of the location and growth rate of flame kernel early in the combustion event were the major reasons for cyclic variation in pressure curves. They noted that the mean velocity remained identical from cycle to cycle and that the kernel "random walk" in the turbulent flow was the reason for variation in kernel displacement and direction.

Using a production engine, Witze et al. (1990) measured flame kernel convection velocity and mean flow velocity using a fiber-optic spark plug and an LDV technique. They found good agreement between convection velocities and the LDV ensemble-average swirl-direction velocities. They observed weak correlation between combustion duration and convection velocity. They concluded that the random convection of the early flame kernel had much less effect on cyclic variation than suggested by Keck et al. (1987).

Bianco et al. (1991) employed the fiber-optic spark plug used by Witze et al. (1990) in a modified Ricardo Hydra research engine capable of generating quiescent, tumble or swirl motion during the induction process. The behaviour of the flame kernel was characterised using an expansion velocity (describing the kernel growth rate) and a convection velocity (indicating the overall movement of the kernel). They found a strong correlation between these two parameters and explained the correlation in terms of three factors: higher turbulent fluctuation with higher bulk motion velocity; larger flame stretch with higher convection velocity due to flame anchoring by the electrodes; reduction in heat losses due to flame convecting out of the spark plug region. However, they found only a weak correlation between the 10-90% burn duration and the initial behaviour.

Shen et al. (1996) suggested that the cylinder volume encompassed a distribution of turbulence intensities; when flame propagates and grows longer, a greater fraction of the overall distribution will influence the flame. From statistics, they demonstrated that when the sample size of an average of a set of observations increases, the variance of the average decreases. Therefore, as the flame propagates and becomes larger, the influence of cycle-by-cycle variations in turbulence will necessarily decrease. They concluded that the turbulence in the small region of the cylinder where spark discharge occurs varies more cycle-by-cycle than does the average turbulence value in the complete cylinder.

Using a PIV technique and recording flame kernel images, Pajot et al. (2000) quantified the effects of the instantaneous local velocity field in the vicinity of the spark plug just prior to ignition on the flame kernel development. They found a good correlation between flame centroid displacement and the velocity at the spark plug. Measuring flame radius at 1 *msec* after ignition, they found the largest flames relatively far from the electrodes and explained this in terms of reduces heat exchange with the electrodes.

In-cylinder peak pressure, $p_{\max}$, and the crank angle at which it occurs, $\theta_{p_{\max}}$, are two important parameters for characterising cyclic variation. Matekunas (1983) investigated the variation of $p_{\max}$ with $\theta_{p_{\max}}$ for different cycles and conditions. Hill

(1988) investigated cyclic variation in terms of engine speed and equivalence ratio, on the lean side of stoichiomery, quantifying variation in terms of the coefficient of variation of peak pressure, $\sigma_{P\max} / \overline{P}_{\max}$. In the range of conditions tested, he found an almost linear correlation between the overall equivalence ratio and the relative standard deviation; his results showed that effects of engine speed on cyclic variations to be much less than that of equivalence ratio.

Cyclic variation has also been quantified on the basis of a combustion parameter describing the completeness of combustion (Ball et al., 1998 and Al-Fakhri et al., 2000). This parameter was based on the Rassweiler-Withrow method of calculating the mass fraction burned (derived from pressure-crank angle records).

A number of investigators have attempted to determine spatial inhomogeneity of mixture and cyclic variation of equivalence ratio by measuring concentrations either at exhaust or in the vicinity of the spark plug prior to or just after ignition; these works have been reviewed by Ozdor et al. (1994).

2.6 Stratified charge spark ignition engines

Lean-burn and stratified charge concepts have received significant attention over the last three decades, because of fossil fuel reserve depletion, air pollution and global warming. Lean combustion enables simultaneous low emissions of CO_2, CO, HC and good fuel economy, under the right conditions. For homogeneous lean burn engines, substantial cyclic variation, initial flame instability and slow burn rates have been reported (Hill, 1988; Itoh et al., 1998). To counter these disadvantages, stratified charge spark ignition concepts have been promoted. The idea behind the stratified charge strategy is to generate a rich mixture close to spark plug at ignition, with a leaner charge towards the cylinder wall such that the combustion is lean overall.

2.6.1 Mixture formation

Mixture formation is very important in lean burn SI engines, since the air-fuel mixing process in the combustion chamber has a dominant effect on the subsequent processes

of ignition, flame propagation and pollutant formation. To create the mixture stratification, a number of different practical approaches have been introduced and developed; e.g. jet (or torch) ignition, mixture injection, port injection, direct- and indirect-injection.

Date et al. (1974) developed a torch-ignition stratified charge engine using an auxiliary fuel system and a small pre-combustion chamber. During intake process, the pre-chamber was fed with fuel-rich mixture generated by the auxiliary fuel system. Simultaneously, a very lean mixture was fed to the main combustion chamber through the main fuel system and intake manifold. During compression, this lean mixture flowed into the pre-chamber; diluting the rich mixture there, to produce an easily ignitable (slightly rich) mixture. After ignition, the rich burning mixture expanded into the main chamber in the form of a jet and ignited the lean charge.

Tabata et al. (1995) developed a "mixture injection" stratified charge SI engine using a similar approach to that of Date et al. (1974), without the pre-chamber. The rich mixture was injected through the port of a mixture injection valve (located at the centre of a pent-roof head) into the centre of bulk swirl motion created by the flow through the two main valves. They noted higher combustion rate and stability under lean operating conditions, c.f. normal homogeneous combustion in a conventional port injection version of the same engine.

Arcoumanis et al. (1996) used a solenoid valve to inject small amount of fuel-air mixture in the vicinity of the spark gap. This injection caused a combination of charge stratification and locally enhanced mean flow and turbulence. With this, they were able to extend the engine's misfire lean limiting equivalence ratio to 0.49 from the homogeneous case limit of 0.61 (for a propane-air mixture). They also noted significant increases in peak pressure and *imep*, as well as considerable reduction in cyclic variation c.f. operation with a homogeneous mixture (at an overall equivalence ratio of 0.7).

Using a port fuel injection engine, with critical fuel injection timing during the induction stroke to produce "barrel-stratification", Kuwahara et al. (1994) applied the lean-burn concept to a large displacement centre-spark 4-valve SI engine. They

studied the in-cylinder flow and mixing and showed that a high degree of tumble was effective in maintaining charge stratification in the compression stroke.

Fujimoto et al. (1995) investigated the effect of mixture stratification pattern on combustion characteristics in a pancake constant-volume combustion chamber. The chamber was equipped with a tangentially oriented port. To create a stratified mixture, they utilised two homogeneous mixtures of different air-fuel; one in the chamber and the other tangentially injected into the chamber. By changing the air-fuel ratio of the two mixtures, they were able to generate "central rich" or "central lean" stratified charge; as well as create a homogeneous mixture with swirl. They concluded that, for an overall lean mixture, the combustion speed was greatest with "central rich" burning; for this case, the initial flame growth was faster and flame development period shorter than with the other arrangements.

Using a constant-volume combustion chamber, Moriyoshi et al. (1996) studied the combustion characteristics of inhomogeneous propane-air mixtures under overall lean burn conditions. Before ignition, the chamber was divided into two zones (charged with lean and rich mixtures) separated by a removable partition inside the chamber. Then the partition was removed and the stratified charge was ignited. They demonstrated that a lean stratified mixture (overall equivalence ratio, $\phi = 0.6$) could burn as long as the spark gap was located in combustible mixture of the stratified charge.

A number of direct injection stratified charge (DISC) engines have been developed over the last decade. Investigations have included improvements to injector features by means of modification in the orientation of the nozzle holes of a multi-hole injector (Zhao et al., 1996), improvement of a swirl hollow cone injector associated with a central spray (Itoh et al., 1998) and development of a slit nozzle injector to form a thin fan-shaped fuel spray (Koike et al., 2000). Hayakawa et al. (2002) simulated the fuel spray of slit nozzle injector using a three-dimensional CFD code. Most of the recent DISC engines have been involved complex chamber geometries with pent-roof cylinder heads and piston crown cavities. These complexities usually prevent full optical access to study the events occurring in the combustion chamber, such that

detailed experimental study of DISC engines has largely been restricted to simpler flat piston or disc-shaped chambers (Ohsuga et al., 1997).

Fuel distribution within stratified charge engines has most usually been investigated using planer laser induced fluorescence (PLIF). For this, a number of different tracers have been used to mix with liquid or gaseous fuel (Ipp et al., 2000; Tabata et al., 1995; Meyer et al., 1994).

Gasoline direct injection (GDI) engines usually operate in one of two modes, based on the time of injection: (i) early injection, in which fuel is injected into the cylinder during the induction process and (ii) late injection, in which fuel is injected late in the compression stroke. These two modes prepare different types of mixture for the combustion period. The early injection mode provides an essentially homogeneous charge, at greater volumetric efficiency than obtainable with a standard port fuel injection (PFI) system (Anderson et al., 1996; Wyszynski et al., 2002). The late injection mode generates stratified charge.

2.6.2 Flow field in DISC engines

In DISC engines, the flow field has a key role in mixing and mixture stratification in addition to its usual role in enhancing turbulent burning. Four important features of in-cylinder flow field include: the mean flow components, the stability of the mean flow, the temporal development of turbulence in compression stroke and the mean velocity in the vicinity of spark plug at ignition timing. In a homogeneous charge SI engine, high turbulence intensity and low mean velocity in the vicinity of spark plug are advantageous (i.e. in PFI engines and GDI engines operating in the early injection mode). In such engines, a flow structure which is able to convert the kinetic energy of the mean flow into turbulent kinetic energy late in the compression stroke is regarded as advantage. However, GDI engines operating with late injection operate best with a flow field with significant mean velocity and low turbulence level, to achieve more stable stratification of the mixture. Therefore, the optimum flow field depends on the injection strategy; this is difficult to achieve for full-range GDI engines which have to operate in both early and late injection modes.

In general, there is a rotating flow structure in the cylinder and combustion chamber. The instantaneous principal axis of this structure is at an angle with the cylinder axis. The rotational vector can be split into parallel and perpendicular components. The parallel component is termed swirl and the other, tumble. To obtain stratified combustion in GDI engines, both swirl- and tumble-dominated flow structures have been used. Kume et al. (1996) used tumble-controlled flow with late injection to achieve stratification at part-load.

Squish motion is another bulk motion which adopted in some GDI systems. Squish motion is only generated as the piston is close to TDC. It can result in increased swirl and tumble; but may increase tendency to auto-ignition, due to extended crevice regions, and can necessitate reduction in compression ratio. Reverse squish, as the piston descends, also affects the flow field and combustion.

Zhao et al. (1999) summarised the principal features of swirl, tumble and squish motions and their roles in GDI combustion system. Swirl produces less viscous dissipation and is maintained longer in compression stroke. It is useful to maintain mixture stratification and is intensified when combined with squish motion. However, it should be noted that high swirl ratio can centrifuge the largest spray droplets towards the cylinder wall, resulting in an increase in fuel wall wetting. Swirl depends upon engine speed; this limits the operating range with adequate fuel-air mixing, because the momentum of the fuel spray is independent of engine speed.

Tumble is converted into turbulence near TDC due to its deformation ("squashing") and the associated velocity gradients generated. It is nearly fully transformed into random turbulence in the case of a flat geometry combustion chamber. When there is incomplete transformation, tumble may result in enhanced mean flow in the vicinity of spark plug, causing greater cyclic variation than noted with swirl motion. It is effective in creating high flow velocity near the cylinder wall, which may be useful in vaporising wall fuel film.

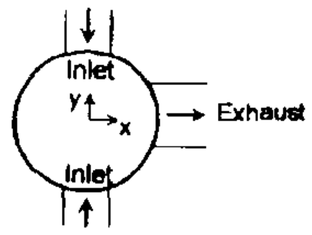

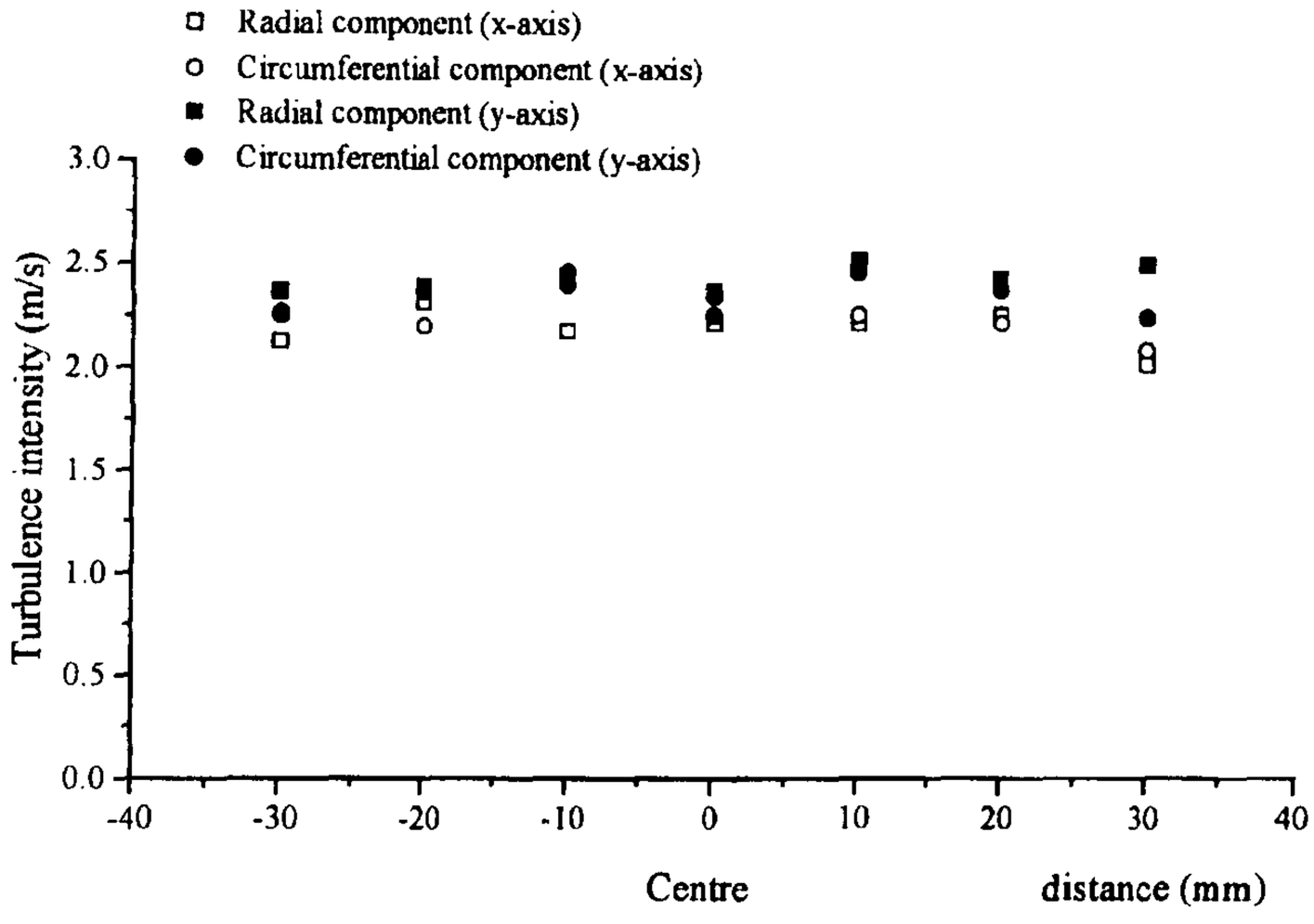

(a)

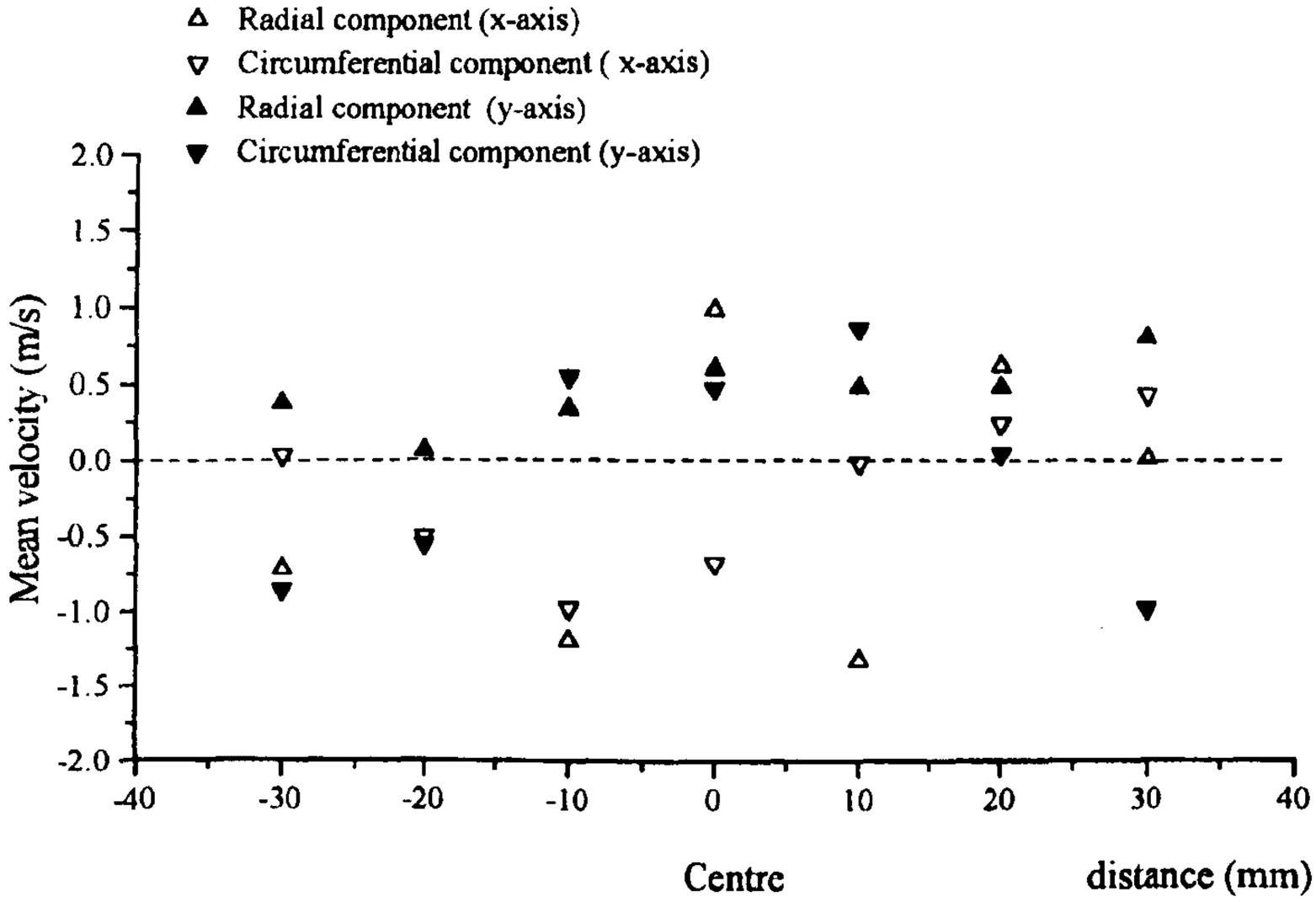

(b)

Figure 2.1 Two-dimensional measurements of **(a)** turbulent intensity and **(b)** mean velocity at the mid-plane at TDC position (1500 rpm engine speed, Atashkari, 1997).

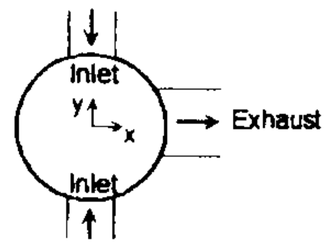

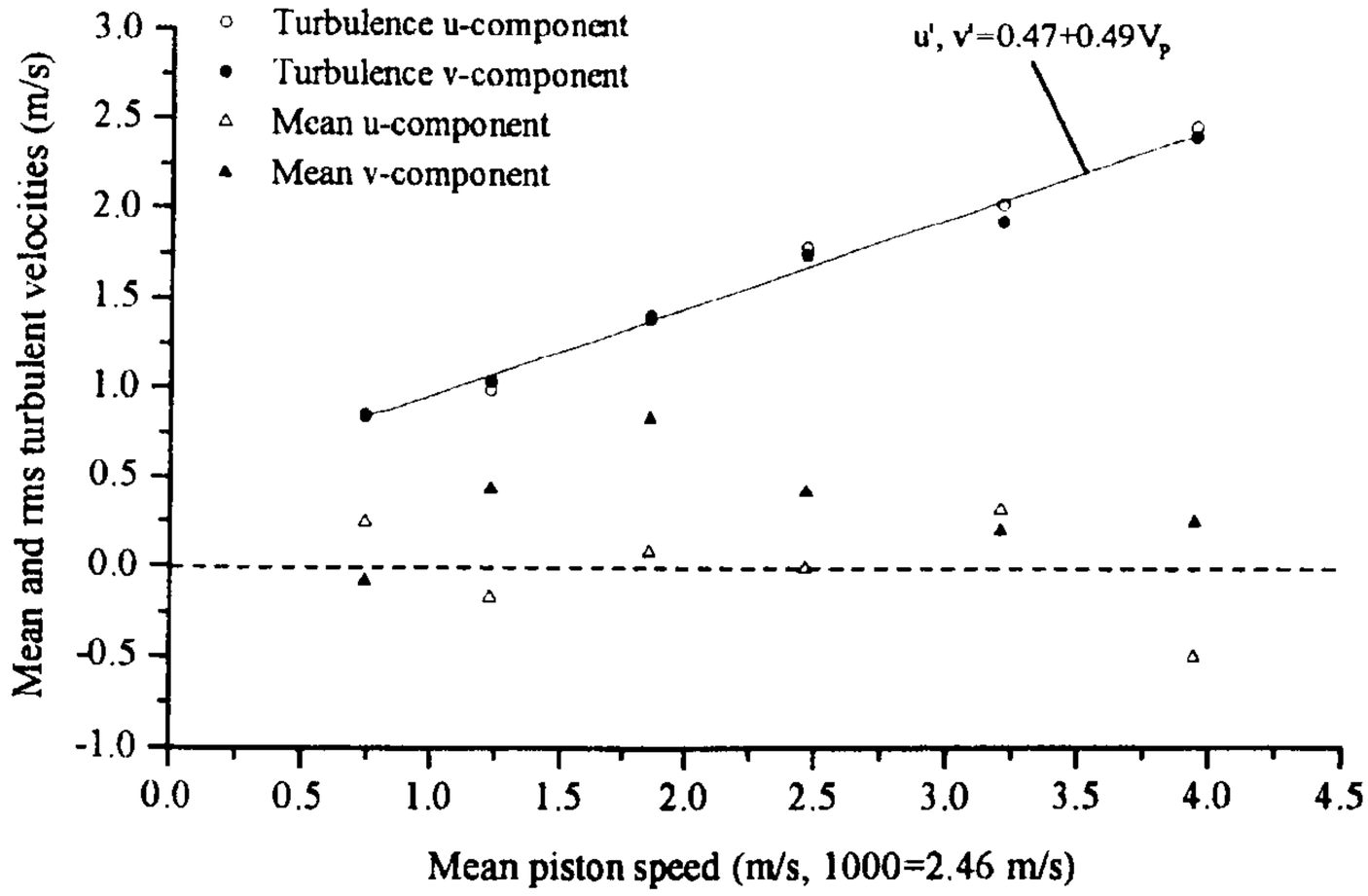

(a)

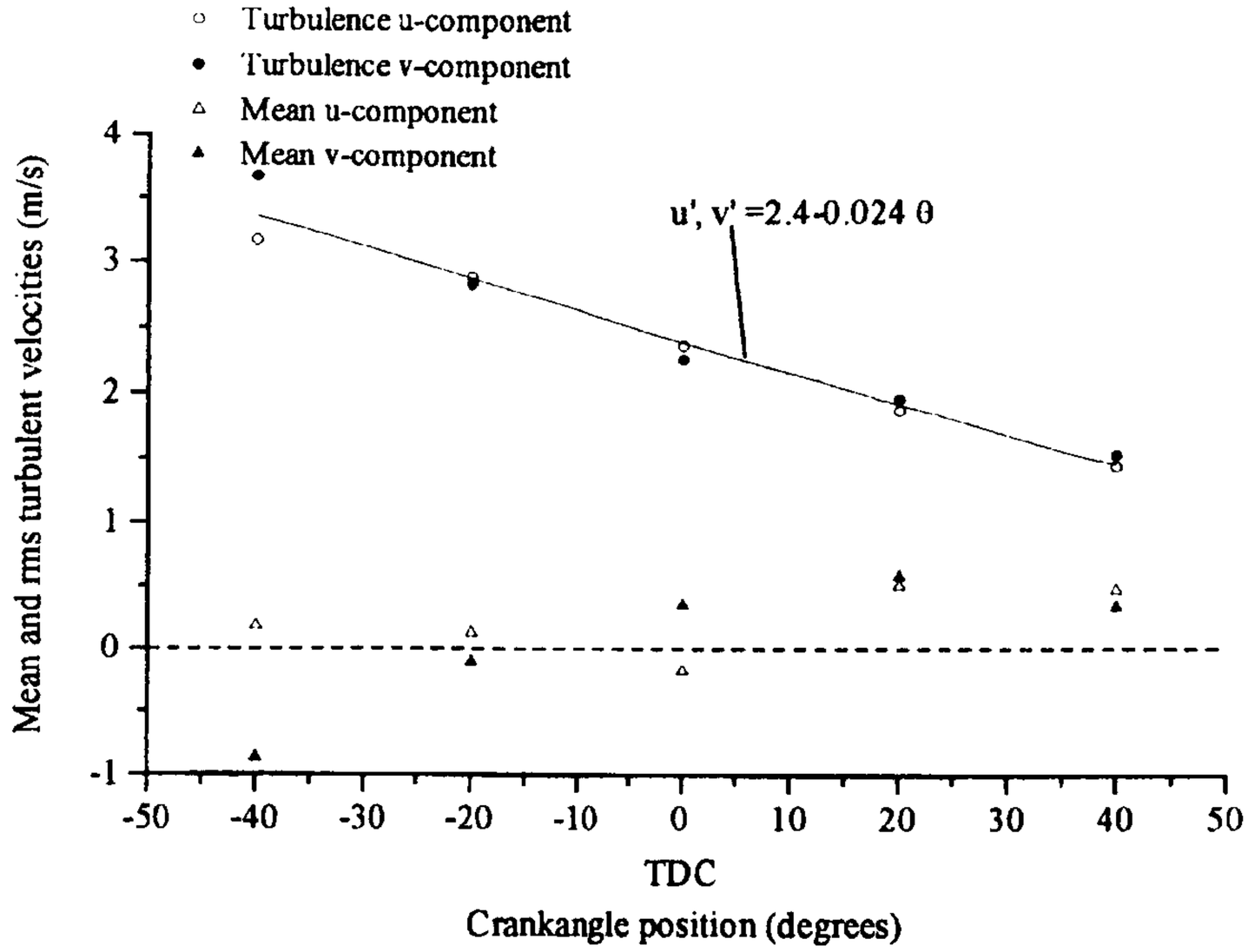

(b)

Figure 2.2 Mean and *rms* turbulent velocities **(a)** at TDC position versus mean piston speed and **(b)** versus crank angle position at 1500 rpm engine speed (Atashkari, 1997).

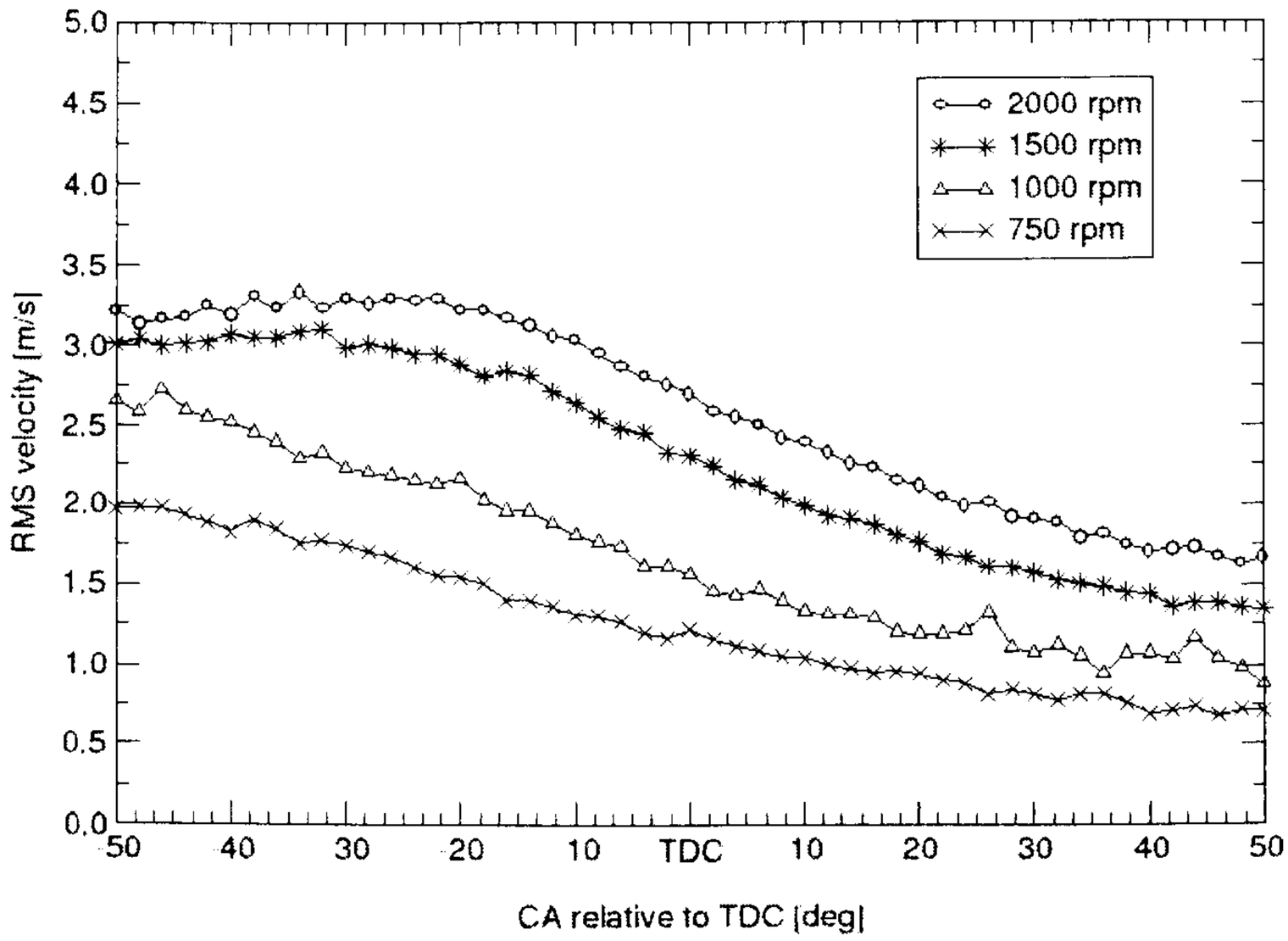

Figure 2.3 RMS turbulent velocity versus crank angle at different engine speeds for 7.6 compression ratio (Jakubík, 2002).

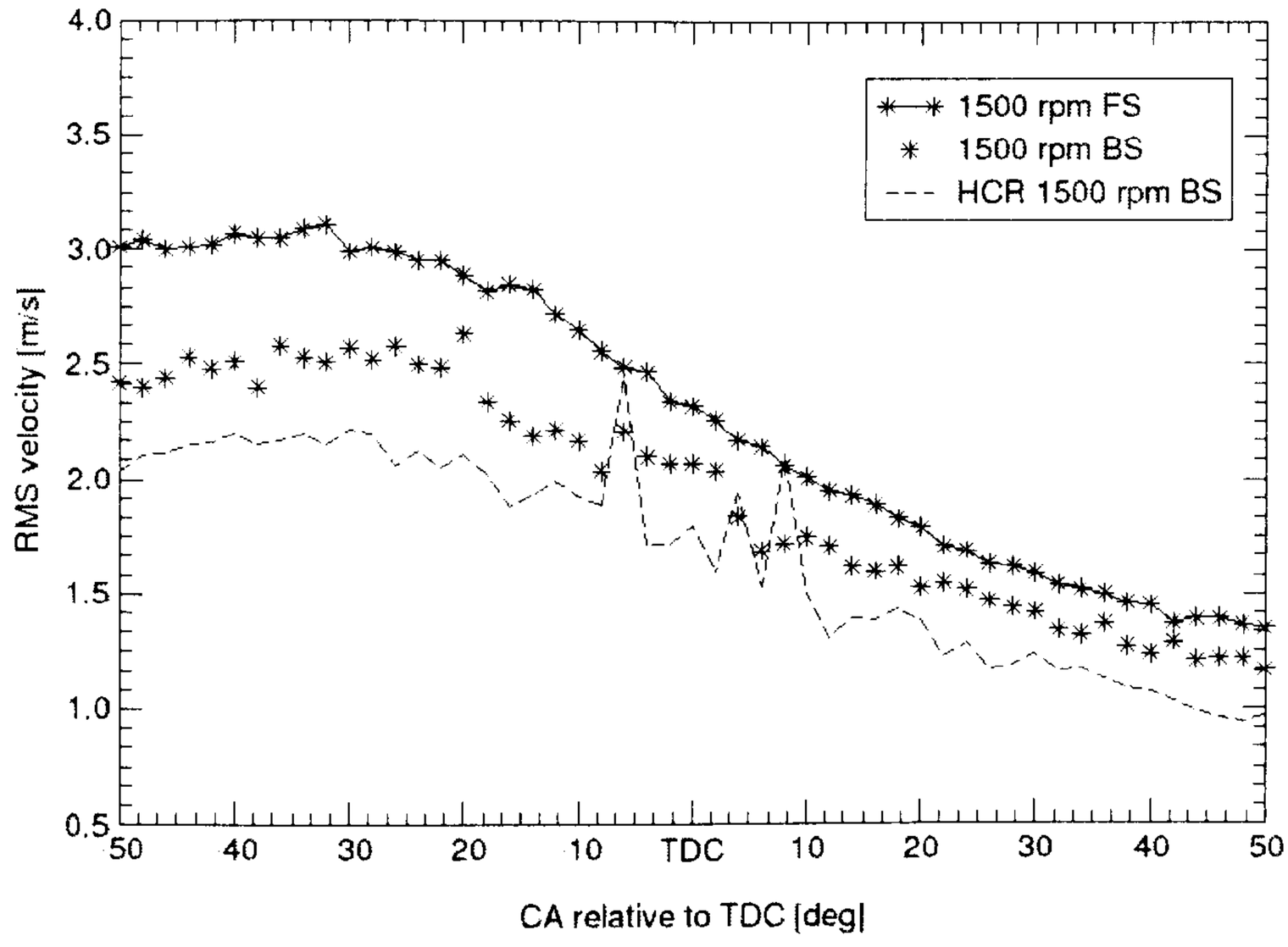

(a)

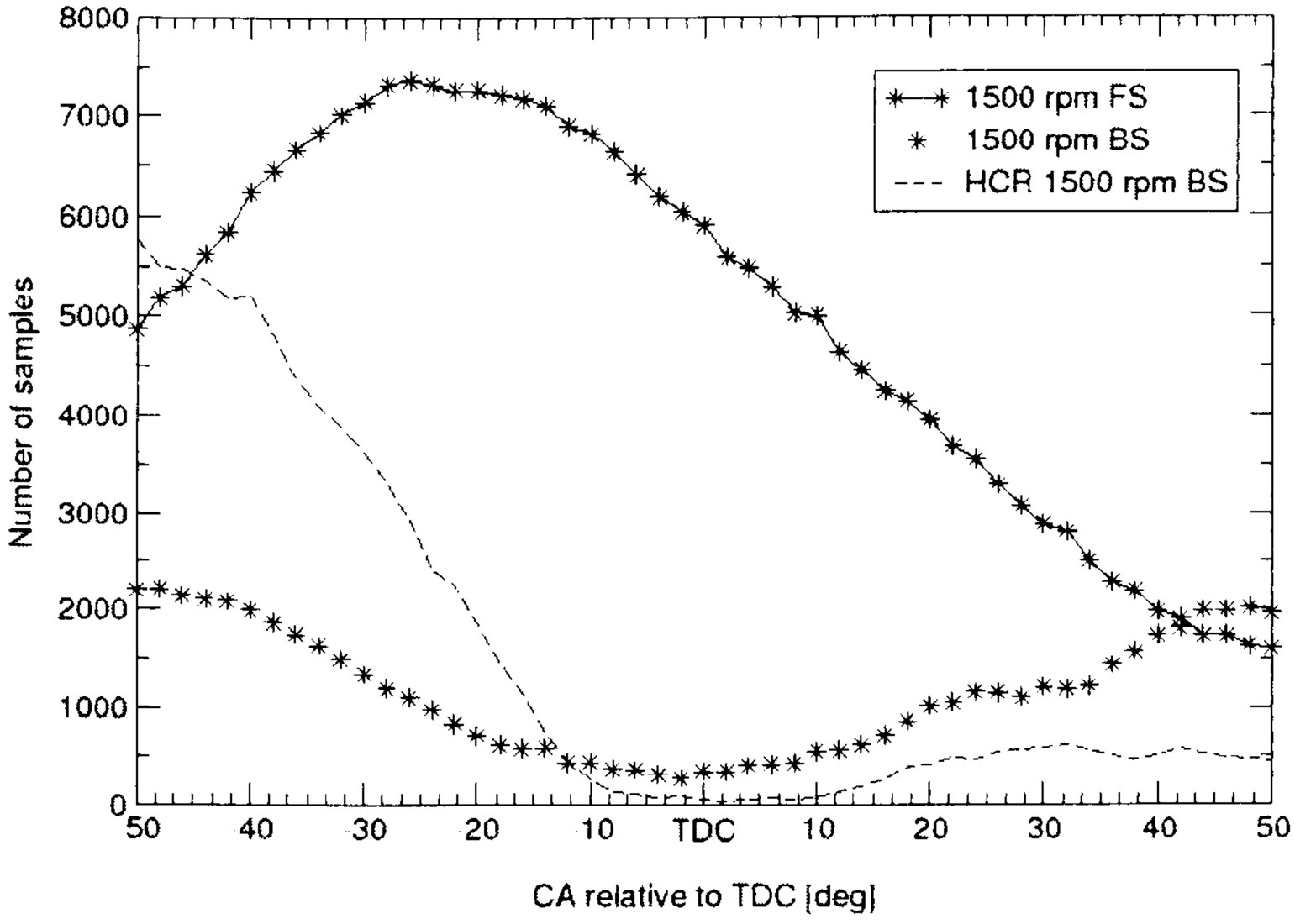

(b)

Figure 2.4 (a) Back-scatter (BS) turbulent intensity at CR=12.4 (HCR) and corresponding back- and forward-scatter (FS) results at CR=7.6 and 1500 rpm **(b)** the related number of samples versus crank angle (Jakubík, 2002).

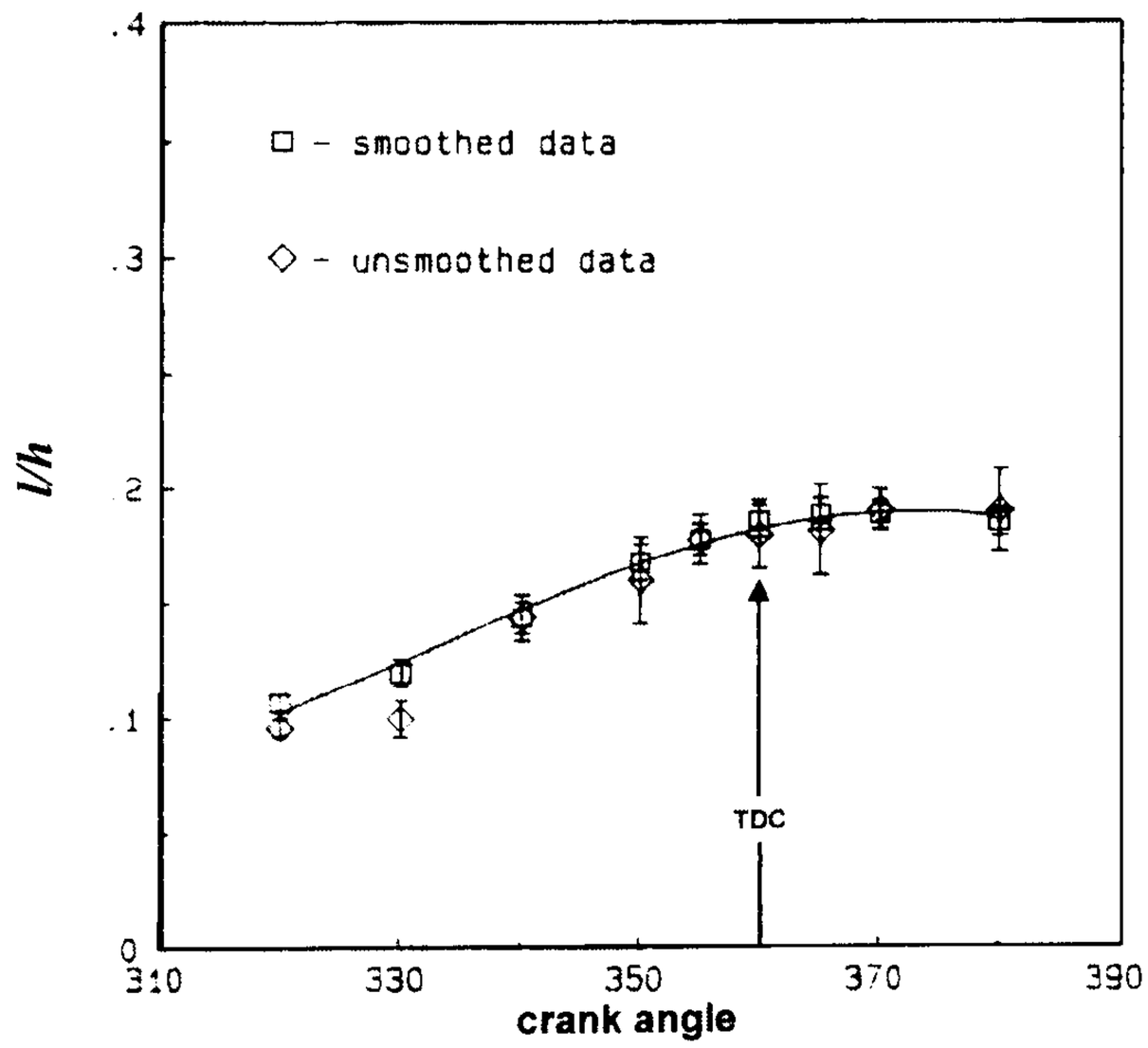

Figure 2.5: The ratio of integral length scale to instantaneous clearance height (*l/h*) versus crank angle for smoothed and unsmoothed data (Fraser et al., 1986).

Chapter 3

Experimental Engine and Instrumentation

3.1 Introduction

A single-cylinder optical research engine, termed LUPOE1 (acronym for Leeds University Ported Optical Engine, Version One), was used to collect experimental data in the currently reported work. The full-bore overhead optical access of this engine enabled observation of the full flame propagation to the cylinder walls. This engine was developed from a commercial single-cylinder two-stroke JLO L372 engine, following substantial modifications by previous research students in Leeds (detailed in Section 3.2). Comprehensive descriptions of the engine control system, auxiliary instrumentation, measurement systems and test procedure are provided in Sections 3.3-3.6.

As a part of the current study, a number of further modifications were made to the barrel design, breathing system and piston of a second generation of the engine, developed from Petter PH1 engine by Butler (1999). The revised engine is termed LUPOE2 in this thesis. Although this engine was not used for data collection in the current study (due to time limitations and an extended manufacturing period), it has provided an excellent basis for the study of combustion events in an idealised version of more conventional SI engines. The modifications to the Petter engine, now being extensively used by fellow researchers at Leeds, are detailed in Section 3.7.

3.2 LUPOE1 engine

The LUPOE1 engine has been developed via many successive modifications made to the original JLO engine. These include changes to the cylinder barrel, cylinder head, piston, breathing and air-fuel supply systems (Hicks, 1994; Lee, 1995; Tindall, 1997; Buran, 1998; Gillespie, 1998). The original JLO engine was a two-stroke, air-cooled, crankcase scavenged SI engine with a dome-shaped piston crown. In his

modifications to the cylinder barrel, Hicks (1994) replaced the original air-cooled JLO barrel with a redesigned one made from spheroidal graphite cast iron and machined to incorporate cylinder head, crankcase, inlet, exhaust and absolute pressure transducer mountings. This barrel had two diametrically opposed square inlet ports and a single rectangular exhaust port at 90° to the inlet ports. The inlet ports were joined to two inlet ducts, or tubes, vertically inclined upwards at an angle of 20°. He also designed a disc shaped optical cylinder head incorporating a top and two side windows. To create a disc shaped chamber (suitable for modelling and Schlieren photography), the original domed piston crown was machined flat; this head yielded a compression ratio of 7.6:1. Shown in Figure 3.1 is the barrel and cylinder head assembly used in the current work. To reduce engine speed variations, Hicks also fitted a new flywheel (of a greater mass and inertia than that the original).

Lee (1995) fitted a simple brass venturi carburettor to each inlet pipe, together with three electrical "band" heaters (2×250W and 1×125W) on each inlet line to increase fuel vaporising rate. Illustrated in Figure 3.2 is the inlet pipe assembly used in the current work. To minimise the effect of crankcase pressurisation during the piston down-stroke on lubrication and gases blowing from the crankcase to the cylinder through the ring pack, Lee (1995) connected the crankcase to the exhaust pipe using a new line incorporating a standard Citröen 2CV oil filter/breather.

Thermocouples were fitted to the barrel (at three different heights) to measure cylinder wall temperature. These provided necessary information for blowby and heat transfer evaluations for the engine simulations represented in Chapter 6. Shown in Figure 3.3 are the locations of the thermocouples and their means of attachment.

For collection of experimental data at a higher compression ratio, another optical head (designed by Tindall, 1997) offering 10.2 compression ratio was used. This head also had full-bore overhead optical access for natural light and Schleiren imaging techniques (Tindall, 1997; Mahmud, 1999). At a later stage, this head was modified for knock study at high compression ratio; the modified head resulted in 12.4 compression ratio with a lower clearance volume height (~4.7 *mm*). In the currently

reported study, this head was used to collect experimental data at high compression ratio.

Details of the LUPOE1 engine geometry for different heads have been provided in Table 3.1 below.

Table 3.1 Engine geometry of the LUPOE1 engine with different heads.

	Head with top and side windows	**Head with top window**	**Modified head with top window**
Bore [*mm*]	80	80	80
Stroke [*mm*]	74	74	74
Clearance volume [*cc*]	40.4	29.0	23.4
Swept volume [*cc*]	372	372	372
Effective stroke [*mm*]	53	53	53
Effective swept volume [*cc*]	266.4	266.4	266.4
Effective compression ratio	7.6	10.2	12.4
Exhaust port open/close (°*a/bTDC*)	108.5	108.5	108.5
Inlet port open/close (°*a/bTDC*)	115.7	115.7	115.7
Connecting-rod length [*mm*]	148	148	148

3.3 Heating and temperature measurement systems

In a research engine such as LUPOE1, heating systems are crucial to control engine conditions, fuel evaporation and engine heat transfer in skip fire mode. To control the inlet and cylinder head temperatures, three heating systems for the two inlet ducts and the cylinder top flange (as shown in Figures 3.1 and 3.2) were utilised.

Shown in Figure 3.4 are schematic diagrams of the heating, temperature measurement and control systems. A digital thermometer-heating control box (Digitron 4801) allowed setting of the inlet and cylinder head temperatures. The heating control

system influenced the heaters according to the difference between set values and those measured by the related thermocouples. For the experiments reported in this thesis, inlet and head temperatures were set to 70° and $80^\circ C$, respectively. When pressure and film data were captured, the temperatures measured by the thermocouples were recorded simultaneously. Slightly differences were observed in the measured wall temperatures with different engine speeds; greater for high and lower for low engine speed. This resulted from a combination of shorter breathing time at higher engine speed (retaining significant quantities of hot residual gas in subsequent motoring cycles in skip fire mode), skip firing (offering shorter time interval between firing cycles at higher engine speed at a fixed skip fire ratio) and friction between the piston-ring pack and cylinder (generating greater friction power at higher engine speed). The mean values for the tests conducted at 1500 *rpm* (the "reference" engine speed in this study) were 74, 72 and $70^\circ C$ for top, middle and bottom points of cylinder barrel and $89^\circ C$ for cylinder head. The inlet temperature was not influenced by engine speed and the mean value was $70^\circ C$ identical to the set value.

3.4 Fuel-air supply and control

Supplying a known mixture composition with identified thermodynamic state was vital for cyclic analysis of experimental data and validation of combustion models. The LUPOE1 engine was designed to be used with a pressurised air-fuel supply. This required air and fuel systems to control inlet flow rate and mixture composition. Under firing conditions, metered fuel supply was introduced through a carburettor fitted to each inlet pipe into a regulated air flow (Figure 3.2). Schematic diagrams of the fuel-air supply and control systems are set out in Figure 3.5.

3.4.1 Air supply system

The components of the air supply system are shown in the lower half of Figure 3.5. A continuous pressurised air was delivered to the air supply system from the department's piped supply system, capable a maximum delivery pressure of 8 *bar*. The air was regulated to 4 *bar* (gauge) and filtered to remove any possible oil and moisture. A solenoid valve was used to prevent air supply whilst the engine was

stationary. The air line was divided into two branches (one for each inlet line) to allow separate control the air flow rate to each inlet. The air flow rate of each line was adjusted using a Brooks 5812N thermal mass flow meter and a needle valve (fine control valve). The meters were calibrated by the manufacturer at a standard condition (1.0133 *bar* and $0^{\circ}C$) for a full-scale deflection (FSD) flow rate of 400 *l/min*, equivalent to 8.6 *g/s*. A Brooks series 5875 display unit was connected to the meters. This unit displayed the flow rate of each line as a percentage of the FSD flow rate. Throughout the experiments reported in this thesis, the meters were adjusted to 40% FSD on each inlet line. To dampen any air pulsations caused by piston motion (which interrupted the air supply), a 5-litre surge tank was installed downstream of each meter.

3.4.2 Fuel supply system

The fuel supply system is illustrated on the upper half of Figure 3.5. Isooctane stored in a one-litre fuel tank was pumped via a fuel filter using a Ford Granada injection pump. To control the fuel delivery pressure, a standard fuel pressure regulator was used. This regulator enabled the pressure to be set to any value between 0 and 4 *bar* above a reference pressure supplied to the regulator (2.7 bar above atmospheric pressure for the experiments reported in this thesis). Downstream of the regulator, flow was divided between two supply lines (one for each inlet). Each inlet supply line was metered using a Platoon 2-25 *cc/min* rotameter and manual control valve.

3.5 Engine ignition and measurement systems

Set out in Figure 3.6 is a schematic diagram for the engine control, ignition and measurement systems used in the currently reported work. These systems are detailed below.

3.5.1 Ignition system

The ignition system included 12V supply battery, a Lucas contactless electronic unit, a standard Lucas ignition coil and a spark plug. Throughout the work reported in this

thesis, the central ignition mode of the engine was adopted. For this, the spark plug was fitted to a hole drilled through the centre of the top window. To minimise interference with the full-bore overhead optical access to the combustion chamber, Lee (1995) and Buran (1998) developed a special spark plug. This plug comprised a 0.5 *mm* diameter steel electrode bonded into a 1.6 *mm* diameter alumina tube. This tube was itself bonded into a 3.2 *mm* brass tube, which was earthed. A small length of brazing rod was soldered to the outer brass tube and bent to form the earth electrode; the spark gap was set at 0.5 mm. The plug assembly was glued into the central hole of the top window of the cylinder head (as seen in Figure 3.1).

The ignition system was activated by the engine control unit according to the set spark ignition timing and skip fire ratio. A delay was observed between the set ignition timing and the crank angle position of the generated spark in a cycle. Once the ignition was set to TDC position and the output signals of the ignition and TDC generated by the engine control unit were monitored through two different channels of an oscilloscope. Engine was run and ignited without fuel supply; the two signals fitted each other on the oscilloscope screen. Therefore, it was found that the engine control unit produced an accurate signal for spark.

To monitor any delay generated by the ignition system, a photo multiplier was used to detect the spark ignition light. The engine control unit ignition signal and the output signal of the photo multiplier were connected to two different channels of an oscilloscope. The engine was run, without fuel, at a known engine speed and ignition timing. The lighting in the test room was switched off, to minimise the effect of any unwanted light on the photo multiplier detection unit. Then the ignition system was activated and both signals were simultaneously monitored on the oscilloscope screen. Shown in Figures 3.7(a) and (b) are typical frozen signals monitored at 1500 and 750 *rpm* engine speed. It can be seen that there was a time-dependent delay in ignition of $\sim 64\mu$sec (equivalent to $0.6^\circ CA$ at 1500 *rpm*); the horizontal scale is 10μsec per division.

3.5.2 Pressure measurement

In-cylinder pressure is a most important measurement for analysis of an engine cycle. This was used to estimate mass fraction burned, indicated mean effective pressure and knock characteristics. The reliability of any derived data depends on the accuracy of the pressure measurement. Randolph (1990) and Kuratle et al. (1992) have provided an excellent review of the sources of engine pressure measurement error.

The pressure measurement system used in the experiments reported in this thesis is illustrated in Figure 3.6. The in-cylinder dynamic pressure was measured using two Kistler 601A piezoelectric pressure transducers, capable of measuring rapidly varying pressure in the range 0-100 *bar*. The low compression ratio (7.6) head, including top and side windows, was fitted with a Kistler 601A dynamic transducer. As there was insufficient space to fit a standard water-cooled adaptor for the transducer, Buran (1998) drilled small holes close to the transducer to provide a degree of water cooling. The moderate and high compression ratio (10.2 and 12.4) head (with no side windows) was fitted with a standard water-cooled Kistler 601A transducer. The output charge of the transducer was converted to a voltage using a Kistler 5007 charge amplifier and transmitted to the data acquisition system (Section 3.5.5).

A piezoresistive pressure transducer Kistler 4045A50 was employed to measure absolute cylinder pressure within the low pressure part of the cycle for referencing purposes. The charge signal of this transducer was amplified by a Kistler 4601A piezoresistive charge amplifier and then conveyed to the data acquisition system (Section 3.5.5).

3.5.3 Crank angle measurement

In the analysis of cylinder pressure data, it is crucial to know accurately the piston position (Kuratle et al., 1992), particularly in the early stages of combustion where the pressure rises due to combustion are small. It is also important to estimate engine speed variation in a cycle (Section 4.2.4).

A Hohner 3202 shaft encoder was coupled to the torque free end of the crankshaft; this encoder was utilised to attain crank angle position every $0.2^{\circ}CA$. The generated electrical signal of this shaft encoder was connected to the engine control system providing TDC, BDC and spark ignition signals in addition to the crank angle. These signals were transmitted to the ADC system (as seen in Figure 3.6).

3.5.4 Flame filming system

All the flame images reported in this thesis were captured employing a natural light filming technique. Two different digital cameras were used at different stages of this study. In the first period, a high speed Kodak Ektapro camera, borrowed from the Textile Department, was used; this was used with a filming rate of 4500 frames per second. Although this camera was simultaneously triggered with the data acquisition system, the frame position was subject to maximum ± 1 error due to the lack of a framing signal. In the second period of this study, a high speed digital Phantom V4.1 camera of 32000 *fps* maximum framing rate (with variable exposure time of 10 μsec, independent of filming rate) was employed. This camera (with a standard memory of 256 Mbytes) was able to generate a framing signal according to the defined exposure time. This signal was stored as a single-bit signal in the Microlink analogue to digital converter (ADC) unit (Section 3.5.5) when the camera was simultaneously triggered with the data acquisition system. The signal provided a more accurate frame position for synchronisation between the framing and shaft encoder signal (described in Chapter 4). The image data stored in the camera were transferred to a personal computer (PC) via Phantom software (supplied with the camera).

3.5.5 Data acquisition system

A Biodata Microlink 4000 analogue to digital converter (ADC) was utilised for simultaneous recording of the absolute and dynamic pressures, TDC, BDC, spark ignition, framing and shaft encoder (external clock) signals. This ADC was able to store up to 128 ksamples for each channel at a maximum sampling rate of 1 MHz. Each channel of the ADC was capable of recording a main signal (such as absolute or dynamic pressures) at 12-bits (4096 levels) resolution together with four single-bit

(binary) minor signals. Two channels of the ADC were utilised: one channel for the dynamic pressure, TDC, BDC, spark ignition and shaft encoder pulses; the other for absolute pressure and framing signals. The ADC could be activated to sample the data by an external clock (such as shaft encoder) or by its own internal clock. For all the work reported in this thesis, the internal clock was used (mostly with a 200 kHz sampling rate). During the tests with the low compression ratio (7.6) variant of the engine, negative thermal drift was observed in the dynamic transducer signal. To prevent any loss of pressure signal with the ADC range set at 0-10 volts, a constant 1 volt offset was applied using the differential input available on the related ADC board (as seen in Figure 3.6).

3.6 Test procedure

The pressure transducer charge amplifiers, the digital camera and the Brooks air flow display unit were switched on at least 30 minutes before any record was made. The inlet and head heaters were turned on and allowed to reach a uniform set condition ($70^{\circ}C$ for the inlets and $80^{\circ}C$ for the head). The main air supply valve was opened and the air pressure regulated to a 4 *bar* gauge pressure prior to running the engine. The engine was motored to the test set engine speed and the air flow rate adjusted after re-checking the air pressure. Then, the fuel pump was switched on and the rotameters set to achieve the required test equivalence ratio, using their calibrated values. For any new conditions, pressure data for motoring conditions were recorded.

In firing tests, the ADC and camera were armed using a trigger signal, simultaneously to capture the film and pressure data. A manual trigger was used for this purpose. After setting the inlet air and fuel rates as mentioned above, ignition timing and skip fire ratio were adjusted on the engine control panel. Then, the ignition system was switched on and both ADC and camera manually triggered after a few firing cycles. The temperatures of inlet mixtures, cylinder wall and head were recorded after the trigger.

After all data was captured, the ignition system and fuel supply were turned off. Then the engine was slowed down to rest and the heaters were switched off. The cylinder windows were checked and cleaned after every run.

3.7 LUPOE2 engine

From flow visualisation experiments with the LUPOE1 engine, Cairns (2001) observed some unexpected large-scale flow features at the time of ignition even for the "quiescent" case (with a pair zero-angle inlets). More complex flow patterns than desired were also noted when the "angled" inlets were adopted to generate axial swirl. These were shown to be associated with having a single exhaust port. This led to the development of a new version of the optical research engine. This, termed LUPOE2, was based on the robust crankcase and connecting rod of a single cylinder Petter PH1 engine, four-stroke compression ignition. This engine was modified to a ported optical spark ignition engine. The longer stroke of this engine, in conjunction with the smaller bore of the JLO engine, permitted a higher effective compression ratio for a given clearance volume. The bore diameter was changed from the original value, 87.3 *mm*, to a modified value, 80 *mm*.

Shown in Figure 3.8 is the assembly of the modified barrel for the LUPOE2 engine. In the design of this barrel, much attention was paid to the possibility of future extra modifications (such as changing flow pattern and EPC or IPC timing) just by manufacturing one or two revised elements of the barrel. To improve engine breathing and control of flow in the cylinder, a large number of small exhaust holes distributed around the barrel were adopted. This allowed "diffusion" of exhaust into an annulus (prior to removal via two exhaust pipes) to prevent the strong exhaust flow through the single exhaust port experienced with LUPOE1. This allowed greater control of the in-cylinder flow via the inlet ports. A greater vertical angle (45°) was used for the inlet tubes to assist scavenging the longer stroke cylinder, with its associated relatively higher piston speed. The barrel includes four main parts: mounting flange, exhaust collar, top collar and liner. These parts are shown in Figure 3.9, separately.

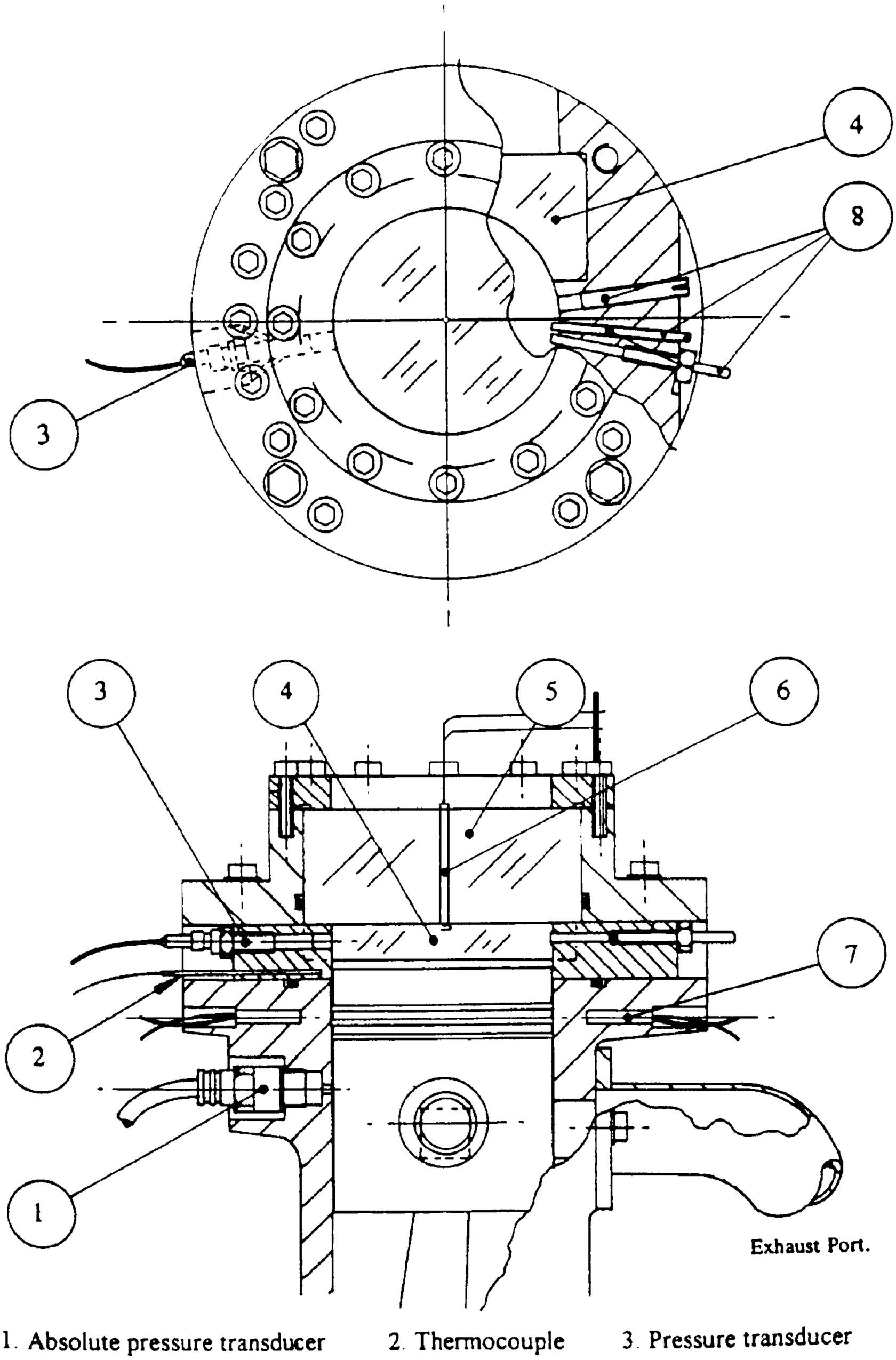

1. Absolute pressure transducer
2. Thermocouple
3. Pressure transducer
4. Quartz insert
5. Quartz window
6. Spark electrode
7. Cartridge heater
8. Blank plugs

Figure 3.1 Disc shaped optical cylinder head assembly of LUPOE1 engine (modified from Hicks, 1994).

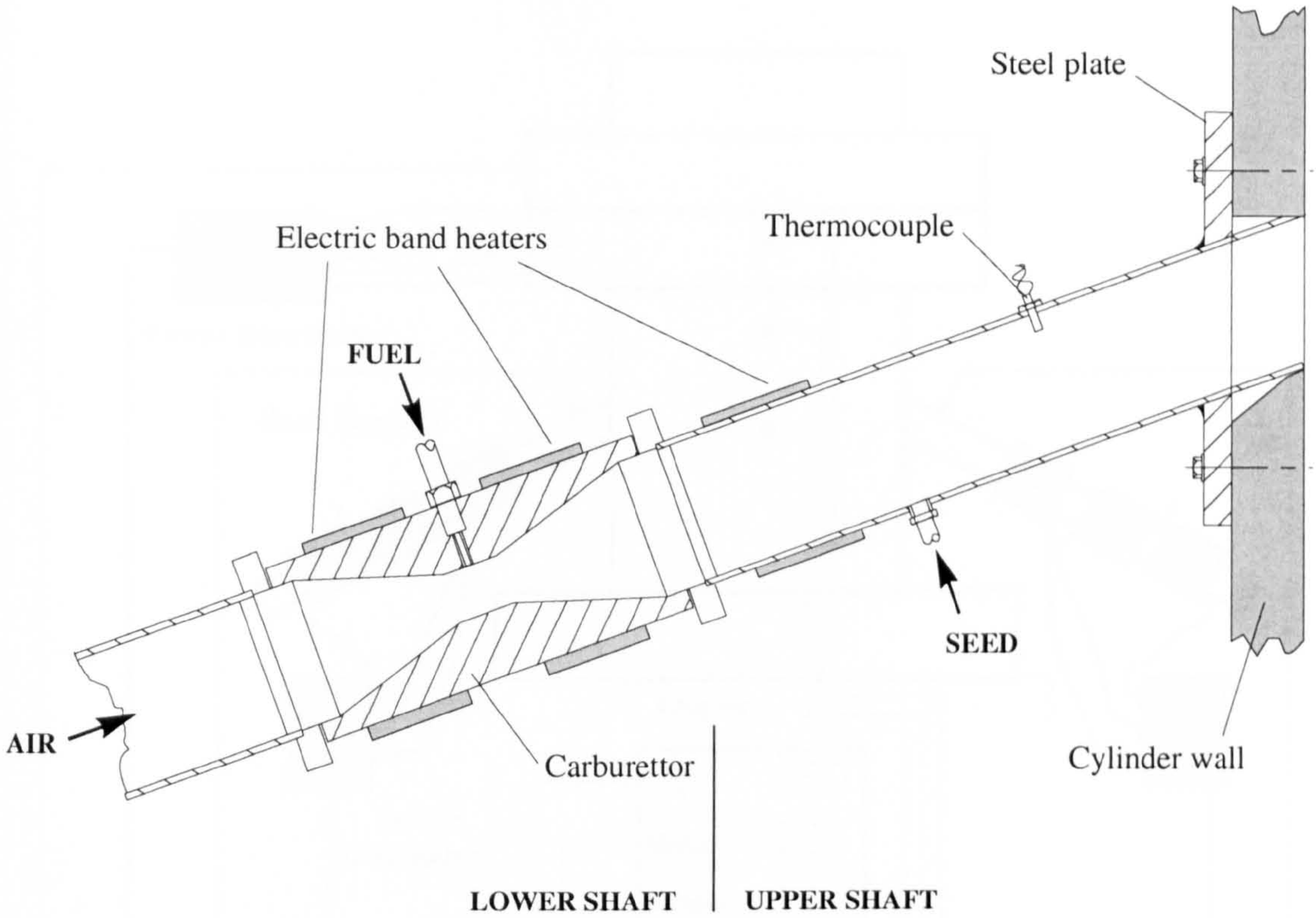

Figure 3.2 Inlet pipe assembly (drawn by Cairns, 2001).

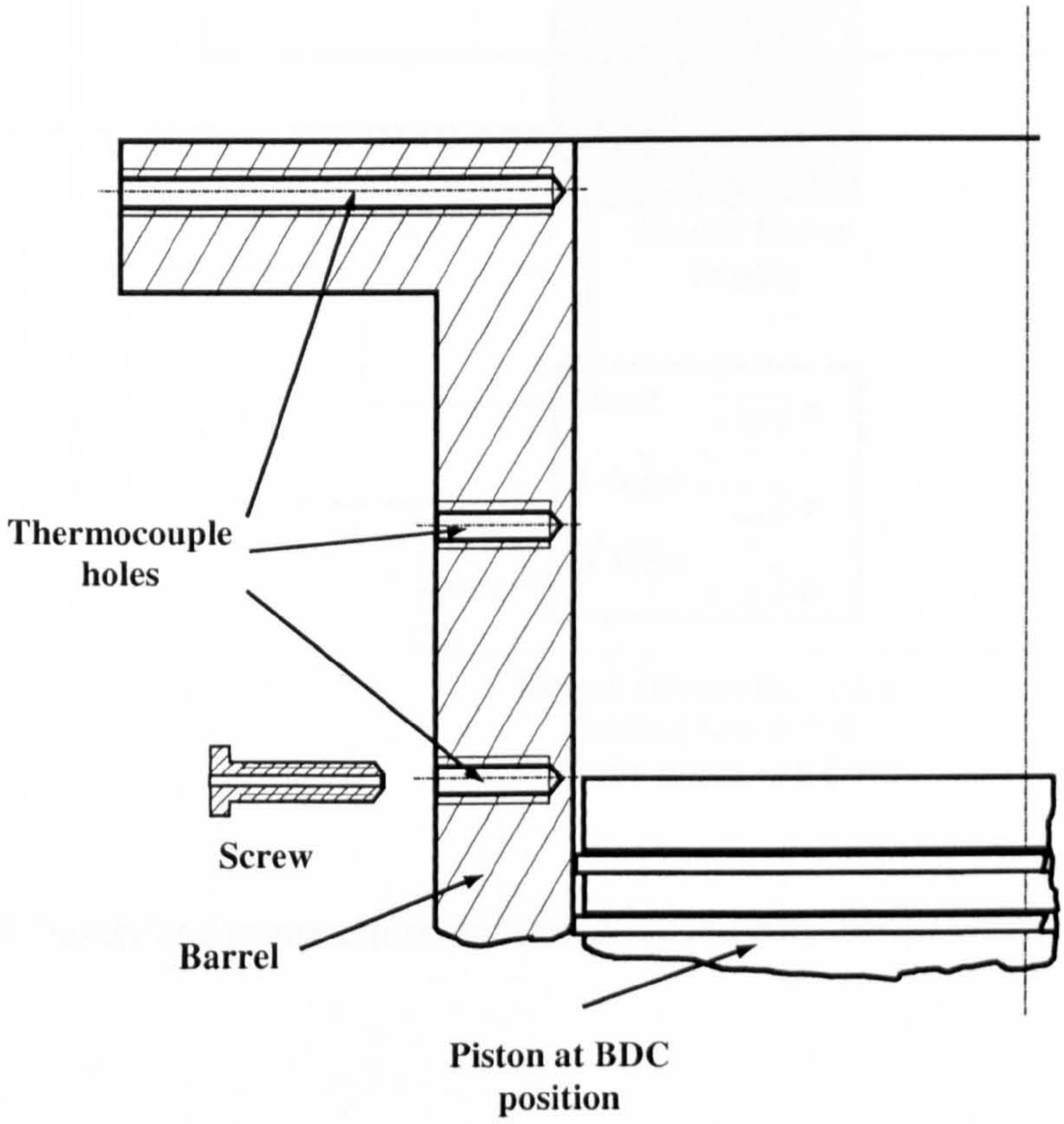

Figure 3.3 The position of thermocouple holes on cylinder and a typical holder screw.

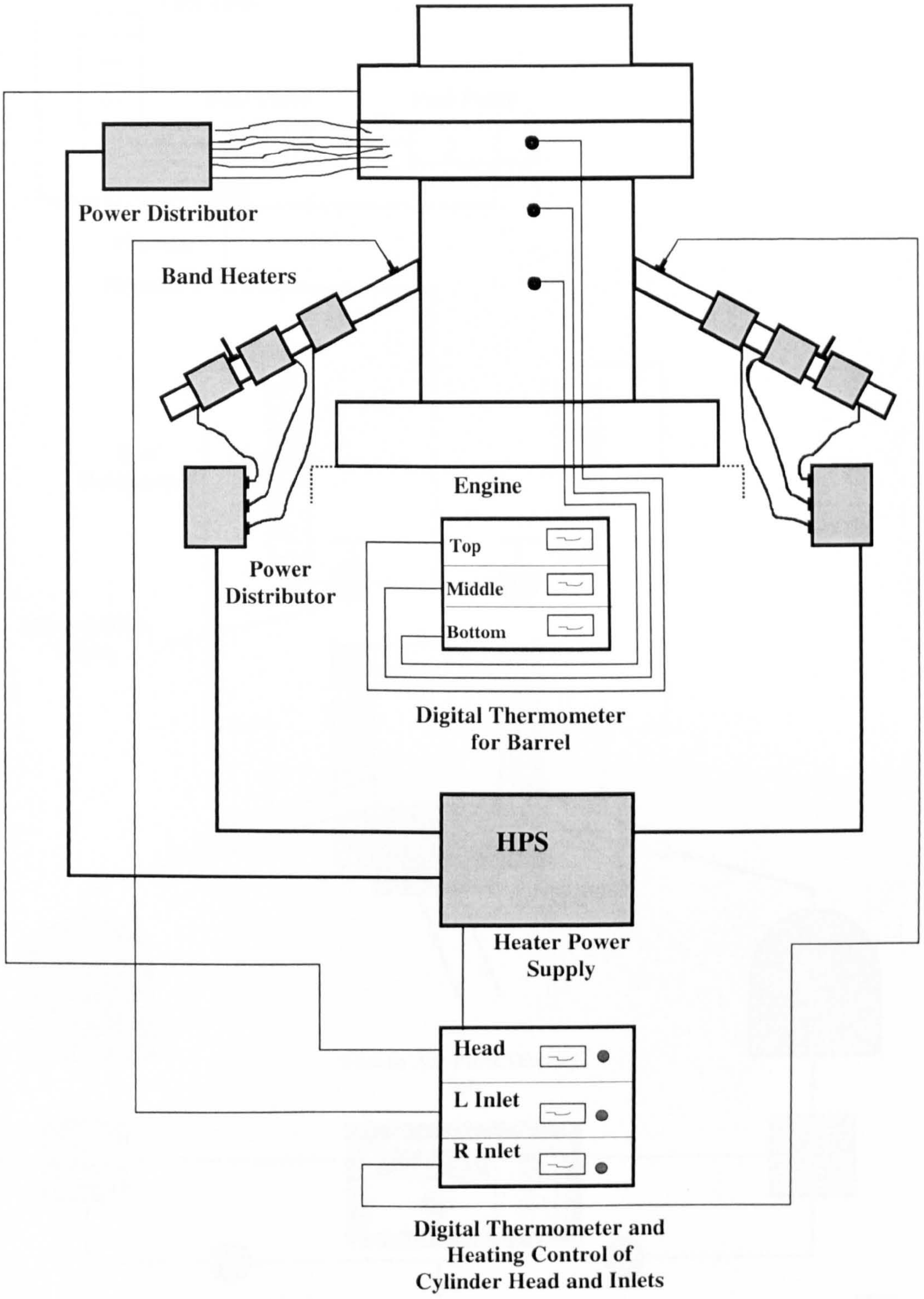

Figure 3.4 Heater and temperature measurement systems for LUPOE1 engine.

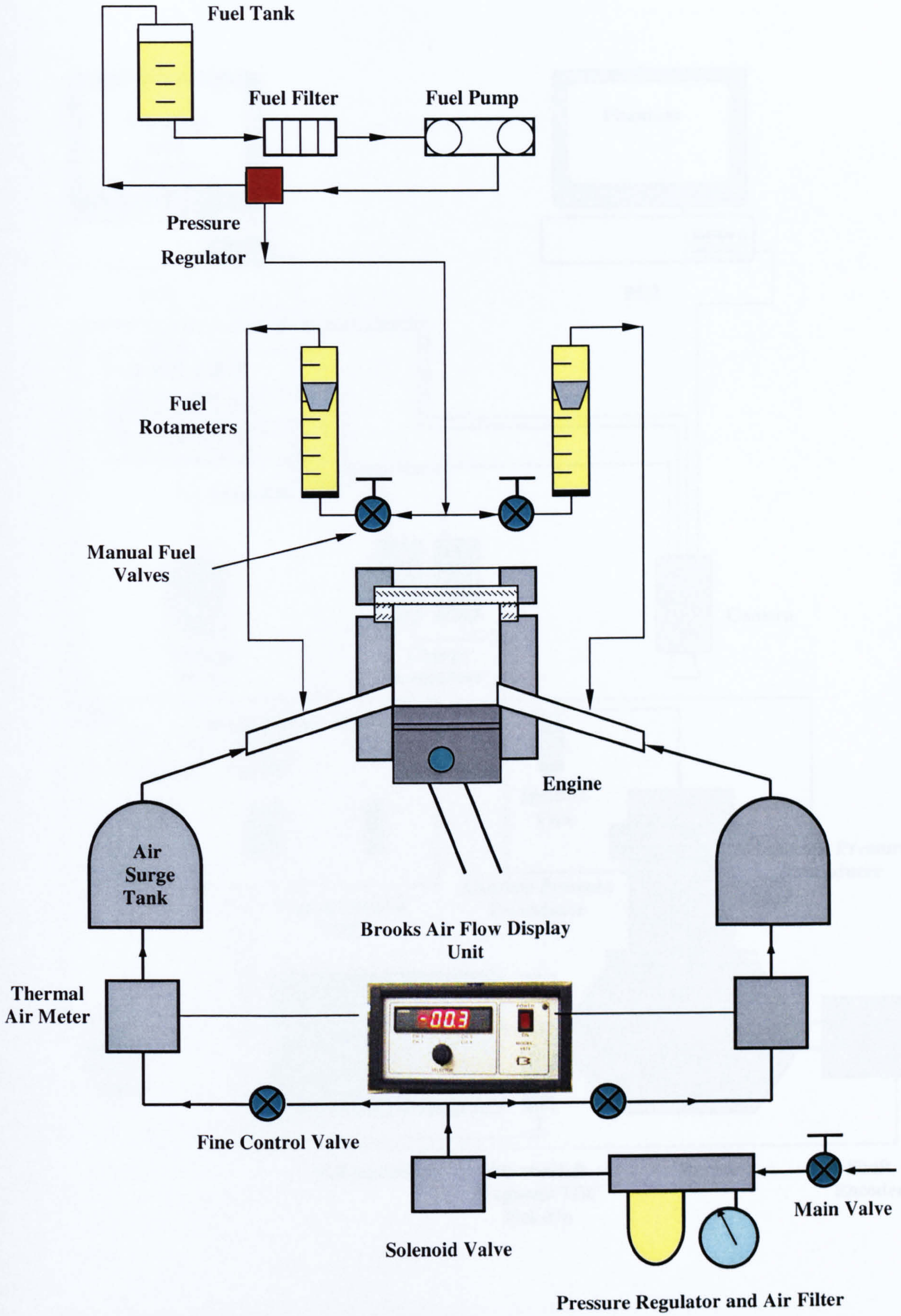

Figure 3.5 Schematic diagrams of the fuel-air supply and control systems.

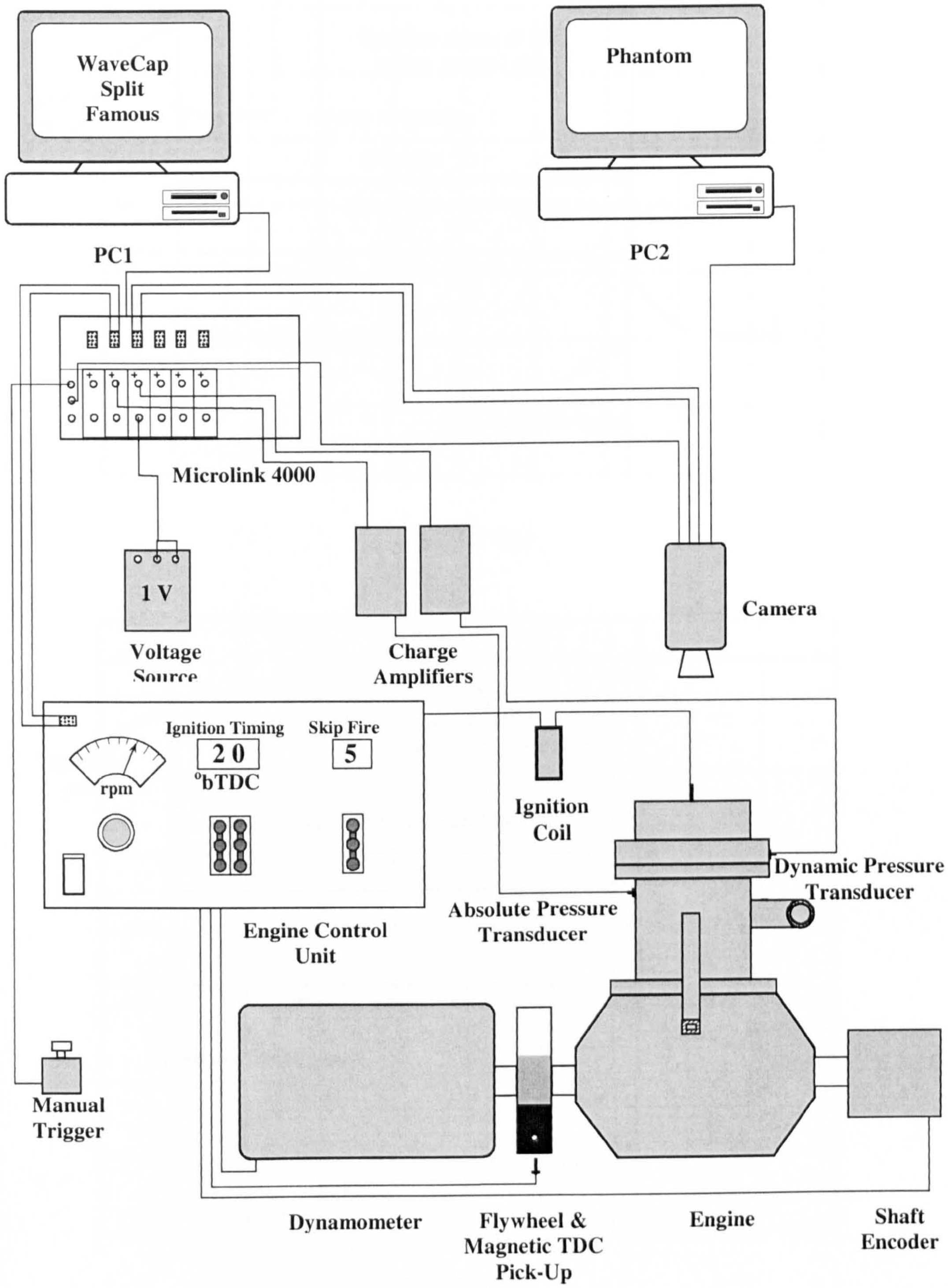

Figure 3.6 Schematic of engine control, pressure and film data acquisition systems.

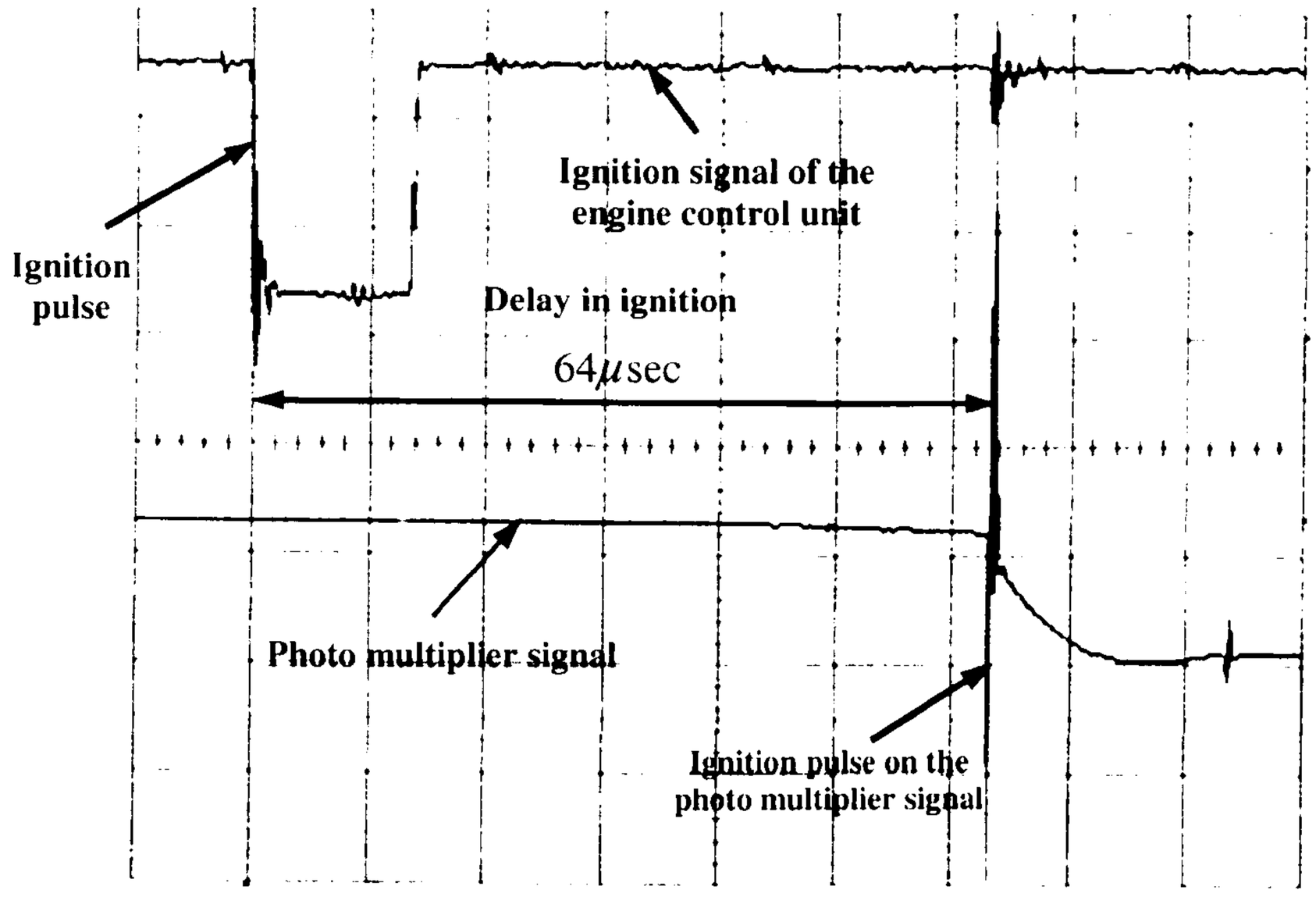

(a) 1500 *rpm*

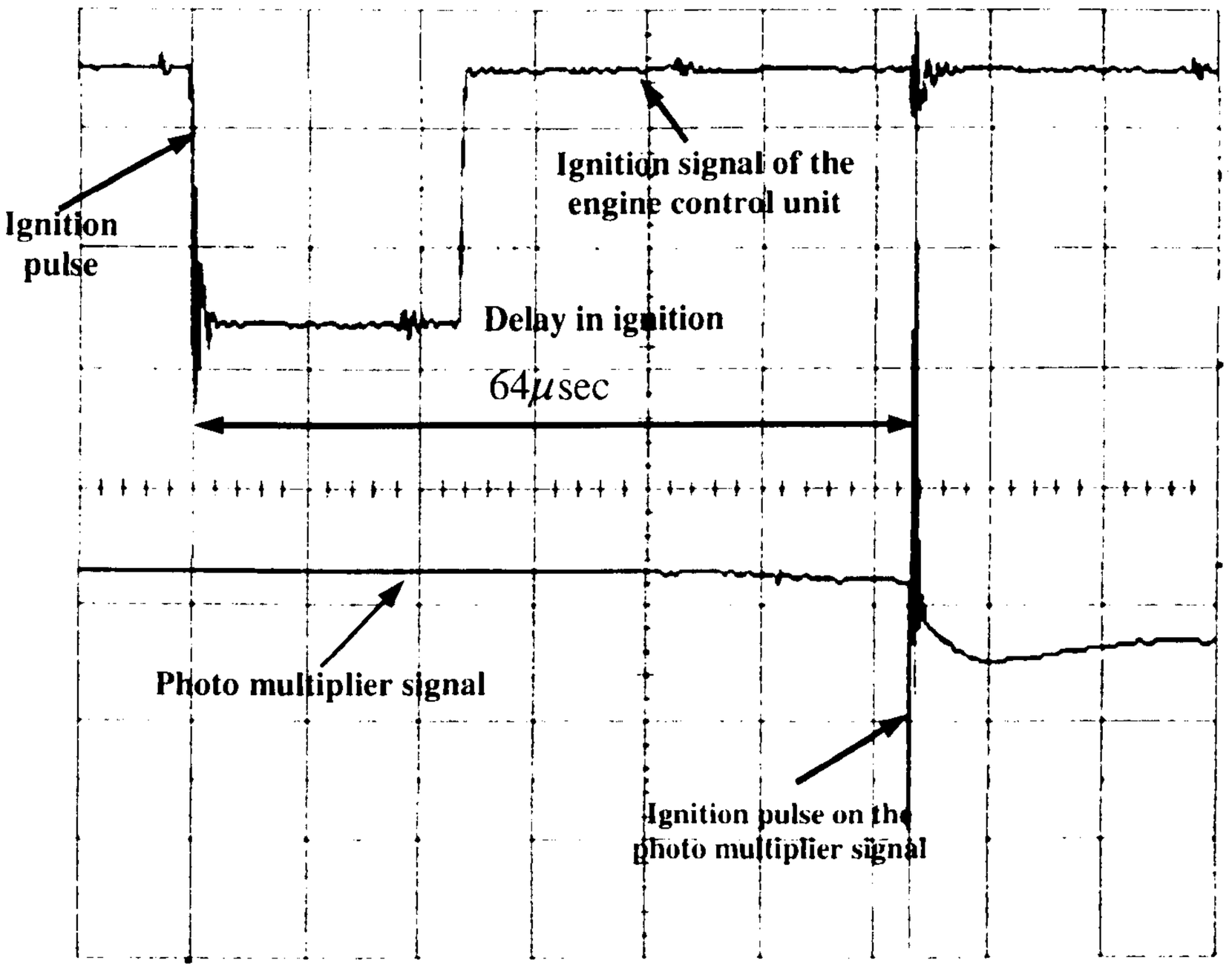

(b) 750 *rpm*

Figure 3.7 The ignition signal of the engine control unit and the output signal of the photo multiplier at **(a)** 1500 *rpm* and **(b)** 750 *rpm* (horizontal scale= 10μsec/ division).

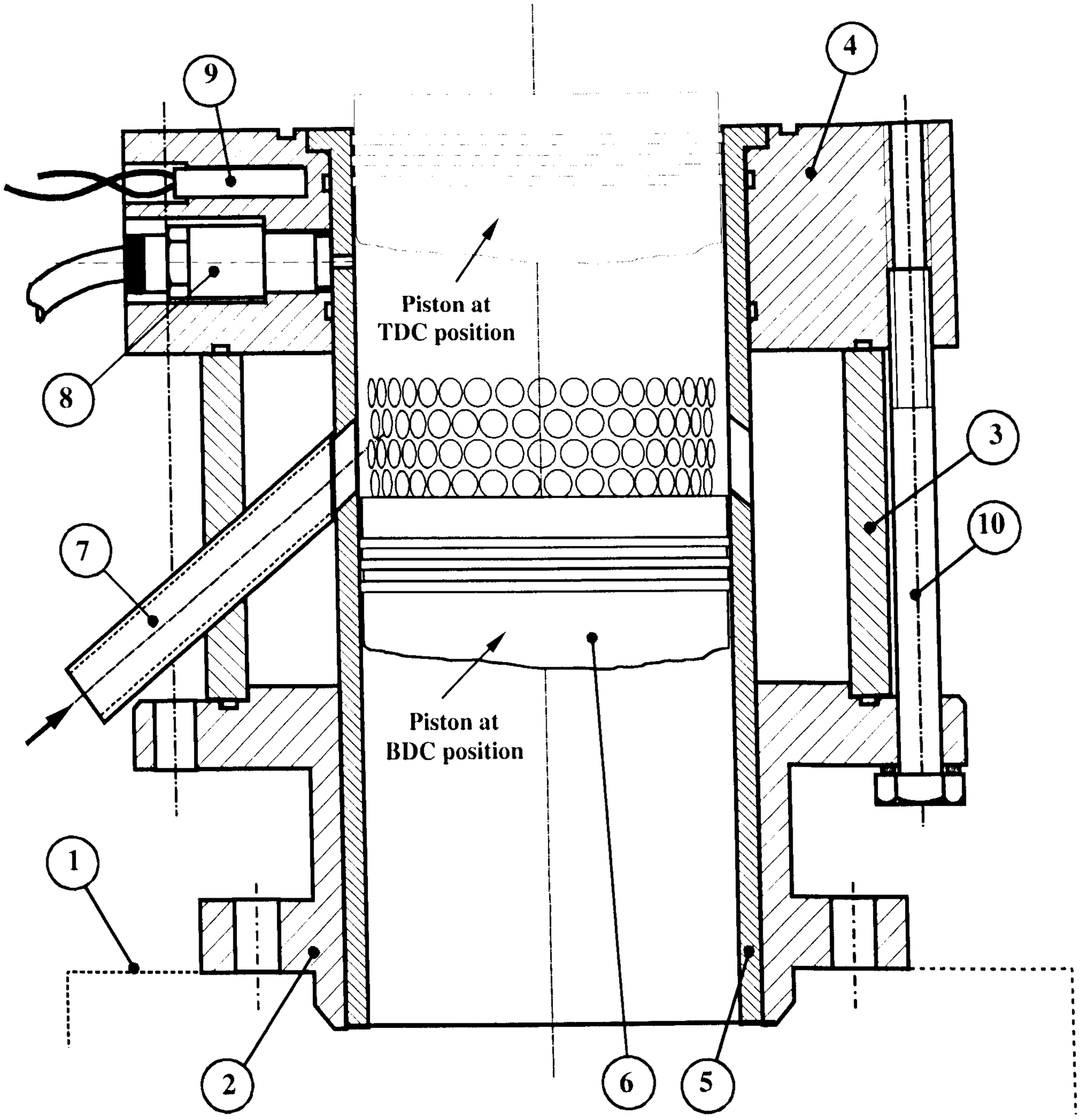

1. Crankcase
2. Mounting flange
3. Exhaust collar
4. Top collar
5. Liner
6. Piston
7. Inlet tube
8. Absolute transducer
9. Cartridge heater
10. Connecting bolt

Figure 3.8 Cylinder-piston assembly for LUPOE2 engine.

(a)

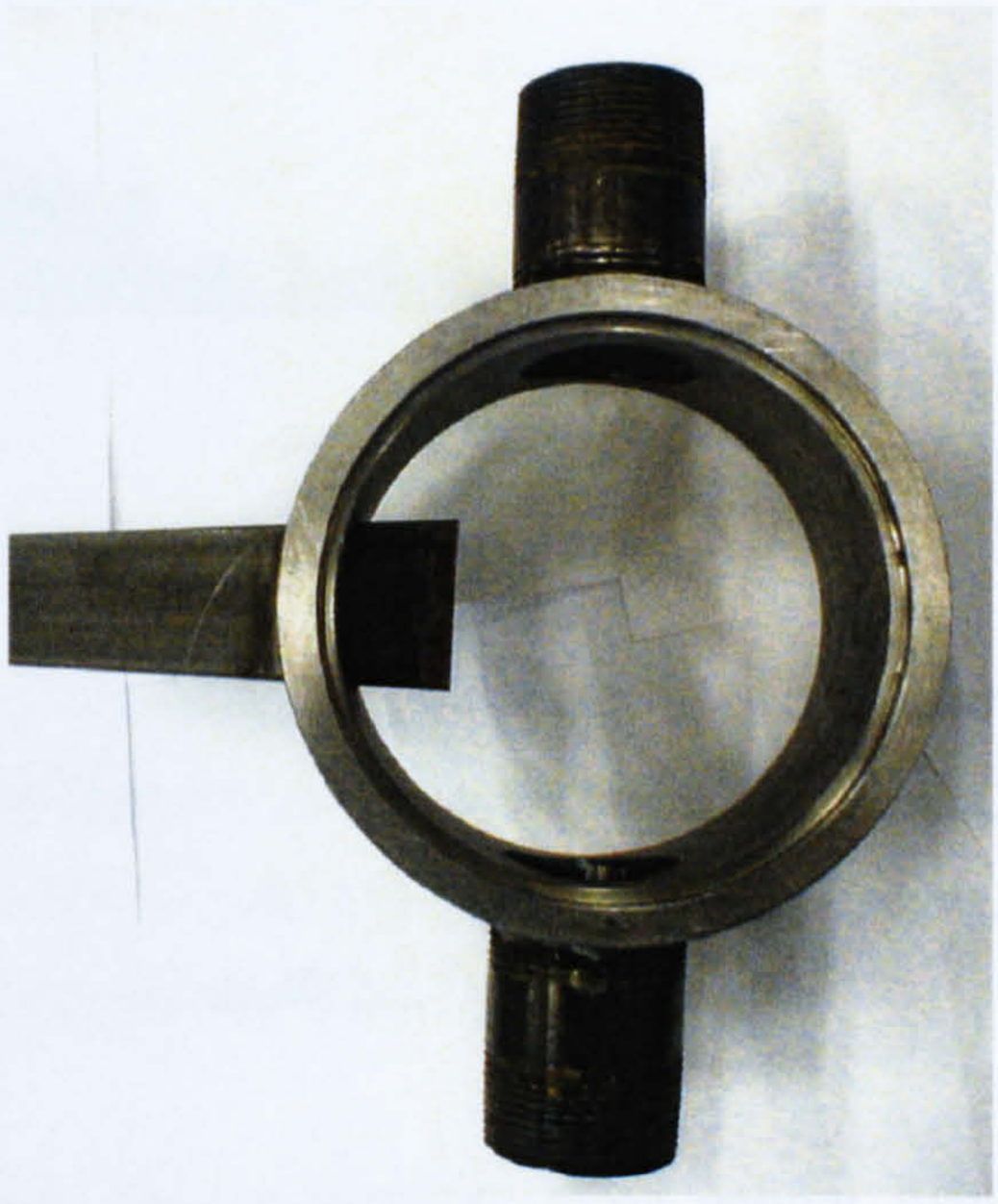

(b)

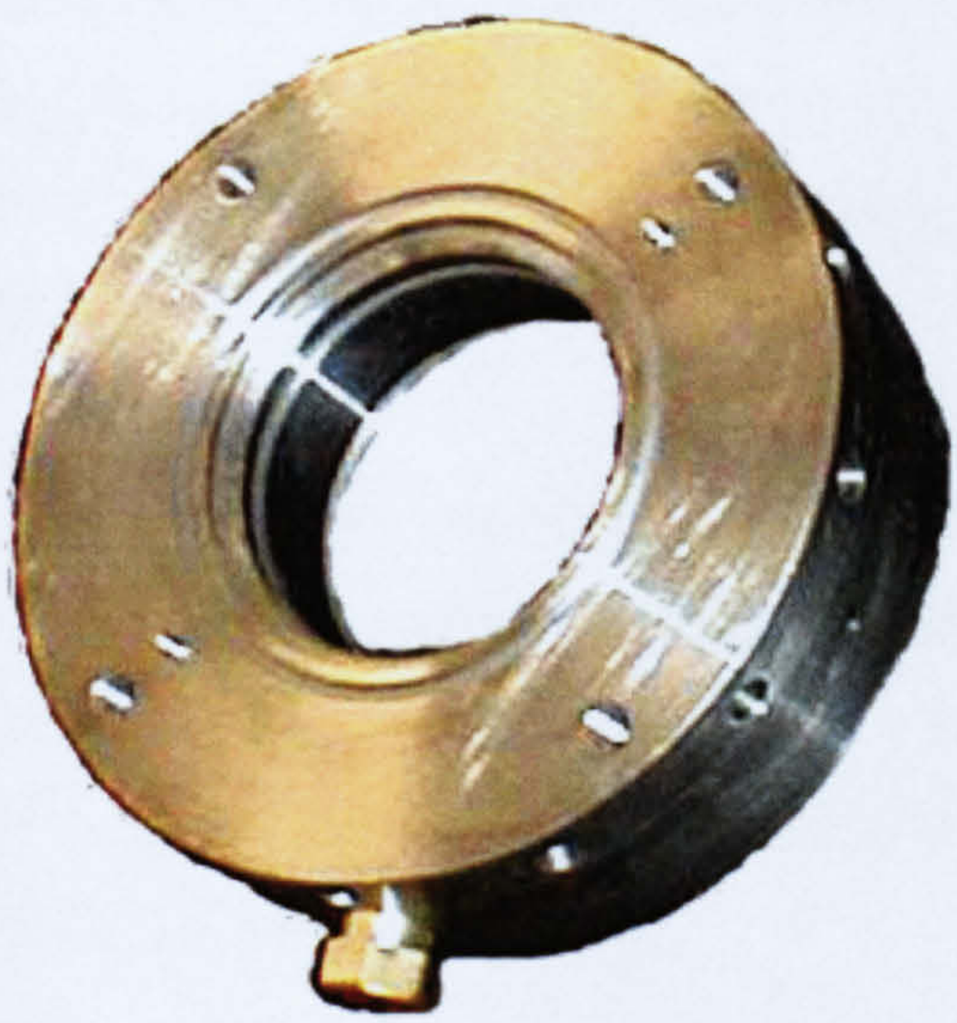

(c)

(d)

Figure 3.9 **(a)** mounting flange, **(b)** exhaust collar with inlet and exhaust tubes, **(c)** top collar and **(d)** liner.

Chapter 4
Data Processing and Analysis Techniques

4.1 Introduction

An extensive bank of data, comprising simultaneous measurement of cylinder pressure and flame position, has been collected for model validation. These data, compiled for more than 1000 firing cycles, with a total of about 10000 raw images, were recorded for a disc shaped central ignition variant of the LUPOE1 engine.

Flame propagation was monitored, through the top window, using natural light imaging with a Kodak Ektapro camera or high speed Phatom V4.1 camera. To process the extensive pressure and film data, commercial software and two substantial Fortran programs (one for pressure processing and the other for film processing, written by the current author) were used to minimise processing time and sort out the final processed data.

A new method, employing external clock signals, was used to resample gauge and absolute pressure data from time to crank angle basis. Variation of engine speed in a cycle and mean engine speed for a cycle were estimated using the external clock data in conjunction with known sampling frequency. These procedures are explained in more detail in Section 4.2.

Raw film data images were subject to several processing stages, using Adobe "Photoshop 5" and Corel "Photo Paint 9" software. Then, quantitative features of flame propagation (e.g. flame edge, enflamed cross-sectional area, centroid, flame radii and edge perimeter) were evaluated using a Fortran program written by the current author. These processes are detailed in Section 4.3.

The external clock data enabled resolution of crank angle versus time ($\theta - t$) data useful for synchronising the pressure and film data over a combustion period. This synchronisation, vital in data analysis, is detailed in Section 4.4.

The results of the various processing methods are illustrated for two successive firing cycles (Cycle A and Cycle B) at a typical test condition with skip fire ratio of five. Set out in Table 4.1 are the operating conditions for this test.

Table 4.1 Operating conditions for the typical test.

Compression ratio	**7.6**
Set engine speed	**750 rpm**
Equivalence ratio	**1.0**
Ignition timing	**10^{o} CA bTDC**
Type of fuel	**Isooctane**

In this chapter, the results of some of the pre-existing and new processing methods are reported, with the differences between the methods highlighted to justify the methods selected for subsequent processing of the substantial experimental database.

4.2 Cylinder pressure data processing

The Microlink "Wavecap" software was employed to store the outputs of two ADC channels used (described in Section 3.5.5). To separate the signals stored via the channels, the software "Split" (Lee 1995) was utilised. All the digitised binary format data needed to be converted into ASCII format using Microlink's "FAMOS" (Fast Analysis and Monitoring Of Signals) software.

4.2.1 Developing the digitised binary data with FAMOS sequences

The binary format data were transferred to ASCII format, a (readable) form suitable for use in subsequent processing and programming. This transfer was effected by loading and running a proper sequence program through FAMOS software. An

improved sequence program was developed from a pre-existing program. Using the BDC signal, this program enabled sorting of the data of any selected cycle, such as a pair of successive motoring and firing cycles, from the continuous skipped firing mode data. The pressure, TDC and external clock data for the cycles were saved in separate ASCII format files. For a number of tests captured in the late period of this study, a binary to ASCII program ("*Bin2asc*") developed by a colleague (C. Wu) in Leeds was used. This minimised the processing time for this stage.

4.2.2 Resampling and arranging the digitised pressure data versus crank angle

The cropped dynamic and absolute pressure data available after the stage of processing described above were in single column form. To resample the single column pressure data by crank angle (with $0.2^\circ CA$ increment) instead of time, two methods were examined: one based on the assumption of uniform engine speed over a cycle; and the other referenced to the external clock (shaft encoder) signals. These methods are detailed in Sections 4.2.2.1 and 4.2.2.2.

4.2.2.1 Uniform engine speed assumption

In this method, the engine speed for the cycle being processed was taken to be uniform. Then, assuming a uniform distribution of data points over the $360^\circ CA$ cycle, the crank angle step was found. Using this step, the corresponding crank angle (relative to TDC) of each data point was calculated and the pressure-crank angle data were arranged. To resample these data with $0.2^\circ CA$ increment from $180^\circ CAbTDC$ to $180^\circ CAaTDC$, pressure data corresponding to the nearest angles to the new arranged angles were selected. This procedure is shown in Figure 4.1, for the initial part of a dynamic pressure data record. This method was used by Lee (1995), Gillespie (1998) and Cairns (2001), averaging the pressure over a few points around each data point.

4.2.2.2 Relative to external clock

A Hohner 3202 shaft encoder, coupled to the torque free end of crankshaft, was utilised in the currently reported work (Chapter 3). This encoder generated an

electrical signal, with a period of $0.2^\circ CA$, when engine was running. Shown in Figure 4.2 is a schematic analogue signal generated by the encoder. This signal was sampled by the analogue to digital converter at the same time as the pressure signal. Illustrated in Figure 4.3(a) and (b) are the digitised shaft encoder signal, termed external clock, and dynamic pressure signal of a typical cycle versus time in the early part of the cycle. The period of the external clock [shown in Figure 4.3(a)] was approximated to $0.2^\circ CA$. The first data point was considered to stand for $180^\circ CA\,bTDC$. Then, by moving one period forward from the first point of the clock data, the similar point in the next period ($179.8^\circ CA\,bTDC$) was determined. Using the number of points passed, the relevant pressure data was found. This procedure was successively applied to resample pressure data over a cycle with the $0.2^\circ CA$ increment.

4.2.3 In-cylinder pressure referencing

Piezoelectric transducers are generally used to measure engine cylinder pressure because of their accuracy, bandwidth, relative thermal stability, durability and size. These transducers measure gauge, rather than absolute, pressure. They also usually experience long and short time "drift" (Kuratle et al. 1992) associated with thermal effects. Therefore, absolute pressure referencing is necessary for each individual cycle.

The absolute pressure transducer (mounted in the cylinder wall, a few millimetres above the exhaust port) was used to measure absolute cylinder pressure over the low pressure and temperature parts of a cycle. Exhaust port closure timing was chosen as the reference point. To reduce referencing error caused by any signal noise, both gauge and absolute records were smoothed by averaging over five points around the referencing point. The gauge pressure reading was then vertically shifted to match the absolute pressure measured at the referencing point. Shown in Figure 4.4 are the referenced cylinder pressures of the two firing cycles (with skip firing ratio 5) versus crank angle at the typical test condition (Table 4.1) using the uniform engine speed assumption.

It can be observed that there is a significant difference in the two in-cylinder pressure traces prior to the ignition timing. Since the engine was operated in skip fire mode (with 4 skipped cycles), this difference cannot be associated with cyclic variation, breathing and blowby differences or errors arising from referencing. Set out in Figure 4.5 are similar referenced pressure traces versus crank angle, for the same cycles, using the method based on external clock signals. There is now coincidence between the pressure traces for the cycles prior to ignition.

To further demonstrate the differences associated with the two processing methods (at the same condition), the processed pressure traces for one cycle (Cycle A) have been plotted in Figure 4.6. In addition to the previously noted difference before ignition, an offset in the peak pressure position is apparent.

4.2.4 Estimation of cycle engine speed

The average engine speed ($\overline{n}$) in a cycle was evaluated using the time duration for the complete $360^\circ CA$ cycle. The elapsed time was calculated using sampling frequency and the number of digitised data points of the cycle;

$$\overline{n}(\text{rpm}) = \frac{60 f(\text{Hz})}{N_{D.P.}} \tag{4.1}$$

where f and $N_{D.P.}$ stand for the sampling (capturing) frequency and the number of digitised points of the cycle. Cyclic variation in the average engine speed was found in successive firing cycles recorded in one test. Also, a deviation between the average engine speed and that set was observed. For example, the average engine speeds of the two firing cycles (Cycle A and Cycle B) were determined to be 761 and 741 rpm, respectively, while the set engine speed was 750 rpm.

The significant difference between the two pressure processing methods (Figure 4.6) suggested a non-uniform distribution of the digitised points and associated non-uniform engine speed in a cycle. Evaluation of the instantaneous engine speed with high accuracy in an engine cycle is difficult, because of a number of problems; e.g.

very short resolution period, angular torsion, rotational vibration and flexible coupling between encoder and engine and/or engine and dynamometer. For estimation of in-cycle engine speed history, the external clock of the shaft encoder was utilised. Using this record, the number of data points in a chosen crank angle increment (angular period $\Delta\theta$) was counted and, using sampling frequency, the corresponding time period (Δt) was evaluated. Then average engine speed over the chosen angular period was computed and taken as that at the middle of the period ($\theta+\Delta\theta/2$). This assumption might cause slightly smoothing of real engine speed. This procedure can be summarised as follows:

$$n(\theta + \Delta\theta/2)[\text{rpm}] = c\frac{\Delta\theta[^\circ\text{CA}]}{\Delta t[\text{msec}]} \tag{4.2}$$

where c is a constant, 500/3 [rpm.msec/$^\circ$CA]; n and Δt are engine speed and the time duration of the angular period ($\Delta\theta$), respectively. This procedure was applied over many individual angular periods in a cycle to determine engine speed history over a cycle. Shown in Figure 4.7 is variation in estimated engine speed, together with "smoothed" speed [generated using a fast Fourier transform (FFT) filter available in "Origin" graphic software] as a function of crank angle for Cycle A. For this, 5°CA was selected as the angular period and 3 points were used for FFT filter smoothing. The relative error of the estimation depends on the sampling time step or frequency. Supposing the maximum absolute error of the elapsed time to be $\pm$ time step, the relative error can be determined as follows,

$$\frac{\Delta n}{n} = \frac{\delta t}{\Delta t} \tag{4.3}$$

in which δt is time step of sampling or digitising. The maximum relative error occurs at minimum Δt (or maximum speed) evaluated by this method. Set out in Figure 4.8, is the maximum relative error of the estimated in this way. It should be noted that this error does not include any uncertainty associated with the data acquisition system.

4.2.5 Fortran program for pressure data processing

A Fortran program was written (by the current author) to include the new processing methods described in Sections 4.2.2.2 and 4.2.4. Due to the easy availability of PCs, it was decided to adopt the program using PC based Salford Fortran "Plato 2" software. Four important points were considered for the program,

- Low processing time
- Ability to apply absolute and dynamic transducer calibrations
- Preparation of necessary information in suitable form for other stages of data processing and model validation
- Output data format easy for plotting by standard graphic software.

The program was written to resample in-cylinder gauge and absolute pressures and to perform pressure referencing. It was able to process a maximum of 20 cycles in one run. All filenames of the data (absolute, dynamic, data point number and external clock) generated by FAMOS "Sequence" could be read through a data file termed '*datain*'. This file comprised capturing frequency, set engine speed and referencing point. This arrangement improved processing time significantly.

The program was improved to calculate time-crank angle ($t-\theta$) and produce a file for each cycle with a '*timcra*' extension. This file was used to apply engine speed variation within a cycle in the modified LUSIE code (detailed in Chapter 6). It was also used to synchronise pressure and film data (described in Section 4.4.3).

In addition to storing all in-cylinder pressure records in individual files, they were collected in one file suitable for plotting by available graphic software. This resulted in reduced plotting time.

4.3 Film processing

Each raw flame image was generally subject to a number of qualitative and quantitative processing stages. The qualitative stages (including adjusting brightness level, cleaning, threshold, dust and scratches noise filter) were used to convert a raw

greyscale image to a binarised black and white one. These stages are detailed in Section 4.3.1.

Quantitative aspects included determination of: enflamed cross-sectional area, flame centroid, flame radius and edge perimeter to characterise flame images. To program evaluation of these parameters, it was necessary that the character of all pixels in an image be readable by the processing program. This was effected by changing the format of the image file from binary to ASCII. This procedure is detailed in Section 4.3.2.

Flame edge processing, used previously to study flame position and the effects of interaction between the flame and the unburned gas flow field (Cairns and Sheppard, 2000), is described in Section 4.3.3.

4.3.1 Converting raw image to black and white

Raw greyscale images, captured by the black and white camera, were converted to binarised black and white images using Adobe "Photoshop 5" software. In Adobe Photoshop, greyscale mode uses up to 256 shades of grey to represent an image. Every pixel of a greyscale image has a brightness value ranging from 0 (black) to 255 (white).

Illustrated in Figure 4.9(a) is a typical greyscale raw image. In the image, the shadows of the spark plug and its connection wires can be observed. Black and white spots can also be seen in the enflamed area. The black spots located on the top window are most likely to be associated with soot particles, resulting from oil droplets burned in the previous cycles. The white spots are images of oil droplets burning in the cycle being processed. To minimise the effects of the spots, the engine was run with very little lubrication oil and the top window was cleaned prior to each test.

In natural light imaging, the brightness intensity across the enflamed area is normally inconsistent and weak at the flame front. This is associated with unburned gas entrainment, 3D flame growth effects and flame motion within the exposure time of each frame. This rendered it difficult to distinguish the flame edge in the raw image.

To recognise the flame edge, the brightness level of each image was adjusted using the "Equalise" command in the Adobe Photoshop environment. The command redistributes the brightness values of pixels in an image. Shown in Figure 4.9(b) is the same image (as that of Figure 4.9(a)) after adjusting the brightness level.

The spark plug and connection wire shadows and the black and white spots were manually "cleaned" using brushes and proper colour available in the imaging software. Illustrated in Figure 4.9(c) is the cleaned version of the previous image.

The "Threshold" command of the software was used to produce a binarised black and white (B/W) image. This binarisation was effected by specifying an appropriate level as a threshold to produce a high-contrast B/W version of the greyscale image. The threshold level was adjusted such that the white area covered the enflamed area of the cleaned image. Shown in Figure 4.9(d) is the thresholded, or binarised, image. This process was performed for each frame, separately.

To remove any dissimilar pixel and smooth the flame edge trace of the thresholded image, the "Dust and Scratches" filter command of the software was used. Shown in Figure 4.9(e) is the resultant image, after applying the command to the thresholded image.

4.3.2 Converting binarised image to ASCII format

To calculate quantitative features of a flame image using a Fortran program, the character of pixels in the image needs to be read. The format of the image file resultant from the qualitative stages was of "Tagged Image File" format, *".tif"* (which is binary). Using PC based Corel "Photo Paint 9" software, the *".tif"* file was saved as an "Encapsulated PostScript", *".eps"* file (a metafile supported by most illustration and page layout programs). By opening the *".eps"* file through ASCII based software, such as Salford "Plato 2" and "Word Pad", the characters of all pixels in the image appeared, following a header. The colour feature of each pixel was displayed with two characters e.g. '*00*' for a black pixel and '*ff*' for a white pixel. All the *".tif"* binarised B/W images were saved as *".eps"* files and, to minimise processing time at this stage, the "recorder" command available in the Coral "Photo Paint" was used.

This was effected by recording the processes of the stage (such as opening *".tif"* file, saving the file as *".eps"*, after typing a name for the file) for one frame of a cycle; saving it as a *".csc"* file; opening the file in "Word Pad"; including the other frames of the cycle; saving the file; opening and playing it through the "recorder" command to process the frames.

4.3.3 Flame edge processing

To find the coordinates of flame edge pixels, the binarised image was used; the character of each pixel in a 256×256 pixels image being stored in a 256×256 array. The cells of each row of the array were checked from left to right. Where the cell character changed from black/white to white/black the coordinates (row and column) of the white cell was memorised. This procedure was also followed for each column of the array from top to bottom. Hence, the coordinates of all pixels located on the flame front were collected. Another 256×256 array with the black pixel character ('*00*') in the all cells was defined. In the array, the characters of the cells having the same coordinates of the flame front pixels were changed to white pixel character ('*ff*').

Using the modified array, a *".eps"* file was created so that a flame edge trace image could be observed by opening the file in the environment of the Corel software. Shown in Figure 4.10(a) is a local part of the binarised image shown previously in Figure 4.9(e). Horizontal and vertical checks (i.e. row and column checks) of the part can be observed in Figure 4.10(b) and (c), respectively. In Figure 4.10(d), the combination of the horizontal and vertical checks is illustrated. Using this method, all frames captured over the combustion period were processed and the related flame edge traces were collected in a file termed '*Result.eps*'. This method was capable of handling multi-loop flame edges, such as those obtained from laser sheet, knock and multi-kernel combustion, without performing any graphical process.

Shown in Figure 4.11 are the flame edge traces over the flame propagation period for a typical cycle (Cycle A) in pixel size scale. To distinguish successive edge traces, two colours were used for the flame edge traces. It can be observed that the frame has not completely included the full cylinder cross-section at the right hand side.

To plot a flame edge using standard graphic software, it was necessary to store the coordinates of flame edge by fully travelling the flame edge loop from a starting point. A two-column array was adopted to store the coordinates of pixels, travelling along the successive flame edge. The first flame edge pixel found by the above-mentioned method was selected as the starting point for this travelling. Using the coordinates of the starting pixel (the main pixel), the neighbour pixels were checked from the west pixel by clockwise spinning around the main pixel. The first white colour pixel along the spine direction was selected as the second flame edge pixel and its coordinates were memorised in the array. The second pixel was then considered as the main pixel and the procedure repeated until arriving back at the starting pixel. Shown in Figure 4.12(a) is a schematic of the procedure for a small part of a flame edge. It should be noted that at some particular positions of flame edge, this procedure results in an infinite loop problem [Figure 4.12(b)]. To avoid this, the coordinates of any selected white pixel along the spine direction were checked with the previously stored pixels. If the pixel had already been stored, it was ignored and the next pixels along the spine direction were checked to find the next white pixel. Finally, the coordinates of all flame edge pixels were arranged according to flame edge travel and stored in an array.

Pixel scale (mm/pixel), an important parameter for quantitative evaluations, was determined using a calibration image before running the engine. A Cartesian co-ordinate (x, y) system, based on the centre of the cylinder with x and y in *mm* was adopted. Using the pixel scale, the co-ordinates of the arranged flame edge pixels (in *mm*) were transformed to Cartesian co-ordinates and recorded.

The axes of the co-ordinates were rotated about the centre by an appropriate angle to a consistent reference configuration relative to inlet and exhaust ports, with the flame edge co-ordinates corrected accordingly. Shown in Figure 4.13(a) and (b), are successive flame front positions for the flame propagation period for the two typical cycles (Cycles A and B). The configurations have been rotated 135° anticlockwise relative to the original axes. For these cycles, the filming rate was $4500 fps$, giving 0.222 *msec* frame step (equivalent to $0.9^{\circ} CA$ at 750 *rpm* engine speed).

4.3.4 Enflamed cross-sectional area and centroid

To evaluate enflamed cross-sectional area of an image, the number of white pixels in the image was counted and multiplied by the square of the pixel scale (with the scales in the two directions identical). Shown in Figure 4.14 is enflamed cross-sectional area versus crank angle for the two cycles considered previously.

The flame centroid of each frame was determined using the co-ordinates of white pixels located in enflamed cross-section area. The distance of the centroid position from the centre of the cylinder bore was estimated as a measure of bulk flame movement. This is illustrated in Figure 4.15 as a function of crank angle for the two cycles over the flame propagation period. To illustrate the movement of the centroid in successive frames, the coordinates of the centroid were recorded over the flame propagation period. Set out in Figure 4.16 is the locus of the flame centroid over flame propagation period for the two cycles. It can be seen that shortly after ignition the flame centroid is relatively far from the cylinder centre, it then moves a few millimetres further away before coming back to the cylinder centre by the time the flame covers the whole cylinder cross-section.

4.3.5 Flame radius and edge perimeter

The flame front imaged using a natural light technique is representative of the "entrainment" flame front (as opposed to the mean reaction front) (Gillespie et al., 2000). Hence, the estimated mean flame radius using the natural light imaging technique can be considered to be a mean turbulent entrainment radius ($\bar{r}_e$). It is clearly an important parameter in validation of entrainment combustion models. Mean flame radius is considered to be that of a circle having identical area to the enflamed cross-sectional area [Cairns (2001)]. Set out in Figure 4.17 is the mean flame radius ($\bar{r}_e$) versus elapsed time from ignition during the flame propagation period for the two typical cycles (A and B). Since engine speed varied throughout the cycles (Section 4.2.4), synchronisation was made between the film data and the external clock signal of the shaft encoder (detailed in Section 4.4.3).

Flame edge perimeter, related to the mean area for interaction between burned and unburned gas, is possibly an important parameter governing combustion rate. For a given enflamed cross-sectional area, the edge perimeter of a distorted flame is longer than that of a circular one. In his study, Cairns (2001) observed that the combustion rate of a more circular flame was higher than that of a distorted one.

Flame edge perimeter was evaluated by integration of length travelled along the flame edge. For travel in north, west, east or south directions, incremental length was one pixel size; for travel in northwest, northeast, southwest or southeast directions, incremental length of $\sqrt{2}$ times pixel size was adopted. To account for contact between the flame and the cylinder wall, a circle with bore diameter and cylinder centre was defined in pixel coordinates. In each image any white noise pixel out of the circle was changed to black. Then any part of flame edge located on the circle was considered as "inactive" for unburned gas entrainment. Shown in Figure 4.18 are the total and active perimeters for the two cycles considered previously, versus crank angle.

It is clear that when any part of flame front hits the wall, that part is inactive for unburned gas entrainment. In other words, the fraction of "active" perimeter for unburned gas entrainment reduces after the flame hits the wall. To highlight this effect, an "Active" Perimeter Fraction (APF) was defined as:

$$\mathrm{APF} = \frac{\text{"Active" perimeter}}{\text{Total perimeter}} \tag{4.4}$$

Shown in Figure 4.19 is APF versus crank angle for the two typical cycles. It can be seen that APF drops from unity late in flame propagation, as the flame hits the wall. Set out in Figure 4.20 is APF against, time-independent, flame radius. The graph shows that APF begins to drop from ~35 *mm* flame radius, in a similar manner for both cycles.

To quantify flame distortion from a circular shape, Buran (1998) and Gillespie (1998) defined a flame "Shape Factor" (SF). Similarly, in the current work, a flame "Shape

Factor" was defined in terms of flame perimeter (P_f) and the perimeter of an equivalent circle having an area identical to the enflamed cross-sectional area (P_e), as follows:

$$\text{Shape Factor} = \frac{P_f}{P_e} \tag{4.5}$$

Shown in Figure 4.21 are values of this Shape Factor versus crank angle for the two cycles (A and B); illustrated in Figure 4.22 are the same data versus mean flame radius.

4.3.6 Fortran program for film processing

A Fortran program was written by the current author to evaluate the quantitative features of flame propagation. All the methods described in the above sections were applied in the program. In line with the previously described improvements in image acquisition and processing methods, the program was successively upgraded via four different versions. In Version 1, flame edge, enflamed cross-sectional area, centroid position and flame radius were included and the set (constant) engine speed used in determination of the corresponding crank angle of image frames. The edge filtering of the late frames of flame propagation and flame perimeter estimations (active and inactive) were developed in Version 2. Synchronisation of film and external clock (shaft encoder) data was considered in Version 3. Most of the film data was directly downloaded from camera into the PC (split into frames). In a few cases, film data were recorded in video as ciné and then downloaded into the PC. When the ciné data were split into frames using the Corel software, frame size was changed to 384×288 pixels, which resulted in different pixel scales for the two directions. To process these types of data, Version 4 was improved.

The input data for the program are: frame size in pixel, pixel scales for the two axes, image rotation angle, cylinder bore diameter, ignition timing, $t-\theta$ data for the cycle (prepared by the pressure processing code), number of the first frame being processed

after ignition (counting the first visible spark light as one), filming rate, the number of image files to be processed and the list of filenames, successively.

The code generates three output files; termed *"Result.eps"*, *"Flameedge"* and *"Flamedata"*. The *"Result.eps"* file was described in Section 4.3.3, the *"Flameedge"* file embodies the coordinates of all flame edges and the *"Flamedata"* file contains flame features (e.g. the flame radii, centroid, cross-sectional area and edge perimeter) versus crank angle.

4.4 Synchronisation between film data and crank position

Combustion events in SI engines are often studied on the basis of measured cylinder pressure and filmed flame propagation; used separately or together. Crank angle, indicating piston-crank position in a cycle, is the most common independent variable used to illustrate the dependent variables of combustion, heat transfer and thermodynamic phenomena. Usually filming rate, which is based on time, is constant over the data capturing period. To evaluate the corresponding crank angle of a frame, it is necessary to use a relation between time and crank angle.

The position of the first frame after ignition within a firing cycle is important for the positions of the subsequent frames. For the film data captured using the Kodak Ektapro camera (which was available for a short period), there was no framing signal and the first frame showing the visible spark light was considered the first frame after ignition. The position of this frame was considered to be one frame period after ignition timing. From the Phantom V4.1 camera, a framing signal was available and the crank angle position of any frame was determined using the simultaneous signals of the framing, ignition and external clock.

Three methods, based on set engine speed, average engine speed of the cycle in question and use of the external clock (shaft encoder) are described in Sections 4.4.1-4.4.3.

4.4.1 Synchronising by set engine speed

In this method, it is assumed that engine speed is constant and equal to the set engine speed. Then the crank angle increment for successive images can be determined using filming rate and set engine speed as follows:

$$\Delta\theta(^{\circ}CA) = \frac{6n_{set}(rpm)}{n_f(fps)} \tag{4.6}$$

where n_{set} and n_f are set engine speed and filming rate, respectively. To illustrate film data versus crank angle, Gillespie (1998) and Cairns (2001) used this method at $1500\,rpm$ set engine speed. Shown in Figure 4.23 is the flame radius versus crank angle for the two typical cycles considered previously.

4.4.2 Synchronisation using average engine speed for the cycle concerned

In this method, the average engine speed of the cycle concerned (which can be evaluated using the sampling frequency of engine data and the number of data points in the cycle) is used. For this method, the digitised BDC signal is required to separate different cycles. Set out in Figure 4.24 is the flame radius versus crank angle for the usual two cycles using this method. This method can be useful to analyse film data with the pressure data processed using the same engine speed assumption (Section 4.2.2.1). However, its use is inconvenient for model validation purposes; because its results can be influenced by engine speed variation within a cycle. In his study, Langridge (1995) used the method to synchronise sequential Schlieren and natural light film images with crank position. Pan (1994) used the average engine speed evaluated over the film sequence for the synchronisation.

4.4.3 Synchronisation using external clock data

Experimental data for crank-piston positions within a cycle can be achieved using information generated by shaft encoder. If both pressure and film data are processed based on the external clock record generated by the shaft encoder, they will also be

synchronised together. Set out in Figure 4.25 is the flame radius in terms of crank angle for the two typical cycles using the method. Since crank angle is directly recorded, the disadvantages mentioned for the two previous methods are avoided.

To clarify the differences, the flame radii computed for the three methods are shown in Figure 4.26 for Cycle B.

4.5 Discussion

To validate SI engine combustion models, experimental cylinder pressure and flame radius are often compared with those of the model. The comparison will be valid if the experimental conditions are applied to the model properly, and the experimental pressure and film data are processed precisely. In the current chapter, a number of different methods of pressure and film data processing have been detailed and illustrated. Significant differences were found between the methods in both pressure and film results (Figure 4.6 and Figure 4.26). In models, parameters such as cylinder volume and cylinder surface are calculated in terms of crank angle, implying piston position. Hence, experimental crank angle determination is vital for validation purposes. In a research engine such as LUPOE1, the shaft encoder is the key to generate signals relative to crank position. Important features of a cycle, such as ignition timing, indicated mean effective pressure, TDC and BDC are determined with respect to shaft encoder signals. Also, in experimental analysis, peak pressure position and combustion duration are usually determined in terms of crank angle. On the basis of the work described in Section 4.4, the third method has been shown to offer the most reliable processing and as a result was adopted in subsequent analysis of the extensive experimental data collected in the work reported in the thesis.

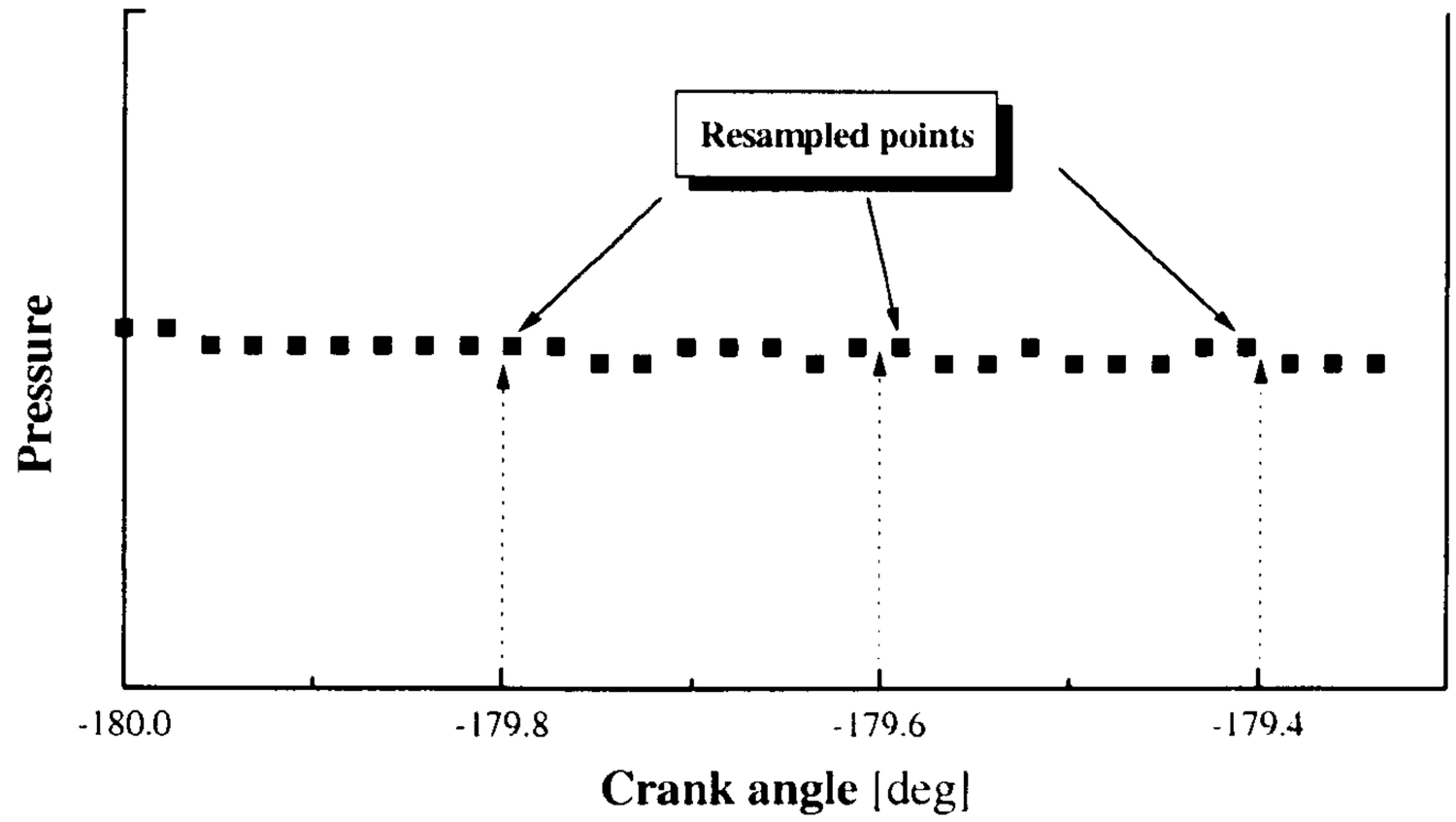

Figure 4.1 Typical resampling of a digitised pressure data using uniform engine speed method.

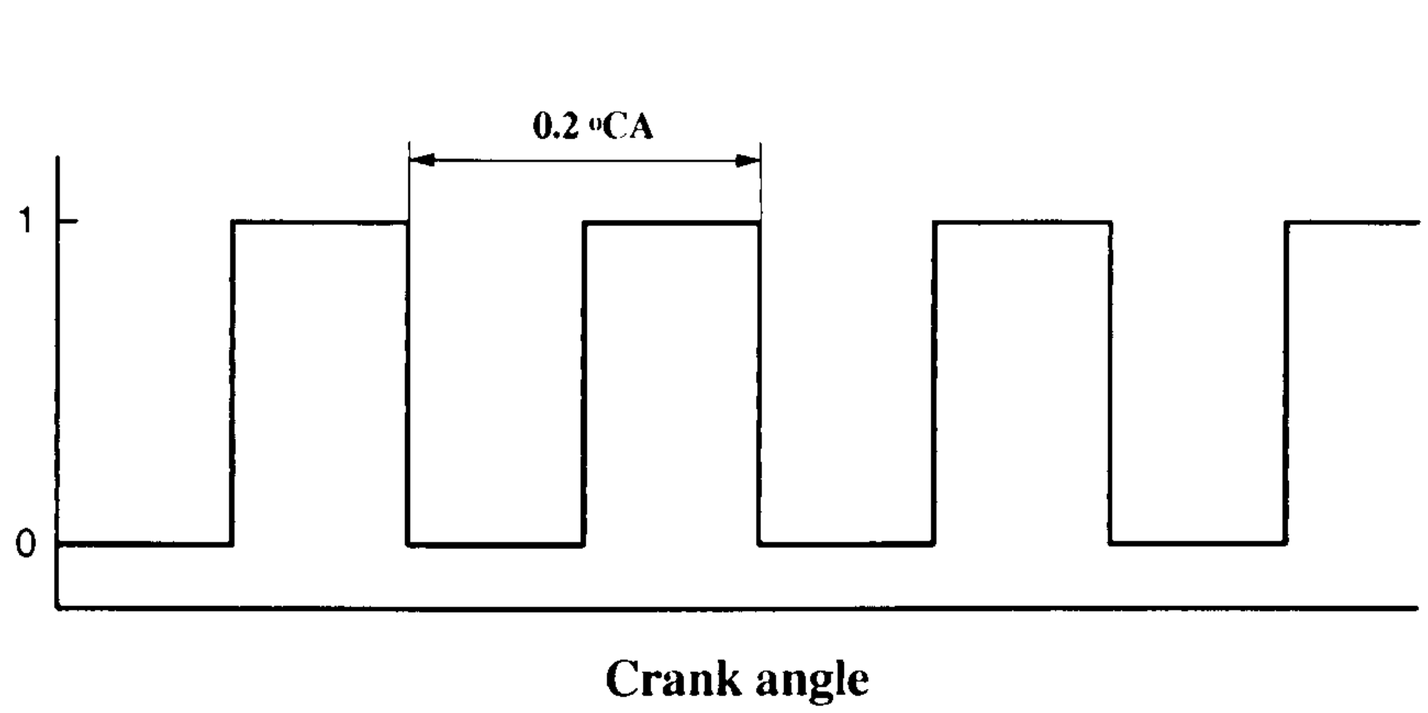

Figure 4.2 Schematic analogue signal generated by shaft encoder.

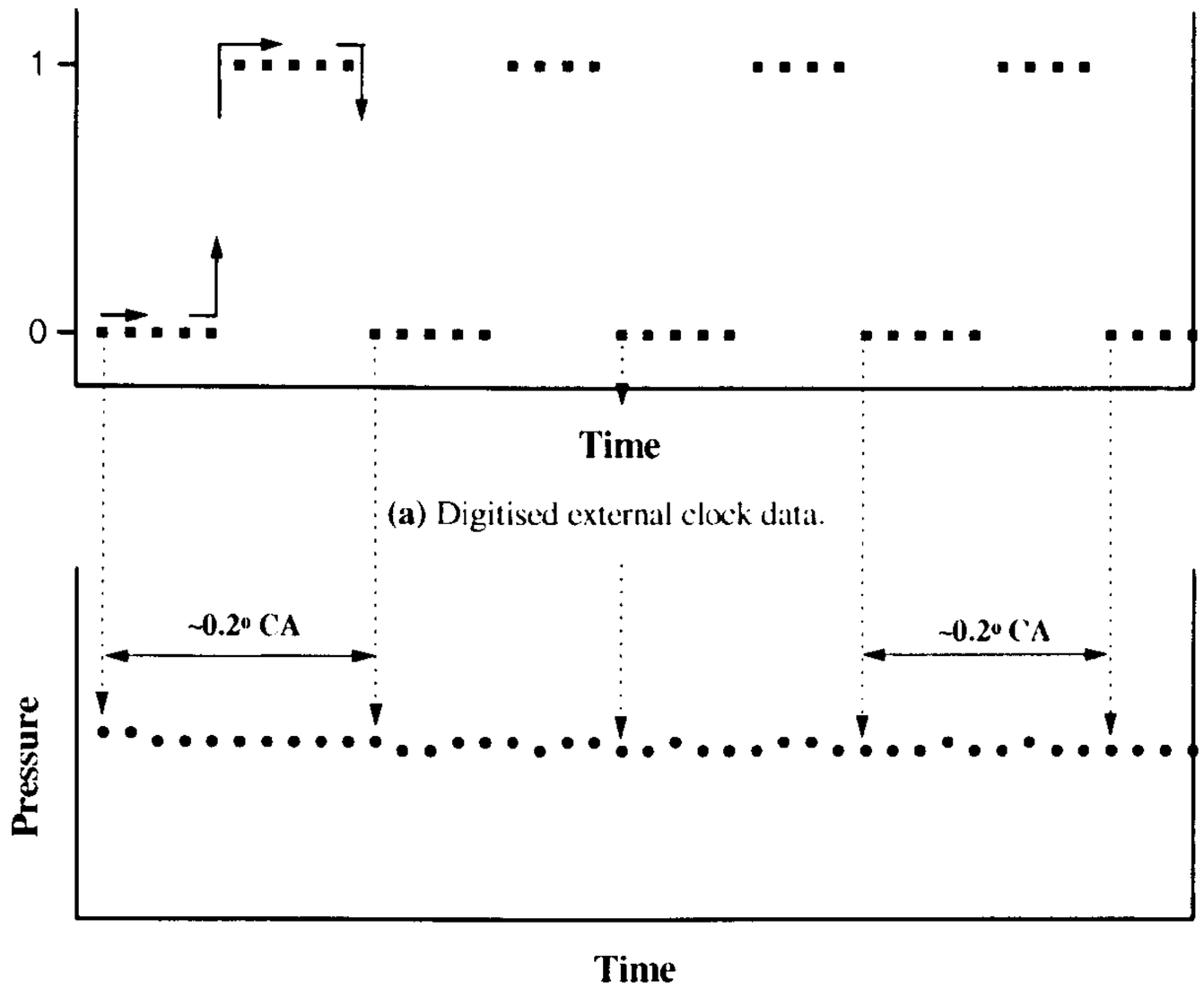

(a) Digitised external clock data.

(b) Digitised pressure data.

Figure 4.3 Digitised **(a)** external clock and **(b)** cylinder pressure data.

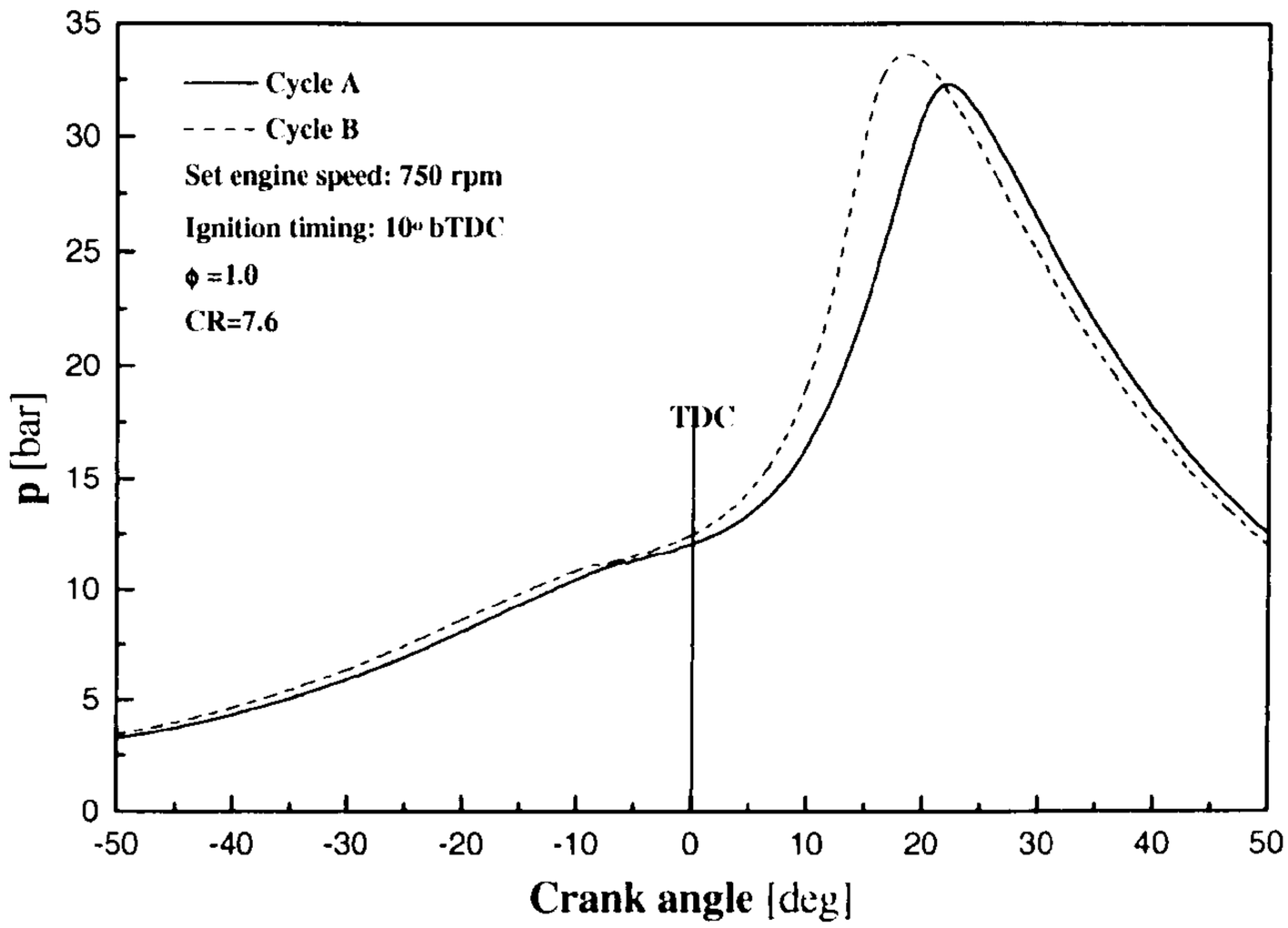

Figure 4.4 Cylinder pressure versus crank angle for the two typical firing cycles using the uniform engine speed assumption.

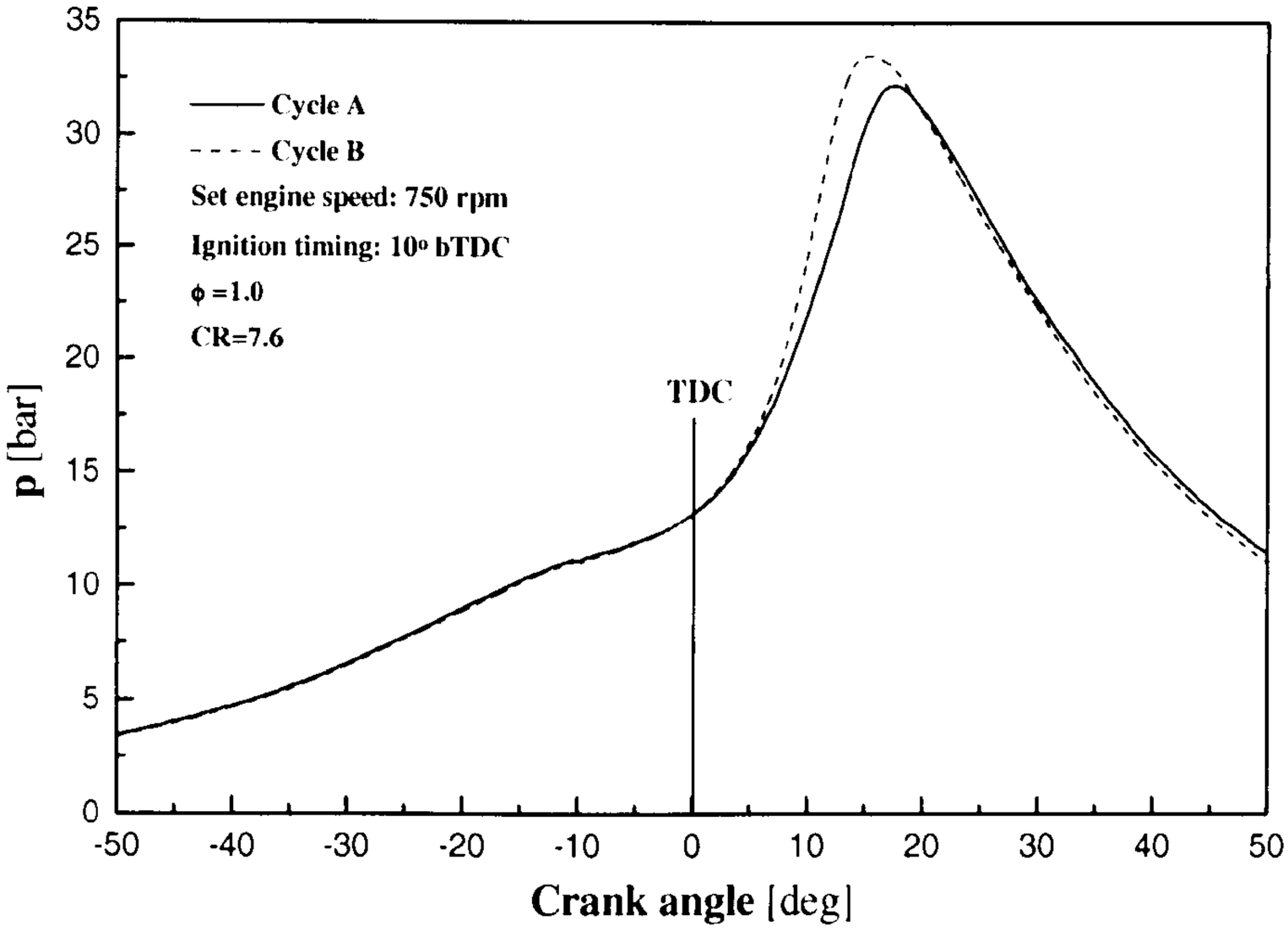

Figure 4.5 Cylinder pressure versus crank angle for the two firing cycles, processed by external clock signals.

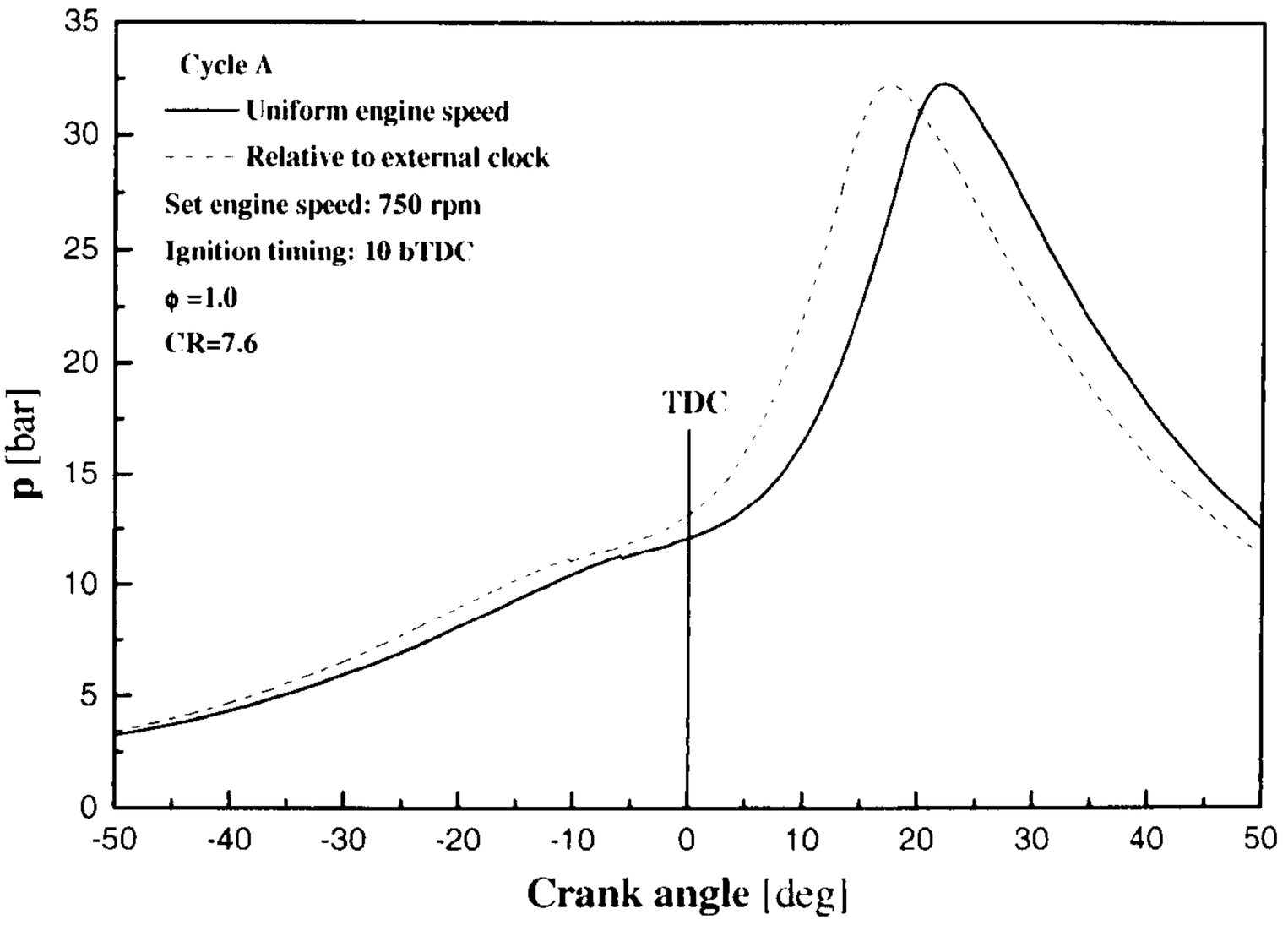

Figure 4.6 Cylinder pressure versus crank angle for Cycle A using the uniform engine speed and external clock methods.

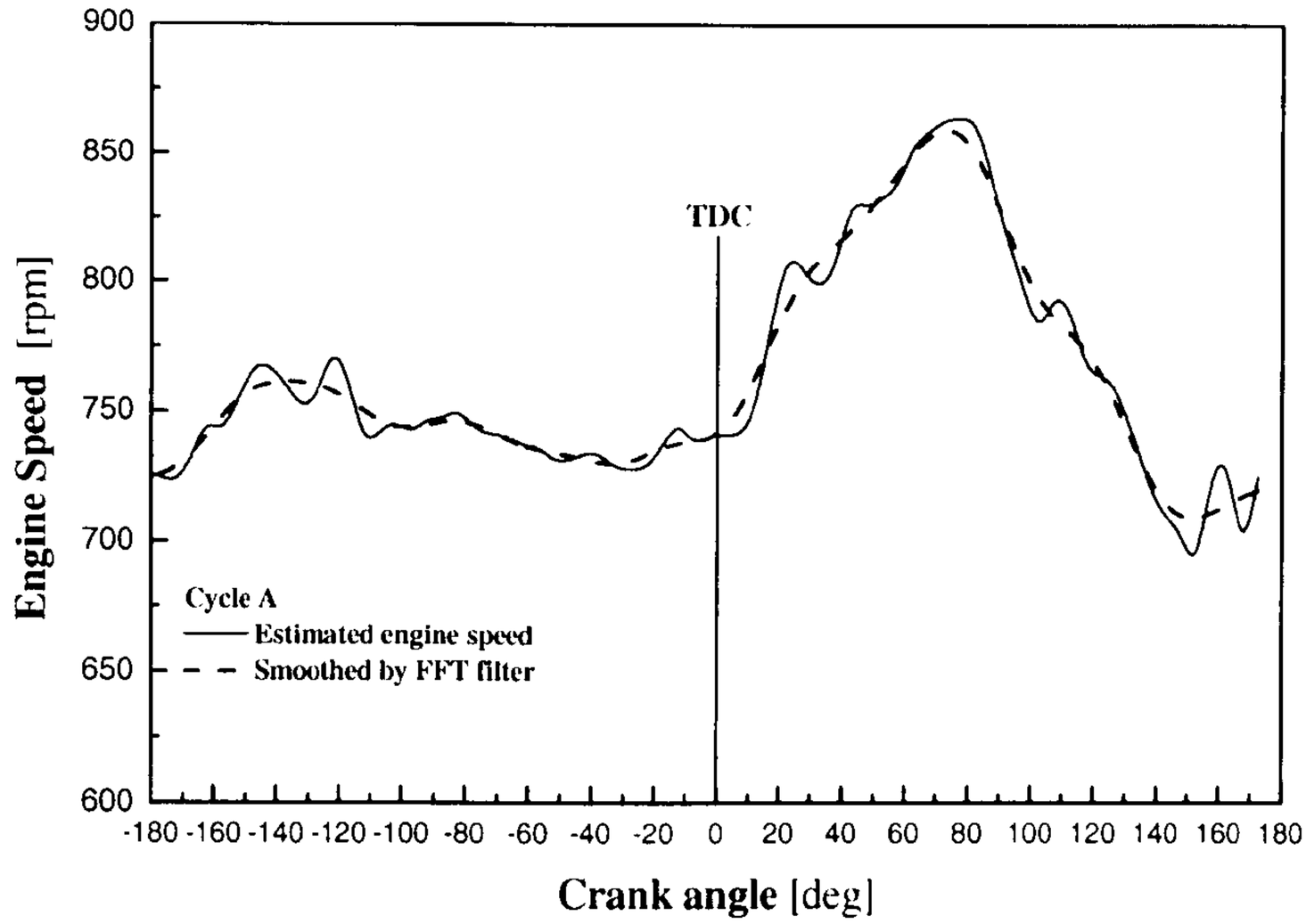

Figure 4.7 Estimated and smoothed engine speed versus crank angle.

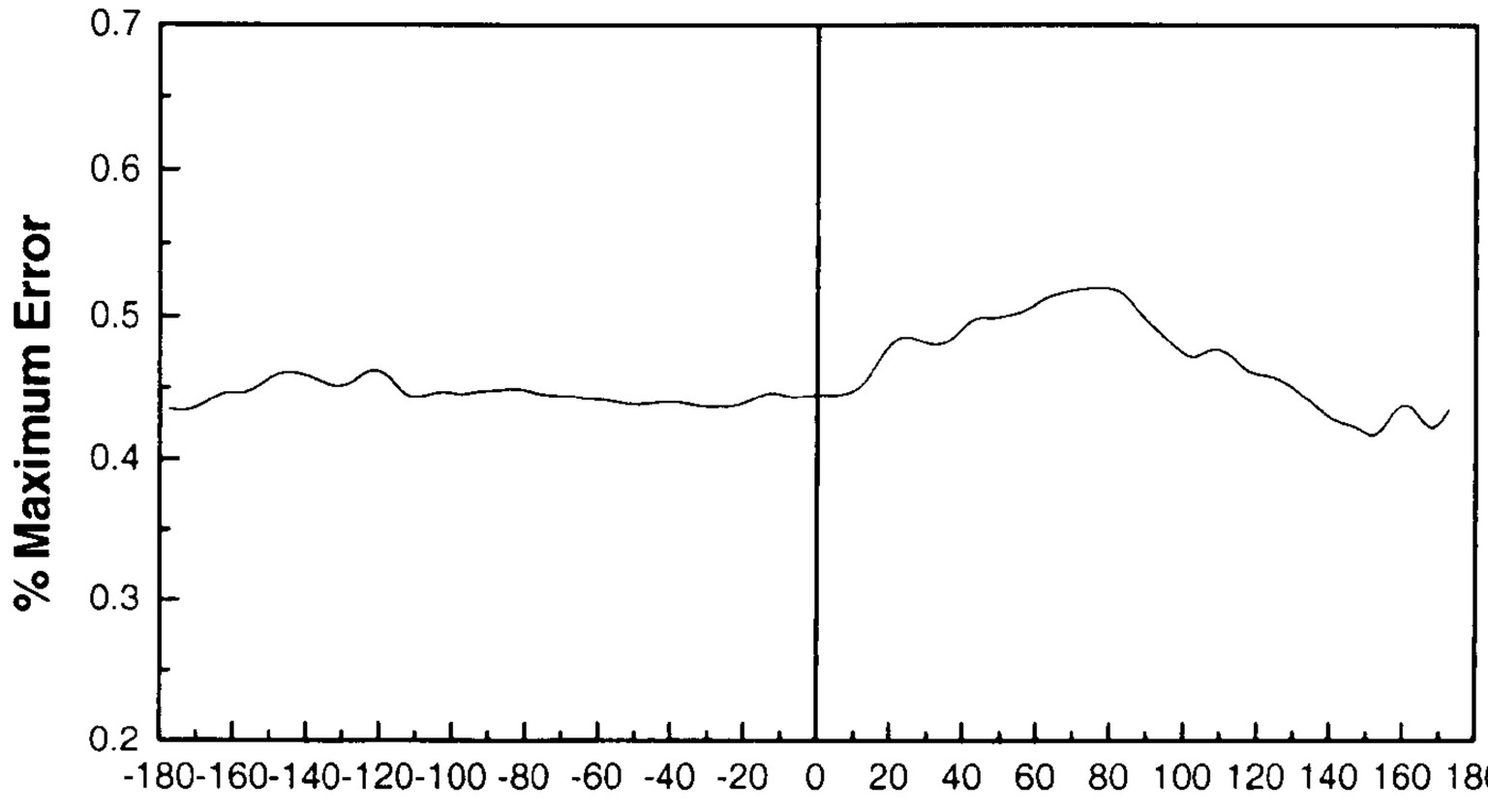

Figure 4.8 Percentage of maximum relative error for engine speed estimation versus crank angle using the suggested method.

(a) Raw image

(b) Adjusting brightness level

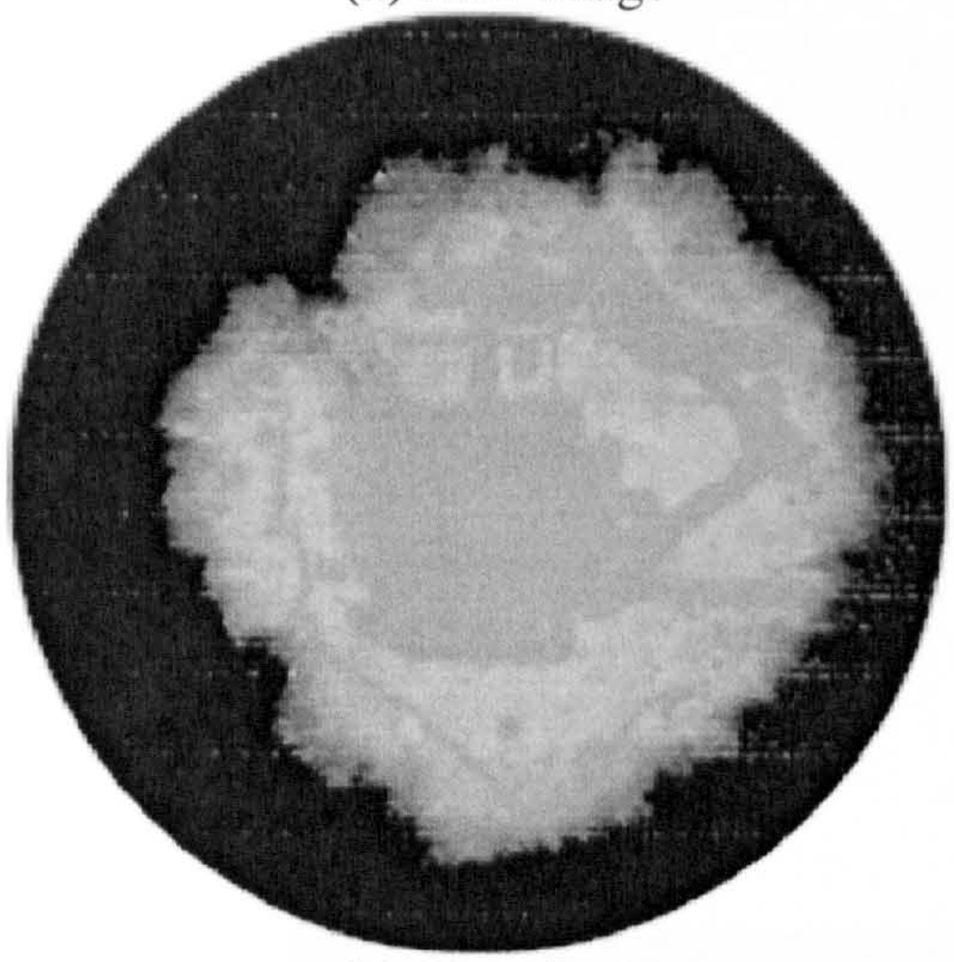

(c) Cleaning

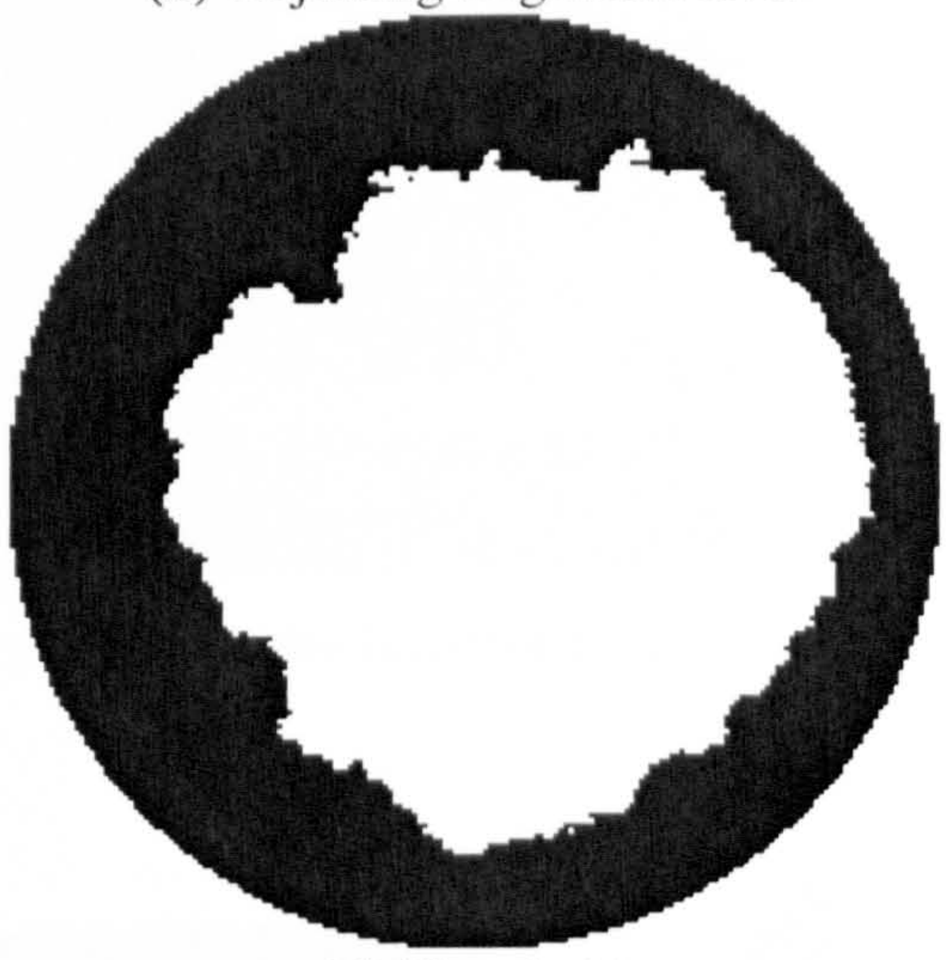

(d) Threshold

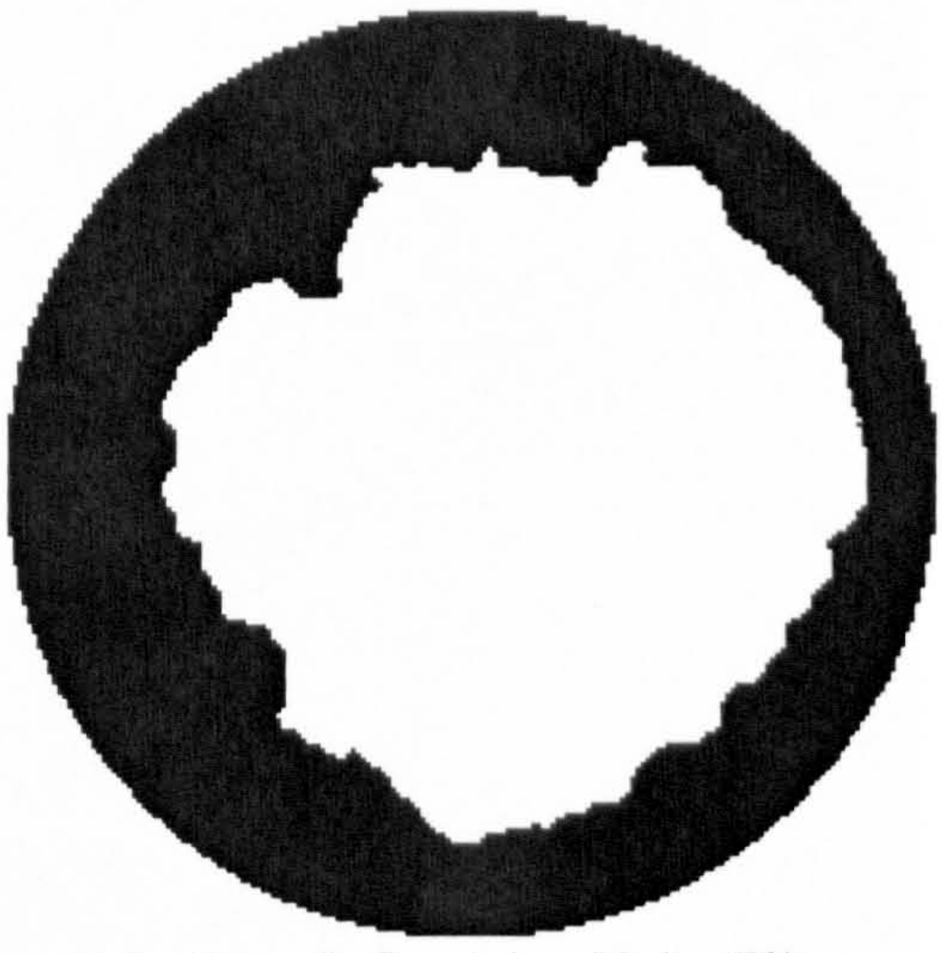

(e) Dust & Scratches Noise Filter

Figure 4.9 Successive stages of qualitative image processing to produce a binarised black and white image from a typical raw image.

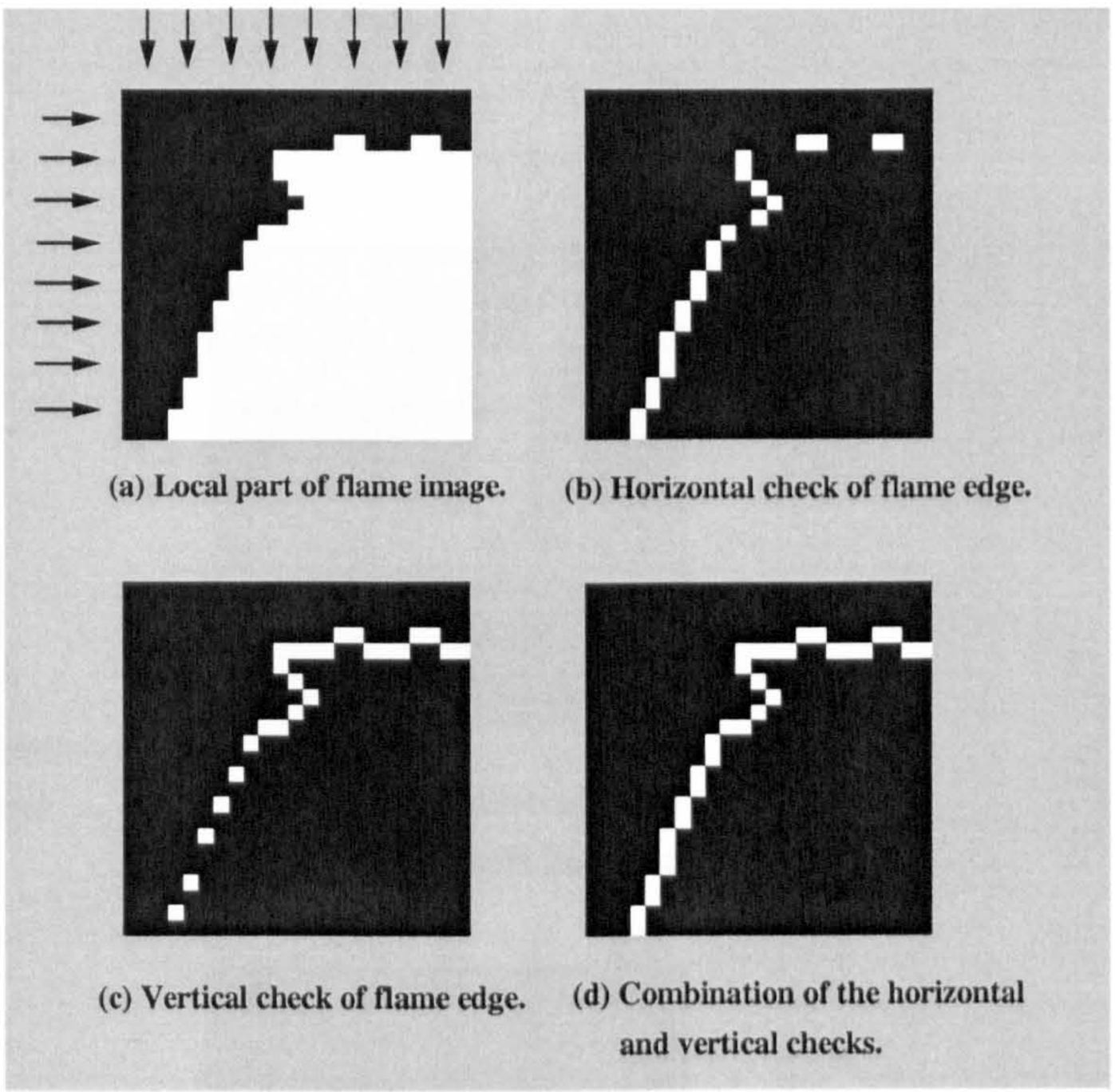

(a) Local part of flame image.

(b) Horizontal check of flame edge.

(c) Vertical check of flame edge.

(d) Combination of the horizontal and vertical checks.

Figure 4.10 Flame contour of a local part of the binarised image.

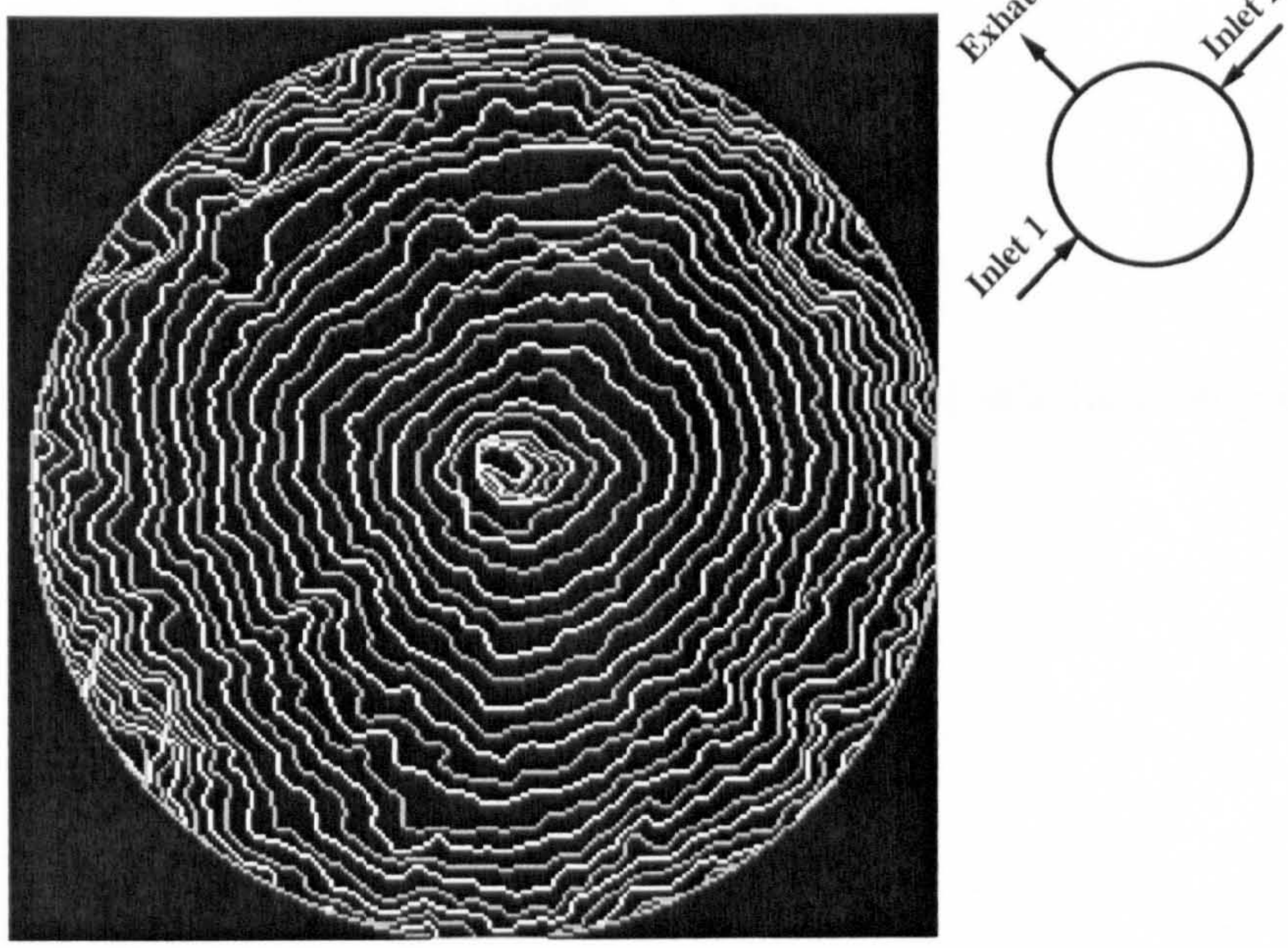

Figure 4.11 Flame edge traces of Cycle A during flame propagation period.

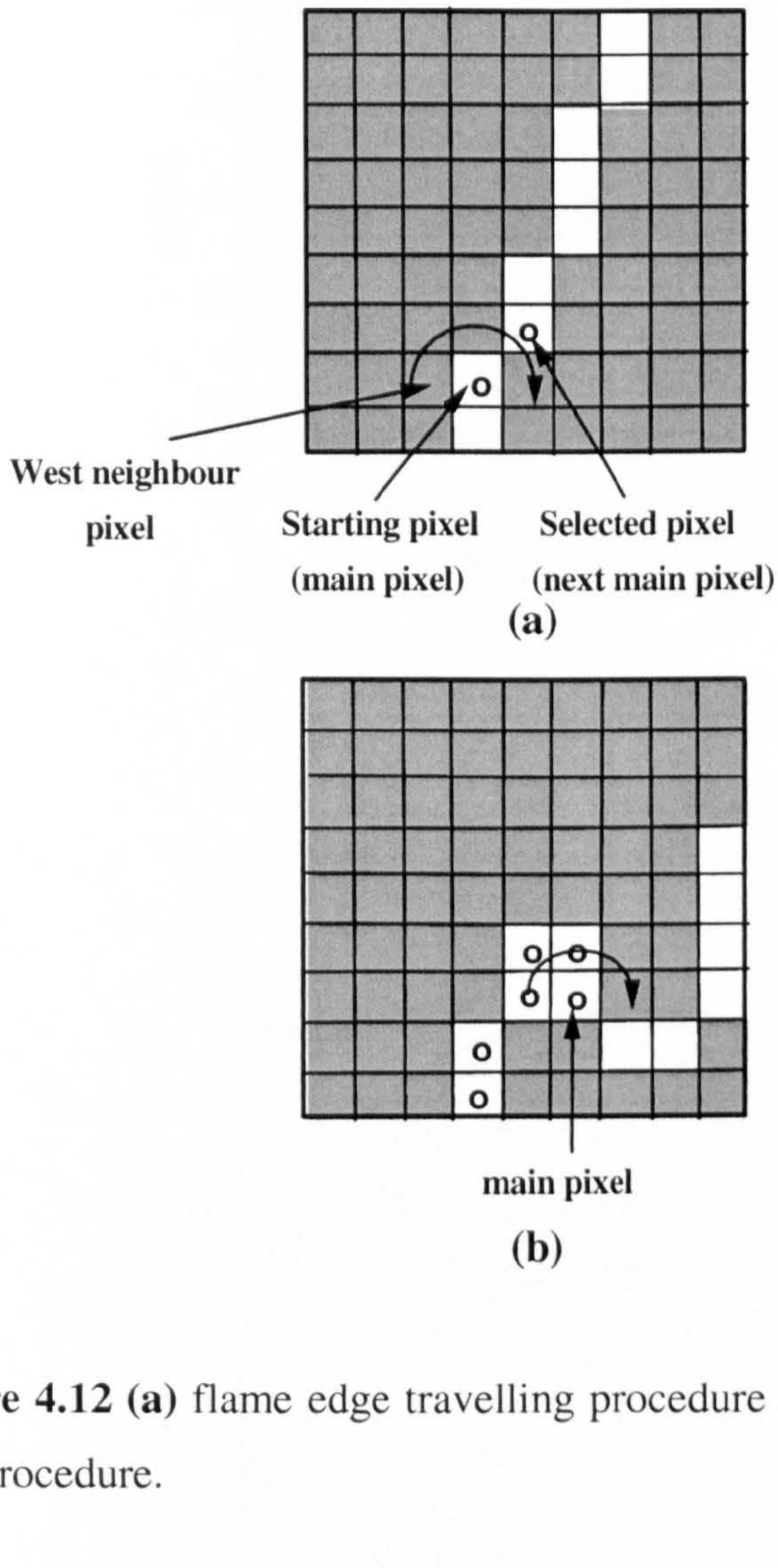

Figure 4.12 (a) flame edge travelling procedure and **(b)** infinite loop problem case of the procedure.

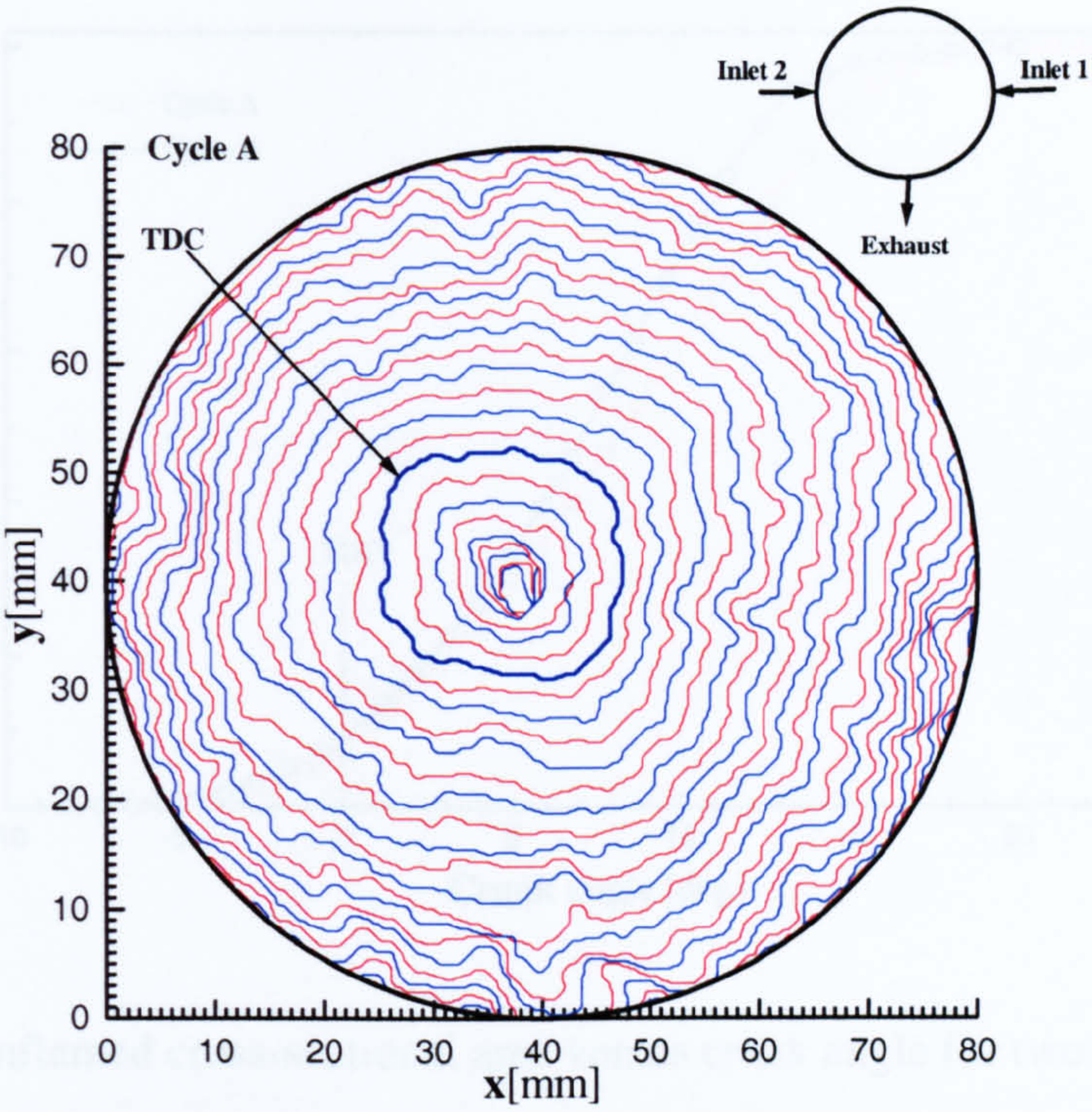

(a)

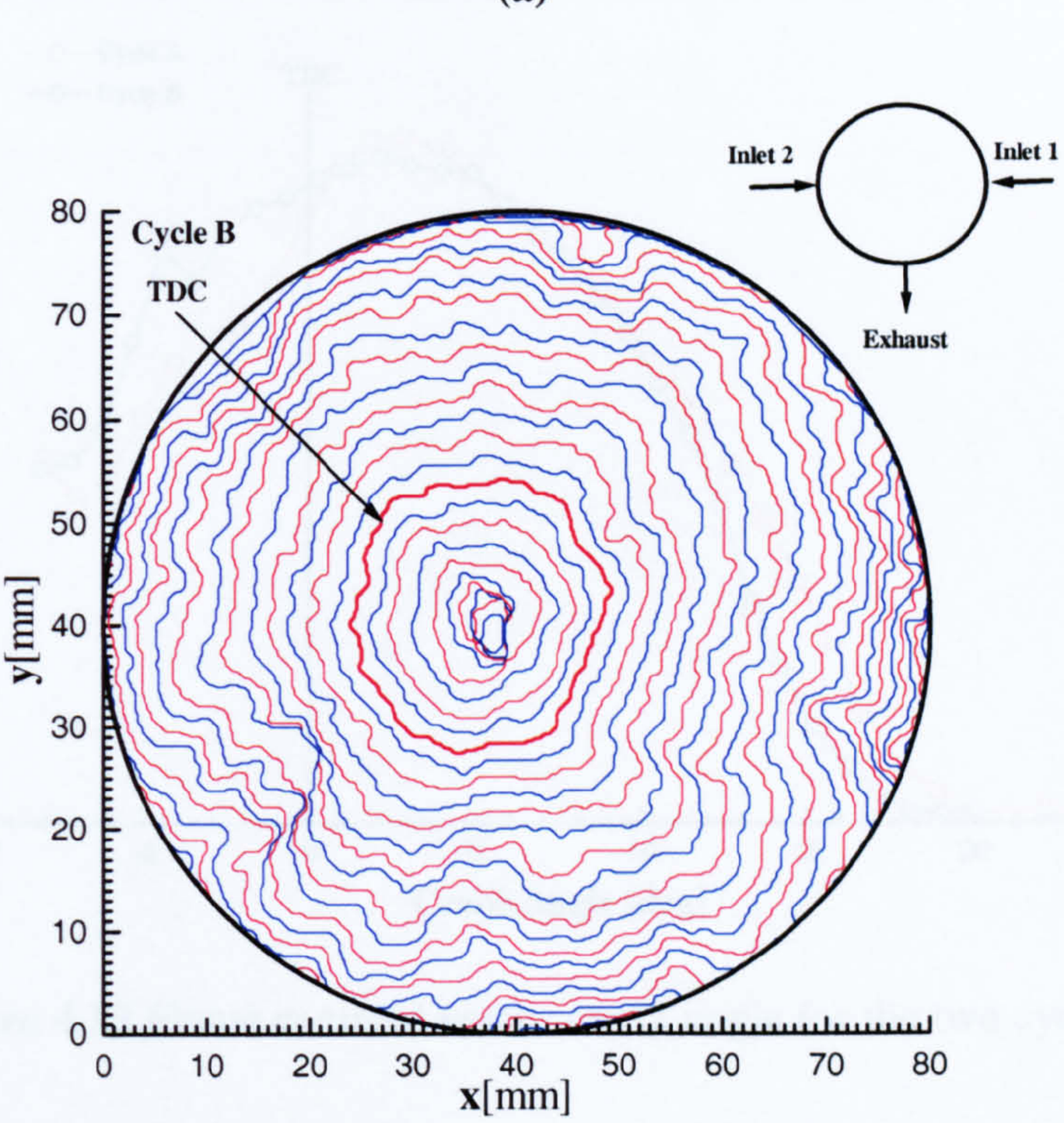

(b)

Figure 4.13 Flame edge positions of **(a)** Cycle A and **(b)** Cycle B.

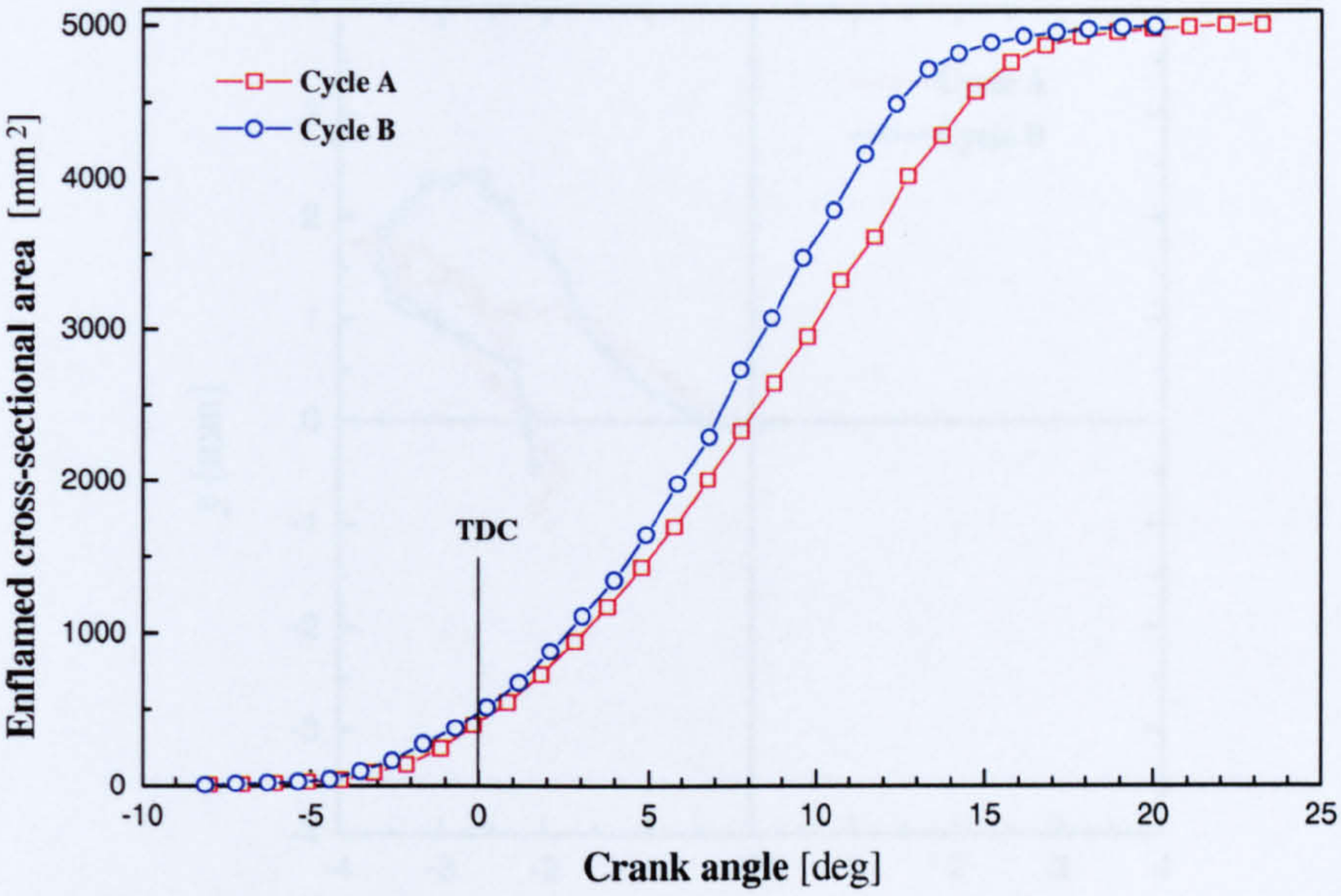

Figure 4.14 Enflamed cross-sectional area versus crank angle for two typical cycles.

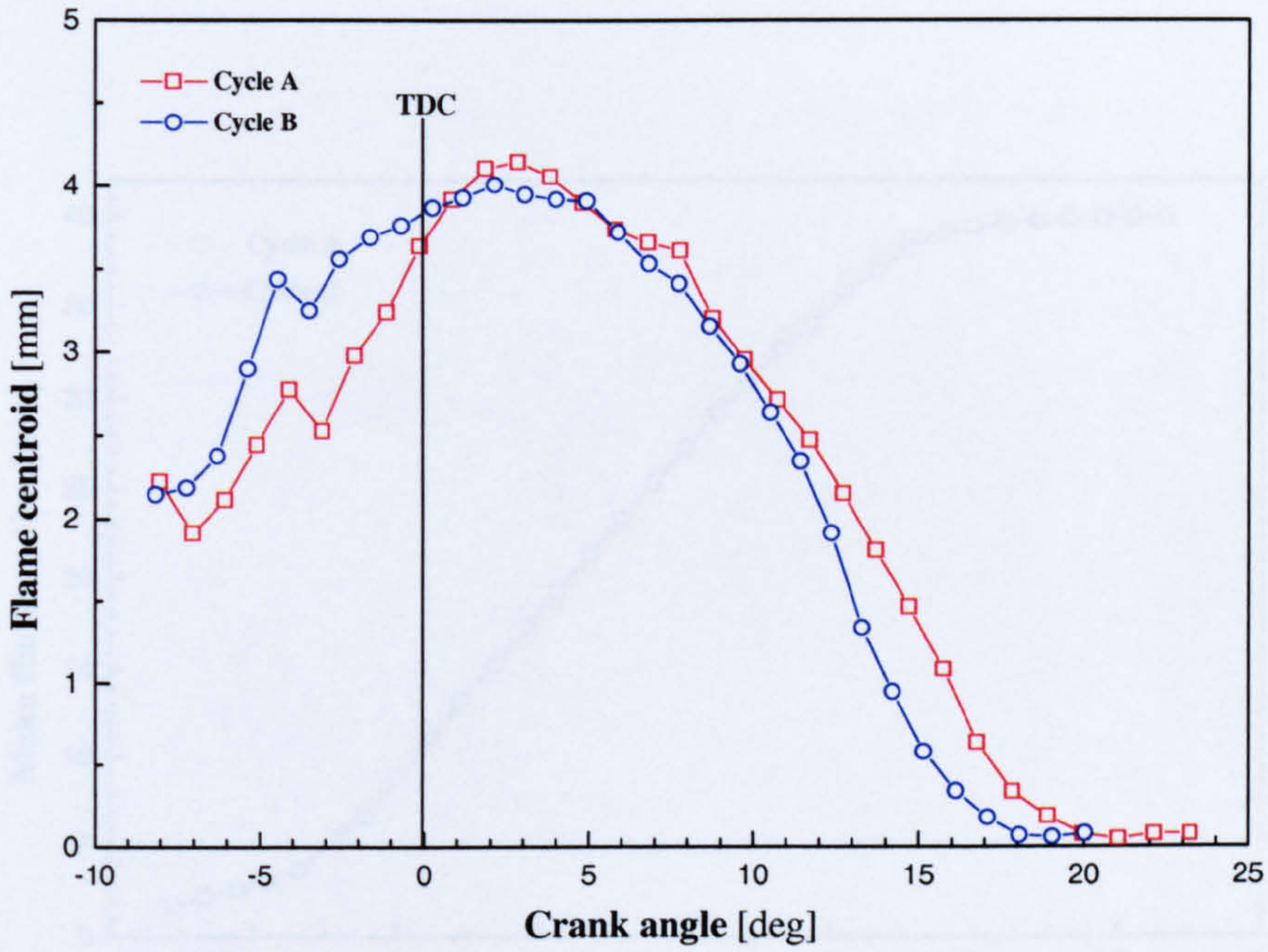

Figure 4.15 Flame centroid versus crank angle for the two cycles.

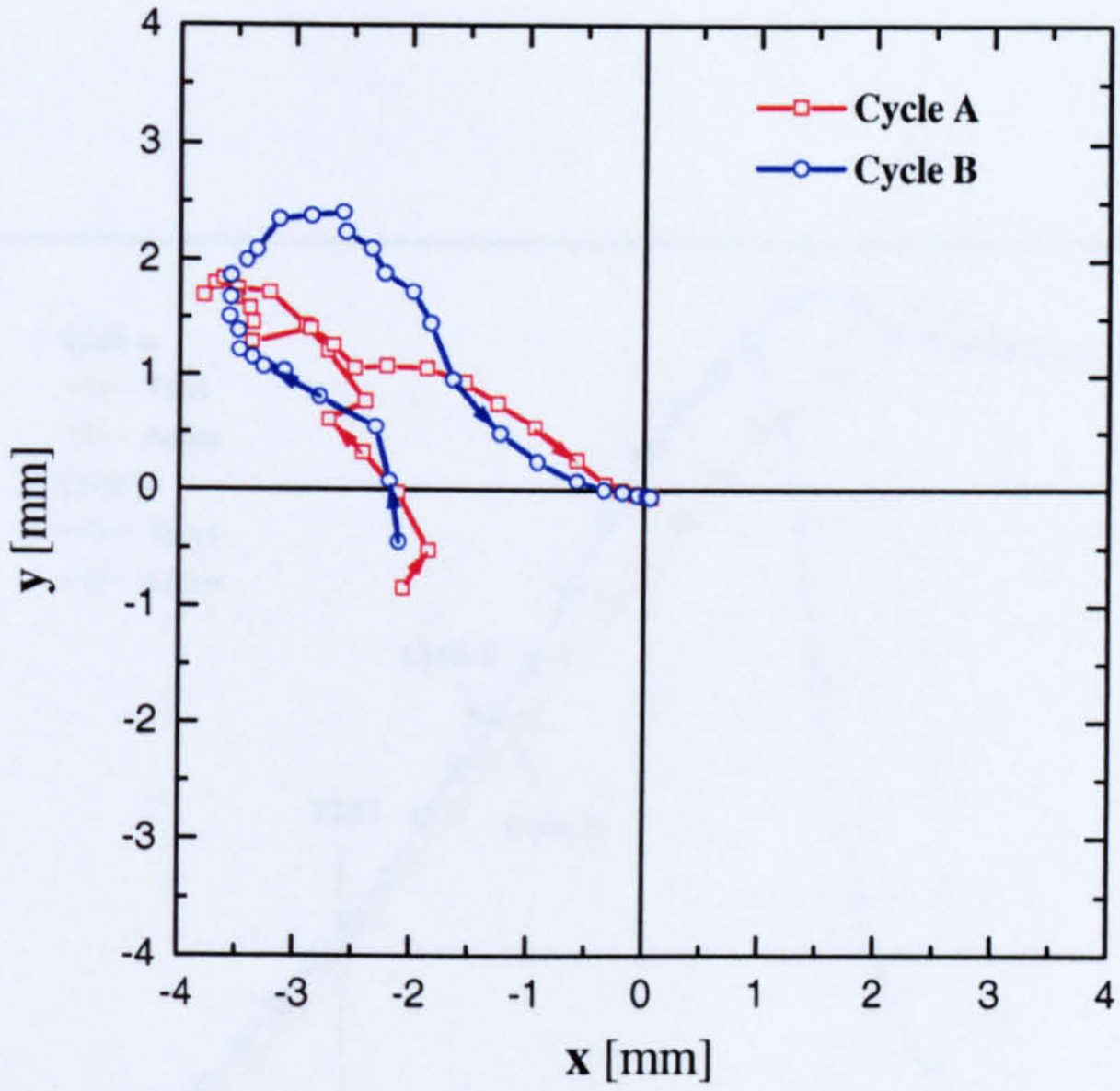

Figure 4.16 The locus of flame centroid over propagation period for the two cycles.

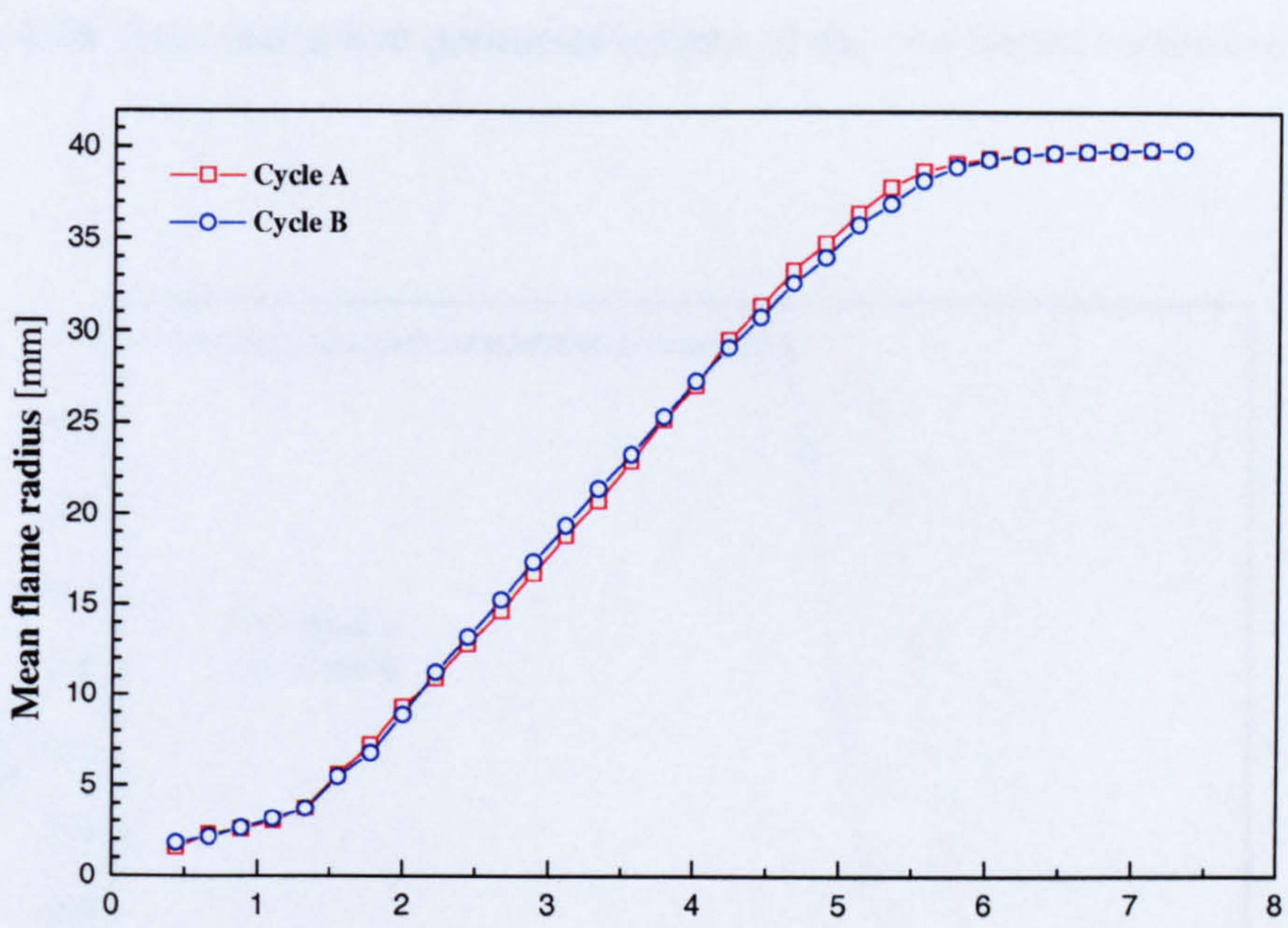

Figure 4.17 Mean flame radius versus the elapsed time from ignition for the typical cycles.

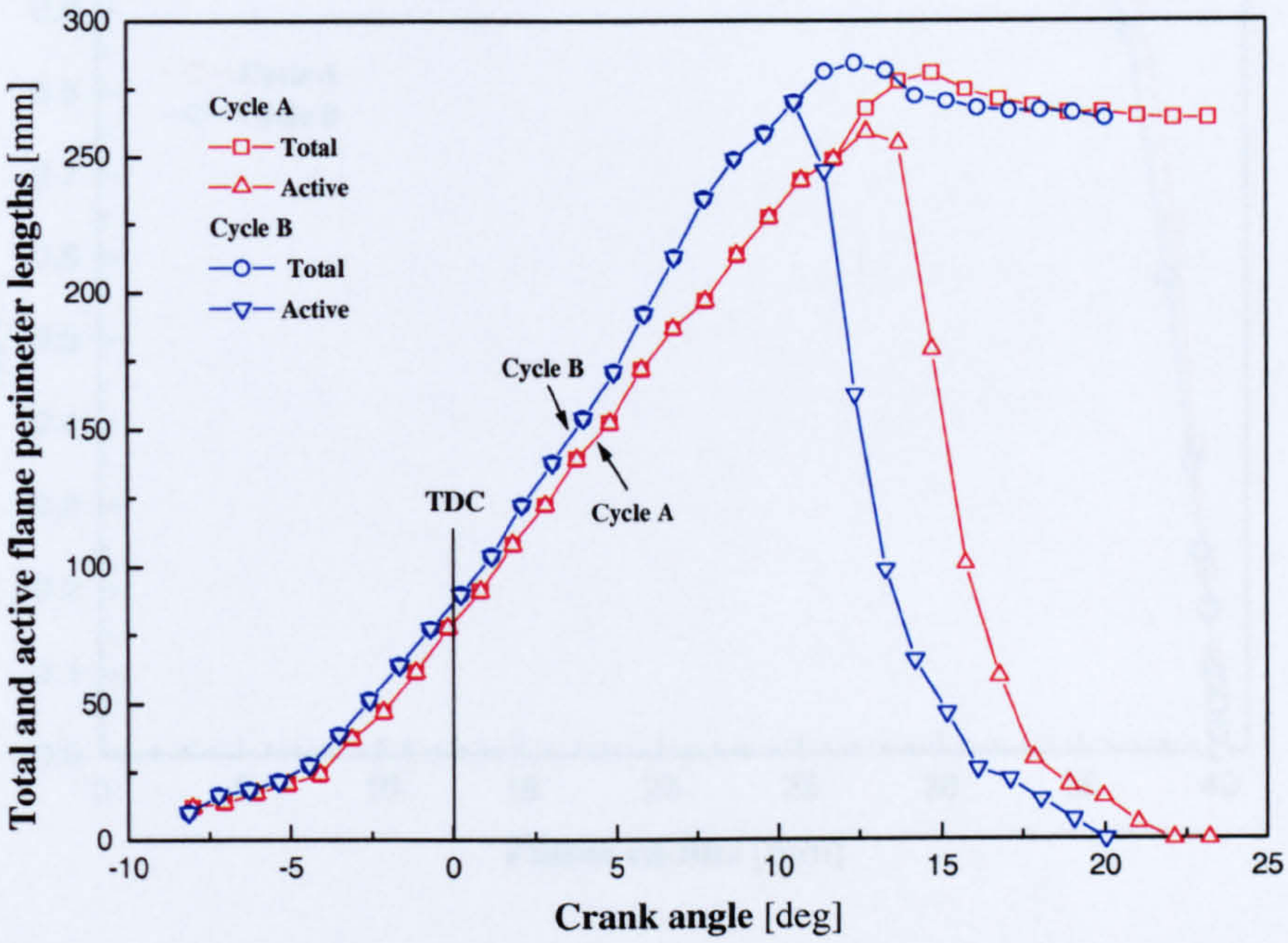

Figure 4.18 Total and active perimeter lengths of the two cycles versus crank angle.

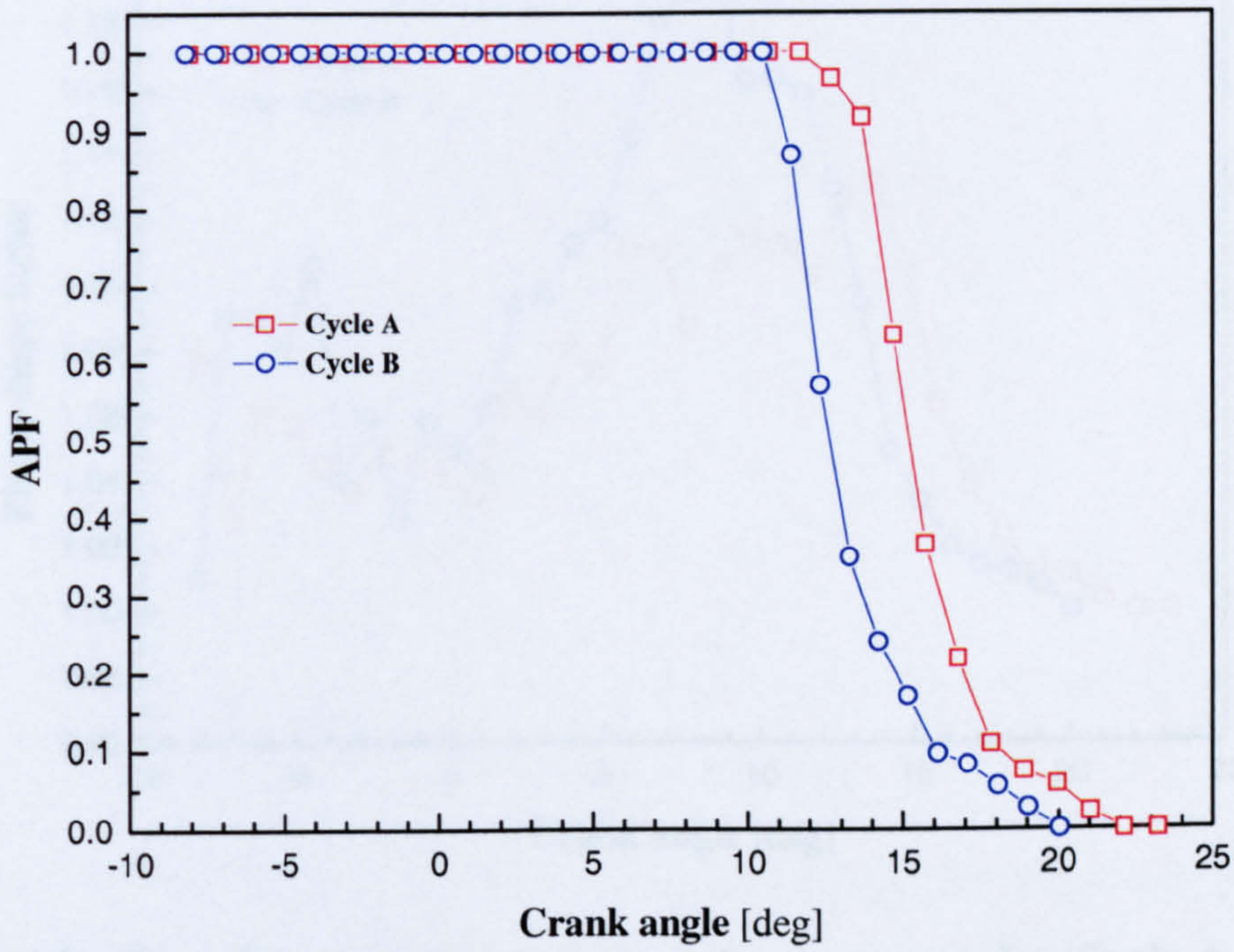

Figure 4.19 Active perimeter fraction versus crank angle for the two typical cycles.

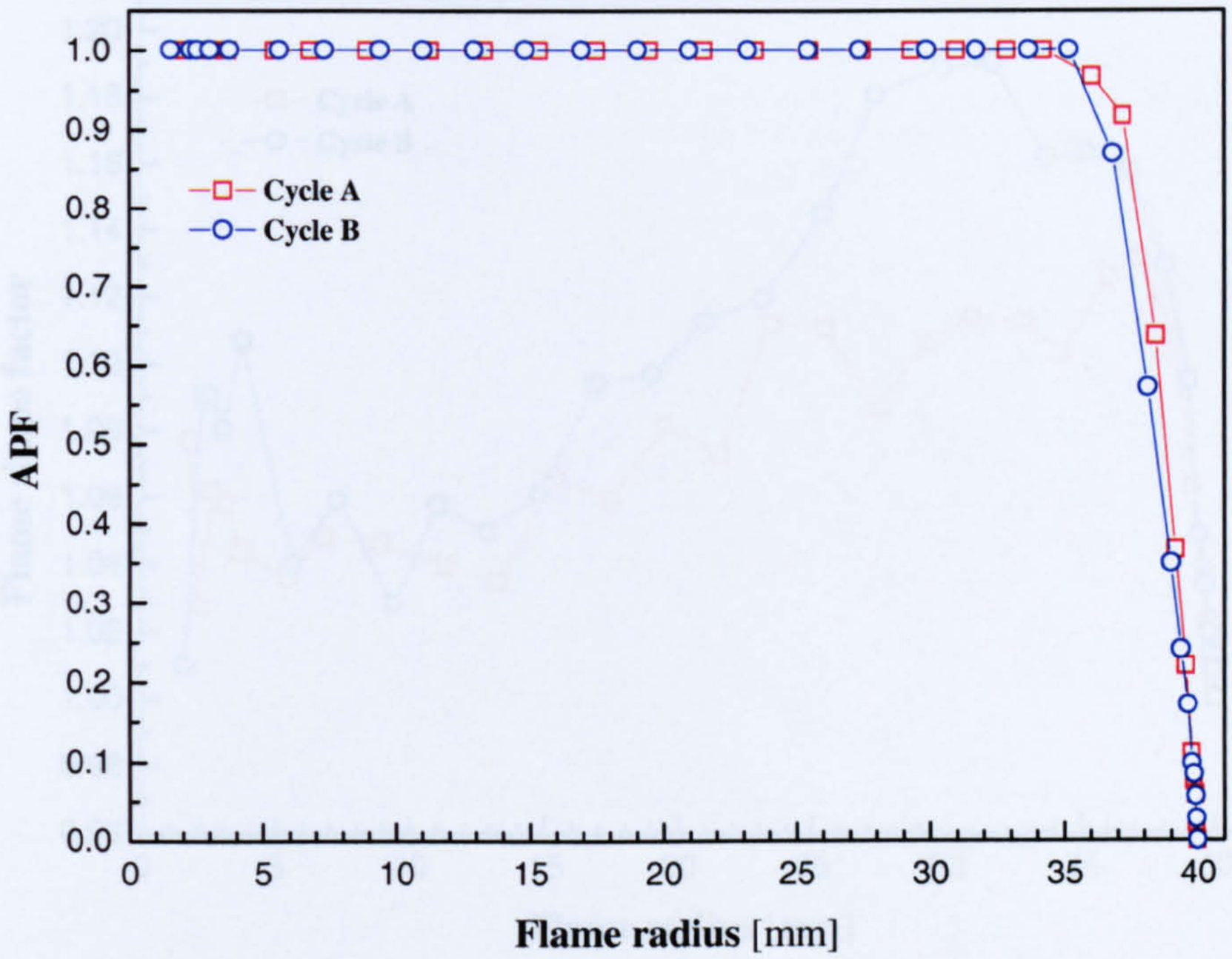

Figure 4.20 Active perimeter fraction versus flame radius for the two cycles.

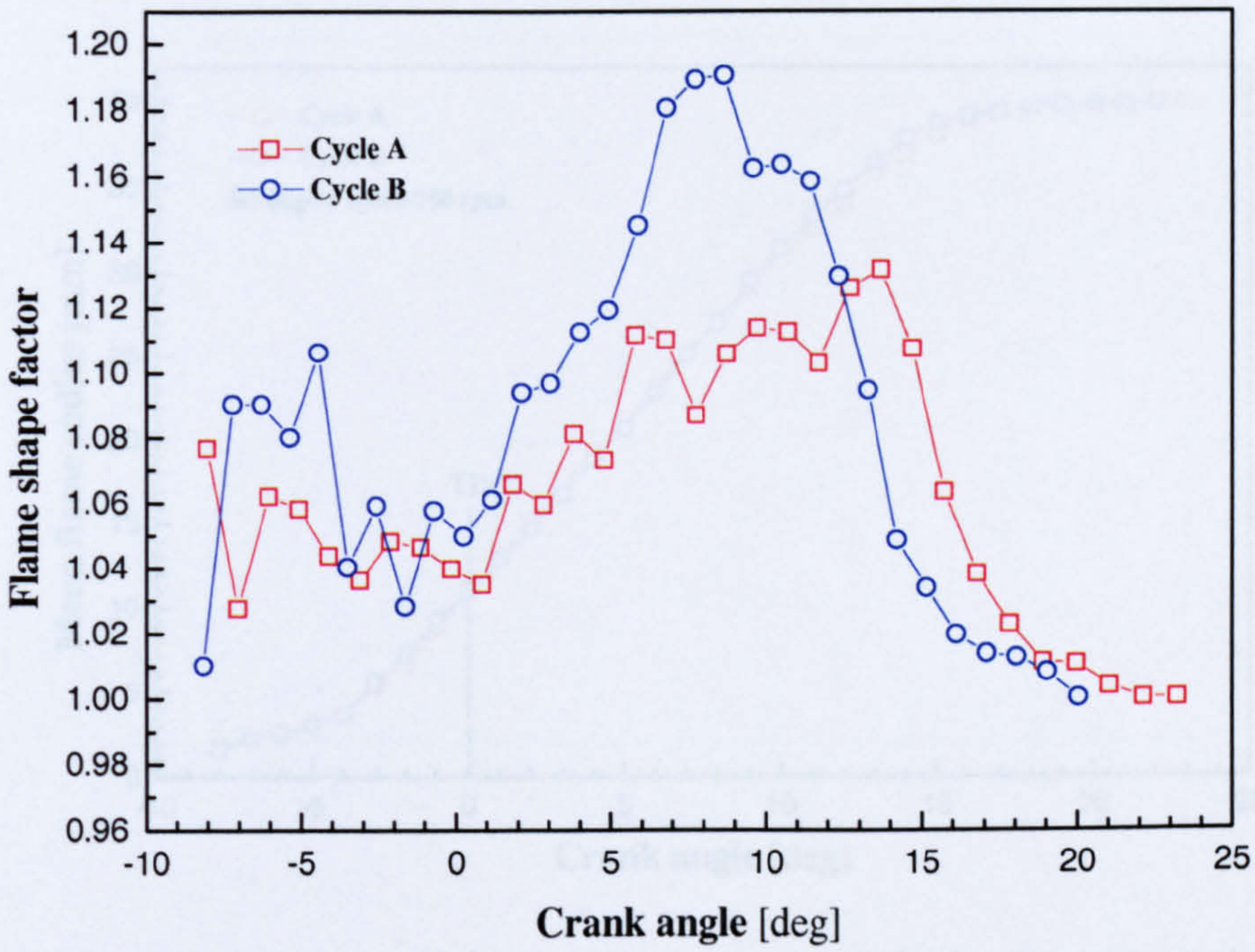

Figure 4.21 Shape Factor versus crank angle for the two cycles (Cycle A and Cycle B).

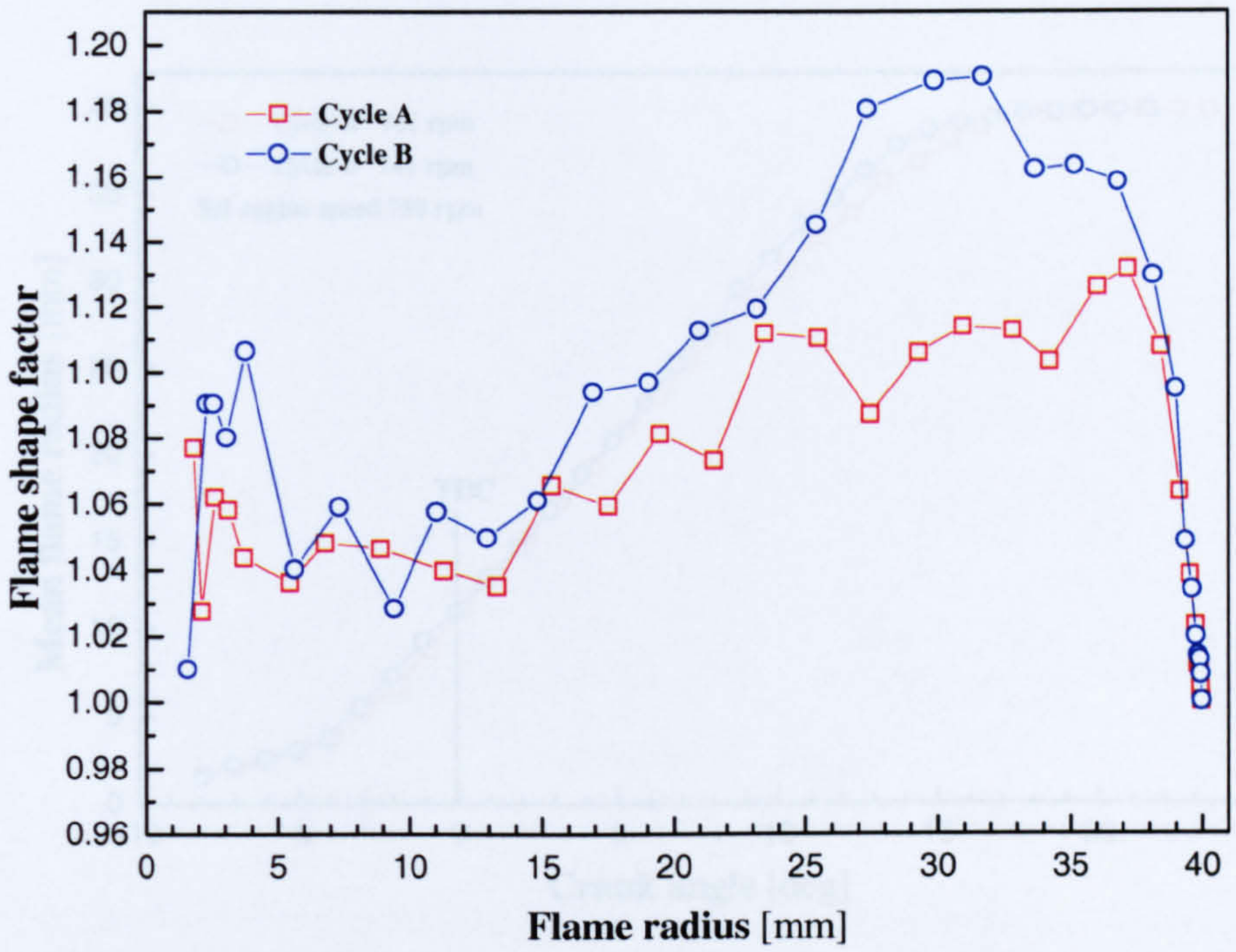

Figure 4.22 Flame shape factor against flame radius for the two cycles (Cycle A and Cycle B).

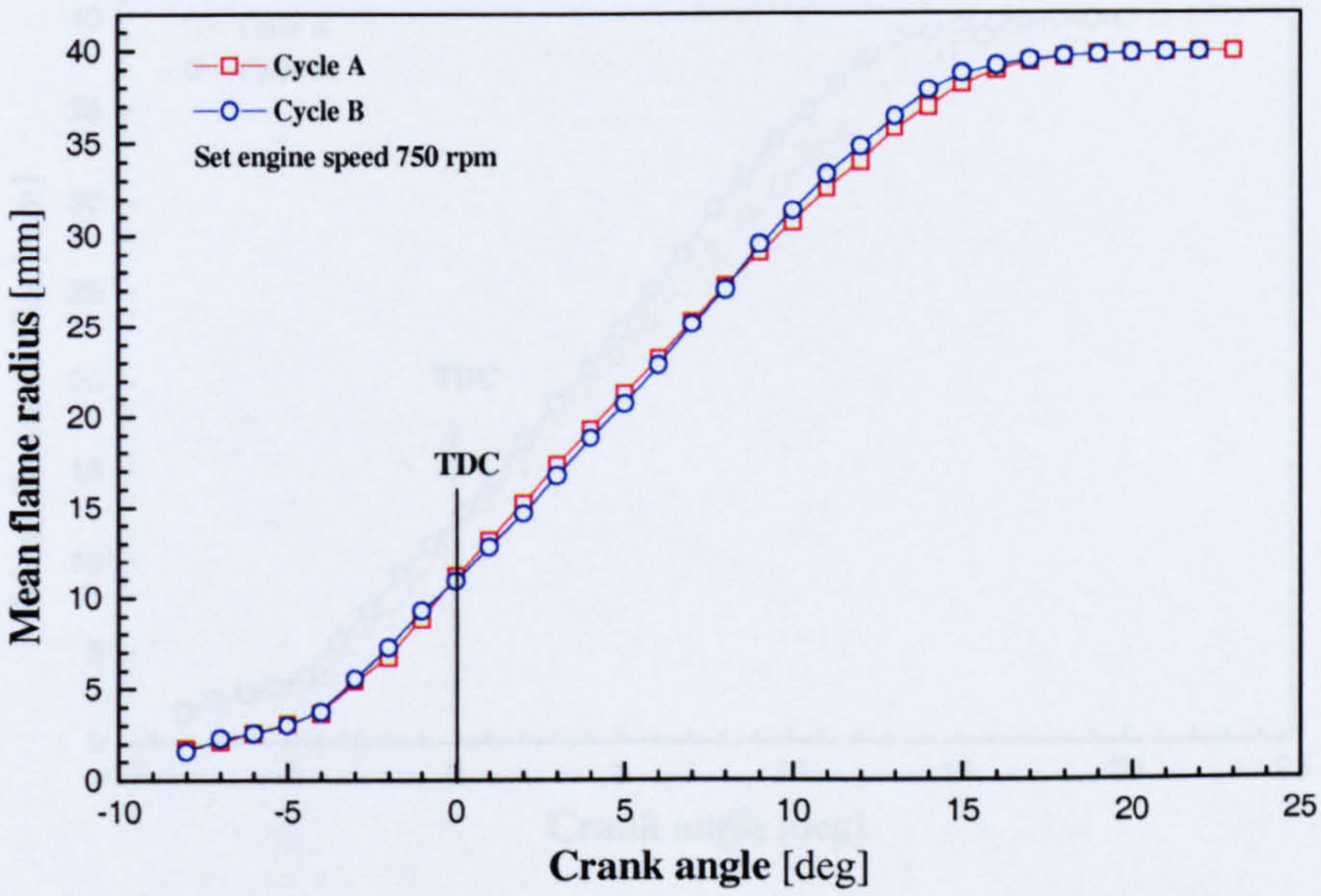

Figure 4.23 Mean flame radius in terms of crank angle for the two typical cycles, using the uniform set engine speed assumption.

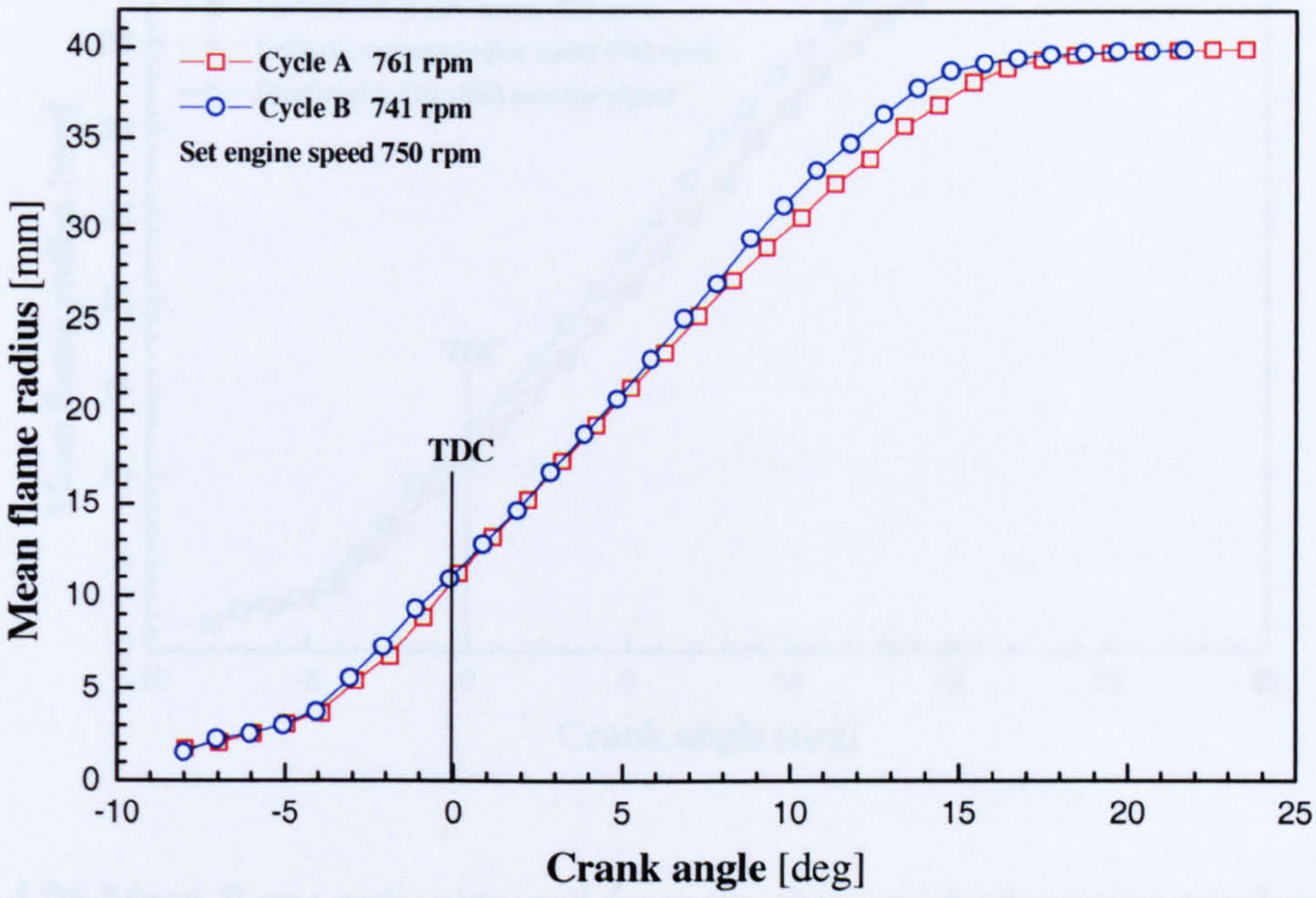

Figure 4.24 Mean flame radius versus crank angle for the two cycles, using the average engine speed of the cycles concerned.

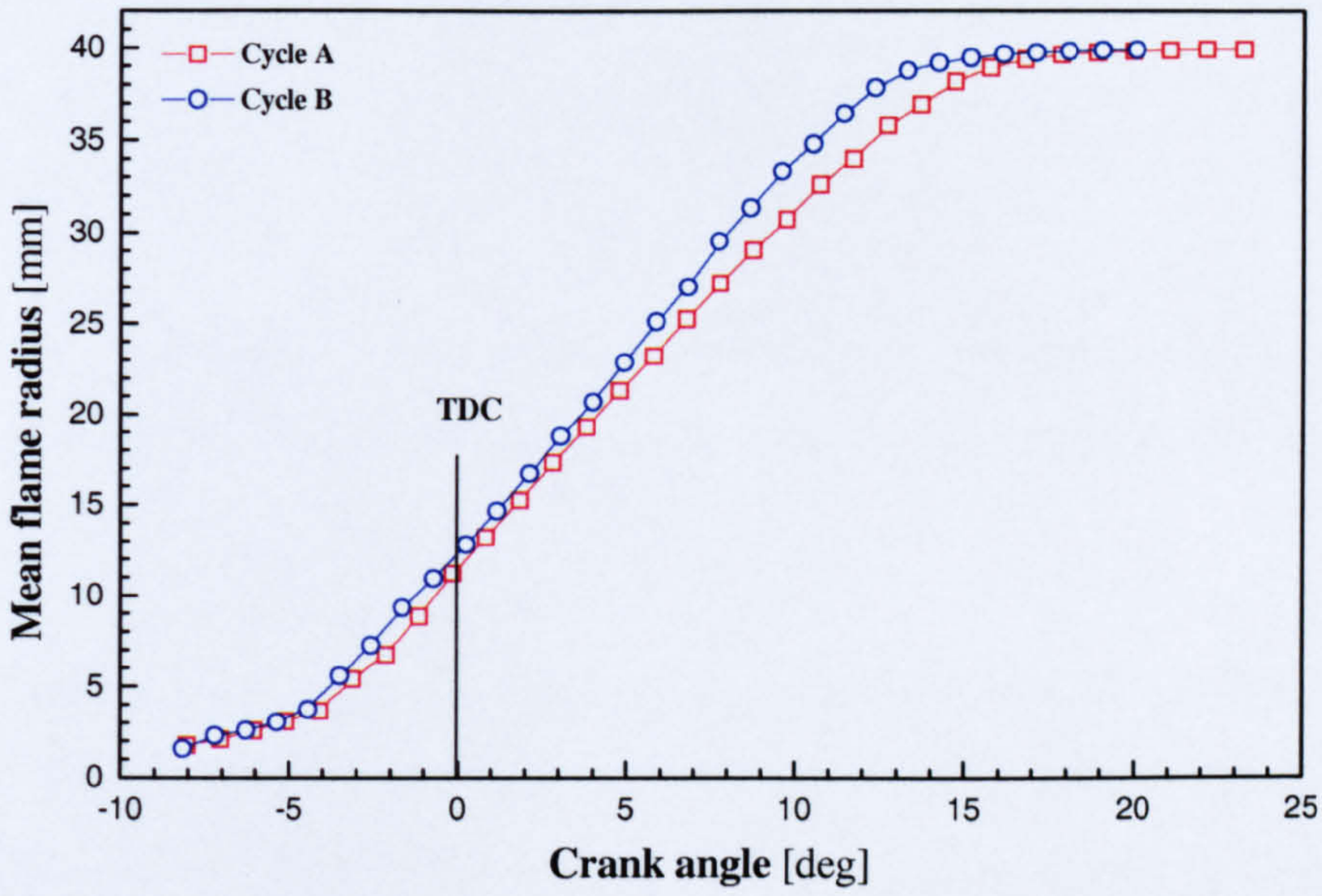

Figure 4.25 Mean flame radius versus crank angle for the two typical cycles using external clock data.

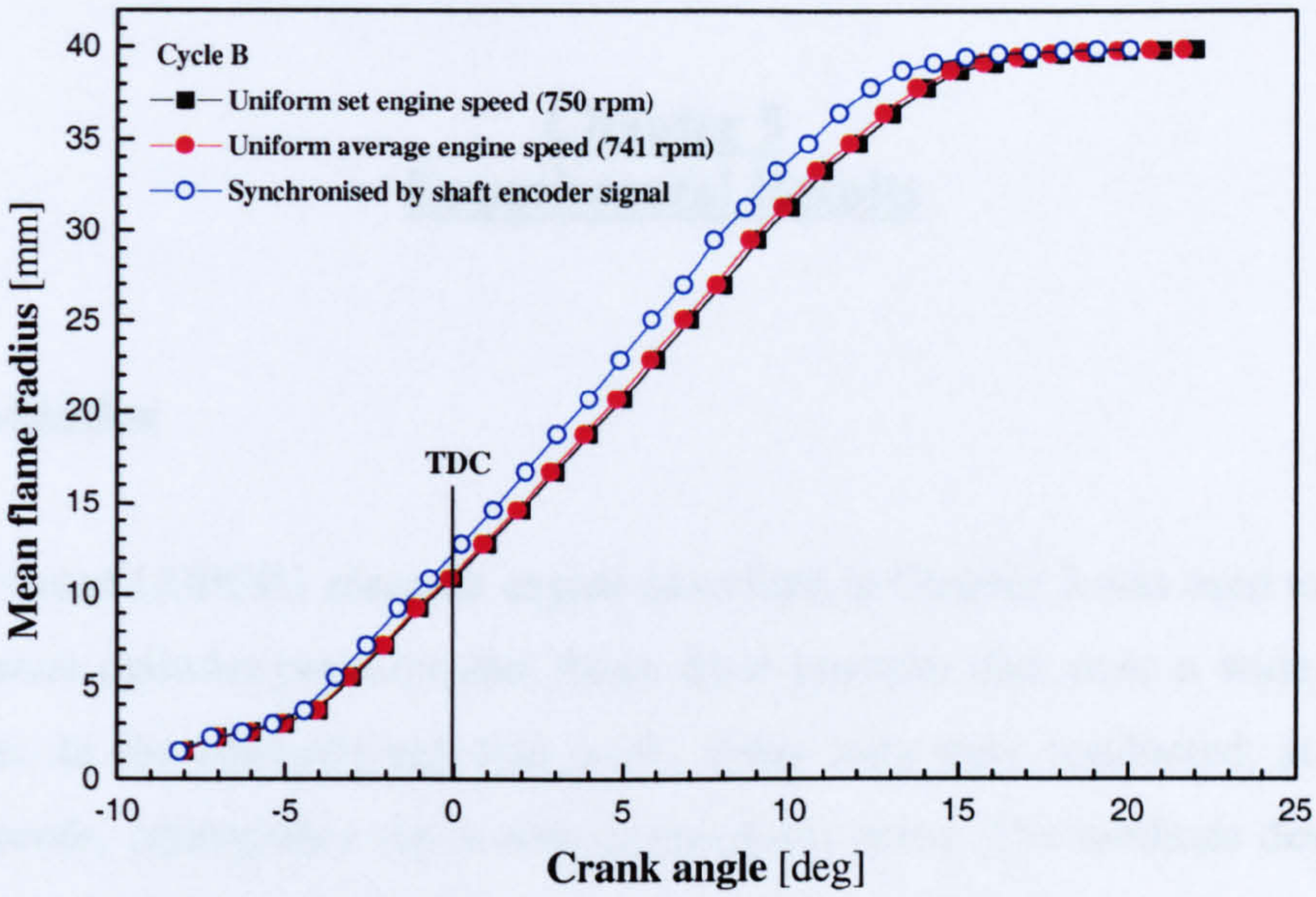

Figure 4.26 Mean flame radii obtained from the three methods versus crank angle for Cycle B.

Chapter 5
Experimental Results

5.1 Introduction

The JLO based LUPOE1 research engine described in Chapter 3 was used to generate simultaneous cylinder pressure and flame front position data over a wide range of conditions. In the currently reported work, many tests were conducted; at different engine speeds, equivalence ratios and compression ratios. The methods described in Chapter 4 were used to process the extensive experimental database.

To take advantage of previously performed research on the engine (useful to supplement the currently reported work), a reference (or base) condition was selected. This condition and the newly obtained results are detailed in Section 5.2.

Three engine speeds (with nominal values of 750, 1500 and 2000 *rpm*) within the operating range of the engine/dynamometer were adopted to examine the effect of engine speed on engine combustion and flame features. The results obtained are detailed in Section 5.3.

The effects of equivalence ratio (lean, $\phi = 0.8$, stoichiometric, $\phi = 1.0$, and rich, $\phi = 1.1$) and compression ratio (7.6, 10.2 and 12.4) are described in Sections 5.4 and 5.5, respectively.

During data processing, it was found that the engine speed varied significantly within a cycle. This variation was recognised to be important in synchronisation of time dependent variables (such as filming) with crank angle (discussed in Chapter 4). It was also necessary to take this into account in providing accurate experimental conditions for model validation purposes (Chapter 7). These LUPOE1 engine speed variation data were compared with equivalent data for the School's Ricardo E6 single

cylinder four stroke engine and for a production VW 1.4 litre four cylinder four stroke engine (VW "standard engine" – VWSE). The findings are detailed in Section 5.6.

Finally, the overall conclusions of the experimental results are summarised and discussed in Section 5.7.

5.2 Reference condition

To study the effects of different parameters on engine combustion, in both experimental and modelling studies, it is often useful to compare performance with that at some "reference" condition. After reviewing investigations conducted by previous research students at Leeds using the central ignition option of the LUPOE1 engine [Lee (1995), Gillespie (1998) and Cairns (2001)], it was decided to adopt the conditions set out in Table 5.1 as the "*reference condition*" for the currently reported study.

Table 5.1 Reference operating conditions.

Compression ratio	**7.6**
Equivalence ratio	**1.0**
Engine speed	**1500 rpm**
Ignition timing	**20^{o} bTDC**
Intake air flow rate	**6.9 gr/sec**
Type of fuel	**Iso-octane**

5.2.1 Cyclic variation

At the reference condition, data for 170 filmed and non-filmed cycles were captured, in four sets over a one year period. Slight set-to-set variation was observed in mean peak pressure and mean crank angle position for occurrence of peak pressure. This was associated with increased leakage due to cylinder-piston-ring wear, which was greater than normal as the engine was generally operated without proper lubrication for filming purposes. For examination of cyclic variation at the reference condition, 65 filmed firing cycles together with 35 non-filmed (pressure record only) cycles captured during the same relatively short time period were considered. The cylinder

pressure records (versus crank angle) for these 100 cycles are shown in Figure 5.1, with the ensemble averaged pressure record highlighted by the thick red line. A degree of electrical noise in some pressure signals, associated with the spark, is apparent at the ignition timing. The small scatter before and just after ignition, is associated with cyclic variation in products from previous cycles, ignition and pressure referencing errors. It can be seen that this scatter (cyclic variation) gets bigger from $10^{\circ} CA\ bTDC$, with a spread of 17.1 *bar* at $14^{\circ} CA\ aTDC$; dropping to an approximately constant spread of about 2 *bar* for the bulk of the expansion period. In the graph a few representative crank angle positions have been highlighted by vertical lines; these correspond to positions where histograms of cylinder pressures were generated to describe cyclic variation (detailed in Section 5.2.2).

Set out in Figure 5.2 is a plot of peak pressure versus the corresponding crank angle for that peak for the 100 cycles considered previously and that value of ensemble averaged cylinder pressure (described in Section 5.2.2). It shows an approximately linear relationship, with the peak pressure dropping the further the corresponding occurrence position from TDC. Slow cycles have longer combustion duration with more mass burning further from the TDC position, where change in cylinder volume by piston motion is significant. This results in low peak pressure, occurring far from the TDC position (for fast cycles the situation is vice versa). In the graph a few middle, fast and slow filmed cycles (defined in Section 5.2.3) have been highlighted by the use of colour. Based on the peak pressures and corresponding crank angle positions, standard deviation, mean value and coefficient of variation (in the form of percentage) were evaluated for the cycles; these are given for the reference condition in Table 5.2.

Table 5.2 Standard deviation (σ), mean value (μ) and coefficient of variation COV for the reference condition.

$CR = 7.6 /\ \phi = 1.0 /\ 1500rpm /\ \ IT = 20^{\circ} aTDC$			
	μ	σ	COV (%)
$p_{max}\ (bar)$	($\overline{p}_{max}$ =) 33.9	2.4	7.1
$\theta_{P_{max}}\ (^{\circ} CA)$	18.7 ($aTDC$)	2.5	

An attempt was made to find a "real" individual cycle matching the calculated ensemble averaged pressure record (highlighted in Figure 5.1) to use for model validation purposes; however, no such cycle could be found; i.e. the ensemble average cycle was representative of no true individual cycle. Therefore, it was decided to examine different definitions of "central" or "typical" experimental cycles; this is detailed in the following section.

5.2.2 "Typical" cycles

In the literature for a set of cylinder pressure data captured at the same operating conditions, a mean pressure-crank angle record derived from ensemble-averaging of the cylinder pressure set at any crank angle is often adopted. Although the derived data provides identical indicated mean effective pressure (*imep*) to mean *imep* of the cycles in question, it has been seen that it can be difficult to find a real cycle having a very similar pressure trace to the ensemble averaged one. From Figure 5.1 it can be seen that there is a smoother curvature around the peak pressure position for the ensemble average pressure than for individual cycles. The point in Figure 5.2 corresponding to the ensemble averaged cycle is towards the lower edge of the spread of peak pressures at that crank angle for peak pressure. It therefore seemed unjustified to adopt the ensemble averaged pressure record to use as the representative cycle for the dataset for model validation purposes, when the basis of comparison was to be with both in-cylinder pressure and simultaneous flame front position.

There are three parameters commonly used to express the "centre" of a set of experimental data: mean, mode and median (Stroud et al., 2001). Mean applies to the arithmetic mean of a data set; in the current case, the ensemble average of pressure recorded at a given crank angle for a number of cycles, Figure 5.3. The mode is defined on the basis of the highest frequency class and its neighbour classes in data frequency histograms. The median divides the frequency histogram into two equal areas. A Fortran program was written by the current author to find these central values of pressure at any crank angle. For the filmed and non-filmed cycles at the reference condition, 11 classes were used to construct a histogram for pressure variation at any given crank angle. Since the mode is sensitive to the number of classes and can easily

jump from class to class in abnormal frequency distributions over combustion period, an unstable result was obtained in terms of crank angle.

Data at a few particular crank angles (illustrated in Figure 5.1) were examined. Set out in Figure 5.4 are histograms showing the distributions in pressure at given crank angle positions, together with the mean, median and mode values in the histograms. On each histogram, pressure range, class width, standard deviation and coefficient of variation (COV_p, in the form of percentage) are displayed. Illustrated in Figure 5.4(a) is a relative frequency histogram of pressure data at $2^\circ CA$ before ignition. This graph illustrates the cyclic variation in cylinder pressure before combustion. These variations result from combinations of cyclic variations in "turbulence", inlet temperature, EPC timing pressure, equivalence ratio, and residual gas; as well as any contribution due to pressure and crank angle referencing errors. By definition, mode and median values are very close and the mean value is slightly lower; all are located in the highest frequency class. Shown in Figure 5.4(b) is the relative frequency histogram at the TDC position. The overall shape approximates a normal distribution and the mean/median/mode values are very close together [but note the rather greater range of pressure values c.f. Figure 5.4(a)]. Set out in Figure 5.4(c) is the relative frequency histogram at $10^\circ CA\ aTDC$. The frequency distribution is now skewed towards the lower limit of the range. The mean and median are within one class whereas the mode locates in the left neighbour class; with the mean > median > mode pressure. The corresponding frequency histogram at $14^\circ CA\ aTDC$ is set out in Figure 5.4(d). Here, the distribution is close to normal and there are two mode values. The mean, median and one of the modes pressures locate in the middle class, with values very close to each other. The relative frequency histogram at $18.2^\circ CA\ aTDC$ (that crank angle yielding peak mean and median pressure attained for the set cycles) is shown in Figure 5.4(e). The distribution is skewed towards higher values, since the pressures of those cycles burning with close to average speed are reaching peak values not dissimilar to those of fast (and higher peak pressure) cycles having passed their peak pressure. The mean, median and mode pressures are located in different classes, mode > median > mean (with the latter most affected by slow cycles). Set out in Figure 5.4(f) is the corresponding histogram at $30^\circ CA\ aTDC$, fairly late in the

combustion event. One can note a return to a fairly normal distribution, with the values of mean, median and mode pressures close to each other.

A "mean" cycle, having the mean (of the distribution) pressure at any crank angle, can be considered as a representative cycle when the frequency distribution in the pressure range is close to normal throughout. However, Figure 5.4 suggests significant changes in frequency distribution over the combustion period. This may lead to an average cycle composed of pressure values at any crank angle being far from any real cycle occurring in the distribution. Therefore, it may be invalid as a representative cycle of a set, for model validation purposes.

A median cycle, with the median (of the distribution) pressure at any crank angle, will yield a value very close to the central one at any given crank angle if the distribution of frequencies in the corresponding class is uniform. However, the continuity of the median pressure versus crank angle diagram depends on the number of frequency occurrences in the median class.

Hence, it was decided to adopt the individual filmed cycles having peak pressure value close to the mean peak pressure, $\overline{p}_{\max}$, highlighted in Figure 5.2, as the "typical" or "representative" cycles for the dataset. The cylinder pressure versus crank angle for the selected "middle" cycles associated with ensemble averaged and motoring cycles are shown in Figure 5.3.

5.2.3 Analysis of representative middle, fast and slow cycles (at reference condition)

To examine the flame features of a set of data and check the compatibility of pressure and film data, a few middle, fast and slow cycles were selected for analysis. From the 100 cycles at the reference condition (Figure 5.1), four filmed cycles having peak pressure close to the mean peak pressure ($\overline{p}_{\max}$) were considered as middle cycles. Based on cycle peak pressure, the four highest and lowest filmed cycles (within the range $\overline{p}_{\max} \pm 2\sigma_{P\max}$) were selected as representative of fast and slow cycles, respectively. The corresponding positions of the selected middle, fast and slow filmed

cycles associated with that of ensemble averaged cylinder pressure have been highlighted in Figure 5.2 ($p_{max} - \theta_{Pmax}$ graph). The features of the cycles are detailed in the following Sub-sections.

(i) Middle cycles

Shown in Figure 5.5 are successive flame front positions for the four middle cycles, Cycles B1-B4. Corresponding pressure-crank angle and mean flame radius-crank angle diagrams for these cycles are set out in Figures 5.6 and 5.7.

Although these cycles have similar overall performance, they have significant differences in flame development. This is highlighted in the development of flame shape factor (the parameter expressing the "circularity" of the flame –Section 4.3.5), Figure 5.8; the movement of the flame centroid (shown as displacement and in the form of loci of successive centroid positions), Figure 5.9; and the active perimeter fraction (APF), Figure 5.10. Most of the parameters are shown both versus crank angle and mean flame radius.

Initial flame development

The random initial displacement of the flame kernels (presumably a function of the local turbulent velocity field at the time of ignition) is quite striking, Figure 5.9. Cycles B2, B3 and B4 can be seen to experience substantial displacements, of 2.5-3*mm* by the time of the establishment of the first analysable flame image, whereas B1 essentially remains close to the spark plug. The centroids can then be seen to migrate randomly, sometimes further away from the plug, sometimes towards it, sometimes remaining fairly stationary and eventually all moving back to the centre late in the combustion event. Cycle B4 experienced rather greater movement than the others. The flame of cycle B1 (with centroid remaining close to the plug) and B4 (which experienced most centroid movement) suffered greatest distortion shortly after ignition, whereas cycles B2 and B3 remained relatively circular, as shown in Figure 5.8. One might expect the more distorted flames (of presumably greater "envelop" flame surface area) to grow faster; however, this seemed not to be the case as the "circular" flame of Cycle B2 exhibited faster growth in mean flame radius than the most "distorted" Cycle B4, Figure 5.6. However, this variation in early flame growth

(to approximately $8^\circ bTDC$) was not reflected in the cylinder pressure, Figure 5.7 – presumably because the mass of fuel burned (and associated heat release) was rather small in each case, such that pressure rise was also small. For a short period before TDC, the pressure development for the initially "circular" Cycle B2 reflected the faster development of mean flame radius, Figure 5.6 – however, by the crank angle of $1^\circ bTDC$, the Shape Factor (Figure 5.8) was similar for all four cycles. This similarity at greater flame radius presumably reflects a greater flame dimension, capable of being affected by more of the spectra of turbulent eddies (Abdel-Gayed et al., 1984). Nevertheless, up to ~$15^\circ aTDC$ (and close to development of peak pressure), pressure and mean flame radius developments were remarkably similar for the four cycles – in spite of the substantial differences in flame distortion and displacement.

Late flame development

There was rather greater variation in pressure development relatively late in the cycles (after ~$15^\circ aTDC$), when the mean flame radius was within a few millimetres of the wall – when it should be noted, nevertheless, that there was a substantial amount of unburned mixture remaining (note the difference in density between burned and unburned gas, greater incremental increase in cylinder volume with increment in flame radius and possible 3-D effects not shown in 2-D projections of the flame). Cycle B4 experienced lower peak pressure and sooner occurrence, Figure 5.7; this reflects the greater distortion, Figure 5.8, and flame centroid displacement, Figure 5.9(b), causing a lower active perimeter fraction during the later stages of flame propagation, Figure 5.10(b).

(ii) Fast and slow cycles

A similar full analysis of four typical "fast" and "slow" cycles was undertaken. The full data sets are available in a School Technical Report (Abdi-Aghdam, 2003); for conciseness, only selected diagrams are shown here.

Pressure and flame radius development

Set out in Figures 5.11 and 5.12 are pressure-crank angle and mean flame radius-crank angle diagrams for the "fast" (F) and "slow" (S) cycles, c.f. those for the "middle" (M) cycles shown previously.

Significant differences in peak pressure (~37.5, 33.5 and 30.5 *bar*) and crank angle for occurrence of peak pressure (~14, 18.5 and 22° *aTDC*) are apparent for the typical F, M and S cycles, respectively (Figure 5.11). Similarly the values of mean flame radius for the F, M and S cycle flames reach 39 mm (i.e. approach within 1.0 mm of the bore) at 7, 12 and 15° *aTDC* , respectively (Figure 5.12). The F cycles can be seen to be fast (i.e. exhibit relatively large mean flame radius) throughout the combustion event; whereas differences between typical M and S burn cycles sometimes becomes apparent only later (albeit at small mass fraction burned) in the cycle, Figure 5.12.

In order to obtain some idea of the mass fraction burned corresponding to the pressure developed and mean entrained flame radius achieved at any crank angle, the following expression (Heywood, 1988) for mass fraction burned (x_b) in terms of volume fraction burned (y_b) was invoked:

$$x_b = \left[1 + \frac{\rho_u}{\rho_b}\left(\frac{1}{y_b} - 1\right)\right]^{-1} \tag{5.1}$$

where the ratio of unburned to burned gas density (ρ_u / ρ_b) was taken as ~4. To evaluate y_b, a mean radius ($\bar{r}_r$) corresponding to the that enclosing the entire reacted (or burned gas) was required; rather than the mean radius ($\bar{r}_e$) of enflamed gas (including some unburned gas). The two radii were related by:

$$\bar{r}_r = \bar{r}_e - 2a' \tag{5.2}$$

where a' is the rms deviation of the flame front leading edge from a mean burned gas radius (i.e. $2a'$ equals half turbulent flame brush thickness) – determined from laser sheet imaging, for the same engine, at the reference condition by Gillespie (1998). The corresponding computed values of y_b and x_b for the fast, middle and slow cycles are shown in Figures 5.13(a) and (b). Not surprisingly, the trends for the F, M and S cycles are much the same. However, the curves (particularly for x_b) do highlight the low volume and mass fraction burned values for flames that have spread quite far (high mean flame radius) across the cylinder. Cyclic variations of factors of

approaching 3 are evident in mass fraction burned (MFB) in the early stages of combustion (even at TDC in this case). The method of calculating MFB was preferred to the well known Rassweiler and Withrow (1938) method, given the relatively large leakage of unburned charge from this ported engine.

Flame development characteristics

As in the case of M group of cycles, within each of the F and S groups of cycles there were considerable variations in the shapes (circular or otherwise) of successive flame front positions and in initial movements and subsequent trajectories of the flame centroids. As before, within the F and S groups there was no significant correlation between these characteristics and the rate of pressure/ flame speed development. Shown in Figures 5.14(a) and (b) are the developments in "Shape Factor" (flame "circularity") with crank angle for the various F, M and S cycles. In Figure 5.14(a), as a function of crank angle (or time), the fast burn cycles appear to become more circular sooner; this is deceptive, as the fast cycles inevitably approach the cylinder walls sooner – and it has already been noted that all flames become more circular (with a centroid moving closer to the centre of the cylinder) as they become constrained by the cylinder walls. The true "flame shape" behaviour is more apparent when plotted against flame radius, Figure 5.14(b). Here, no significant difference can be seen between flame circularity and size for F and M cycles. Arguably, on the average, the slow cycles exhibit greater symmetry (Shape Factor nearer to unity) early in combustion event; however, it is clear that some of the M and F cycles are in fact more "circular" than some of the S cycles. It is again stressed that, overall, there was no consistent relationship between flame shape, initial displacement or centroid trajectory and flame growth rate. This has subsequently been confirmed by a colleague adopting close-up Schlieren photography to study initial flame development in the same engine; also, adopting simultaneous natural light and Schlieren cine imaging, he demonstrated remarkable agreement between mean flame radius development using the two techniques (so validating the simpler natural light method adopted here in order to acquire a very large database) [Murad – thesis in preparation].

Set out in Figures 5.15(a) and (b) are values of active perimeter fraction (APF) versus crank angle and mean flame radius respectively for the three sets of four cycles. As seen previously for the M cycles, the values of APF for the F and S cycles fall progressively to zero as the flames (asymmetrically) touch the cylinder wall and less of the flame circumference becomes active for propagation. The values of APF fall sooner for the faster groups of cycles (and also sooner for the faster individual cycles within a group) as the faster burn cycles touch the walls sooner, Figure 5.15(a). However, expressed as a function of mean flame radius (Figure 5.15(b)), the APF profiles were remarkably similar – a fact which later proved most useful in modelling the cycles, Chapter 6.

5.3 Effect of engine speed

The experiments reported in the previous section (for the "reference" 1500 *rpm* case) were repeated for higher (2000 *rpm*) and lower (750 *rpm*) engine speeds at the same equivalence ratio (ϕ=1.0) and compression ratio (CR=7.6); ignition timing was adjusted to yield mean maximum indicated mean effective pressure at each speed ($31^\circ bTDC$ and $10^\circ bTDC$, respectively). Set out in Figures 5.16(a) and (b) are $p_{\max} - \theta_{p_{\max}}$ diagrams for filmed cycles at the higher and lower engine speeds, respectively. As before, those of the selected "fast", "middle" and "slow" cycles are highlighted in the diagrams.

5.3.1 Higher engine speed (2000 *rpm*)

As at the reference condition, four middle cycles displaying pressure development close to the mean peak pressure ($\overline{p}_{\max}$) were analysed in detail; together with "fast" (F) and "slow" (S) groups of four filmed cycles closest to being two standard deviations (based on peak pressure) from the mean peak pressure [highlighted in Figure 5.16(a)]. Shown in Figure 5.17 are the plotted successive flame front positions for the four M cycles. These show considerable cyclic variation but, overall, no discernable differences to those at the "reference" condition (1500 *rpm*), Figure 5.5. Similarly no significant differences were observed between the successive flame

"contours" and flame centroid, initial displacements and centroid loci, for the M, F and S groups of cycles.

Set out in Figures 5.18 (a) and (b), are cylinder pressure and mean flame radius versus crank angle diagrams for the F, M and S groups of four cycles at 2000 *rpm*. In general, the pattern of behaviour proved very similar to that observed at the reference condition, Figure 5.11. As before, the F cycles proved faster throughout (arguably with greater variation within the group at the higher engine speed) and differences in pressure development and flame speed between M and S cycles only become apparent after the initial combustion period.

Variation in flame "Shape Factor" (SF) and "Active Perimeter Fraction" (APF) are shown in Figures 5.19(a) and (b), respectively. As before, Figure 5.14(b), there was no significant correlation between flame circularity and speed of flame development (F, M or S); although SF values were generally similar to those at the reference condition, one or two cycles exhibited rather greater irregularity in shape at the higher engine speed. The APF versus mean flame radius profiles proved very similar to those at the reference condition, Figure 5.19(b) c.f. Figure 5.15.

5.3.2 Lower engine speed (750 *rpm*)

Set out in Figure 5.20 are (a) pressure and (b) mean flame radius versus crank angle diagrams for typical fast (F), middle (M) and slow (S) groups of cycles (selected on the same basis as before) – at this engine speed only two typical cycles per group were fully analysed. The pattern of behaviour proved very similar to that observed previously at 1500 and 2000 *rpm*. Likewise, no striking differences in Shape Factor or Active Perimeter Fraction [Figures 5.21(a) and (b), respectively] were noted.

At the nominal engine speed of 750 *rpm*, it proved rather more difficult to maintain the set speed; in addition, engine speed within a given cycle was more variable, Figure 5.22. This results in variable time increments for a given step in crank angle, as well as possible differences in u' (which is related to mean piston speed, $\overline{u}_p$) which might have been significant when modelling these particular cycles, Section 7.4.1.

5.3.3 Variation of (middle cycle) behaviour with engine speed

Shown in Figures 5.23 and 5.24 are pressure (versus crank angle) and mean flame radius (versus crank angle and time from ignition) diagrams for the M cycles at the three adopted engine speeds. The related maximum flame speed over the propagation period and its occurrence crank angle versus engine speed are set out in Figure 5.25. Significant difference can be seen between the motoring $p-\theta$ diagram at 750 *rpm* and those at 1500 and 2000 *rpm*. The lower motoring pressure for the lower engine speed may be associated with changed performance of the pressurised breathing system (described in Chapter 3) for the ported engine. This resulted in 10% lower cylinder pressure at EPC for 750 *rpm* (vis-à-vis the higher speeds), as well as increased blowby and heat transfer.

During early flame development (until $\bar{r}_f$ ~7 *mm*), insignificant difference can be seen between firing and motoring pressures, Figures 5.23 and 5.24(a), due to very small MFB [see Figure 5.13(b) for the reference condition]. Within this period, the higher engine speed cycles experience slower flame development, Figure 5.24(b), because of greater ignition advance (relative to TDC) resulting in lower laminar burning velocity (predominant in early flame growth). Maximum flame speed over the propagation period was evaluated for the three different conditions; this proved greater at higher engine speed, Figure 5.25.

An increased scatter in magnitude of peak pressure with engine speed is apparent, Figure 5.23; this is confirmed in Figure 5.26, where the scatter (including all recorded cycles, i.e. pressure record only (as well as imaged) and all F, M and S cycles) is expressed in terms of standard deviation ($\sigma_{p_{max}}$, *bar*) and coefficient of variation ($COV_{p_{max}}$, %) in peak cylinder pressure. The values of these increase significantly with nominal engine speed.

Set out in Figures 5.27(a) and (b) are comparisons of Shape Factor (SF) and APF for the M cycles at all three speeds. The SF's can be seen to be very much the same for all engine speeds early and late in the flame propagation; however, at mid flame radius there seems to be a clear trend for increasing distortion from circular flame

shape with increased engine speed. This could be associated with reduced eddy lifetime ($l/u' \propto l/\overline{u}_p$) and possibly may contribute to the noted greater cyclic variation at higher engine speed. As seen before, the consistency of APF behaviour with mean flame radius, Figure 5.27(b), was remarkably consistent.

5.4 Effect of equivalence ratio

The reference test condition experiments (CR=7.6, 1500 rpm and ϕ=1.0) were repeated for a richer (ϕ=1.1) and a leaner (ϕ=0.8) mixture strength [in each case at the optimum (for maximum mean *imep*) ignition timing – 18° and 31° *bTDC*, respectively]. Initially, rather fewer cycles were imaged at each condition (12, plus 12 pressure record only, for the richer and 20 for the leaner condition). Hence, it was not possible to select middle, fast and slow filmed cycles for analysis on a reliable statistical basis (close to mean peak pressure, $\overline{p}_{max}$, and $\pm 2\sigma_{p_{max}}$ from the mean) as in the case of the ϕ=1.0 results. As a result, in the following sections the middle (M_3) cycles were selected as the three showing closest to the mean peak pressure; the fast (F_3) and slow (S_3) groups being the 3 fastest and 3 slowest imaged cycles recorded in the batch of tests, Figure 5.28. When comparing results with the ϕ=1.0 cases, these differences in definitions of F, M and S and F_3, M_3 and S_3 should be borne in mind. A later batch of experiments was conducted in an attempt to extend the rich and lean database – however, although the results showed the same trends in flame progress, kernel trajectories, SF, APF, etc, the peak motoring and firing pressures were noticeably lower (peak pressure by ~4 *bar*). This was associated with excessive ring/cylinder wear caused by extended running with poor lubrication (for filming). Hence, for consistency with the reference condition results, only the first batch of results are shown here.

5.4.1 Rich mixture (ϕ=1.1)

The optimum ignition timing for the rich mixture was 18° *bTDC*. Similarly, the contours of traced successive flame front positions showed the same features; to save

space they are not shown here, but are available in a School Technical Report (Abdi-Aghdam, 2003).

Set out in Figures 5.29(a) and (b) are the usual pressure and mean flame radius versus crank angle data for the three selected fast (F_3), middle (M_3) and slow (S_3) cycles for the rich mixture (ϕ=1.1, at 1500 *rpm*). In each case, there was little departure from the motoring pressure for the first 10° *CA* or so following ignition. The F_3 cycles can be seen to be faster than the M_3 cycles, which were in turn faster than the S_3 cycles, throughout the combustion event. This was contrary to the behaviour at ϕ=1.0, where differences between M and S cycles tended to develop only later in the cycle. As before, no consistent differences in flame centroid displacement, between the F_3, M_3 and S_3 cycles (or the fastest and slowest within a group) was apparent, Figure 5.30(a) and (b). However, the F_3, M_3 and S_3 cycles all appeared to have initial kernel displacements in the first, fourth and second quadrants, respectively [Figure 5.30(b)]. This behaviour may or may not be significant, it is contrary to the random behaviour noted at the reference condition – where rather more cycles were available for analysis. As before, there was no consistent trend in SF [Figure 5.31(a)] and the values of APF [Figure 5.31(b)] fitted the usual pattern.

5.4.2 Lean mixture (ϕ=0.8)

For the lean mixture, ignition had to be advanced by 11° *CA* (to 31° *bTDC*) relative to that at ϕ=1.0 – in order to compensate for rather slower burning. Shown in Figures 5.32(a), (b) and (c) are successive flame contours for selected "fast", "middle" and "slow" cycles. The selection of these diagrams was relatively random (as before, no particular correlation of flame speed with "distortion" was evident), by comparison with earlier diagrams of this nature, the slower flame progress (smaller increment in flame progress in one frame, with camera framing rate constant) is evident.

Although the selection of the three cycles representative of "middle", "fast" and "slow" behaviour was less statistically significant than for the reference condition, a greater degree of variation in pressure and mean flame radius behaviour with crank angle, Figures 5.33(a) and (b), is noticeable. The differences in pressure between the

F_3 and M_3 cycles proved somewhat larger than in mean flame radius; this may be associated with the greater difficulties in properly defining the flame edge for lean mixtures (as flame luminosity was rather lower than for ϕ=1.0). The S_3 flames were noticeably very much slower, Figure 5.33(b).

The graphs of SF and APF for the lean mixture, Figures 5.34(a) and (b), show the usual features.

5.4.3 Variation of (middle cycle) behaviour with equivalence ratio

The greater cyclic variation in cylinder pressure with lean mixtures was referred to above. This is shown more graphically in the form of standard deviation and coefficient of variation of peak pressure with equivalence ratio in Figure 5.35. This correlates with the expected trend in laminar burning velocity for the three mixtures (rather lower for ϕ=0.8 and probably peaking near ϕ=1.1); the higher "natural" burning rate giving the richer flames more resistance to flame straining/stretch for the given turbulence level (likely to be similar in each case, as the engine speed is constant).

The values of SF versus mean flame radius, Figure 5.36(a), can be seen to be similar for the stoichiometric and rich flames, although somewhat larger for the lean mixture over the bulk of the flame propagation. This may reflect the greater time available for the range of turbulent eddies to distort the flame, with the slower burning mixture. The values of APF, Figure 5.36(b), can be seen to be relatively independent of mixture strength, except for the lean case. The extended combustion period has given more time for the turbulence to distort the flame such that towards the end of combustion (after much of the flame perimeter has touched the cylinder wall), hence APF at a given mean flame radius falls – resulting in slow final "burn-out" of the mixture.

5.5 Effect of compression ratio

The results presented to date have been with the engine compression ratio set at 7.6:1. This was to match conditions used by earlier workers at Leeds, selected to extend the life of mirror attached to the piston for Schlieren photography and to maintain a reasonably large clearance height for single and multiple laser sheet mie-scatter imaging (Hicks, 1994; Cairns, 2001). The compression ratio was raised in two steps (to 10.2 and 12.4) to be more representative of modern engine operation, to help promote end-gas autoignition and knock (Murad, thesis in preparation) and to provide an additional condition (of elevated temperature and consequent laminar burning velocity at ignition) for model validation. The modifications were effected by reducing the already quite small TDC clearance height from 7.8 *mm* to 5.8 *mm* and 4.7 *mm*, respectively. This resulted in a very shallow combustion space of relatively high surface area to volume ratio. All other parameters were maintained at the reference condition values (ϕ=1.0, 1500 *rpm* and 20° *bTDC* ignition timing).

5.5.1 Medium compression ratio (CR=10.2)

The optimum, mean *imep*, ignition advance for this condition was 20° *bTDC*. In this exercise, sixteen imaged and eight non-imaged (pressure only) firing cycles were recorded; the associated peak cylinder pressure and crank angle for this peak pressure for these cycles are given in Figure 5.37. As in the case of varying mixture strength, there were insufficient cycles for applying a proper statistical approach to select "middle" cycles close to the mean peak pressure and "fast" and "slow" cycles $\pm 2\sigma_{P\max}$ as the reference case. Hence, as before, three cycles exhibiting typical "middle" (M_3), "fast" (F_3) and "slow" (S_3) behaviour were selected – as shown in Figure 5.37. The corresponding diagrams illustrating successive flame front positions for these cycles are available elsewhere (Abdi-Aghdam, 2003) and their pressure and mean flame radius versus crank angle data are set out in Figures 5.38(a) and (b). In a number of cases, particularly the faster ones, there was a trace of oscillation in the pressure records – indicative of knock. There was no clear evidence of end gas autoignition in the filmed images – although it is possible that very small regions of autoignition may have occurred (very late in the flame propagation) which could not

be resolved at the framing rate used (4500 *fps*). Alternatively, any knock might have been associated with overly fast main flame propagation (Ricardo et al., 1968). The delay from ignition, in departing from the motoring pressure trace was typically $9^\circ CA$ at this compression ratio; rather sooner than at the reference condition ($12^\circ CA$). The faster initial kernel development might be associated with a higher gas temperature at ignition (at the higher compression ratio).

Unlike the earlier cases, here there seems little correlation between early burn behaviour and that later in the combustion event, Figure 5.38(b), and the link between increased pressure development and growth in mean flame radius was less clear. There was no obvious correlation between initial kernel displacement and flame centroid locus, Figure 5.39; nor between value of SF [Figure 5.40(a)] and subsequent burn rate. Initial flame kernel projection was predominantly into the first and second quadrants, never into the fourth, Figure 5.39(a) – this is possibly associated with bulk flows influenced by the single exhaust port (Cairns, 2001), which led to the revised exhaust design described in Chapter 3.

The values of APF versus mean flame radius for these cycles generally followed the pattern observed previously, albeit less consistently, Figure 5.40(b). This is possibly associated with generally more marked flame kernel centroid displacements, perhaps exacerbated by the greater two-dimensionality caused by the reduced clearance height.

5.5.2 High compression ratio (CR=12.4)

Corresponding results for the highest compression ratio adopted are set out in Figures 5.41-5.44. The optimum ignition timing remained at $20^\circ bTDC$, as for a compression ratio of 10.2:1. Perhaps surprisingly, although the expected higher combustion pressures were evident, there was no evidence in the records of pressure oscillation (or knock).

At this higher compression ratio, the faster cycles tended to become faster fairly early in the combustion event and then remain faster throughout, Figures 5.42(a) and (b).

The slowest burning cycle seems to have become slow at about $7^\circ bTDC$ after a relatively normal early development.

As at a compression ratio of 10.2:1, initial kernel developments were predominantly in the first and second quadrants, Figure 5.43(b). The values of SF follow their normal random pattern, while the APF values are consistent with those seen previously, Figures 5.44(a) and (b).

5.5.3 Variation of (middle cycle) behaviour with compression ratio

Set out in Figure 5.45 is cylinder pressure and mean flame radius versus crank angle for the selected middle cycles at the three compression ratios. The derived maximum flame speed and the corresponding crank angle occurrence versus compression ratio are shown in Figure 5.46. The delay, from ignition, in departing from the motoring pressure trace was typically $8^\circ CA$ at high compression ratio; rather sooner than at the reference condition ($12^\circ CA$). The faster initial kernel development at the high compression ratio might be associated with a higher gas temperature at ignition. After this early development, maximum flame speed (generated from gradient of mean flame radius) for the low compression ratio case (reference condition) proved greater than the other two cases, in spite of a lower unburned gas temperature expected for the low compression ratio condition, Figure 5.46. This might be associated with the higher "rms" turbulent velocity (the predominant factor controlling flame speed after the early laminar-like flame growth) measured for the low compression ratio case than for the highest compression ratio (highlighted in Figure 2.4(a), Jakubík, 2002). Care should be exercised in making either any quantitative comparison between the data of, or compatibility between the conditions pertaining in, Figures 5.45(a) and (b); because different compression ratios result in different temperature, pressure, cylinder mass (due to blowby), u' and length scale over combustion period. Also, all these differences can create different flame brush thickness development (not seen in natural light filming) for the different compression ratios. It should be noted that the mean flame radii for the medium compression ratio (CR=10.2) case are subject to a maximum ±1 frame period ($\pm 2^\circ CA$) error in synchronisation with crank angle (as discussed in Section 3.5.4).

Cyclic variation in peak cylinder pressure with compression ratio, again expressed in terms of standard deviation and coefficient of variation, are shown in Figure 5.47. These variations are not large and, arguably, not statistically significant (given the relatively small number of cycles analysed at some of the conditions). The values of SF again show no correlation with burn rate at this condition, Figure 5.48(a); likewise, the values of APF follow the now "normal" pattern of behaviour, Figure 5.48(b).

5.6 Engine speed variation within a cycle

From analyses of shaft encoder records, it was apparent that the LUPOE1 engine speed varied (from cycle to cycle and within any cycle) even though it had been fitted with a new flywheel of rather greater inertia than that supplied by the manufacturer (Hicks, 1994). During the current study, this variation was recognised to be important for data processing (Sections 4.2 and 4.4) and combustion modelling (Section 6.5.3). This prompted consideration of the engine speed variation under different operating conditions.

Engine speed variation can result from variation of torque acting on the crankshaft. In a commercial engine, this torque is the resultant of the gas pressure (acting on the piston) torque, the reciprocating inertia torque, the friction plus valve train torque, the torque required to drive auxiliaries and the load torque. Even at nominally steady state operating conditions, the torques of gas pressure, reciprocating inertia, friction and valve train vary with crank angle and produce variations in crankshaft angular speed. Extensive research has been conducted to determine the relationship between engine speed variation and gas pressure torque, especially in conjunction with misfiring detection (Chen et al., 1993; Guezenec et al., 1999; Gyan et al., 2000; and Taraza, 2001). Taraza (2002) presented a method to determine *imep* and gas pressure torque for a multi-cylinder engine using the data obtained from measurements of crankshaft speed variation.

In the current study, in addition to the tests conducted to clarify the effect of the various operating conditions on the LUPOE1 engine, comparative data were collected for a commercial single cylinder 4-stroke research engine (Ricardo E6) and a production 4-cylinder 4-stroke normally aspirated engine (1.4 litre VWSE). In these

tests, engine speed fluctuation was defined as the difference between instantaneous engine speed and the temporal mean engine speed taken over the cycle. Additionally, a normalised engine speed variation was characterised as the ratio of instantaneous engine speed to the mean value.

5.6.1 LUPOE1

In the LUPOE1 research engine, the torque acting on the crankshaft is the combination of the torques of gas pressure, reciprocating inertia, friction and load (here, dynamometer). In skip fire mode, the torques of the gas pressure, friction (unusually large under minimal lubrication filming mode) and load can significantly change from cycle-to-cycle. Shown in Figure 5.49 are the normalised engine speed fluctuations versus crank angle for the "middle" cycles at the reference condition. It can be seen that during the combustion period, (from ~20° *bTDC* to ~20° *aTDC*), the deviation from the mean engine speed is negative (by ~4% of the nominal value). This is important for data processing and imposing experimental conditions on an engine combustion model. Set out in Figure 5.50 are values of normalised engine speed versus crank angle, for representative "middle" cycles at nominally different engine speeds (750, 1500 and 2000 *rpm*). The range of variation is more significant for the low engine speed, presumably because the inertia of the flywheel is inadequate to stabilise engine speed.

In addition, the engine speed variation was evaluated for normal motoring (free from the skipping effect) and motoring without the cylinder head fitted (absence of effective gas pressure torque); this is shown in Figure 5.51, together with data for a typical firing cycle. Considerable engine speed variations are evident, even for motoring without the cylinder head fitted (where the torque acting on the crankshaft is a combination solely of friction, reciprocating inertia and dynamometer load torques). The dip in the curves around TDC demonstrates the strong role of reciprocating inertia on engine speed variation. Around TDC and BDC, the accelerations of the piston and connecting rod are very significant, due to the change in direction of motion.

5.6.2 Engine speed variations in single and multi-cylinder four-stroke engines

To check whether the speed variation effect noted in the unusual LUPOE1 ported optical engine was unrepresentative of more normal 4-stroke engines, comparable data were generated for a single-cylinder Ricardo E6 research engine and a VWSE production engine. Set out in Figure 5.52 are the noted variations in engine speed versus crank angle for both firing and motoring conditions for the Ricardo engine. These engine speed fluctuations can be seen to be very similar under the two conditions, with the lowest speed occurring at about the TDC and BDC positions. The range of speed variation ~ ±4% (at 1500 rpm, nominal) was not dissimilar to that noted for LUPOE1. The recorded engine speed variations for the four-cylinder four-stroke VWSE spark ignition engine are set out in normalised form, for three nominal engine speeds, in Figure 5.53. This information was generated from raw data [captured by a colleague (C. Wu) in Leeds]. As in the case of the LUPOE1, Figure 5.50, there were differences in normalised engine speed variation with crank angle at the three engine speeds (1500, 3000 and 5000 *rpm*). However, the basic pattern of behaviour was very similar at the three speeds. As with the other engines, minimum engine speed occurred close to TDC and BDC. Engine speed variations of ~ ±5% at 1500 *rpm* were noted, similar to the other engines; at 5000 *rpm* the variation in a cycle amounted to as much as ~ ± 12%.

It has already been stated that engine speed variation within a cycle for the LUPOE1 engine is significant and needs to be taken into account in simulations (in terms of variable time interval per crank angle increment for flame propagation, autoignition development and NO_x formation). In such simulations, a uniform engine speed assumption is regularly adopted. The Ricardo and VW data suggest that this phenomenon is not restricted to the perhaps unusual LUPOE1 engine, but also may need to be taken into account when modelling more regular engines.

5.7 Summary and conclusions

The principal objective of collecting the data reported in this chapter was for model calibration and validation. As reported in Chapter 7, models were calibrated (fitted) at the "reference condition". The other tests were designed to test the validity of the

simulations under conditions involving change of model input parameters, with one parameter dominant in each case (e.g. engine speed, u'; mixture strength, u_l; compression ratio, P and T_u).

The changes in engine performance with these various parameters were not particularly new or unexpected. The value of the experiments lies in the establishment of a uniquely large and consistent database of simultaneous cylinder pressure (well referenced, using the cylinder barrel absolute pressure transducer) and mean flame radius data – useable in conjunction with information on turbulence and turbulent flame brush thickness obtained for the same engine by previous researchers at Leeds [Atashkari (1997); Gillespie (1998); Jakubík (2002)]. Nevertheless, some experimental findings in cyclic variation, flame features and engine speed variation, interesting in their own right, have been made. The ensemble averaged cylinder pressure did not fit any individual real cycle and may not be appropriate to use as the "representative cycle" for a dataset for model validation purposes. Analysis of flame shape for the typical "fast", "middle" and "slow" cycles at different conditions suggested no correlation between flame Shape Factor and burning rate. The Active Perimeter Fraction versus mean flame radius followed a consistent overall pattern, as seen in Figure 5.54 for "middle" cycles at seven different engine operating conditions. This correlation proved useful in combustion modelling employing the usual spherical flame growth assumption (Section 6.5.6), allowing for non-symmetric flame-wall contact during late flame propagation. The observed engine speed variation, within any cycle, was also to prove significant in correctly modelling engine behaviour, Section 6.5.5.

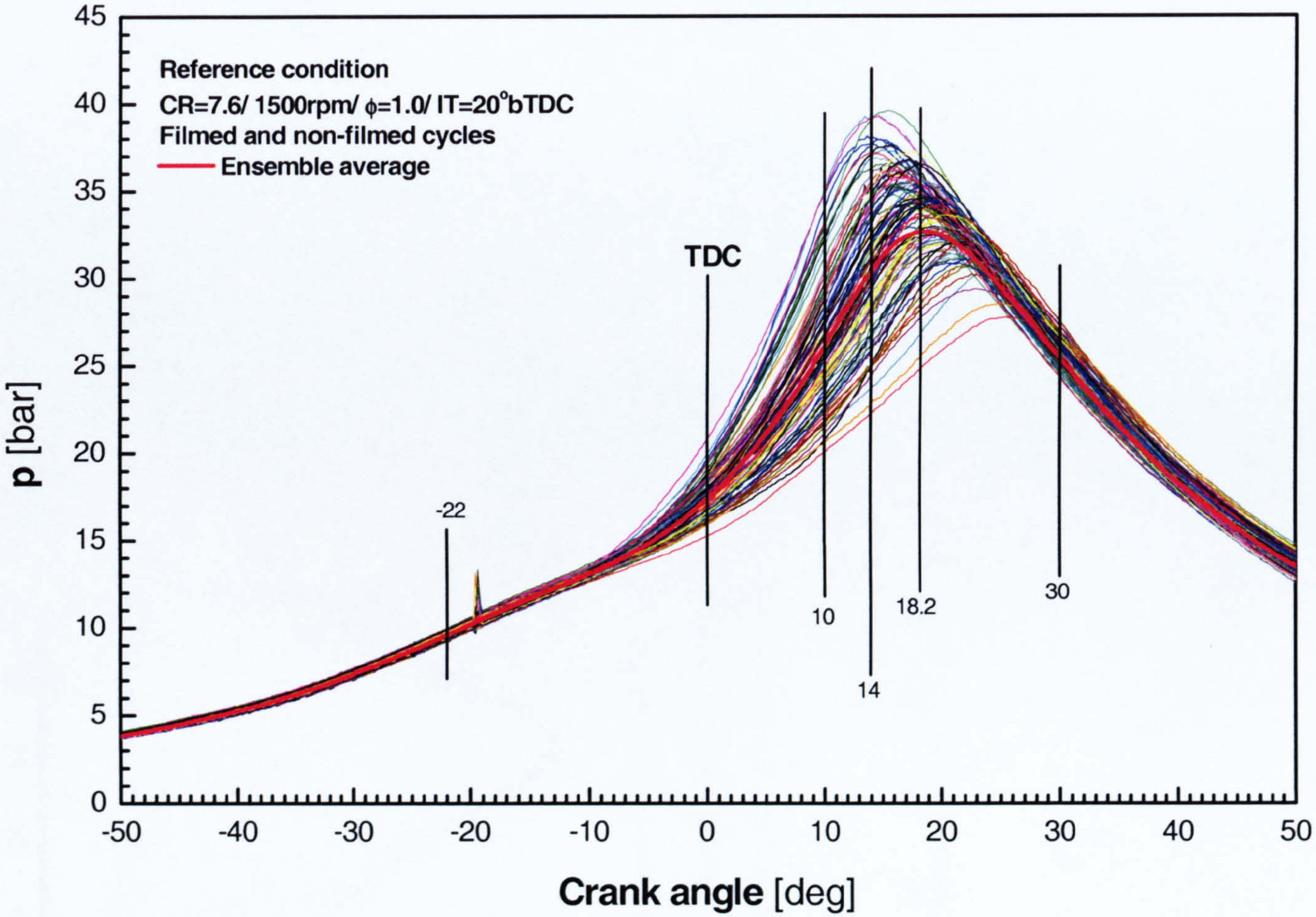

Figure 5.1 Cylinder pressures of 65 filmed and 35 non-filmed cycles associated with ensemble average value versus crank angle.

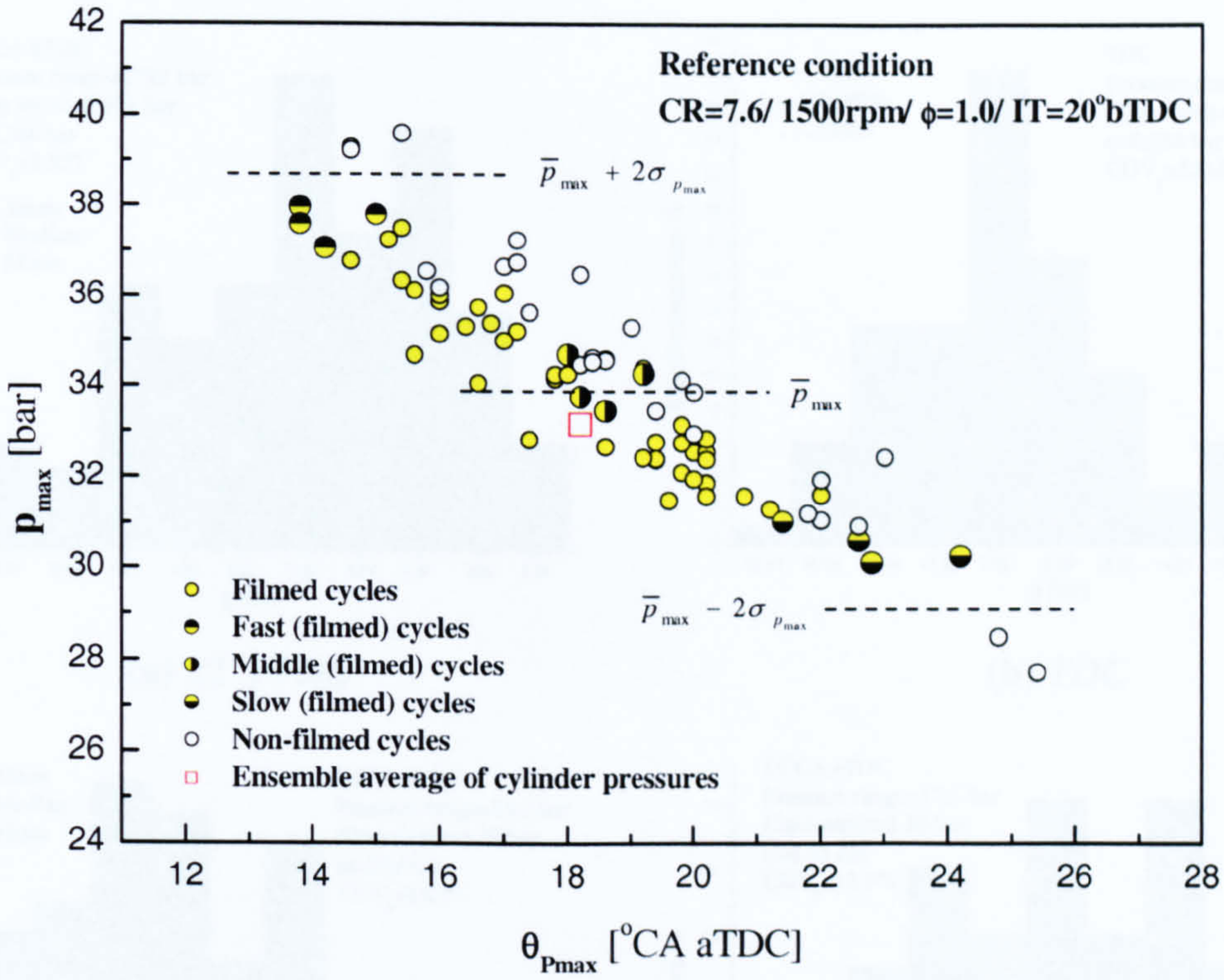

Figure 5.2 Peak pressure versus the corresponding crank angle occurrence for the filmed and non-filmed cycles associated with that of ensemble average.

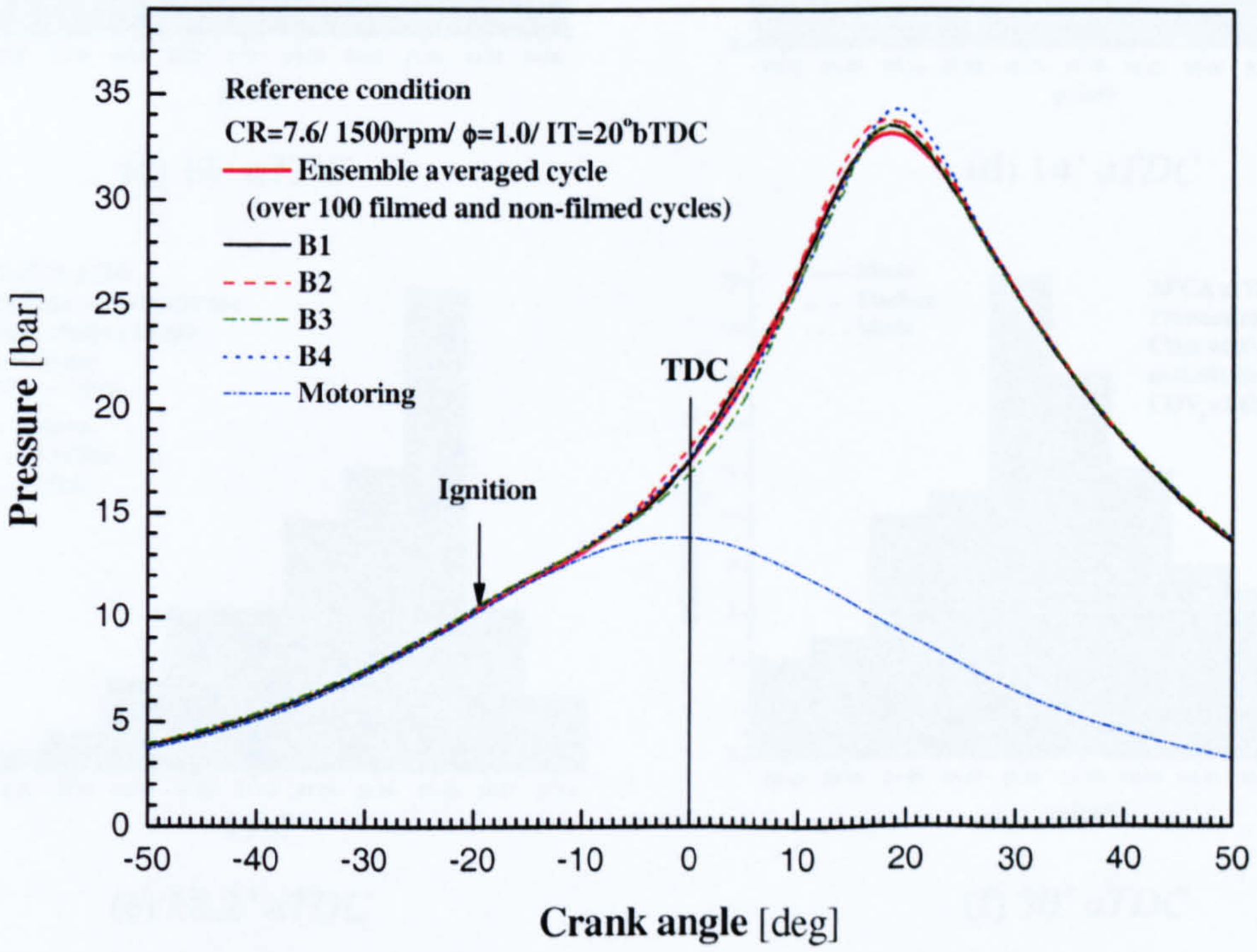

Figure 5.3 Cylinder pressure versus crank angle for selected middle filmed cycles associated with ensemble averaged and motoring cycles.

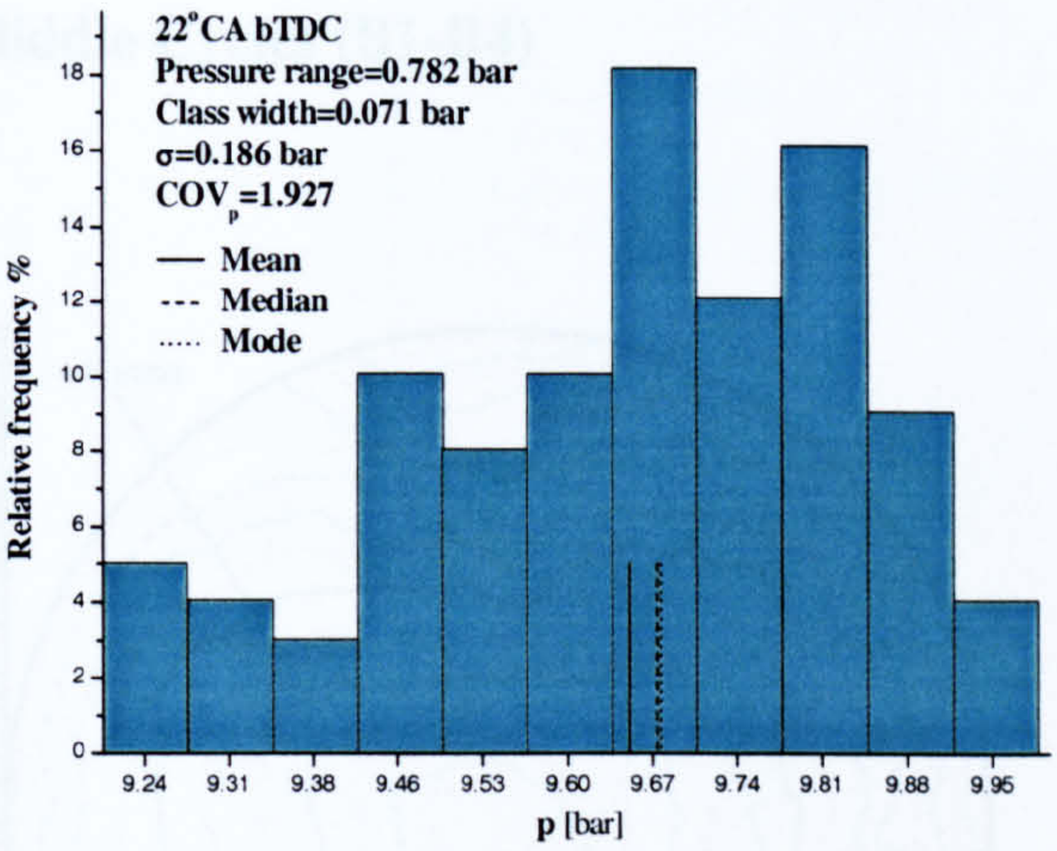

(a) *22° bTDC*

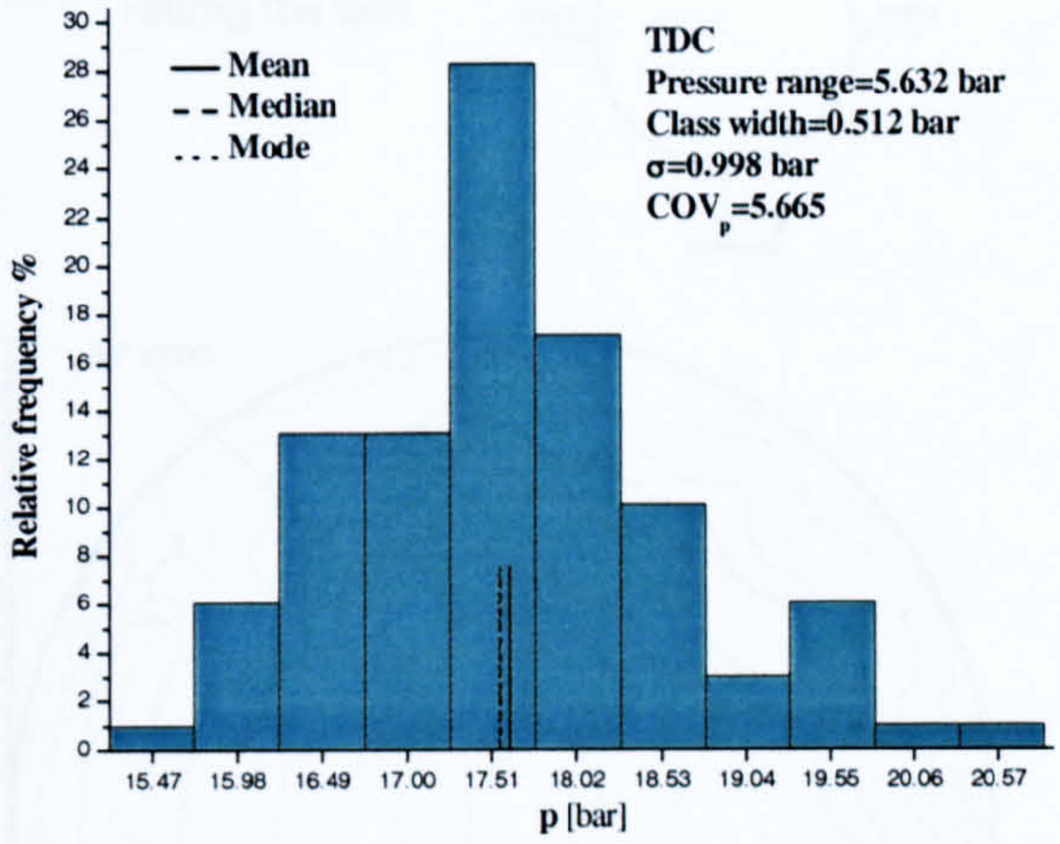

(b) *TDC*

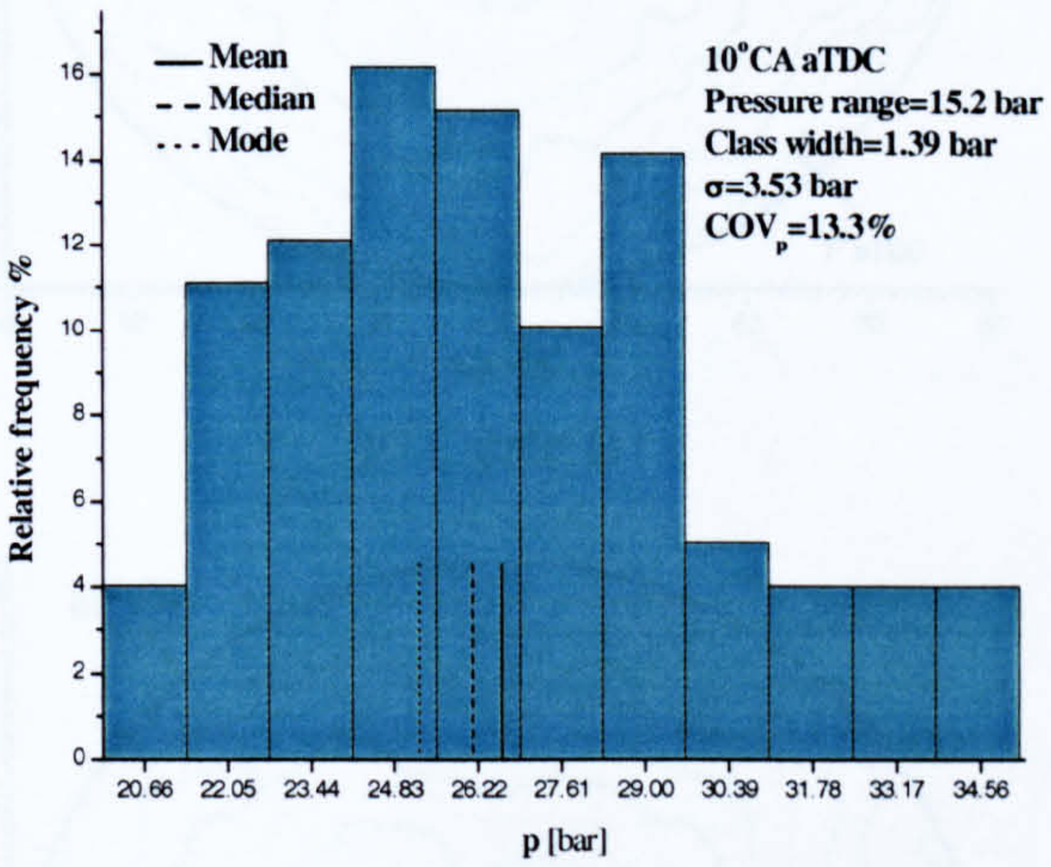

(c) 10° *aTDC*

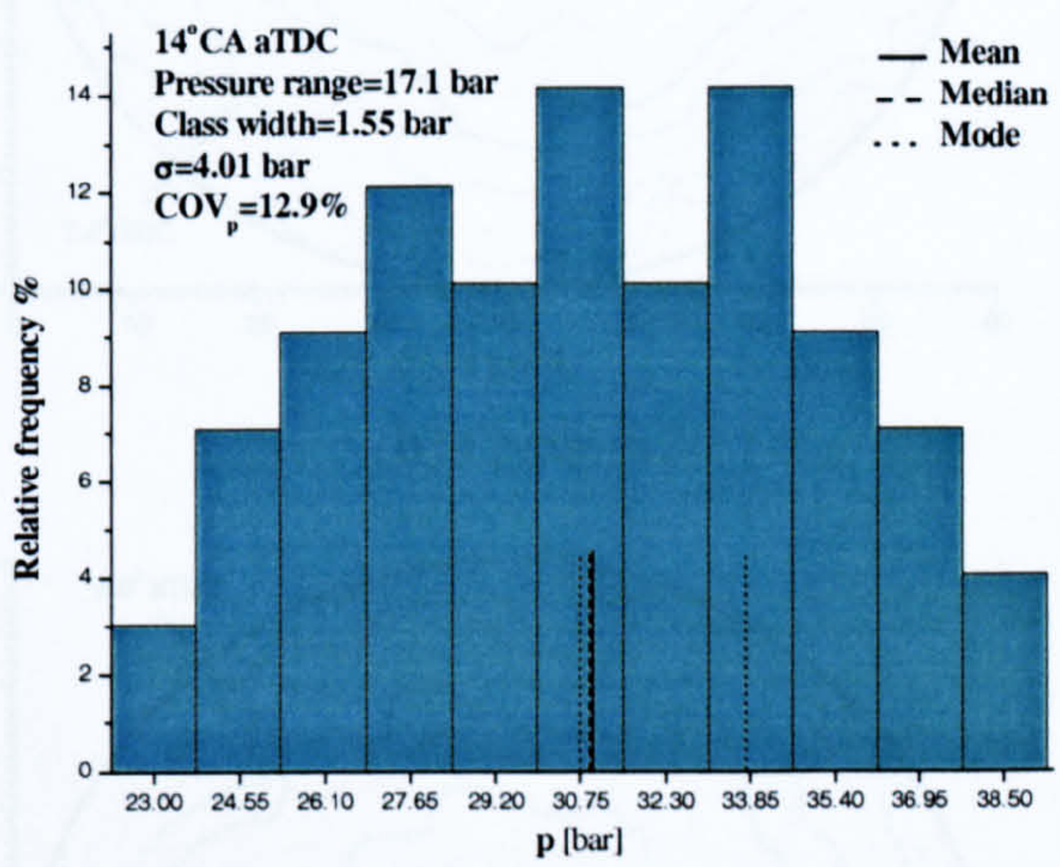

(d) 14° *aTDC*

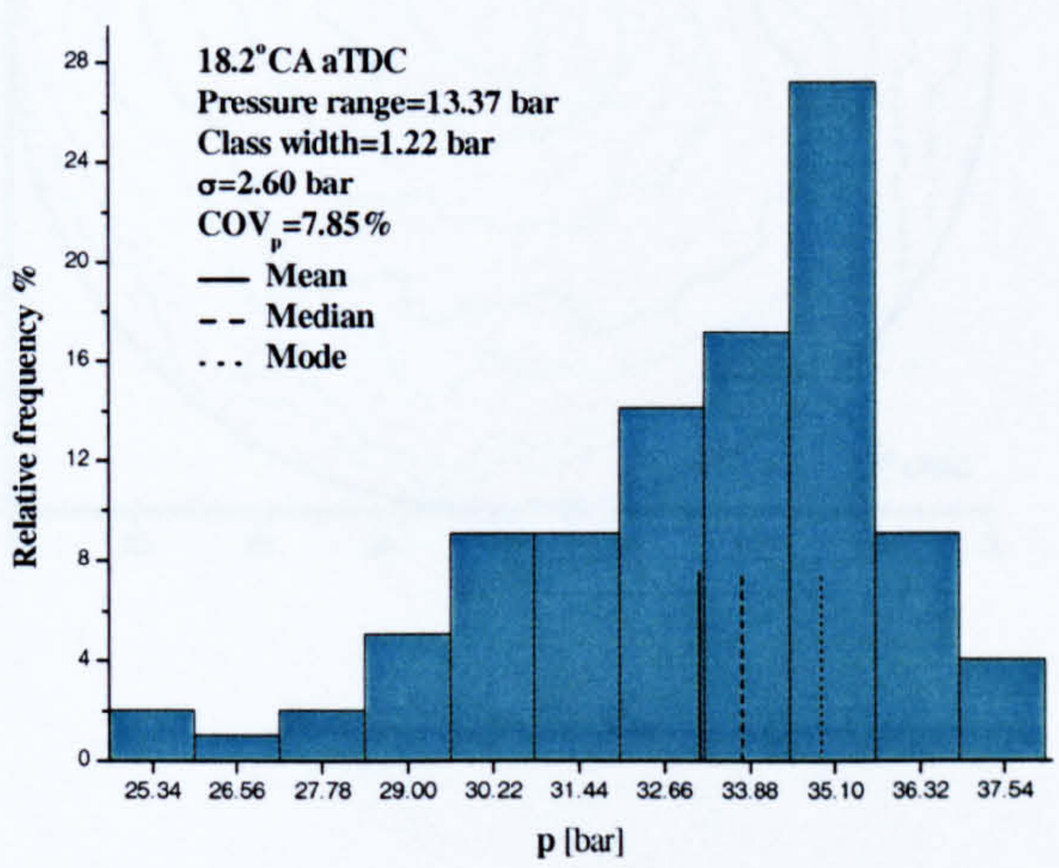

(e) 18.2° *aTDC*

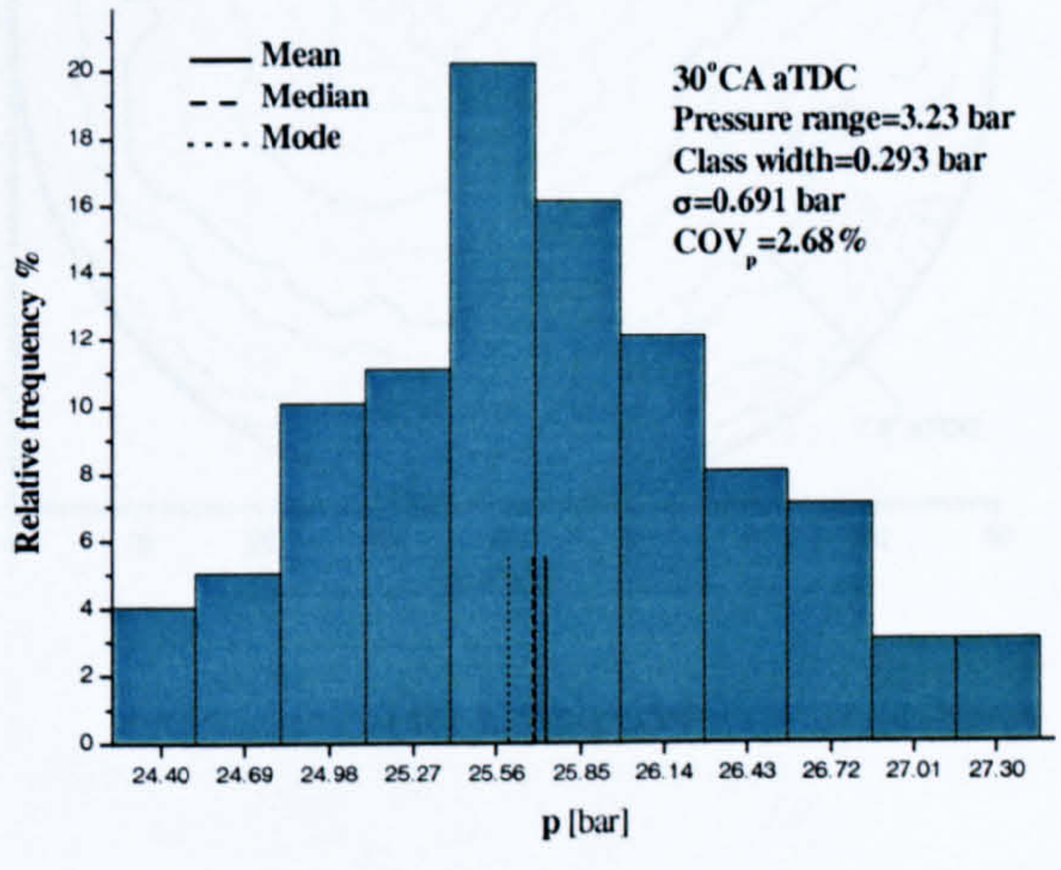

(f) 30° *aTDC*

Figure 5.4 Histograms of six selected sections in Figure 5.1 associated with mean, median and mode positions.

$CR = 7.6 / 1500rpm / \phi = 1.0 / IT = 20^{\circ} bTDC$

Middle Cycles (B1-B4)

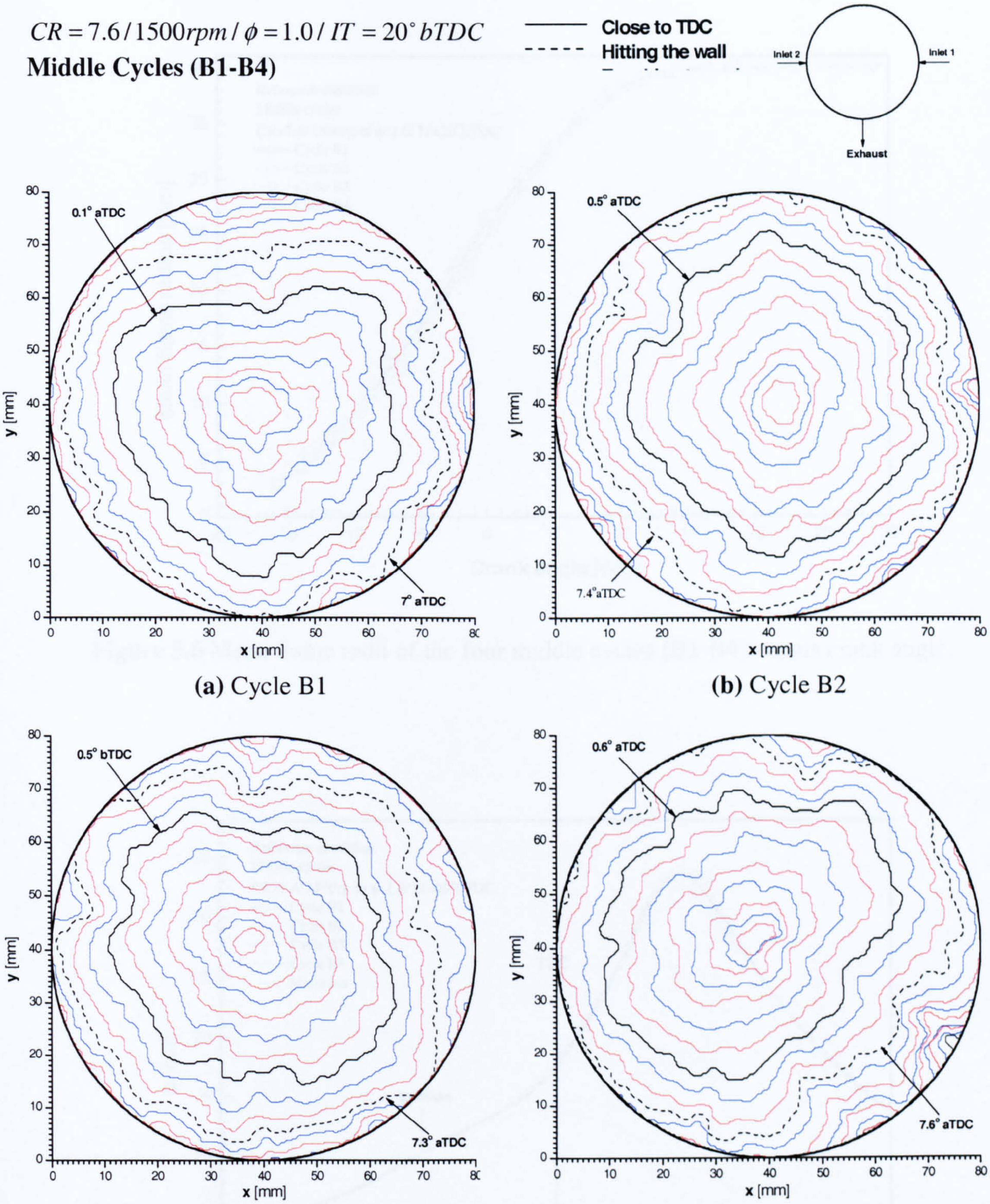

(a) Cycle B1

(b) Cycle B2

(c) Cycle B3

(d) Cycle B4

Figure 5.5 Successive flame positions of the four middle cycles (B1-B4) over the flame propagation period.

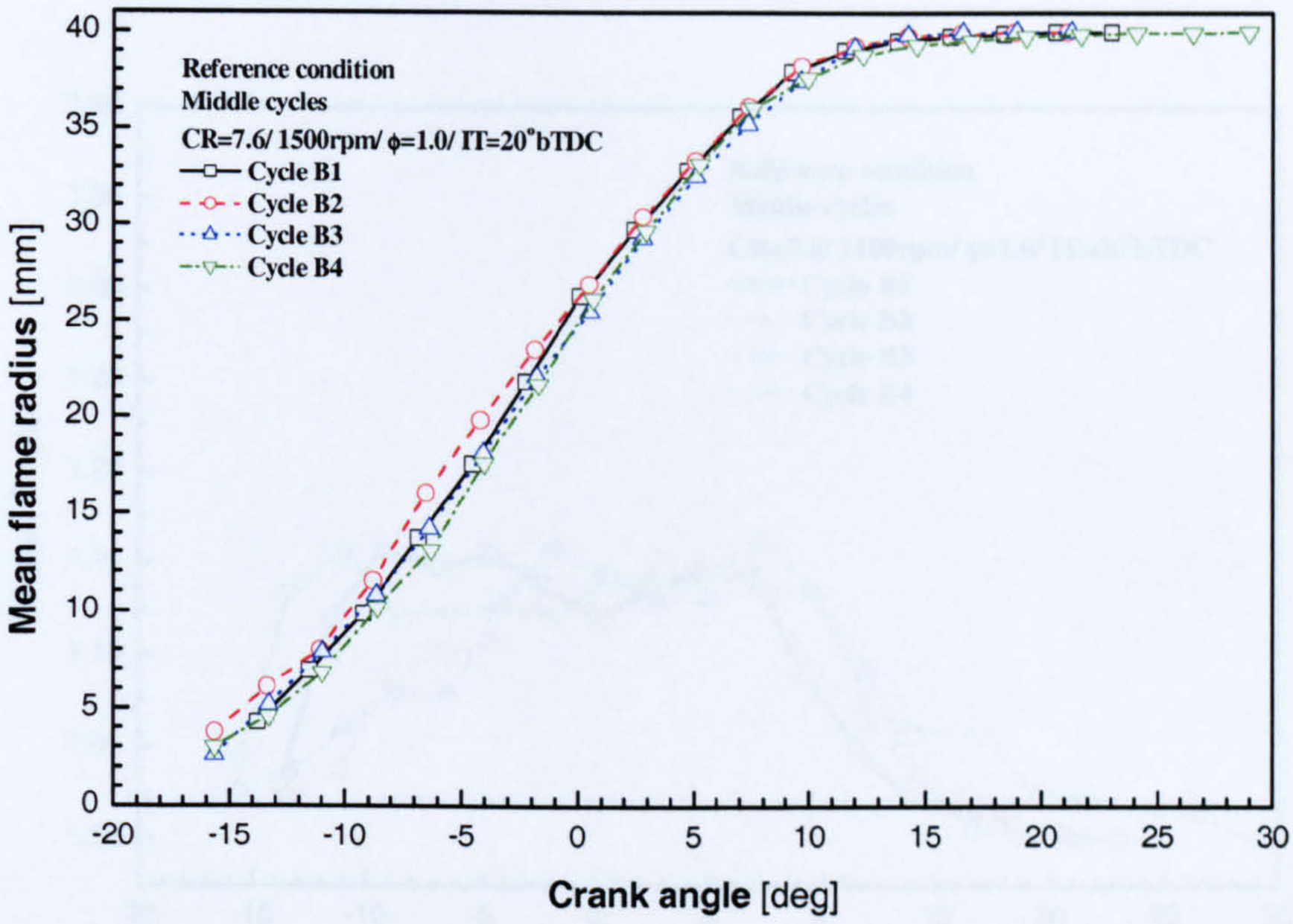

Figure 5.6 Mean flame radii of the four middle cycles (B1-B4) versus crank angle.

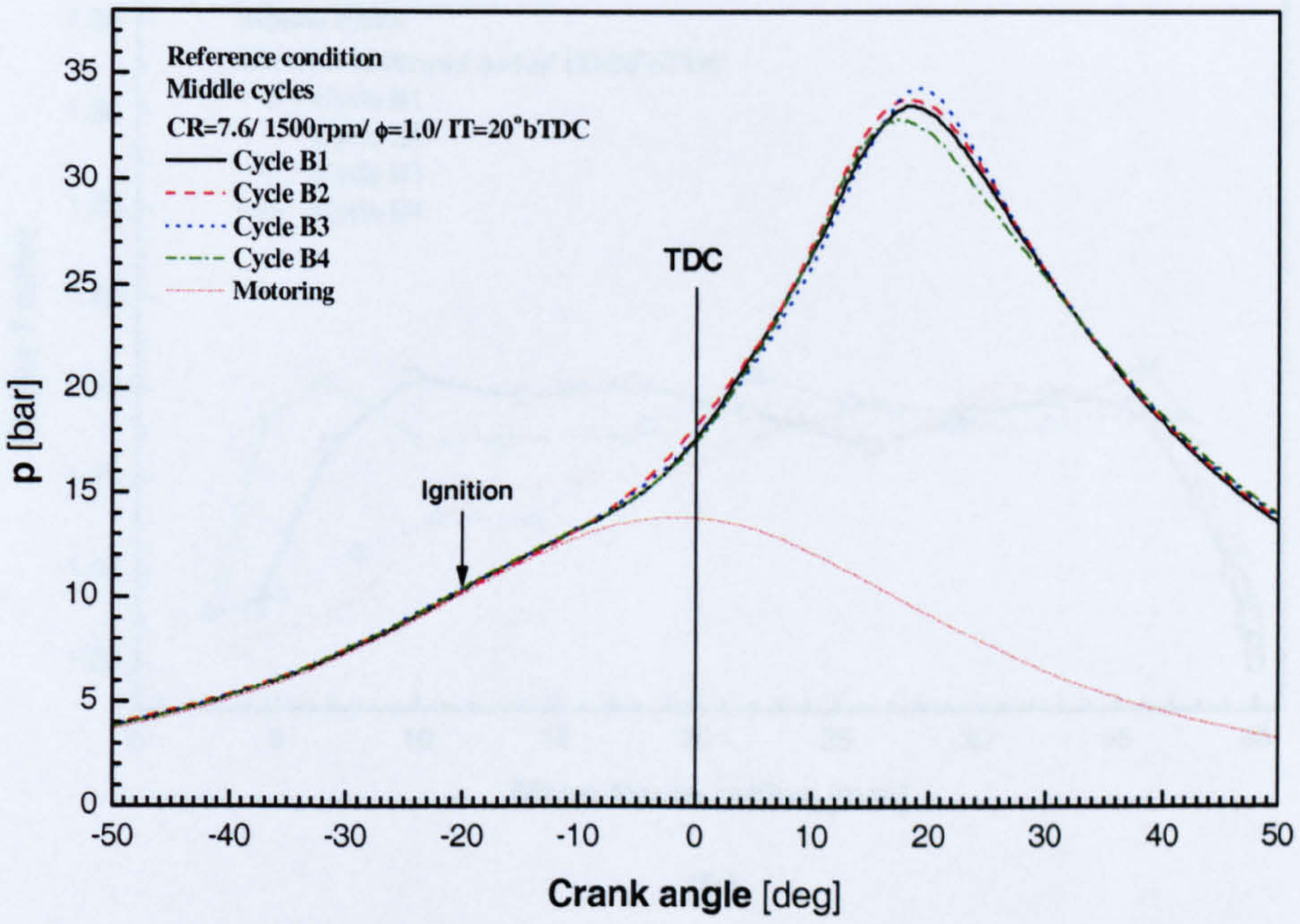

Figure 5.7 Cylinder pressure in terms of crank angle for the four middle cycles (B1-B4).

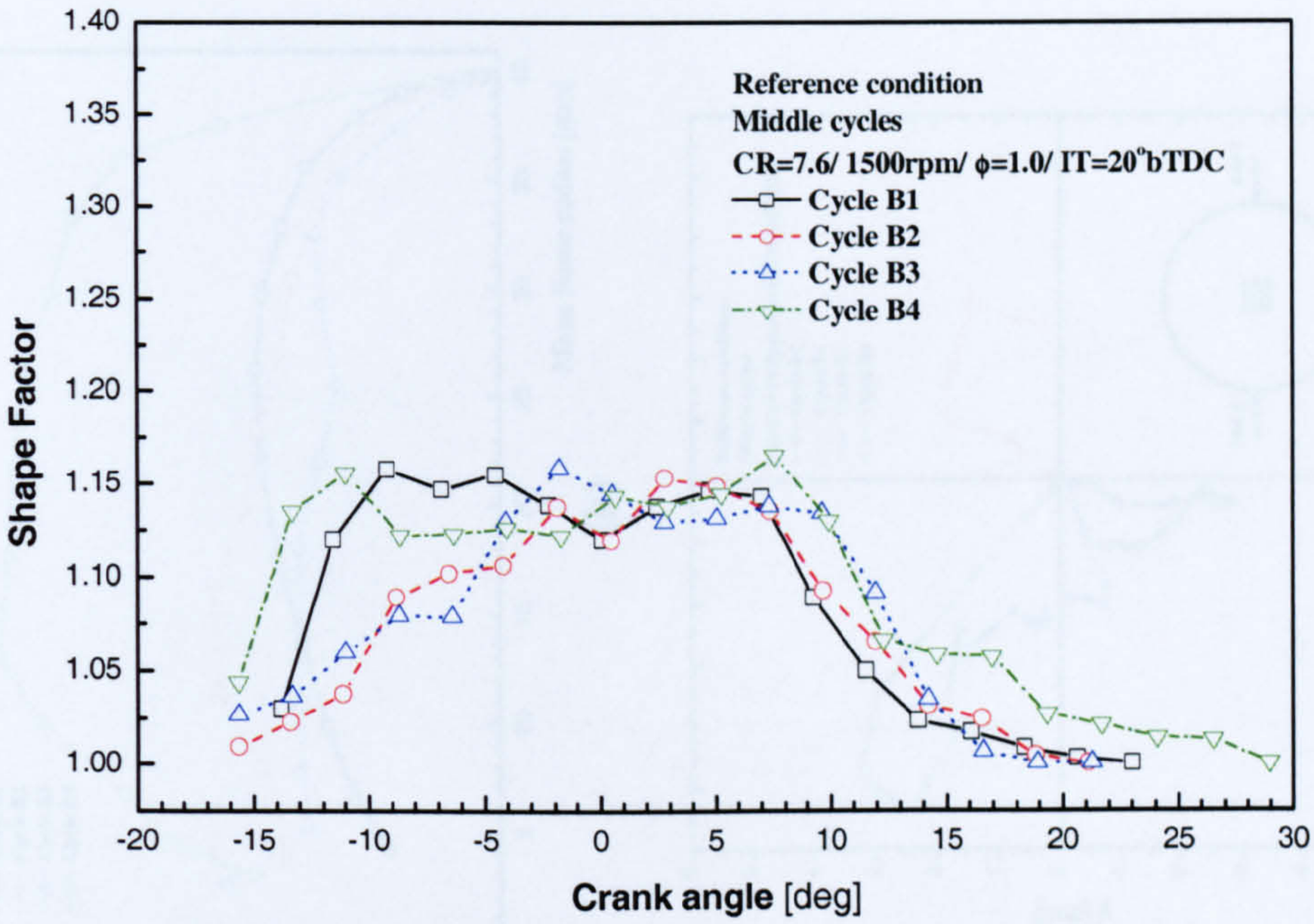

(a)

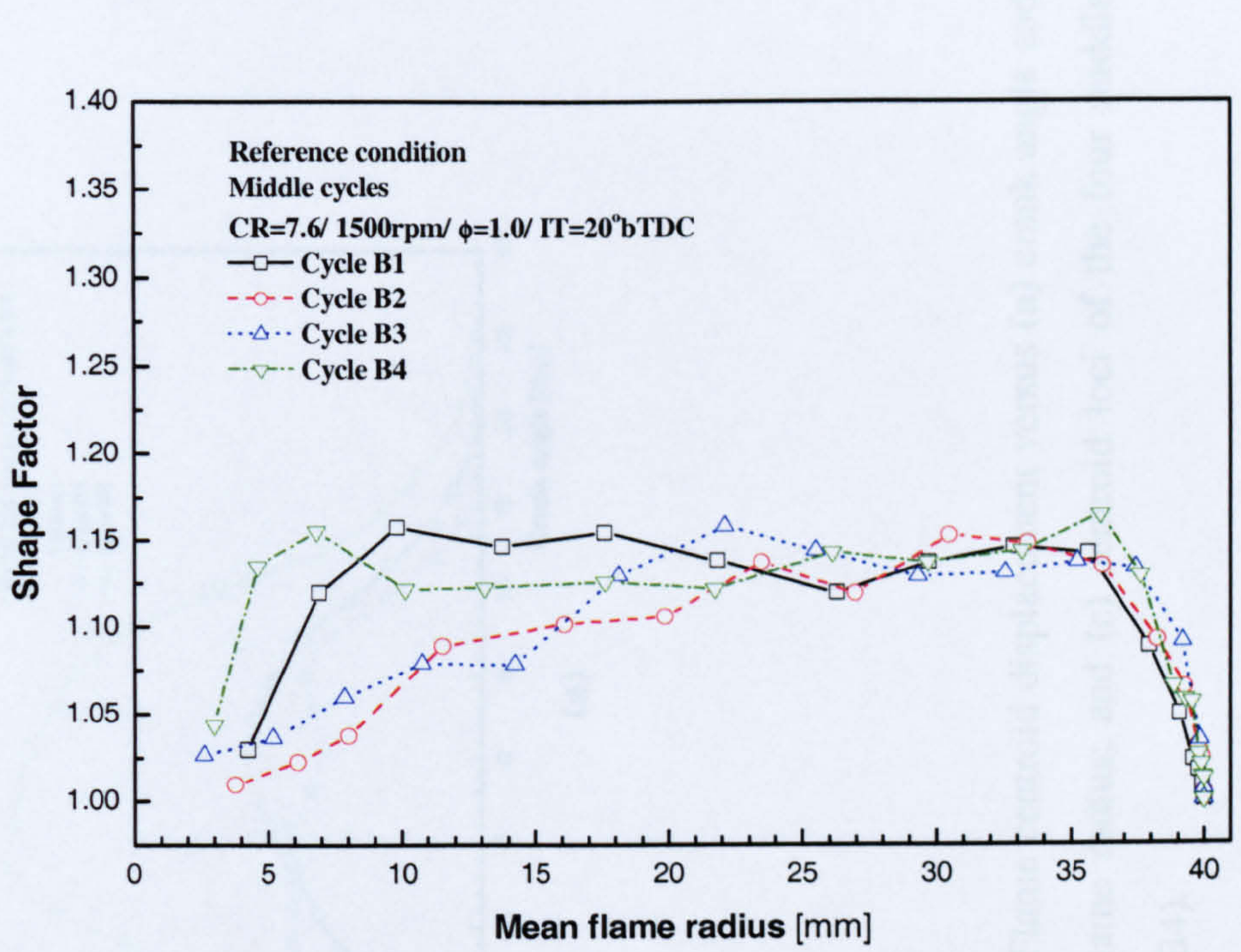

(b)

Figure 5.8 Flame shape factor versus **(a)** crank angle and **(b)** mean flame radius for the four middle cycles (B1-B4).

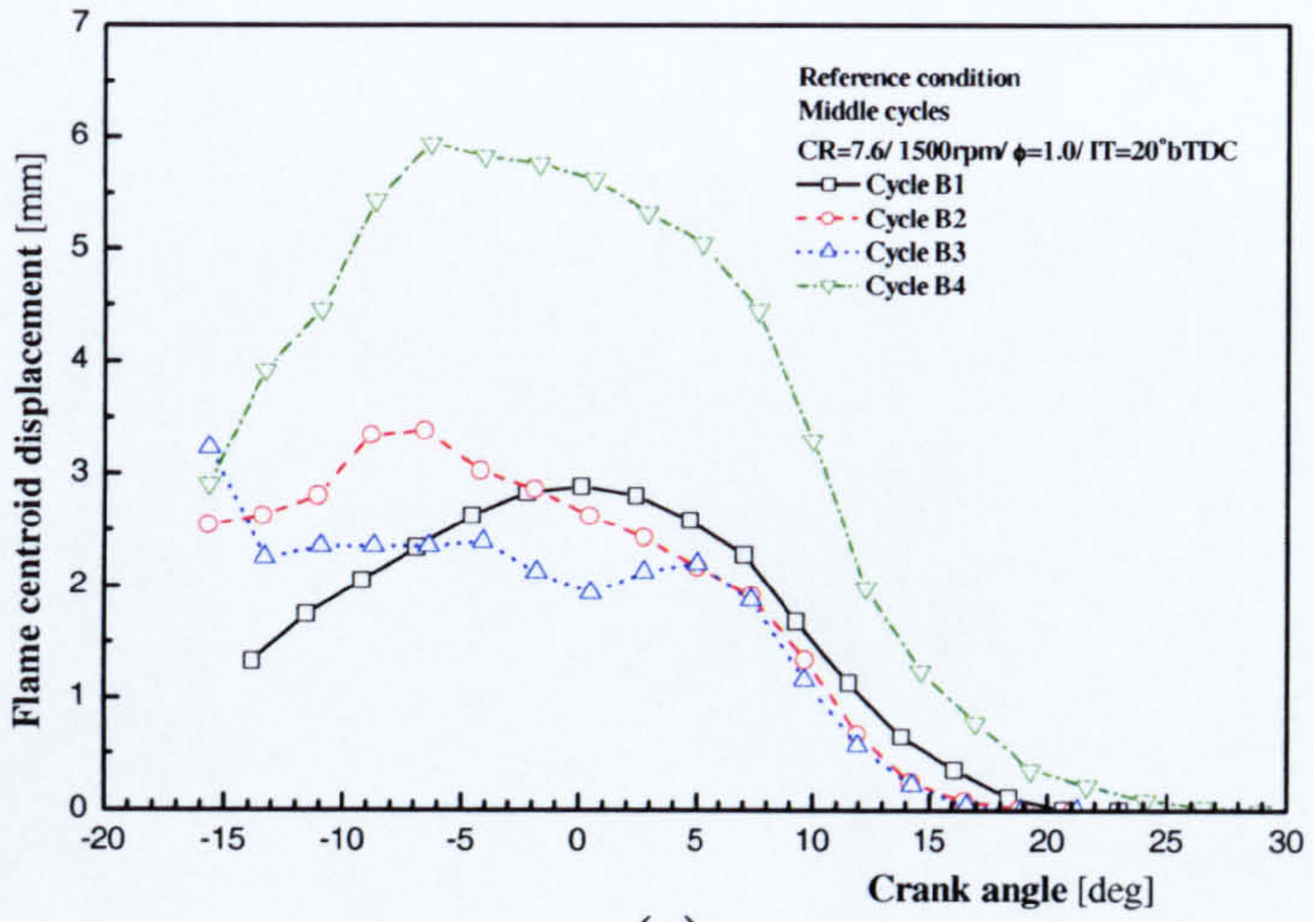

(a)

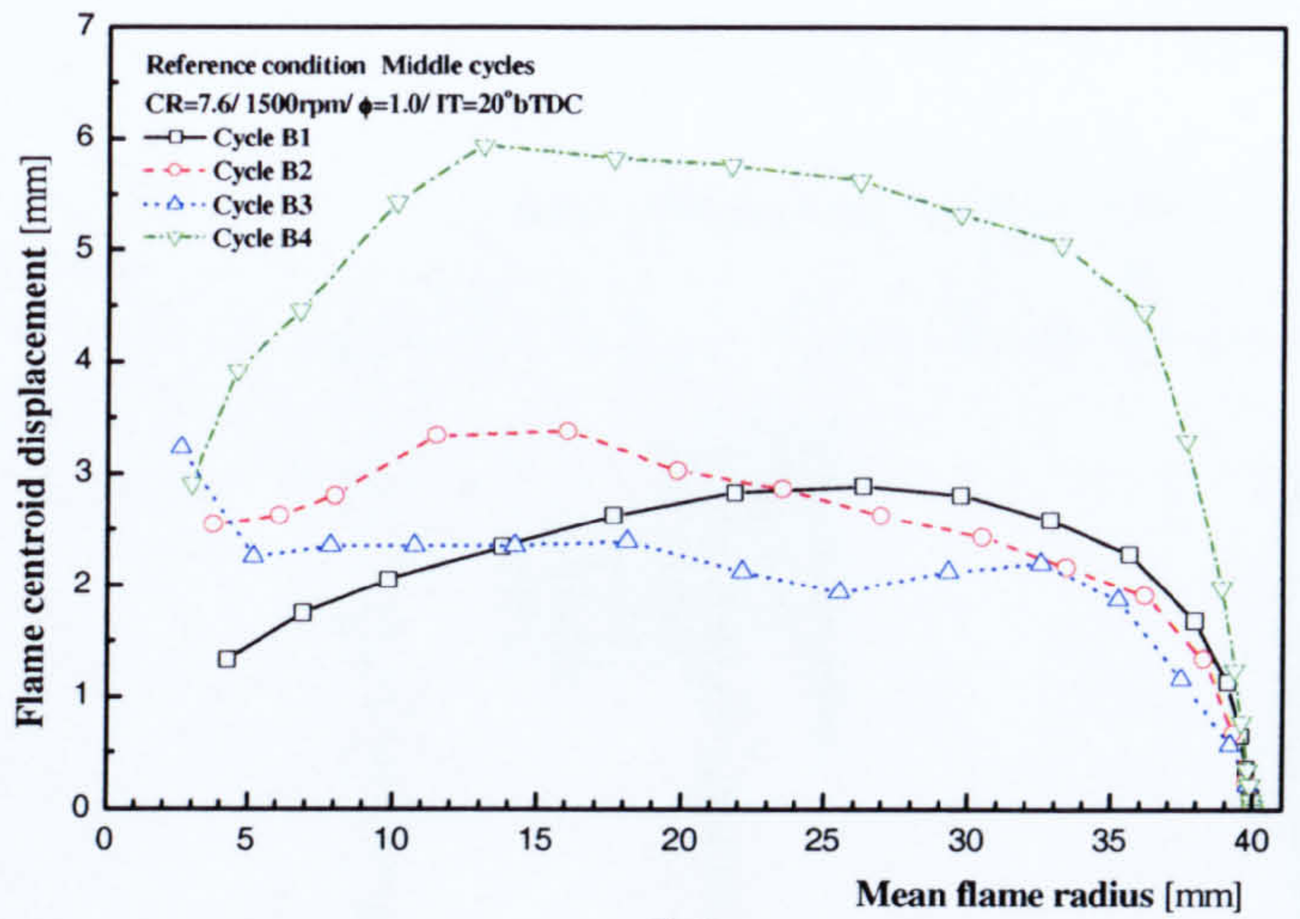

(b)

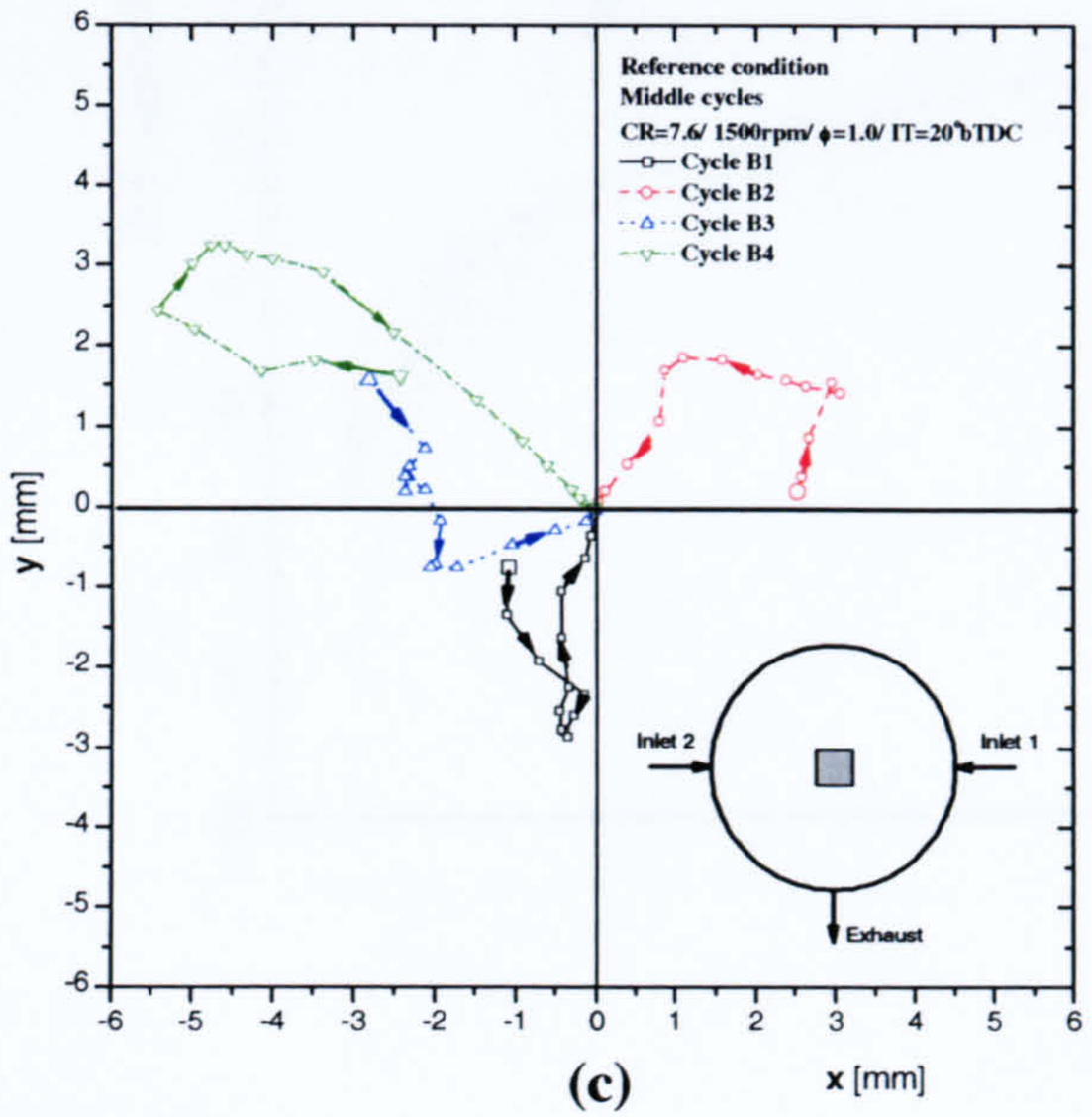

(c)

Figure 5.9 Flame centroid displacement versus **(a)** crank angle and **(b)** mean flame radius; and **(c)** centroid loci of the four middle cycles (B1-B4).

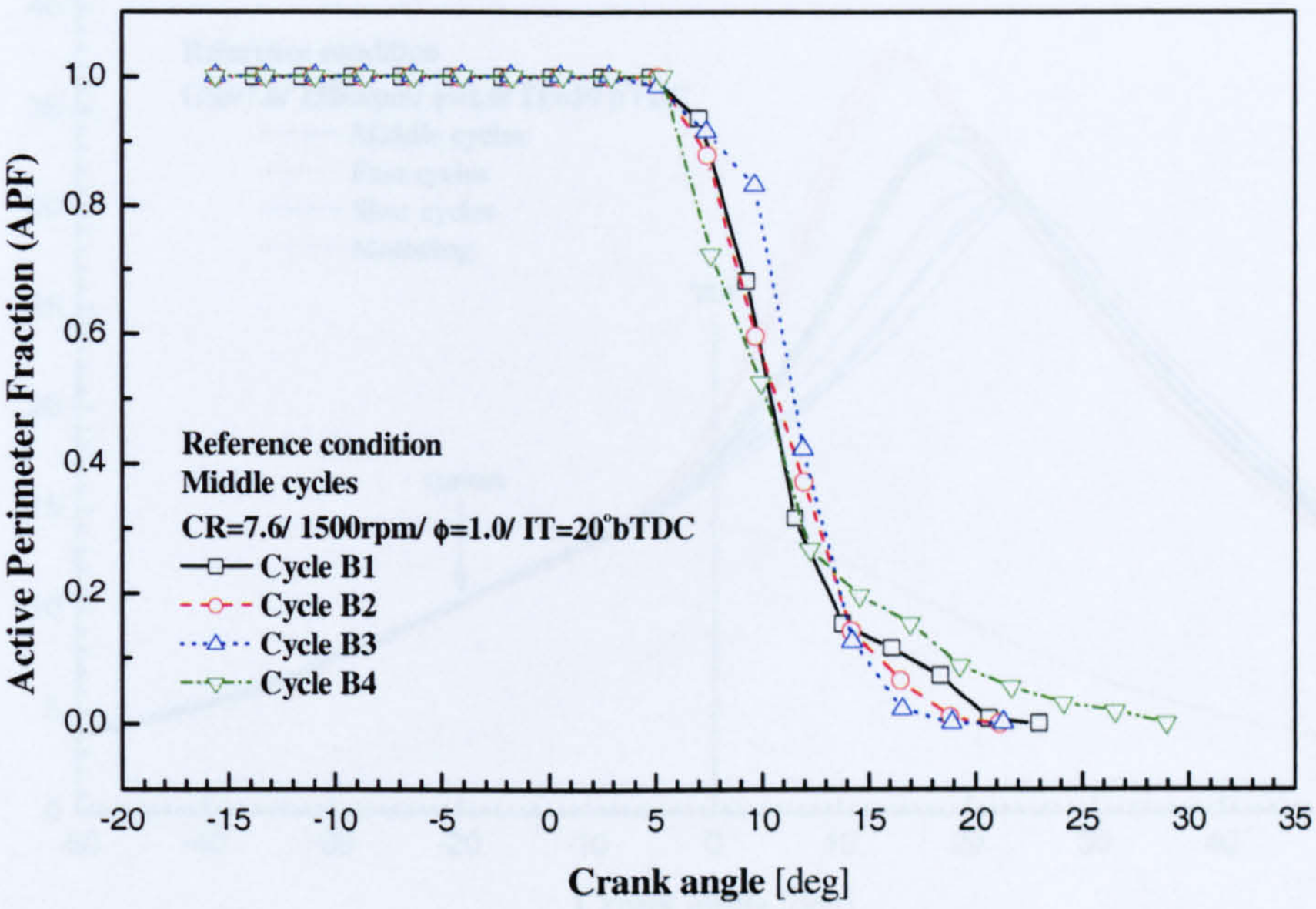

(a)

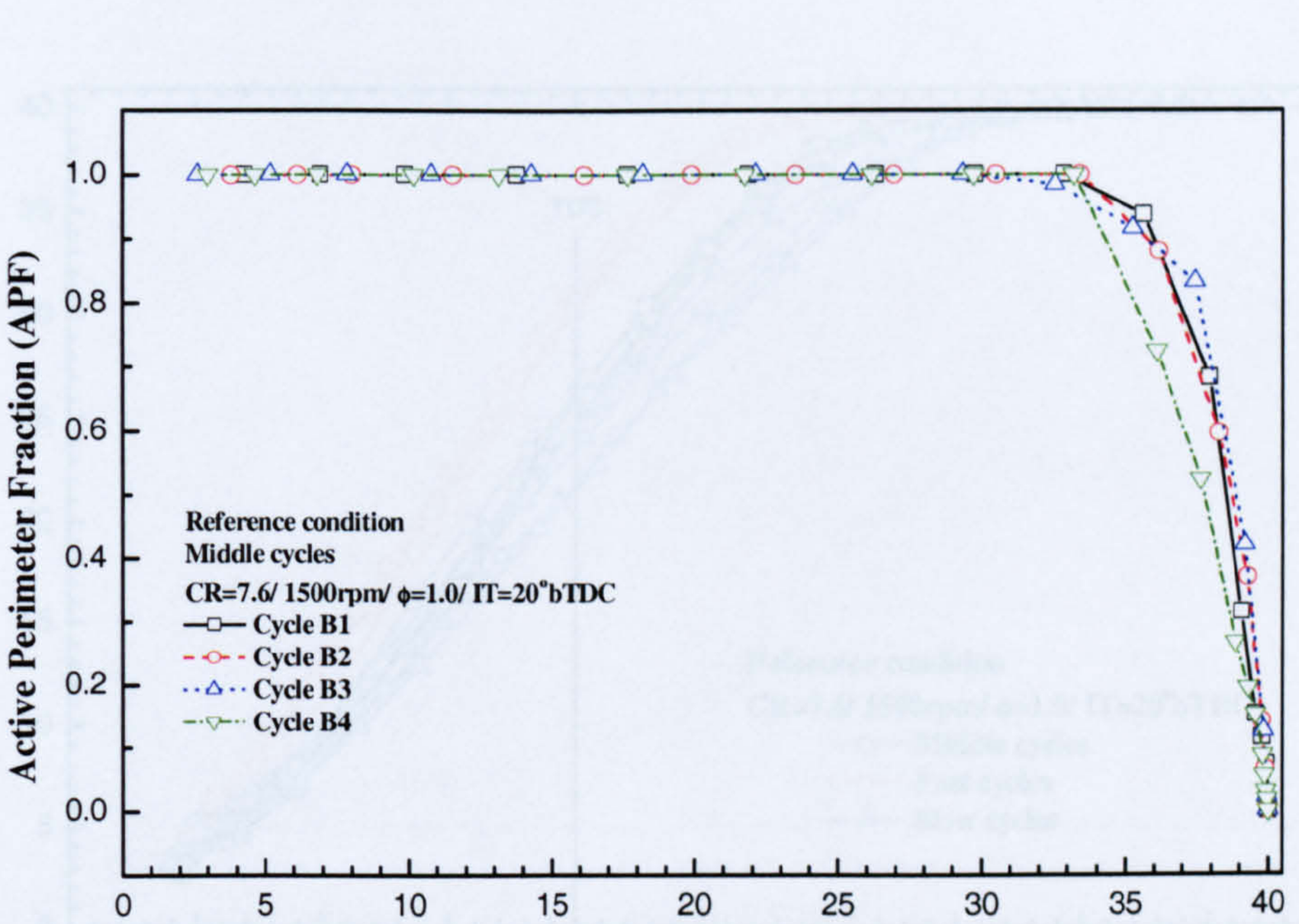

(b)

Figure 5.10 Active perimeter fraction versus **(a)** crank angle and **(b)** mean flame radius for the four middle cycles (B1-B4).

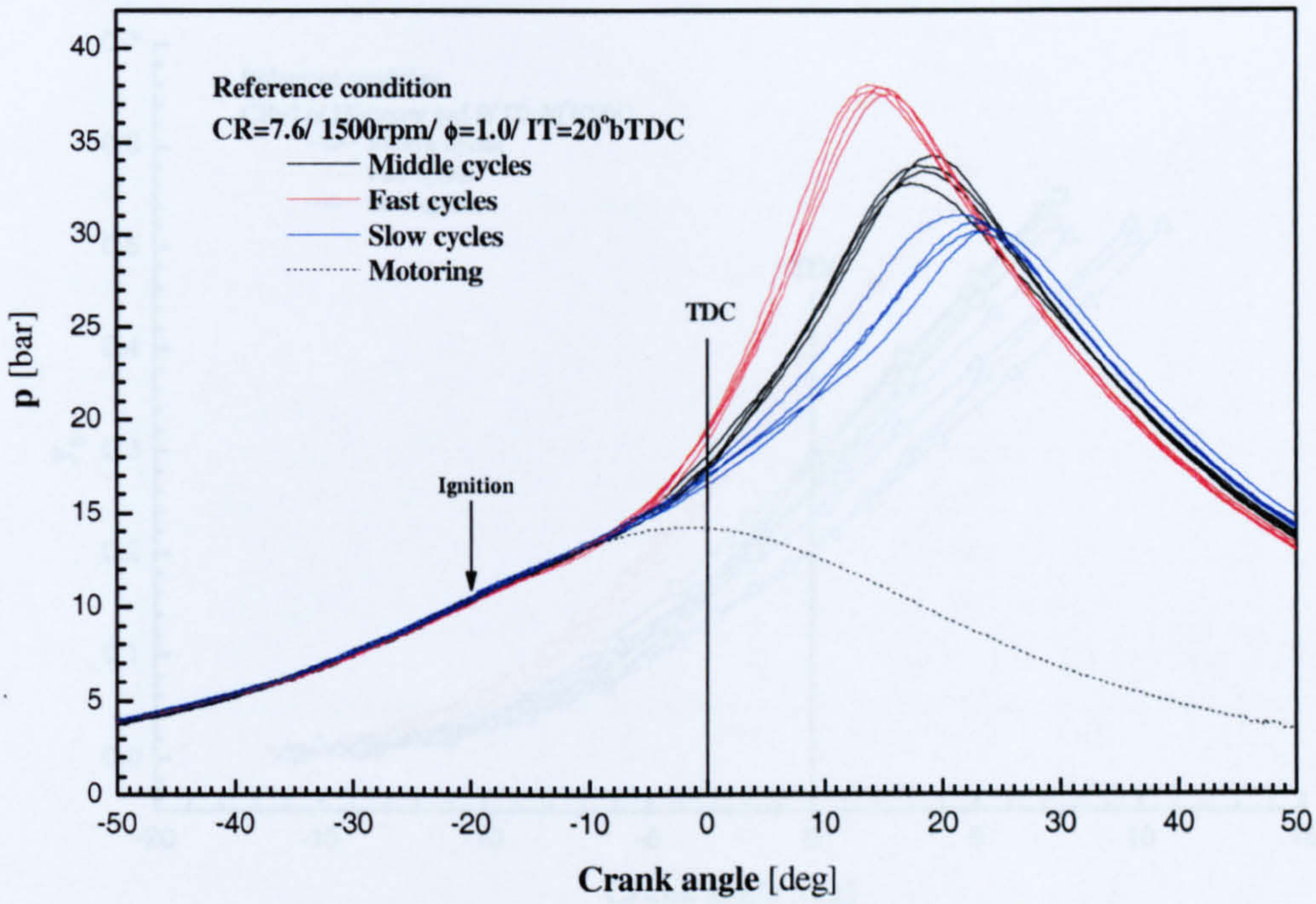

Figure 5.11 Cylinder pressure in terms of crank angle for the middle, fast and slow cycles at the reference condition (B1-B12).

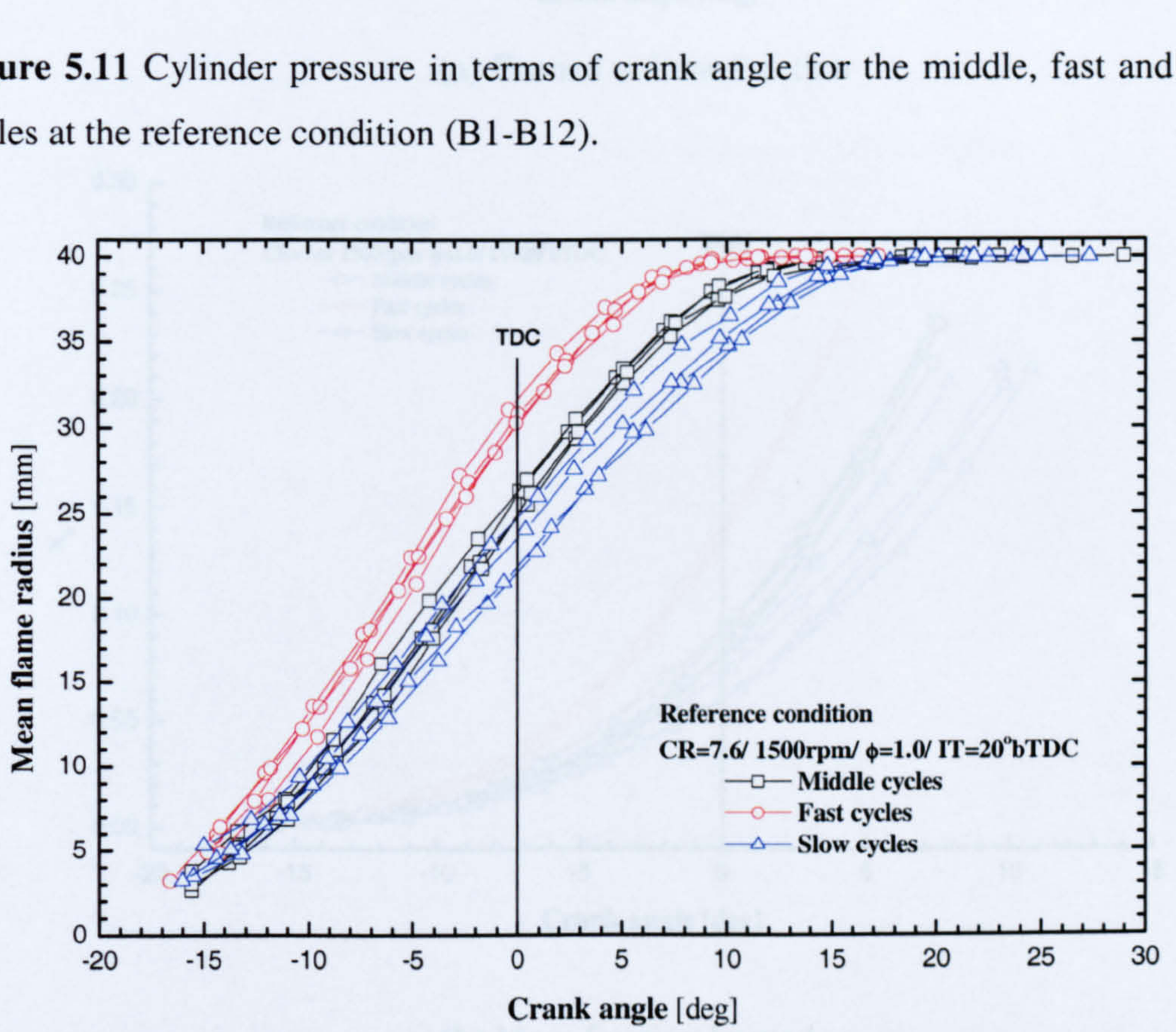

Figure 5.12 Mean flame radius versus crank angle for the middle, fast and slow cycles at the reference condition (B1-B12).

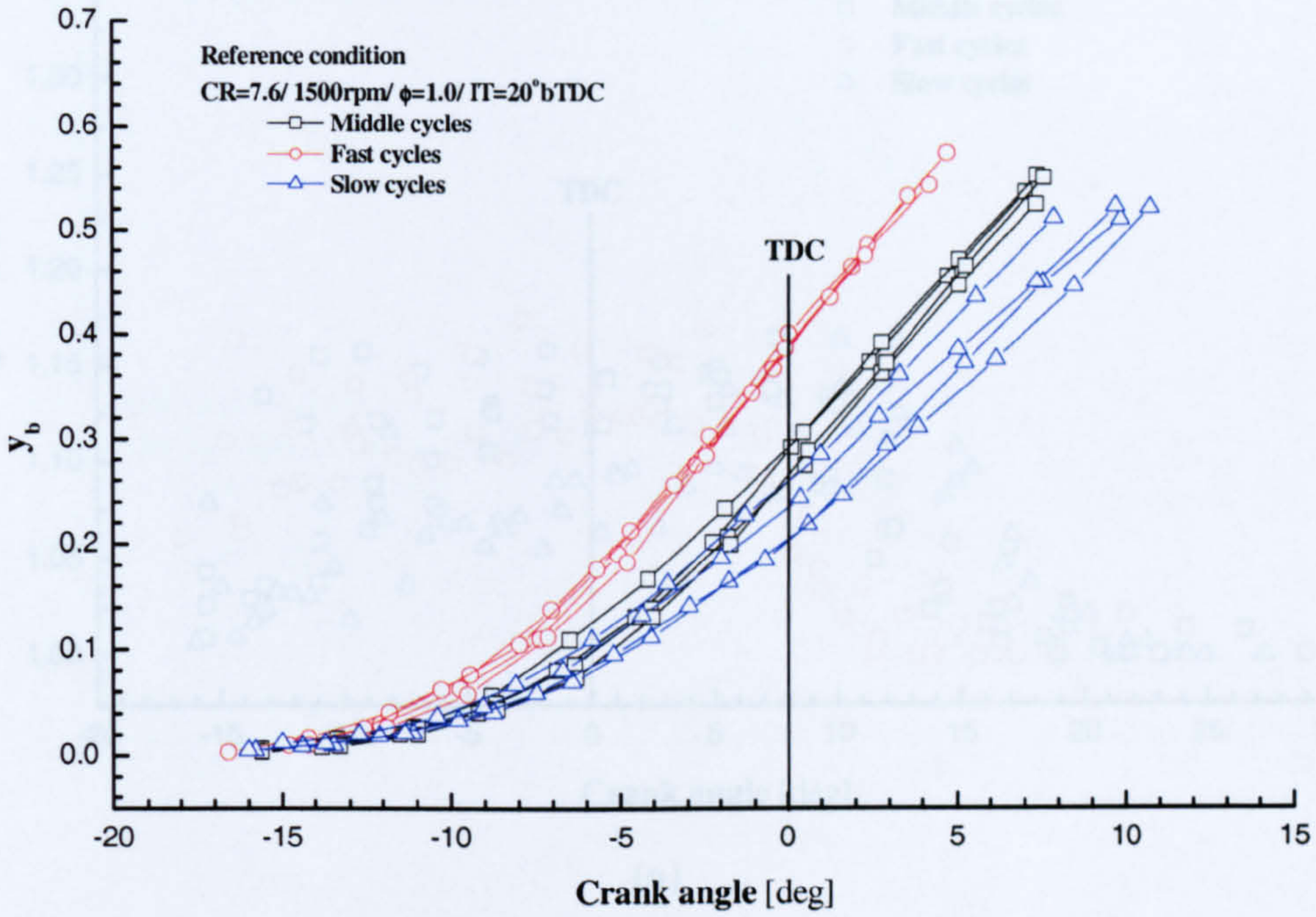

(a) Burned volume fraction

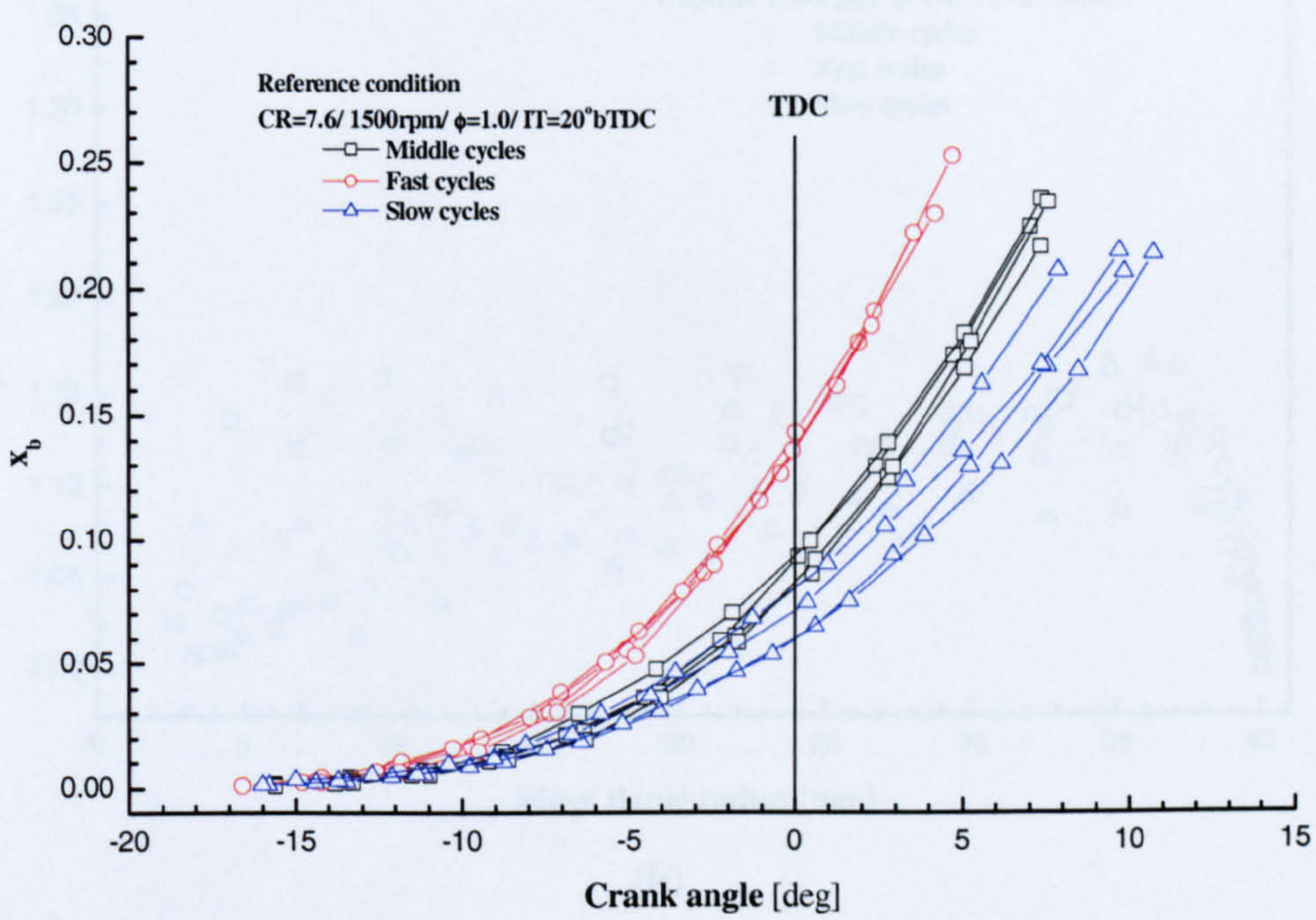

(b) Mass fraction burned

Figure 5.13 (a) Burned volume fraction derived from mean flame radius development and **(b)** mass fraction burned for the selected cycles at the reference condition.

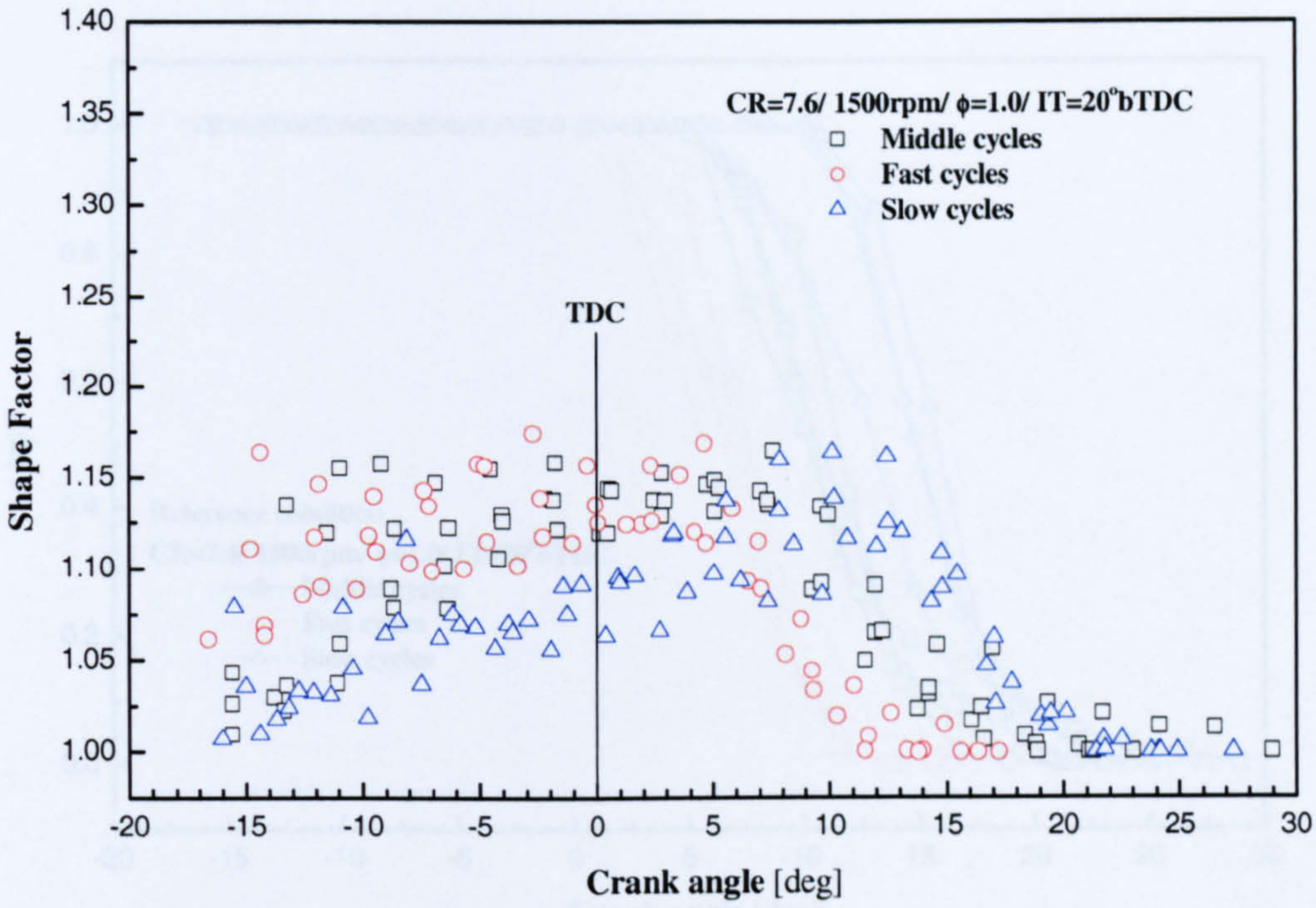

(a)

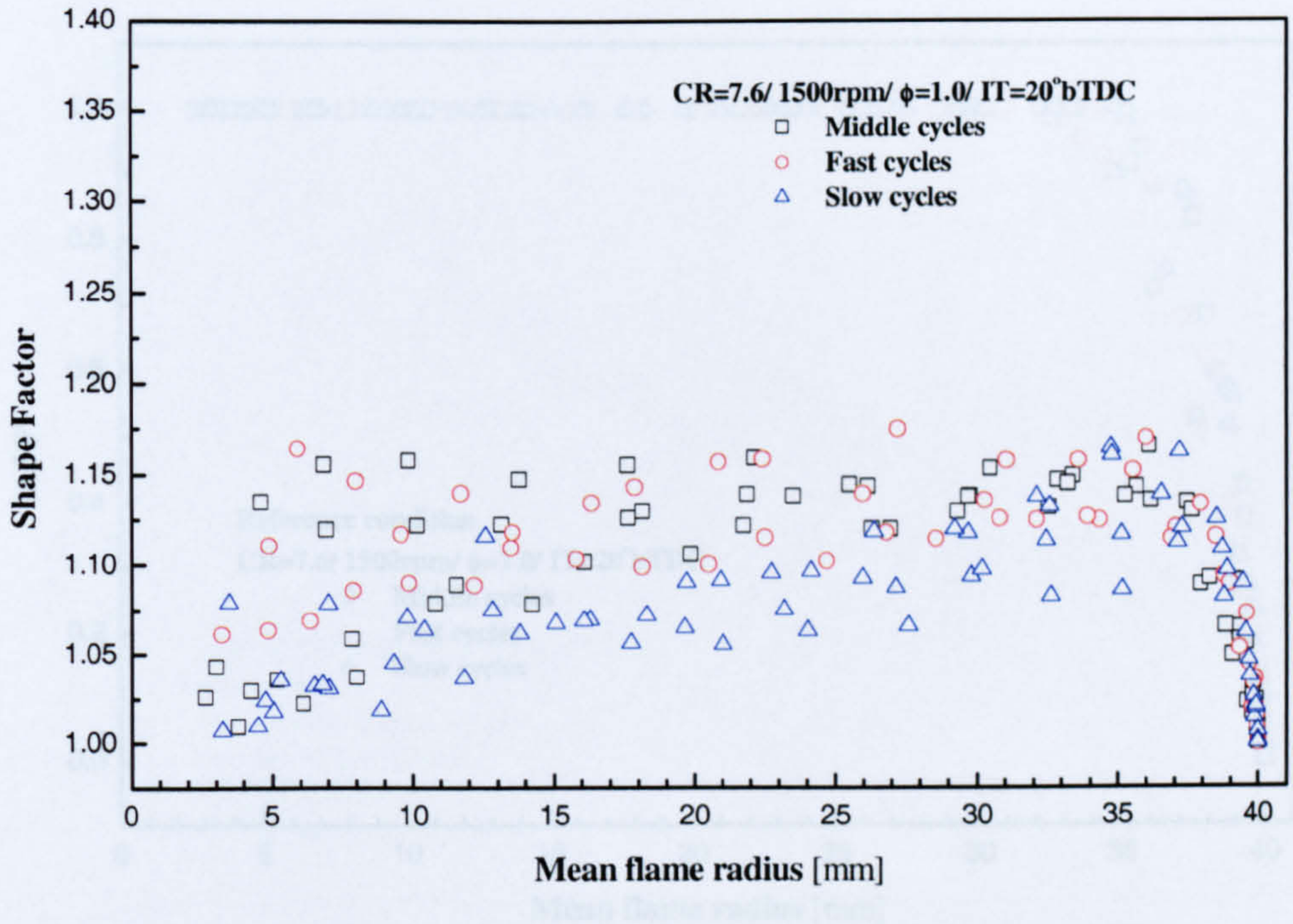

(b)

Figure 5.14 Flame Shape Factor versus **(a)** crank angle and **(b)** mean flame radius for the middle, fast and slow cycles at the reference condition (B1-B12).

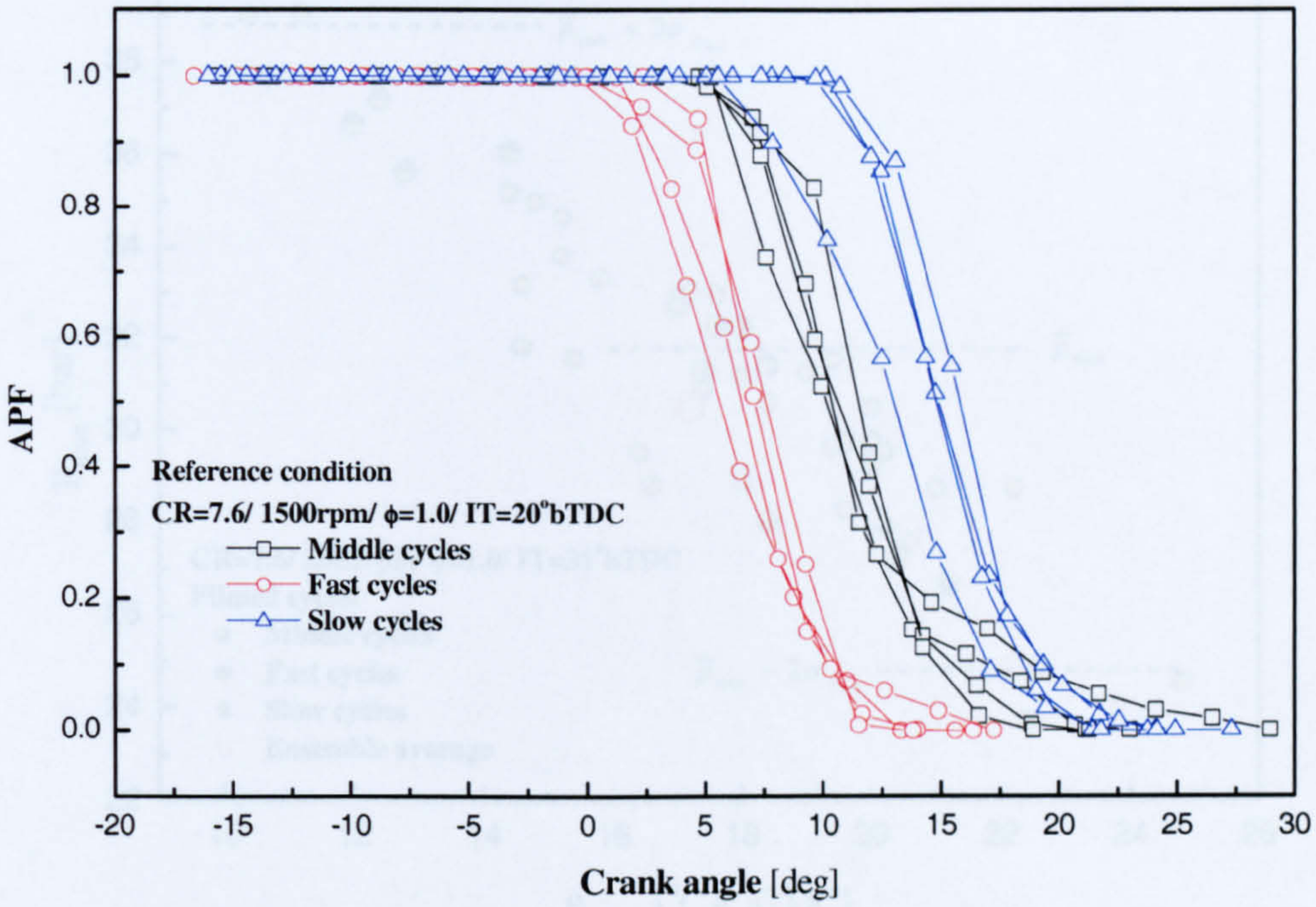

(a)

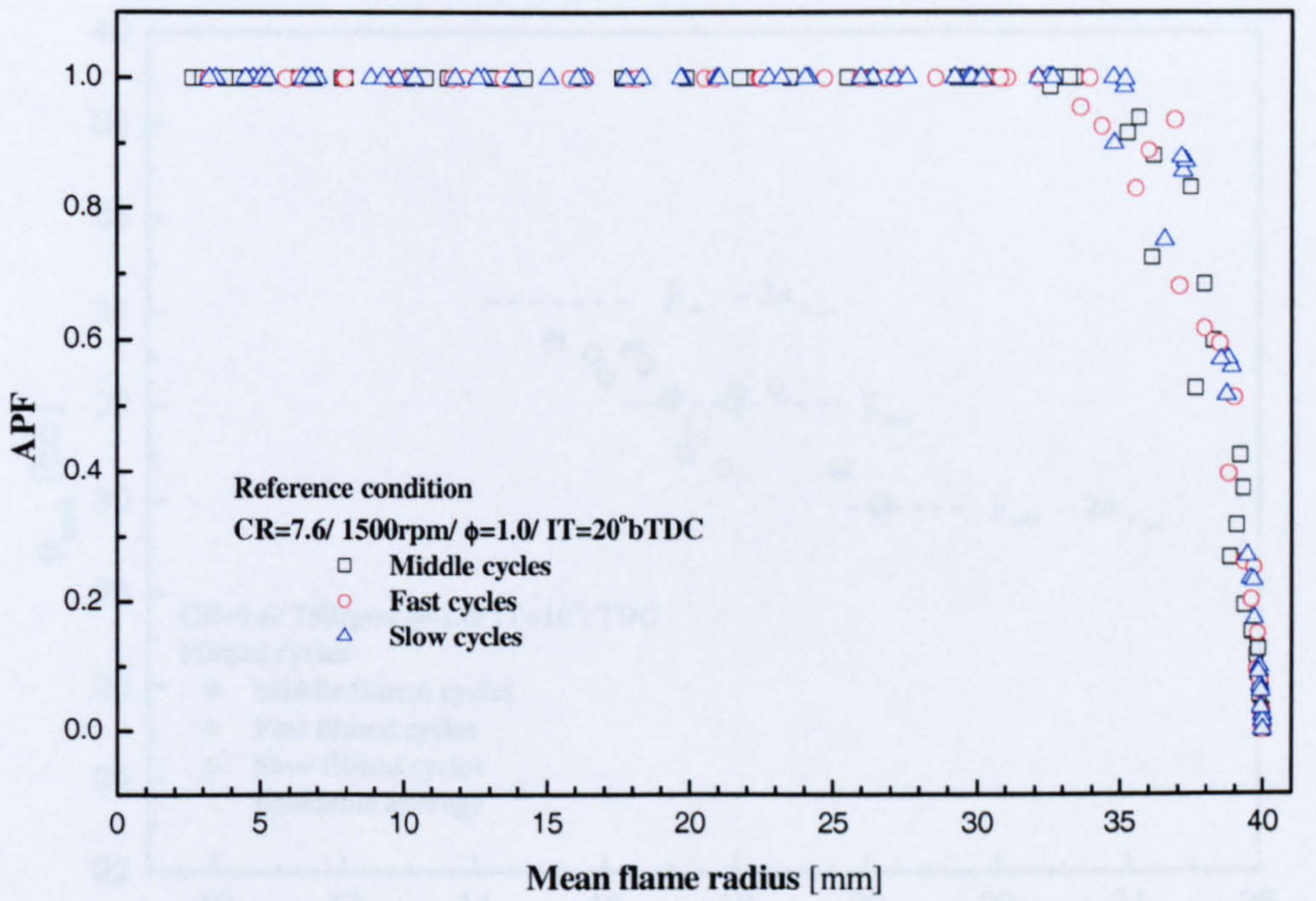

(b)

Figure 5.15 Active Perimeter Fraction (APF) versus **(a)** crank angle and **(b)** mean flame radius for the middle, fast and slow cycles at the reference condition.

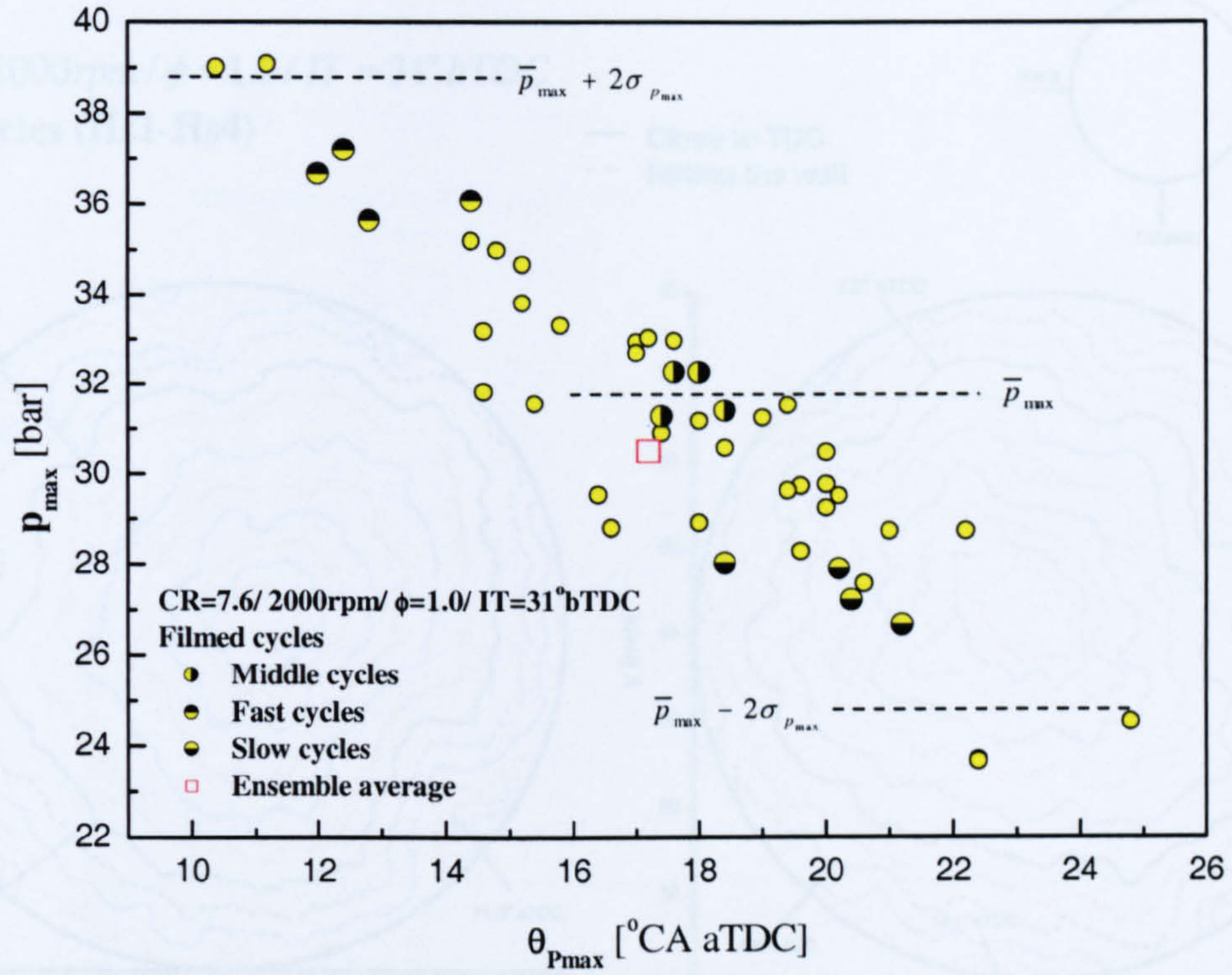

(a)

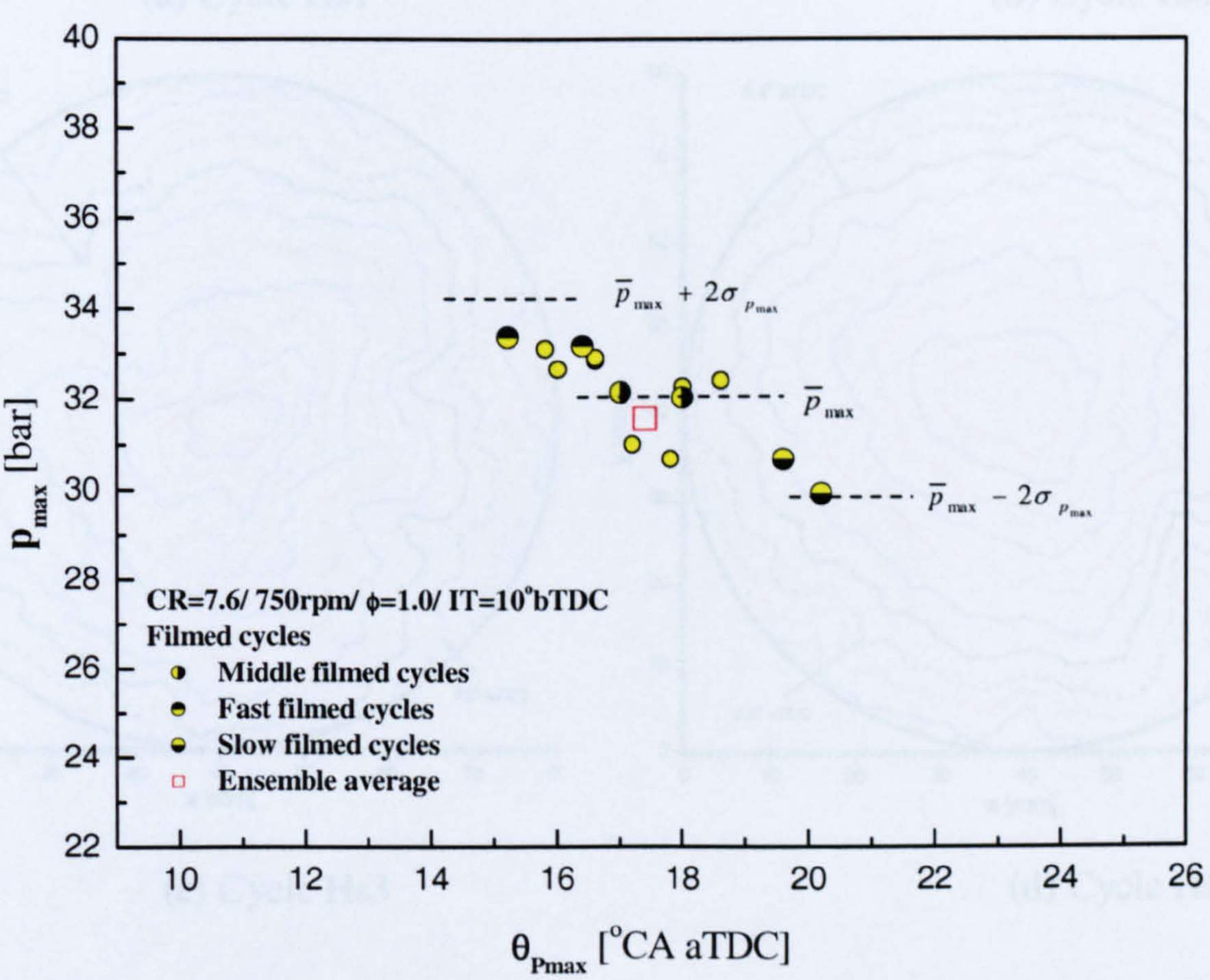

(b)

Figure 5.16 Peak pressure versus the corresponding crank angle occurrence associated with that of ensemble average for **(a)** 2000 *rpm* and **(b)** 750 rpm.

$CR = 7.6 / 2000rpm / \phi = 1.0 / IT = 31^{\circ} bTDC$

Middle Cycles (Hs1-Hs4)

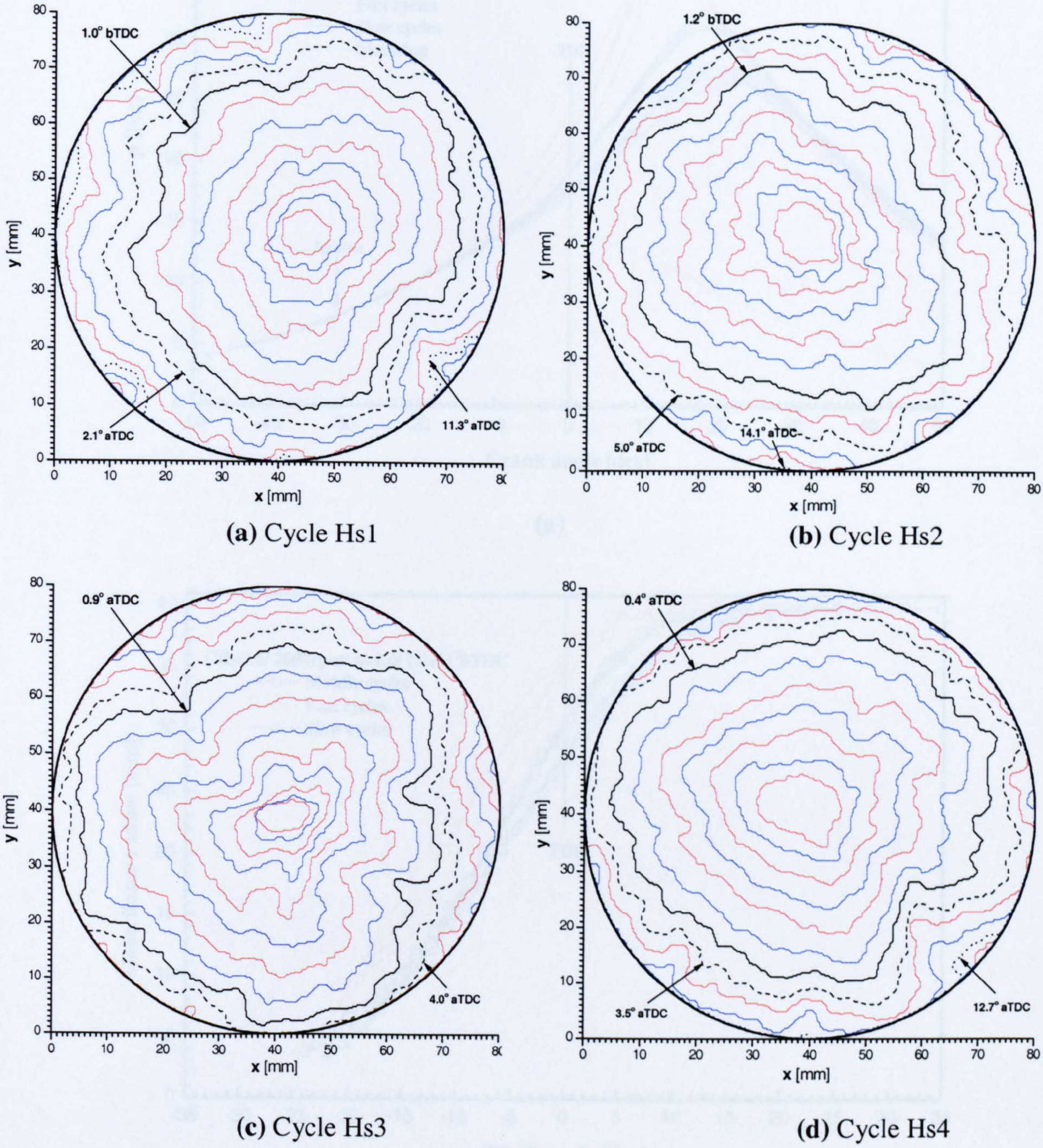

(a) Cycle Hs1

(b) Cycle Hs2

(c) Cycle Hs3

(d) Cycle Hs4

Figure 5.17 Successive flame positions of the four middle cycles (Hs1-Hs4) over propagation period.

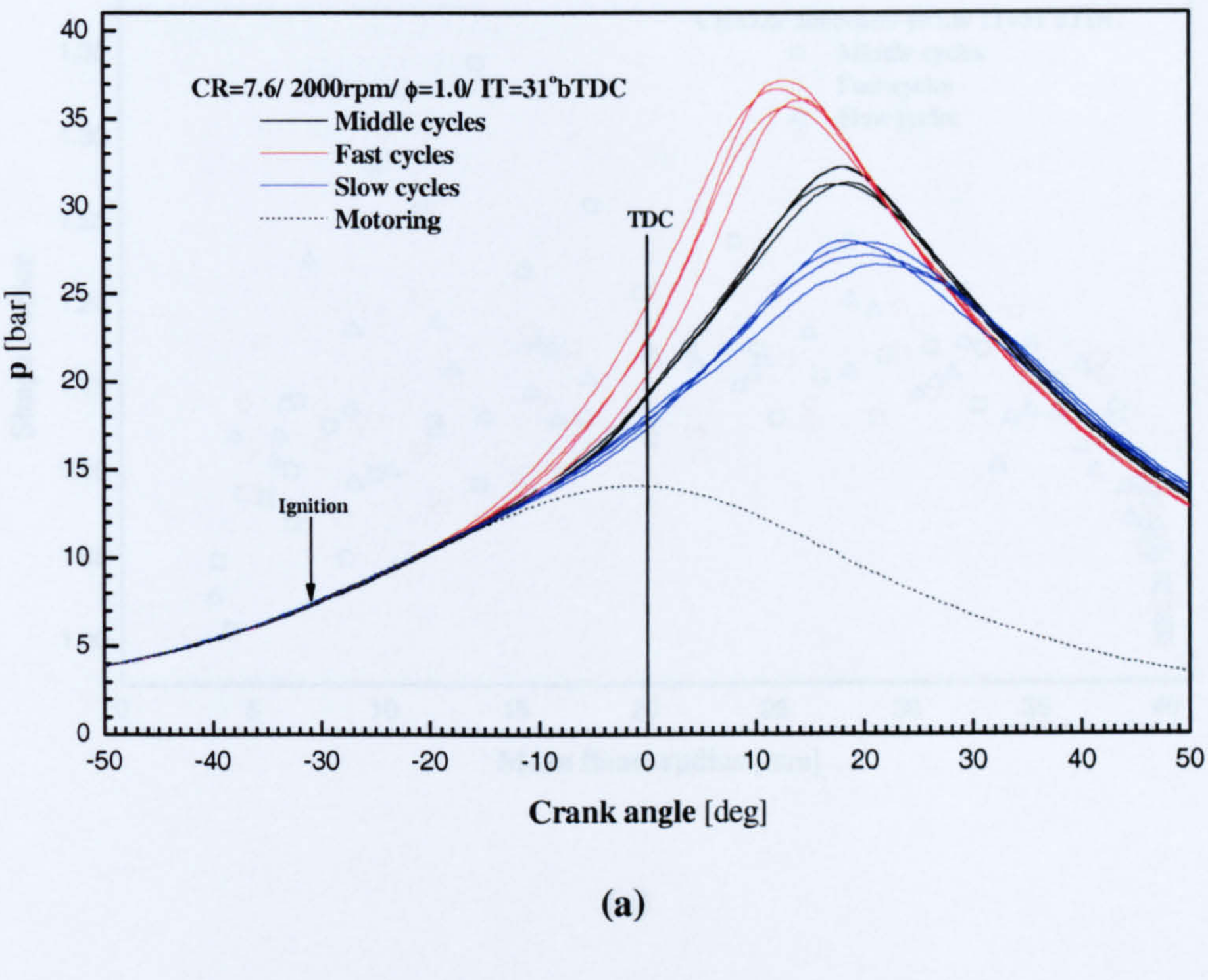

(a)

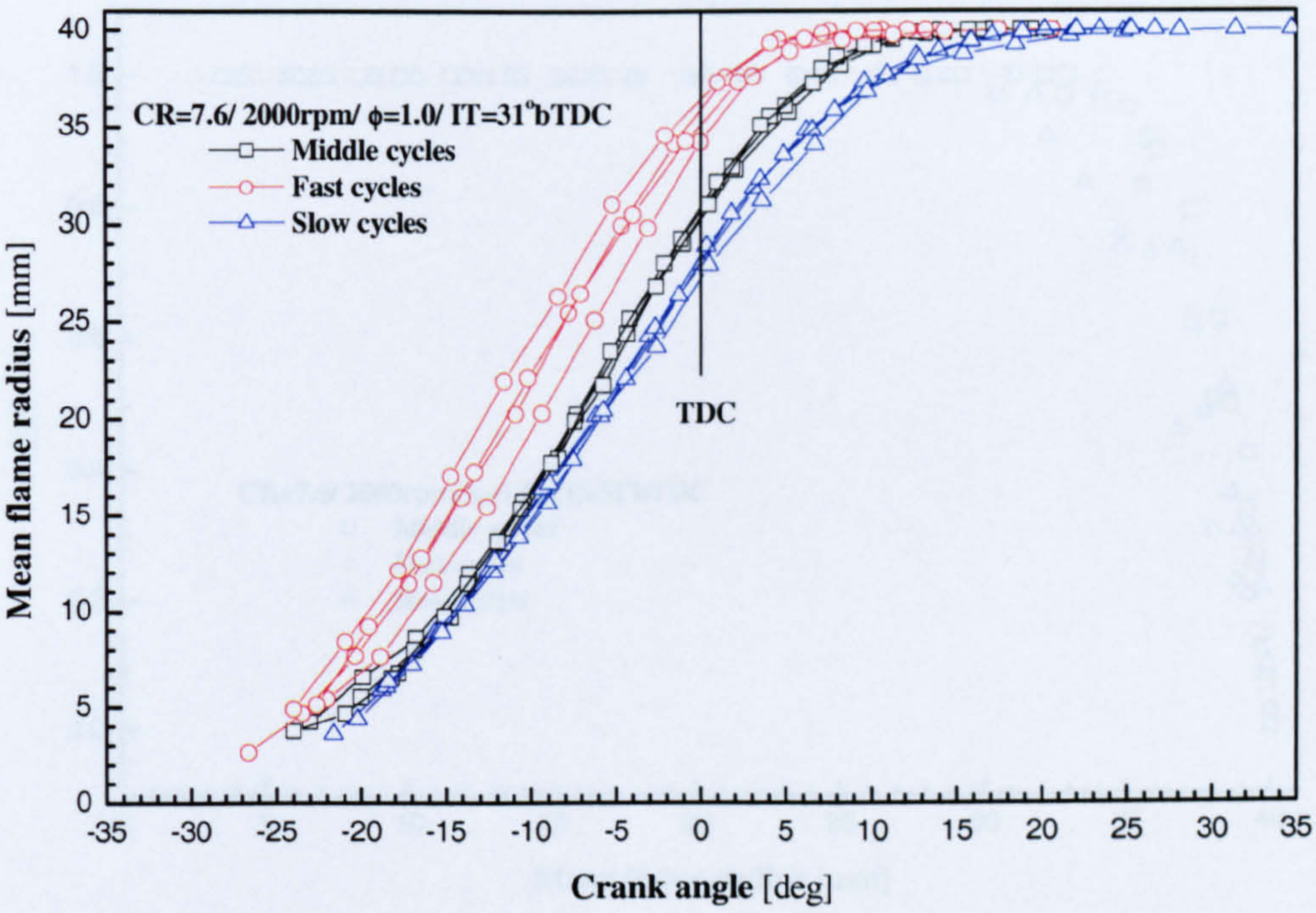

(b)

Figure 5.18 (a) Cylinder pressure and **(b)** mean flame radius versus crank angle for the middle, fast and slow cycles (Hs1-Hs12).

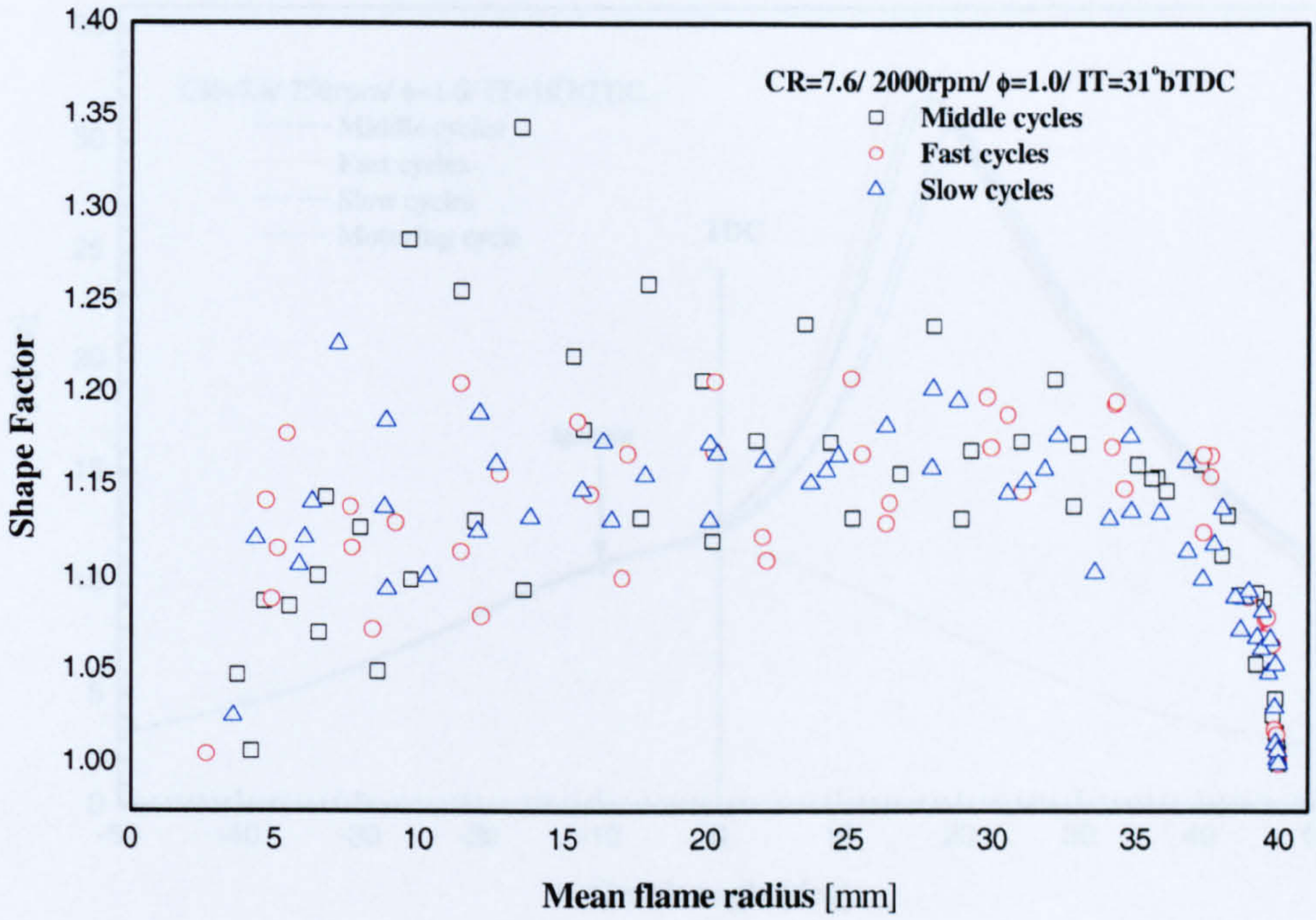

(a)

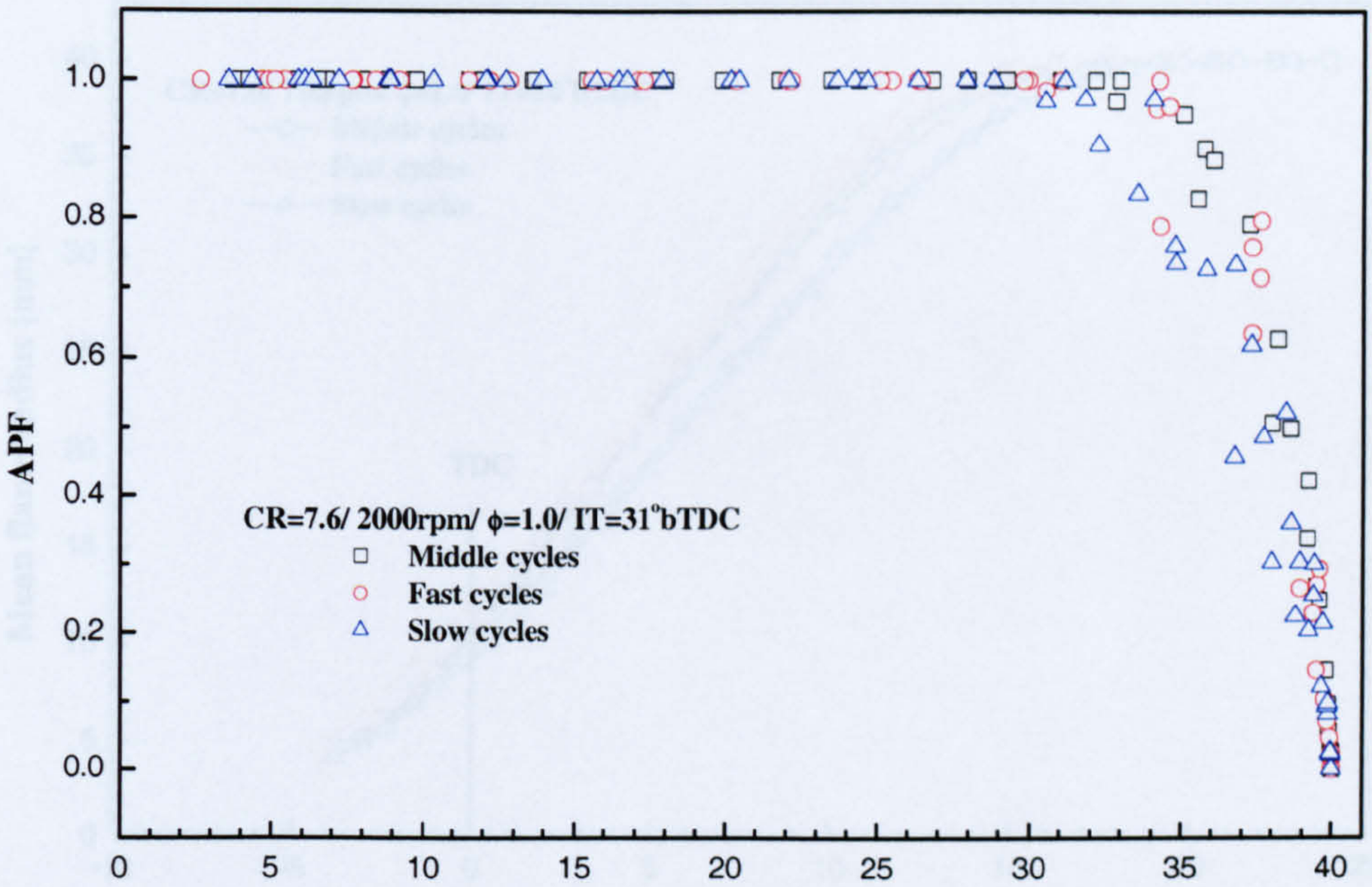

(b)

Figure 5.19 (a) Flame shape factor and **(b)** active perimeter fraction versus mean flame radius for the middle, fast and slow cycles (Hs1-Hs12).

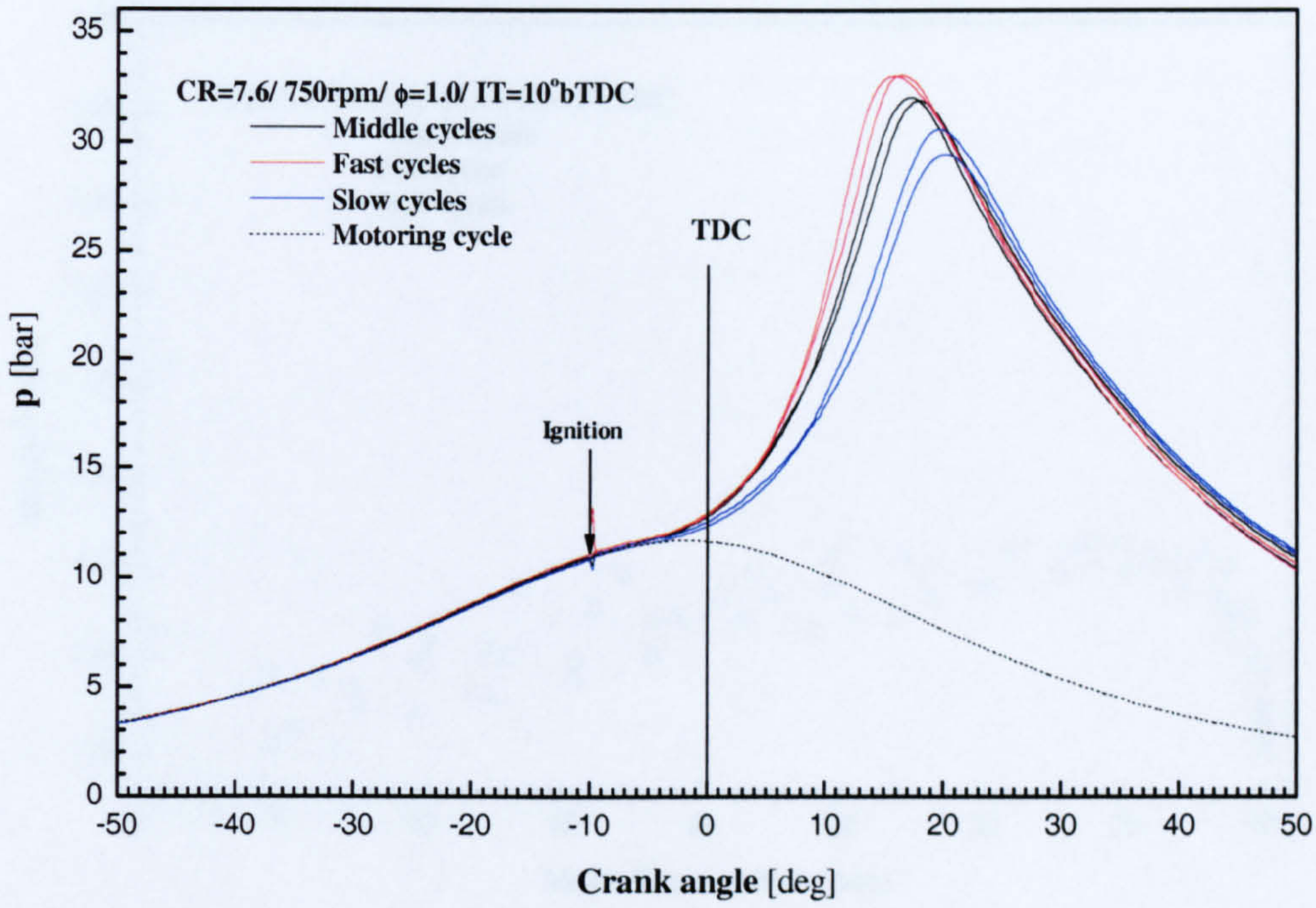

(a)

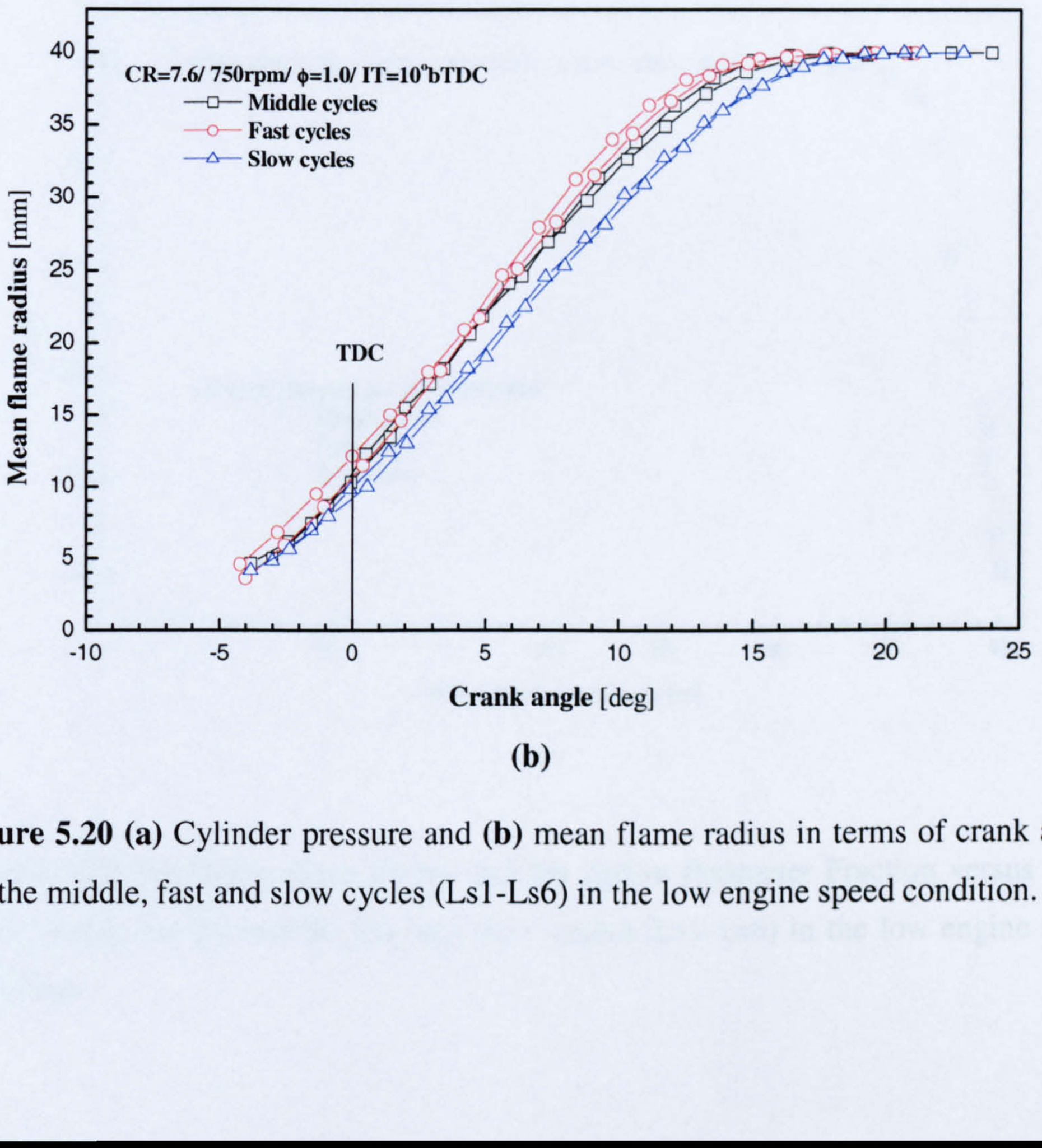

(b)

Figure 5.20 (a) Cylinder pressure and **(b)** mean flame radius in terms of crank angle for the middle, fast and slow cycles (Ls1-Ls6) in the low engine speed condition.

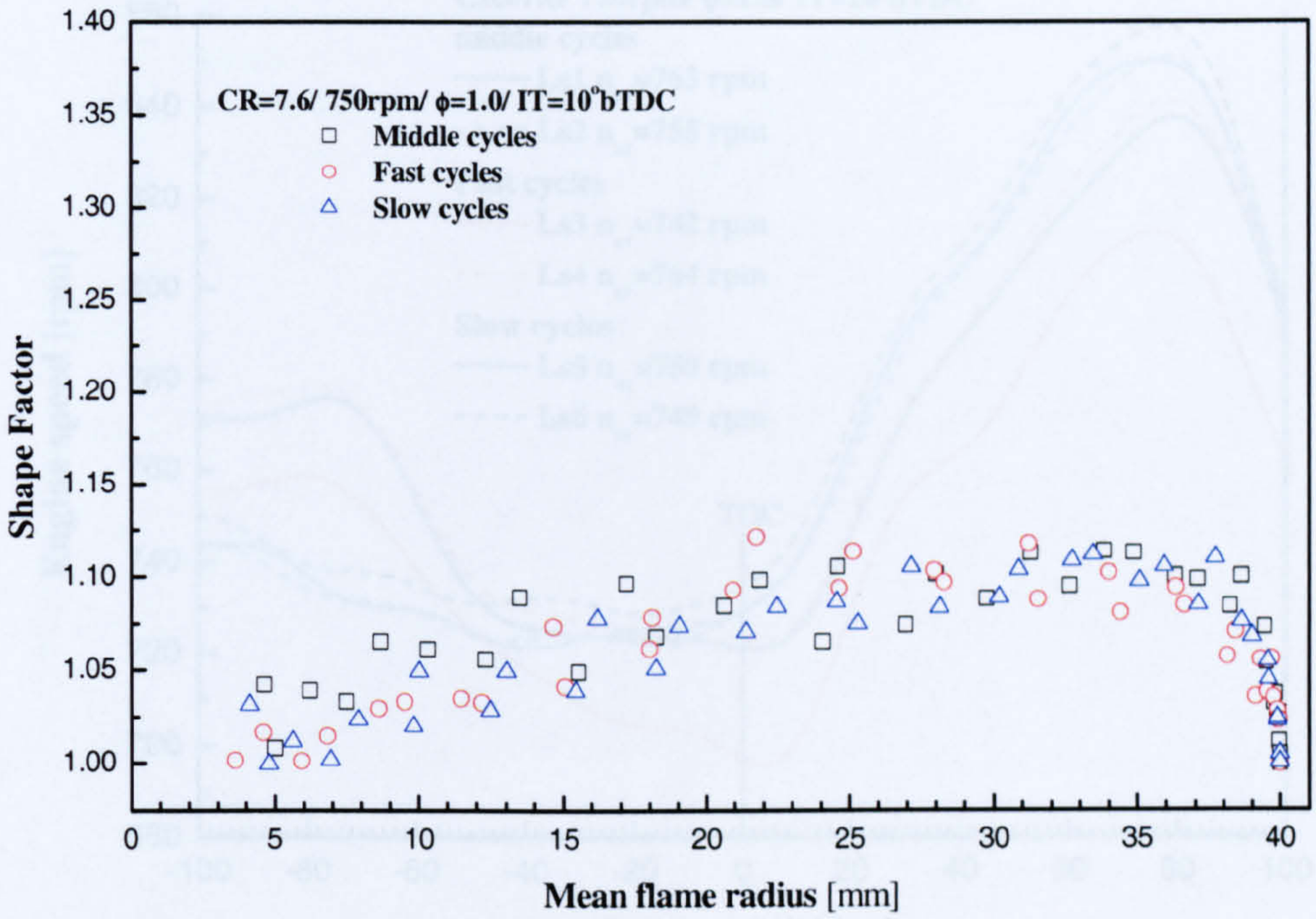

(a)

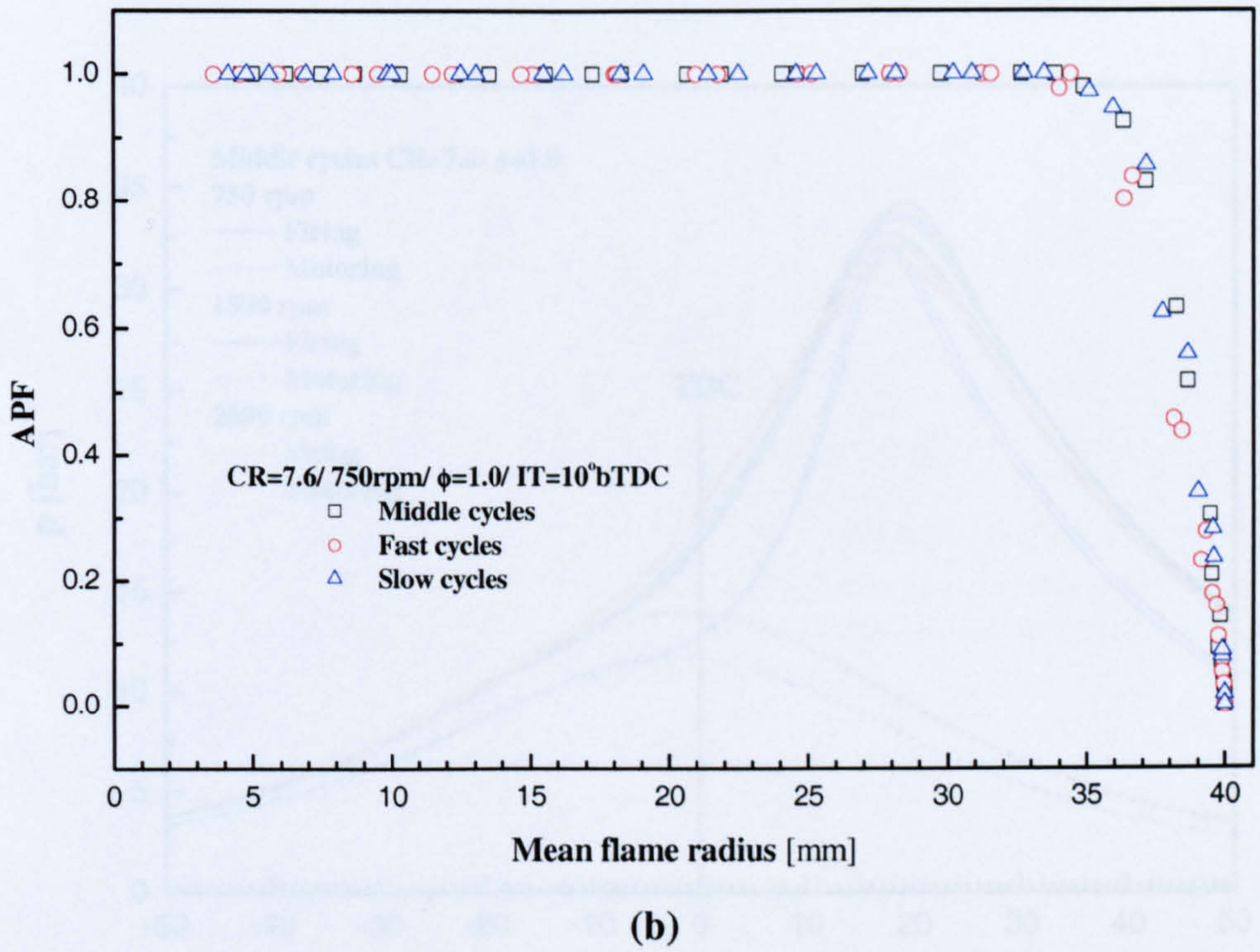

(b)

Figure 5.21 (a) Flame shape Factor and **(b)** Active Perimeter Fraction versus mean flame radius for the middle, fast and slow cycles (Ls1-Ls6) in the low engine speed condition.

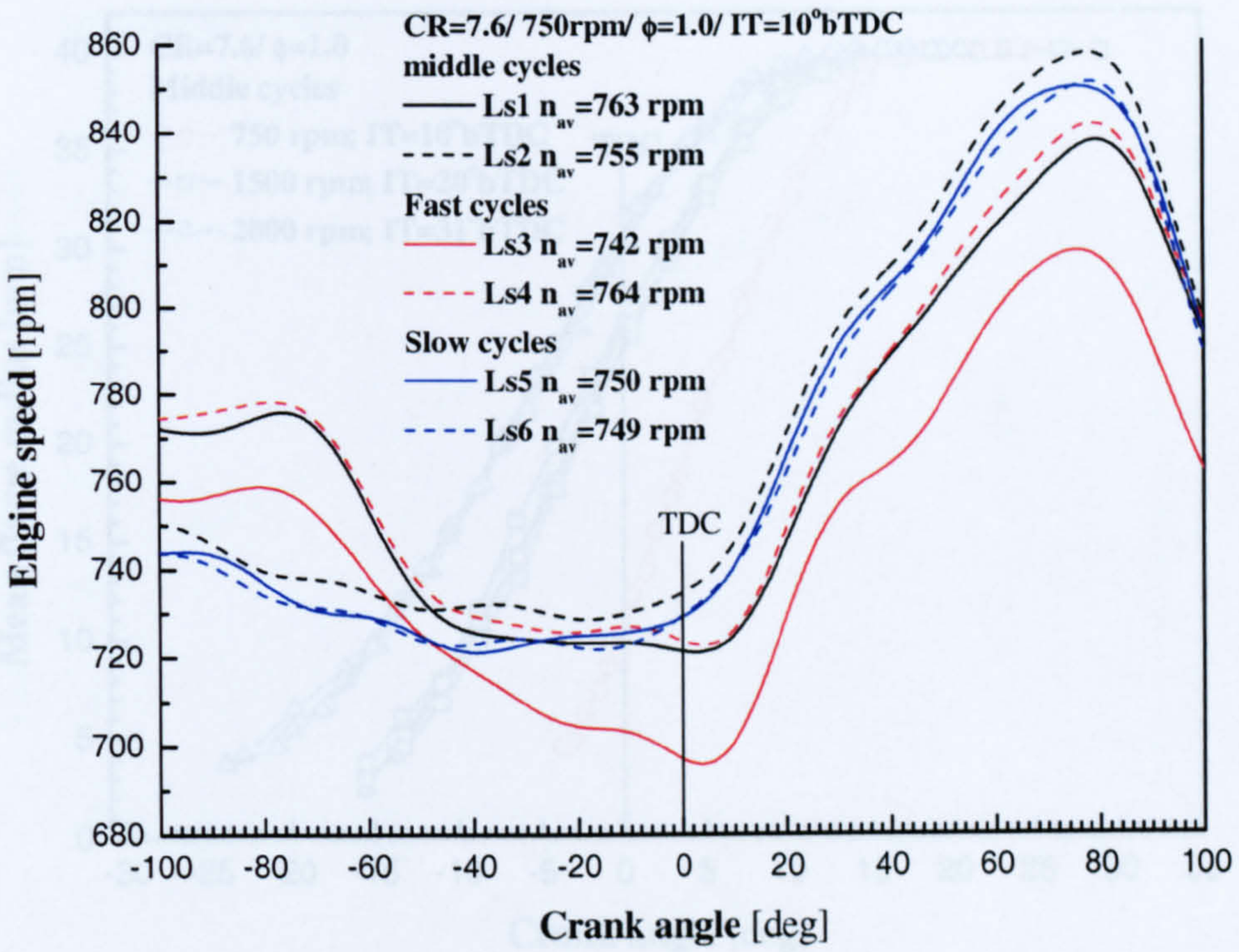

Figure 5.22 Engine speed versus crank angle for the six selected cycles at low engine speed (750 *rpm*).

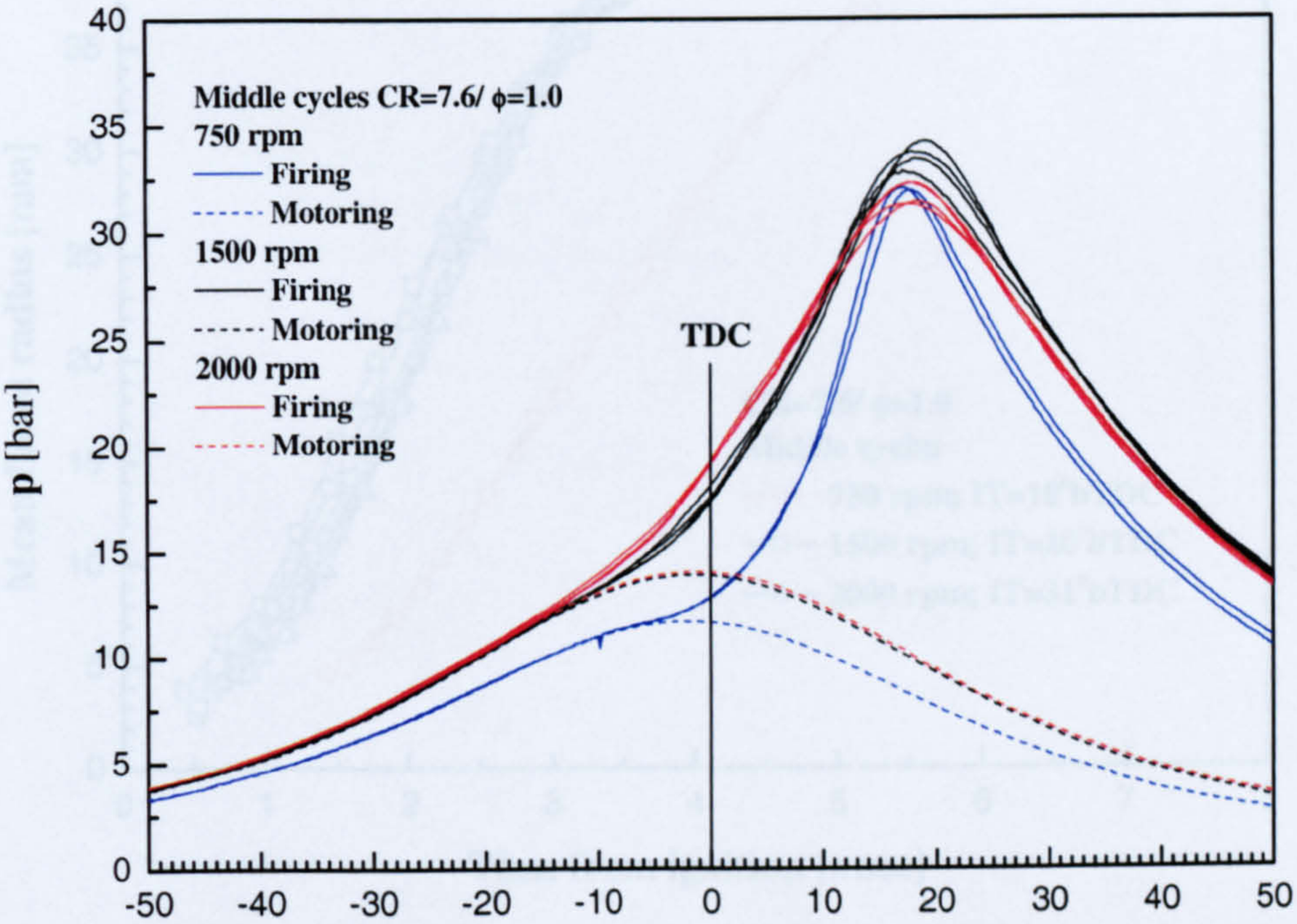

Figure 5.23 Cylinder pressure versus crank angle for the middle cycles associated with those of motoring cycles at the three engine speeds.

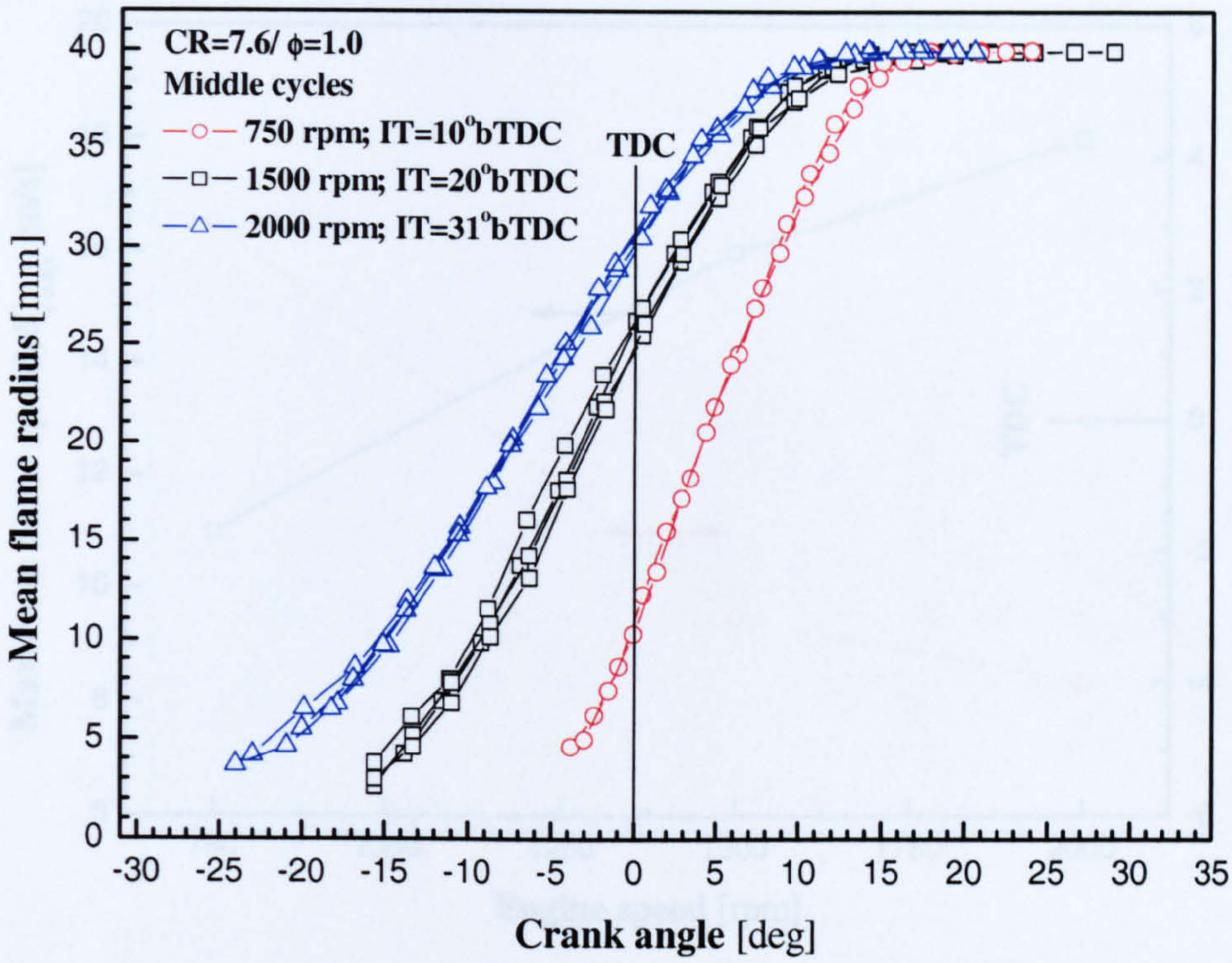

(a)

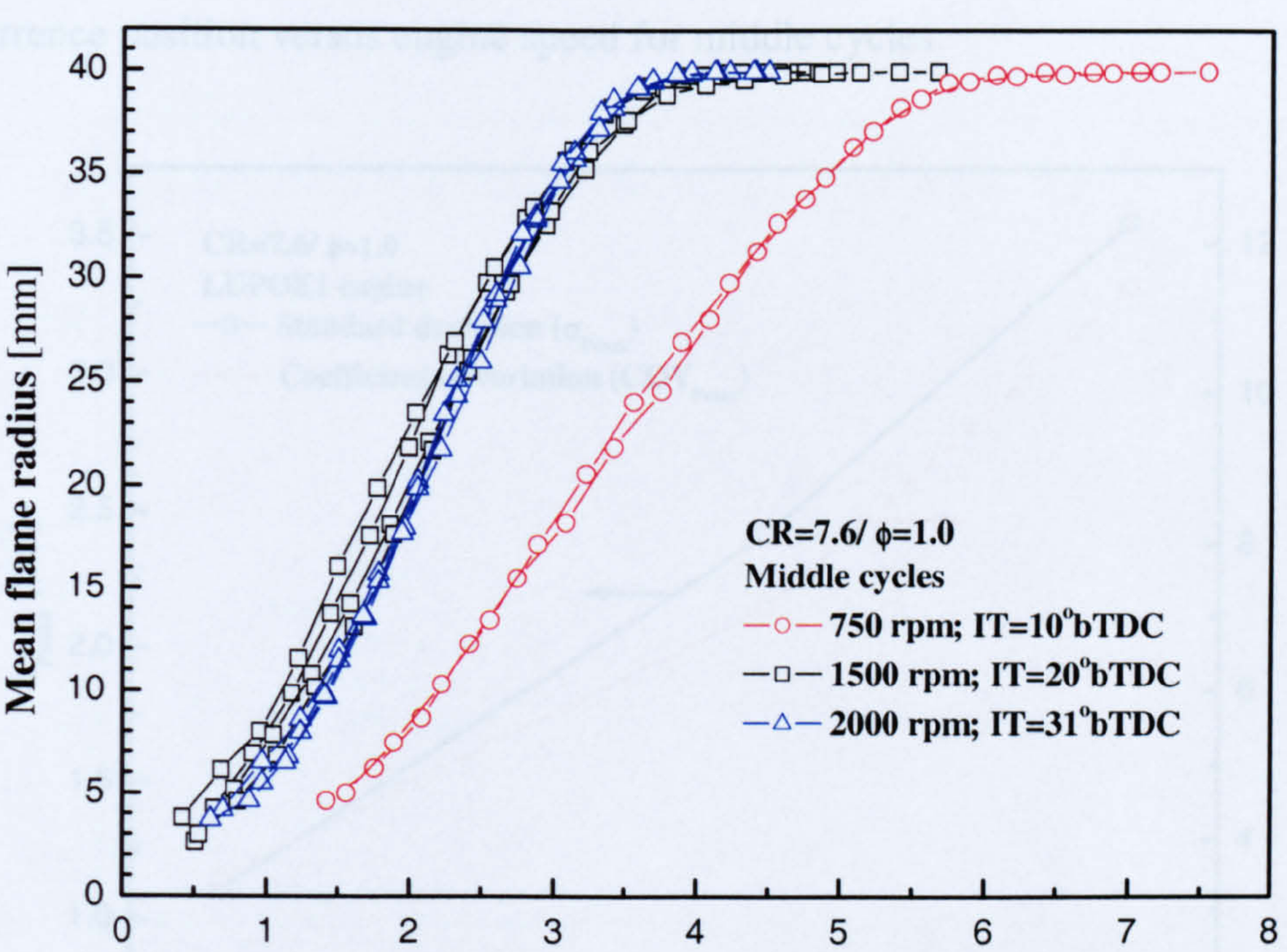

(b)

Figure 5.24 Mean flame radius versus **(a)** crank angle and **(b)** time from ignition for the middle cycles of the three engine speeds.

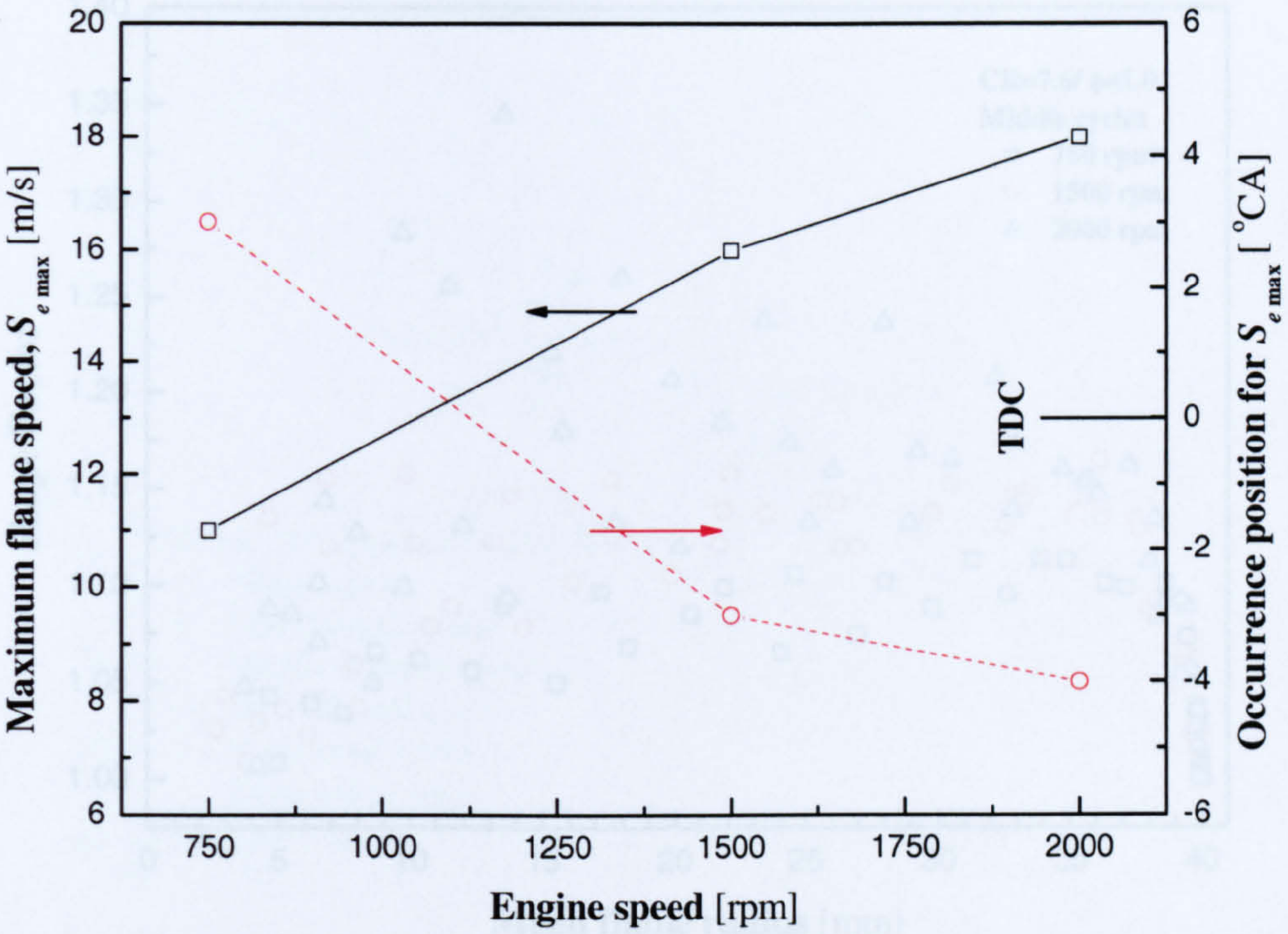

Figure 5.25 Maximum flame speed (estimated from flame development) and its occurrence position versus engine speed for middle cycles.

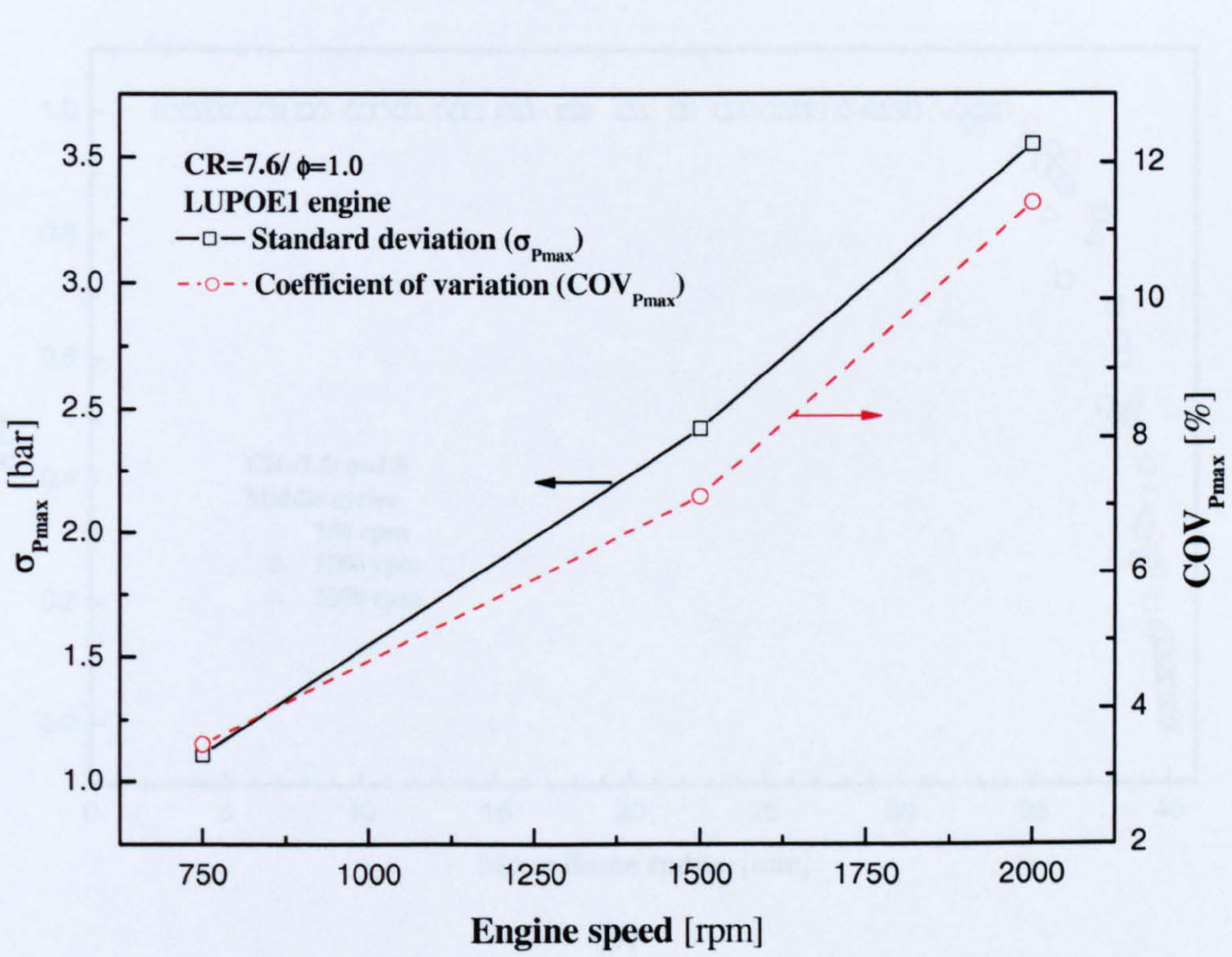

Figure 5.26 Standard deviation and coefficient of variation based on peak pressure versus engine speed.

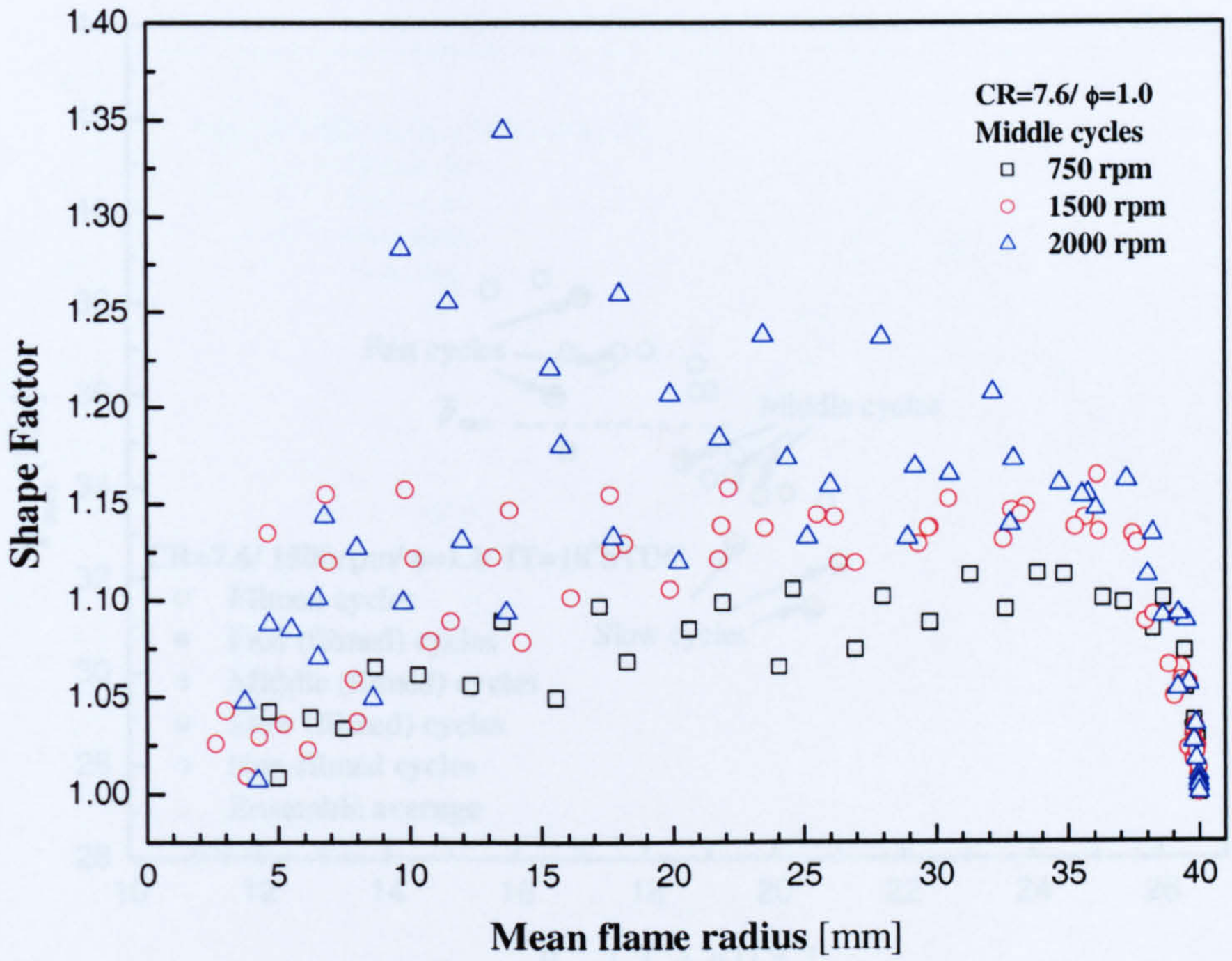

(a)

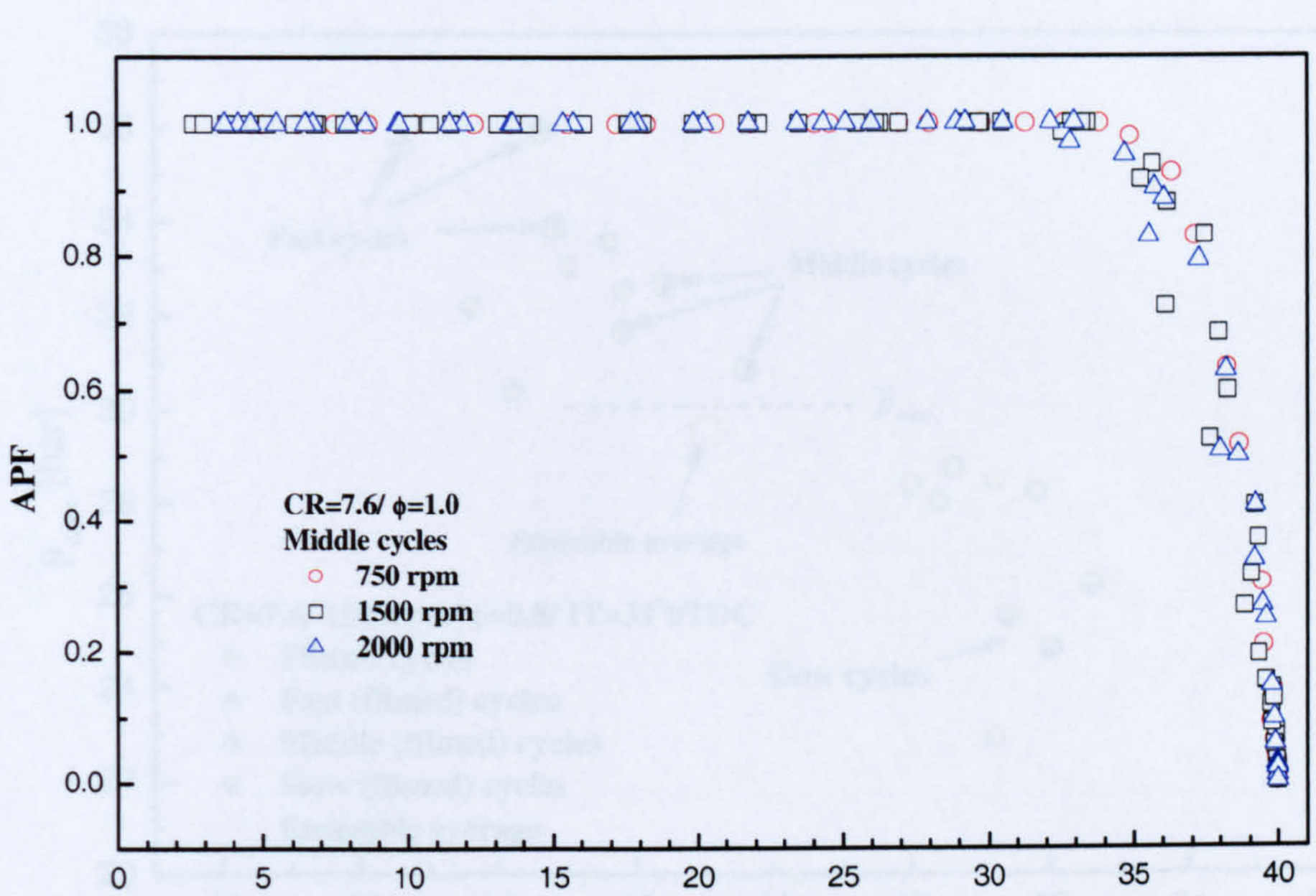

(b)

Figure 5.27 (a) Shape Factor and **(b)** Active Perimeter Fraction versus mean flame radius for the middle cycles of the three engine speeds (750, 1500 and 2000 rpm).

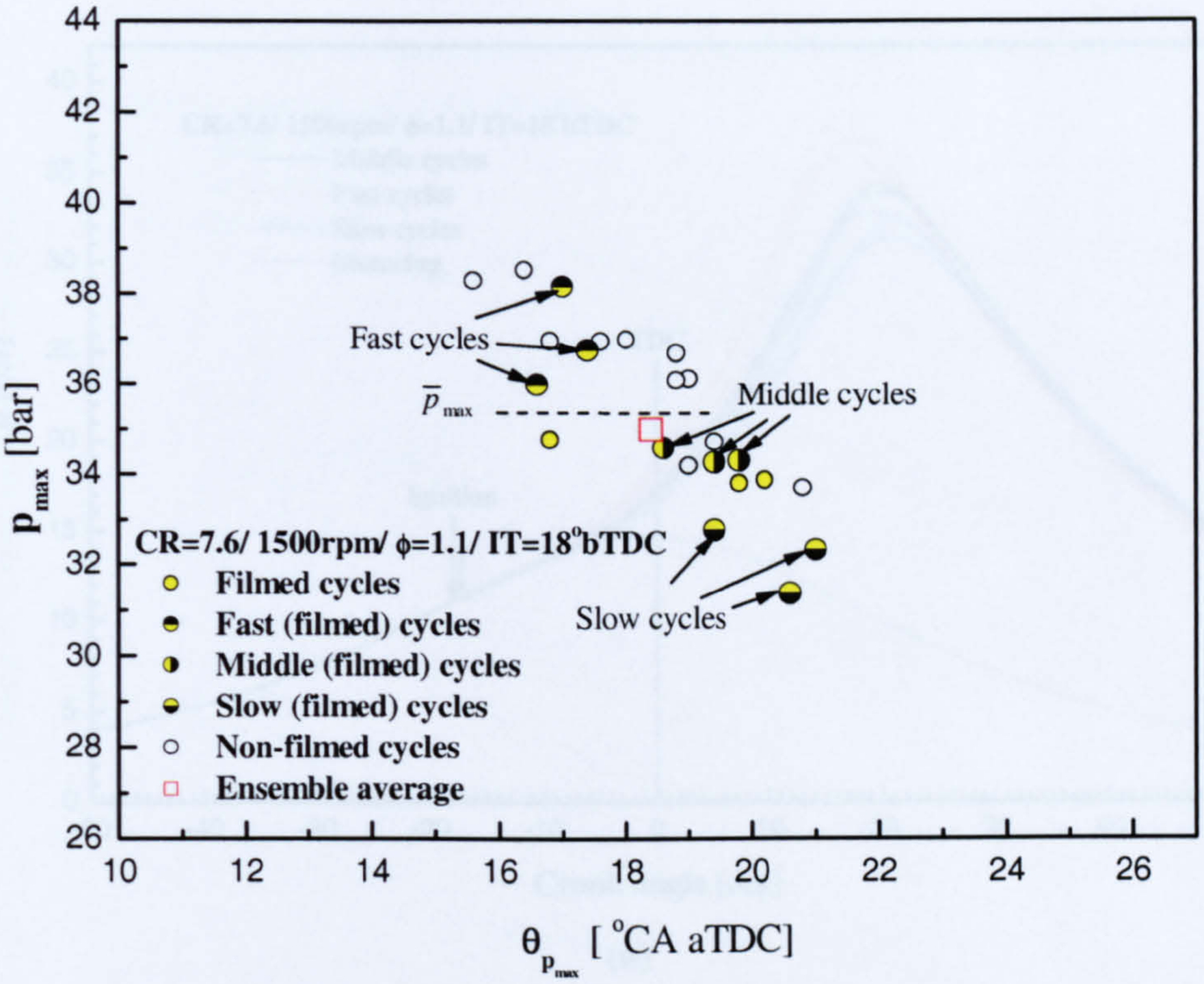

(a) Rich mixture

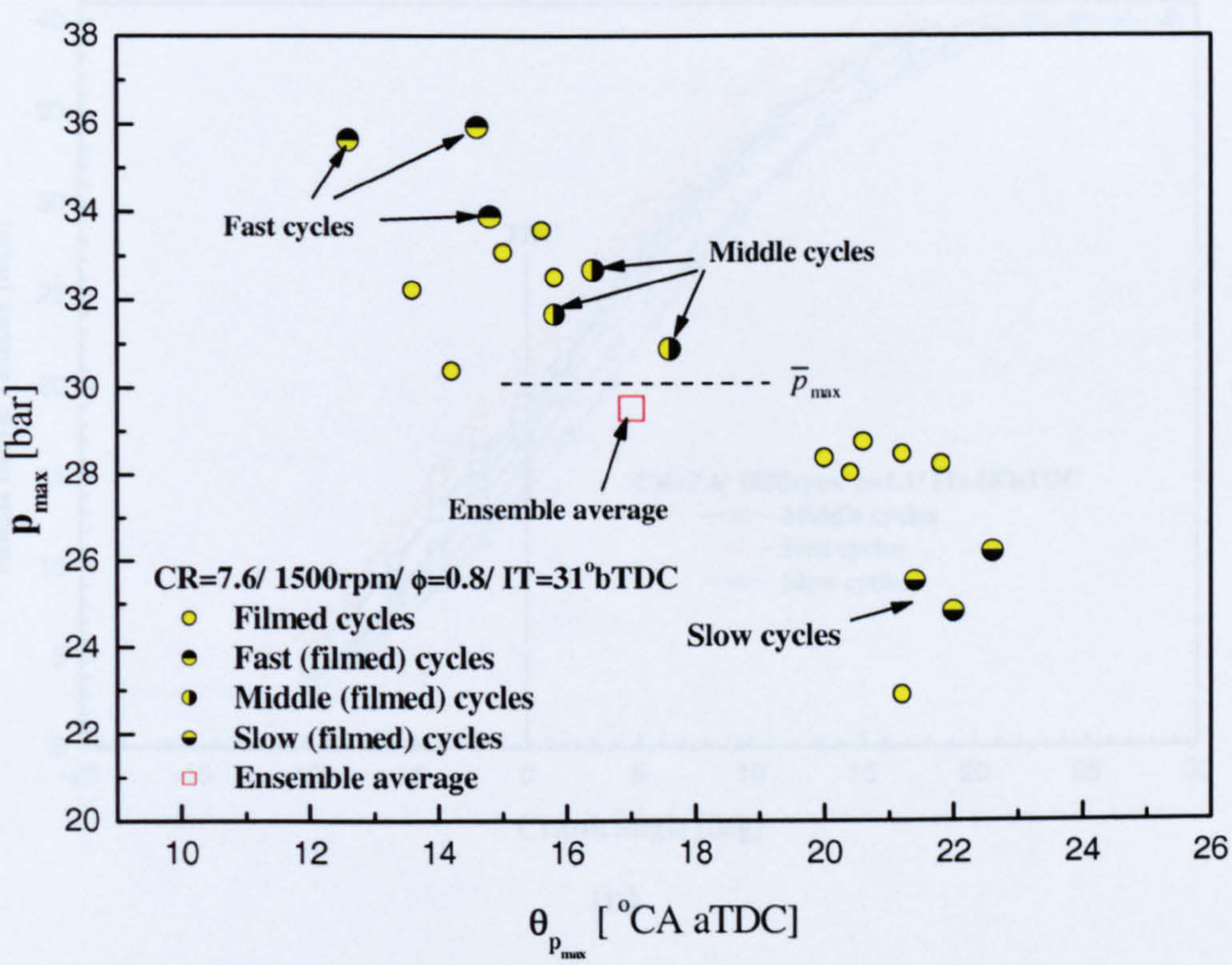

(b) Lean mixture

Figure 5.28 Peak pressure versus the corresponding crank angle occurrence for **(a)** rich and **(b)** lean mixture conditions.

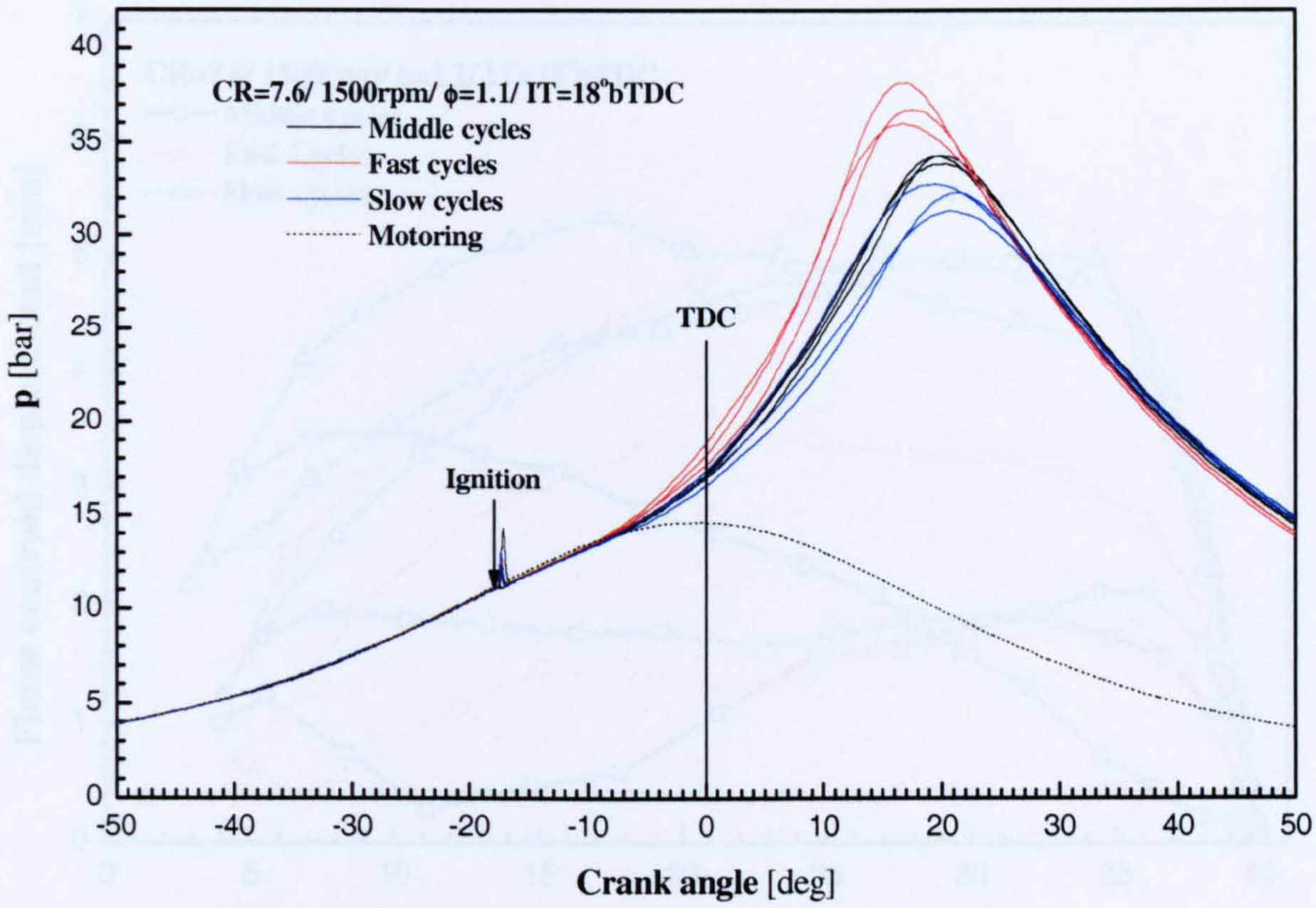

(a)

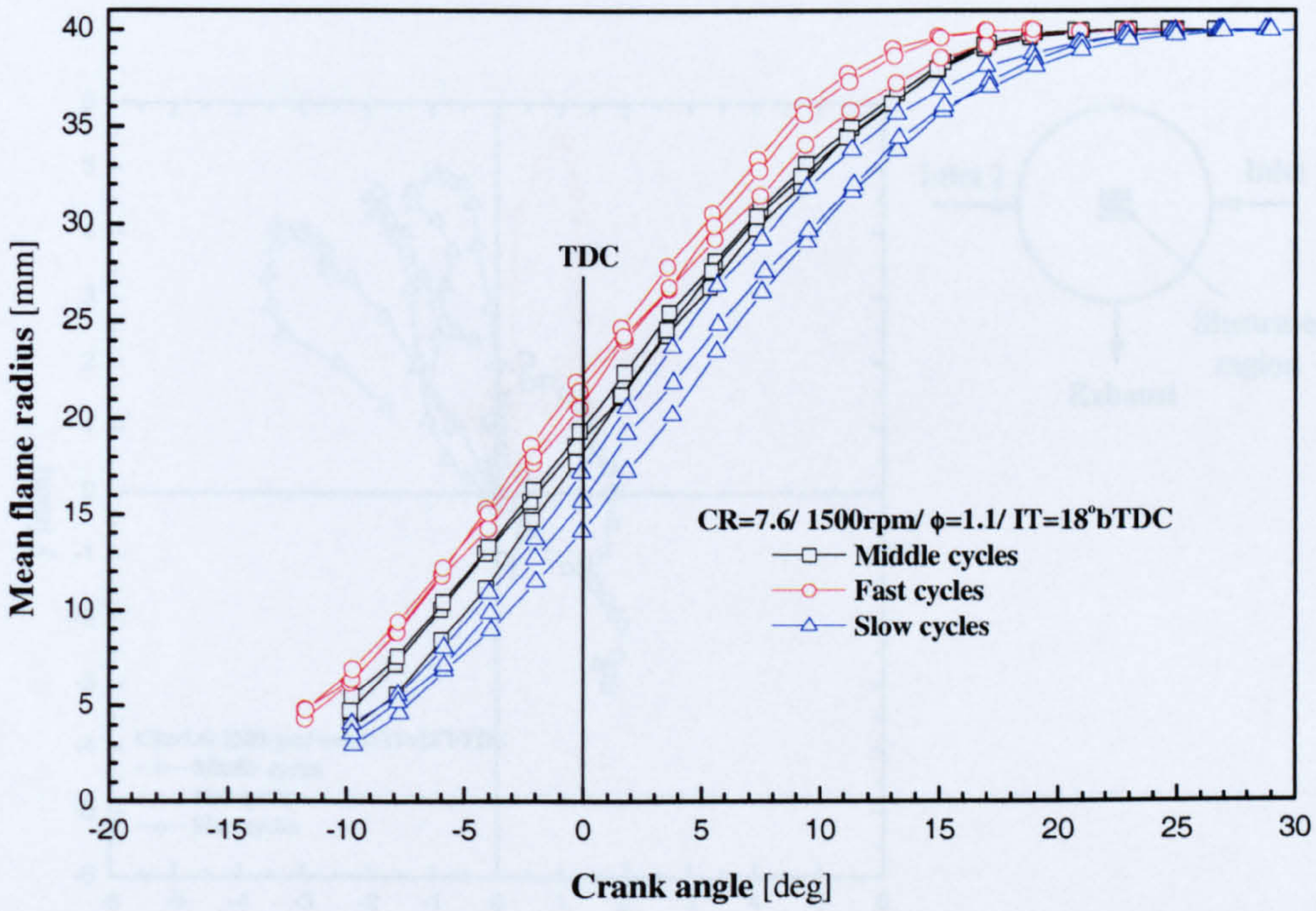

(b)

Figure5.29 **(a)** Cylinder pressure and **(b)** mean flame radius versus crank angle for the middle, fast and slow cycles at the rich condition.

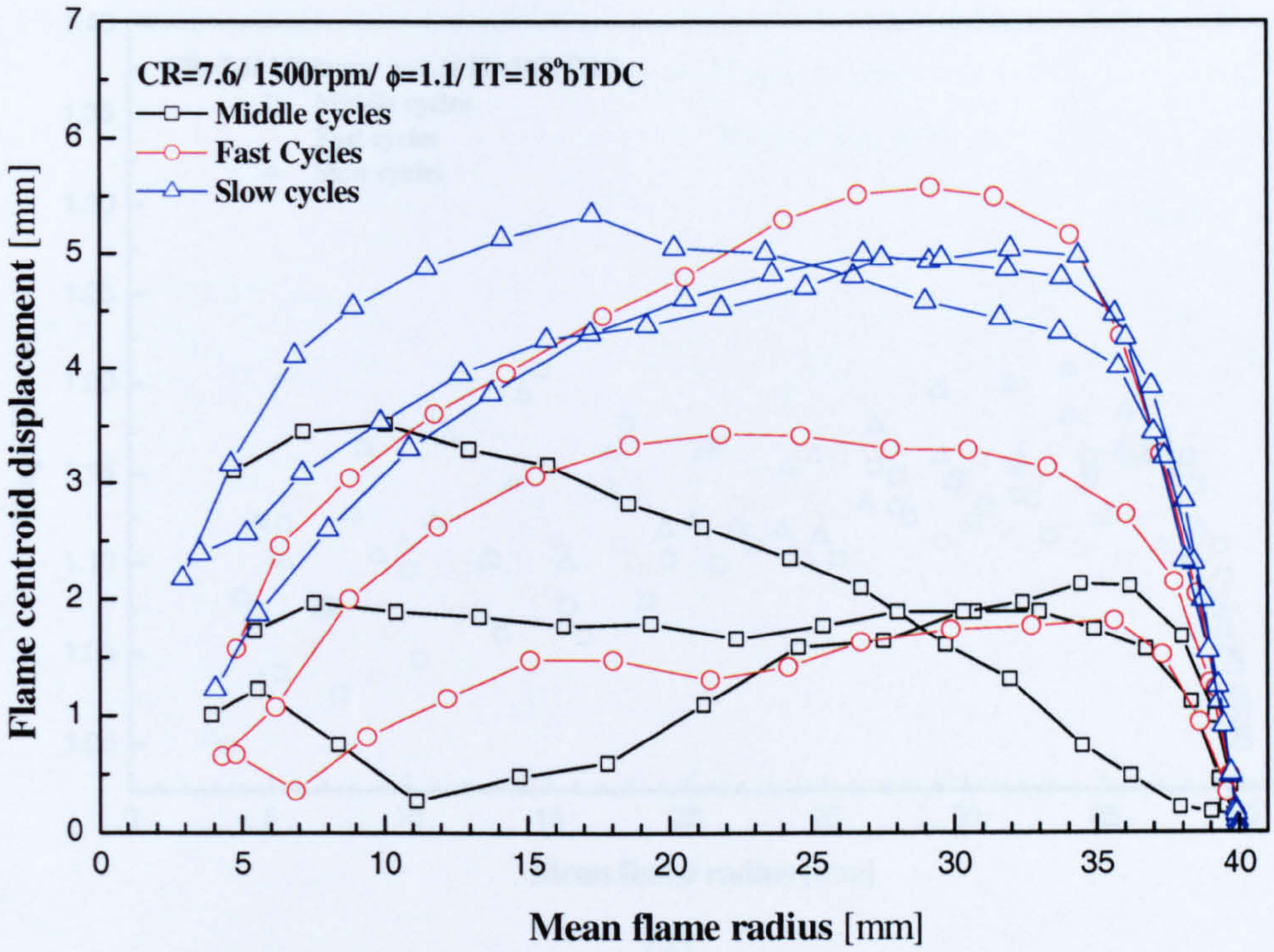

(a)

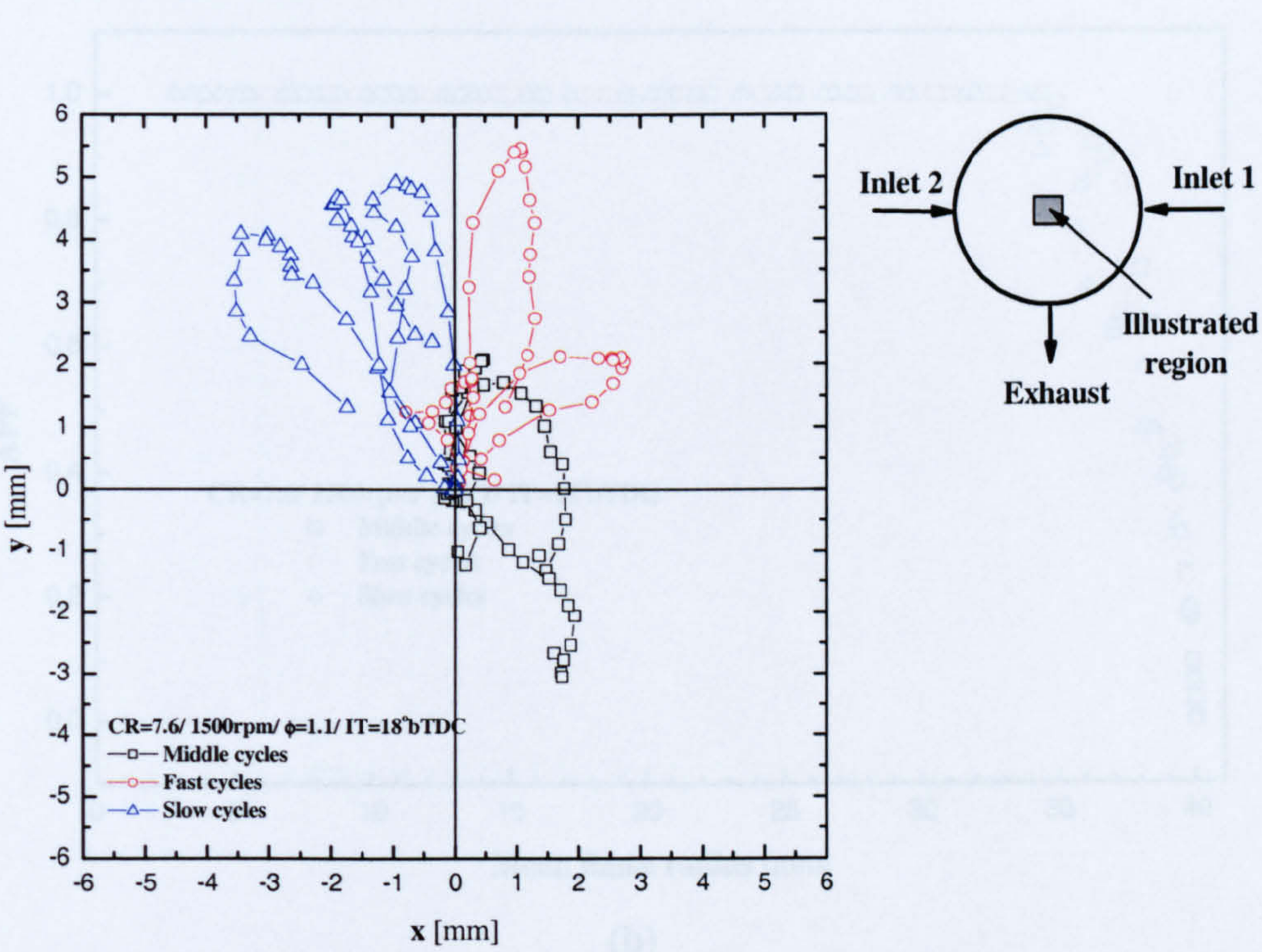

(b)

Figure 5.30 (a) Flame centroid displacement versus mean flame radius and **(b)** flame centroid locus for the middle, fast and slow cycles at the rich mixture condition.

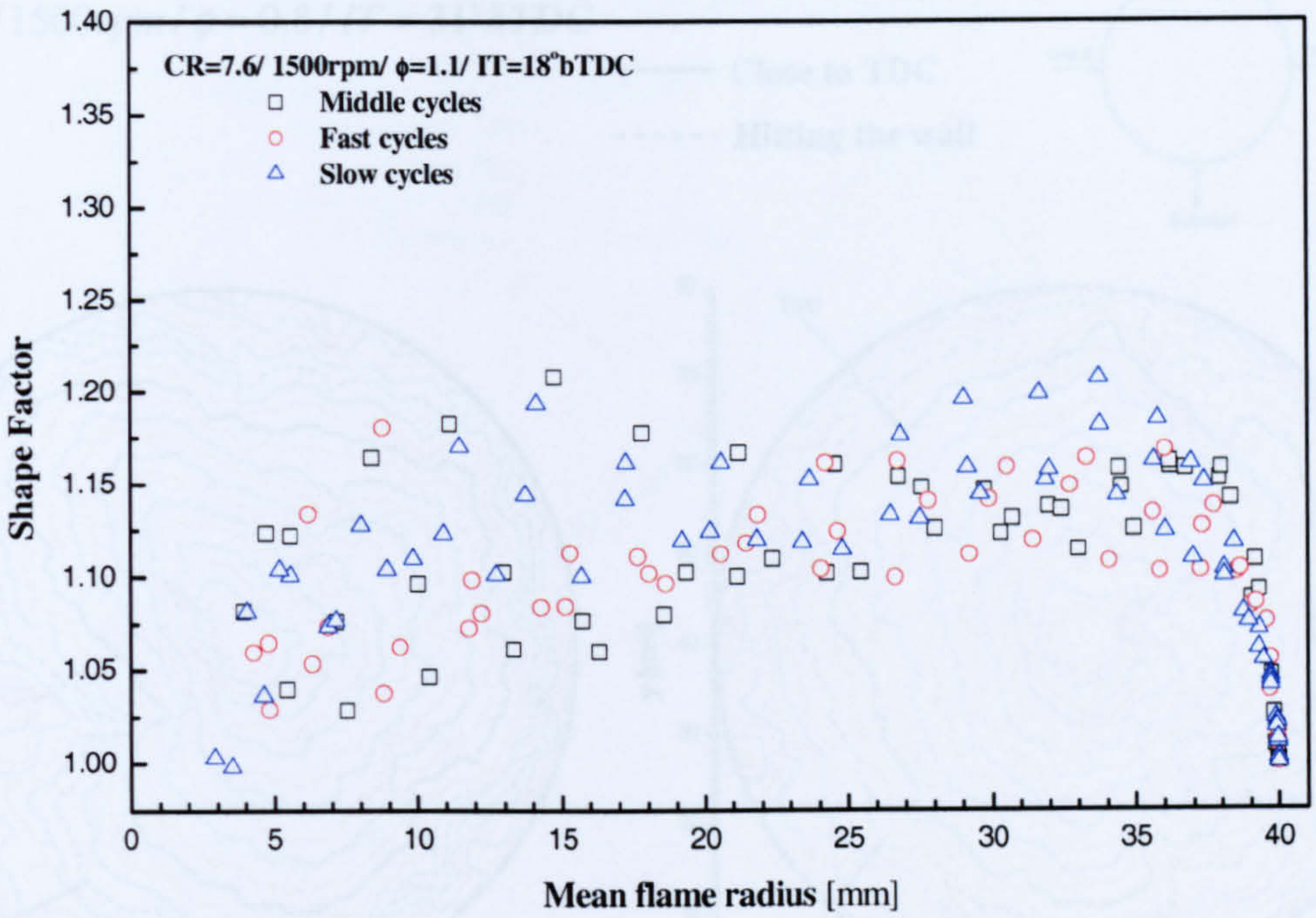

(a)

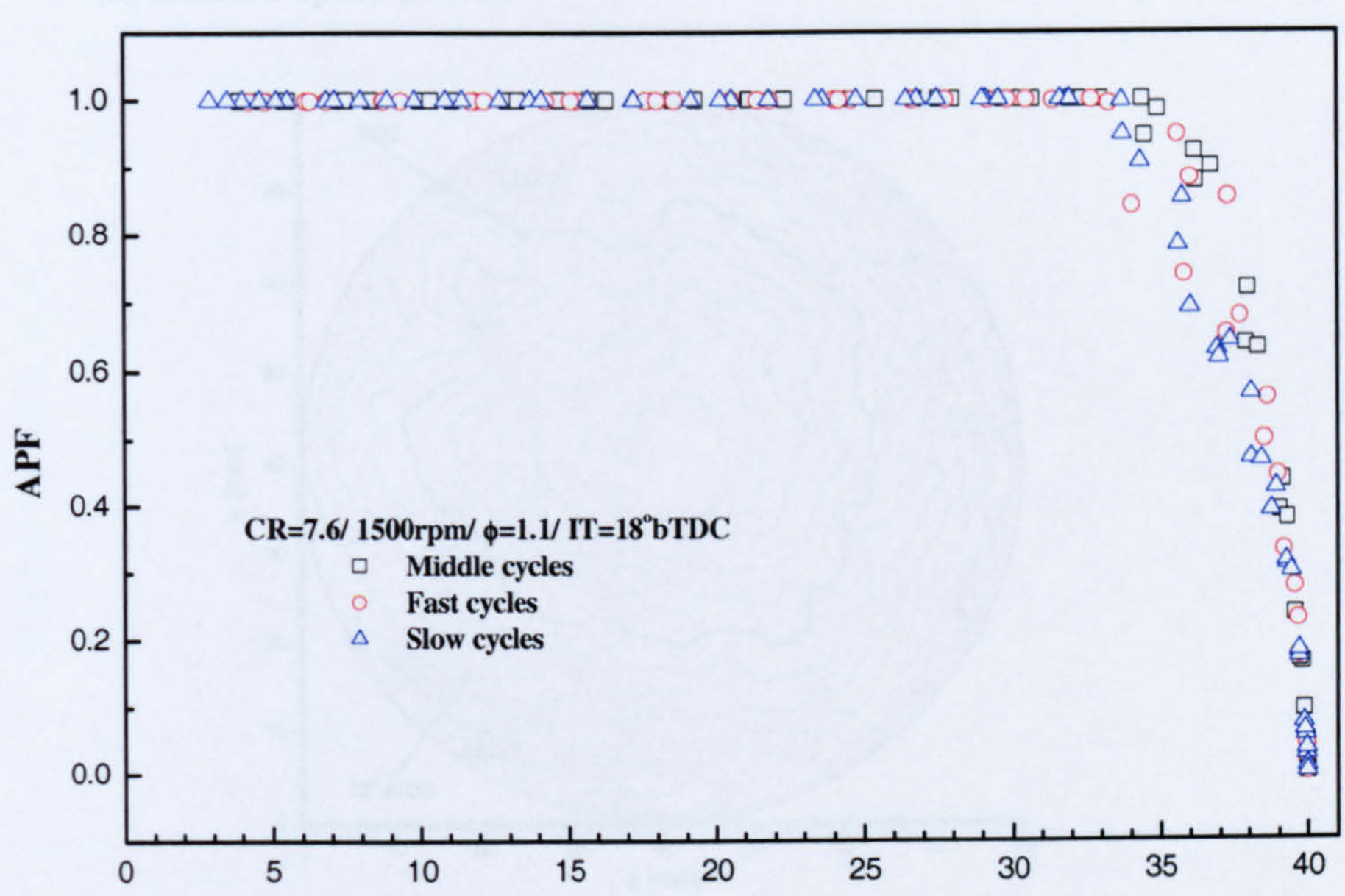

(b)

Figure 5.31 (a) Flame Shape Factor and **(b)** APF versus mean flame radius for the middle, fast and slow cycles at the rich condition.

$CR = 7.6 / 1500 rpm / \phi = 0.8 / IT = 31^{\circ} bTDC$

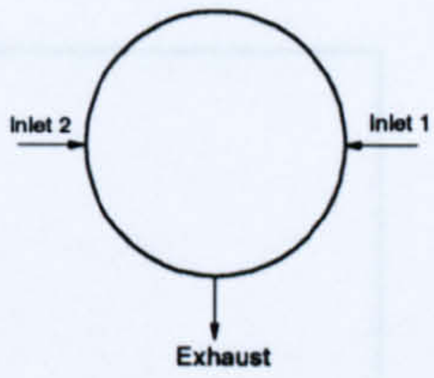

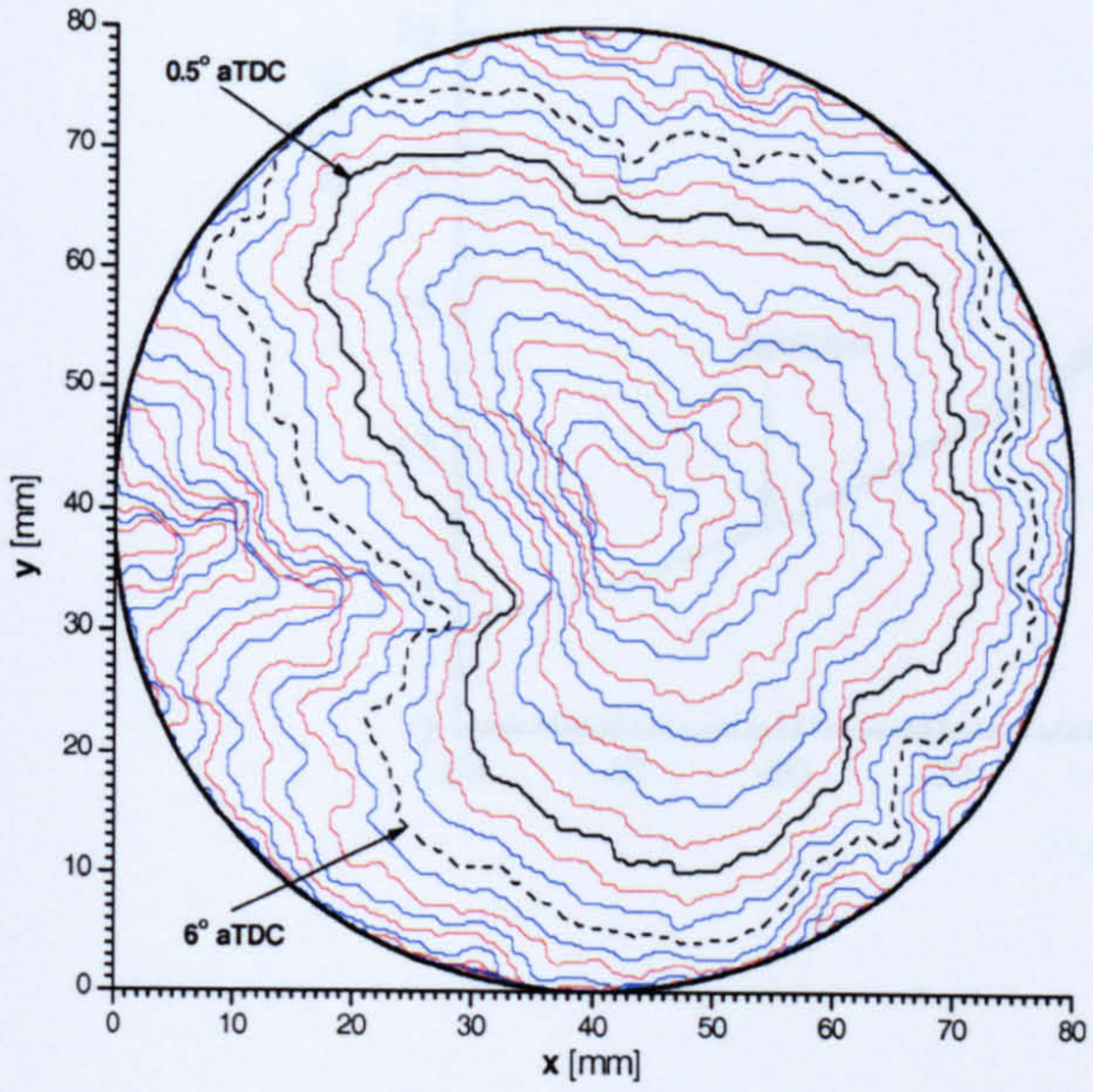

(a) Middle cycle (Lm3)

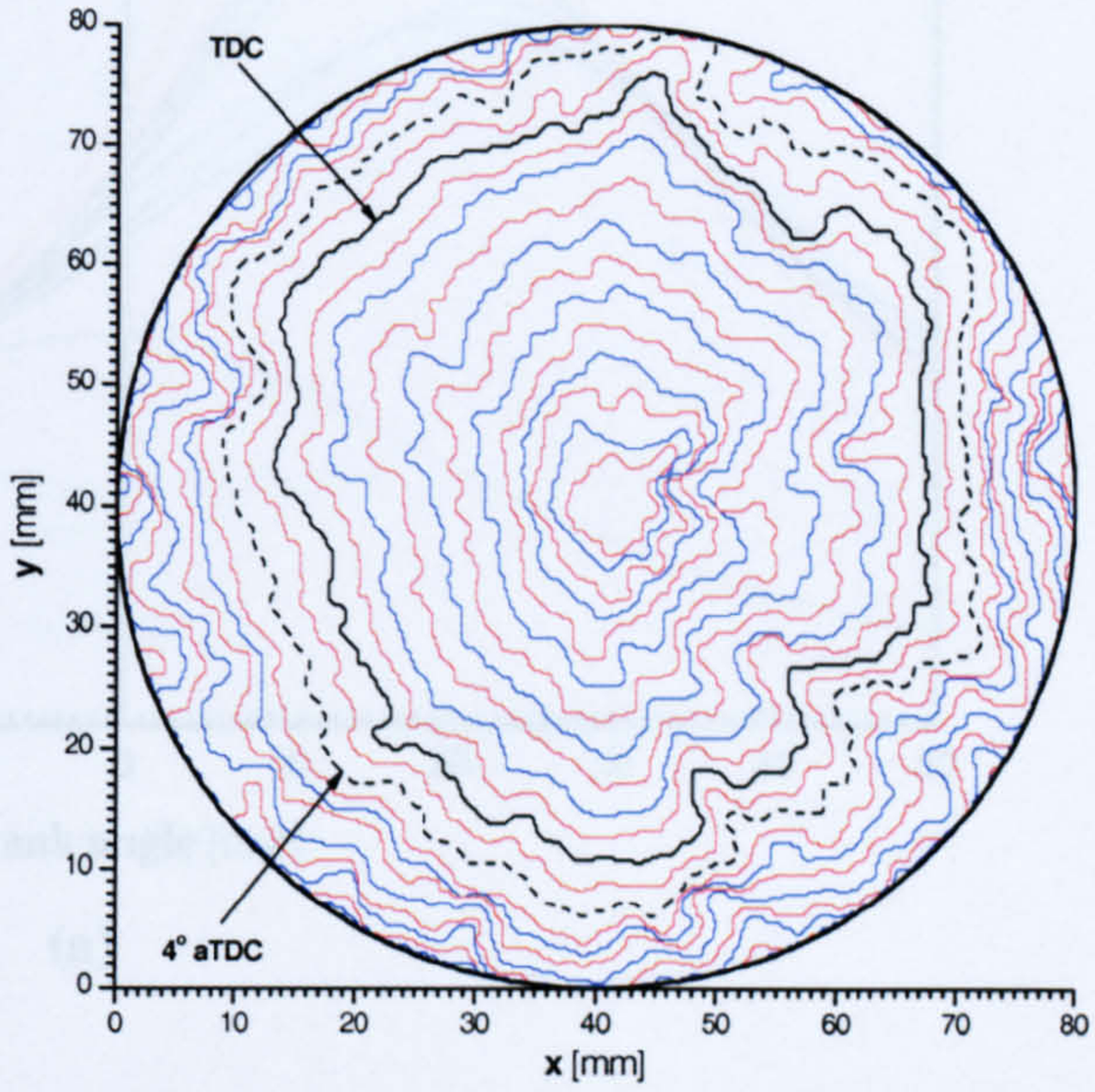

(b) Fast cycle (Lm4)

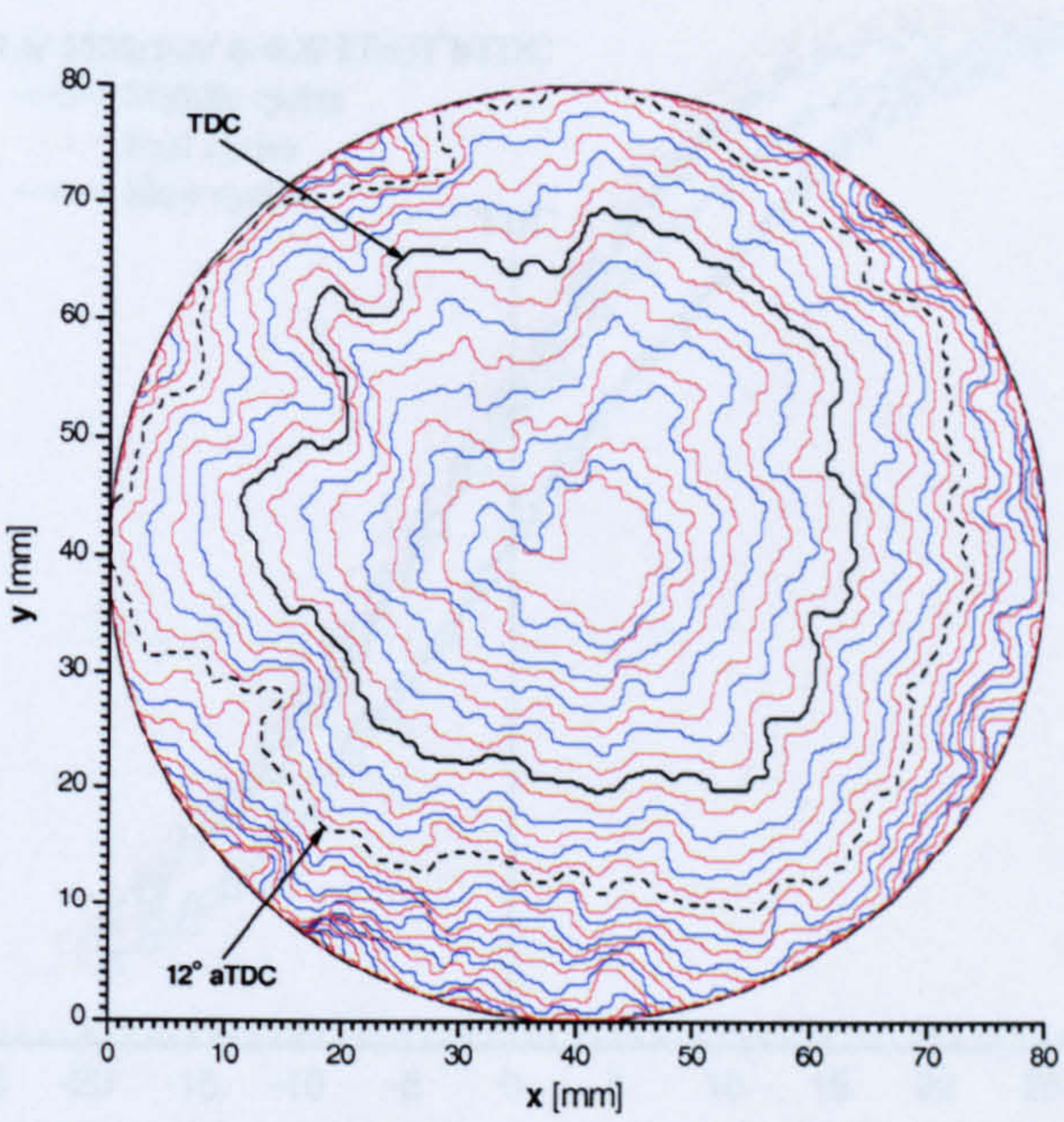

(c) Slow cycle (Lm7)

Figure 5.32 Successive flame contours for selected **(a)** middle, **(b)** fast and **(c)** slow cycles at the lean mixture condition.

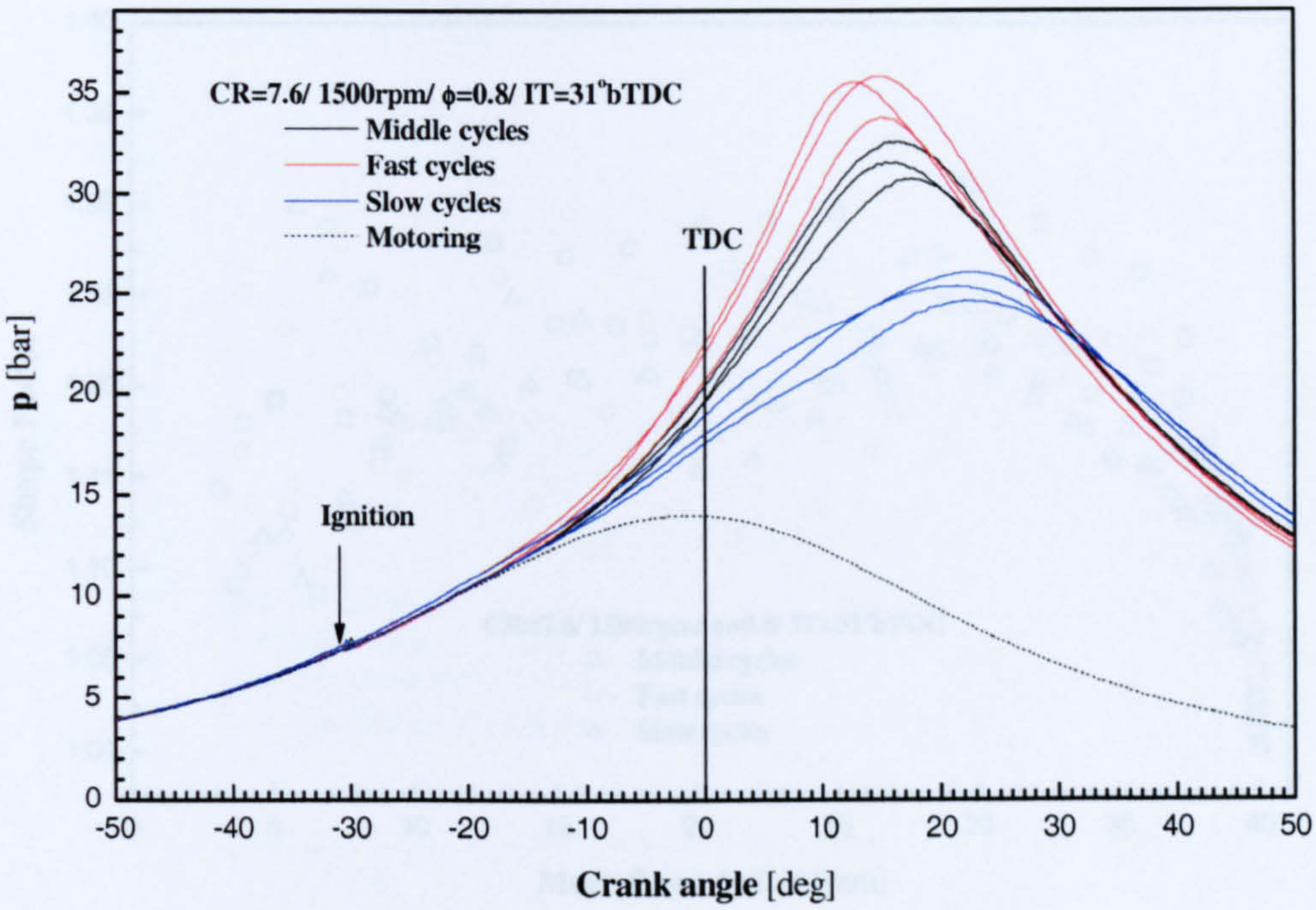

(a)

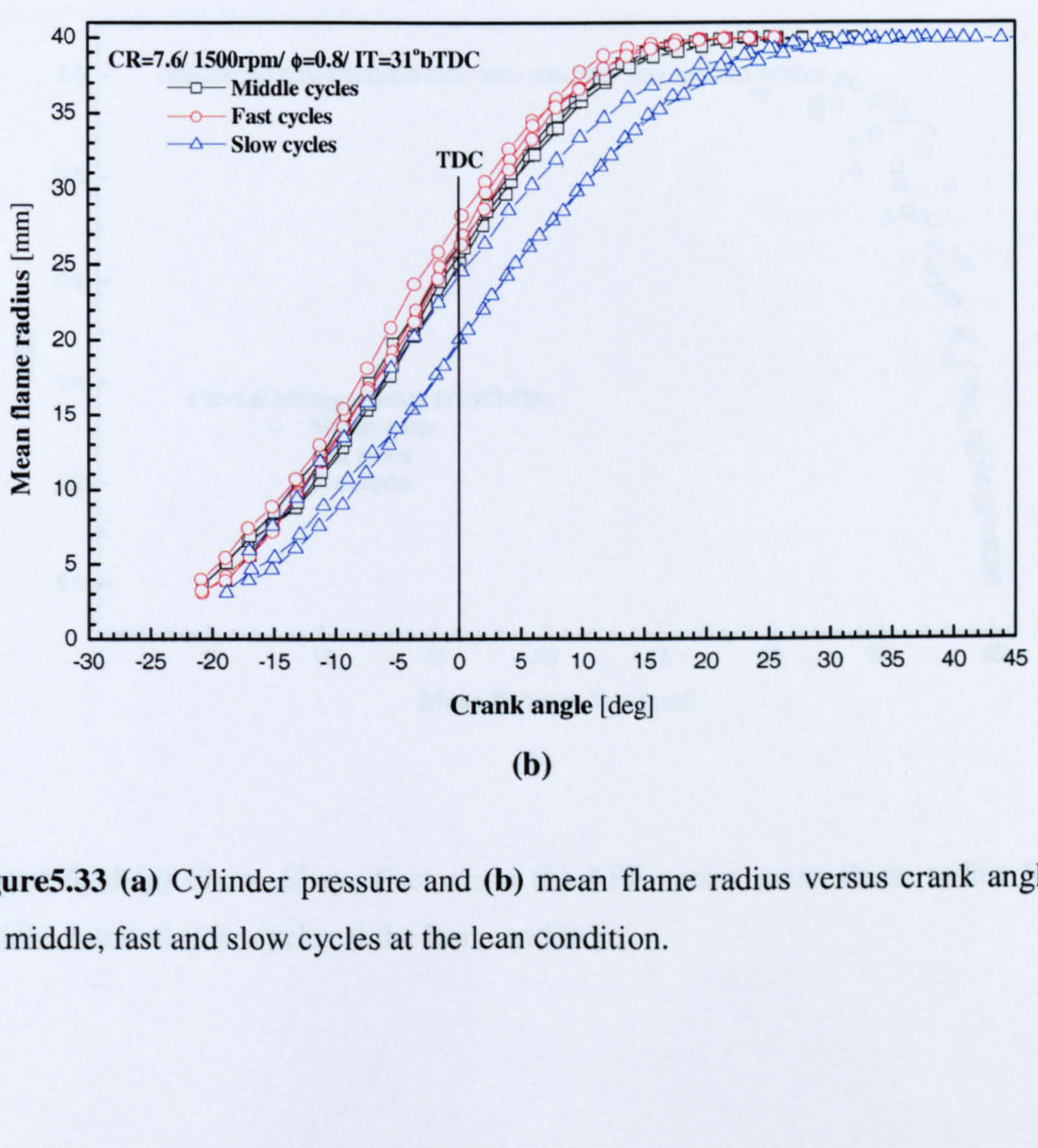

(b)

Figure5.33 (a) Cylinder pressure and **(b)** mean flame radius versus crank angle for the middle, fast and slow cycles at the lean condition.

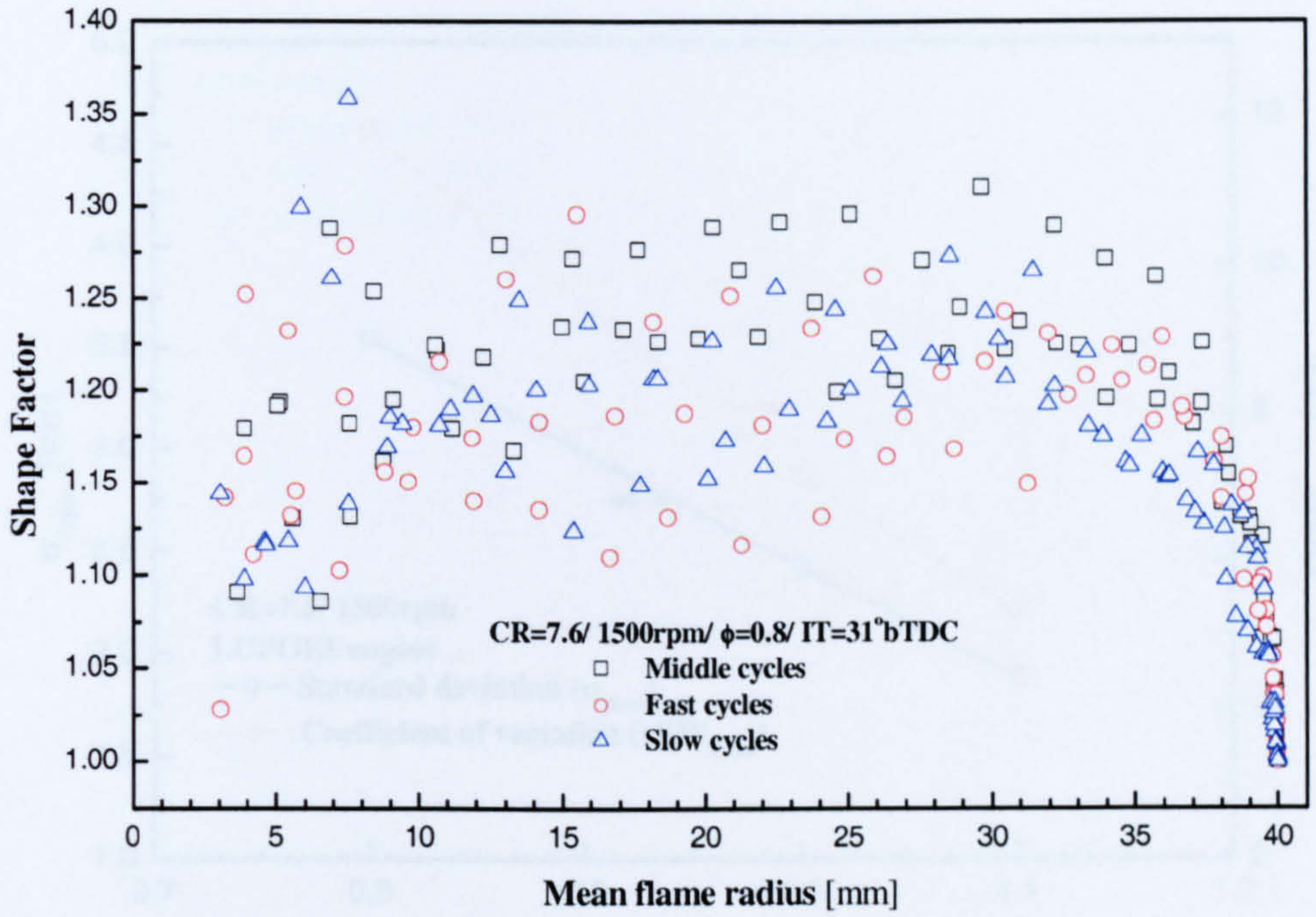

(a)

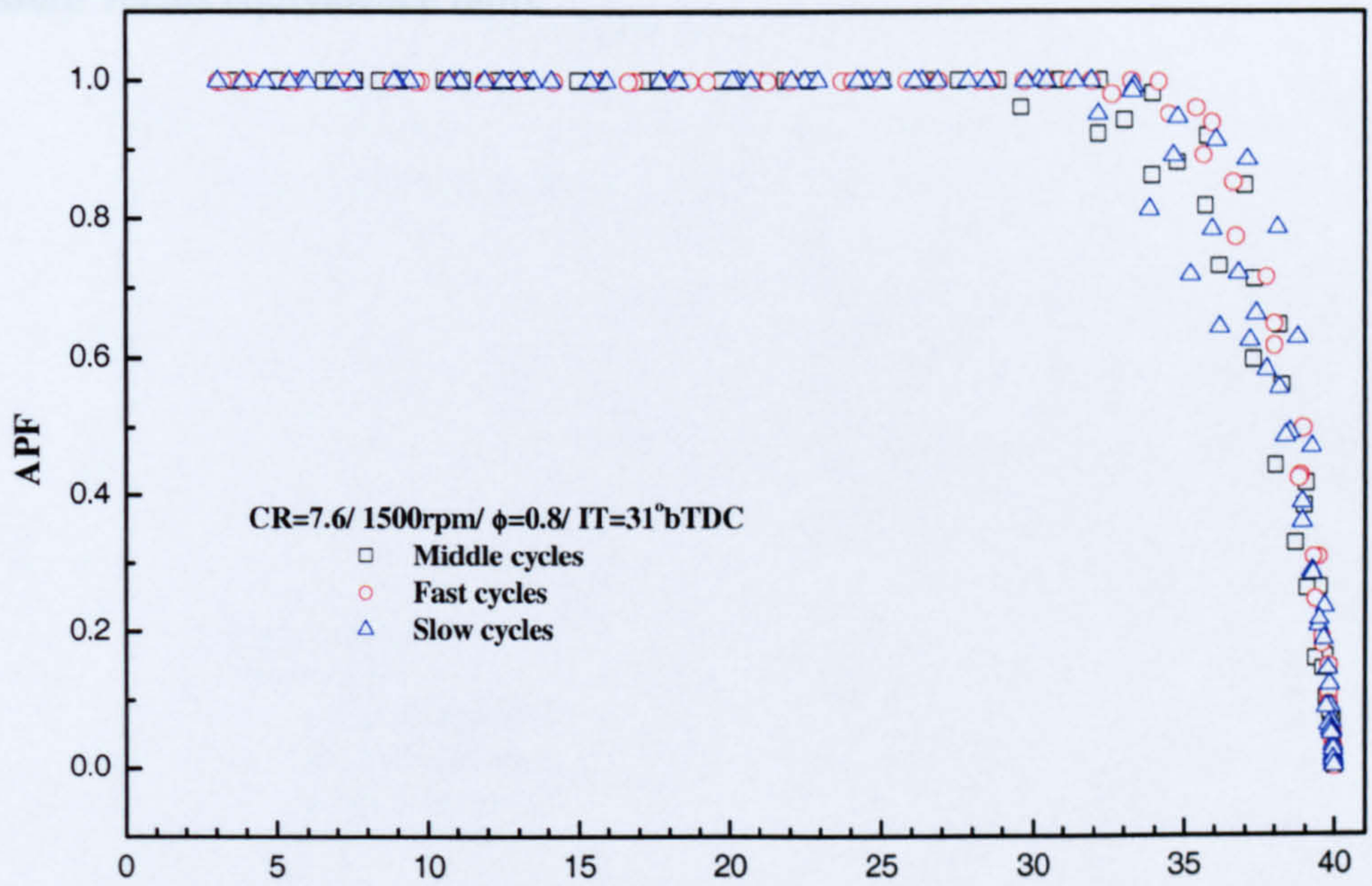

(b)

Figure 5.34 (a) Flame Shape Factor and **(b)** APF versus mean flame radius for the middle, fast and slow cycles at the lean condition.

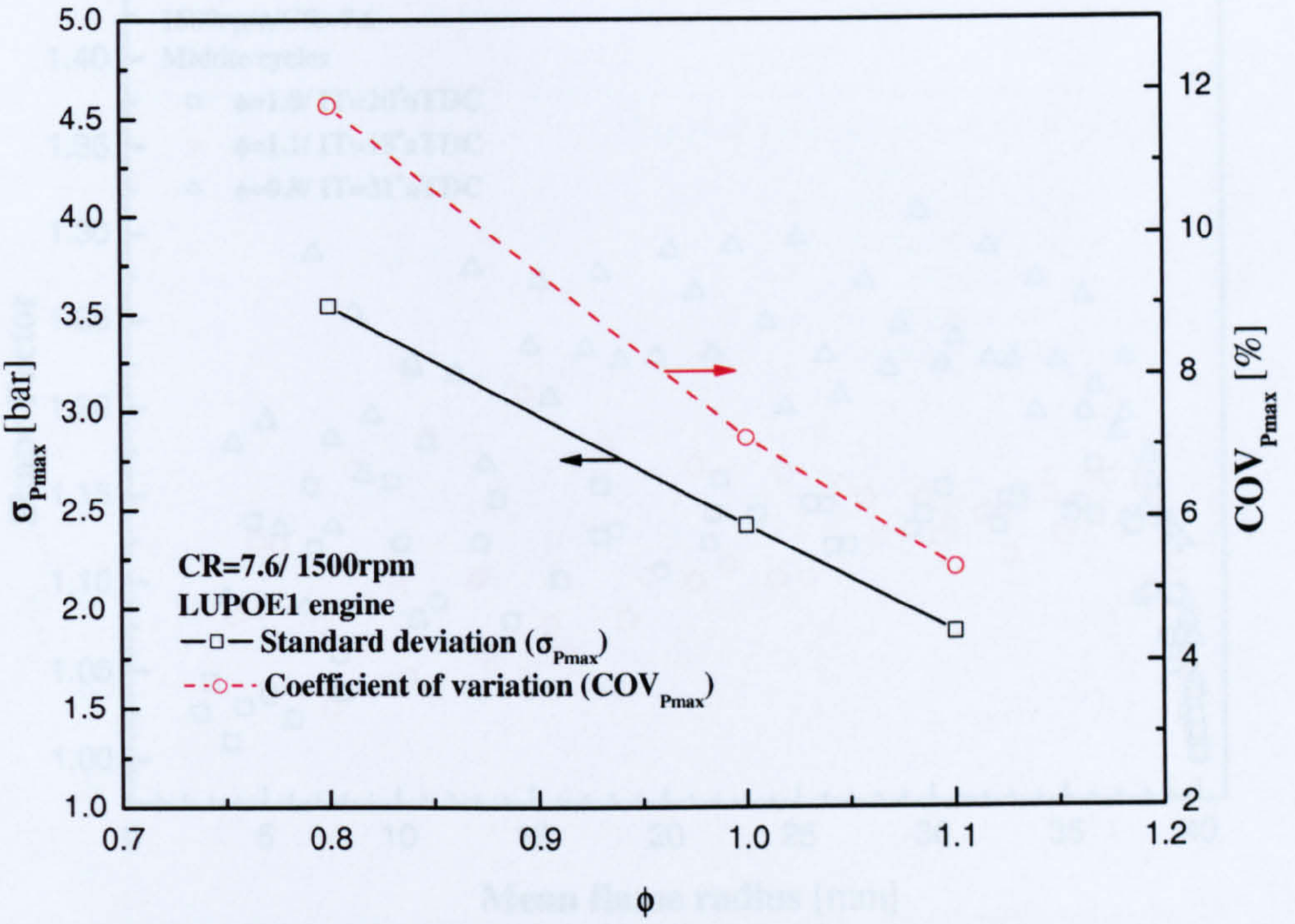

Figure 5.35 Standard deviation and coefficient of variation based on cylinder peak pressure versus equivalence ratio.

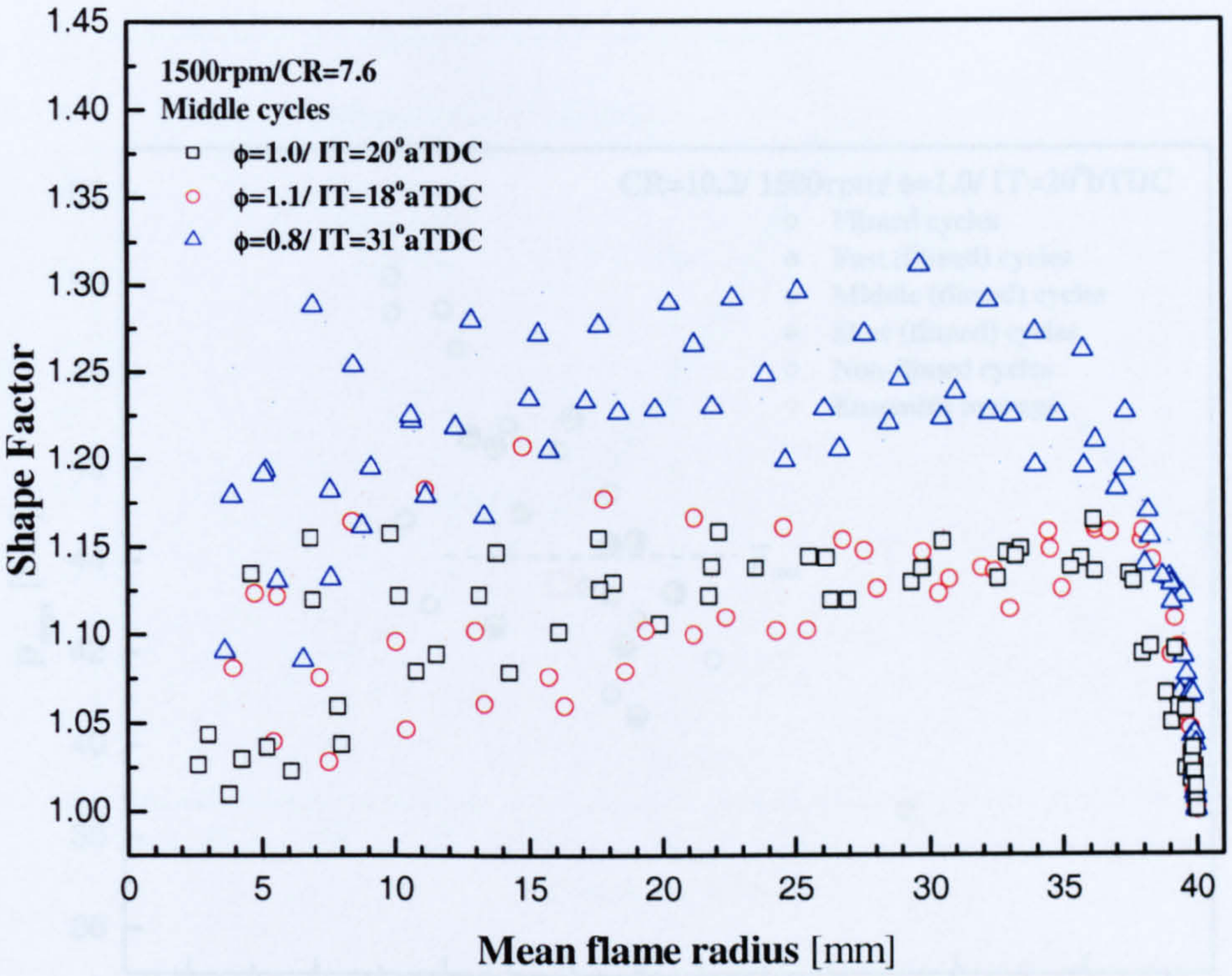

(a)

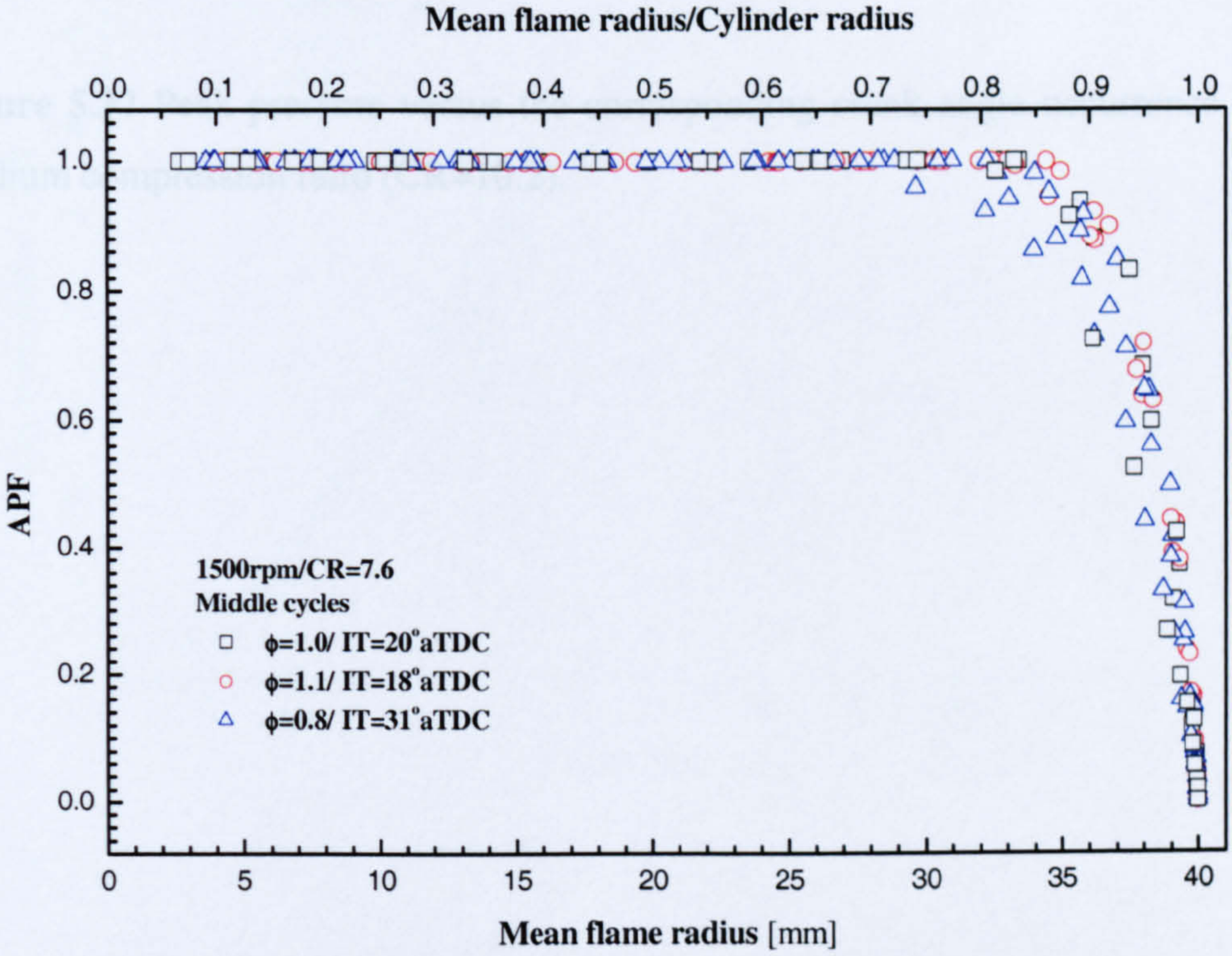

(b)

Figure 5.36 (a) Flame Shape Factor and **(b)** APF versus mean flame radius for the selected middle cycles at the three equivalence ratios ($\phi = 0.8$, 1.0 and 1.1).

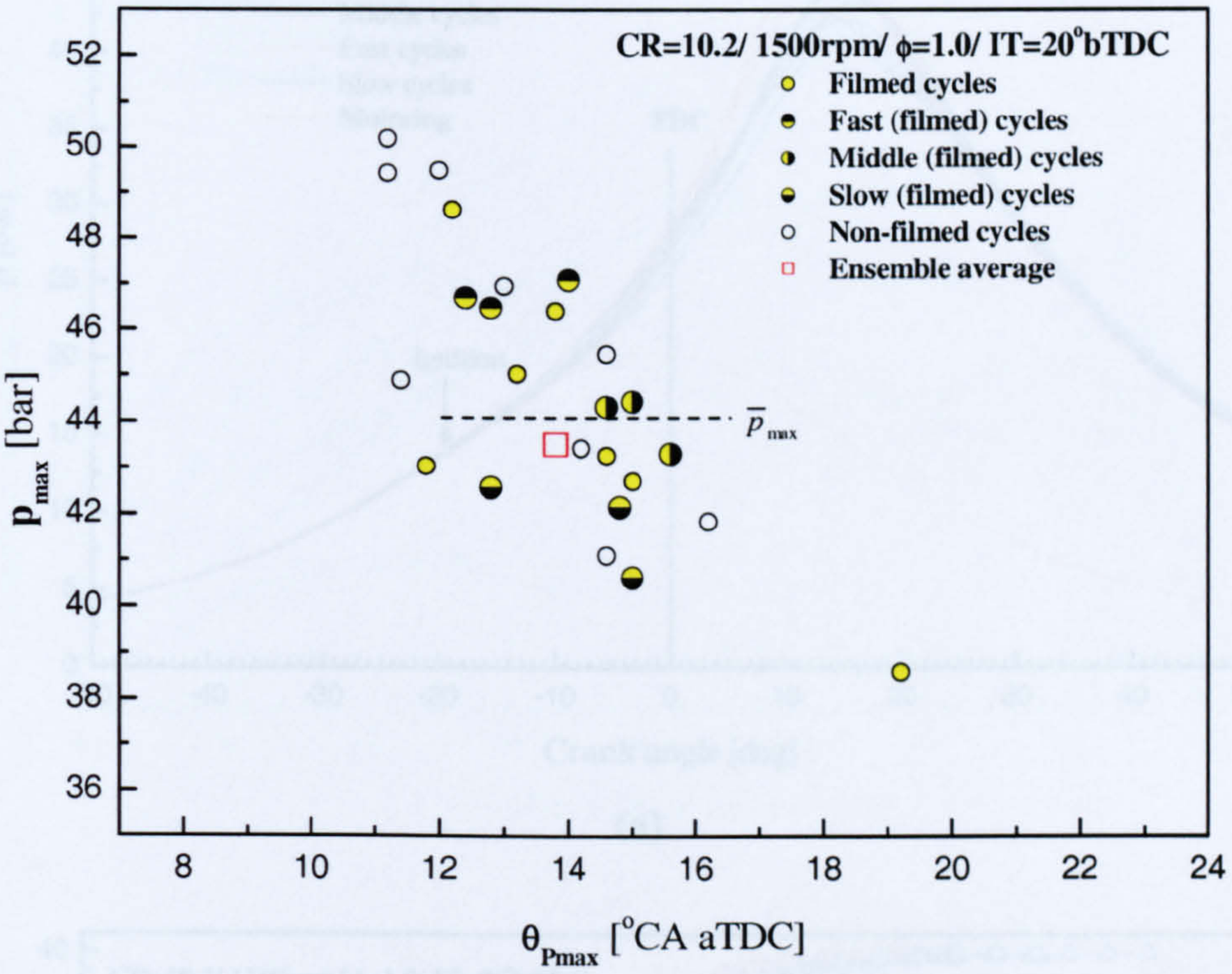

Figure 5.37 Peak pressure versus the corresponding crank angle occurrence for the medium compression ratio (CR=10.2).

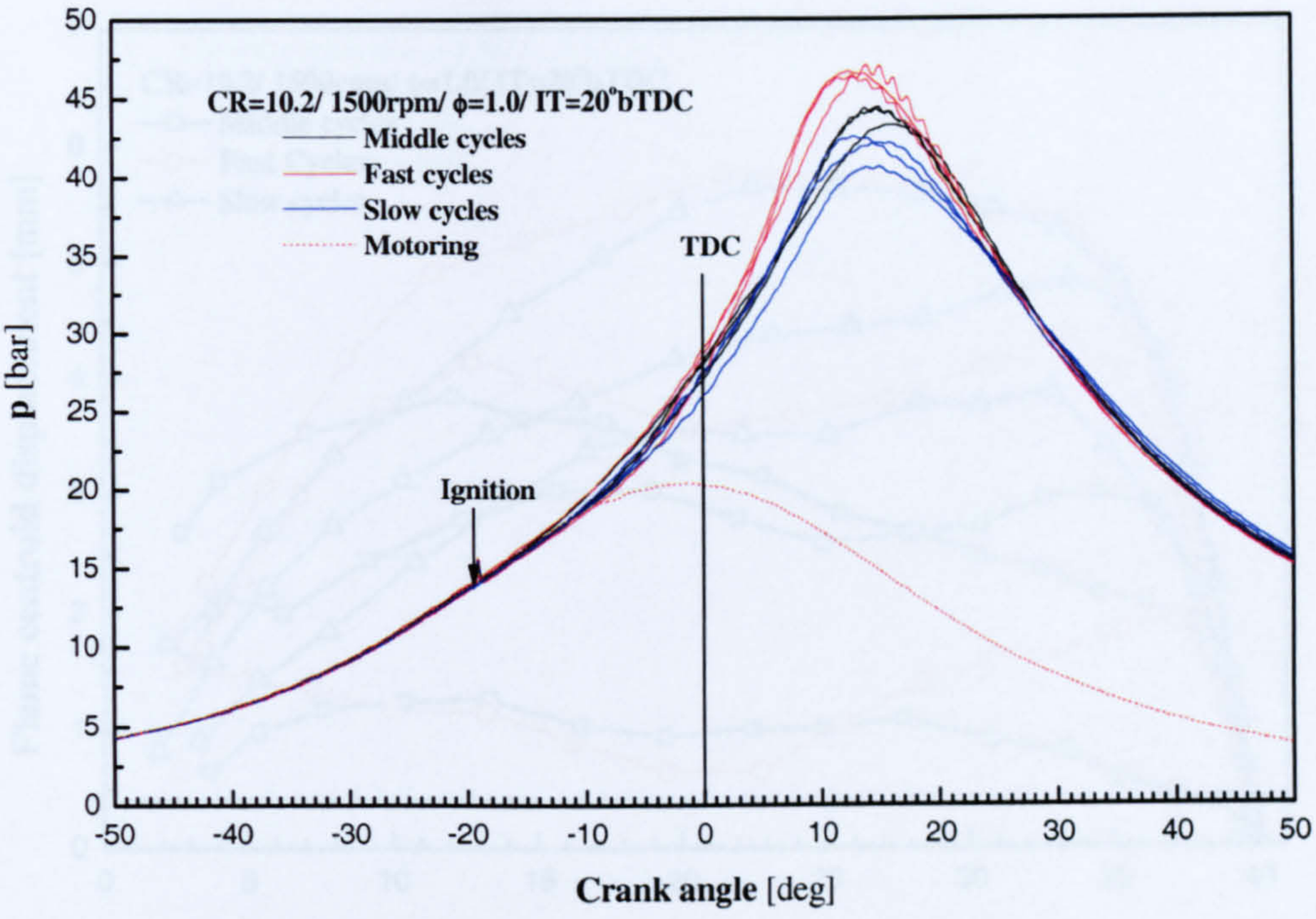

(a)

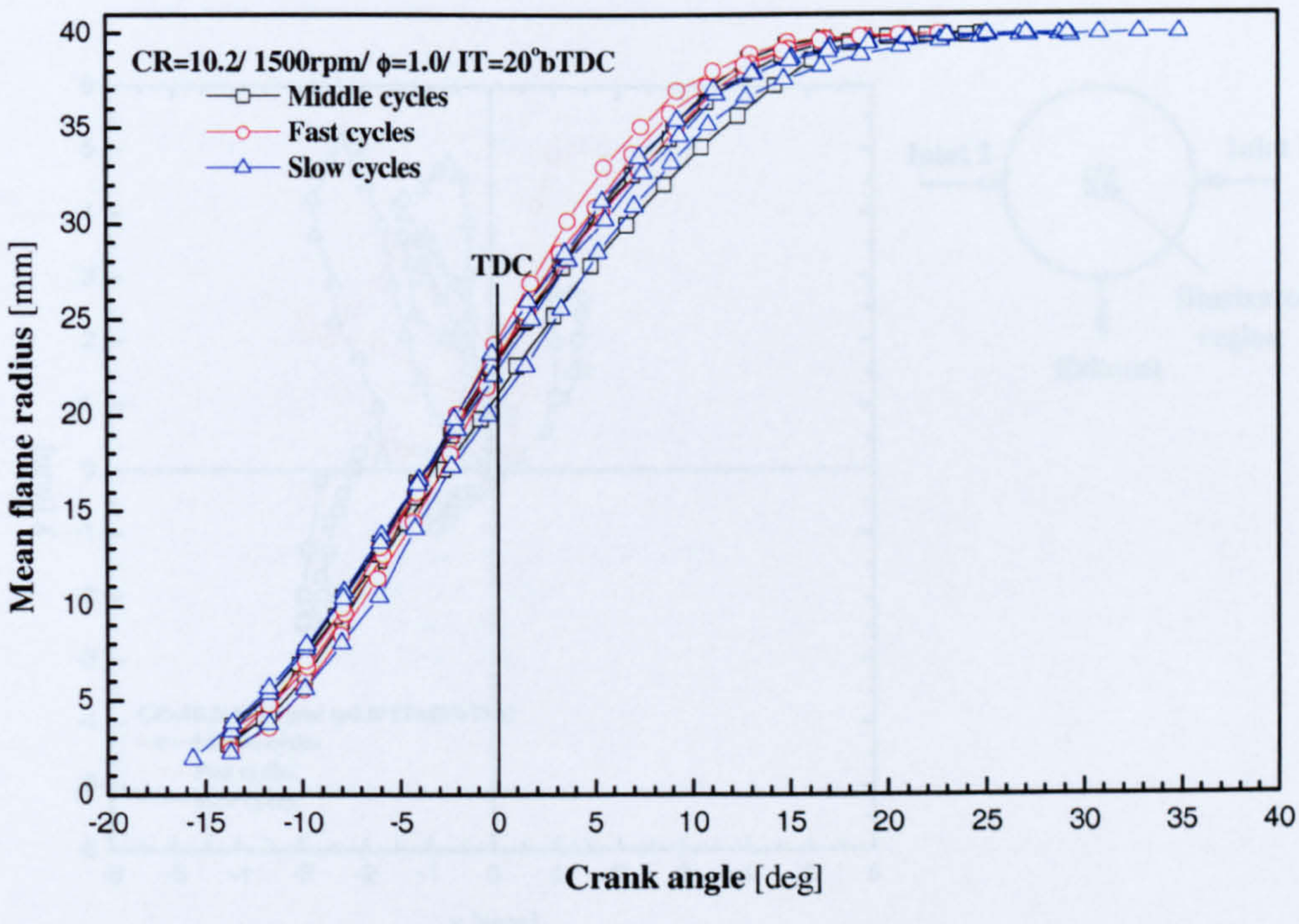

(b)

Figure5.38 (a) Cylinder pressure and **(b)** mean flame radius versus crank angle for the middle, fast and slow cycles at the medium compression ratio (CR=10.2).

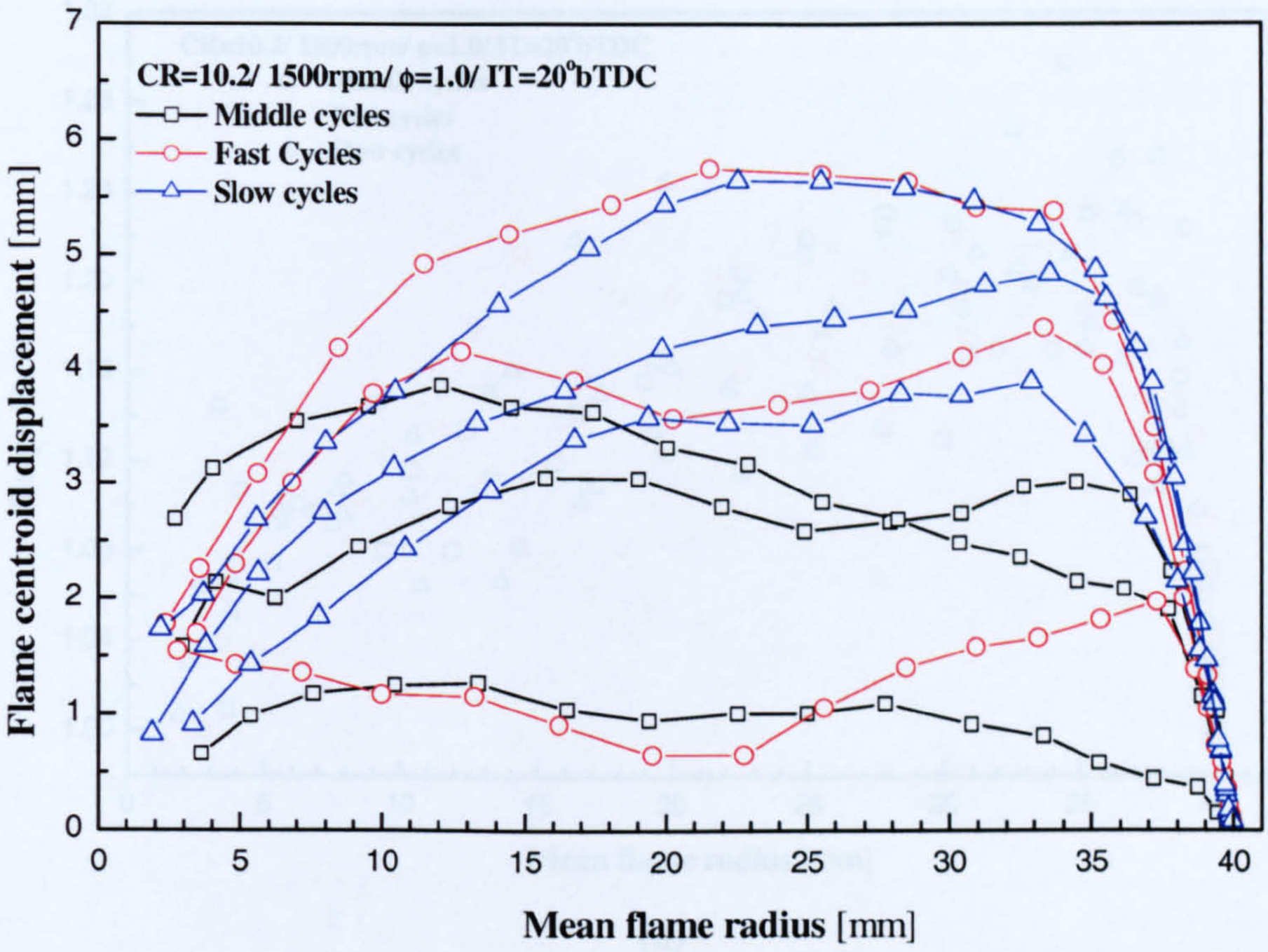

(b)

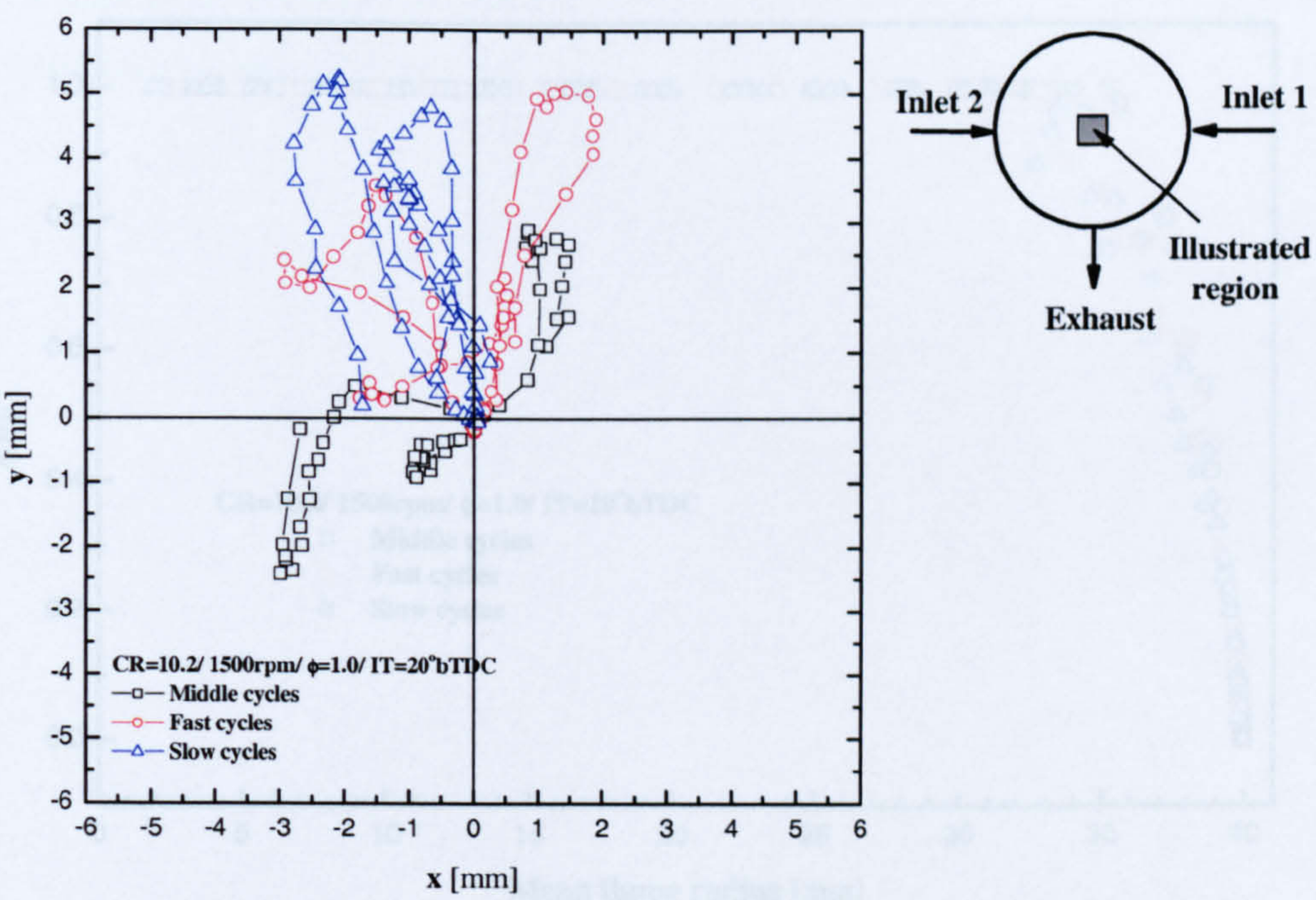

(b)

Figure 5.39 (a) Flame centroid displacement versus mean flame radius and **(b)** flame centroid locus for the middle, fast and slow cycles at the medium compression ratio (CR=10.2).

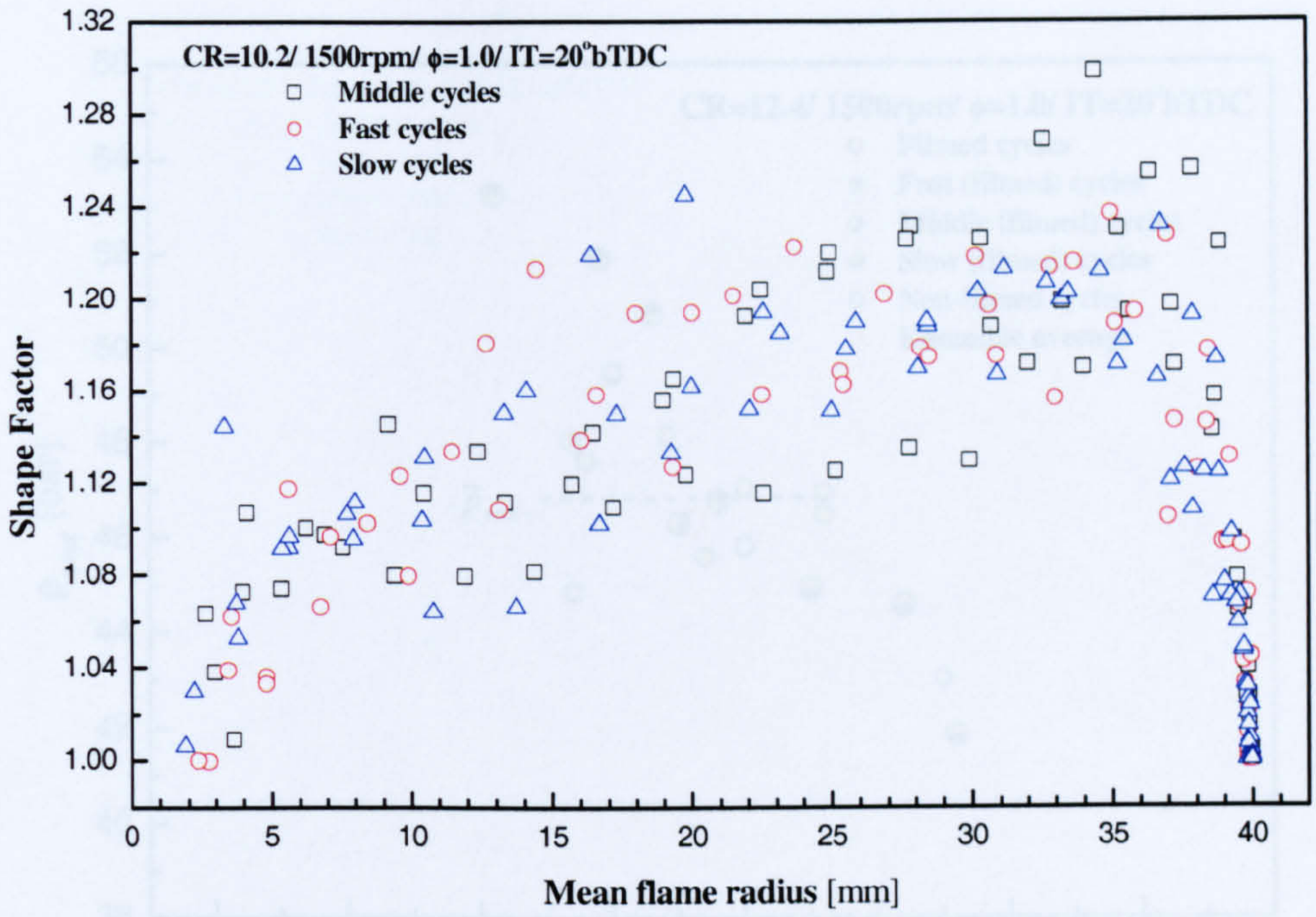

(a)

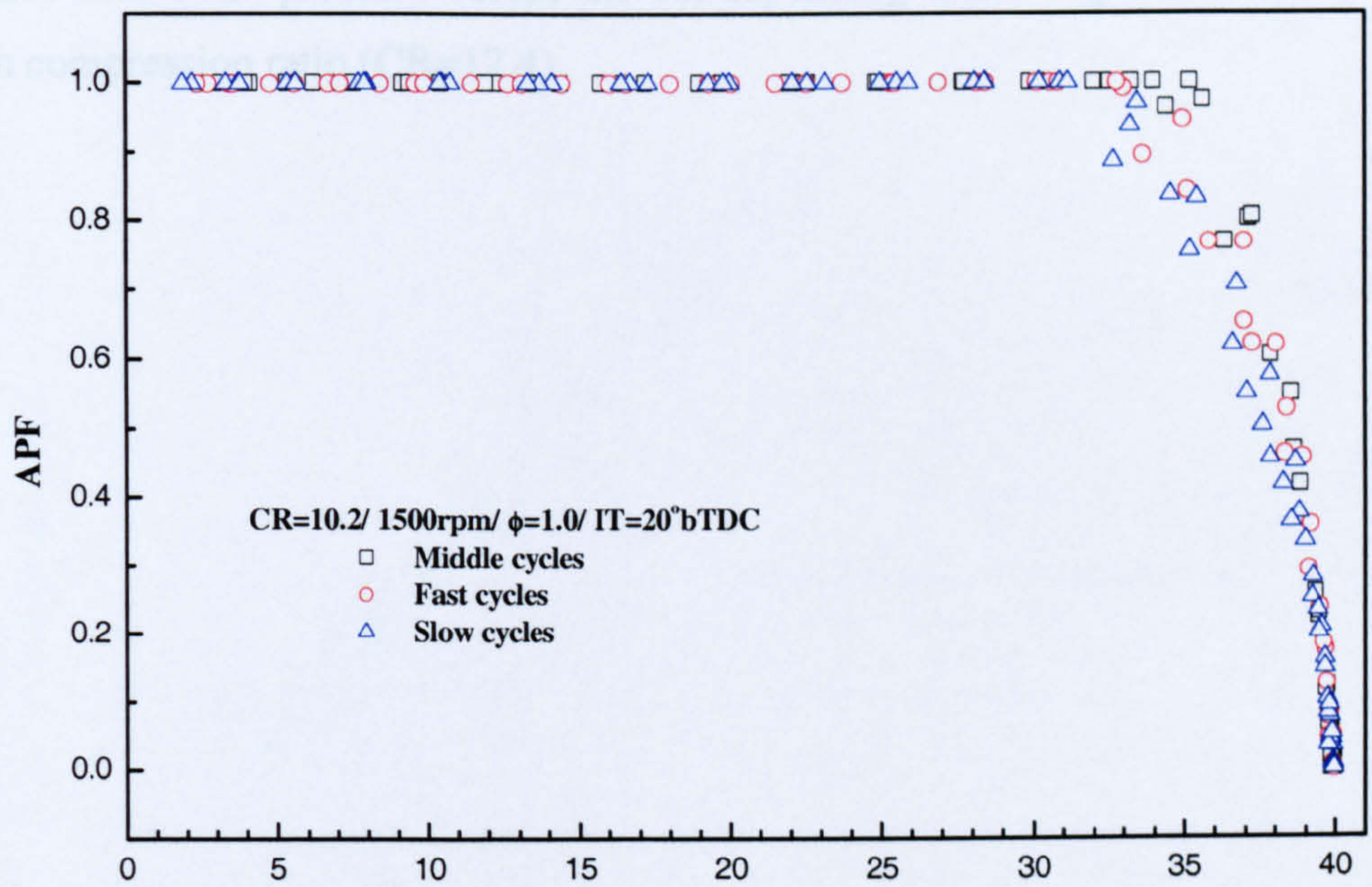

(b)

Figure 5.40 **(a)** Flame Shape Factor and **(b)** APF versus mean flame radius for the middle, fast and slow cycles at the medium compression ratio (CR=10.2).

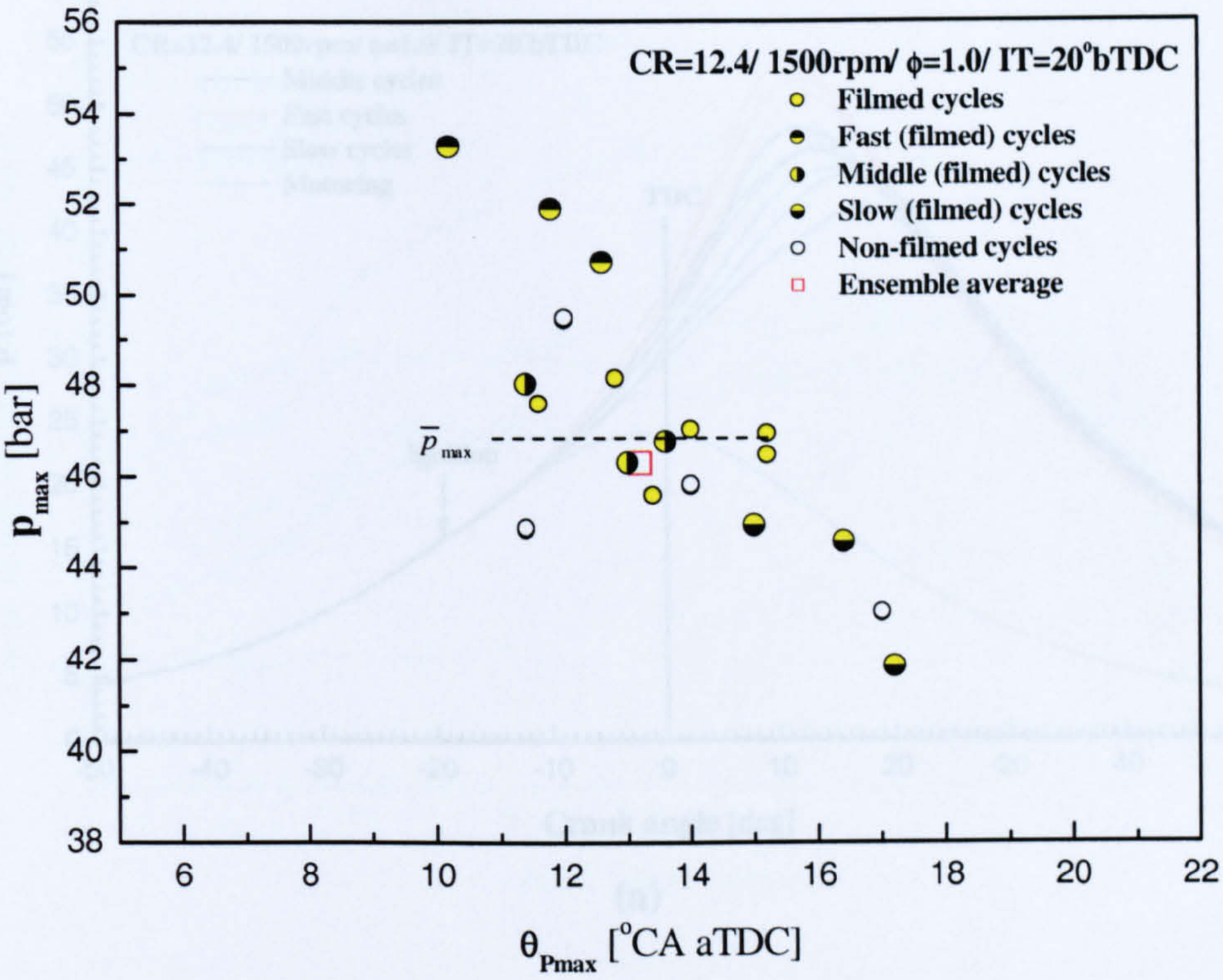

Figure 5.41 Peak pressure versus the corresponding crank angle occurrence for the high compression ratio (CR=12.4).

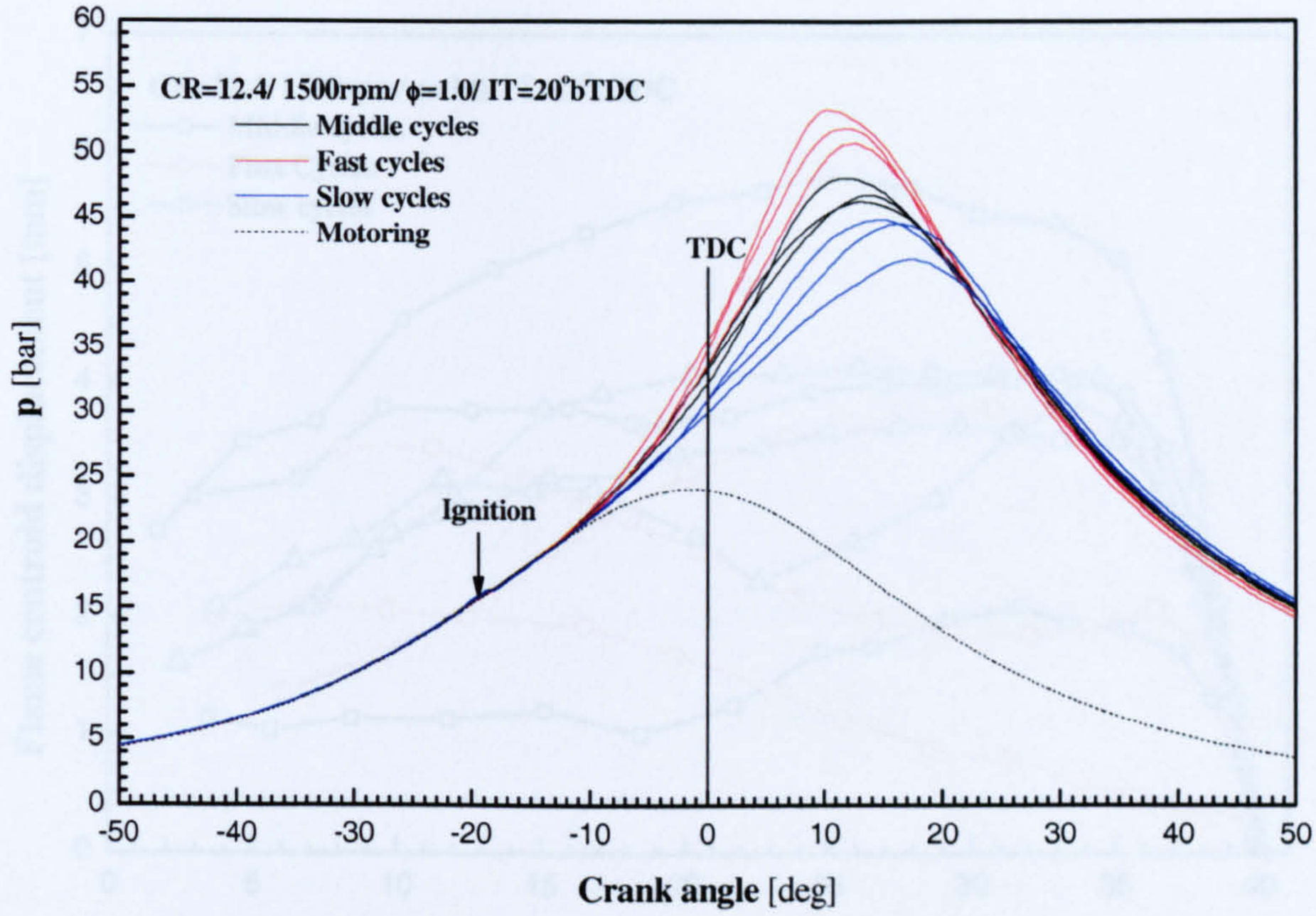

(a)

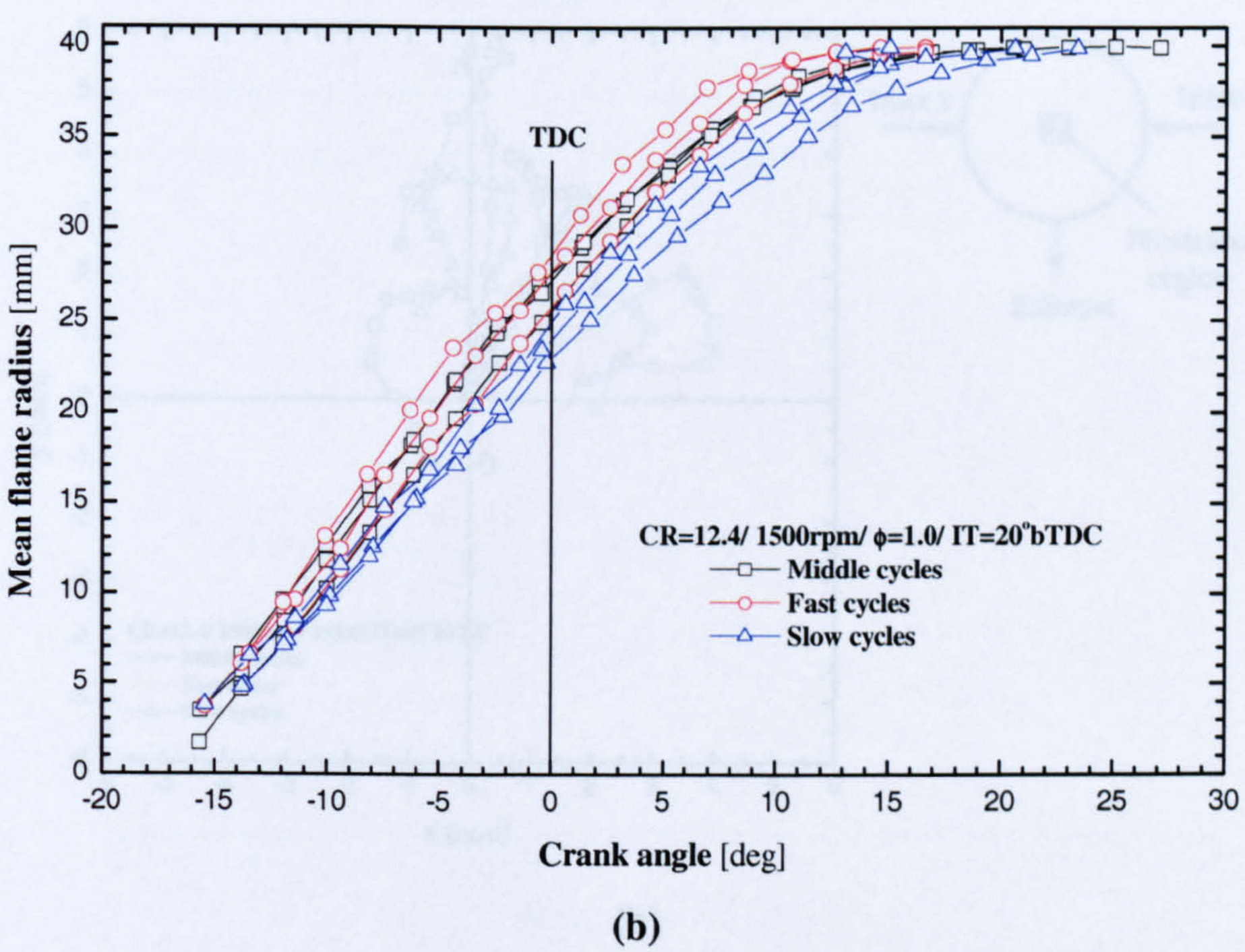

(b)

Figure5.42 (a) Cylinder pressure and **(b)** mean flame radius versus crank angle for the middle, fast and slow cycles at the high compression ratio (CR=12.4).

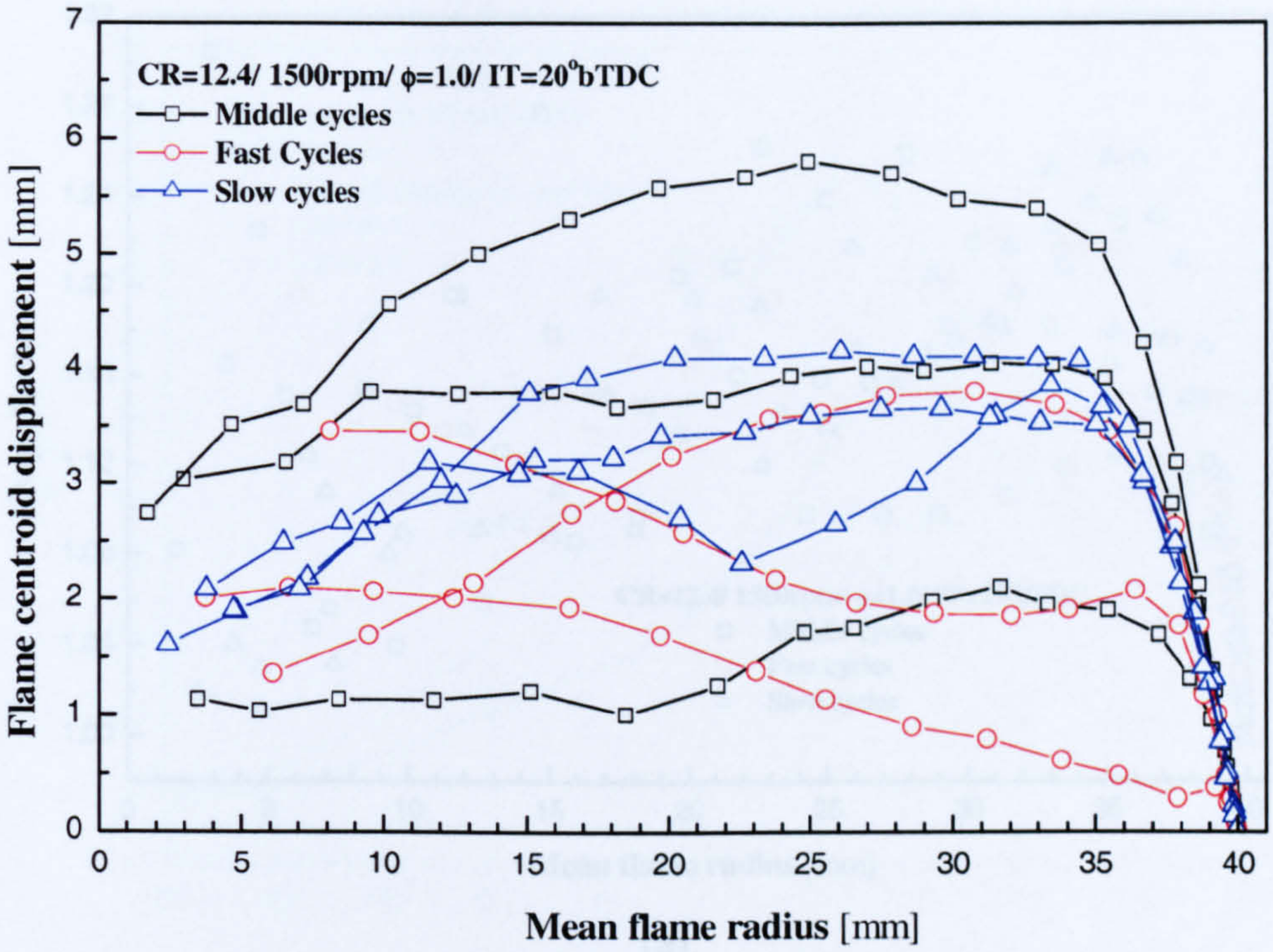

(a)

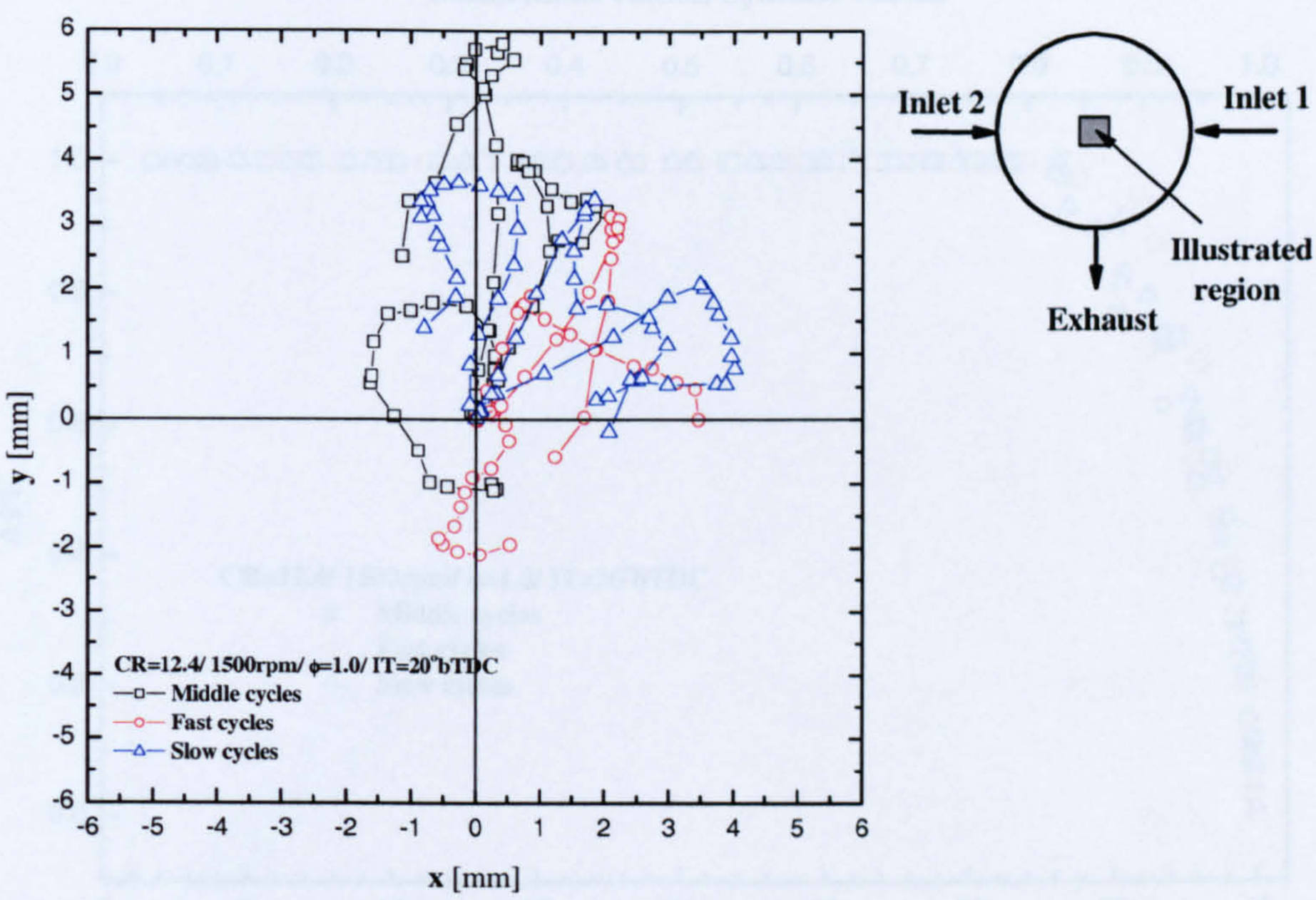

(b)

Figure 5.43 (a) Flame centroid displacement versus mean flame radius and **(b)** flame centroid locus for the middle, fast and slow cycles at the high compression ratio (CR=12.4).

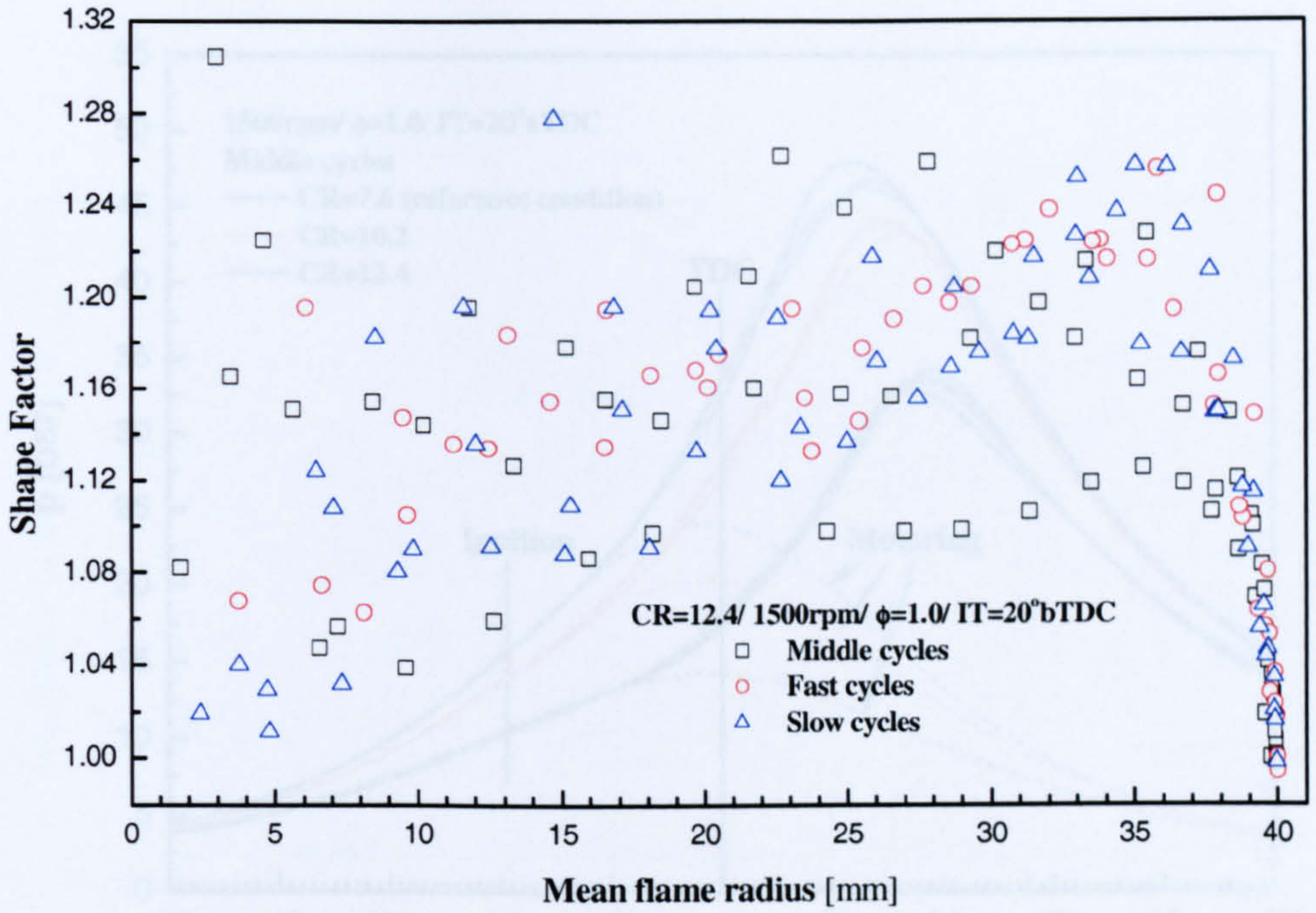

(a)

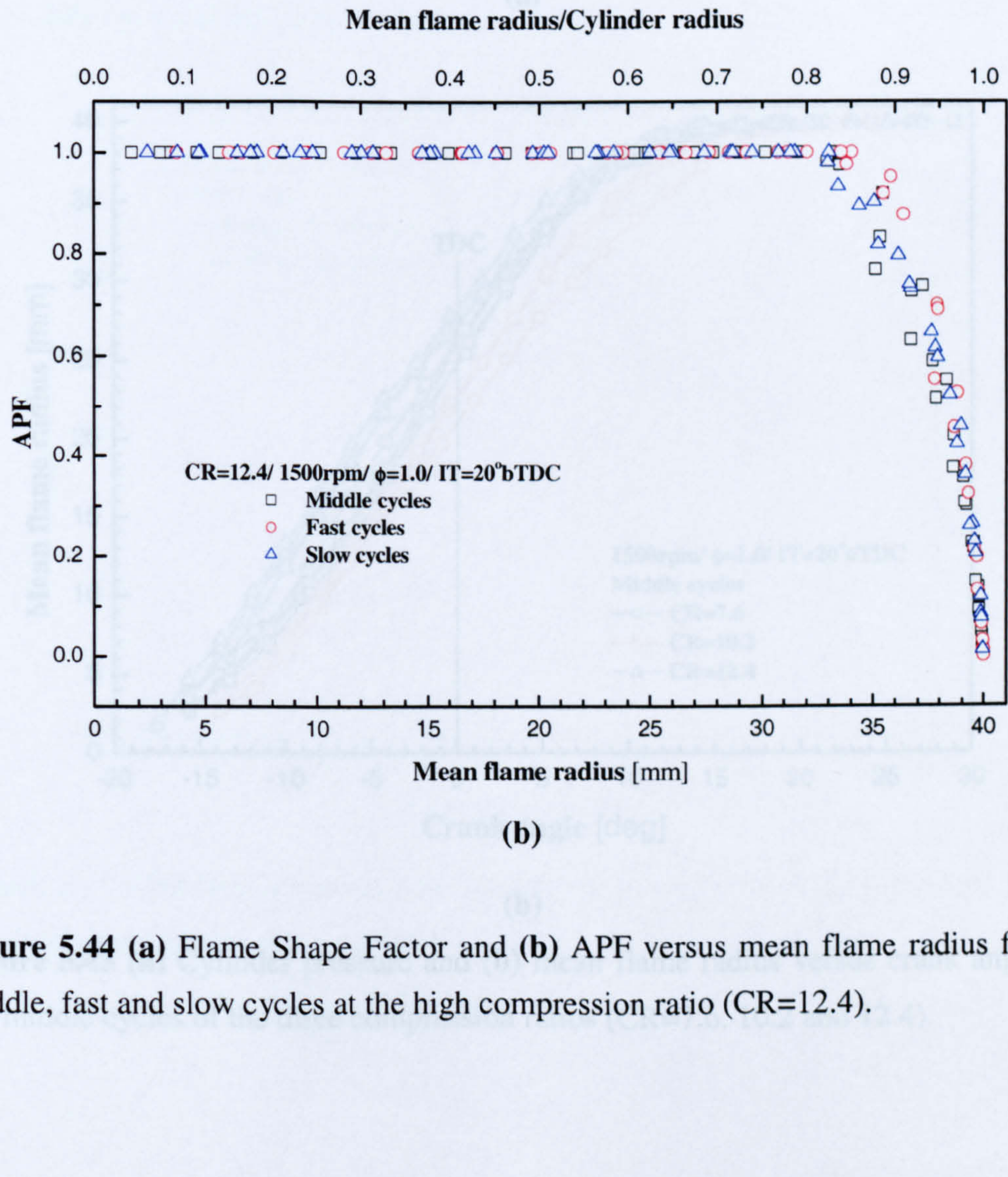

(b)

Figure 5.44 (a) Flame Shape Factor and **(b)** APF versus mean flame radius for the middle, fast and slow cycles at the high compression ratio (CR=12.4).

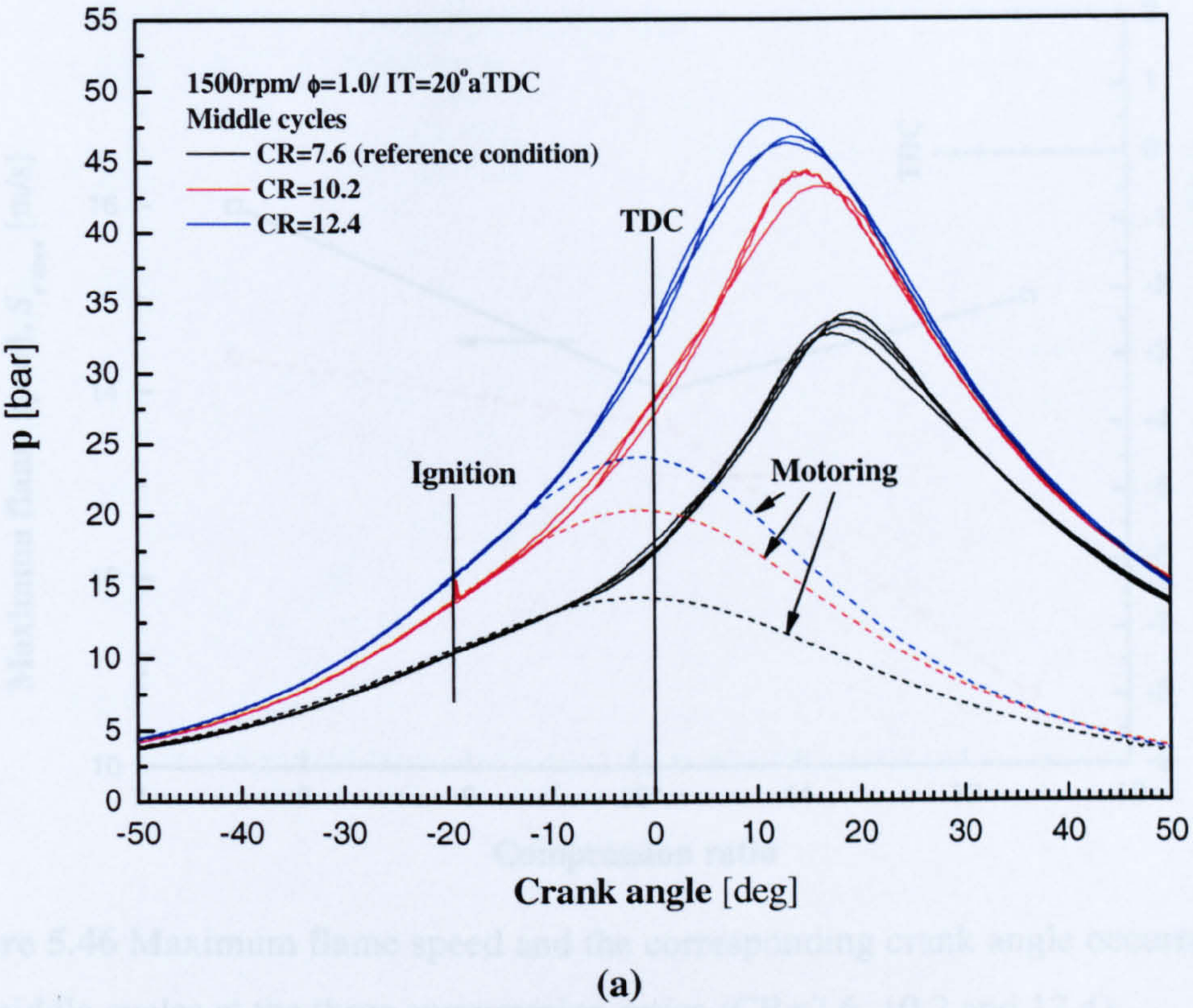

(a)

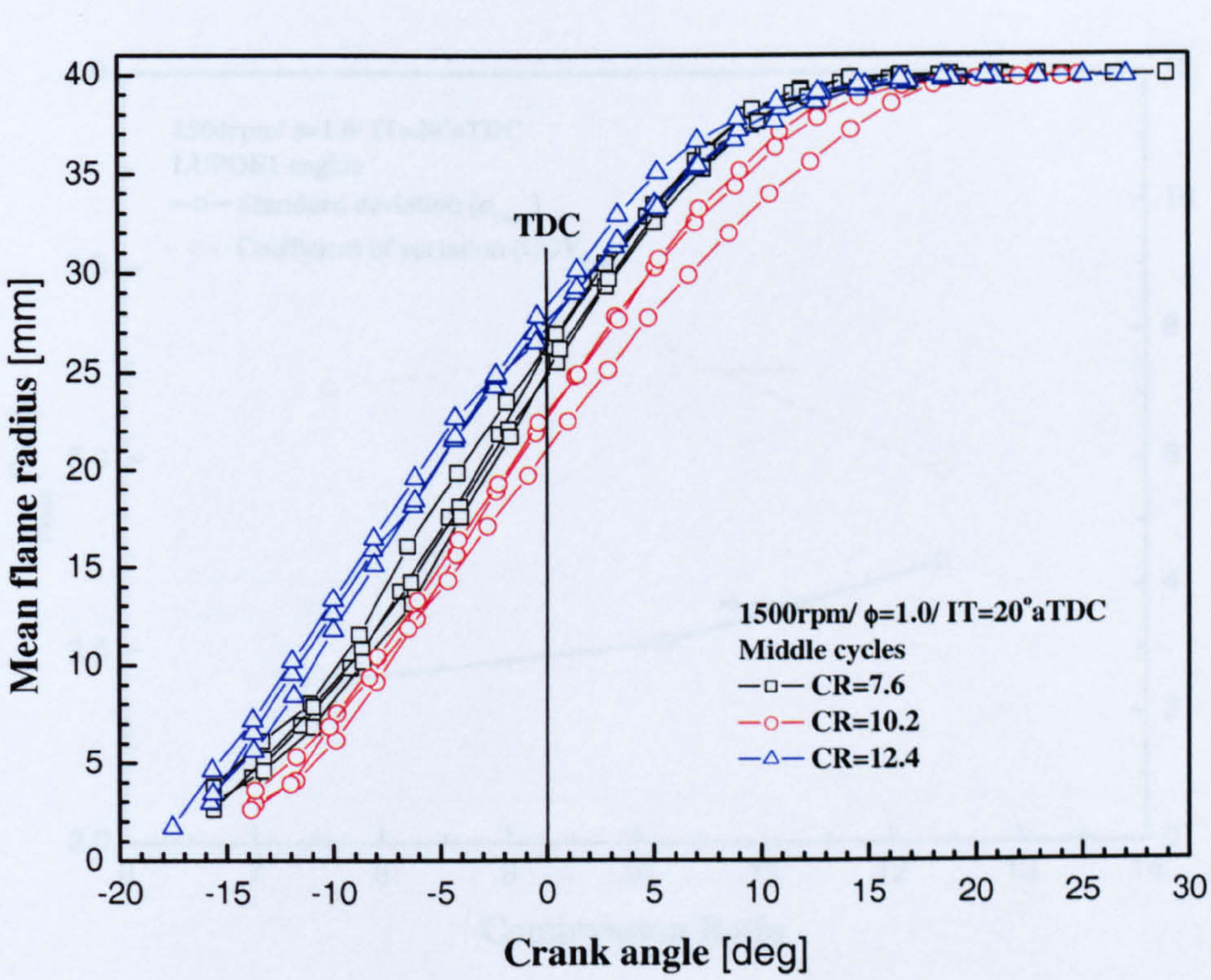

(b)

Figure 5.45 (a) Cylinder pressure and **(b)** mean flame radius versus crank angle for the middle cycles of the three compression ratios (CR=7.6, 10.2 and 12.4).

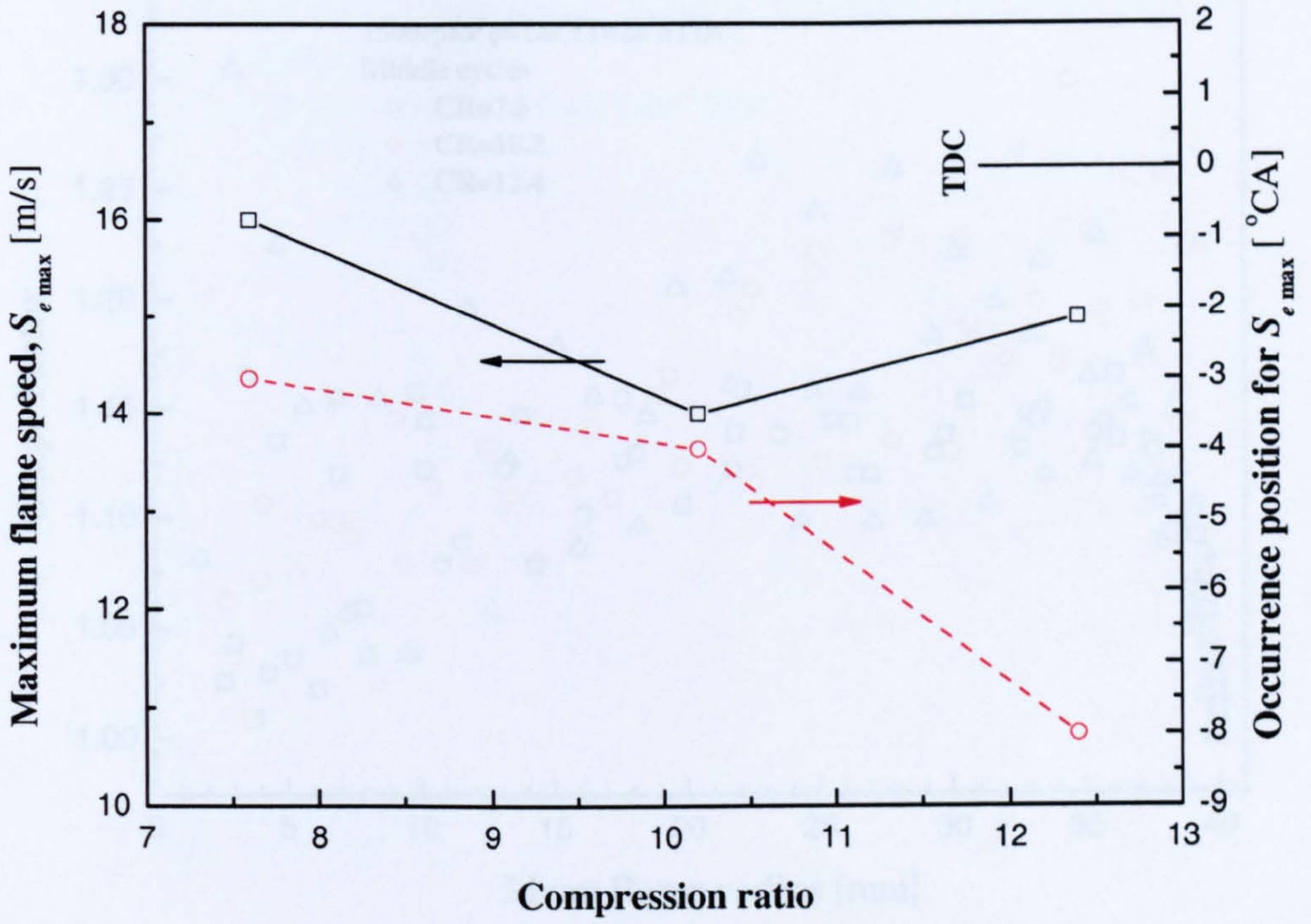

Figure 5.46 Maximum flame speed and the corresponding crank angle occurrence for the middle cycles at the three compression ratios (CR=7.6, 10.2 and 12.4).

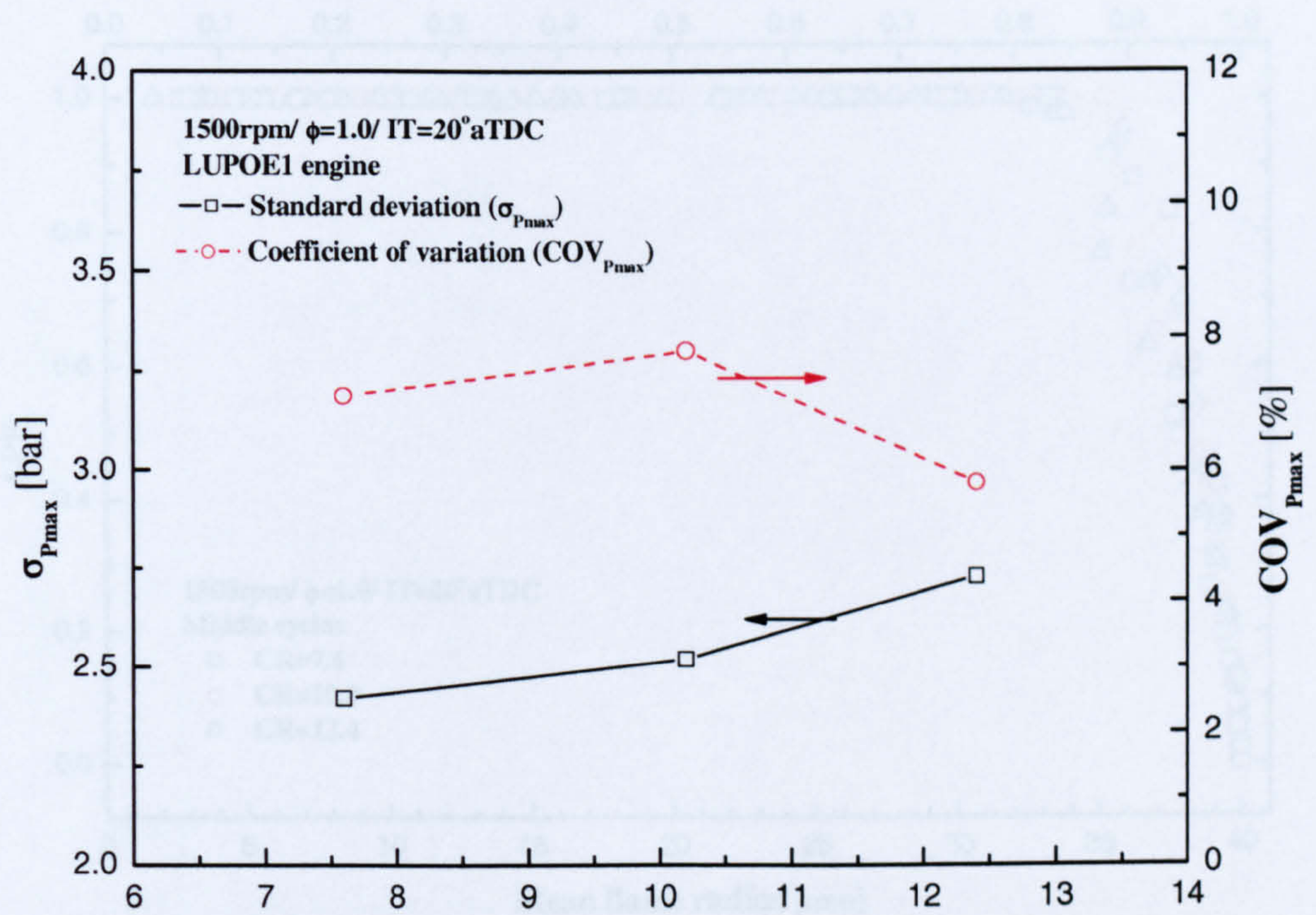

Figure 5.47 Standard deviation and coefficient of variation based on cylinder peak pressure versus compression ratio.

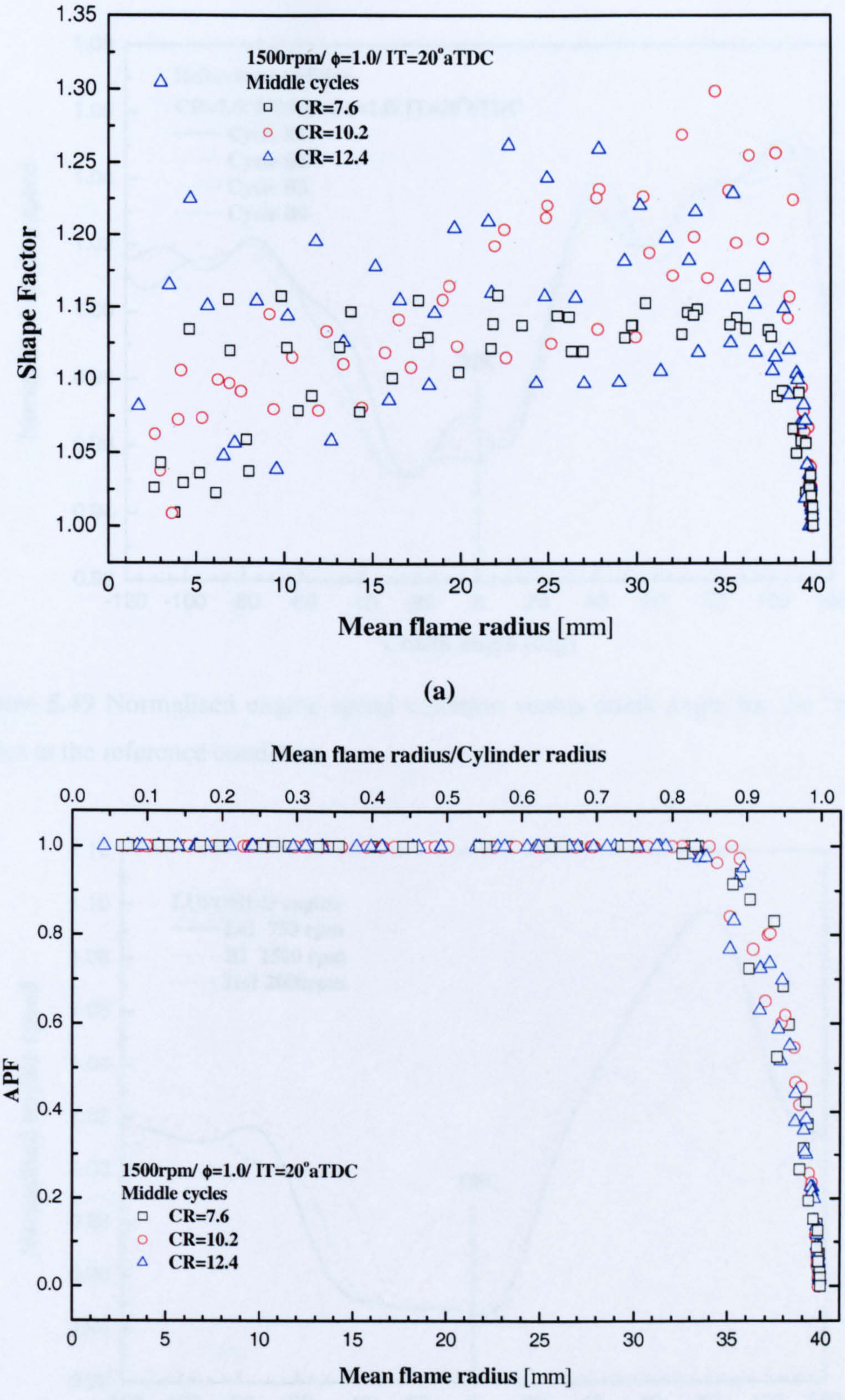

Figure 5.48 **(a)** Flame Shape Factor and **(b)** APF versus mean flame radius for the middle cycles of the three compression ratios (CR=7.6, 10.2 and 12.4).

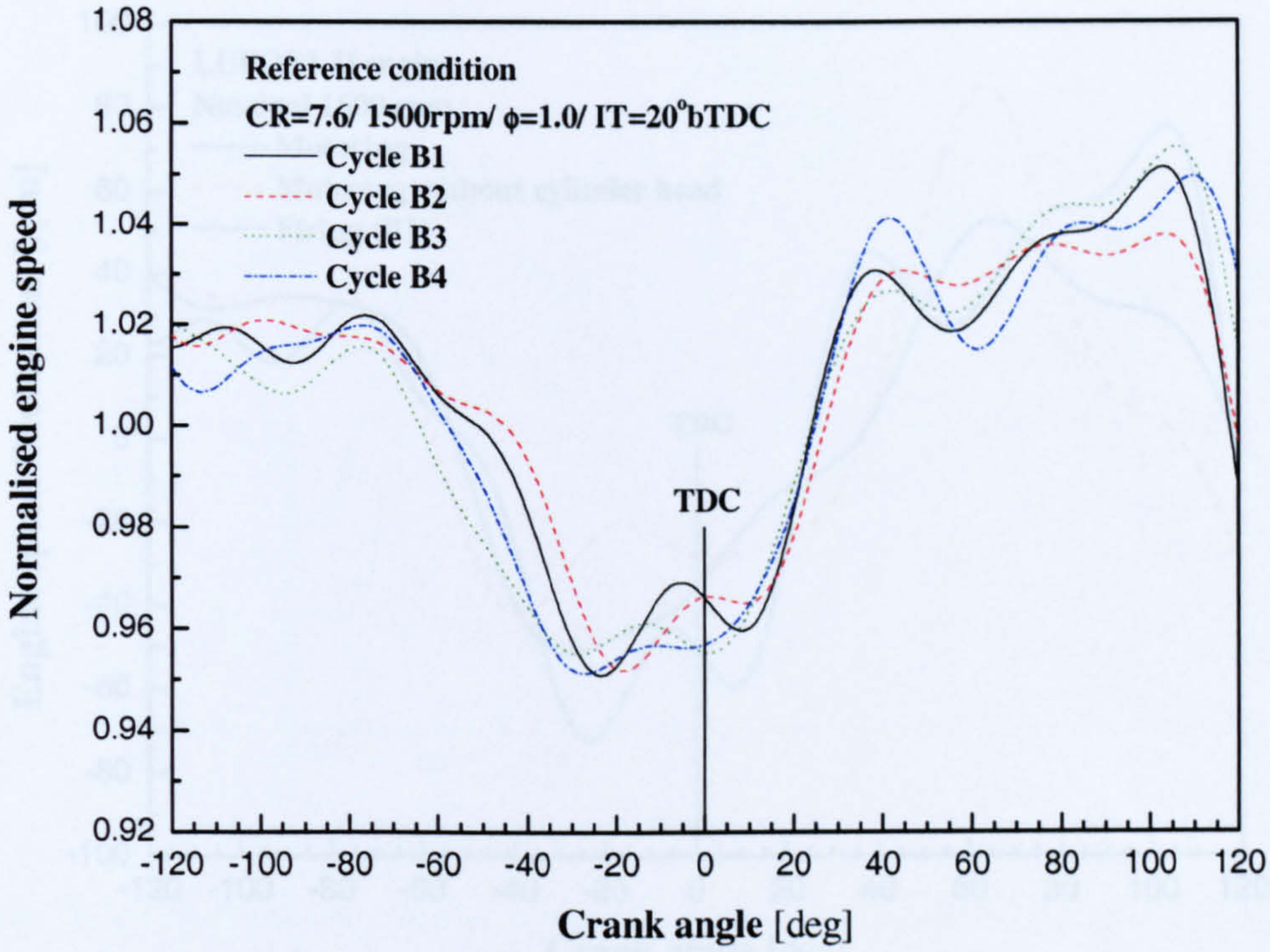

Figure 5.49 Normalised engine speed variation versus crank angle for the "middle" cycles at the reference condition.

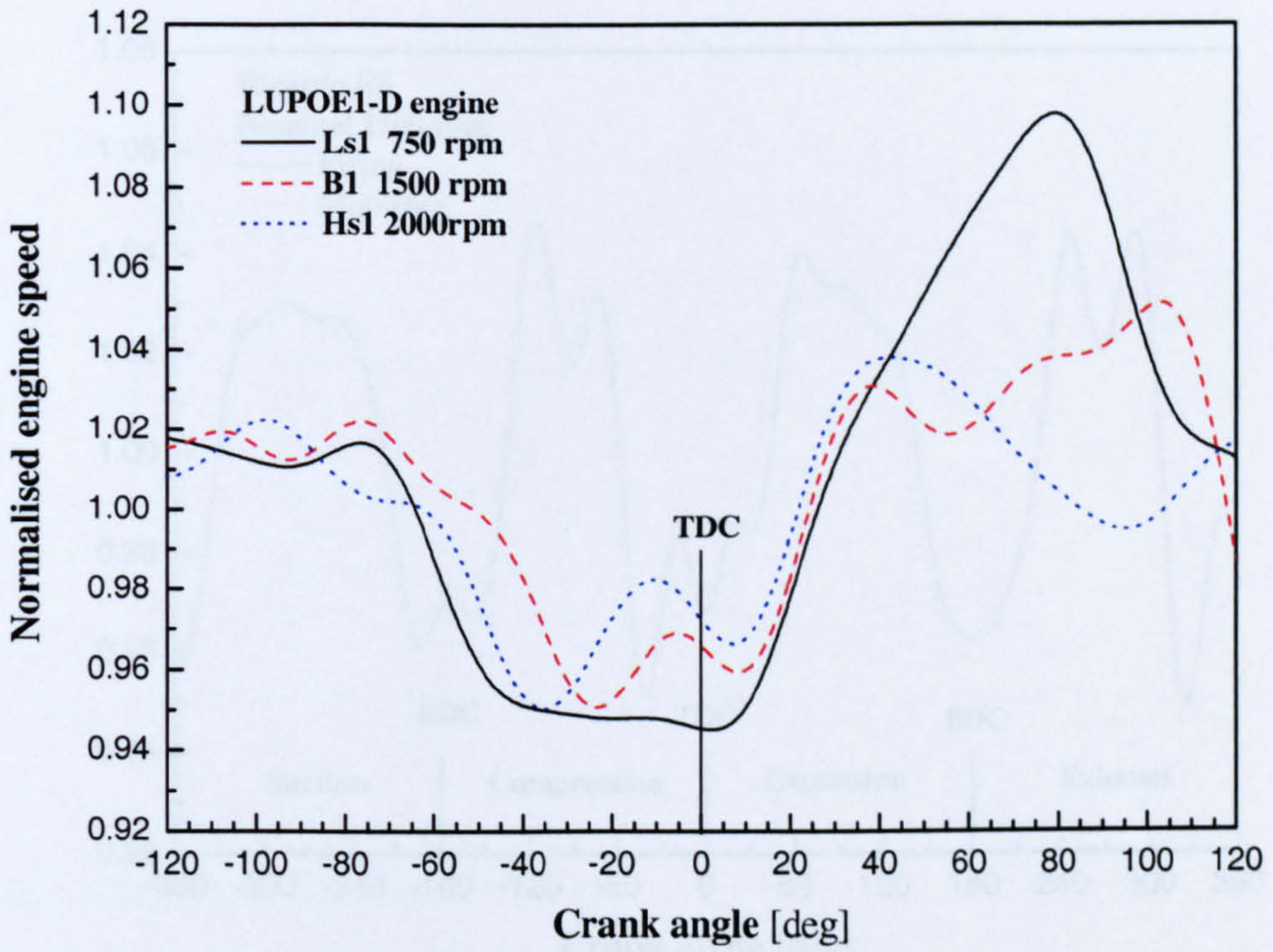

Figure 5.50 Normalised engine speed variation versus crank angle for typical middle cycles at different engine speeds.

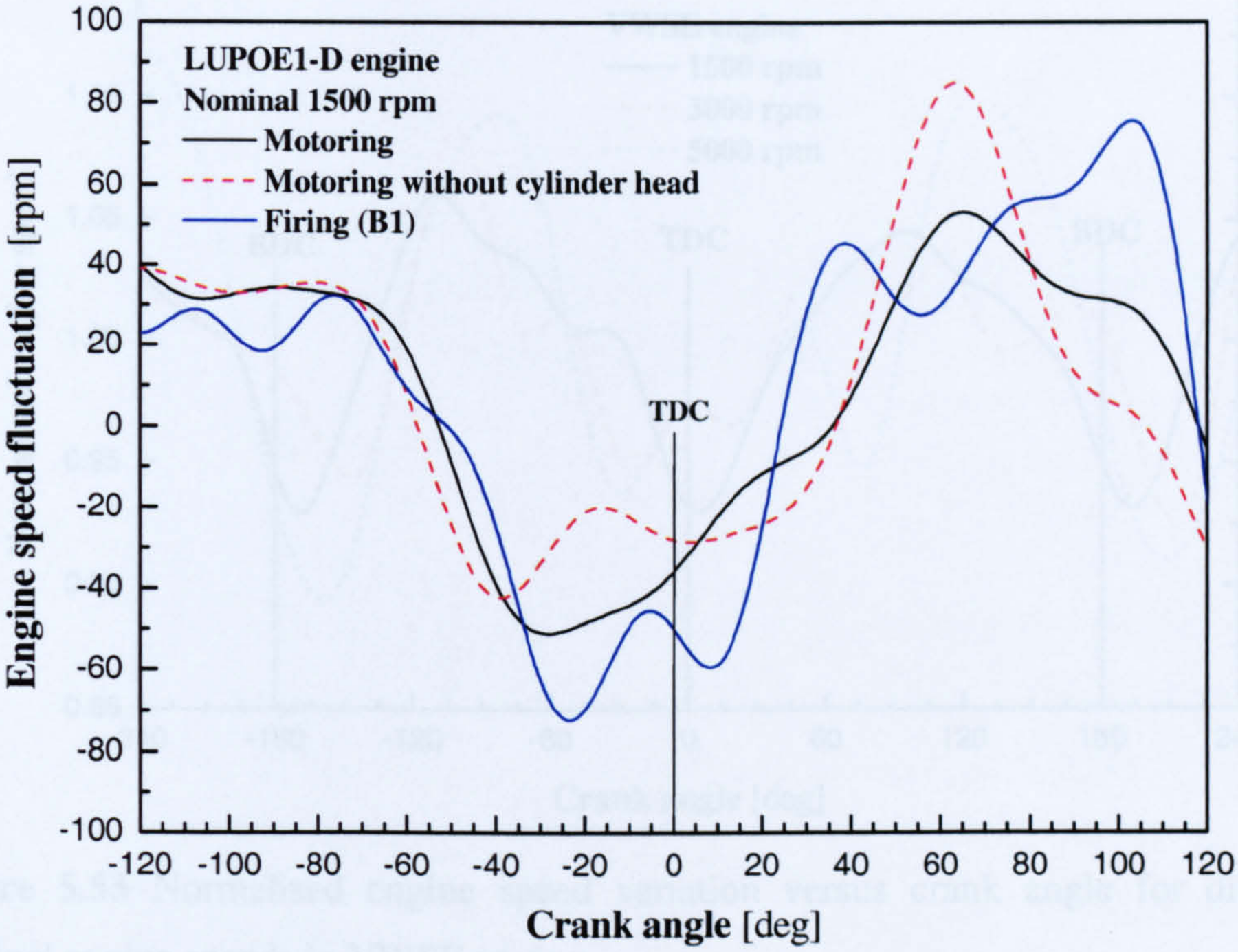

Figure 5.51 Engine speed fluctuations versus crank angle for normal motoring and motoring without cylinder head associated with a typical firing cycle in LUPOE1-D.

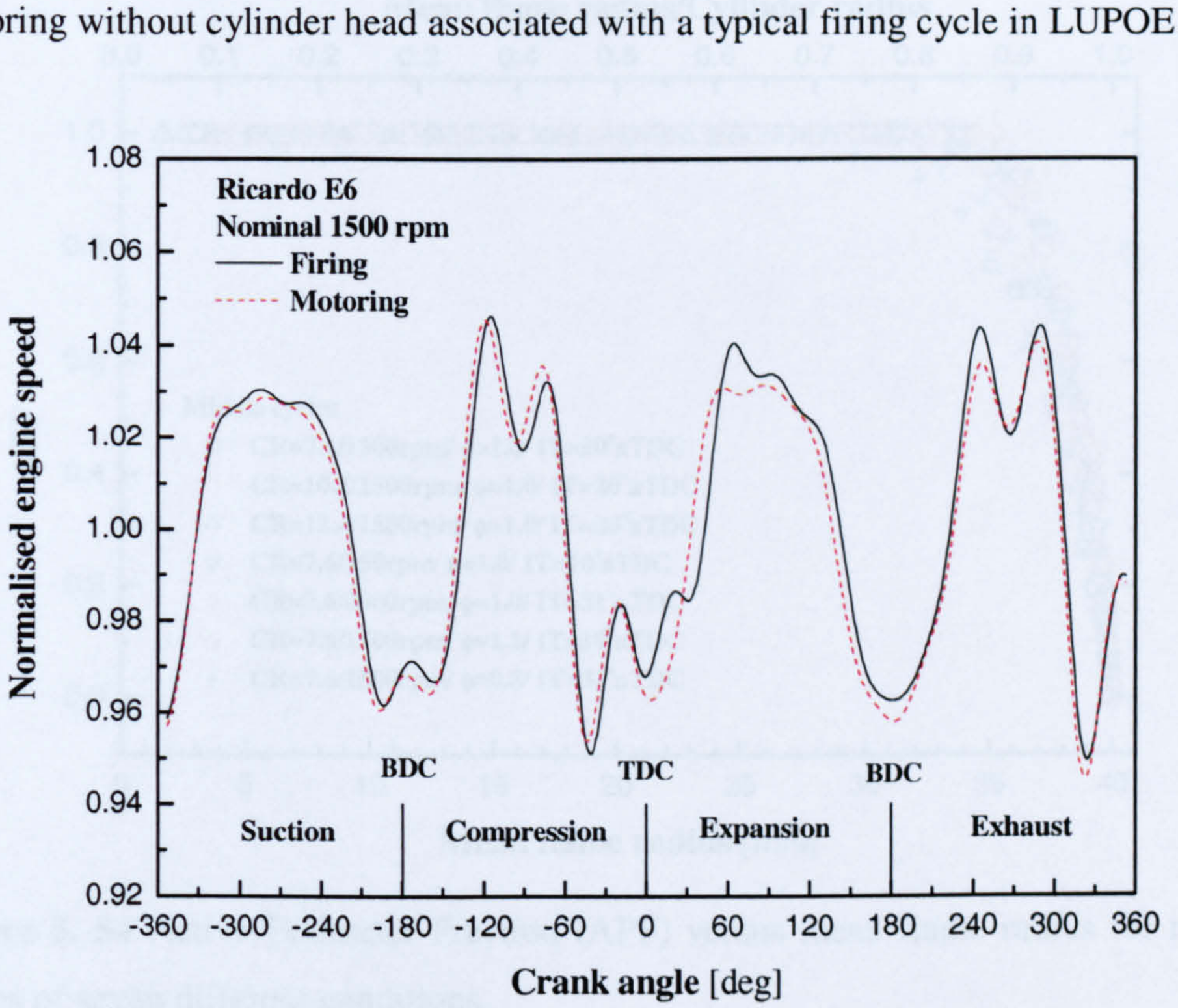

Figure 5.52 Normalised engine speed variation versus crank angle for motoring and firing conditions in Ricardo E6 engine.

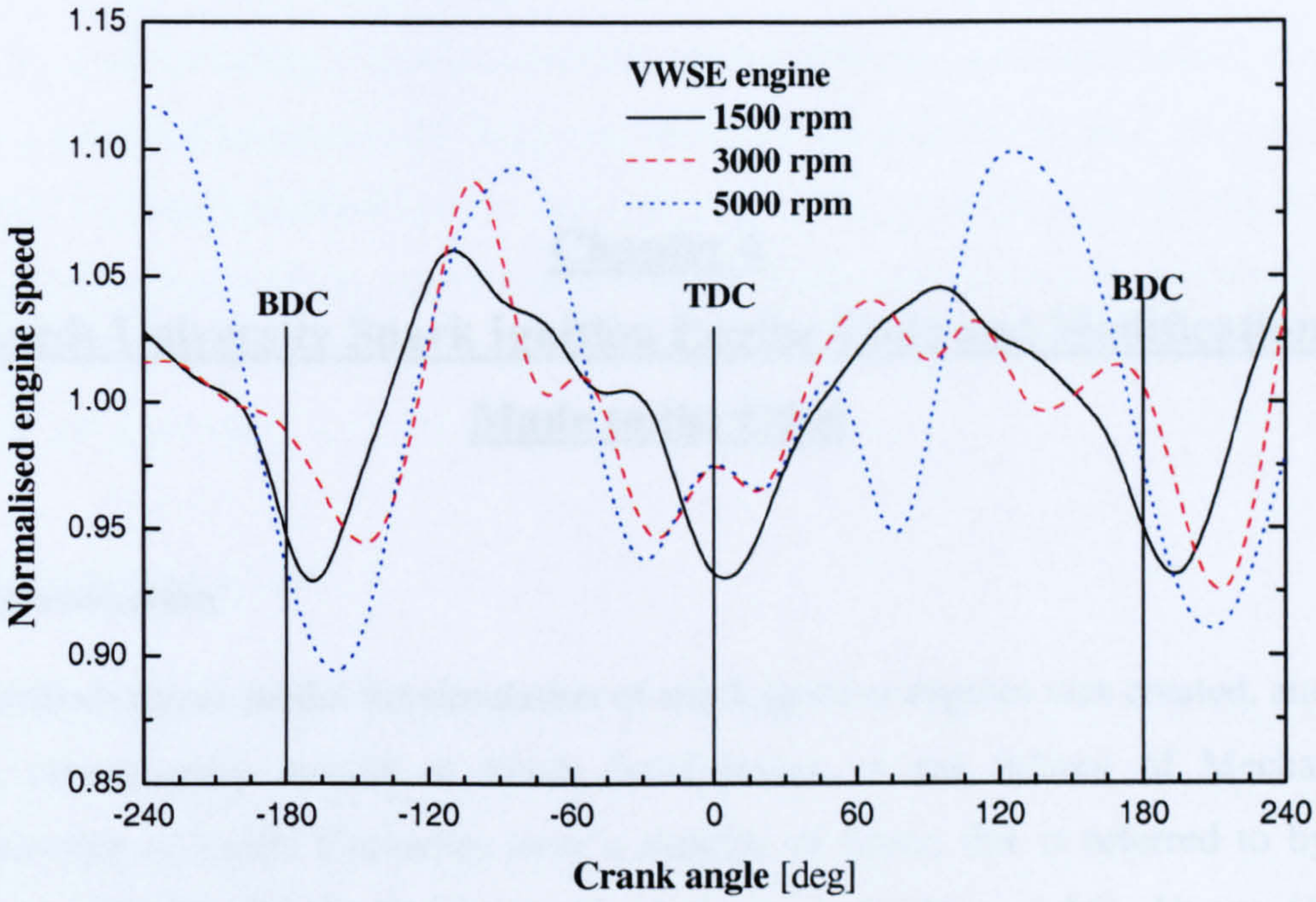

Figure 5.53 Normalised engine speed variation versus crank angle for different nominal engine speeds in VWSE engine.

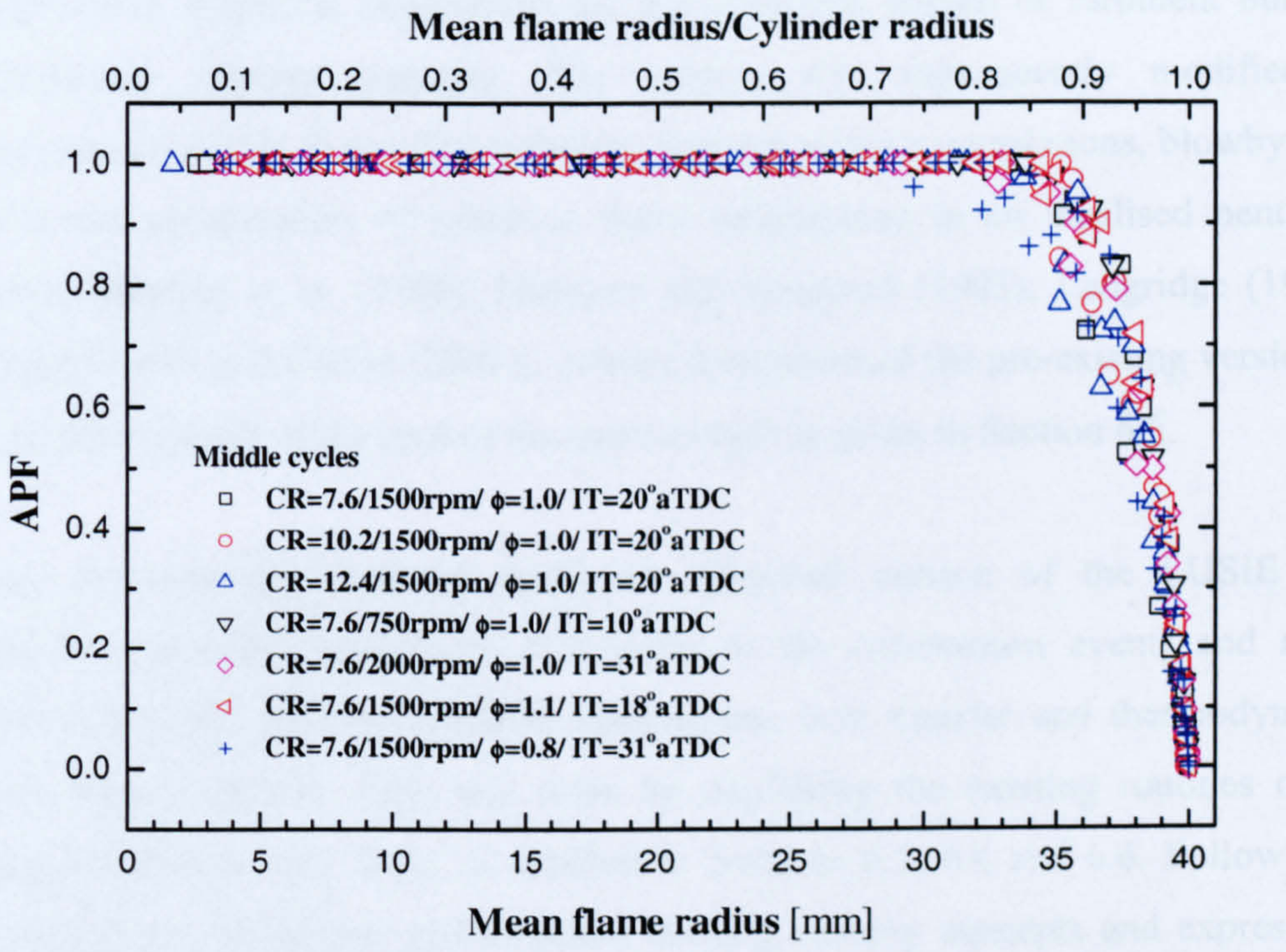

Figure 5. 54 Active Perimeter Fraction (APF) versus mean flame radius for middle cycles of seven different conditions.

Chapter 6

Leeds University Spark Ignition Engine Code and Modifications Made to the Code

6.1 Introduction

A thermodynamic model for simulation of spark ignition engines was created, and has been subsequently subject to much development, at the School of Mechanical Engineering at Leeds University over a number of years; this is referred to by the acronym LUSIE (Leeds University Spark Ignition Engine model). Hynes (1986) introduced the original version of this model, modifying a pre-existing equilibrium cycle model (Desoky, 1981; Al-Mamar, 1983) to incorporate burning rate control through either empirical expressions for mass fraction burned or turbulent burning (entrainment) velocity concepts. The version was subsequently modified to incorporate the Leeds *K* and *KLe* turbulent burning velocity correlations, blowby sub-models and computation of spherical flame propagation in an idealised pent-roof chamber [Bradley et al. (1988); Merdjani and Sheppard (1993); Langridge (1995); Merdjani (1996) and Cairns (2001)]. A brief discription of the pre-existing version of the LUSIE available at the start of the current study is given in Section 6.2.

During the currently reported study, the inherited version of the LUSIE was extensively modified (especially in relation to the combustion event) and many deficiencies in the blowby, pressure equalisation, heat transfer and thermodynamic aspects were corrected. This was done by modifying the existing routines or by writing completely new code, as detailed in Sections 6.3, 6.4 and 6.6. Following a brief discussion of laminar and turbulent burning velocity concepts and expressions (Sections 6.5.1.1 and 6.5.1.2), the Leeds *K* and *KLe* turbulent burning velocity correlations are described in Section 6.5.2. In addition, a new turbulent burning velocity model, based on Damköhler number and termed the "Zimont model" (described in Section 6.5.3) was incorporated into the code. This model was used as a

predictive option in the currently presented work. The combustion modelling was improved by including numerical solution of the "burn-up" equation, taking account of engine speed variation and flame approach to the wall (Sections 6.5.4-6.5.6). In addition to these modifications, in the light of the current interest in stratified direct injection gasoline engines, a new sub-model for flame development in radial stratified charge within a disc-shaped chamber has been developed and incorporated into the LUSIE program (detailed in Section 6.7).

6.2 Pre-existing LUSIE

The pre-existing LUSIE code encompassed treatment of the various thermodynamic processes occurring in four-stroke spark ignition engine cycles: including intake, compression, combustion, expansion and exhaust. Shown in Figure 6.1 is a brief flow chart for the LUSIE code, including both motoring and firing variants. For the firing option, two alternative procedures for combustion process were included: one incorporating empirical mass burn rate expressions and the other adopting turbulent burning velocity concepts. In the empirical burning rate variant, the mass fraction of mixture burned at any given crank angle was defined as a function of elapsed time (or crank angle) from ignition. The routine included a "linear" burn rate function and "cosine law" function as well as the more commonly adopted "Wiebe" function [Hynes (1986) and Cairns (2001)]. In the currently reported work, the more relevant part of the pre-existing code was that of combustion controlled by turbulent burning velocity concepts, described in Sections 6.2.3 and 6.5.

Three important sub-models (blowby, heat transfer and flame geometry) can be seen in the LUSIE flow chart (Figure 6.1). The blowby and heat transfer subroutines were called in compression, combustion and expansion parts of the code, as explained in Sections 6.2.1-6.2.4. The flame geometry sub-model was incorporated in the code by Hynes (1986), who provided a few geometrical sub-files for different spark locations within disc shaped chambers. Merdjani (1996) and Cairns (2001) later developed a geometrical module, entitled "GEOM", for spherical flame propagation in idealised pent-roof chambers. Engine geometries and spark position were required inputs to the geometrical routine. This routine was called several times in the combustion part of the code to evaluate flame front area, enflamed volume and flame-wall contact areas.

For disc shaped chambers, a number of mathematical expressions, derived for spherical flame over a range of flame radii, were employed (detailed by Hynes, 1986); these expressions were used in the currently reported work. The GEOM model was programmed to create a chamber wall mesh by dividing the piston crown, cylinder and head surfaces into a series of flat triangular facets and a large number of spherical flame meshes centred on the spark position. For a new engine geometry, GEOM could generate a look-up table of enflamed area, enflamed volume and flame-wall contact areas versus flame radius at different piston positions. This was effected by interacting the chamber wall mesh and spherical flame meshes [detailed by Merdjani (1996) and Cairns (2001)]. When the routine was called for a given flame radius at a known piston position, it computed the related values from the look-up table using a bilinear interpolation. For a given enflamed volume at a known piston position, the geometrical routine was also programmed to find the related flame radius.

The compression, combustion, expansion, exhaust and intake processes are briefly reviewed in the following sections.

6.2.1 Compression

During the compression part of the code, computations were carried out for increments of increasing crank angle assuming isentropic compression of a gas mixture of uniform frozen composition. At the end of each increment, cylinder mass lost was either neglected or computed using a multi-ring blowby model developed by Langridge (1995). Then heat transfer was evaluated utilising the selected option [based on either the Woschni (1967) or Annand (1963) expressions] for the known gas properties and work done was calculated using the derived cylinder pressure and known change in volume. For simulation of motoring cycles, the computations proceeded direct to the expansion process (Section 6.2.4), as seen in Figure 6.1; for firing computations the code moved next to the combustion routine (Sections 6.2.2 and 6.2.3).

6.2.2 Ignition

In the code, a simplified approach was adopted for ignition process, as described by Merdjani and Sheppard (1993). Illustrated in Figure 6.2 is a flow diagram for the successive processes invoked to create an initial flame kernel due to ignition. An empirically derived kernel size at a known period after ignition ($\Delta\theta_{ker}$) was input to the code. Following an isentropic compression for the cylinder charge over the period, mass lost from cylinder to top land crevice was computed through the available blowby routine. The decreased cylinder pressure was then determined by assuming isentropic expansion to remaining charge in the cylinder. For the unburned gas in the spherical kernel, a constant volume adiabatic combustion process was considered. This was followed by applying a pressure equalisation process between the burned kernel and unburned gases. The constant volume adiabatic combustion and pressure equalisation processes are described in Sub-sections 6.2.3(iv) and 6.2.3(ii), respectively.

After creating the burned and unburned zones, incremental computations were pursued using the concepts of entrainment and mass burning rates, as detailed in the section below.

6.2.3 Combustion

As mentioned earlier, for the currently reported work, the more relevant part of the pre-existing code was that of combustion controlled by turbulent burning velocity concepts. This method was based on the entrainment concept used by Blizard and Keck (1974), described in Sub-section 6.2.3(iii).

In a spark ignition engine, during the combustion event, a number of simultaneous phenomena occur: change in cylinder volume, pressure and temperature due to piston motion; flame development and associated expansion of the burned gas and compression of the previously burned and unburned gases; unsteady heat transfer from the burned and unburned in-cylinder gases to (varying area) combustion chamber walls (due to substantial temperature gradients); and mass transfer between

the cylinder and crevices (because of pressure gradients). In a thermodynamic model, these instantaneous and simultaneous phenomena are often considered as a succession of sequential incremental computations to the satisfaction of mass conservation and the laws of thermodynamics.

Illustrated in Figure 6.3 is a flow diagram for the successive processes incorporated in the turbulent burning velocity option of the inherited version of LUSIE. The processes are described in more detail in the following sub-sections.

(i) *Isentropic compression or expansion of burned and unburned zones due to piston motion*

This process was incorporated to consider any property changes due to piston motion during a crank angle increment in the combustion period. At the start of each increment, the ratios of specific heats for the burned and unburned gas zones were calculated, using the mixture properties of the two zones. The total cylinder volumes at the start and end of the increment were computed on the basis of the engine geometry and the two crank angle positions. Then the pressure and temperatures of the zones at the end of the increment of piston motion were determined for ideal gas isentropic compression (or expansion, dependent on the motion direction) assuming equal pressure in the two zones. These calculations were performed in the code using the Newton-Raphson method.

(ii) *Mass transfer between cylinder and top land crevice and the related effect on cylinder charge*

Mass exchange between the cylinder and the top land crevice could be evaluated using a blowby routine incorporated in the code. This routine was a three-ring model provided by Langridge (1995). His routine could predict mass lost from cylinder over the whole period between EPC and EPO in both motoring and firing cycles; however, it was incapable of predicting return of mass to the cylinder after attainment of peak pressure, Figure 6.10 (for motoring cycle). This routine computed the amount of cylinder mass lost in addition to estimating pressures and mass exchange in the crevices. In the code, the mass lost was considered as unburned gas. The reduced

pressure of the unburned gas zone in the cylinder due to the mass loss was determined by assuming isentropic expansion of the unburned gas to remaining in the cylinder. This process was reasonable when the blowby routine predicted mass loss from the cylinder; however, for the case of mass gained, the procedure was more questionable. With a proper multi-ring model, return of mass to the cylinder after peak pressure occurrence will occur (as in practice) and the above-mentioned assumption cannot be employed. This part of the code was therefore improved by incorporating a revised subroutine in the code, as described in Section 6.6.3.

In the next step, the pressures of unburned and burned gases were equalised, employing a two-zone pressure equalisation routine. In this routine, isentropic compression (IsC) and isentropic expansion (IsE) of the low- and high-pressure zones, respectively, was assumed. This method proved flawed and was replaced by an alternative procedure, as discussed in Section 6.4.

(iii) *Evaluation of incremental entrained and burned masses*

The turbulent burning velocity option in the LUSIE code was based on an entrainment model. Hynes (1986) incorporated a number of alternative expressions for turbulent burning velocity; including the simplest model of Damköhler (1940), the burning velocity ratio correlations of Lancaster (1976), Groff and Matekunas (1980) and Hamid (1986). Later, Bradley et al. (1988) and Merdjani and Sheppard (1993), the Leeds *K* and *KLe* turbulent burning velocity correlations were also incorporated into the code.

As mentioned earlier, the entrainment model was based on that proposed by Blizard and Keck (1974). They suggested that the rate of unburned gas entraining into the leading edge of turbulent flame was given by:

$$\frac{dm_e}{dt} = \rho_u u_{te} A_e \tag{6.1}$$

where m_e is the unburned mass entrained into the flame front, ρ_u the unburned gas density, u_{te} turbulent burning (entrainment) velocity and A_e the area of entrainment flame front. To evaluate incremental mass entrained in the code, the "instantaneous" turbulent burning velocity (u_{te}) was first estimated using the unburned gas properties. Then the change in flame radius due to the incremental mass entrainment was calculated by:

$$r_{fe2} - r_{fe1} = u_{te}\Delta t \tag{6.2}$$

where r_{fe1} and r_{fe2} are the flame radii before and after the entrainment, respectively; Δt is incremental time step. The incremental volume entrained was evaluated from advancing the spherical flame front from r_{fe1} to r_{fe2} using the flame geometry routine. As described earlier, this routine could determine enflamed volume for a given flame radius at a known crank angle. The incremental mass entrained (Δm_e) was then evaluated from:

$$\Delta m_e = \rho_u \Delta V_e \tag{6.3}$$

where ΔV_e is the incremental volume entrained. In the inherited version of LUSIE, the incremental mass entrained was multiplied by a factor (termed "flame shape factor") to account for the effect of non-spherical flame shape on the entrainment rate. This factor, generally greater than unity, was determined on the basis of experimental flame image data.

The rate of mass burning was evaluated by:

$$\frac{dm_b}{dt} = \frac{m_e - m_b}{\tau_b} \tag{6.4}$$

in which τ_b is characteristic burning time, generally determined from:

$$\tau_b = k_\tau \frac{X}{u_l} \tag{6.5}$$

where k_τ is a constant of proportionality, X is a characteristic length scale and u_l is the laminar burning velocity. In the original paper (Blizard and Keck, 1974), the length scale (X) was considered proportional to valve lift, which is of the order of the integral length scale, l. In the currently reported work, X was taken as integral length scale in Equation (6.5). In the code, incremental solution of Equation (6.4) was effected by the following expression for ith increment (Hynes, 1986):

$$m_{b_i} = m_{e_i} - \sum_{j=1}^{i} \Delta m_{e_j} \times \exp\left[-(i - j + \frac{1}{2})\frac{\Delta t}{\tau_{b_i}}\right] \tag{6.6}$$

where m_{b_i} and m_{e_i} are total burned and entrained masses until the end of ith increment, j is a counter, Δm_{e_j} entrained mass during jth increment, Δt time increment and τ_{b_i} characteristic burning time in ith increment. Finally, the mass burning, Δm_{b_i}, in the ith increment was evaluated by:

$$\Delta m_{b_i} = m_{b_i} - m_{b_{i-1}} \tag{6.7}$$

(iv) *Constant volume adiabatic combustion of the burning zone*

The mass of charge burned in a crank angle increment was assumed to undergo a constant volume adiabatic combustion process. The composition and elevated pressure and temperature of the burned gas were calculated assuming thermochemical equilibrium, energy conservation and the ideal gas law – the routine considered 10 product species and invoked dissociation reactions (Desoky, 1981).

(v) *Three-zone pressure equalisation process*

The freshly burned gas was then allowed to expand (isentropically), compressing (also isentropically) both unburned and previously burned gases in the cylinder to

achieve pressure equalisation. This procedure employed the same routine discussed in Sub-section 6.2.3(ii) and was modified by the current author, as described in Section 6.4.

(vi) *Mixing process of the newly and previously burned zones*

Mixing of the gas freshly burned in the increment with previously burned gas to form a single burned gas region was then invoked. A constant volume adiabatic mixing process was assumed, applying the First Law of Thermodynamics and themochemical equilibrium. Using a related routine, the final state of the mixed zone was determined. Following this mixing process, the model again considered just two zones (burned and unburned). Any resulting pressure difference between these two zones was eliminated by adopting the (IsC-IsE) pressure equalisation routine described before.

(vii) *Heat transfer from burned and unburned zones to chamber wall*

At the end of the crank angle increment, convective heat transfer between the burned and unburned gas zones and the combustion chamber walls, cylinder head and piston were computed on the basis of one of two expressions (Annand or Woschni, reviewed in Sections 6.6.4.1 and 6.6.4.2). From the geometrical routine embodied in the code, the contact areas of the burned and unburned zones with the combustion chamber (cylinder wall, head and piston) were evaluated. Then heat transfer from each zone was individually determined according to the gas properties of the zone and the selected heat transfer option (note that any possible heat exchange between the zones was ignored). The First Law of Thermodynamics was applied to each zone assuming a heat transfer process at constant volume and the final internal energy of each zone was calculated. The corresponding temperature, pressure and mixture composition (just for burned zone) of the zones were evaluated using gas properties, the ideal gas law and thermochemical equilibrium (just for burned zone). This process was followed by a pressure equalisation process, as described earlier. Within the heat transfer routine, a number of problems were encountered and eradicated in the current work (described in Section 6.6.4.3).

The final states of the two zones (burned and unburned) were transferred as the initial conditions for the next crank angle increment and the sequence of procedures was repeated until a pre-determined mass fraction burned in the cylinder was achieved. Thereafter calculations were performed using the expansion routine described below.

6.2.4 Expansion

The expansion routine of the code, for both motoring and (post combustion) firing cycles, was very similar to that for the compression stroke. In a motoring cycle, charge composition was considered uniform and frozen. For a firing cycle, a single zone of uniform burned gases in thermochemical equilibrium was assumed. It should be noted that this assumption applied also to any mass returned from crevices – resulting an unrealistic assumption of instantaneous combustion of such gases. It proved necessary to change this, as outlined in Section 6.6.7.

6.2.5 Exhaust and intake

Hynes (1986) incorporated idealised exhaust and intake processes in LUSIE to predict residual gas mass fraction and composition in a four-stroke cycle. The code was principally developed to consider the combustion process and more precise treatment of the exhaust and intake processes was considered inappropriate. In the currently reported work, this part of the code was ignored, as (skip fire mode – no residual) LUPOE1 engine measured EPC pressure and inlet temperature were imposed at the start of compression.

6.3 Blowby modelling

Many researches have been conducted on the "blowby" phenomenon, i.e. gas flow through the cylinder-piston-ring crevices. This phenomenon is important for validation of engine combustion simulation, analysis of bore wear pattern and estimation of hydrocarbon emissions. A one dimensional orifice-volume method has been mostly widely used in analysis of such crevice flow. Ting and Mayer (1974), in a study of bore wear pattern in reciprocating engines, developed a model to estimate gas pressure in piston-cylinder crevices which incorporated a series of chamber and inter-

ring spaces connected by orifices. Namazian and Heywood (1982) investigated the effect of the gas flow through the piston-cylinder-ring crevices on hydrocarbon emissions in a four-stroke spark ignition engine. In their investigation, they imposed experimental cylinder pressure data to a blowby model (based on the orifice-volume method). Ruddy et al. (1981), of the Leeds University School of Mechanical Engineering Engine Tribology Group, employed a volume-orifice method to predict the gas pressures within the ring packs of a large bore diesel engine.

Abdel Salam (1992), Langridge (1995) and Mahmud (1999), working in the same research group as the current author, also studied blowby using the volume-orifice method for an earlier version of the engine outlined in Chapter 3. Abdel Salam and Langridge considered a three ring model. Langridge's blowby modelling suggested a 30% mass loss in motoring and rising to as much as 50% in a firing cycle. Mahmud simplified the complex gas flow through the crevices by representing the three rings by just a single ring (based on the work of Ramos, 1989). Cairns (2001) utilised this single ring model in his modelling study. Pan (1994) estimated mass loss in motoring cycles using motoring data and two simple theoretical methods. In addition, he conducted a static leakage test for estimating the mass loss from the engine by supplying pressurised air to the combustion chamber. He reported that when the piston just covered the exhaust port, a very high air flow rate was necessary even to maintain a pressure of 2 bar.

Since the single ring model of Mahmud (1999) and Cairns (2001) was unable to predict the crevice flow properly (especially after peak pressure occurrence), initially it was decided to improve the blowby model of Langridge (which was available in the inherited version of LUSIE). However, many problems and errors were discovered in the inadequately commented three-ring model (which employed somewhat confusing dimensionless expressions). Therefore, it was decided to develop a completely new one dimensional multi-ring blowby routine using dimensional governing equations. This routine is described in more detail in Section 6.3.3.

6.3.1 Piston-ring-cylinder pack crevices

To minimise in-cylinder mass loss through the narrow space between the piston skirt and cylinder, a number of piston rings (located in piston ring-grooves) are generally adopted. These rings divide the narrow space into a number of "crevices": the "top land crevice", connected to combustion chamber and bounded by the piston, the top ring and cylinder; "inter-ring crevices" (two for three-ring pack) bounded by two successive rings, piston and cylinder; and the crevice connected to the crankcase, which is bounded by the bottom of the lowest ring, piston and cylinder (illustrated in Figure 6.4). The rings significantly reduce the gas leakage into crankcase; nevertheless, small gaps in the rings allow gas flow between crevices due to inter-ring pressure differences. Illustrated in Figure 6.5 are a few typical shapes of ring gaps encountered in internal combustion engines. In a four-stroke engine, normally, the ring gap is similar to those shown in Figures 6.5(a), (b) and (c). In ported engines, such as LUPOE1, circumferential motion in the ring-groove is usually prevented to avoid interference between the rings and ports. This is generally effected by fitting a pin in the ring-groove at the ring gap position and designing the ring gap to match the pin, shown in Figure 6.5(d). This is the method employed for the LUPOE1 engine.

6.3.2 Mass flow through crevices and ring gaps

Cylinder pressure rise due to compression and combustion generates a pressure gradient between the cylinder and top land crevice. This causes a gas flow from cylinder into the top land crevice through a relatively large entrance cross-section area; the gas cools to the temperature of surroundings (because of a large surface to volume ratio of the narrow passage). The pressure gradient between the top land and first inter-ring crevice produces a gas flow through the top ring gap. This flow increases the pressure in the first inter-ring crevice and generates a pressure gradient with the crevice below (which is connected around its periphery to crankcase) as seen for a 2-ring pack in Figure 6.4. This results in flow through the second ring-gap into the crankcase. In the expansion stroke, after peak pressure has been attained in the cylinder, the direction of the pressure gradient between the cylinder and top land crevice reverses and a gas flow back into the cylinder occurs. The direction of flow through the ring gaps can also change, according to pressure difference between the

connected volumes. Using a transparent engine with a square-cross section piston and adopting a schlieren technique, Namazian and Heywood (1982) observed a low velocity flow from the top land crevice back into the cylinder following cylinder peak pressure. They also noticed a jet-type flow through the top ring gap when the top land crevice pressure dropped below than in the first inter-ring crevice.

6.3.3 Volume and orifice blowby theory

The "volume and orifice" theory of blowby is based on two essential expressions: one for mass flow rate through an orifice due to pressure gradient and the other for determining the change of pressure in a volume due to mass flow in or out of that volume through the orifices. Shown diagrammatically in Figure 6.6 is the three-ring-piston assembly used in the LUPOE1 engine. In the assembly, a series of three crevices (including top land and two inter-ring crevices) connects the cylinder to the crankcase (ignoring the crevice below the lowest ring for this ported engine). Assuming the top land entrance section as a large orifice, one can consider four orifices for the flow through the ring pack.

Set out in Figure 6.7 is the simplified volume and orifice model representing the three-ring assembly considered in the currently reported work. The flow is assumed one dimensional, with change in gas properties in the flow direction but not normal to the flow. It is assumed that the crevice volumes and orifice cross-section areas remain constant, regardless of piston motion. There is significant heat exchange between the gases in the crevice volumes and surroundings (cylinder wall, piston and rings). Furuhama and co-worker (1961a) examined the temperature of gas flowing through piston-ring crevices using a stationary piston and a reciprocating cylinder. They concluded that the temperature of the gas flowing through the piston-ring crevices is nearly equal to that of the gas on the piston surface. In the currently adopted model, the gas temperature in the crevices was assumed uniform and equal to the wall temperature.

On the basic of isentropic flow through an orifice, the mass flow rate can be expressed in terms of orifice upstream and downstream pressures (Furuhama et al., 1961b; Ting and Mayer, 1974 and Heywood, 1988). For an orifice located between the *i*th and

(i+1)th volumes (i = 1, 2, 3, 4 and 5), according to pressure ratio the mass flow rate is given by one of the four following expressions:

(i) If $\frac{p_{i+1}}{p_i} \le 1$ and $\frac{p_{i+1}}{p_i} > \left(\frac{2}{\gamma_i + 1}\right)^{\gamma_i/(\gamma_i - 1)}$, the mass flow rate will be:

$$\frac{dm_{i,i+1}}{dt} = C_{d_{i,i+1}} A_{i,i+1} \left[\frac{2\gamma_i}{(\gamma_i - 1)RT_i}\right]^{\frac{1}{2}} p_i \left(\frac{p_{i+1}}{p_i}\right)^{\frac{1}{\gamma_i}} \left[1 - \left(\frac{p_{i+1}}{p_i}\right)^{\frac{\gamma_i - 1}{\gamma_i}}\right]^{\frac{1}{2}} \tag{6.8}$$

where $C_{d_{i,i+1}}$ and $A_{i,i+1}$ are discharge coefficient and orifice cross-section area, respectively, flow is from ith to the (i+1)th volume; γ_i is the ratio of specific heats for the gas mixture in the ith volume.

(ii) If $\frac{p_{i+1}}{p_i} \le 1$ and $\frac{p_{i+1}}{p_i} < \left(\frac{2}{\gamma_i + 1}\right)^{\gamma_i/(\gamma_i - 1)}$, the flow will be choked and the mass flow rate becomes:

$$\frac{dm_{i,i+1}}{dt} = C_{d_{i,i+1}} A_{i,i+1} \left[\frac{\gamma_i}{RT_i}\right]^{\frac{1}{2}} \left(\frac{2}{\gamma_i + 1}\right)^{(\gamma_i + 1)/2(\gamma_i - 1)} p_i \tag{6.9}$$

(iii) If $\frac{p_{i+1}}{p_i} > 1$ and $\frac{p_{i+1}}{p_i} < \left(\frac{2}{\gamma_{i+1} + 1}\right)^{-\gamma_{i+1}/(\gamma_{i+1} - 1)}$, the mass flow rate is given by:

$$\frac{dm_{i,i+1}}{dt} = -C_{d_{i+1,i}} A_{i+1,i} \left[\frac{2\gamma_{i+1}}{(\gamma_{i+1} - 1)RT_{i+1}}\right]^{\frac{1}{2}} p_{i+1} \left(\frac{p_i}{p_{i+1}}\right)^{\frac{1}{\gamma_{i+1}}} \left[1 - \left(\frac{p_i}{p_{i+1}}\right)^{\frac{\gamma_{i+1} - 1}{\gamma_{i+1}}}\right]^{\frac{1}{2}} \tag{6.10}$$

where the negative sign denotes reversed flow direction (from bottom to top); $C_{d_{i+1,i}}$ and $A_{i+1,i}$ are discharge coefficient and orifice cross-section area, respectively, and flow is from (i+1)th to the ith volume.

(iv) If $\frac{p_{i+1}}{p_i} > 1$ and $\frac{p_i}{p_{i+1}} \le \left(\frac{2}{\gamma_{i+1} + 1}\right)^{\gamma_{i+1}/(\gamma_{i+1} - 1)}$, the flow will be choked and the mass flow rate is given by:

$$\frac{dm_{i,i+1}}{dt} = -C_{d_{i,i+1}} A_{i+1,i} \left[\frac{\gamma_{i+1}}{RT_{i+1}}\right]^{\frac{1}{2}} \left(\frac{2}{\gamma_{i+1}+1}\right)^{(\gamma_{i+1}+1)/2(\gamma_{i+1}-1)} p_{i+1} \tag{6.11}$$

Assuming that the gas in the crevice volumes obeys the ideal gas low, the rate of pressure change (due to mass exchange) in the *j*th crevice with constant volume and temperature will be:

$$\frac{dp_j}{dt} = \frac{RT_j}{V_j}\left(\frac{dm_{j-1,j}}{dt} - \frac{dm_{j,j+1}}{dt}\right) \tag{6.12}$$

in which j can be 2,3 and 4 for the three-ring model.

From development of Equation (6.12), three differential equations can be derived for the three crevice volumes. The time base equations can be easily converted to crank angle base using engine speed ($d\theta/dt = \omega$, ω is rotational engine speed), summarised as follows:

$$\frac{d}{d\theta}\begin{bmatrix} p_2 \\ p_3 \\ p_4 \end{bmatrix} = \begin{bmatrix} f_1[\theta, p_2, p_3, p_4] \\ f_2[\theta, p_2, p_3, p_4] \\ f_3[\theta, p_2, p_3, p_4] \end{bmatrix} \tag{6.13a}$$

where f_1, f_2 and f_3 are determined via Equations (6.8-6.12), and:

$$\frac{dP}{d\theta} = F(\theta, P) \tag{6.13b}$$

where P and F include three components (p_2, p_3 and p_4) and (f_1, f_2 and f_3), respectively.

6.3.4 Blowby geometric parameters

Key blowby geometric parameters (orifice cross-sectional areas, top land and inter-ring crevice volumes) change with cylinder, piston and ring temperatures; due to different thermal expansion coefficients of the cylinder and piston materials. The thermal expansion coefficient of aluminium alloys is about 2.3 times that of cast iron (Gere et al., 1985). A simple calculation for the LUPOE1 engine showed that a $100^{\circ}C$ increase in the cylinder and piston temperature would decrease the top land crevice cross-sectional area and related volume by about 25 and 18.5%, respectively (cf the blowby geometric parameters measured at ambient temperature). The necessary temperature corrections at running conditions were incorporated into the modelling code.

The critical cross-section (orifice) areas directly depend on the shape of piston ring gaps. Shown diagrammatically in Figure 6.8 is the piston ring pack assembly for the LUPOE1 engine. The shape of the ring gap and the position of the pin fitted in the ring groove can be seen in the diagram. The width of the ring gap varies from a small value at the top to a large value at the bottom of the ring. For this case, the orifice cross-section area would be a function of the largest width pertaining at the bottom of the ring and the radial clearance as the bottom of the ring settles on the lower surface of the ring-groove. It is obvious that the orifice cross-section area will be different if the top of the ring locates on the top surface of ring-groove. This can happen in the expansion stroke due to vertical motion of the ring relative to the ring-groove (resulting from piston acceleration, ring-wall friction and variation of pressure in crevices). This type of ring motion has been considered in the work of Namazian and Heywood (1982). In the currently reported work, good agreement was found between experimental and model results when neglecting the possible ring motion; therefore, to reduce the complexity of the model, such ring motion was not considered.

The discharge coefficient of an orifice depends on its shape and dimensions (upstream and downstream) and compressibility (Shapiro, 1953). Furuhama et al. (1961a) experimentally investigated the discharge coefficient through the narrowest gas

passage. They concluded that the discharge coefficient should be approximately 0.86; this value was adopted in the currently presented work.

6.3.5 Numerical aspects of the blowby model

The differential equation set [Equation (6.13b)] was numerically solved using a Runge-Kutta order two method. The blowby model was incorporated into LUSIE in the form of three subroutines and one function (all written by the current author). In the blowby routine, the main computational increment was subdivided into several sub-increments adequately to cope with the large pressure difference between the small crevice volumes. In each sub-increment, mass flow rate for each orifice was determined and then totalled to yield the mass flow from the orifice in the main increment.

Setting of the blowby model constants and comparison between model predictions and an experimental motoring cycle, and additional information from the modelling results, are described in Section 7.2. In the current chapter, quantitative and qualitative comparisons with the previously reported works in Leeds are considered. Substantial differences were observed between the predictions of the three-ring blowby model developed in the currently reported work and those of previous workers in Leeds. Shown in Figure 6.9 are the predicted masses lost from the chamber using the single-ring model presented by Cairns (2001) and those obtained using the model developed in the current study for a similar motoring condition for the LUPOE1 engine. The single-ring model shows little mass loss over the period in which the exhaust port is connected to the top land crevice (TLC); whereas the three-ring model suggests a mass loss of 2.4% by the end of this period ($88^\circ bTDC$). Thereafter, the rate of mass loss suggested by the single-ring model increases faster than predicted by the three-ring model. The former yields a maximum mass loss of 22% at $7^\circ aTDC$, which is more than twice the peak loss predicted by the three-ring model. At the EPO position, the single-ring model predicts ~11% mass loss; c.f. the three-ring computation of ~6%.

Illustrated in Figure 6.10 is the predicted percent of mass flow across the TLC boundary and through the piston rings versus crank angle from the three-ring model of Langridge (1995), for a modified version of the JLO engine under motoring conditions. Although this version of the JLO was not used in the currently presented work, substantial differences can be seen in the overall pattern of mass lost from the cylinder. There is no evidence of any reverse flow to the cylinder in the expansion stroke, as predicted in the computations shown in Figure 6.9 for both models. The peak value of mass lost (~30%) is significantly higher than that predicted by the currently developed model under firing conditions (19%, described in Section 7.3.3); the crank angle position for peak mass loss is also rather different.

6.4 Pressure equalisation subroutine

As outlined in Section 6.2, a key subroutine in the inherited LUSIE code was that allowing pressure equalisation between zones (separated by an imaginary partition) containing gases at different conditions following a change in the thermodynamic state of one of the zones, Figure 6.11. In the original version of LUSIE, this process was considered to occur by isentropic compression of the low-pressure zone and isentropic expansion of the high-pressure zone, abbreviated IsC-IsE here. An improved, alternative, method (termed IsC-COIE) was developed in the current work. This assumed constraints of isentropic compression for the low-pressure zone and constant overall internal energy of the two zones. The governing equations of the original and revised methods are detailed, and the differences highlighted by numerical examples, below.

6.4.1 Governing equations

Shown diagramatically in Figure 6.11(a) are the initial states of two isolated zones (A and B) within a rigid volume. These zones, with different pressures ($P_{a1} < P_{b1}$ here), are assumed separated by an imaginary transportable partition. By the end of the pressure equalisation process, the partition moves to some final position such that both zones are both at pressure, p_f, as shown in Figure 6.11(b). To find the five

unknown parameters at the final condition ($T_{a2}, P_f, V_{a2}, T_{b2}$ and V_{b2}), five equations are required. They may be generated as below:

(i) Application of the ideal gas law to the two zones yields:

$$\frac{P_f V_{a2}}{T_{a2}} = \frac{P_{a1} V_{a1}}{T_{a1}} \tag{6.14}$$

and

$$\frac{P_f V_{b2}}{T_{b2}} = \frac{P_{b1} V_{b1}}{T_{b1}} \tag{6.15}$$

(ii) Noting the constraint on the total volume of the system:

$$V_{a2} + V_{b2} = V_{a1} + V_{b1} = V_t \tag{6.16}$$

where V_t is the total volume.

(iii) Assuming isentropic compression of the low-pressure zone (Zone A) from the initial state to the final state:

$$V_{a2} = V_{a1}\left(\frac{P_{a1}}{P_f}\right)^{1/\gamma_a} \tag{6.17}$$

where γ_a denotes the ratio of specific heats of the gas mixture in Zone A.

(iv) In the inherited version of LUSIE, an isentropic expansion assumption for the high-pressure zone (Zone B here) was adopted to provide the necessary fifth equation:

$$V_{b2} = V_{b1}\left(\frac{P_{b1}}{P_{b2}}\right)^{1/\gamma_b} \tag{6.18}$$

where γ_b is the ratio of specific heats for the gas mixture in Zone B.

6.4.2 Revised pressure equalisation routine

It was found that the isentropic assumption in the inherited version resulted in violation of the First Law of Thermodynamics. Hence, a revised pressure equalisation method was developed in the current work. In this, the required final equation is derived via the application of the First Law to the isolated (closed) system comprising both zones. During the pressure equalisation process, the system does not exchange heat and work with surroundings; hence the total internal energy of the system must remain constant, then:

$$U_{a1} + U_{b1} = U_{a2} + U_{b2} = U_t \tag{6.19}$$

where U_t is the total internal energy of the zones.

In this revised pressure equalisation subroutine (IsC-COIE), the unburned gas composition is assumed frozen and the burned gas is considered to be in thermochemical equilibrium. Illustrated in Figure 6.12 is a brief flowchart for the routine. The initial states of the two zones are input and the total volume and internal energy calculated (Equations 6.16 and 6.19). The zone of initial lower pressure is taken as Zone A in the flowchart. The final pressure of the two zones is first guessed:

$$P_g = \frac{P_{a1}V_{a1} + P_{b1}V_{b1}}{V_t} \tag{6.20}$$

and T_{a2}, U_{a2} and V_{a2} are evaluated for isentropic compression of Zone A. Then for Zone B, V_{b2} and U_{b2} are determined using the total volume constraint (Equation 6.16) and the First Law of Thermodynamics (Equation 6.19). The corresponding temperature (T_{b2}) is evaluated by a numerical procedure (quadratic interpolation method) until the relative error in internal energy is less than a defined tolerance ($tolU$); then, p_{b2} is determined using the ideal gas law. Then any pressure difference ($difP$) between the two zones is evaluated. If the difference is less than the imposed

tolerance (*tolP*), the routine terminates; otherwise, a revised guess of final pressure is made:

$$p'_g = \frac{p_g V_{a2} + p_{b2} V_{b2}}{V_t} \tag{6.21}$$

and the whole procedure repeated until the set tolerances are met.

6.4.3 Comparison of original and revised subroutines

The outputs from the two pressure equalisation methods were initially compared by considering a $50\,cm^3$ constant volume containing a stoichiometric isooctane-air mixture at 5 *bar* pressure and $500^\circ K$ temperature. It was assumed that one-third of the total mass followed a constant volume adiabatic combustion (CVAC) process. Then the pressure equalisation methods were applied between the burned and unburned zones. For the burned region, LUSIE's usual thermochemical of dissociation reactions and equilibrium routines were adopted. Shown in Figures 6.13(a), (b) and (c) are the initial state, that following constant volume adiabatic combustion (CVAC) of Zone B and that following pressure equalisation between the two zones for constant total volume.

Illustrated in Figure 6.14 is a *T-s* diagram for the processes occurring in the two zones. Since the gas properties change significantly in the combustion, for compactness, the processes for the two zones are displayed separately. That for the unburned gas is displayed using the left and bottom axes (shown by black lines) and that for the burned gas by the right and top axes (shown by red lines). Before combustion both zones are at the same state (pressure, temperature and composition), and identified in Figure 6.14 by States, *a1* and *b1*. Following the CVAC process, there is a change of composition and state for the gases in Zone B (p_{b2}=29.75 *bar* and T_{b2}=2760 *K*). The composition in Zone A remains unchanged, as does the State (*a2*). Following pressure equalisation, the states of both zones change (as does the composition in Zone B, to that of thermochemical equilibrium at the revised pressure and temperature). Adopting the original IsC-IsE pressure equalisation method, the

unburned zone follows isentropic compression process (*a2-a3*, from 5 *bar* and 500*K* to a final state at 12.46 *bar* and 620*K*); the burned zone finally reaches State *b3* (12.46 *bar* and 2400*K*). However, using the IsC-COIE method, the final pressure is computed to be 13.57 *bar* (c.f. 12.46 *bar* with the original method). The fixed composition gas mixture in the unburned zone follows isentropic compression (*a2-a3'*, from 5 *bar* and 500*K* to 13.57 *bar* and 630*K*) and the state of the burned zone changes from *b2* to *b3'* (13.57 *bar* and 2620*K*).

The two calculation methods yield significant differences in the final temperature (180*K* for the burned and 10*K* for the unburned gases) and pressure (~1.1*bar*). The final composition of the burned gas mixture (at thermochemical equilibrium in each case) is also different (since the final pressures and temperatures are different). The lower final temperatures of the burned and unburned gases with the IsC-IsE method also result in a lower final internal energy for the complete system (Zone A plus Zone B), defying the First Law of Thermodynamics.

The IsC-COIE method was incorporated into the full LUSIE code. To examine the effect of using the two different calculation methods on the subsequent model predictions, the code was run separately for each method at a fixing running condition (the experimental "reference" condition, Chapter 5). Set out in Figure 6.15 are the resultant computed cylinder pressure and mass fraction burned (based on the instantaneous cylinder mass), versus crank angle, for the two methods. The values of crank angle at which peak pressure is achieved are close, ~20° *aTDC*, for the two calculation procedures. However, the peak pressure with the IsC-COIE routine is 5.5 *bar* greater than that calculated using the original IsC-IsE routine. At the crank angle for peak cylinder pressure, the mass fraction burned with IsC-COIE is 0.70; that with IsC-IsE is 0.61. The corresponding unburned and burned gas temperatures (versus crank angle) are shown in Figure 6.16. The computed burned gas temperatures predicted with the IsC-COIE method are ~330*K* greater than using the IsC-IsE through most of the combustion event. Following ignition, the unburned gas temperature calculated using the two methods differ (in accord with computed differences in calculated pressure), with a difference of about 35*K* by the crank angle for peak cylinder pressure. The difference in unburned gas temperature has a feedback

effect, resulting in increased laminar and turbulent burning velocities and (consequently) cylinder pressure.

In the thermodynamic models presented by Beretta et al. (1983) and Arsie et al. (1998), isentropic compression of unburned gas (excluding boundary layer) and energy balance of combustion chamber have been used. In their multi-zone thermodynamic equilibrium model, Mann and co-workers (2000) used the assumption of isentropic compression of unburned and previously burned zones, thermochemical equilibrium and energy balance to evaluate the states of zones. All these confirmed that the IsC-COIE method was reasonable assumption for the pressure equalisation process used in the LUSIE.

6.5 Combustion modelling

The turbulent entrainment model proposed by Blizard and Keck (1974) was invoked for modelling combustion development in the work reported in this thesis. As detailed in Sub-section 6.2.3(iii), turbulent burning (entrainment) velocity is a key controlling parameter for the entrainment model [Equation (6.1)]. In the current study, two turbulent burning velocity correlations (termed *K* and *KLe*) developed in Leeds and previously incorporated into the LUSIE code [Bradley et al. (1988) and Merdjani and Sheppard (1993)] were examined (Chapter 7). Following a brief discussion of laminar and turbulent burning velocity concepts and expressions (Sections 6.5.1.1 and 6.5.1.2), both correlations are described in Section 6.5.2. In addition to these existing options, a promising recent simple turbulent burning velocity model (termed the "*Zimont model*", Lipatnikov et al., 1997) was incorporated as a new alternative within LUSIE in the currently presented work. The output of this model was compared with experimental engine data, as detailed in Chapter 7. This model and a number of modifications made in the combustion modelling of the code are described in Sections 6.5.2-6.5.5.

6.5.1 Burning velocity and flame propagation

The burning velocity of a flammable mixture is the velocity of the cold reactants, normal and into the plane that comprises the cold front of the flame (Bradley et al.,

2000). This velocity can be characterised in terms of flow field, fuel type, equivalence ratio, shape of flame propagation and mixture properties. On the basis of the nature of the flow, burning velocity may be categorised as either a laminar burning velocity (in which mass and heat transfer rates essentially occur in molecular level) or a turbulent burning velocity (where turbulent diffusivity plays the main role in mixing and transfer rates).

6.5.1.1 Laminar burning velocity

A number of notable investigations have been undertaken to establish values of laminar burning velocity: using visualization or time-pressure record techniques in constant volume bombs (Bradley et al., 1998; Gülder, 1982; Metghalchi and Keck, 1982; Ryan and Lestz, 1980) and Bunsen burners (Dugger and Graab, 1952; Heimel and Weast, 1957; Gibbs and Calcote 1959). Müller et al. (1997) numerically calculated the laminar burning velocities of lean-to-stoichiometric n-heptane-, isooctane- and methanol-air mixtures using elementary reaction mechanisms consisting of a few hundred reactions. James (1987) reviewed published values of laminar burning velocities of isooctane-air mixtures and the various techniques used to evaluate laminar burning velocity.

The advancing flame can be stretched by flow velocity components and curvature, which affect the laminar burning velocity. If u_l and u_n are unstretched (corresponding to a flat flame surface) and stretched laminar burning velocities, respectively, then it has been shown that (Bradley and co-workers, 2000):

$$u_l - u_n = L\left(\frac{1}{A}\right)\left(\frac{dA}{dt}\right) \tag{6.22}$$

where A is flame surface area, $(1/A)(dA/dt)$ is the stretch rate and L is a proportionality constant; termed the Markstein length. Equation (2.9) can be written in dimensionless form as:

$$\frac{u_l - u_n}{u_l} = \left(\frac{1}{A}\right)\left(\frac{dA}{dt}\right)\left(\frac{\delta_l}{u_l}\right)\left(\frac{L}{\delta_l}\right) = K_l Ma \tag{6.23}$$

where δ_l is laminar flame thickness, K_l is laminar Karlovitz stretch factor (comprised the first three bracketed terms) and the dimensionless group $\left(L/\delta_l\right)$ is the Markstein number. From analysis of experimental data, Bradley et al. (1998) found that Markstein number approached zero with increasing isooctane-air mixture pressure, resulting in u_n close in value to u_l.

Although the nature of the flow field in a spark ignition engine is turbulent, the turbulent burning velocity of a mixture is related to the laminar burning velocity, such that the latter is a key controlling character in the most turbulent burning models and correlations utilised for SI engine simulations. Metghalchi and Keck (1982), Gülder (1982) and Bradley et al. (1998) have all presented empirical correlations of the laminar burning velocity for isooctane-air mixtures in terms of temperature and pressure, in the following form:

$$u_l = u_{l,0}\left(\frac{T_u}{T_0}\right)^{\alpha}\left(\frac{p}{p_0}\right)^{\beta} \tag{6.24}$$

where $u_{l,0}$, α and β are functions of equivalence ratio; T_0 and p_0 are reference temperature and pressure. There is wide scatter with values of laminar burning velocity predicted by the various expressions; presumably because of the uncertainties arising from the techniques used, analysis methods adopted and the assumptions made; these differences have been highlighted by Bradley et al. (1998).

The ranges of equivalence ratio, temperature and pressure used for a correlation are crucial for its applicability over the full range of engine operating conditions. For their correlation, Metghalchi and Keck (1982) examined a large number of time-pressure data captured from a constant volume bomb using wide ranges of equivalence ratio (0.8-1.5), temperature (298-700 *K*), pressure (0.4-50 *atm*) and diluent mass fraction (0-0.2). They evaluated laminar burning velocity by imposing the time-pressure records to a thermodynamic model. Since the range covered the full spread of

unburned gas conditions for the engine used in the currently reported study, this correlation was preferred for use in the turbulent burning velocity expressions used in the modelling part of the study; even though the effect of flame stretch (which may not be that important at high pressure) and possible cellularity were not considered in the thermodynamic analysis adopted in their derivation (Gillespie et al., 2000). The form of the Metghalchi and Keck correlation is:

$$u_l = u_{l,0}\left(\frac{T_u}{298}\right)^{\alpha} p^{\beta}(1-2.1f) \tag{6.25}$$

in which f is diluent mass fraction, T_u is unburned gas temperature in Kelvin and p is pressure in atmosphere. For an isooctane-air mixture, $u_{l,0}$, α and β are:

$$u_{l,0}[cm/\sec] = 26.32 - 84.72(\phi - 1.13)^2 \tag{6.26a}$$

$$\alpha = 2.18 - 0.8(\phi - 1) \tag{6.26b}$$

and

$$\beta = -0.16 + 0.22(\phi - 1) \tag{6.26c}$$

6.5.1.2 Turbulent burning velocity

Gillespie et al. (2000) defined two turbulent burning velocities, one based on mass rate of entrainment of fresh unburned gas into the flame (u_{te}) and the other on mass reacting rate (u_{tr}). In a laminar flame, since the flame thickness is very small, these two definitions are essentially identical; however, turbulent flame thickness is many times thicker than laminar flame thickness and as a result u_{te} and u_{tr} can be very different in a developing turbulent flame. At any instant (k), the relation between flame speed, turbulent burning velocity and the local gas velocity can be expressed, for the entrainment rate, as:

$$(S_e)_k = \left(\frac{dr_e}{dt}\right)_k = (u_{te})_k + (u_{ue})_k \tag{6.27a}$$

a similar relationship holds in terms of u_{tr}:

$$(S_r)_k = \left(\frac{dr_r}{dt}\right)_k = (u_{tr})_k + (u_{ur})_k \qquad (6.27b)$$

where S_e and S_r denote entrainment and reaction flame speeds; r_e and r_r represent flame front radius (visible in cine/Schlieren photographs) and mean reaction front radius (visible in sheet image or evaluated from pressure record assuming mean spherical growth); u_{te} and u_{tr} are turbulent burning velocities based on mass entrainment and mass reacting rates; u_{ue} and u_{ur} denote the speed of unburned gas ahead of the entrainment flame front and reaction front, respectively. Bradley et al. (2003) discussed alternative definitions of turbulent burning velocities and associated flame areas at length and gave a correlation between u_{tr}, density ratio and the flame speed determined from high speed Schlieren photography.

Many models and correlations have been developed to express turbulent burning velocity in terms of physical and physicochemical properties of a turbulent mixture; however, in most cases either the basis of the flame front expression (i.e. u_{te} or u_{tr}) is not clear or the "developing" effect of turbulence on the flame (discussed below) is not included.

In a developing spherical flame, flame is initially wrinkled by only the smallest scales of turbulence; the larger scales merely convect the flame kernel without significant wrinkling of the flame front (Ting et al., 1995; Abdel-Gayed et al., 1987). In a few of the available turbulent burning expressions, the turbulent flame development has been incorporated on the basis of either dimensionless elapsed time (Abdel-Gayed et al., 1987; Lipatikov et al., 1997) or dimensionless flame radius (Mann et al., 2000; Brehob and Newman, 1992; Wahiduzzaman et al., 1993; Ho et al., 1997).

Lipatnikov and Chomiak (2002) recently reviewed many turbulent flame models and correlations. They concluded that the "Zimont" model was the most promising tool for engineering applications, due to its numerical efficiency and robustness in a number of industrial applications, as well as its simplicity. During the currently

reported work, this model was incorporated into LUSIE (detailed in Section 6.5.1). Two correlations developed in Leeds by Bradley et al. (described in the next section) have also been adopted in the current study.

6.5.2 Leeds *K* and *KLe* correlations

After analysing a large collection of experimental data (1650 measurements), Abdel-Gayed et al. (1987) introduced a correlation of turbulent burning velocity in terms of flame straining rates and the effective *rms* turbulent intensity. They tried to relate turbulent burning velocity with the flame straining through dimensionless Karlovitz flame stretch factor, K, defined as follows:

$$K = [u'/\lambda] \cdot [\delta_l / u_l] \tag{6.28}$$

in which δ_l is the laminar flame thickness. Using an approximate expression for δ_l, this can be simplified:

$$K = 0.157 (u'/u_l)^2 R_L^{-0.5} \tag{6.29}$$

To obtain the effective turbulent intensity affecting a developing turbulent flame kernel at any instant, they used a dimensionless power spectrum from LDV measurements of isotropic turbulence in a fan-stirred bomb. Then the effective turbulent intensity, u'_k, was determined from the following expression:

$$u'_k = u' \left[\int_{\bar{F}_k}^{\infty} \bar{S}(\bar{F}) d\bar{F} \right]^{1/2} \tag{6.30}$$

where $\bar{S}(\bar{F})$ is the dimensionless power spectrum, $\bar{F} = f\tau_a$ dimensionless frequency (f frequency and τ_a integral timescale) and $\bar{F}_k = t_k / \tau_a$ (t_k elapsed time from ignition); further details can be found in the original paper (Abdel-Gayed et al., 1987). They found that Lewis number (*Le*, the ratio of thermal diffusivity to the diffusion coefficient of deficient reactant) had an important effect; they found it necessary to

subdivide their correlations into two separate ranges of Lewis number, namely $Le \leq 1.3$ and $Le > 1.3$. Illustrated in Figures 6.17(a) and (b) are the correlations for these two ranges of Lewis number. The horizontal axis relates to the ratio of the effective *rms* turbulent intensity to the laminar burning velocity, u_k' / u_l, and the vertical axis relates to the ratio of turbulent to laminar burning velocities.

Using extensive experimental data, Bradley et al. (1992) later presented a correlation of turbulent burning velocity in terms of the product of the Karlovitz stretch factor and Lewis number, referred to hereafter as the "*KLe*" correlation. Shown in Figure 6.18 is this correlation. They also derived an approximate relationship expressing these correlations:

$$u_t / u_k' = 0.88(KLe)^{-0.3} \tag{6.31}$$

Since most of the data adopted in the correlations came from Schlieren photography, the u_t in the correlations might best be considered to be u_{tc} (rather than u_{tr}).

6.5.3 Zimont model

Zimont (1979) developed a turbulent combustion model valid for high Reynolds and Damköhler numbers. The basic assumption of Zimont's model (Zimont, 1979) is that there is an equilibrium between the turbulent entrainment of fresh mixture into the flame brush and the consumption of this mixture in the thickened reaction zone. The equilibrium flame speed is given by:

$$u_{t,0} = Au'^{3/4} u_l^{1/2} \alpha^{1/4} l^{1/4} \tag{6.32}$$

where $u_{t,0}$ is the developed turbulent burning velocity, A is a constant, u' is root mean square (*rms*) turbulent velocity, u_l laminar burning velocity, α thermal diffusivity and l integral length scale. The dimensionless form of the equation is:

$$\frac{u_{t,0}}{u'} = ADa^{1/4} \tag{6.33}$$

where *Da* is Damköhler number $[(l/u')/(\delta_l/u_l)]$. To cover low turbulence applications, Lipatnikov and Chomiak (1997) included a laminar element in the expression:

$$\frac{u_{t,0}}{u_l} = 1 + A\frac{u'}{u_l}Da^{1/4} \tag{6.34}$$

The only constant in the Zimont model is *A*. This constant was introduced as an empirical parameter of the order of unity in the original paper of Zimont (1979). From reviewing a number of published papers in which the Zimont model has been considered, different values have been suggested for the constant, A, (Zimont and Lipatnikov, 1995; Lipatnikov and Chomiak, 1997; Biagioli and Zimont, 2002). In his conceptual model, Gülder (1990) suggested a value of 0.62 in an expression similar to Equation (6.34). Overall, values of this constant (*A*) in the range of 0.4-1 have been reported.

Following the ideas of Zimont, Lipatnikov and Chomiak (1997) considered a time-based development of the turbulent burning velocity, as below:

$$\frac{u_{t,t_k}}{u_{t,0}} = \left\{1 + \frac{\tau'}{t_k}\left[Exp\left(-\frac{t_k}{\tau'}\right) - 1\right]\right\}^{1/2} \tag{6.35}$$

where t_k is the elapsed time from ignition, u_{t,t_k} is the undeveloped turbulent burning velocity at the time of t_k and τ' is a turbulent time scale defined by:

$$\tau' = \frac{D_{t,0}}{u'^2} \tag{6.36a}$$

where $D_{t,0}$ is the developed turbulent diffusivity (predictable by a $k-\varepsilon$ turbulence model). From their considerations, the following relation was found for τ' in terms of eddy life time ($\tau_t = l/u'$):

$$\tau' = 0.55\tau_t \tag{6.36b}$$

Equation (6.35) can be related to the instantaneous ratio of effective turbulent intensity to a fully developed value (u'_k / u') expressed by Abdel-Gayed et al. (1987). Shown in Figure (6.19) is u'_k / u' versus dimensionless time, $\bar{t}_k$, for the Bradley correlation and for the Zimont model; associated with this, the ratio of the two expressions; $\bar{t}_k$, is given by:

$$\bar{t}_k = c\frac{t_k}{\tau_t} \tag{6.37}$$

where c is a constant, $(8/\pi)^{1/2}$ (Abdel-Gayed et al., 1987; Merdjani and Sheppard, 1993). Although the ratio of the two expressions significantly varies early in flame development, it is between 0.7 and 0.9 within a typical range of application at 750 and 1500 *rpm*. This is based on the related values of l and u' at TDC position in the LUPOE1 engine. Illustrated in Figure 6.20 is the relation between $\bar{t}_k$ and t_k (or crank angle) from ignition at 750 and 1500 *rpm*. This graph clearly shows that the turbulent burning velocity is unlikely to achieve the developed value in the wide range of operating conditions.

6.5.4 Numerical solution of burn-up equation in the entrainment model

The entrainment model incorporated in the LUSIE was described in Section 6.2.3. This model included two differential equations: one for entrained mass rate, Equation (6.1) and the other for mass burning rate, termed the "burn-up" equation, Equation (6.4). In the inherited version of LUSIE, the incremental entrained mass was evaluated by applying a "flame shape factor" and the solution of the burn-up equation was approximated using Equation (6.6). In the currently reported work, the flame shape factor was not applied (discussed in Section 6.5.6) and numerical solution of the burn-up equation was employed.

In Equation (6.5), characteristic burning time was defined as a function of a characteristic length scale and laminar burning velocity. For the length scale, both integral and Taylor length scales have been used in literature (Blizard and Keck,

1974; Brehob and Newman, 1992; Merdjani and Sheppard, 1993; Wahiduzzaman et al., 1993; Shen et al., 1996; Cairns, 2001). During the combustion period, the scales and laminar burning velocity vary due to piston motion, unburned gas pressure and temperature. Therefore, the characteristic burning time is a function of time. However, Equation (6.6) assumes that the characteristic burning time (τ_b) is independent of time.

Illustrated in Figure 6.21 are computed variations of l/u_l and λ/u_l using the modified version of LUSIE at the "reference condition" (Section 7.3). There are ~40% differences (based on maximum value) between the highest and lowest values; i.e. τ_b is a variable. As a result, when using Equation (6.6), errors were introduced when the shape factor was eliminated from the computations or when the size of the time increment was reduced.

In the currently presented work, this part of code was improved by applying the Runge-Kutta order two numerical method to solve the burn-up equation. This application led to the following expression for the total burned mass at *i*th increment, m_{b_i} :

$$m_{b_i} = \left[1 + \frac{\Delta t(\Delta t - \tau_{b_i} - \tau_{b_{i-1}})}{2\tau_{b_{i-1}}\tau_{b_i}}\right] m_{b_{i-1}} + \frac{\Delta t(\tau_{b_i} - \Delta t)}{2\tau_{b_{i-1}}\tau_{b_i}} m_{e_{i-1}} + \frac{\Delta t}{2\tau_{b_i}} m_{e_i} \qquad (6.38)$$

where $m_{b_{i-1}}$ and $m_{e_{i-1}}$ are total burned and entrained masses at (*i*-1)th increment, m_{e_i} total entrained mass at the *i*th increment, τ_{b_i} and $\tau_{b_{i-1}}$ characteristic burning times at the *i*th and (*i*-1)th increments, and Δt is the time increment.

6.5.5 Application of engine speed variation within a cycle

Engine speed variation within a cycle was experimentally observed (described in Chapters 4 and 5). This variation (mostly with a lower value at around the TDC position) was crucial for time-dependent phenomena over the combustion period. The overall configuration of the variation varied with nominal engine speed. Therefore,

the code was modified so that an experimental engine speed variation could be imposed on the model to allow correct comparison (model validation) between experimental and predicted cylinder pressures and flame positions. For each experimental cycle, a crank angle-time data (with $0.2^{\circ}CA$ increment derived from shaft encoder record) was stored in a file and fed to the model as an input. Engine speed variation was thereafter available as an option in LUSIE, the required modification was made to compute the time increment by the input file.

Illustrated in Figure 6.22 is a typical engine speed variation within a cycle versus crank angle associated with the related mean engine speed over the cycle. This variation was resulted from a test conducted at the "reference" condition. Between ignition timing and $27^{\circ}aTDC$, the graph shows a lower engine speed than the mean value; this is followed by greater engine speed after $27^{\circ}aTDC$.

Shown in Figure 6.23 are cylinder pressure and mass fraction burned versus crank angle for the uniform engine speed (UES) and variable engine speed (VES) variants. A faster pressure development can be seen, with a peak value of 33.9 *bar* at $18.5^{\circ}aTDC$ for the VES c.f. slower development for the UES with a peak value of 32 *bar* at $20^{\circ}aTDC$. Within the range from the ignition to the peak pressure position ($19.5^{\circ}bTDC$-$18.5^{\circ}aTDC$), the instantaneous engine speed is lower than the mean (Figure 6.22); consequently, the related time of the range is greater for the VES case; this results in faster mass fraction burned versus crank angle and higher pressure as seen in Figure 6.23. It should be noted that there is a feedback effect on unburned gas temperature causing greater laminar burning velocity from the faster pressure rise; also, pressure rise due to combustion of a given unburned mixture depends on cylinder volume, greater for small volume (Raswiler and Withroth, 1935).

Set out in Figure 6.24 are the burned and unburned gas temperatures versus crank angle for the two options. Higher peak unburned ($726K$ at $17.5^{\circ}aTDC$) and burned ($2630K$ at $15^{\circ}aTDC$) gas temperatures can be seen for the VES variant. For the UES, the unburned and burned gas temperatures achieve peak values of $718K$ at $18.5^{\circ}aTDC$ and $2620K$ at $16.5^{\circ}aTDC$, respectively; they reach values close to those

of the VES at ~24° *aTDC*; at later crank angles, higher values are predicted as a result of faster predicted burning rate.

6.5.6 Non-circularity of flame propagation

Although experimental observations of flame propagation reveal wrinkled and distorted flame edges, most thermodynamic models adopt a spherical growth assumption. Merdjani and Sheppard (1993) and Cairns (2001) used an empirically derived "shape factor" to compensate the effects of the mean flame surface distortion. Through his limited data, Cairns (2001) observed faster development for circular cycles.

During the currently reported work, the influence of flame "shape factor" was examined by analysis of a much wider image database generated over a wide range of conditions. As noted in Chapter 5, no overall correlation was found between the flame "shape factor" and flame development. Sometimes distorted flames were accompanied by faster flame development, sometimes not. Therefore, the flame "shape factor" was not used in the currently reported modelling work.

Further attention was paid to the shape and development of flame at the late stages of propagation, when the flame hit the cylinder wall. It was found that the lower flame active perimeter fraction (APF defined in Chapter 4) resulted in slower flame development in the later stages of combustion. This behaviour was investigated for a considerable number of filmed images, at different conditions (Chapter 5). Remarkably consistent correlation between APF value and flame radius was found to pertain (Figure 5.54). Hence to allow for the effects of the partial contact between the flame and cylinder wall on entrainment rate during late flame propagation, the APF was applied to the model. The computed "spherical" flame front area was multiplied by the APF to compensate the reduction of the entrainment flame front area due to the partial contact with the cylinder wall.

Shown in Figure 6.25 (for the "reference" test condition) is the computed mean flame radius versus crank angle, with and without application of the APF. Differences begin

from ~36 *mm* mean flame radius at 9° *aTDC*; this results in a smoothed curve at the late stage of flame development with application of APF (with 4° *CA* delay in completion of the entrainment).

Illustrated in Figure 6.26 are the associated computations of cylinder pressure and mass fraction burned with and without applying APF; this shows slower peak pressure development, with ~1 *bar* difference in peak pressure value and 1° *CA* in peak pressure position, with APF applied.

6.6 Other modifications

In addition to the described modifications, a number of minor modifications were made in the compression, ignition, combustion and expansion parts of the code; these are briefly discussed below.

6.6.1 Compression stroke

For the pre-existing code, in the compression stroke, sequential computations were performed to account for piston motion, cylinder mass loss and heat transfer (as described in Section 6.2.1). In a minor modification by the current author, the processes were merged into a single-step; applying the First Law of Thermodynamics and mass conservation to determine the change in state for each crank angle increment, as follows:

$$m_2 u_2 - m_1 u_1 = Q_{1-2} - W_{1-2} - m_l h_l \tag{6.39}$$

where m_1 and m_2 are the mass in the cylinder at the initial and final states of the increment; u_1 and u_2 are specific internal energy at the initial and final states of the increment; and $m_l = m_1 - m_2$ and h_l are the mass lost and the related specific enthalpy; Q_{1-2} and W_{1-2} are the heat transfer to the cylinder charge and work done by the charge, respectively. The original sequential and revised, single-step, methods resulted in identical predictions.

6.6.2 Ignition period

Treatment of the ignition process in the pre-existing code was explained through a flow chart (Figure 6.2) in Section 6.2.2. As seen in Figure 6.2, heat transfer from the cylinder charge was ignored over the ignition period. As a minor modification, a heat transfer process (similar to that described in Sub-section 6.2.3(vii)) was considered between the constant volume adiabatic combustion and pressure equalisation processes.

6.6.3 Effect of cylinder mass loss on unburned gas zone

The blowby part of the inherited version of LUSIE was completely replaced with the revised version (described in Section 6.3). To evaluate the effect of the mass lost (or gained) on the state of unburned gas zone, a subroutine was prepared. In this routine the unburned gas zone was assumed to be a constant volume adiabatic open system. Then the first law of thermodynamic was applied for the system between the states before and after the predicted mass lost (or gained), as follows:

$$m_{u2}u_{u2} = m_{u1}u_{u1} - m_l h_l \tag{6.40}$$

where from mass conservation:

$$m_{u2} = m_{u1} - m_l \tag{6.41}$$

and m_{u1} and m_{u2} are the mass in unburned gas zone before and after blowby; u_{u1} and u_{u2} are the specific (mass) internal energy before and after the mass exchange; m_l and h_l are the mass and the related specific (mass) enthalpy exchanged between the unburned zone and top land crevice. When there was mass flow from the cylinder to the top land crevice, m_l was considered positive and $h_l = (h_{u1} + h_{u2})/2$. For the case of mass flow from the top land crevice to the cylinder, m_l was assumed negative and $h_l = h_{TLC}$ (h_{TLC} is specific enthalpy of top land crevice gas).

6.6.4 Cylinder charge heat transfer

Two widely used expressions for engine heat transfer, the Annand (1963) and Woschni (1967) equations (based on steady turbulent convection heat transfer) were incorporated as options in the LUSIE code. In both expressions, forced convection was considered to be the principal heat transfer mechanism. The heat transfer expressions are briefly reviewed, below.

6.6.4.1 Annand equation

In his original correlation, Annand (1963) published the relationship below for instantaneous heat flux:

$$q = a\frac{k}{D}\mathrm{Re}^{0.7}(T - T_w) + b(T^4 - T_w^4) \quad [kw/m^2] \tag{6.42}$$

where q is heat flux, a a constant (0.35-0.8 depending on in-cylinder flow field), k thermal conductivity and D cylinder bore diameter. The second term incorporates heat flux due to radiation. In their expression, Borman and Nishiwaki (1987) converted Annand's recommended dimensional coefficient, b, to SI units. This took the value of $3.3\times10^{-11}\ kw/m^2k^4$ for diesel engines and $4.3\times10^{-12}\ kw/m^2k^4$ for spark ignition engines. Annand suggested that gas properties were best evaluated using the bulk-mean-temperature (T) derived from the ideal gas law. The Reynolds number was based on the mean piston speed and cylinder bore diameter.

6.6.4.2 Woschni equation

In his original Paper, Woschni (1967) adopted a similar expression, with the heat flux incorporated via Nusselt number:

$$Nu = c\,\mathrm{Re}^{0.8} \tag{6.43}$$

where $c = 0.035$ and the Reynolds number is based on cylinder bore and the mean gas velocity affecting heat transfer. This mean velocity is given by:

$$w = \left[c_1 \bar{V}_p + c_2 \frac{V_s T_1}{p_1 V_1} (p - p_m) \right] \tag{6.44}$$

where V_s, p and p_m are the displacement (swept) volume and cylinder pressures of firing and motoring at the same crank angle, respectively; p_1, V_1 and T_1 are the cylinder charge pressure, volume and temperature at some reference state (e.g. inlet valve closing or start of combustion). In the present work, p_1, V_1 and T_1 were taken at the moment of exhaust port closure (EPC). For different parts of a cycle, c_1 and c_2 were recommended by Woschni (1967) as below.

For the gas exchange process; c_1 =6.18, c_2 =0.

For the compression process; c_1 =2.28, c_2 =0.

For the combustion and expansion processes; c_1 =2.28, $c_2 = 3.24 \times 10^{-3}$ $[m/s.K]$.

Note that c_2 has dimensions, requiring consistent units in its use.

6.6.4.3 Modification in heat transfer routines

A few problems were found in the heat transfer part of the inherited version of LUSIE. Each problem, together with the corresponding modification adopted to correct it, is described below:

- During the combustion period heat transfer from the unburned gases was being ignored. This problem was solved by modifying the heat transfer sub-files.

- In applying the Woschni method, the motoring pressure had been evaluated by assuming isentropic processes in compression and expansion periods. However, heat and mass losses can affect the cylinder pressure even in the motoring cycle. Hence the code was modified to store the cylinder pressure versus crank angle generated by running the code for motoring conditions.

- The coefficient c had been set at 0.8 at some stage in the code's history (in fact the set value of this coefficient is more like that in the alternative Annand correlation, in which a different velocity was used in the calculation of Reynolds number); also, the dimensional coefficient c_2 had been set at value

of 3.24×10^{-3} whereas the length units in the code were centimetre. The coefficients were reset at Woschni's original recommended values, $c = 0.035$ and c_2=0.324 $[cm/s.^{\circ}K]$.

- Instead of displacement volume (V_s), the instantaneous cylinder volume had been used in Equation (6.34). The code was modified to use the displacement volume, as in the original Woschni equation.

Shown in Figure 6.27 is the cylinder pressure versus crank angle before and after the heat transfer modifications made in the code. Significant differences can be seen over whole period of the cycle (especially over the combustion and expansion periods) arising from the above problems. These results were derived at the time of making the heat transfer routine modifications (at an early stage of the currently reported study), running the code at the "reference" condition. Hence, not all later modifications to the code are included – leading to inconsistencies with later computations. Nevertheless, the data save to show the effects of the changes made. Illustrated in Figure 6.28 are the related burned and unburned gas temperatures versus crank angle for the two cases. Due to the modifications, substantial differences can be seen in both burned and unburned gas temperatures. Over the expansion period, the rate of drop in burned gas temperature is higher for the inherited case; resultant from the greater coefficient used in the Woschni expression. Also, after $18^{\circ}aTDC$, the predicted unburned gas temperature by the modified version dramatically decreases; presumably due to a greater heat loss from a small amount of unburned gas associated with the expansion effect whereas the heat transfer from the unburned gas was not counted in the inherited version.

6.6.5 Thermodynamic properties

To calculate the thermodynamic state of the cylinder charge, continuous thermodynamic properties of all possible species comprising the working fluid are needed. These must cover the full feasible range of temperature and pressure. These are generally available in a number of polynomial expressions. These expressions result from fitting tabulated thermodynamic property data for the chemical species.

The LUSIE code incorporated two six-order polynomials for each species over two temperature ranges (300-2000K and 2000-6000K) presented by Prothero (1969). These polynomials were for molar specific heat at constant pressure, $\widetilde{c}_p$, given by:

$$\widetilde{c}_p = a_1 + a_2 x + a_3 x^2 + a_4 x^3 + a_5 x^4 + a_6 x^5 + a_7 x^6 \qquad (6.45)$$

for $0.3 \le x \le 2$

and

$$\widetilde{c}_p = a_8 + a_9 x + a_{10} x^2 + a_{11} x^3 + a_{12} x^4 + a_{13} x^5 + a_{14} x^6 \qquad (6.46)$$

for $2 \le x \le 6$

where $x = T/1000$, T gas temperature in Kelvin and a_1 to a_{14} are the derived coefficients. In the LUSIE, the molar specific enthalpy of a mixture at a given temperature, T, was evaluated by:

$$\widetilde{h}(T) = \sum_{i=1}^{j} \widetilde{x}_i \widetilde{h}_i(T_0) + \sum_{i=1}^{j} \widetilde{x}_i \int_{T_0}^{T} \widetilde{c}_{p_i}(T) dT \qquad (6.47)$$

where j was the number of species in the mixture, $\widetilde{x}_i$ mole fraction of ith species and T_0 reference temperature (298.15K here). In the inherited version of LUSIE, the molar specific internal energy of a mixture was computed by:

$$\widetilde{u}(T) = \widetilde{h}(T) - \widetilde{R}(T - T_0) \qquad (6.48)$$

where $\widetilde{R}$ is the universal gas constant. This expression was in disagreement with the definition of specific internal energy by specific enthalpy ($u = h - pv$). Therefore, the expression was modified as:

$$\widetilde{u}(T) = \widetilde{h}(T) - \widetilde{R}T \qquad (6.49)$$

Hynes (1986) original program was written for a leak free (no blowby) closed thermodynamic system where, in application of the First Law of Thermodynamics

between two states of a closed system, the two expressions gave the same results; however, they yielded different results for an open system (e.g. a "leaky" ported engine). To examine the effect of using the two different expressions on the subsequent model predictions, the LUSIE code was run separately for each expression at a fixed running condition. Shown in Figure 6.29 are the resultant computed cylinder pressure and unburned gas temperature (versus crank angle) for the two expressions. With the inherited expression, the code predicted greater unburned gas temperatures (even before ignition), with a peak value of $756K$ at $17^{\circ}aTDC$. This is associated with the effect of cylinder mass lost before the peak pressure position. However, after peak pressure occurrence, there is a flow back from the TLC into the cylinder and the original expression results in more rapid fall in the unburned gas temperature. The temperature predicted by the inherited expression at $80^{\circ}aTDC$ is $310K$, which is lower than the input wall temperature ($345K$).

6.6.6 Structure of combustion routine

The structure of combustion routine was successively developed during the currently reported work. Once the three-zone pressure equalisation process had been replaced with a two-zone one (between previously and newly burned zones), no difference was observed in the obtained results. Consequently, the simple two-zone pressure equalisation routine was considered instead of the more complex three-zone one. Set out in Figure 6.30 is the final revised structure of LUSIE in the current work (note that this structure is available as an option in the modified version of LUSIE). The idea behind the revised structure was to reduce the number of the successive processes considered in the combustion routine. This was important for minimising the running time and associated numerical error. In comparison with the inherited structure, two pressure equalisation processes were omitted.

6.6.7 Expansion stroke

As mentioned in Section 6.2.4, when the expansion routine was used in a firing cycle, all unburned gas left at the end of the combustion period (defined by limitation of mass fraction burned in model) or gained from crevices were considered to convert

instantaneously to burned gases in thermochemical equilibrium. In the currently reported work, this unrealistic assumption of instantaneous combustion was avoided by extending the range of the entrainment model to cover most of the expansion stroke; for this, after complete cylinder charge entrainment, any unburned mass returned from crevices was counted as entrained mass and consumed by the mass burn-up equation [Equation (6.4)].

Single-step application of the First Law of Thermodynamics (described in Section 6.6.1) was also adopted in the expansion routine. In the firing variant, this routine was only invoked once all cylinder charge was burned and there was mass lost to the top land crevice (possible when the top land crevice was connected to the exhaust port). For a motoring cycle, a negative sign for any mass gained from the top land crevice was employed in Equation (6.29).

6.7 Radial stratified charge

Experimental observations suggest that an overall lean stratified mixture, in which a rich region is located in the vicinity of spark gap, can improve flame stability, reduce cyclic variation, extend the lean misfire limit, accelerate burning, improve low cold start *HC* emissions and produce better engine performance (Itoh et al., 1998; Arcoumanis et al., 1996; Tabata et al., 1995). Although homogeneous engines have been extensively modelled using thermodynamic cycle codes, stratified charge engines have received less attention.

Reported in this section is an extension to the LUSIE code to permit study of flame propagation in a centrally ignited disc-shaped combustion chamber with an imposed radial stratified charge. A key factor in this was the effect of the expansion of burned gas on the radial distribution of unburned gas mixture; this is described in Section 6.7.1; calculation of the average equivalence ratio of an annular element is detailed in Section 6.7.2. The effects of successive burned gas expansions on unburned gas stratification are then considered in Section 6.7.3. Finally, flame development, for both linear and parabolic distributions of equivalence ratio prior to ignition, are examined and discussed in Section 6.7.4.

6.7.1 Burned gas expansion and unburned gas stratification

In this section, the effects of burned gas expansion on the unburned gas stratification is analysed; assuming cylindrical flame propagation from the centre of a disc-shaped chamber. Shown in Figures 6.31(a) and (b) are the situations in such a system, before and after expansion of burned gas. In the figure, R is the chamber radius, r_1 and V_{b1} denote burned zone radius and volume before expansion, r_2 and V_{b2} the radius and volume after expansion and V_{u1t} and V_{u2t} the total unburned gas volume before and after expansion. Before expansion of the burned gas, an infinitesimal annular mass element of unburned gas is situated at radius r; this element is displaced to r' after burned gas expansion. In Figure 6.32, $V_{u1}(r)$ and $V_{u2}(r')$ represent the unburned gas located between the element and burned gas before and after the expansion, respectively. These volumes can be calculated as:

$$V_{u1}(r) = \pi h(r^2 - r_1^2) \tag{6.50a}$$

and,

$$V_{u2}(r') = \pi h(r'^2 - r_2^2) \tag{6.50b}$$

Assuming spatially uniform pressure and temperature for the unburned gas, the following relation can be derived from application of the ideal gas law:

$$\frac{V_{t2u}}{V_{t1u}} = \frac{V_{u2}(r')}{V_{u1}(r)} \tag{6.51a}$$

or,

$$\frac{(R^2 - r_2^2)}{(R^2 - r_1^2)} = \frac{(r'^2 - r_2^2)}{(r^2 - r_1^2)} \tag{6.51b}$$

hence,

$$r = \left[r_1^2 + \frac{1 - (r_1/R)^2}{1 - (r_2/R)^2}(r'^2 - r_2^2) \right]^{1/2} \tag{6.52a}$$

or,

$$r' = \left[r_2^{\,2} + \frac{1-(r_2/R)^2}{1-(r_1/R)^2}(r^2 - r_1^{\,2}) \right]^{1/2} \tag{6.52b}$$

Supposing frozen composition of the unburned gas, the equivalence ratio of the mass element will remain constant during the expansion; hence,

$$\phi_2(r') = \phi_1[r(r')] \tag{6.53}$$

where function $r(r')$ is defined by Equation (6.52a). Equation (6.53) characterises the relationship between the equivalence ratio distributions of unburned gas before and after the expansion. Before expansion, if the distribution is linear:

$$\phi_1(r) = a + br \tag{6.54}$$

where a and b are constants, then after expansion it will become:

$$\phi_2(r') = a + b\left[r_1^{\,2} + \frac{(R^2 - r_1^{\,2})}{(R^2 - r_2^{\,2})}(r'^2 - r_2^{\,2}) \right]^{1/2}$$

$$\phi_2(r') = a + (a_1 + b_1 r'^2)^{1/2} \tag{6.55}$$

in which a_1 and b_1 are constant. It is clear that the distribution will not remain linear after expansion.

6.7.2 Evaluation of average equivalence ratio

The local equivalence ratio of unburned gas is a function of local fuel mass concentration or mole fraction. Assuming an infinitesimal fuel-air mixture of mass dm (including dm_f fuel and dm_a air) and volume dV, the relation between local equivalence ratio and local fuel mass concentration (or mole fraction) can be evaluated using the reactant components. A fuel-air mixture containing hydrocarbon

fuel C_nH_m (including n carbon atoms for m hydrogen atoms) and air at equivalence ratio (ϕ) may be represented as follows:

$$\phi C_nH_m + (n + m/4)\ (O_2 + 3.764N_2) \tag{6.56}$$

The fuel mole fraction ($\tilde{x}_f$) and mass fraction (x_f) are given by:

$$\tilde{x}_f = \frac{\phi}{4.764(n + m/4) + \phi} \tag{6.57a}$$

and

$$x_f = \frac{\phi}{\phi + (A/F)_{st}} \tag{6.57b}$$

in which $(A/F)_{st}$ is stoichiometric air/fuel ratio by mass and

$$\phi = (A/F)_{st}(dm_f/dm_a) \tag{6.58}$$

Similarly, the average equivalence ratio of a stratified charge is defined as follows:

$$\phi_{av} = (A/F)_{st}\left(\int dm_f / \int dm_a\right) \tag{6.59}$$

Obtaining dm_f from Equation (6.58) and substituting in Equation (6.59):

$$\phi_{av} = \frac{\int \phi dm_a}{\int dm_a} \tag{6.60}$$

Using air partial pressure and the ideal gas law,

$$dm_a = \frac{(1 - \tilde{x}_f)\,pdV}{R_aT} \tag{6.61}$$

where p is total pressure and R_a is the particular gas constant for air. From combination of Equations (6.57a), (6.61) and (6.60), it can be shown that:

$$\phi_{av} = \frac{\int_{\phi + 4.764(n+m\ 4)}^{\phi} dV}{\int_{\phi + 4.764(n+m\ 4)}^{1} dV} \tag{6.62}$$

This equation illustrates the effects of both equivalence ratio distribution and type of hydrocarbon fuel on the average equivalence ratio by mass. Under the integrals, variations of ϕ will change the denominators, slightly (especially in the use of heavy hydrocarbon such as isooctane); therefore, ignoring the denominators, a simple estimation is given by:

$$\phi_{av} = \frac{1}{V}\int_{V}\phi dV \tag{6.63}$$

where V is the volume of the unburned gas for which average equivalence ratio is calculated. In cylindrical stratification, the average equivalence ratio of an annular volume limited between two radii, r_a and r_b will become:

$$\phi_{av} = \frac{2}{r_b^{\ 2} - r_a^{\ 2}}\int_{r_a}^{r_b}\phi(r) r dr \tag{6.64}$$

6.7.3 Successive incremental burned gas expansions and unburned gas stratification

In Section 6.7.1, it was shown that the unburned gas stratification was affected by the burned gas expansion. Since the thermodynamic, physical and chemical properties of unburned gas ahead of flame vary significantly with equivalence ratio, it is crucial to identify the equivalence ratio distribution in the unburned gas during incremental computations of flame propagation. In this section, it is shown how the equivalence ratio distribution of unburned gas in an increment can be obtained from the equivalence ratio distribution prior to ignition. It should be noted that only the effect of burned gas expansion is considered in the current study; the turbulent flow field will also have an effect and it is recommended that this be explored in some future work.

Assuming that r_{1i} and r_{2i} denote the radii of burned zone before and after expansion of the i th increment, the relationship between r_i and r_{i+1} [of the i th and the $(i+1)$th increments] which have identical equivalence ratio can be derived using Equation (6.52b) as follows:

$$r_{2,i}^2 = r_{2,i}^2 + K_i(r_i^2 - r_{1i}^2) \tag{6.65}$$

and

$$r_{2,i} = \sqrt{r_{2,i}^2 + K_i(r_i^2 - r_{1i}^2)} \tag{6.66}$$

where K_i is constant and given by:

$$K_i = \frac{1-(r_{2,i}/R)^2}{1-(r_{1,i}/R)^2} \tag{6.67}$$

Differentiating from both sides of Equation (6.65):

$$r_{2,i}dr_{2,i} = K_i r_i dr_i \tag{6.68a}$$

Similarly,

$$r_i dr_i = K_{i-1} r_{i-1} dr_{i-1} \tag{6.68b}$$

Therefore, the relation between first and i th increments becomes:

$$r_i dr_i = P_i r_1 dr_1 \tag{6.68c}$$

where P_i is constant defined as:

$$P_i = \left(\prod_{1}^{i-1} K_i\right) = K_1 \times K_2 \times \ldots \times K_{i-1} \tag{6.69}$$

Therefore, to evaluate the average equivalence ratio of an annular volume of mixture in the *i*th increment, Equation (6.64) can be used employing the following equivalent integral:

$$\int_{r_{ai}}^{r_{bi}} \phi(r_i) r_i dr_i = P_i \int_{r_{a1}}^{r_{b1}} \phi(r_1) r_1 dr_1 \tag{6.70}$$

where r_{a1} and r_{b1} can be evaluated from r_{ai} and r_{bi} by applying Equation (6.66). This leads to the following expression:

$$\phi_{av} = \frac{2P_i}{r_{bi}^2 - r_{ai}^2} \int_{r_{a1}}^{r_{b1}} \phi(r_1) r_1 dr_1 \tag{6.71}$$

where $\phi(r_1)$ is the equivalence ratio distribution of the initially known radial stratified charge.

6.7.4 Flame development in radial stratified charge

The above was coded into LUSIE and employed to examine the effect of the radial charge stratification on cylindrical flame propagation. For this exercise, the geometry of the LUPOE1 engine (Chapter 3) was employed with operating conditions at ignition the same as for the "reference" condition described in Chapter 5. As the equations developed for stratified charge assume cylindrical flame propagation (as opposed to the spherical flame propagation assumed in the earlier homogeneous charge study), as a preliminary, differences in model output for cylindrical and spherical flame development were considered (just for homogeneous charge). Identical initial kernel volume was considered for both cases. Shown in Figure 6.31 are cylinder pressure and mass fraction burned (based on instantaneous cylinder mass) versus crank angle for the two cases. The performance can be seen to be very similar for cylindrical and spherical flame development. Set out in Figure 6.34 are entrainment radius (r_e) and mean flame radius containing all reacted burned gas radius (r_f) versus crank angle for the two cases. As seen in the figure, the supposition of identical initial kernel volume results in smaller kernel radius for the cylindrical case. However, in general, assumption of cylindrical flame radius (necessary for the

stratified charge case, which follows) leads to results very similar to those obtained earlier assuming spherical growth.

For the cylindrical charge stratification case, cylindrical flame propagation from an imaginary cylindrical kernel was considered. The Zimont model for turbulent burning velocity (validated in Chapter 7) was employed; operating conditions were again assumed identical to those at the "reference" condition apart from local equivalence ratio; blowby, engine speed variation and APF were ignored for this theoretical study. Turbulent entrainment burning velocity was evaluated using local properties of the entrained unburned gas in each increment. During each increment, the average equivalence ratio of the unburned zone was computed to determine the mean properties for this zone. The mean properties were employed in heat transfer and pressure equalisation processes for the unburned zone. The mixing process of the freshly and previously burned zoned (modified for the stratified case) provided a burned zone with a uniform composition mixture. For the heat transfer and pressure equalisation processes in the burned zone, the properties of the uniform burned mixture were utilised.

To incorporate the stratified variant as an option in LUSIE, significant modifications were made to the code; these required writing new functions and subroutines and including additional features in existing routines. For the compression stroke, prior to ignition, the unburned gas mixture composition and properties were calculated using an average equivalence ratio.

Two types of imposed radial stratification prior to ignition were considered: linear distribution of equivalence ratio (detailed in Sub-section 6.7.4(i)) and parabolic distribution (described in Sub-section 6.7.4(ii)). For both cases, a maximum equivalence ratio of 1.1 at the cylinder centre and a minimum value of 0.8 at the cylinder wall were imposed.

(i) *Linear distribution*

Assuming maximum equivalence ratio (ϕ_{max}) at the cylinder centre ($r = 0$) and minimum (ϕ_{min}) at the cylinder wall, the initial linear distribution in equivalence ratio in terms of radius, r, was defined as:

$$\phi(r) = \phi_{max} - \left(\frac{\phi_{max} - \phi_{min}}{R} \right) r \tag{6.72}$$

where R is the cylinder radius. The modified code was run in stratified option with ϕ_{max}=1.1 and ϕ_{min}=0.8. The unburned zone equivalence ratio distribution modified by the burned gas expansion as flame development proceeded is set out in Figure 6.35; this shows the distribution of equivalence ratio in the unburned zone versus radius for a few selected crank angle positions (including that at ignition timing). The overall average equivalence ratio ($\phi_{av} = 0.9$), derived for the initial distribution of ϕ, is also shown (by a horizontal dashed line). The initially linear distribution becomes non-linear, due to burned gas expansion [Equation (6.55)]. The equivalence ratio of the unburned gas just ahead of the burned gas falls below the overall average value only in the last 5 *mm* of burning, albeit there is a large mass contained in that last burning.

To compare the performance of stratified flame growth with that of an equivalent homogeneous charge, the code was run at the same operation condition with uniform equivalence ratio i.e. $\phi_{min} = \phi_{max} = \phi_{av}$. Shown in Figure 6.36 is cylinder pressure and fuel mass fraction burned (FMFB) versus crank angle for the stratified and homogeneous cases. Faster pressure development can be seen for stratified charge with peak pressure 38.1 *bar* at $19.5^{\circ} aTDC$, c.f. 32.9 *bar* at $23^{\circ} aTDC$ for the homogeneous charge. The FMFB diagram also clearly shows faster burning for the stratified case.

(ii) *Parabolic distribution*

The methods incorporated into the modified version of LUSIE can predict flame development for any defined initial charge stratification. To examine the effects of the

initial charge distribution a second option, that of radial parabolic stratification, was incorporated in the code. To define the distribution function, the following assumptions were made:

- Equivalence ratio is a function only of radius from the cylinder axis.
- Maximum equivalence ratio (ϕ_{max}) occurs at the cylinder axis (r =0).
- Minimum equivalence ratio (ϕ_{min}) occurs at the cylinder wall (r =R).
- The gradient of the function at the cylinder axis is zero i.e. $\left.\frac{d\phi}{dr}\right|_{(r=0)} = 0$.

For the radial parabolic distribution in equivalence ratio, this yields:

$$\phi(r) = \phi_{max} - \frac{(\phi_{max} - \phi_{min})}{R^2} r^2 \qquad (6.73)$$

This expression was incorporated into the code; with ϕ_{max} and ϕ_{min} again set at 1.1 and 0.8, respectively. For this, the overall average equivalence ratio was calculated to be 0.95. Setting all the other operating conditions as at the "reference" condition, the code was run for the parabolic initial stratified charge and equivalent homogeneous mixture (at the average equivalence ratio).

Set out in Figure 6.37 is the equivalence ratio distribution in the unburned zone in terms of radius at a few selected crank angle positions (including the initially prescribed stratification; the black line); also shown is the equivalence ratio of the unburned gas just ahead of the burned zone versus the related radius (blue line). Although the mean equivalence ratio of the charge is lean, burning stays rich to ~32.5 *mm* radius and has an equivalence ratio above the average value to ~35.5 *mm*.

Illustrated in Figure 6.38 are cylinder pressure and fuel mass fraction burned for the "parabolic" stratified charge and the equivalent homogeneous mixture. To examine the effect of stratification on combustion parameters, identical ignition timing ($19.5^\circ bTDC$) was considered for both cases. The cylinder pressure of the stratified case again develops faster, with a peak value of 41.4 *bar* at $18.5^\circ aTDC$ c.f. the homogeneous case of 37.2 *bar* at $21^\circ aTDC$. Similarly, the fuel mass fraction burned

for the stratified case develops faster, due to the stratification and the feedback effect of the faster development; this rises the temperature of the unburned gas which, in turn, increases laminar and turbulent burning velocities. Shown in Figure 6.39 are the variation of unburned gas temperature and equivalence ratio (at the entrainment radius and equivalent burned flame radius) with crank angle for the two cases. Due to the faster burning, the unburned gas temperature of the stratified case increases faster, to a peak value of 759 K at $17.5^\circ aTDC$, than that of the homogeneous charge, which more gradually develops to a peak value of 746 K at $20.5^\circ aTDC$. For stratified charge, the equivalence ratios at the entrainment and burned flame radii (solid and dot black lines, respectively) are different.

The combined effects of the unburned gas temperature, pressure and equivalence ratio on the laminar burning velocity of the freshly entrained gas can be seen in Figure 6.40; the laminar burning velocity of the stratified case is the greater until $10^\circ aTDC$. Also shown is the derived turbulent burning velocity (u_t); which depends on turbulent intensity, laminar burning velocity, elapsed time from ignition and gas properties. Here, u_t was determining using the Zimont model expression. The graph shows generally greater turbulent burning velocity for stratified charge, with a peak value of 734 *cm/s* at $6.5^\circ aTDC$. However, u_t then drops to a minimum value of 650 *cm/s* at $14.5^\circ aTDC$, mainly due to the lower laminar burning velocity associated with low equivalence ratio. The stratified turbulent burning velocity grows to be above the equivalent homogeneous case by ~50 *cm/s* by $1.5^\circ aTDC$. However, the stratified and homogeneous u_t values become similar by $11^\circ aTDC$. Thereafter, homogenous burning has the greater u_t by as much as 64 *cm/s* at $14^\circ aTDC$.

6.8 Summary

In the present chapter, the pre-existing LUSIE code has been briefly described, concentrating mostly on the combustion part of the turbulent burning velocity variant. A new multi-ring blowby sub-model, based on the "orifice-volume" method has been developed and incorporated in the code. Application of this sub-model in LUSIE revealed substantial differences with the results obtained by previous workers in Leeds. The original pressure equalisation routine (IsC-IsE) incorporated in the pre-

existing code was reviewed and found to defy the First Law of Thermodynamics. Therefore, a revised pressure equalisation routine (IsC-COIE) was developed and incorporated in the code. Significant differences were observed between the predicted cylinder pressure, burned and unburned gas temperatures by the code with the original and revised pressure equalisation routines (greater values for the revised one).

The "Zimont" turbulent burning velocity expression has been described and its incorporation as a new option in the combustion modelling part of the code discussed. The mass burn rate expression of the entrainment model was improved by including a numerical solution of the "burn-up" equation in the code. Engine speed variation, observed within an experimental cycle, has also been incorporated as an option in the code. This modification resulted in a greater peak pressure with a sooner occurrence, c.f. those obtained with the uniform engine speed assumption. The application of flame "shape factor" was avoided and the empirically derived flame active perimeter fraction (APF) has been applied for the final stage of flame propagation to account for contact between the flame and the cylinder walls. The results obtained showed associated effects on mean flame radius and cylinder pressure.

A number of further minor modifications and their incorporation into the code have been described. The heat transfer part was intensively reviewed; a few problems were found and corrected, based on the original literature recommended expressions. These corrections significantly changed the predictions of cylinder pressure, unburned and burned gas temperatures. A deficiency was observed in the derivation of internal energy from the enthalpy of mixture; this was described and modified. This modification again resulted in substantial changes in the cylinder pressure predicted by the code over the compression, combustion and expansion periods for a "leaky" ported engine.

A new sub-model for flame propagation in radial stratified charge within a disc-shaped chamber has been developed and incorporated into the code. Two types of radial stratification (linear and parabolic) were separately imposed in the code and the effect of flame development on unburned gas stratification was examined. The obtained results showed that the burned gas expansion considerably modified the initial charge stratification.

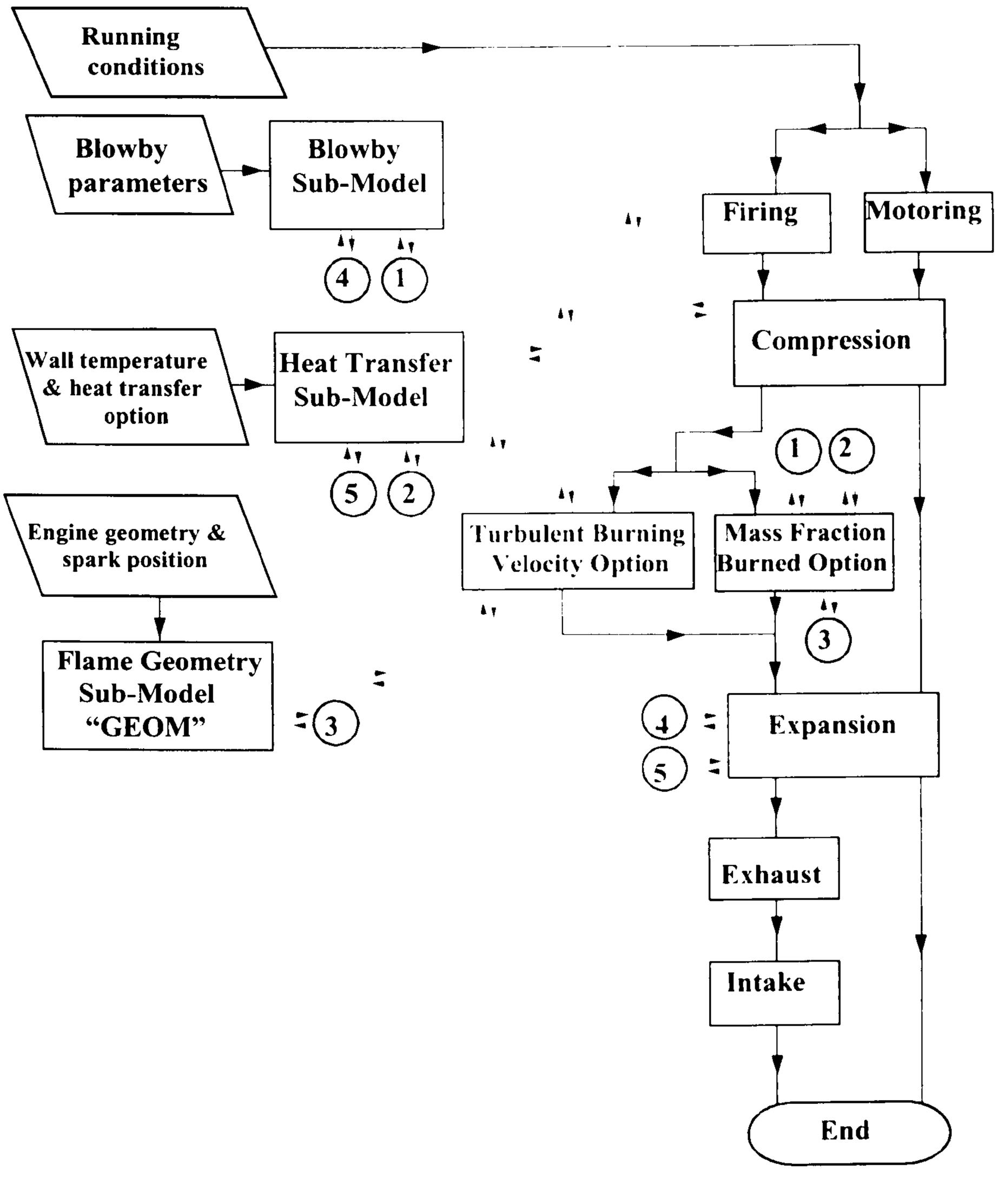

Figure 6.1 A brief flow diagram for the LUSIE code.

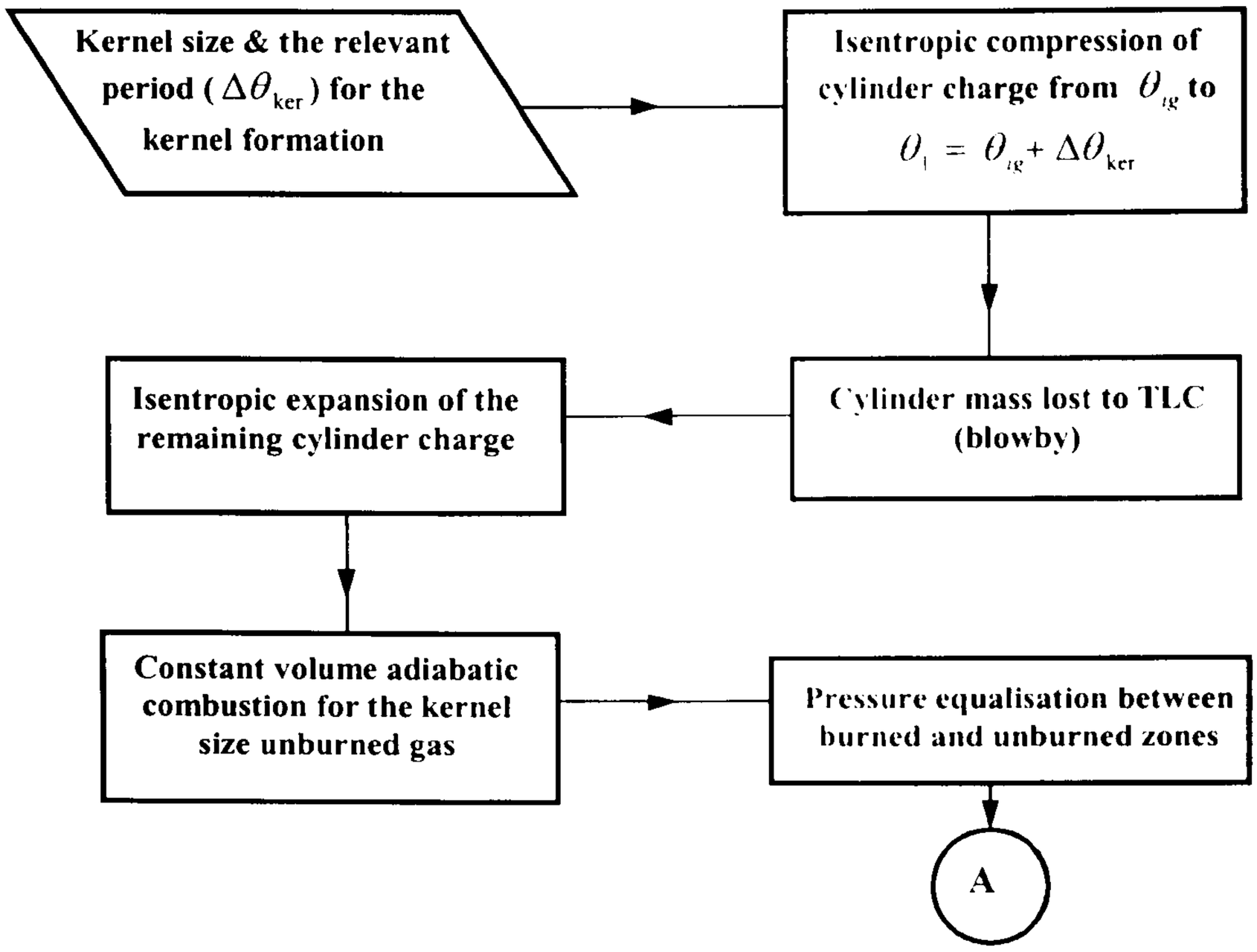

Figure 6. 2 Flow diagram for initial ignition kernel in the pre-existing LUSIE.

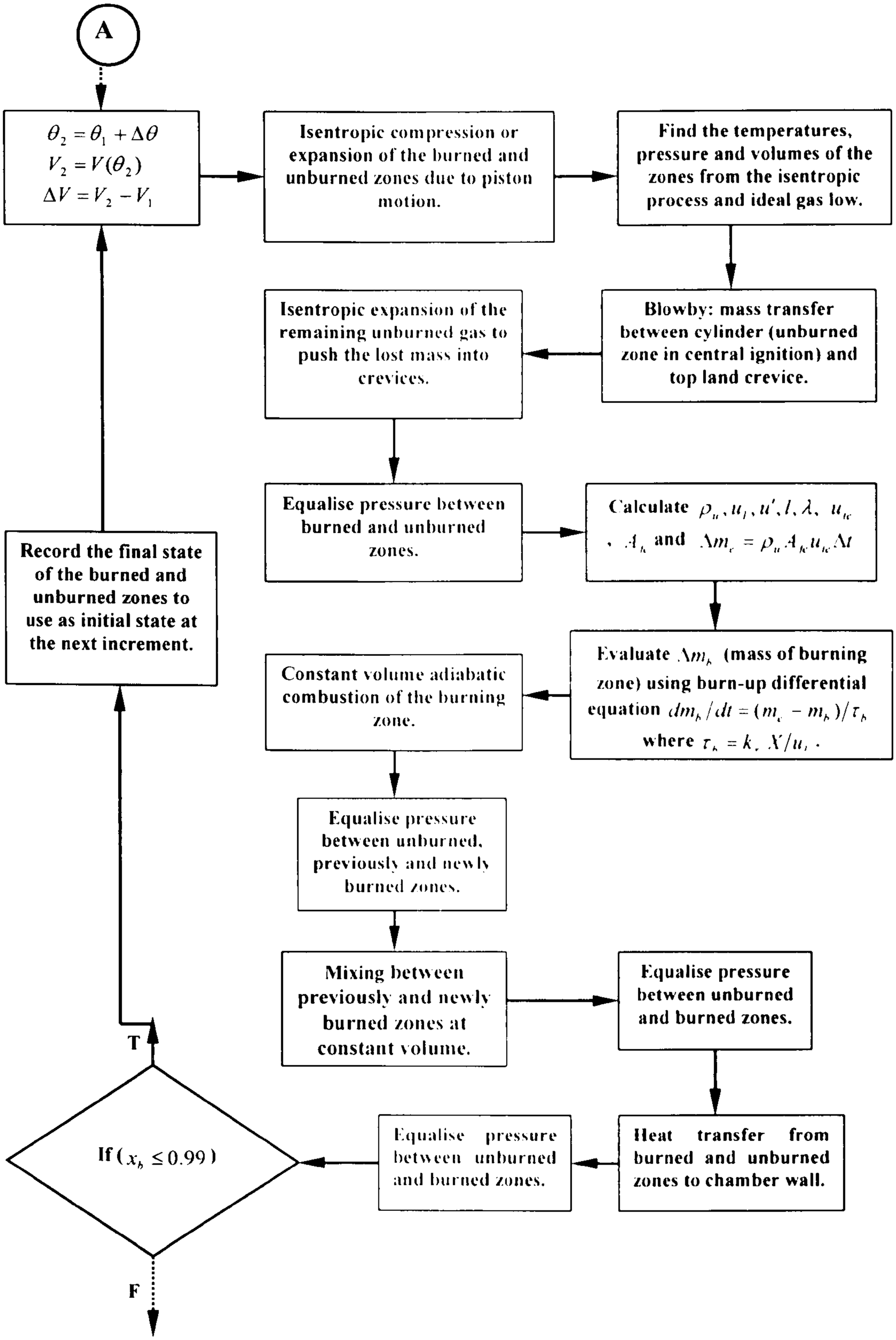

Figure 6.3 Structure of successive processes incorporated in the burning velocity option of the inherited version of LUSIE.

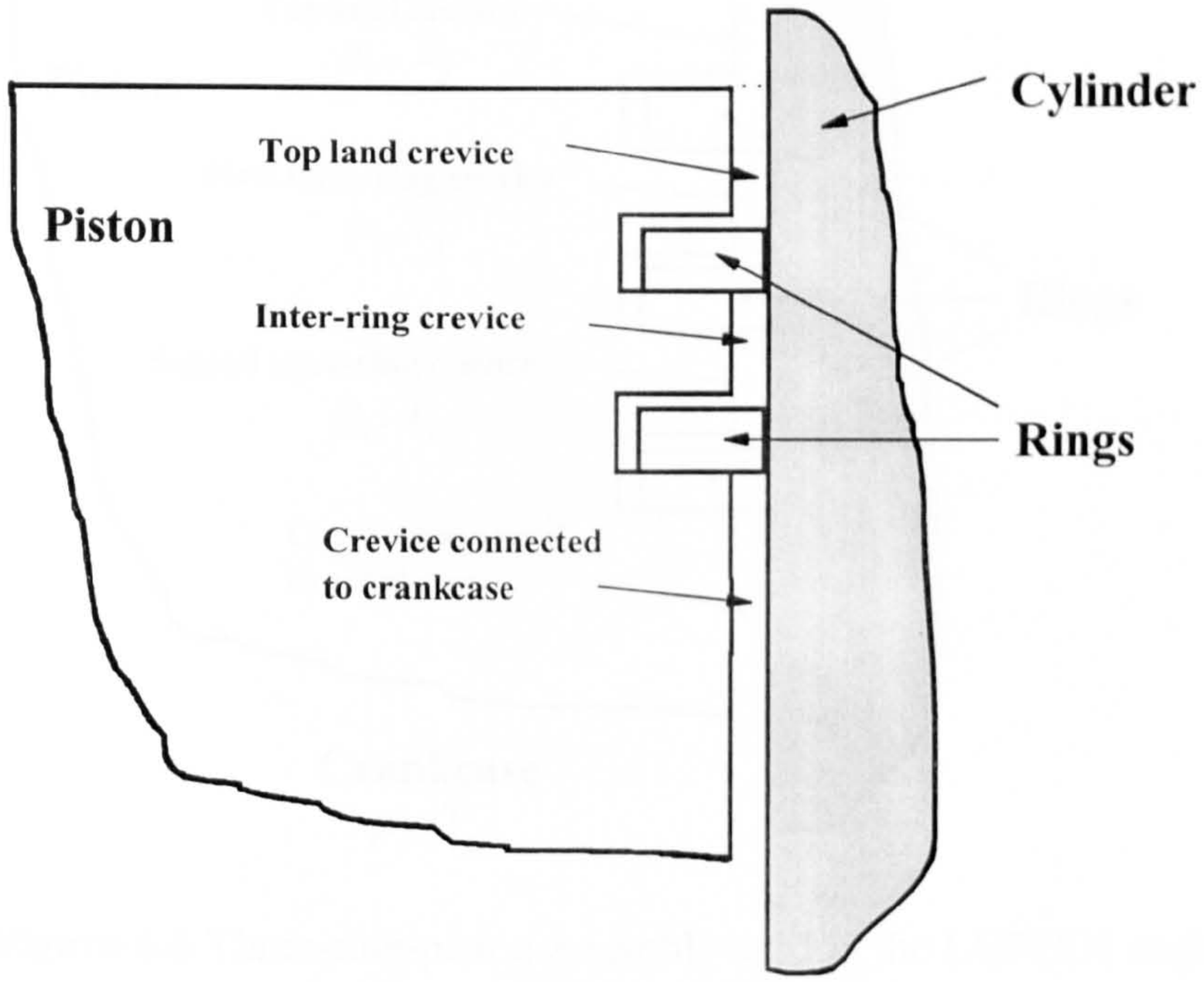

Figure 6.4 Piston-ring assembly for a two-ring pack.

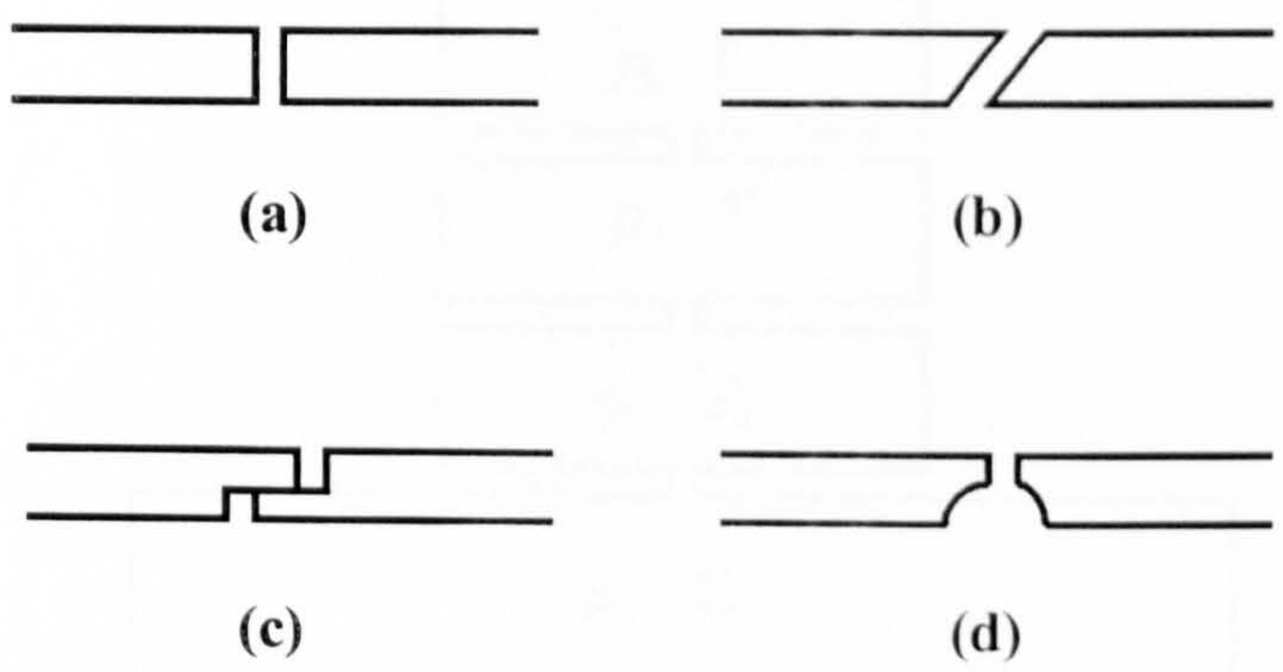

Figure 6.5 A few typical shapes of ring-gaps used in reciprocating engines.

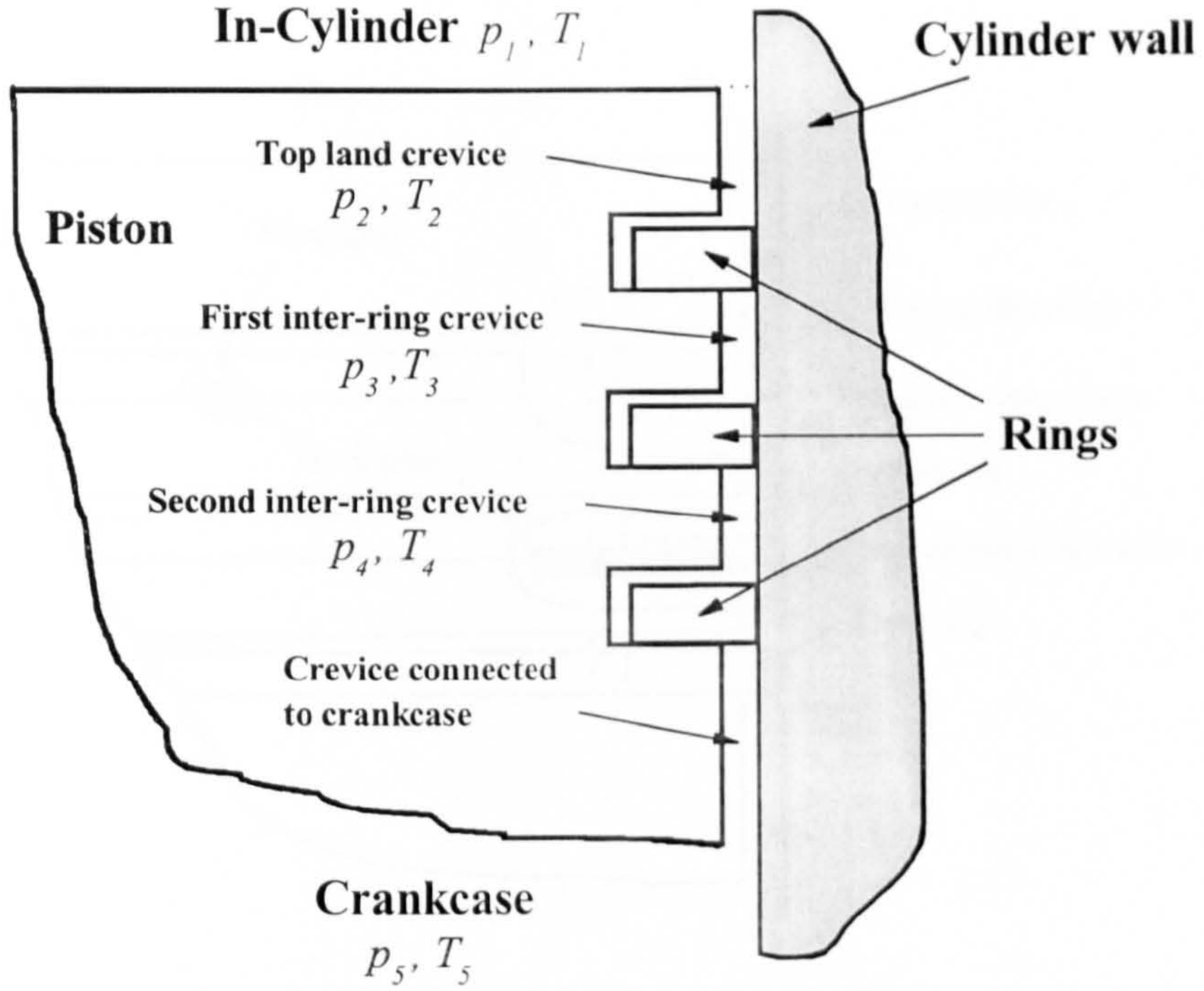

Figure 6.6 Three-ring-piston assembly used in the LUPOE1 engine.

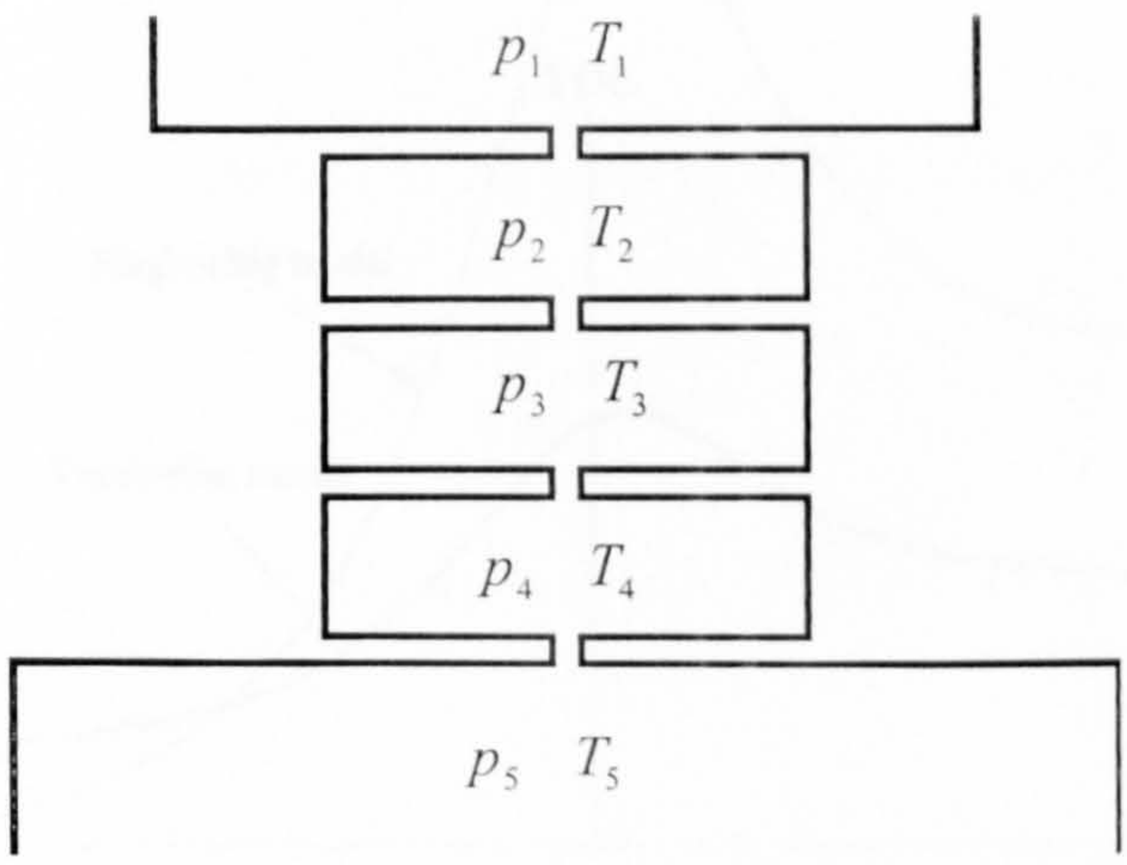

Figure 6.7 Simplified volume and orifice model for a three-ring assembly.

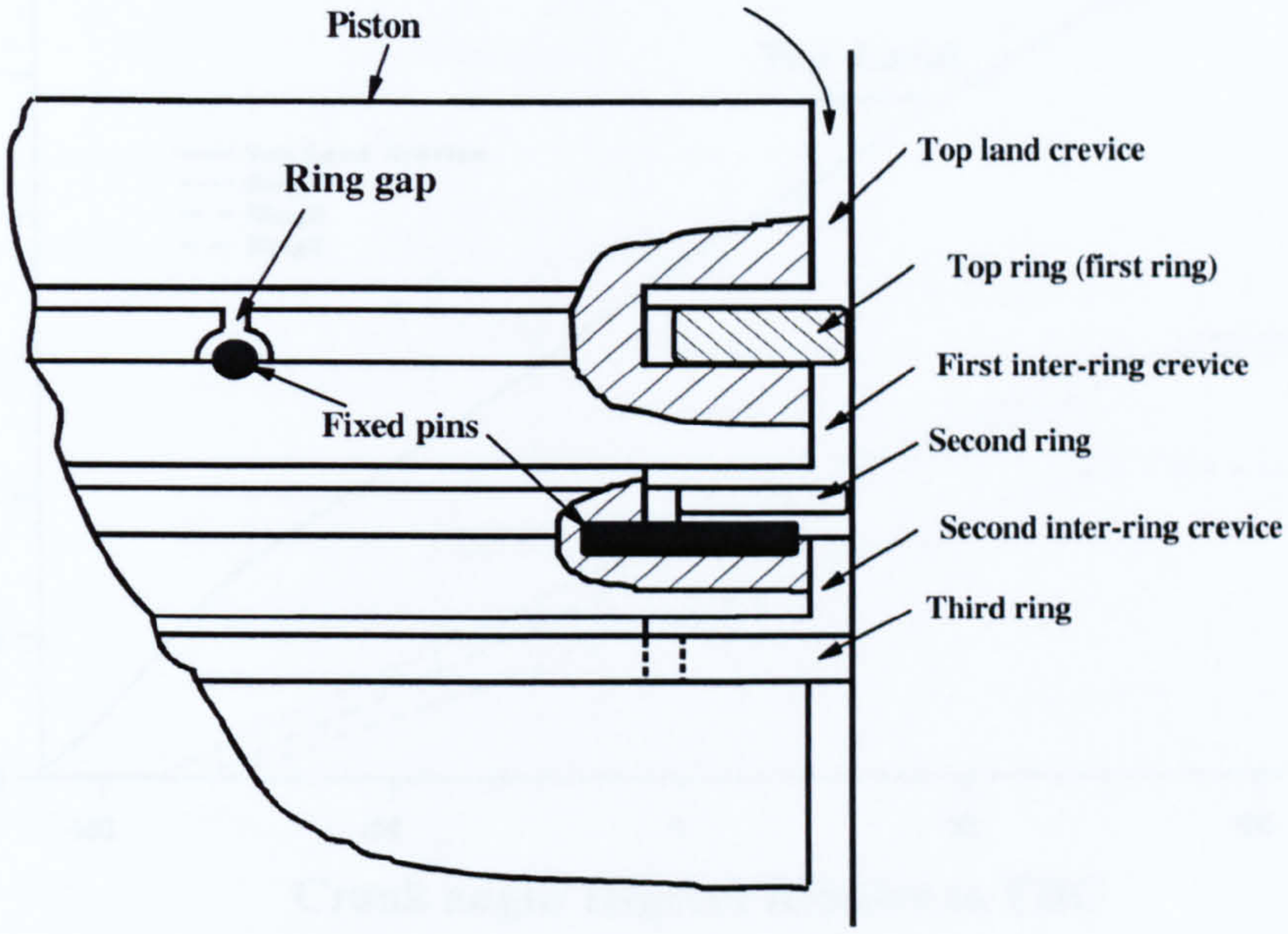

Figure 6.8 Schematic of ring gap and the fixed pin location in the ring-piston assembly of the LUPOE1 engine.

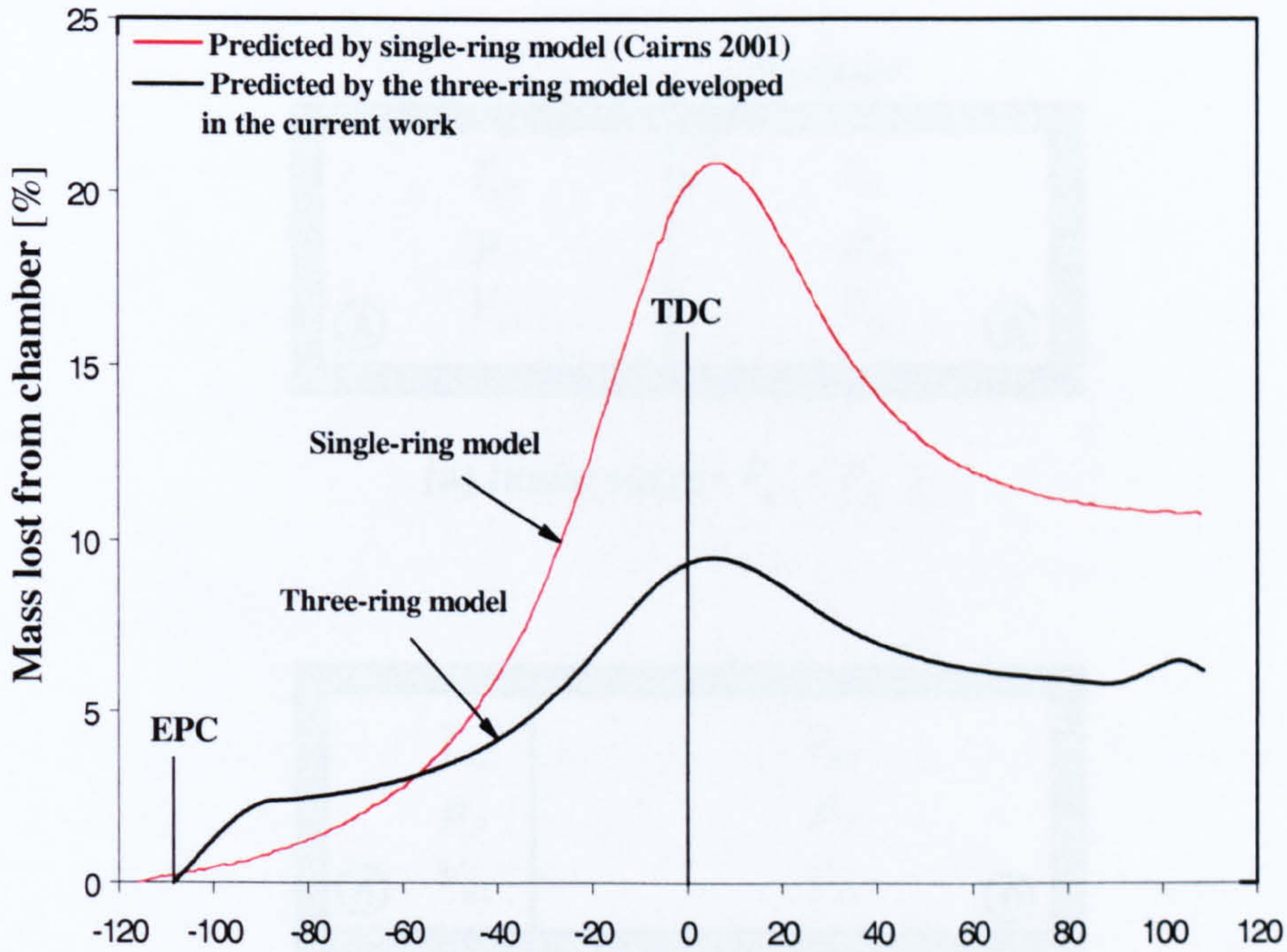

Figure 6.9 Predicted mass lost from chamber (based on the percent of cylinder charge mass at EPC) versus crank angle by single-ring model (Cairns, 2001) and three-ring model (developed in the current work) at 1500 *rpm* motoring condition.

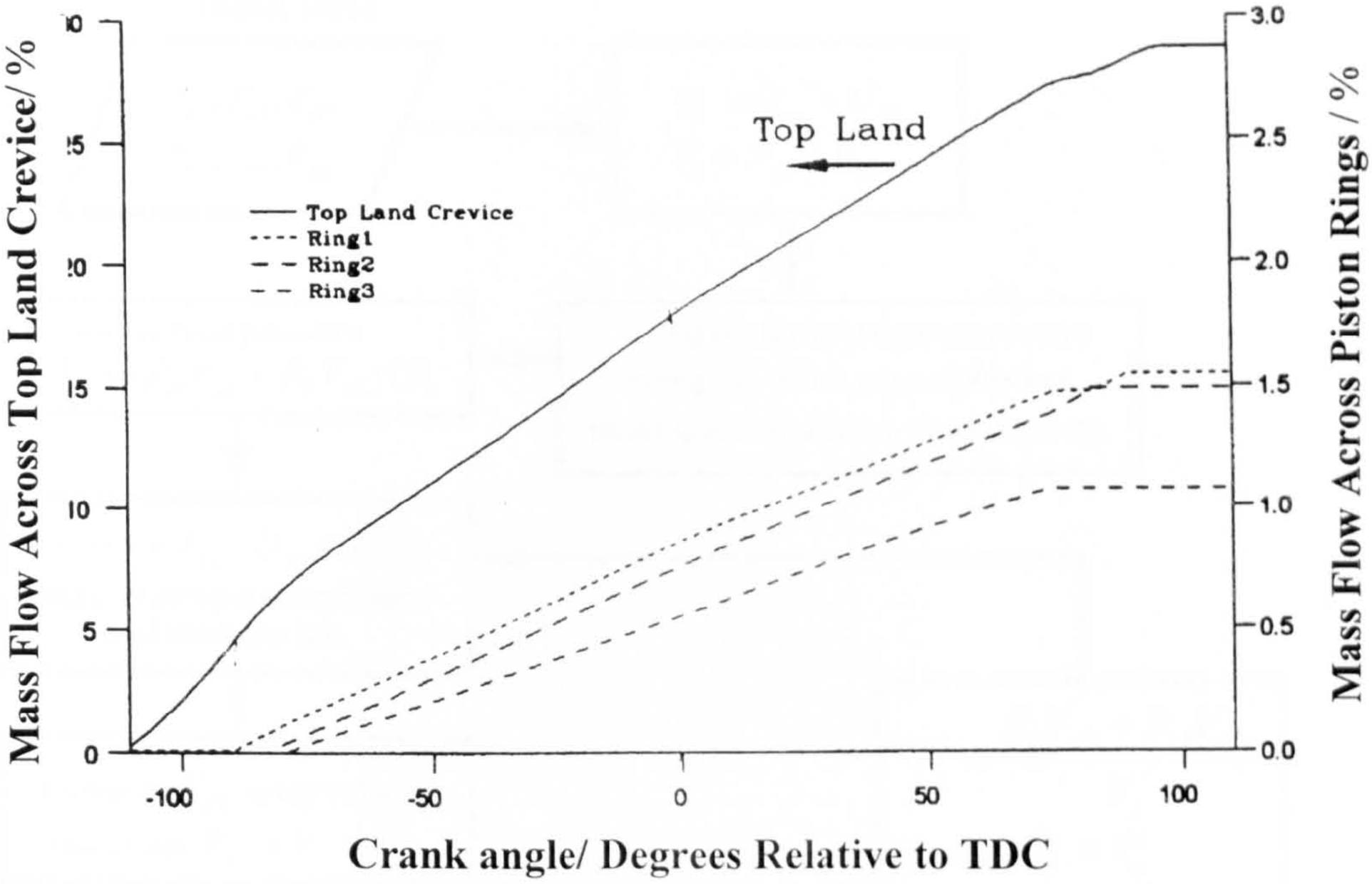

Figure 6.10 Mass flow across the top land crevice entrance and piston rings for a motoring cycle (modified JLO; Langridge, 1995).

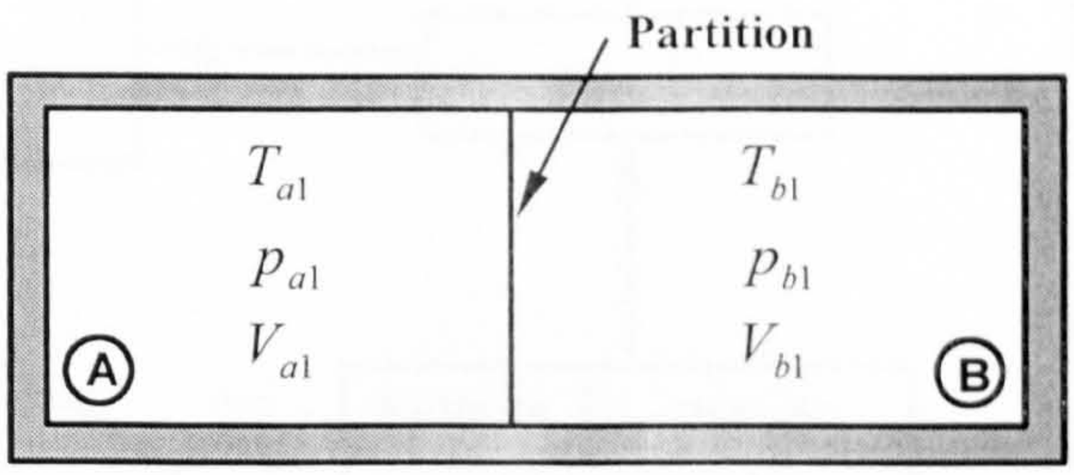

(a) Initial states ($P_{a1} < P_{b1}$)

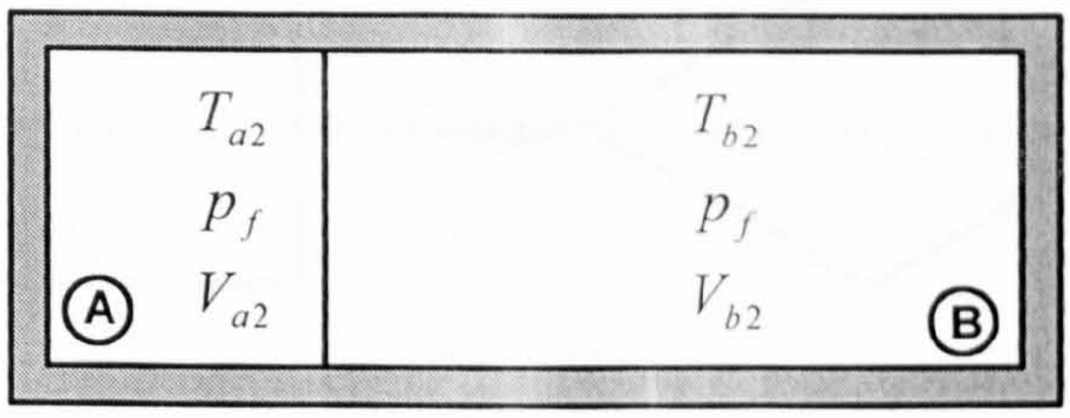

(b) Final state

Figure 6.11 (a) Initial and **(b)** final states of two zones in pressure equalisation process.

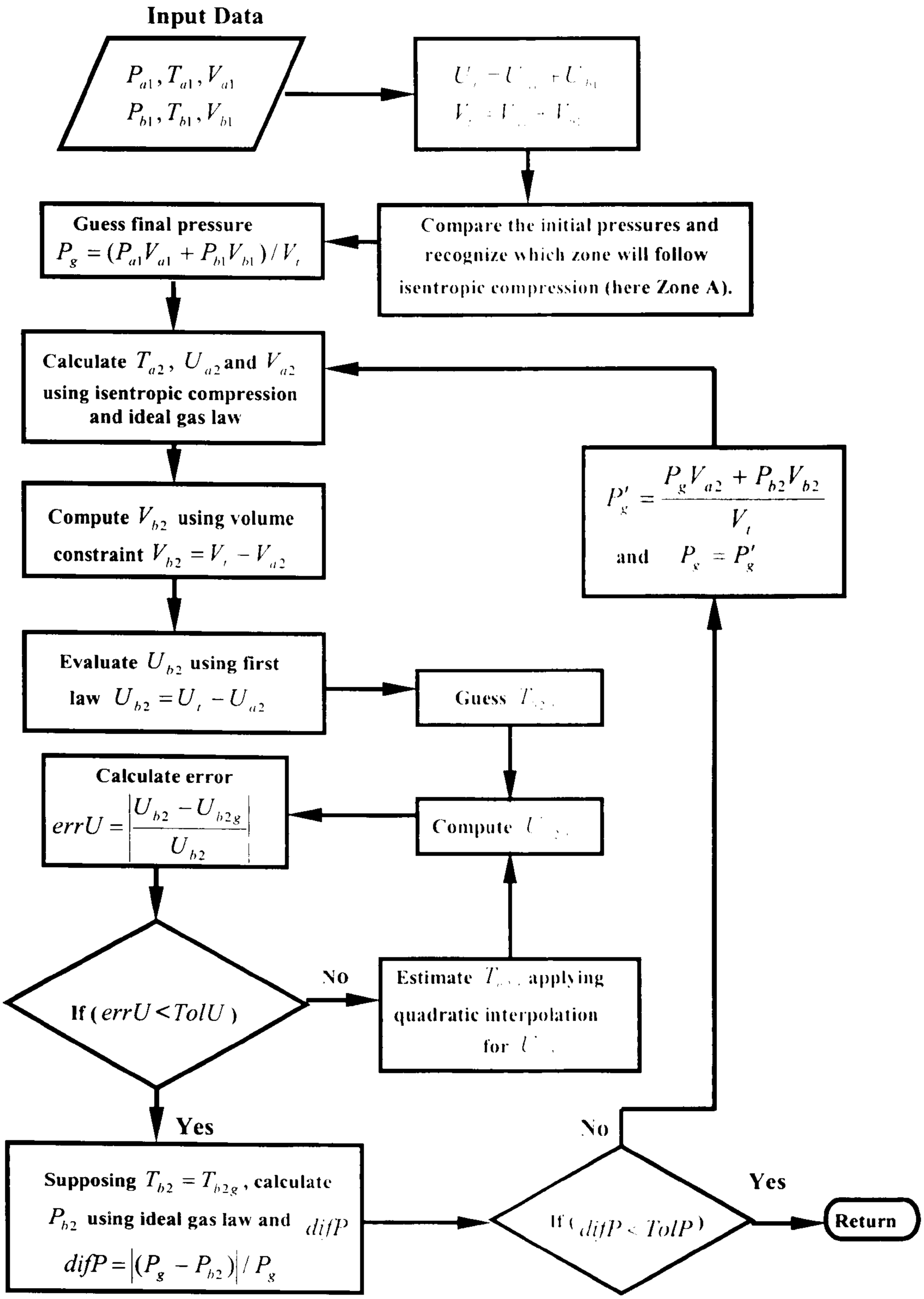

Figure 6.12 Flowchart of the IsC-COIE pressure equalisation subroutine.

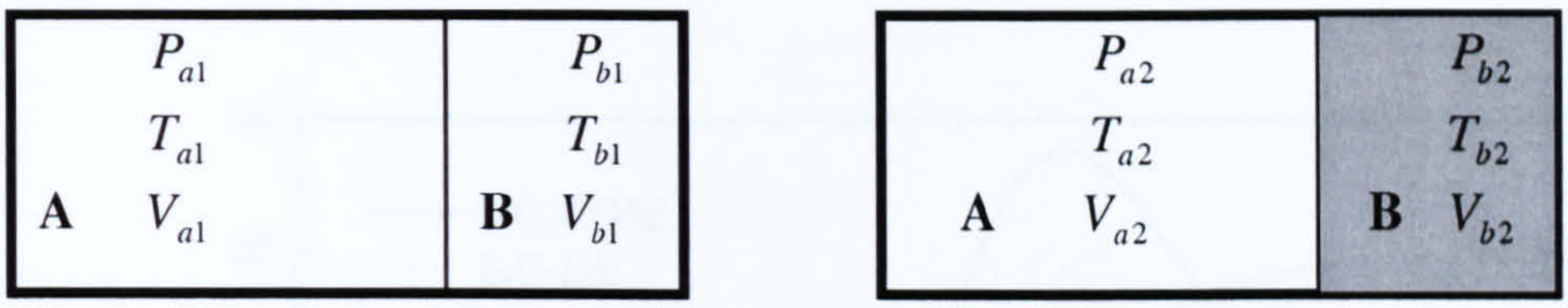

(a) $P_{a1} = P_{b1}$ and $T_{a1} = T_{b1}$

(b) CVAC process ($P_{a2} \neq P_{b2}$)

(c) Pressure equalisation ($P_{a3} = P_{b3}$)

Figure 6.13 **(a)** Initial conditions of the two zones, **(b)** that following the CVAC process in Zone B and **(c)** that at the end of the pressure equalisation process.

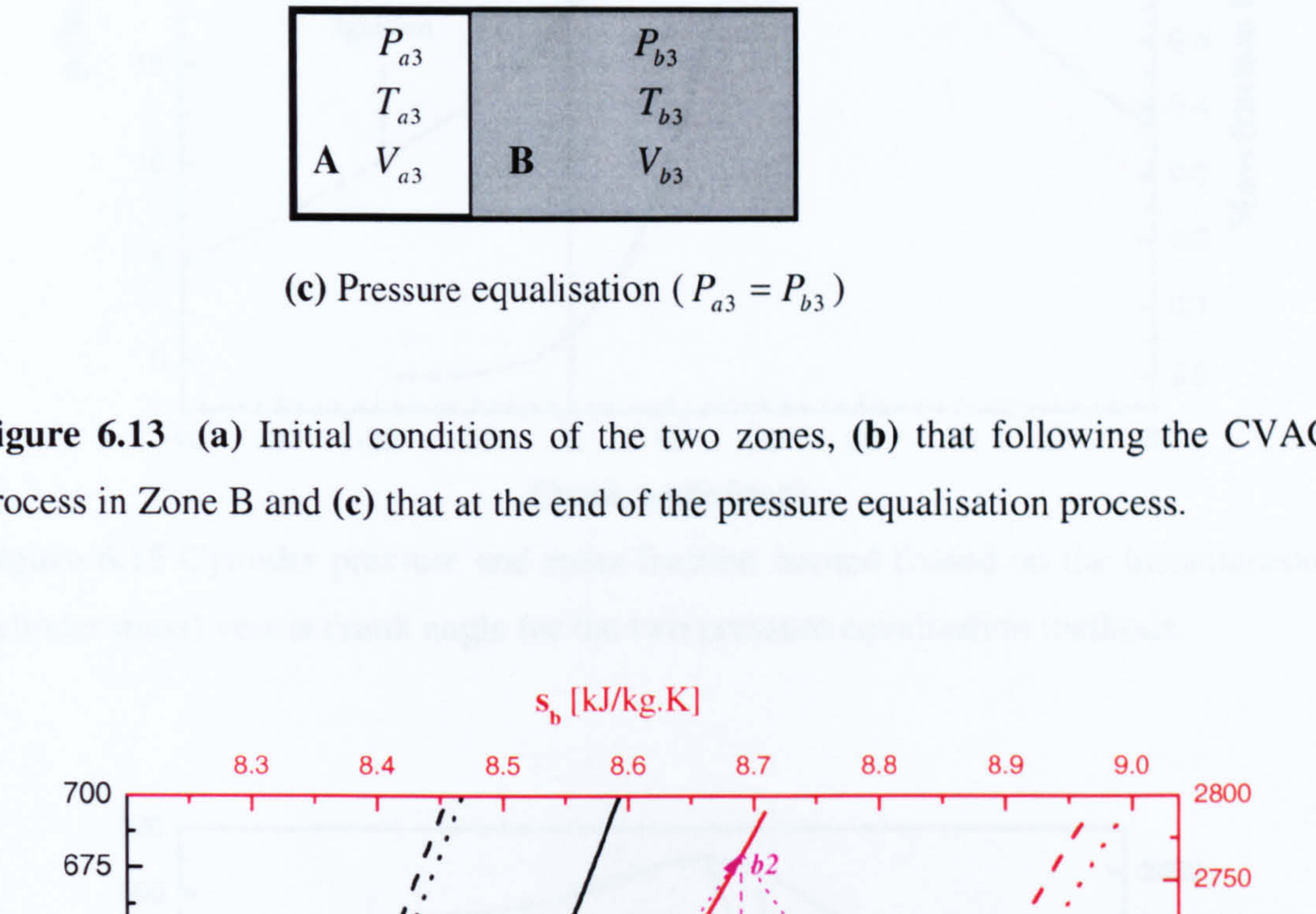

Figure 6.14 Two-layer T-s diagram for CVAC process of Zone B and pressure equalisation process of Zone A and B.

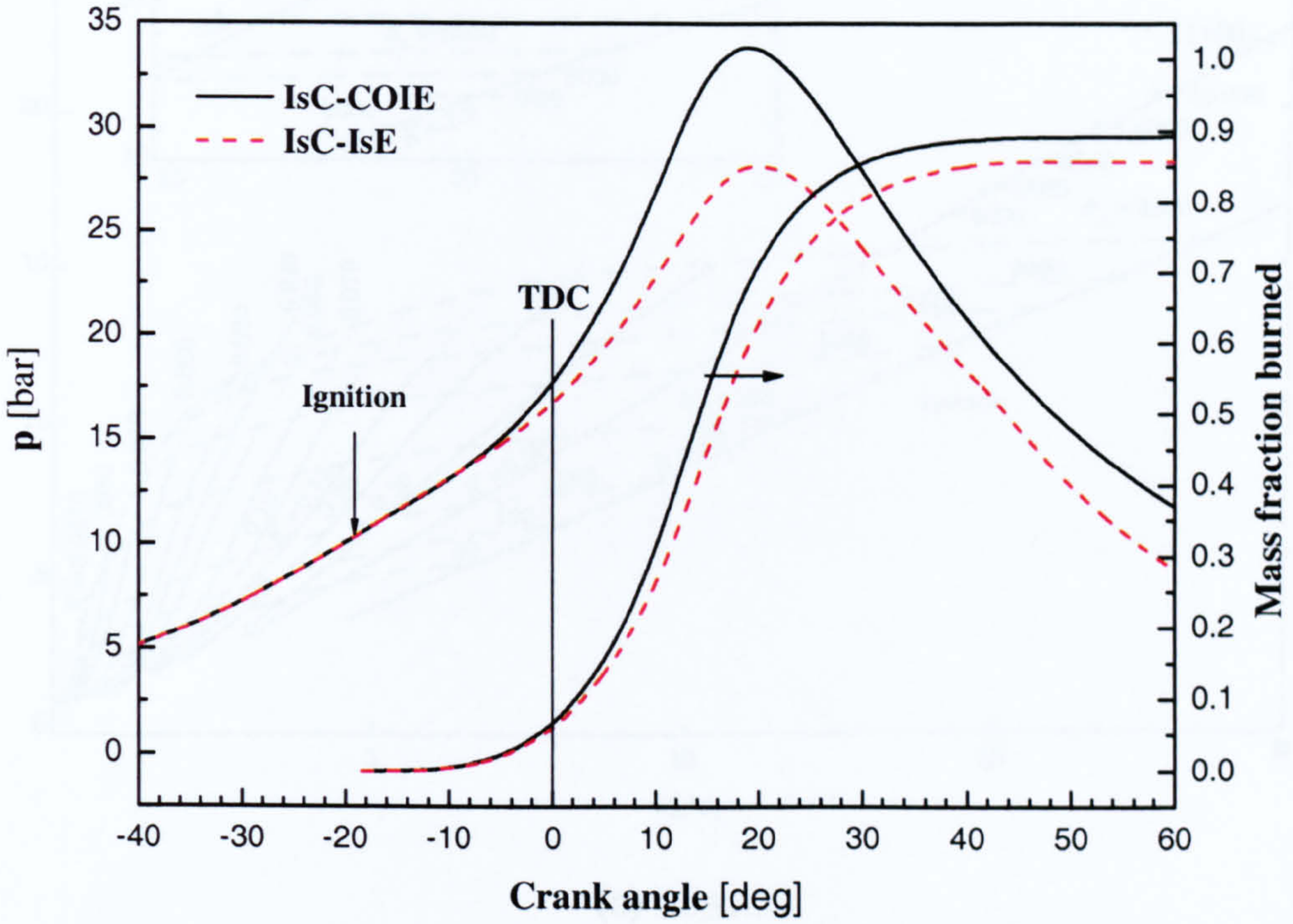

Figure 6.15 Cylinder pressure and mass fraction burned (based on the instantaneous cylinder mass) versus crank angle for the two pressure equalisation methods.

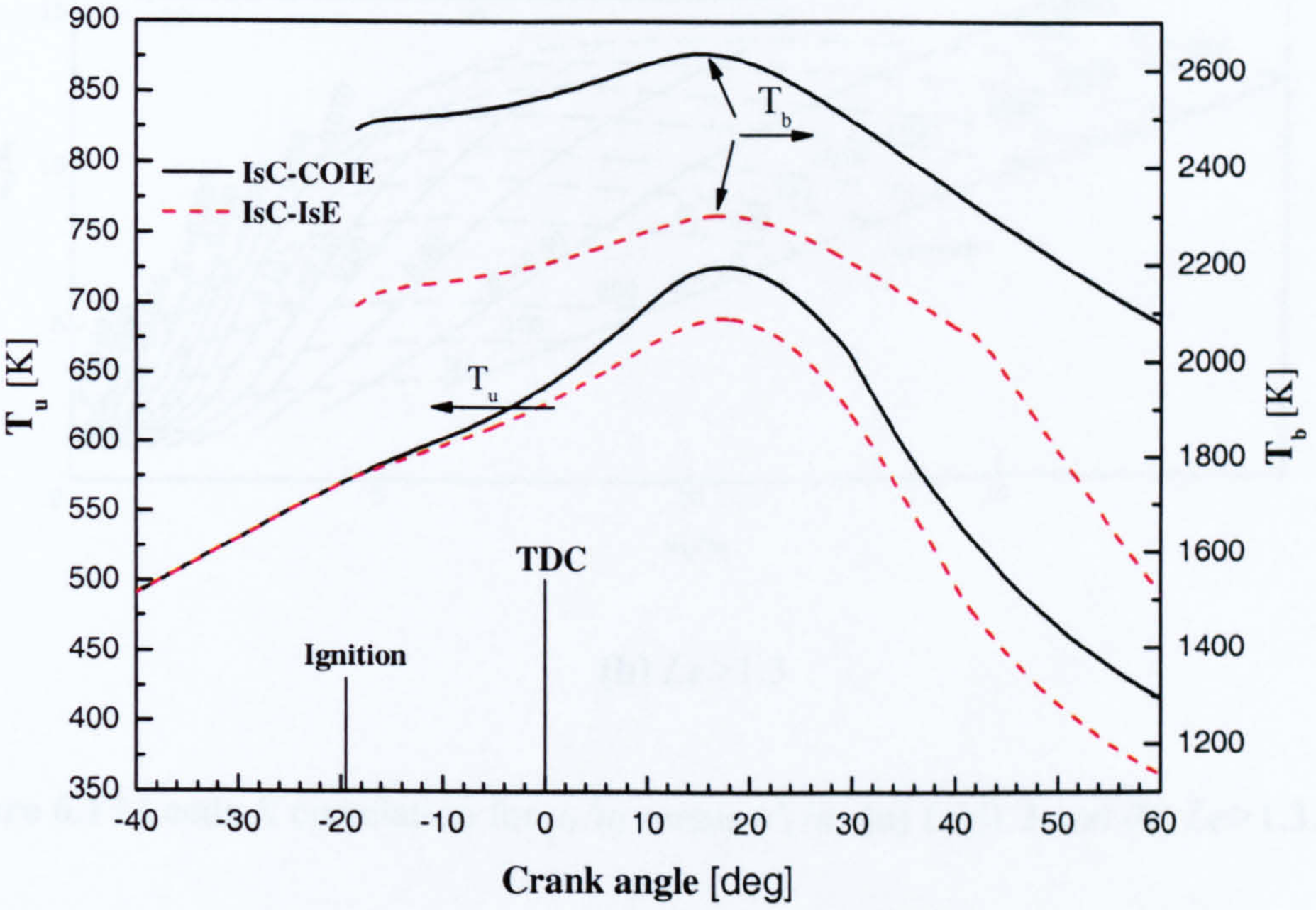

Figure 6.16 Unburned and burned gas temperatures versus crank angle resulted from the two pressure equalisation methods.

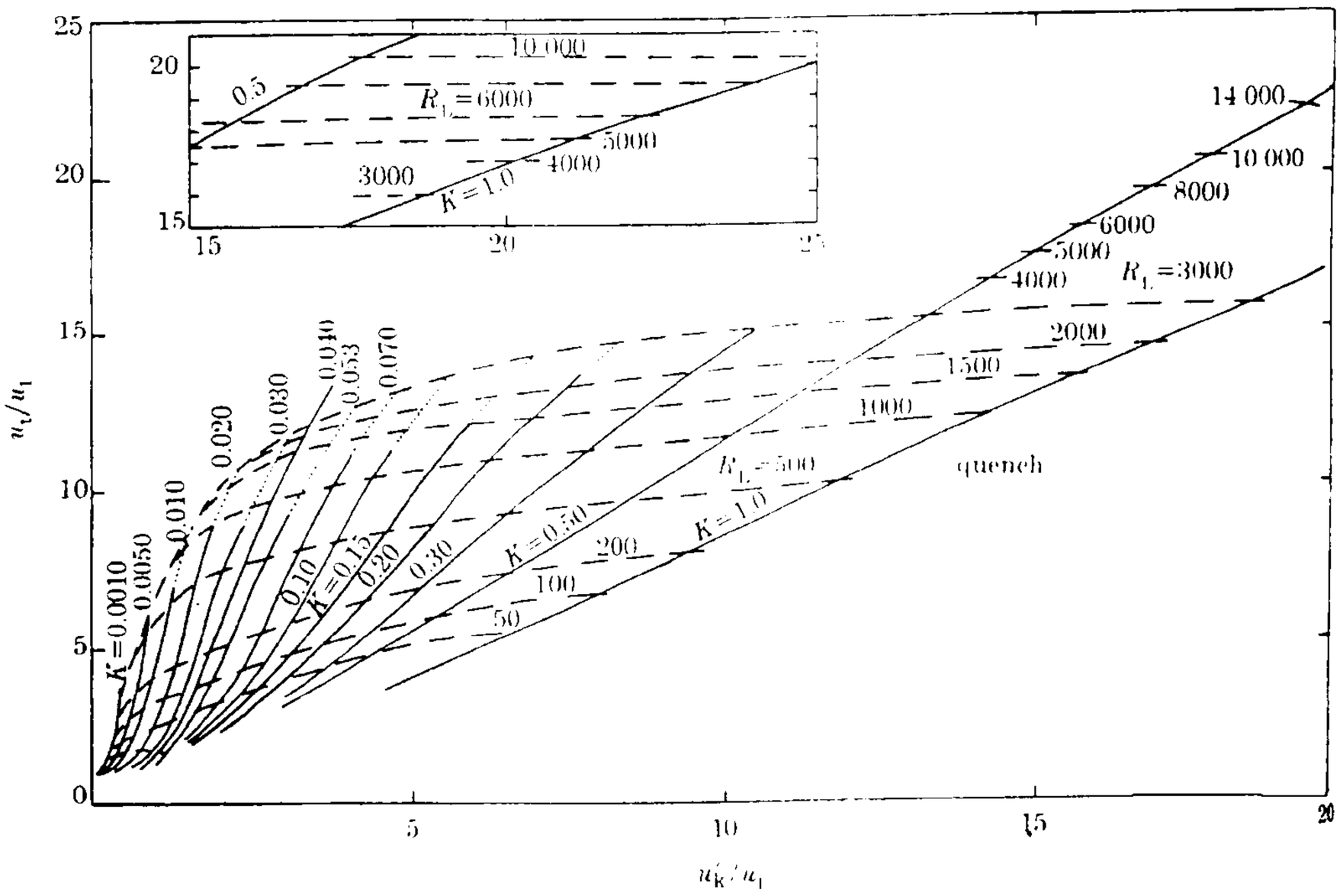

(a) $Le \leq 1.3$

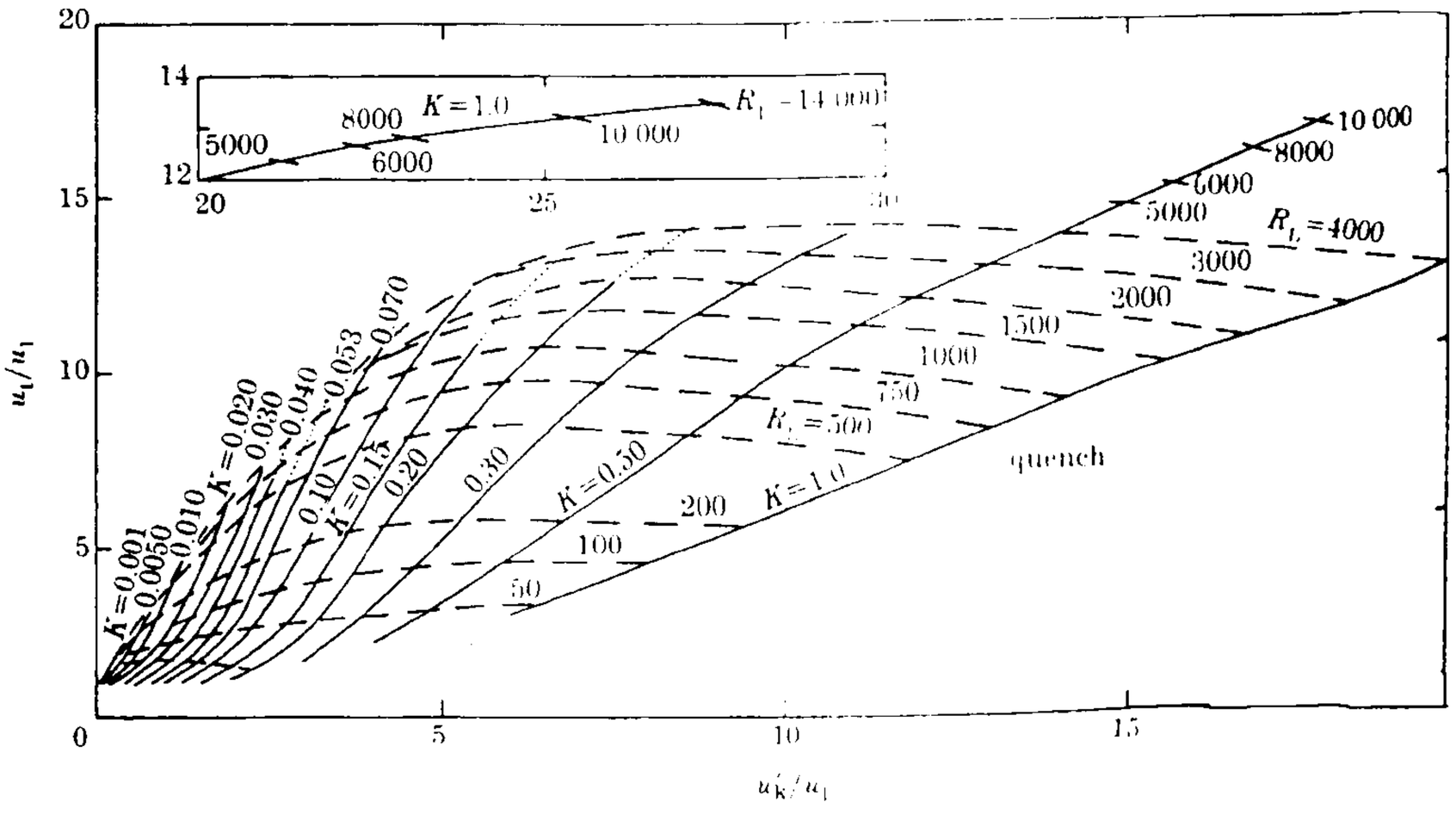

(b) $Le > 1.3$

Figure 6.17 Leeds K correlation for u_t/u_l versus u'_k/u_l **(a)** $Le \leq 1.3$ and **(b)** $Le > 1.3$.

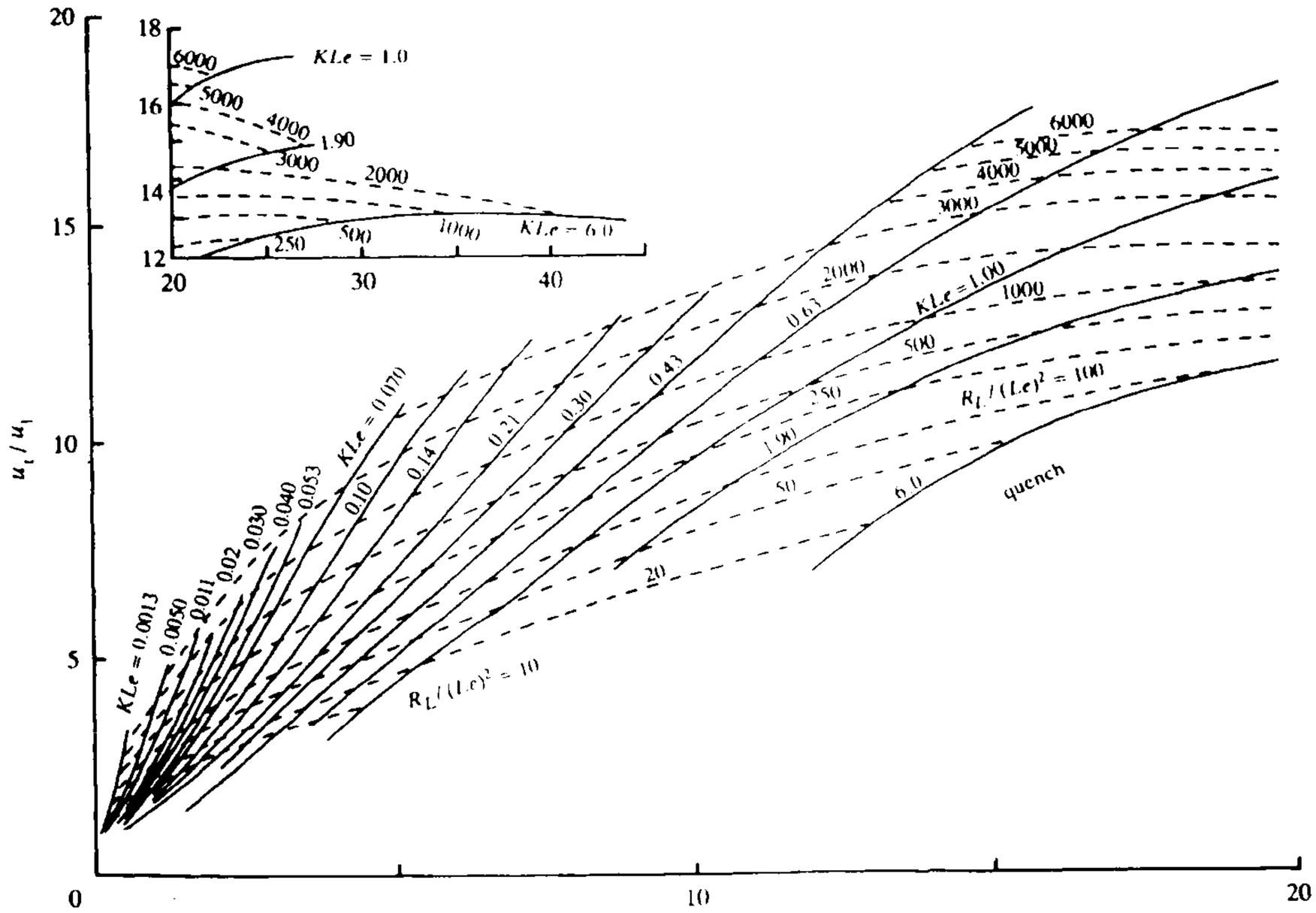

Figure 6.18 Leeds *KLe* correlation for u_t/u_l versus u'_k/u_l.

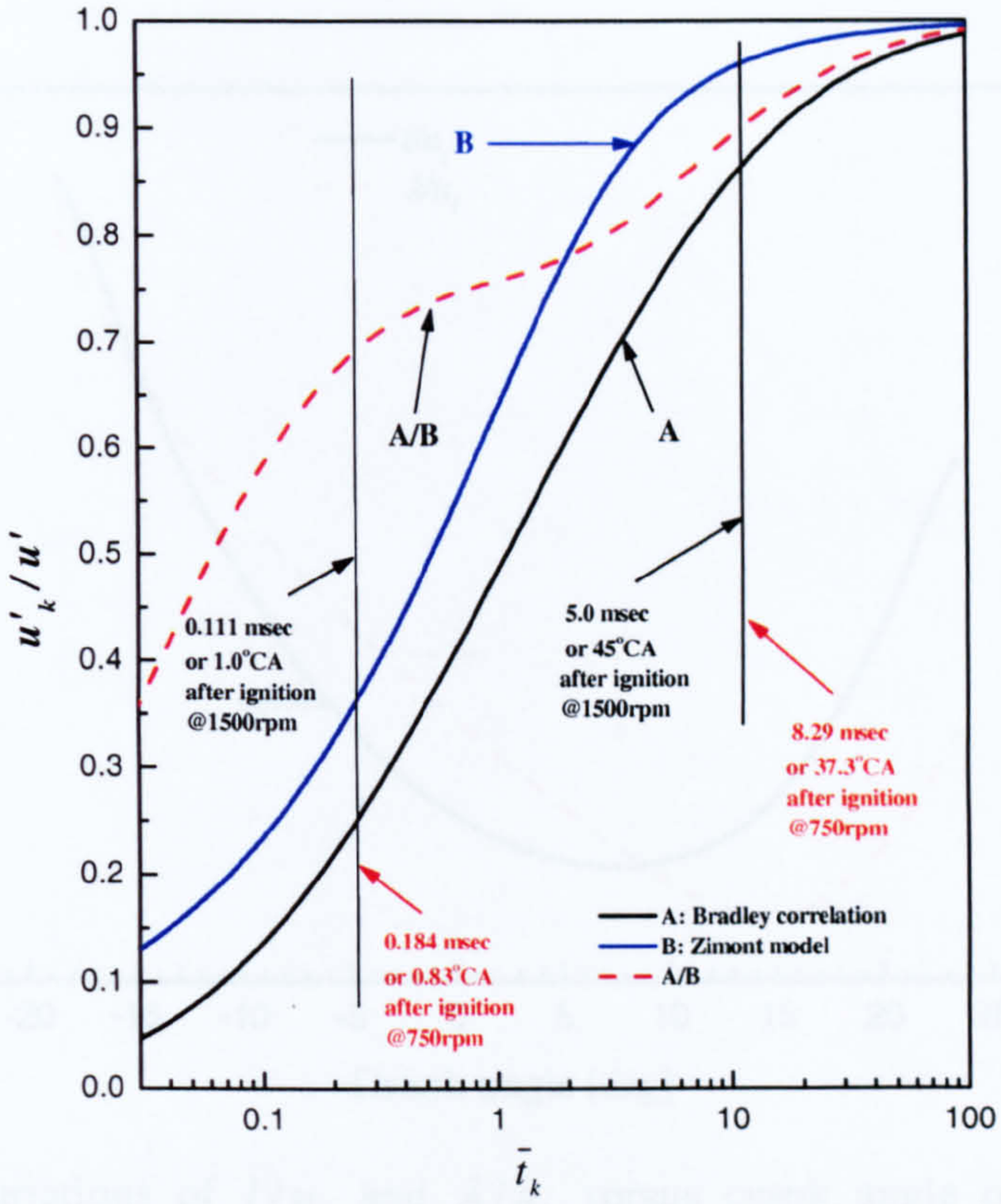

Figure 6.19 u'_k / u' versus dimensionless time, $\bar{t}_k$, for Bradley correlation and Zimont model associated with the ratio of the two expressions.

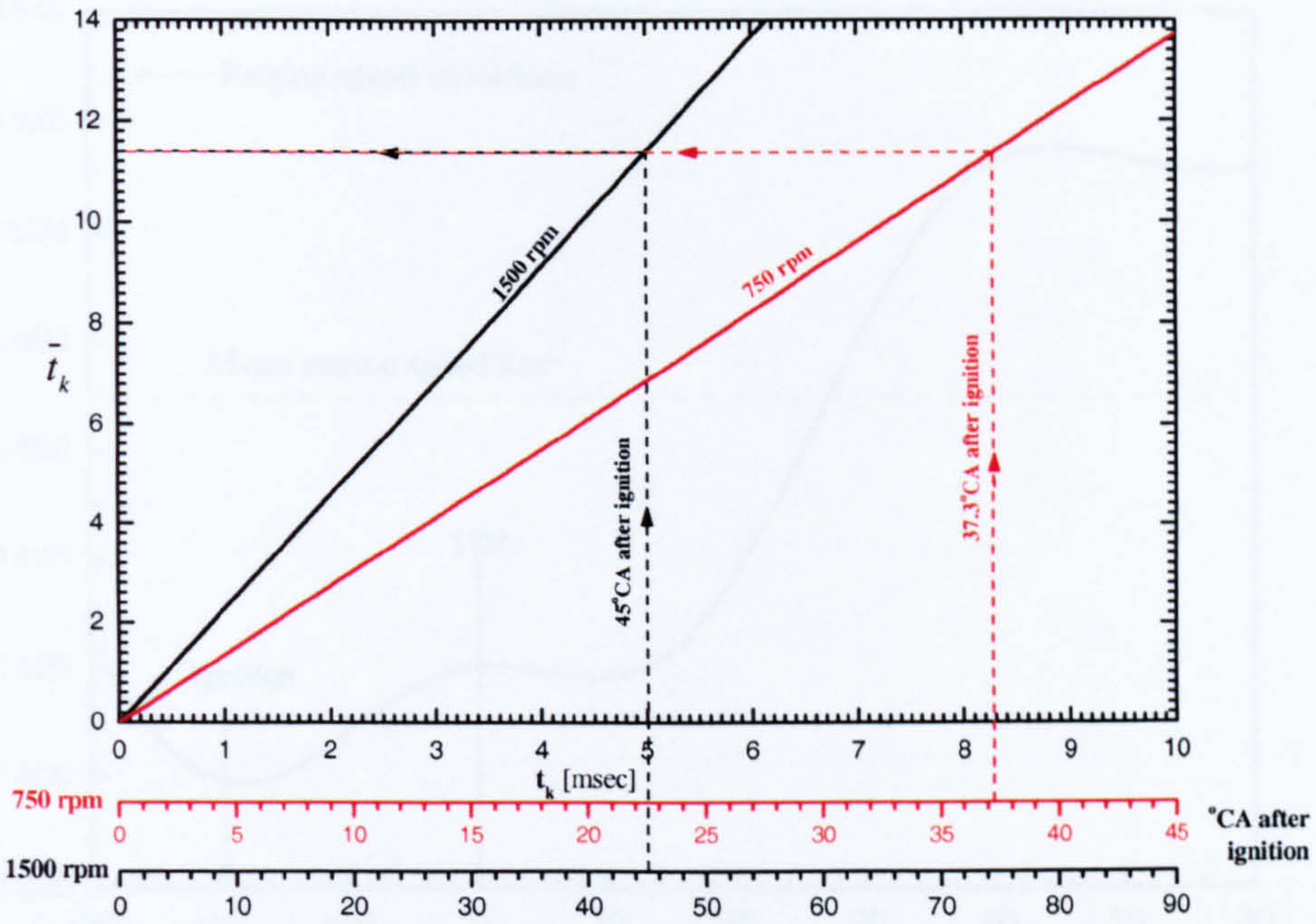

Figure 6.20 the relation between $\bar{t}_k$ and time, t_k, (or crank angle) from ignition for 750 and 1500 *rpm* based on integral length scale and u' at TDC position in LUPOE1.

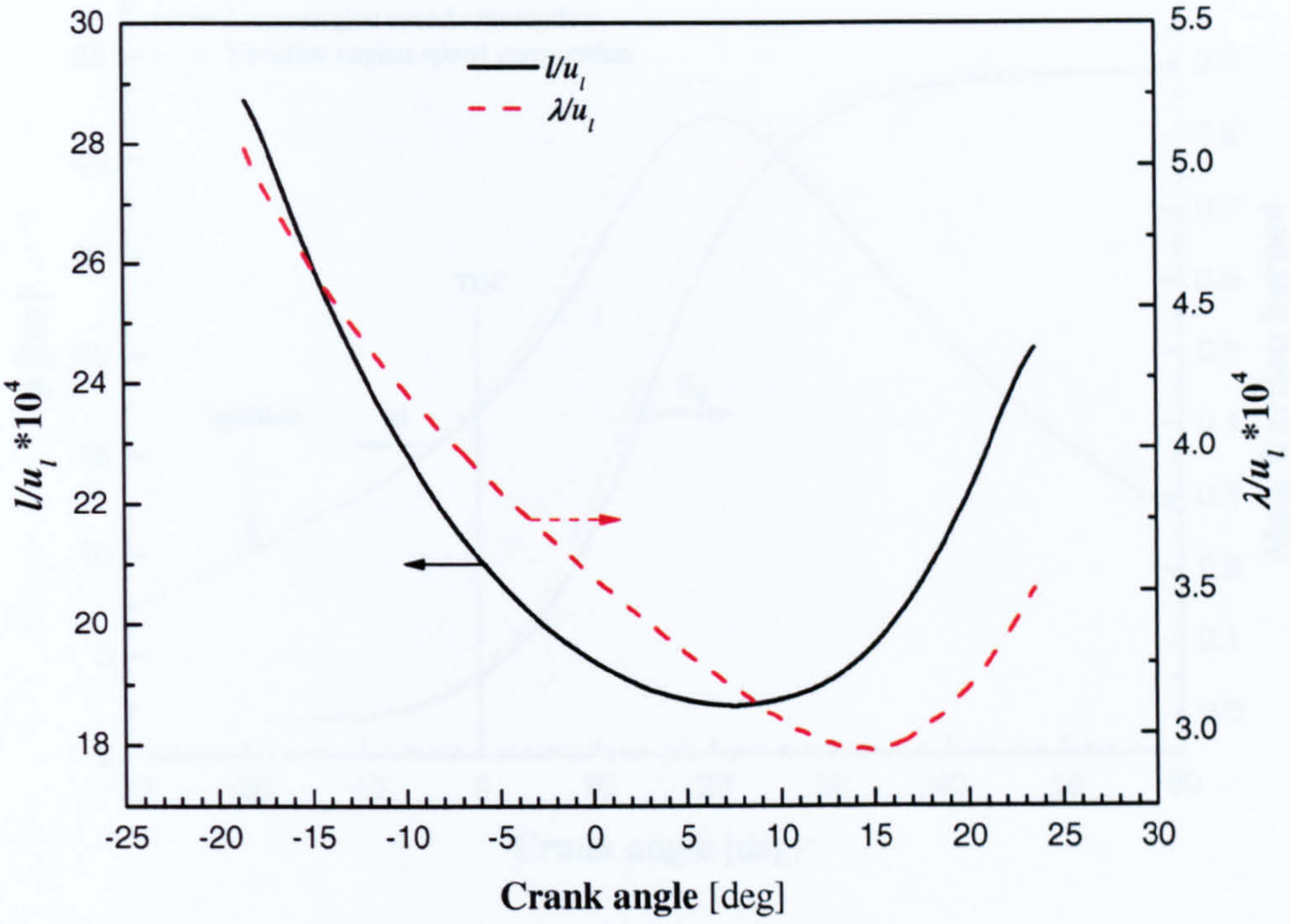

Figure 6.21 Variations of l/u_t and λ/u_t versus crank angle obtained from the modified version of LUSIE at the reference condition.

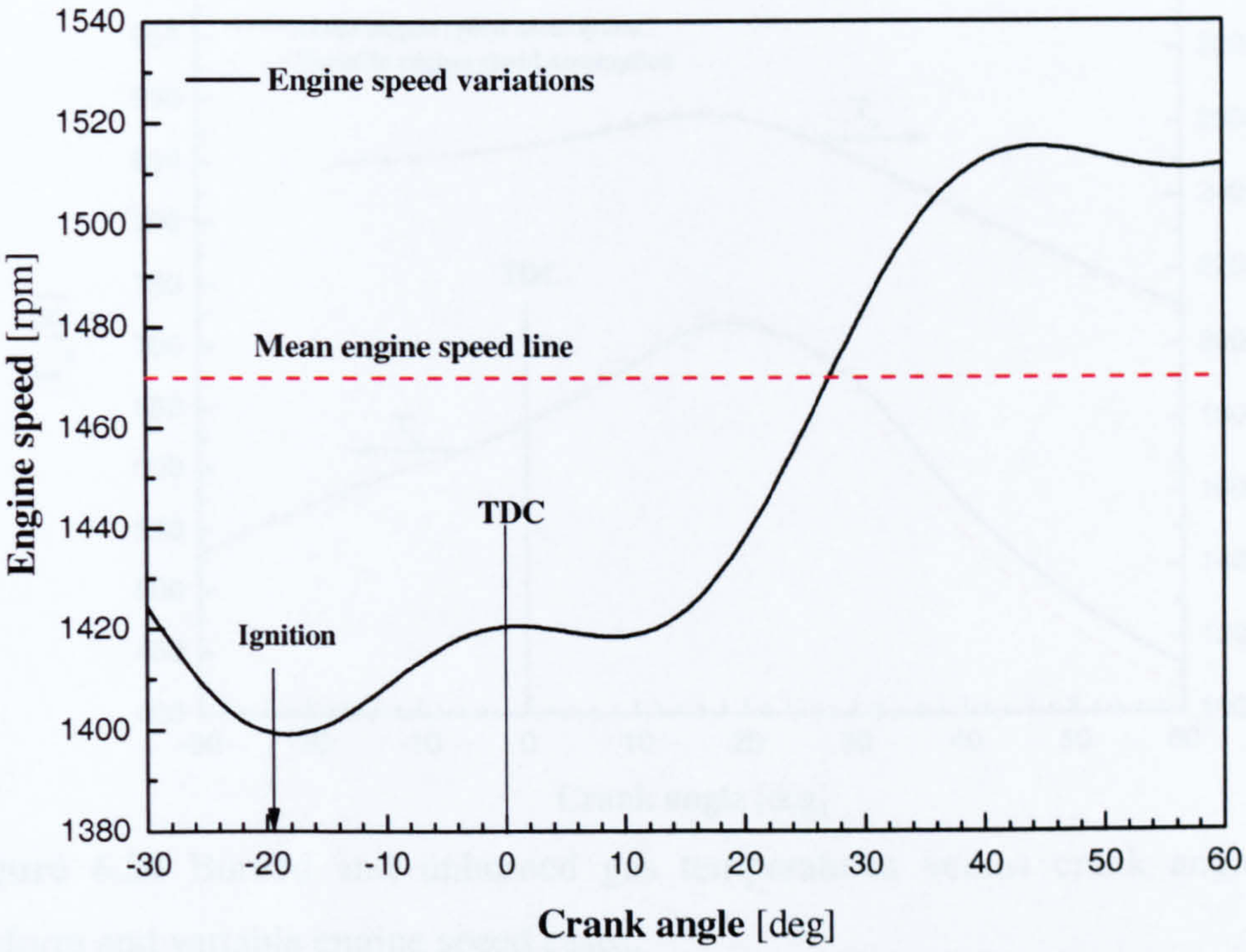

Figure 6.22 Engine speed variations of a typical cycle in terms of crank angle.

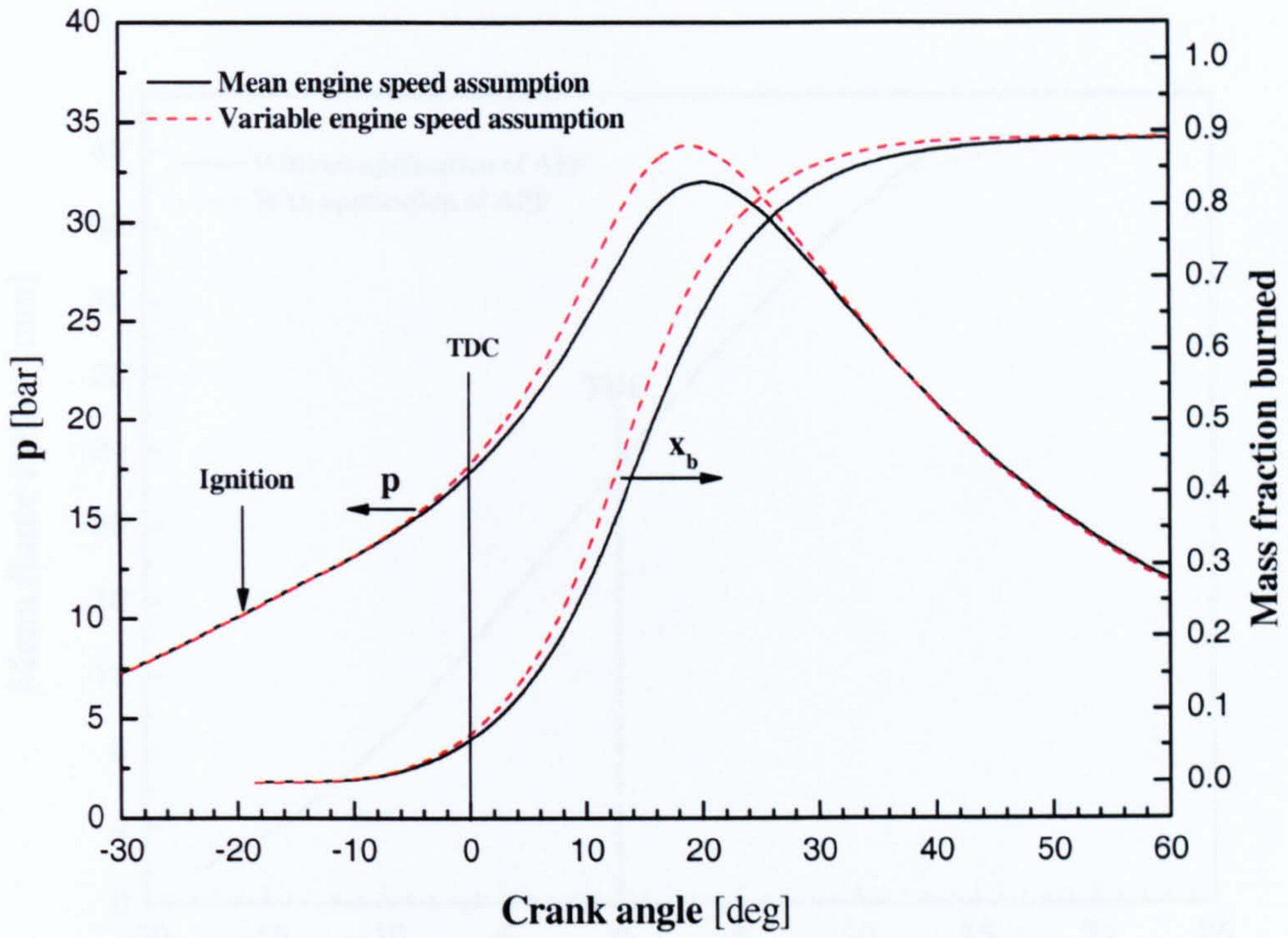

Figure 6.23 Cylinder pressure and mass fraction burned (based on the instantaneous cylinder mass) versus crank angle for the uniform and variable engine speed cases.

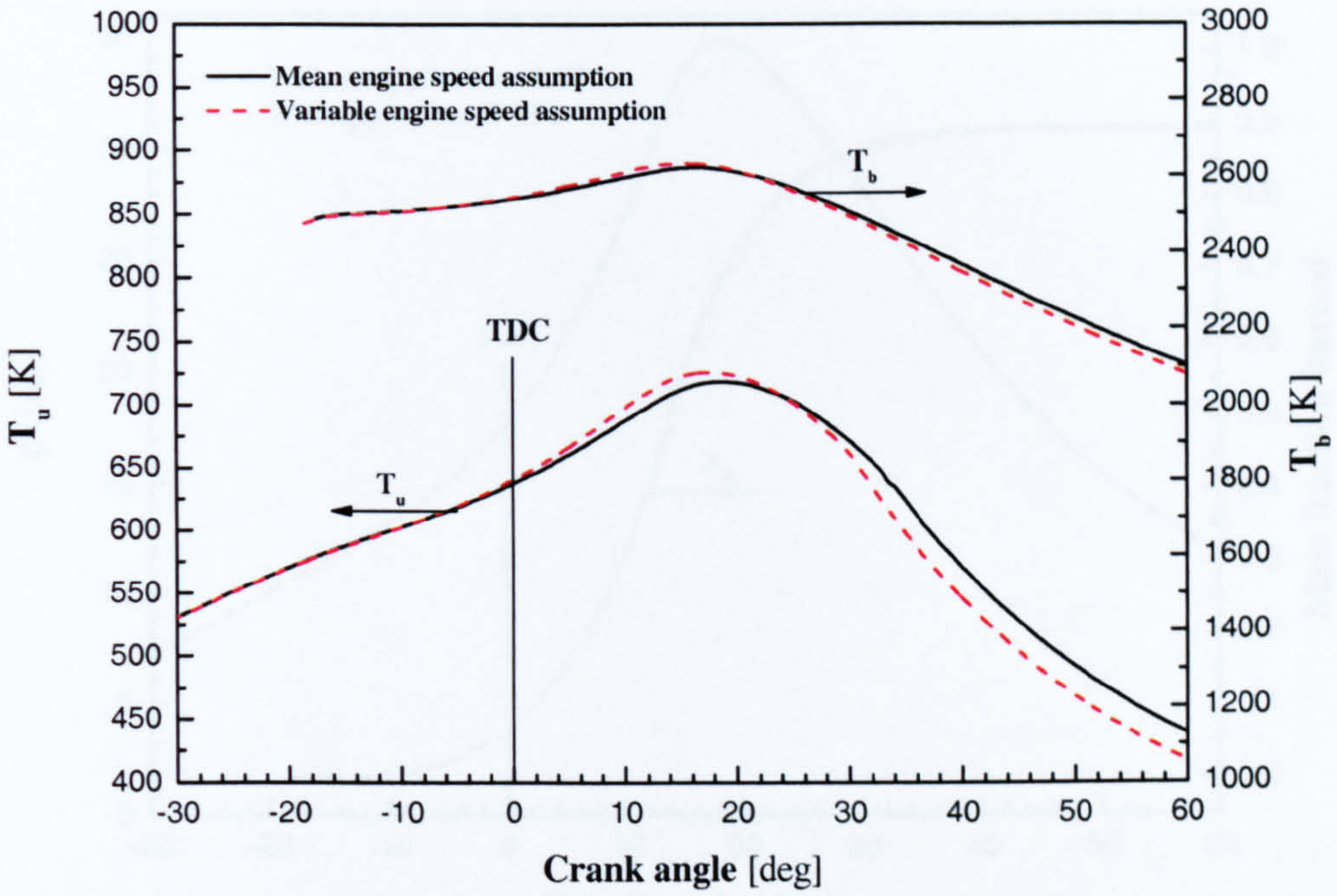

Figure 6.24 Burned and unburned gas temperatures versus crank angle for the uniform and variable engine speed cases.

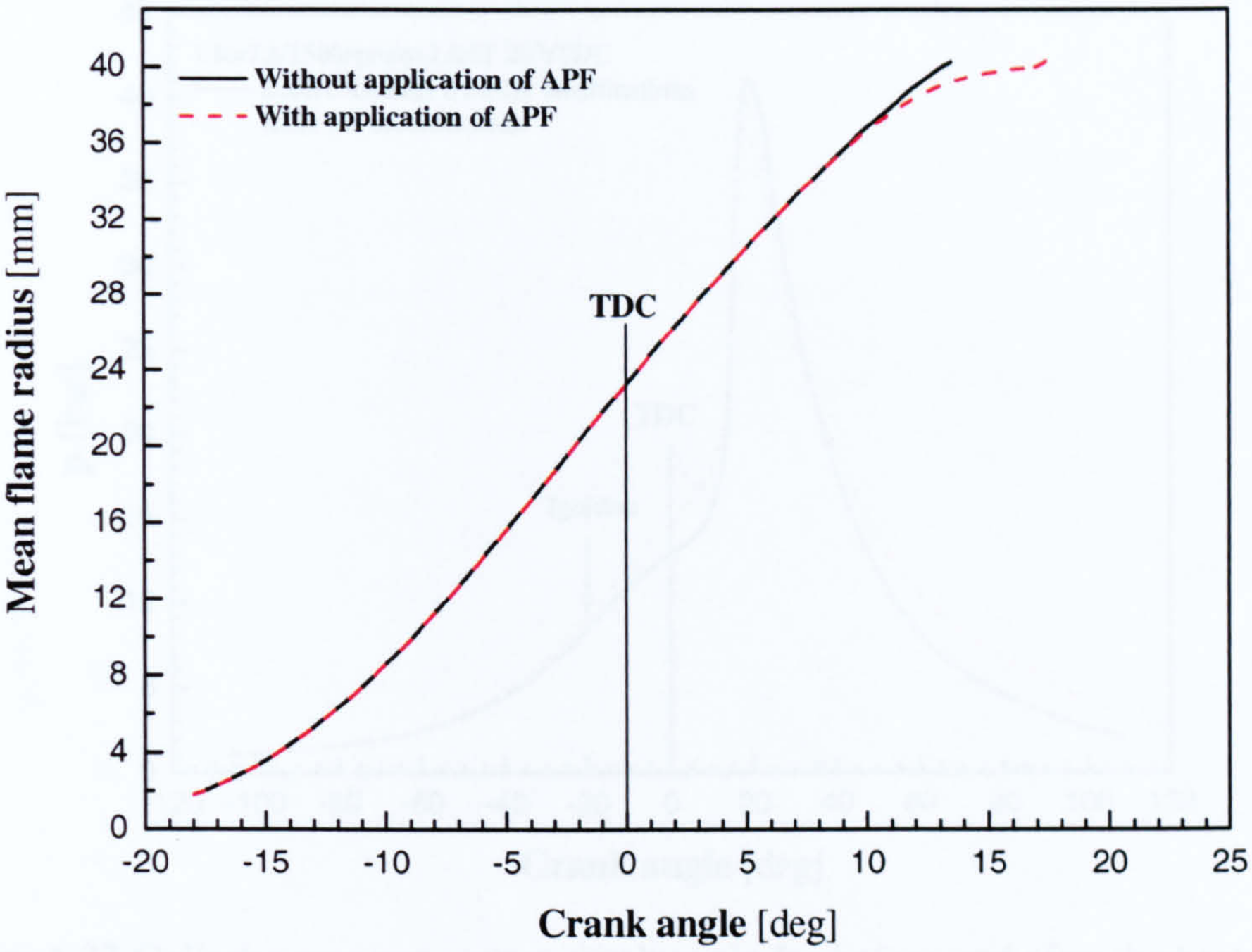

Figure 6.25 Mean flame radius versus crank angle for without and with application of APF.

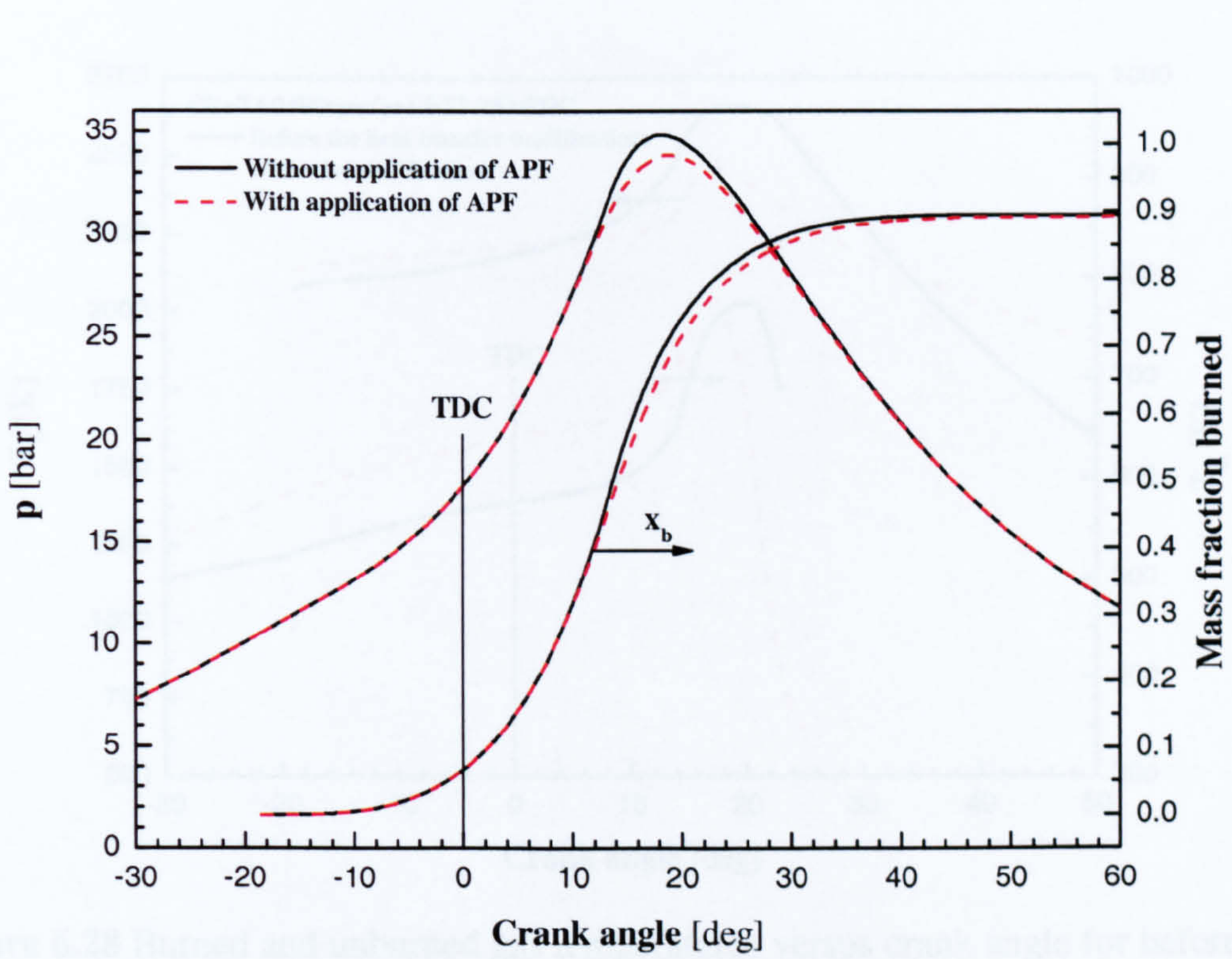

Figure 6.26 Cylinder pressure and mass fraction burned (based on the instantaneous cylinder mass) versus crank angle for without and with application of APF.

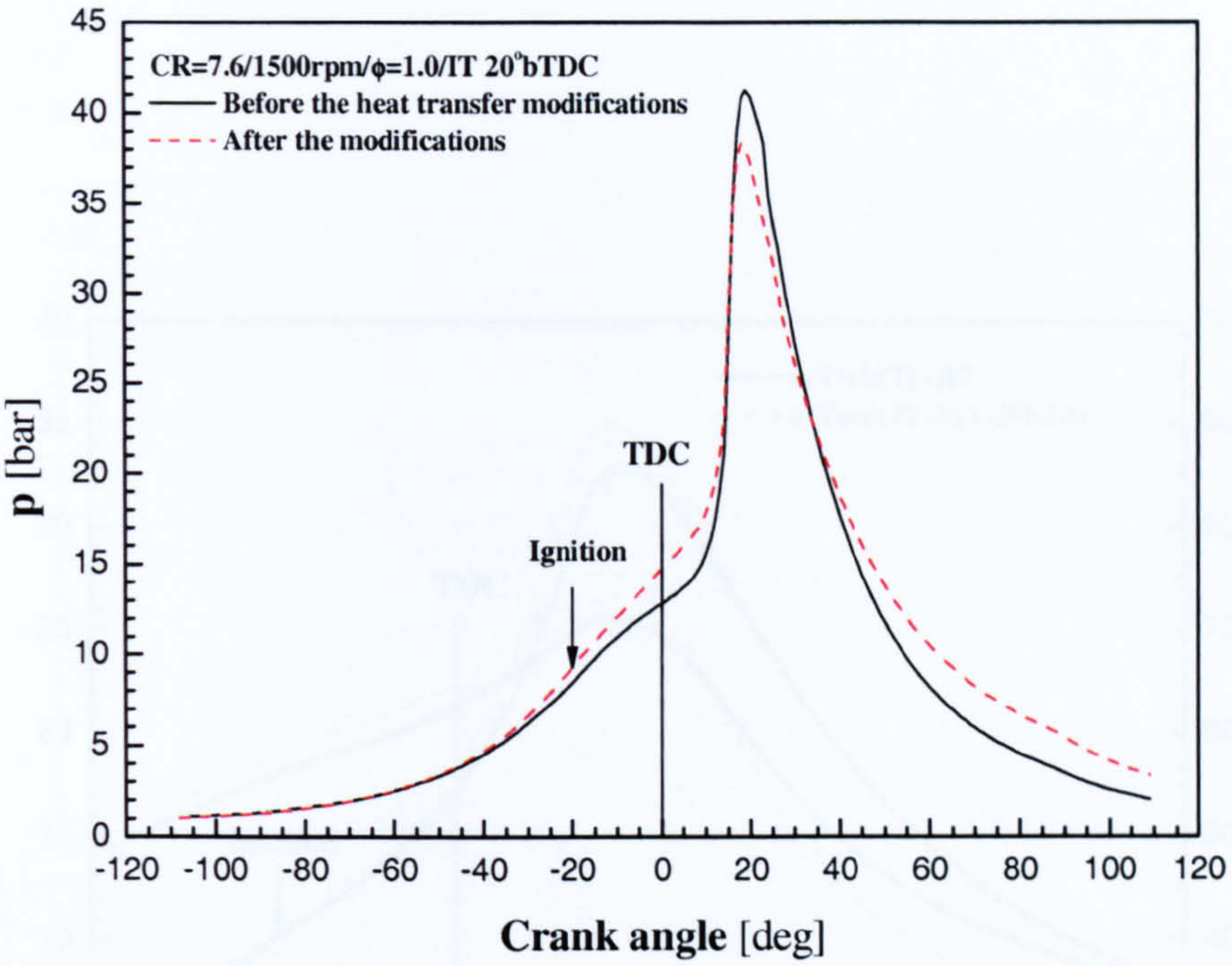

Figure 6.27 Cylinder pressure versus crank angle for before and after the heat transfer modifications at the reference condition.

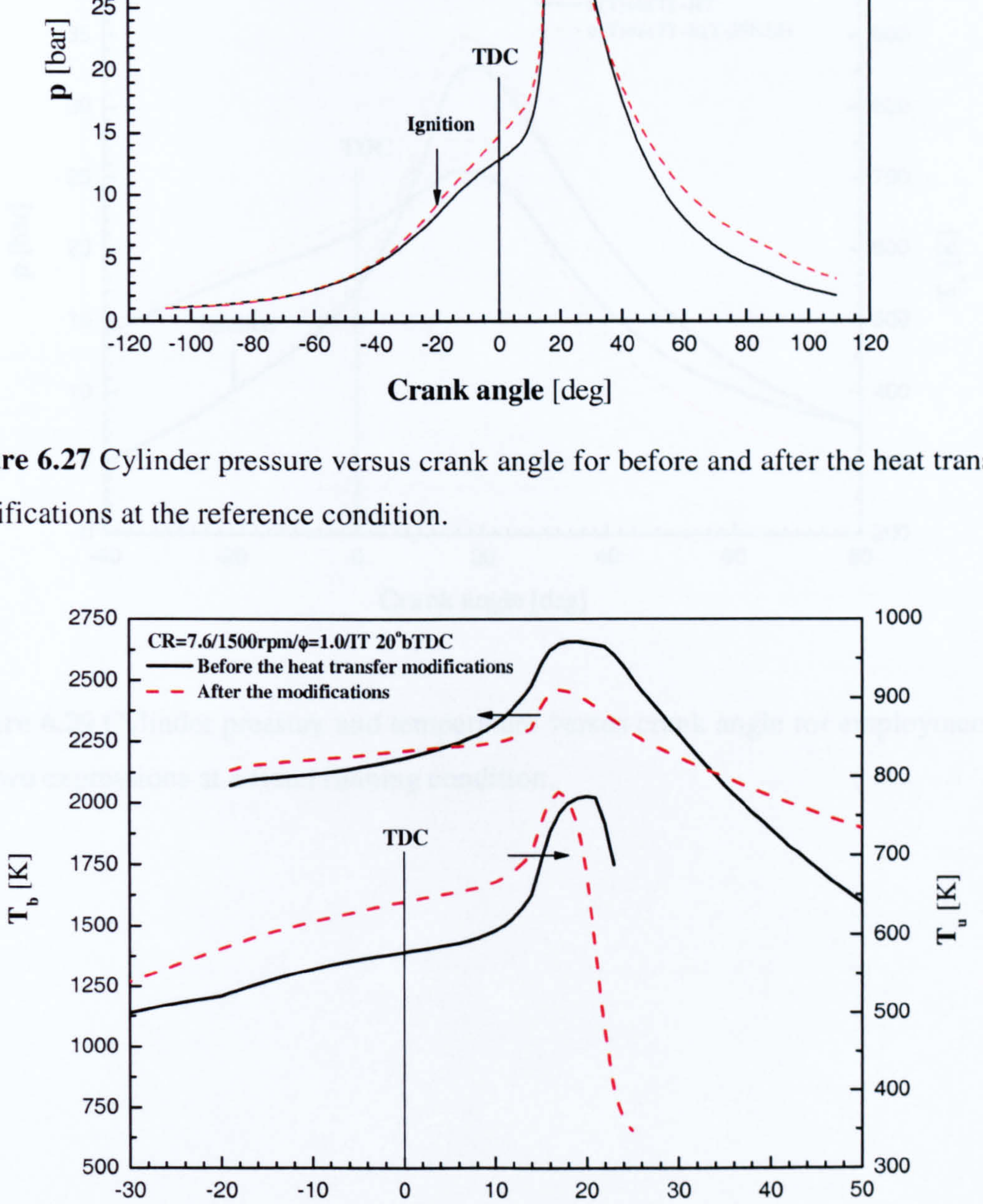

Figure 6.28 Burned and unburned gas temperatures versus crank angle for before and after the heat transfer modifications at the reference condition.

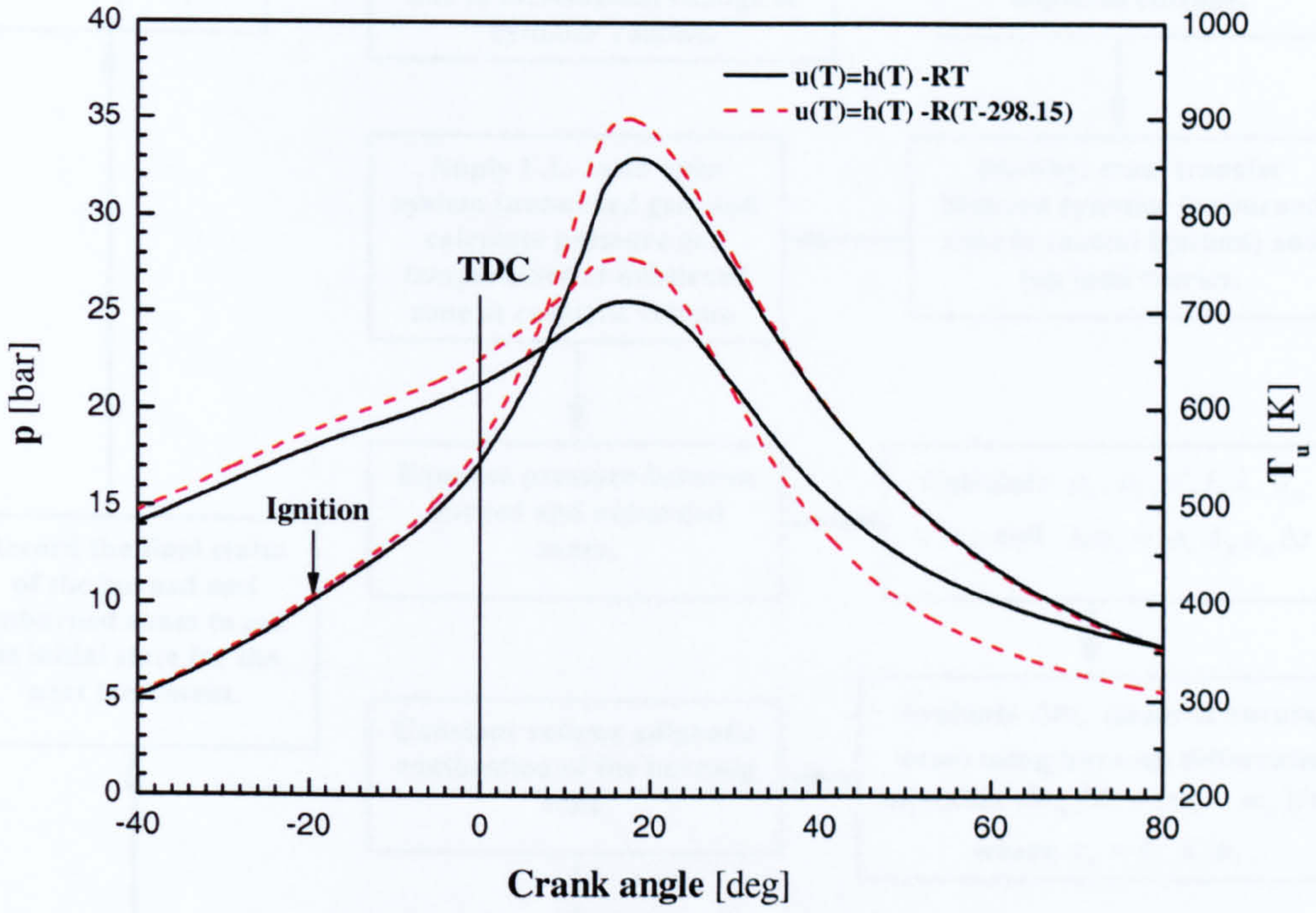

Figure 6.29 Cylinder pressure and temperature versus crank angle for employment of the two expressions at a fixed running condition.

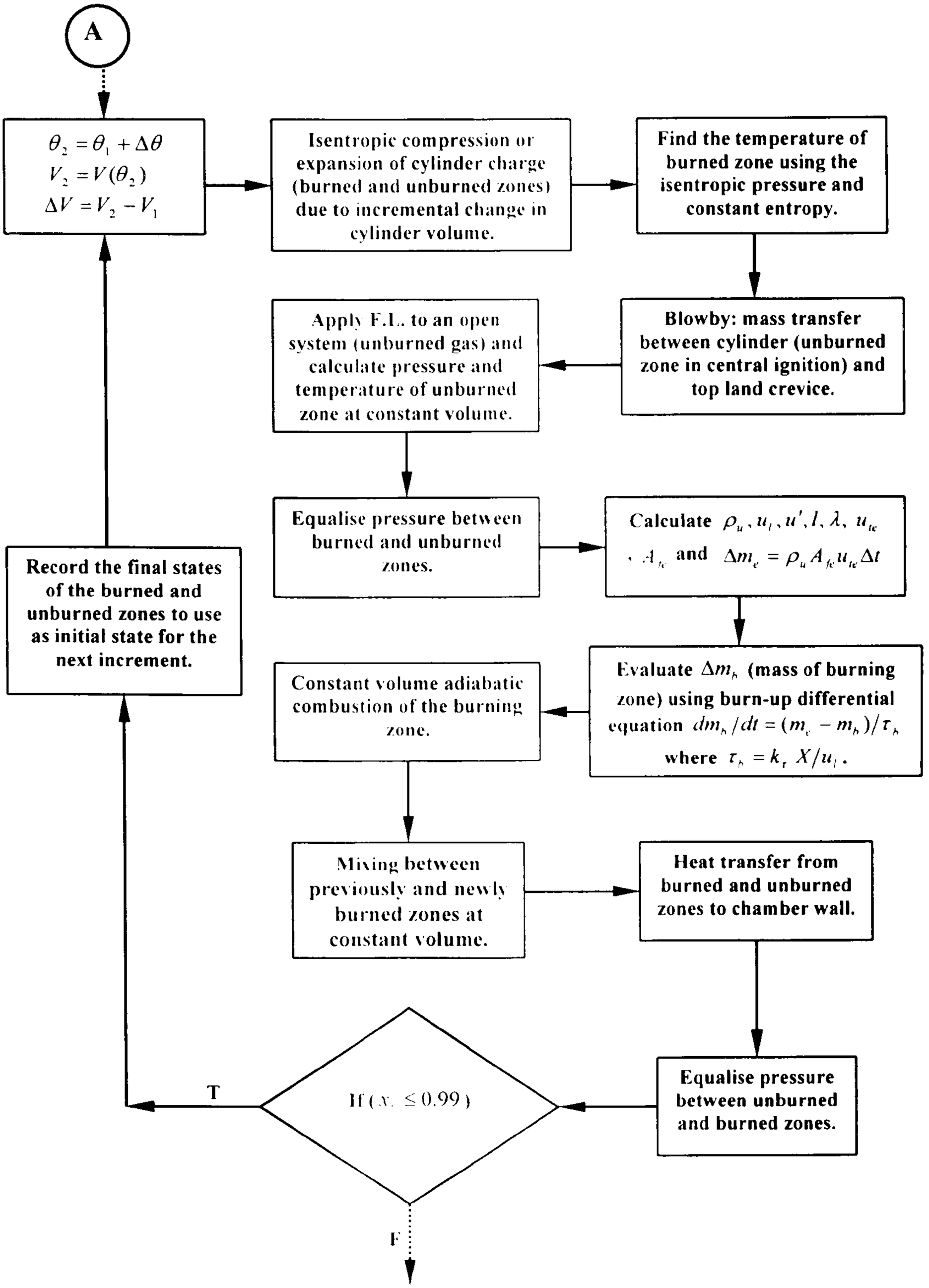

Figure 6.30 Modified structure of the burning velocity combustion routine.

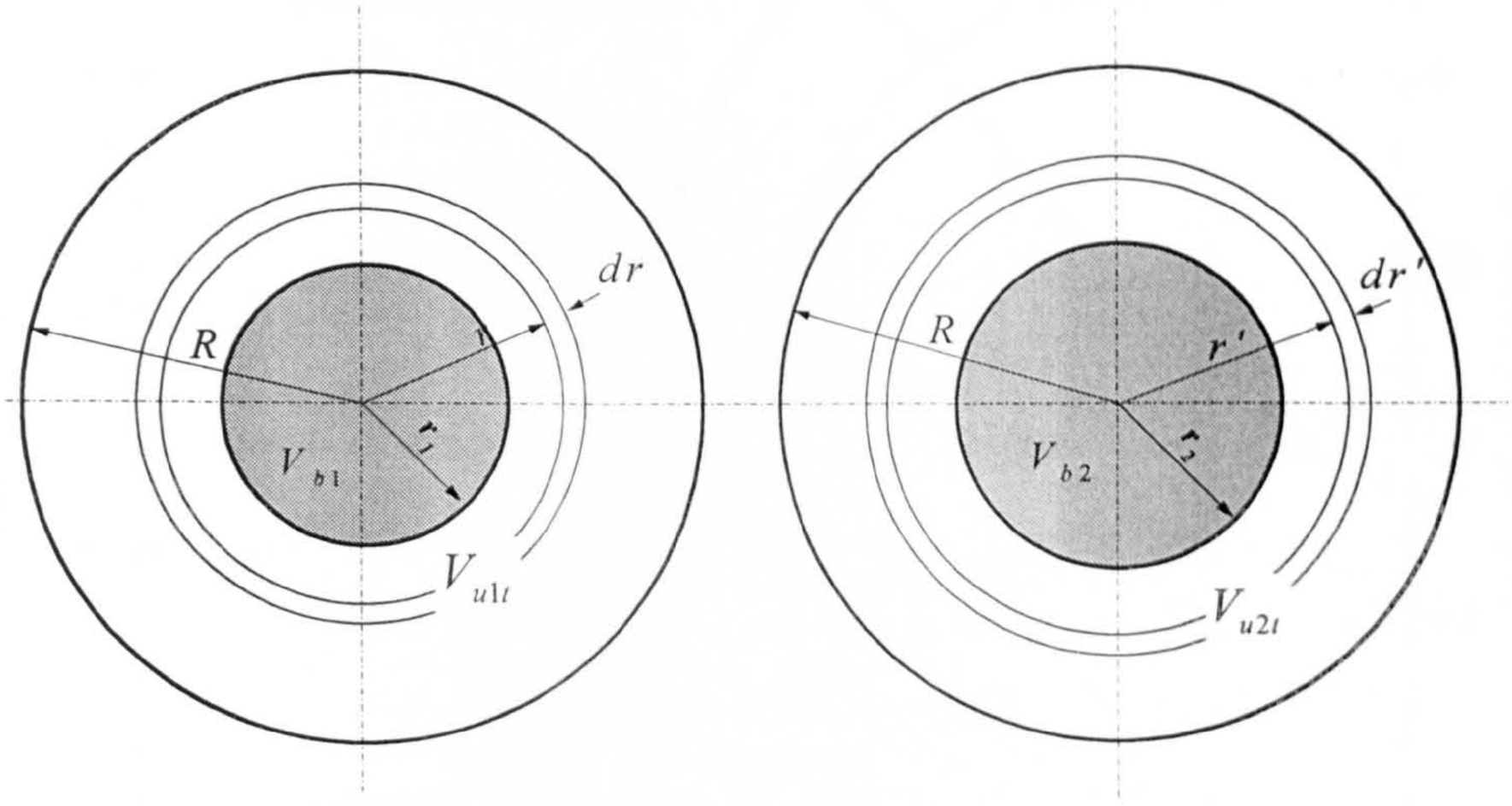

(a) Before expansion.

(b) After expansion.

Figure 6.31 Burned and unburned zones before and after burned gas expansion.

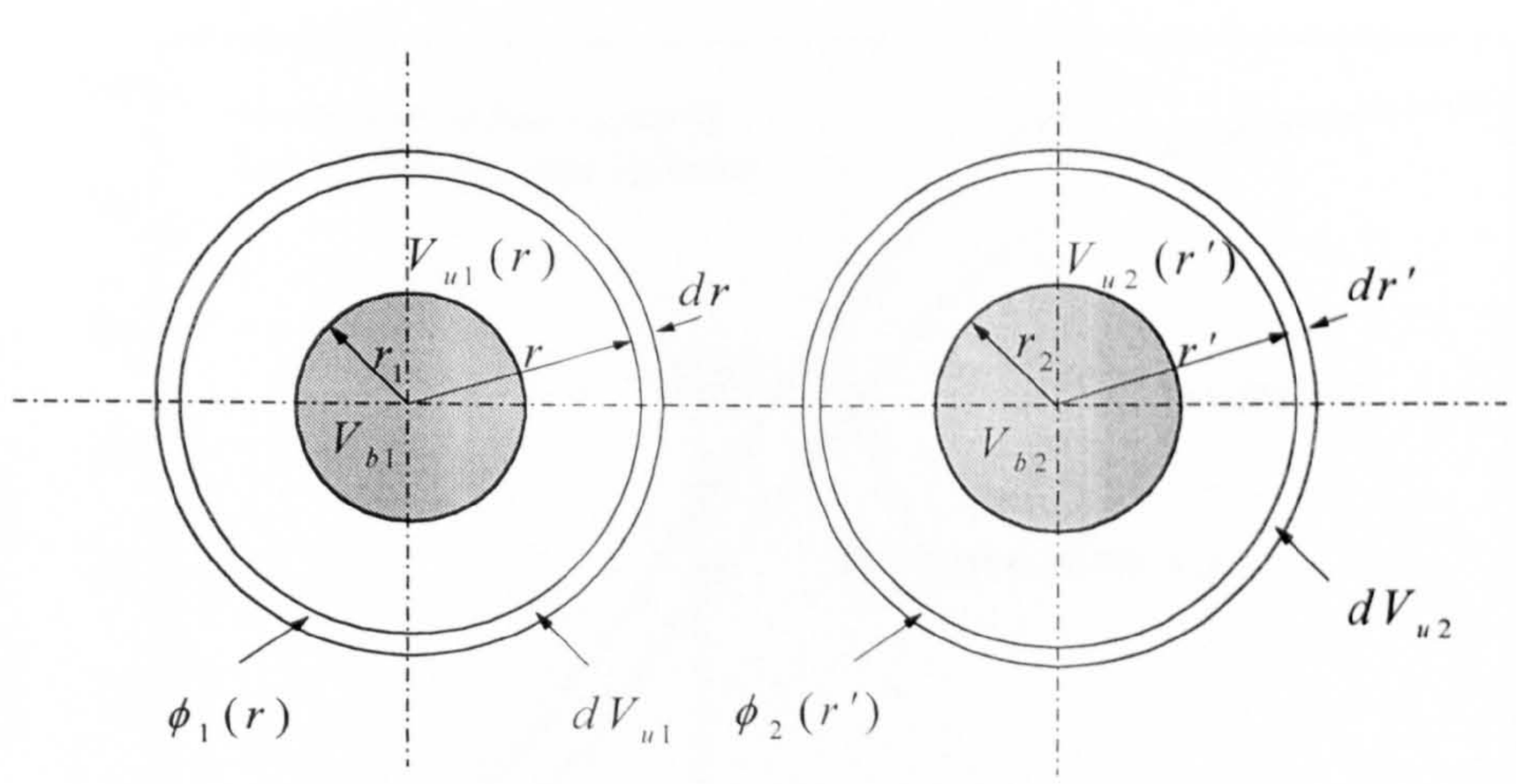

(a) Before expansion

(b) After expansion

Figure 6.32 The situations of burned zone and an infinitesimal elective annular element in unburned zone before and after burned gas expansion.

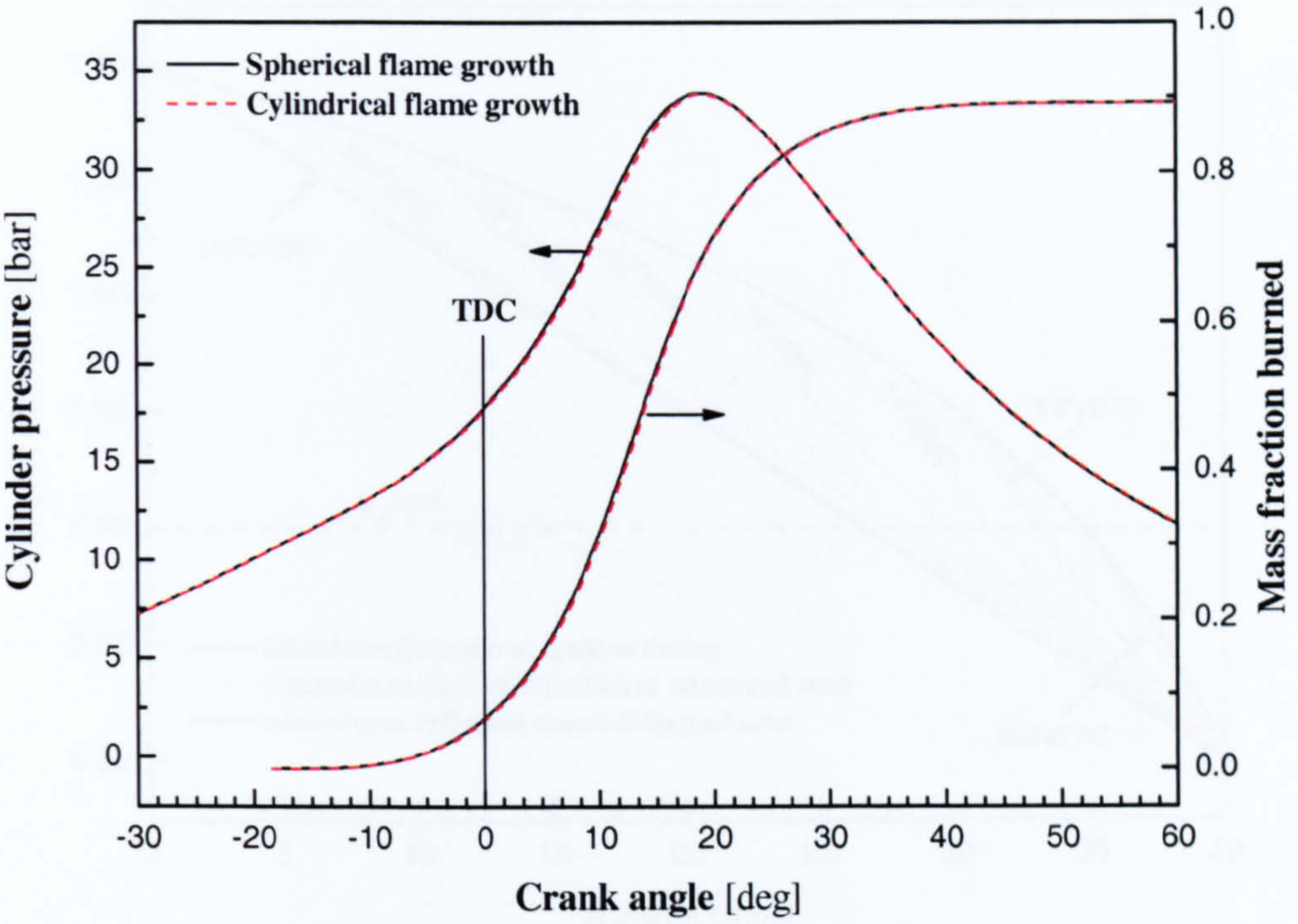

Figure 6.33 Cylinder pressure and mass fraction burned versus crank angle for the assumptions of spherical and cylindrical flame growths.

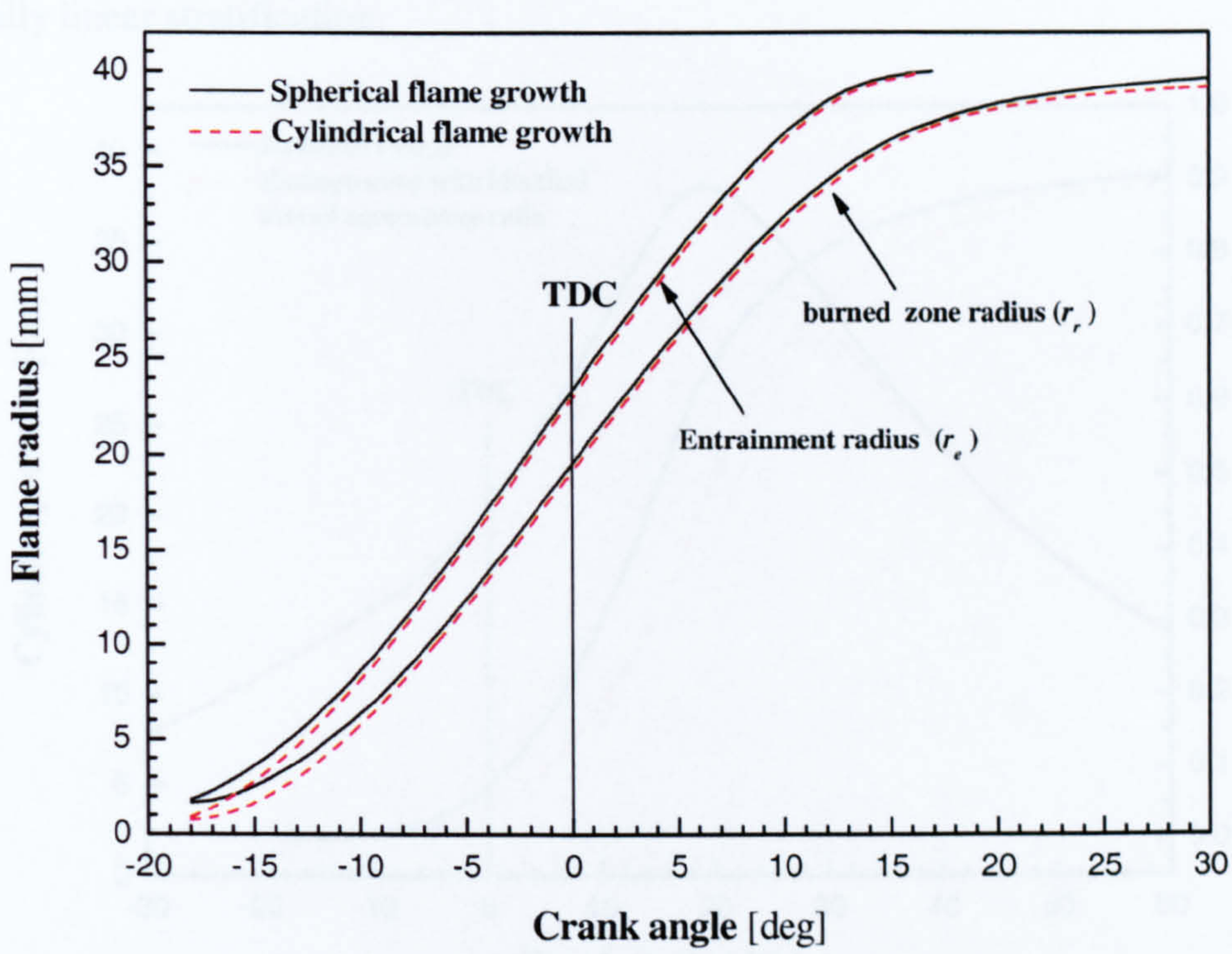

Figure 6.34 Entrainment and totally burned flame radii versus crank angle for the assumptions of spherical and cylindrical flame growths.

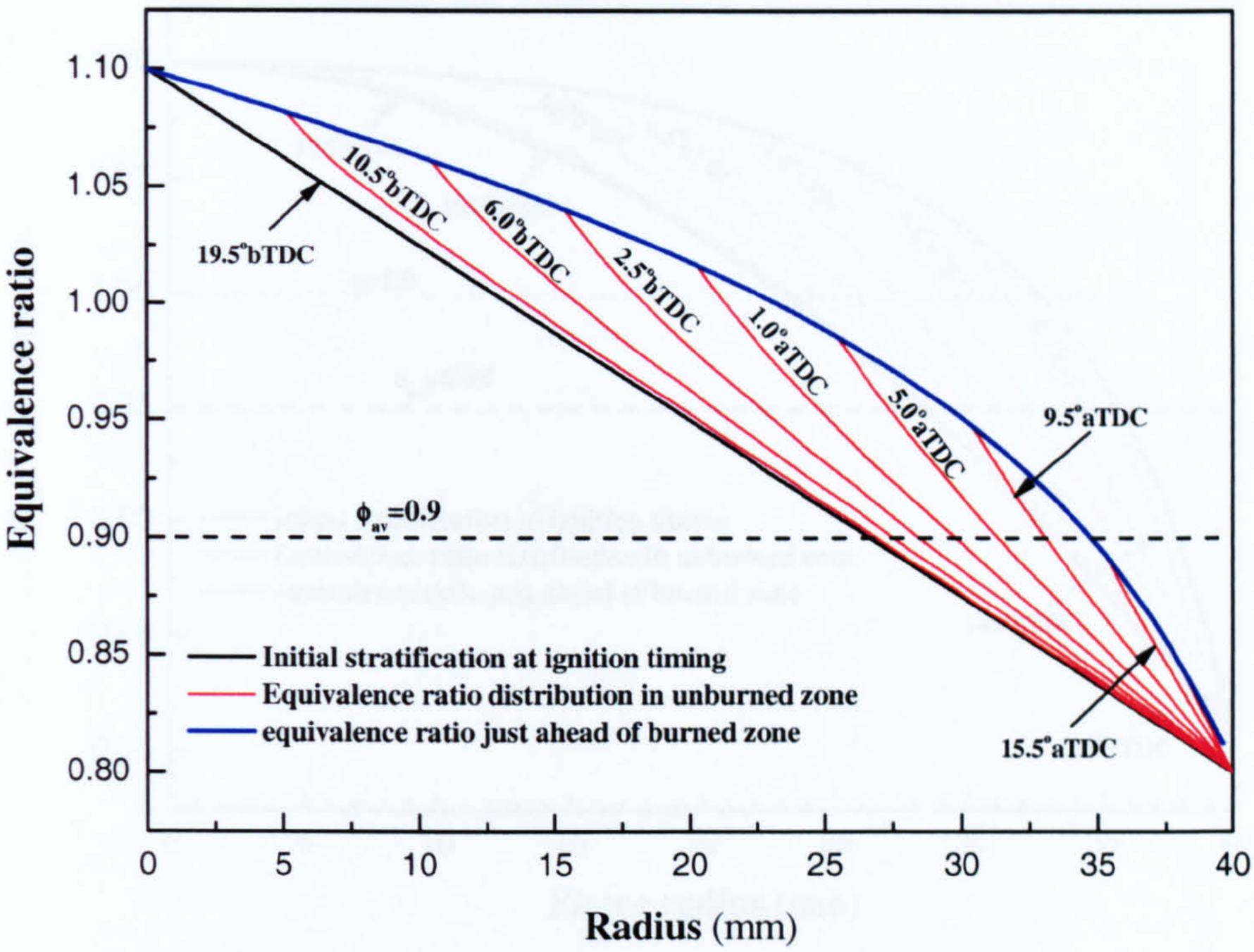

Figure 6.35 Distribution of equivalence ratio in unburned zone at different crank angle positions and equivalence ratio just ahead of burned zone versus radius for the initially linear stratification.

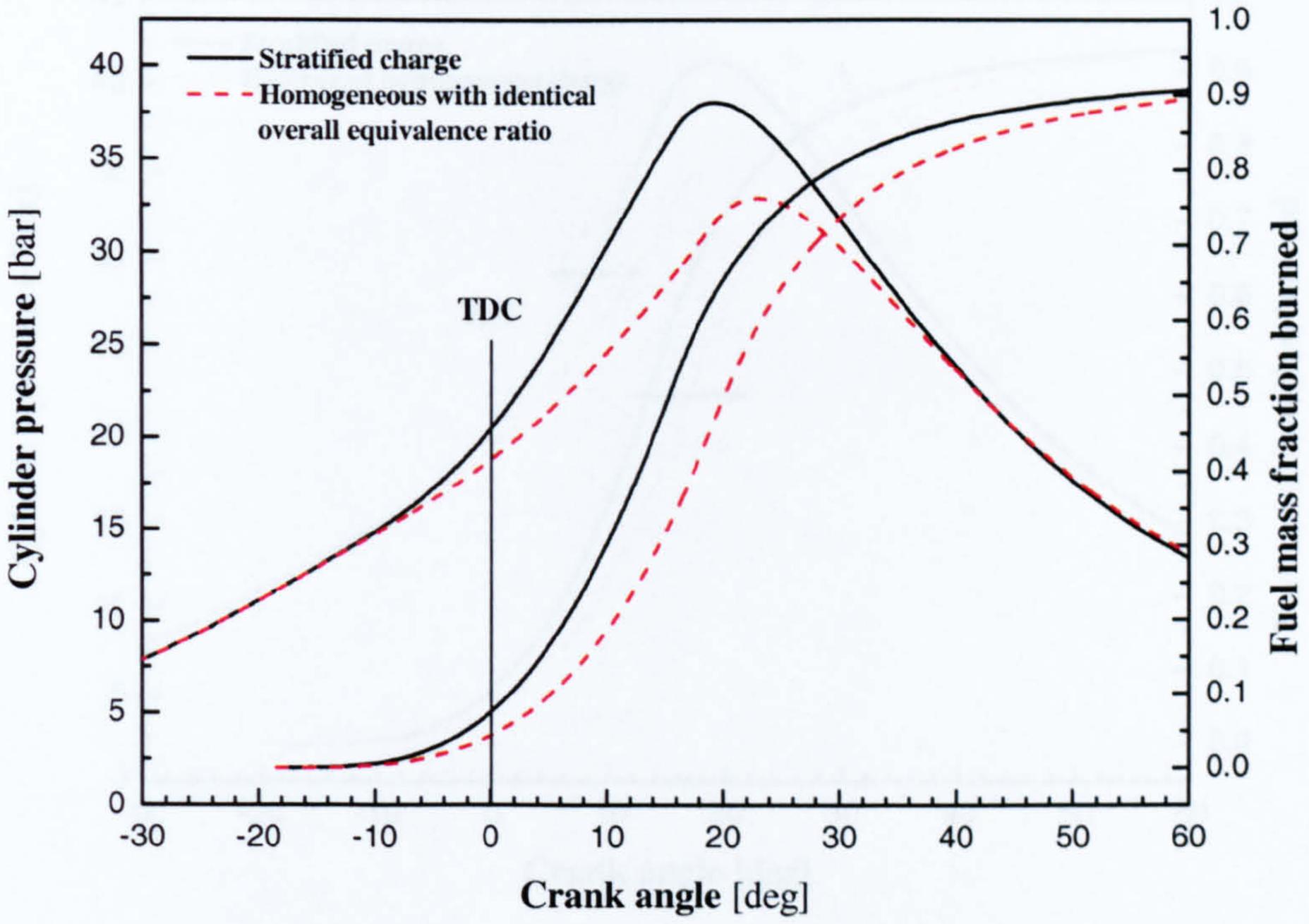

Figure 6.36 Cylinder pressure and fuel mass fraction burned versus crank angle for the stratified and equivalent homogenous charges.

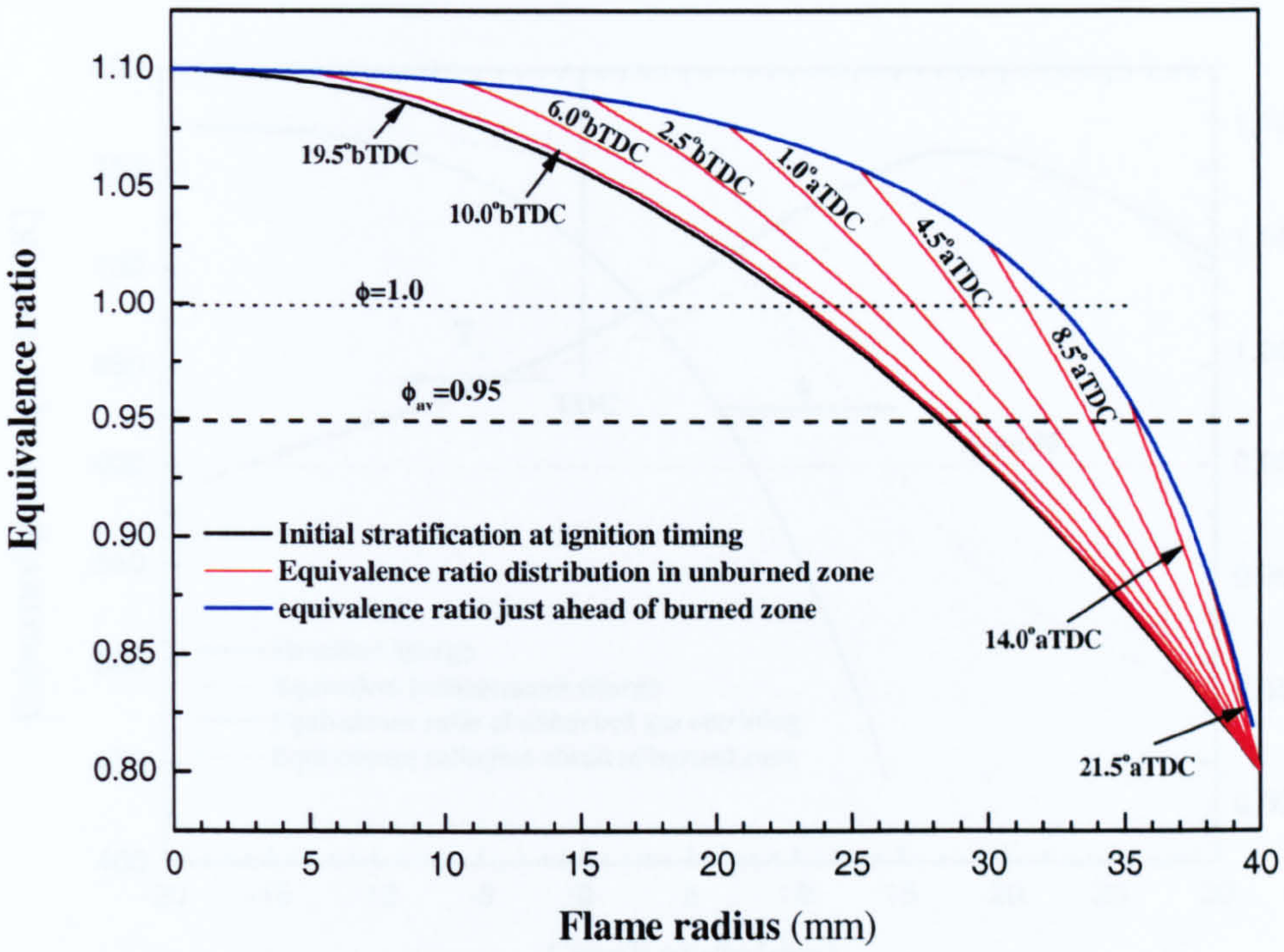

Figure 6.37 Distribution of equivalence ratio in unburned zone at different crank angle positions and equivalence ratio just ahead of burned zone versus radius for the initially parabolic stratification.

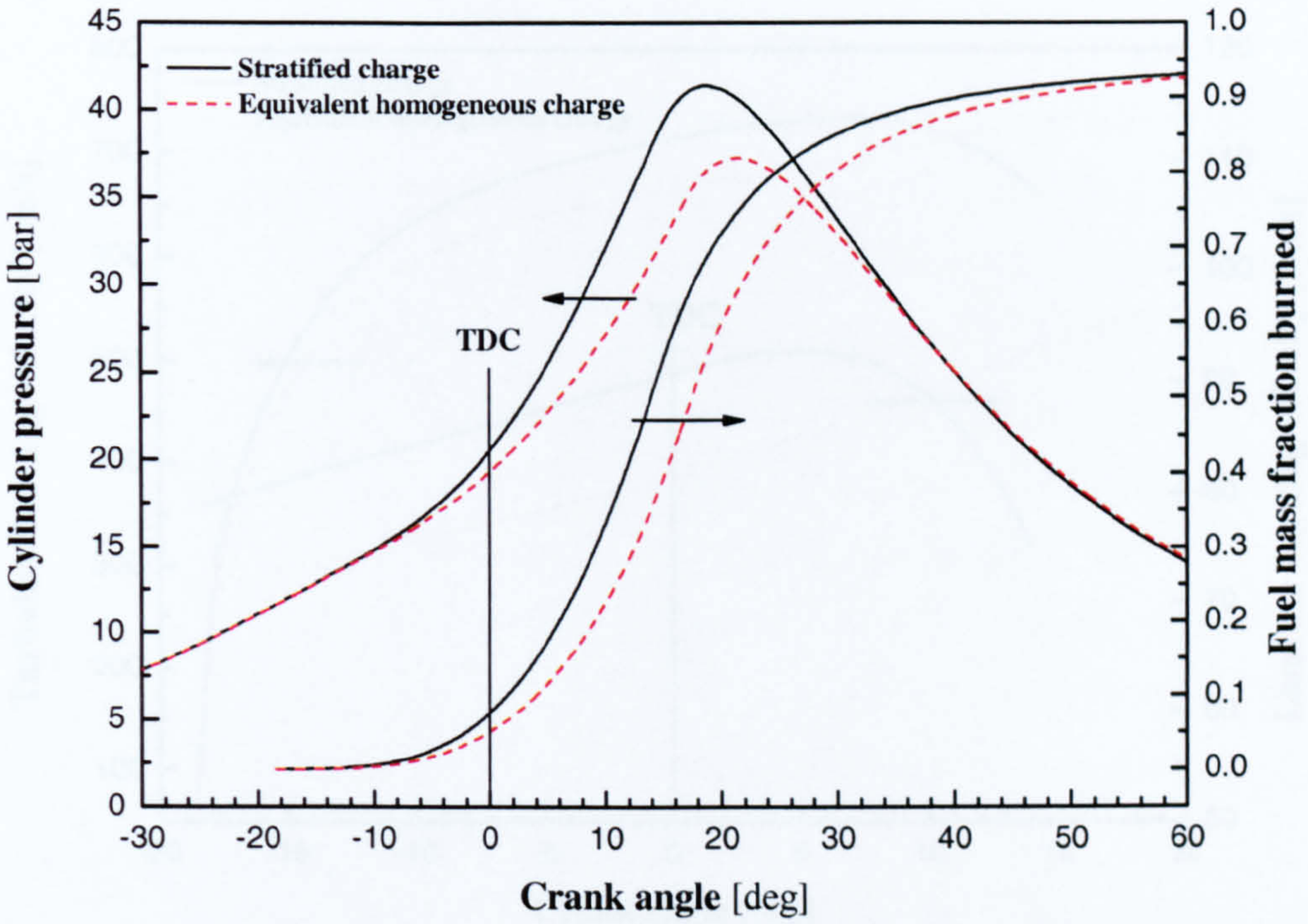

Figure 6.38 Cylinder pressure and fuel mass fraction burned versus crank angle for the stratified and equivalent homogenous charges.

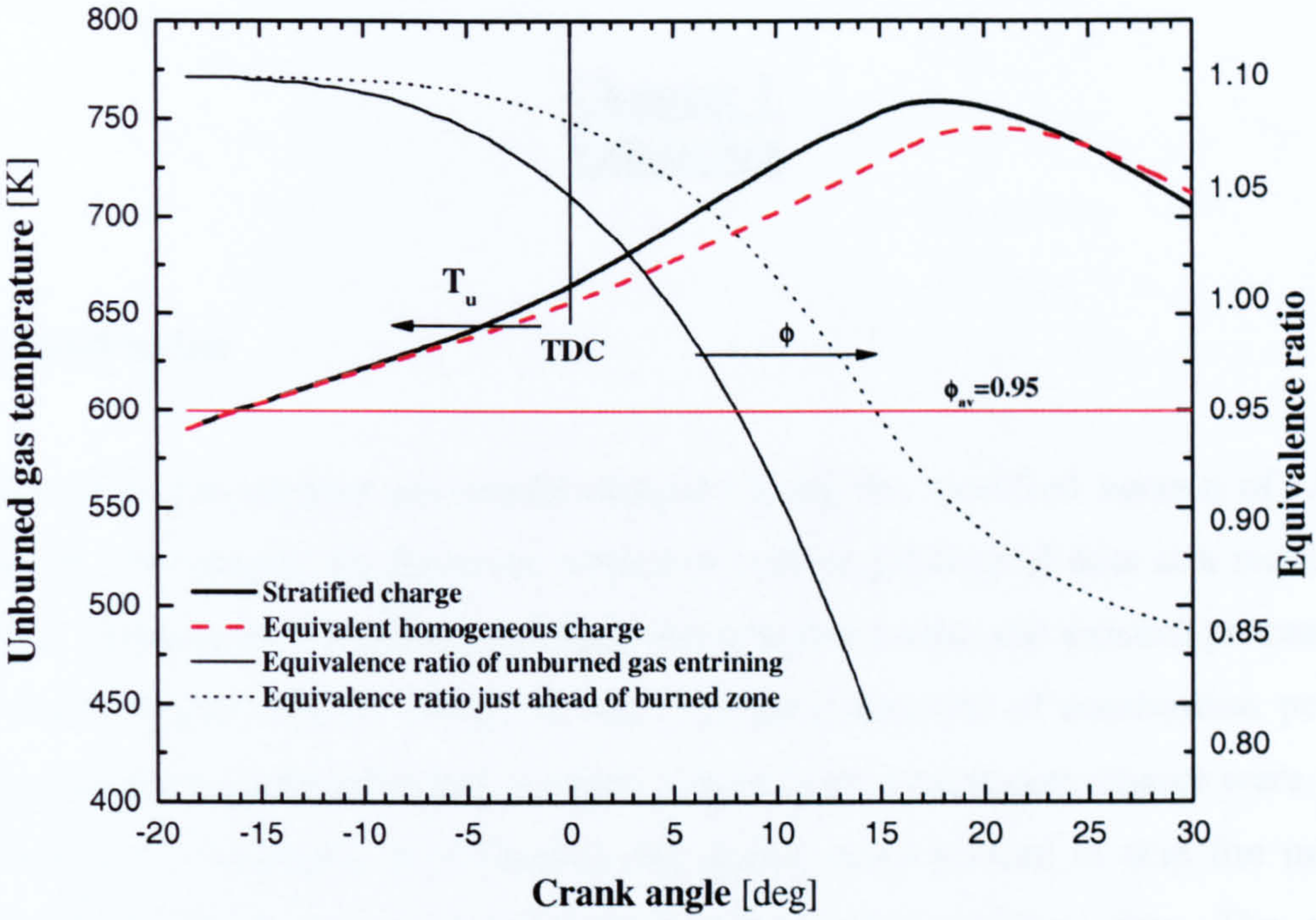

Figure 6.39 Unburned gas temperature and equivalence ratios at entrainment and burned flame radii versus crank angle for the stratified and equivalent homogeneous charges.

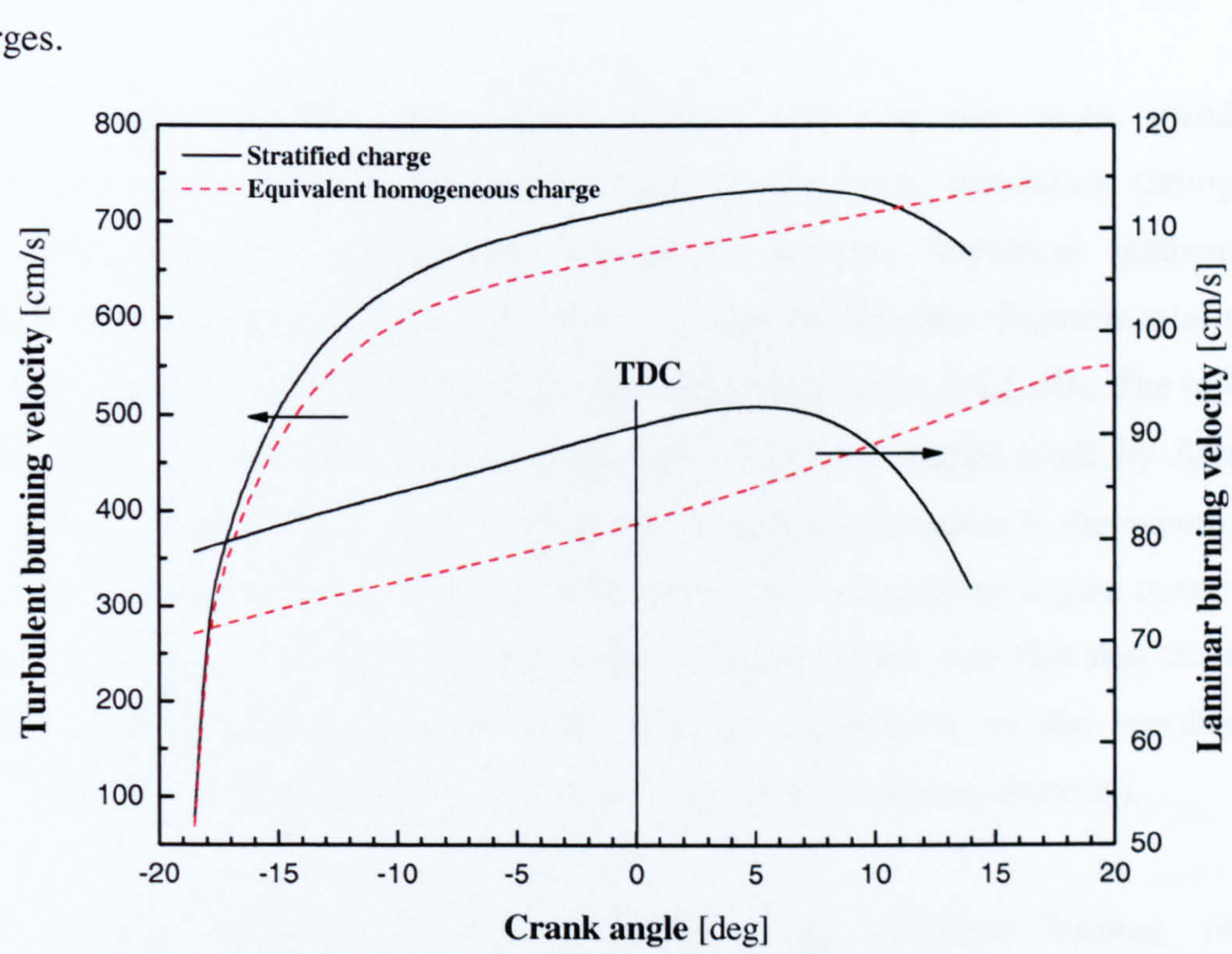

Figure 6.40 Laminar burning velocity at entrainment flame radius and entrainment turbulent burning velocity versus crank angle for the stratified and equivalent homogeneous charges.

Chapter 7
Validation

7.1 Introduction

Presented in this chapter are results obtained using the modified version of LUSIE (described in Chapter 6); these are compared with experimental data at a number of different conditions. To avoid modelling the complex intake and exhaust processes in the ported engine (which could, in turn, change prediction of combustion period), measured inlet temperatures and cylinder pressures at exhaust port closure were fed to the model. As described in Chapter 3, the engine was operated in skip fire mode hence the mixture was considered homogeneous and residual free. The model generated output data between Exhaust Port Closure (EPC) and Exhaust Port Opening (EPO).

A disc-shaped chamber with central ignition and zero-inlet angle (producing nominally zero mean velocity and isotropic homogeneous turbulence through the combustion space) permitted the use of an accurate analytical mathematical expression for spherical flame growth in a cylindrical chamber. Experimental values of rms turbulent velocity and integral length scale were input to LUSIE. The turbulent rms velocity ("intensity") measurements within LUPOE1 engine made by Atashkari (1997) and Jakubík (2002) were utilised. As described in Chapter 3, the experimental cylinder pressure and flame progress data were collected with the engine operating in skip fire mode, to minimise residual gases in firing cycles; this liberated the model from the ambiguities involved with correctly assignment of the residual gas temperature and species (i.e., the model was run for zero residual fraction).

The blowby constants, geometry (Section 6.3.4), turbulent burning velocity expression [Equation (6.34)], burn-up time [Equation (6.5)] and ignition kernel size were set to produce a good match to the experimental data at the reference condition.

Their values were then left unchanged when the model was used at other conditions. These setting are detailed in Sections 7.2 and 7.3.

Proper comparison of a model against experimental data requires extensive experimental information. From the experimental results, engine speed variation within a cycle (Section 5.6.2), correlation of late flame propagation (APF, Figure 5.54) and "delay" in spark ignition (Chapter 3) were available. These findings were incorporated into the model. Previous users of LUSIE had used a shape factor; this was not used here. The crucial effects of the incorporations were highlighted in Chapter 6. The comparison between model and experiment at the "reference" and other conditions are detailed in Sections 7.3 and 7.4.

To compare the Zimont model predictions with other turbulent burning velocity expressions in literature, two fully available correlations developed in Leeds referred to Leeds K and KLe (described in Section 6.5.2) were used. The comparisons are detailed, for both homogeneous and stratified charge variants, in Section 7.5.

7.2 Blowby model setting for motoring condition

Data for warmed-up engine, fuelled, motoring cycles were used to set the blowby sub-model constants. The blowby geometrical factors (crevices and orifices) were measured at ambient temperature. These included the dimensions of the cylinder, piston and rings. Uniform and identical temperatures for the cylinder, piston and rings (equal to the average of the measured wall temperature) were assumed; then the dimensions were corrected for the hot motoring condition. Shown in Table 7.1 are the computed values derived from the measurements at ambient temperature, values corrected for the hot condition and the values used in LUSIE to fit the experimental motoring data. The values used in the model were those calculated at $72^{\circ}C$ (wall temperature) except for the top land crevice (TLC) volume. This was increased to account for the other crevices connected to the cylinder in the optical engine (e.g. spark plug crevices, imperfect gasket fit, optical window and pressure transducer clearances etc); its value was tuned to match the motoring cylinder pressures of model and experiment. The comparison with the experimental motoring cycle, the model

predictions of mass loss and crevice pressures in the cycle are detailed in the sections below.

Table 7.1 The blowby geometric parameters at ambient and hot conditions and those used in LUSIE.

Blowby geometric parameters	Calculated from the Measurements at 20°C	Corrected for the hot condition 72°C	Preferred values to use in LUSIE
TLC cross-section area [mm^2]	62.6	55.9	55.9
TLC volume [mm^3]	970	889	1200
Ring orifice area [mm^2]	0.95	0.99	0.99
Inter-ring volume [mm^3]	353	338	338

7.2.1 Comparison with experimental motoring

A hot motoring test was conducted at 1500 *rpm*, with a stoichiometric mixture, after warming up the engine. Setting the blowby geometric parameters as mentioned above and applying the measured conditions (including inlet temperature, cylinder pressure at EPC, wall temperature and engine speed variation), the code was run in motoring mode. Shown in Figure 7.1 are the measured cylinder pressure and that predicted by the code, versus crank angle, for this motoring condition. Very good agreement can be seen between the experimental data and model prediction over the period between EPC and EPO. To magnify the differences, relative differences based on the experimental pressure data were calculated at each data point; Figure 7.2. The maximum relative difference over the whole period can be seen to be less than 3%; even less than 1.5% for the period between $50^\circ bTDC$ and $50^\circ aTDC$ (the crucial period in a firing cycle). The differences are considered reasonable in relation to

possible uncertainties associated with the cylinder pressure measurement (detailed by Kuratle et al., 1992) and the assumptions made in the model.

7.2.2 Additional motoring predictions

In addition to cylinder pressure, the model predicted the pressures in TLC, first and second inter-ring crevices; it also computed the net mass flow across TLC entrance and ring orifices. Shown in Figure 7.3 are these predicted pressures together with those measured with the absolute pressure transducer versus crank angle. The absolute transducer, which was principally for pressure referencing purpose, had connection with the inside of the cylinder through a 4 *mm* diameter passage (as seen in Figure 3.1). The ring thickness and inter-ring crevice height (2.5 and 3 *mm*, respectively) were smaller than the passage hole diameter. This could result in some leakage from a crevice to the next one when the ring partially covered the hole; also, the passage volume could influence the inter-ring pressures when the passage connection changed from one crevice to the next one. These types of influences were not included in the blowby sub-model; nevertheless, the predicted values over the connection periods between the absolute transducer and crevices (ranges "**A**, **A′**, **B** and **B″**" in Figure 7.3) are close to those measured.

Illustrated in Figure 7.4 are the predicted percentages of net mass loss (based on percentage of the cylinder mass at EPC timing) across the TLC entrance and ring orifices versus crank angle. The rate of mass loss from the cylinder to TLC is greater when the exhaust port is open to the TLC; the mass loss is 2.4% by the time the top ring closes the port (position "**D**"). The maximum mass loss reaches 9.5% at $5.4^\circ aTDC$ (~$6^\circ CA$ after the peak pressure position, due to the fact that the TLC loses mass to the first inter-ring crevice and the rate of change in cylinder pressure is lower around the TDC position). After that the flow direction at the TLC entrance reverses and there is mass gain to the cylinder yielding a minimum (post TDC) mass loss of 5.8% at $88.2^\circ aTDC$, when the exhaust port is open to the TLC. The return mass which has flowed across the first ring orifice reaches a peak value of 3.7% at $23.4^\circ aTDC$; after that it gradually reduces to 3.6% due to flow back to the TLC. There is ~3.5% mass lost to crankcase/exhaust across the bottom ring orifice.

7.3 Model constant setting at the reference condition

To set up the entrainment model at the "reference" condition, the initial kernel size (at a set elapsed time from ignition) was fixed at the value (0.2 *mm* diameter at 0.11 *msec*, 1°*CA*, after ignition) used previously (on the basis of detected kernel imaging) by Cairns (2001). The cylinder pressure and mean flame radius versus crank angle were modelled using LUSIE and compared to experiments. Three turbulent burning velocity expressions were used: the Zimont model, Leeds K and KLe correlations (Sections 6.5.3 and 6.5.2). For the Zimont model, good agreement was obtained at the reference condition with k_τ=0.6 and A=0.86 [Equations (6.5) and (6.34)]. The value of A is well within the range (0.4-1) suggested in the literature.

In this section and in Section 7.4, the results obtained with the Zimont model are compared with experimental results at the reference and other conditions. The results for the three alternative burning velocity expressions are then compared in Section 7.5.

7.3.1 Comparison between model output and experiment

Shown in Figure 7.5 are cylinder pressure versus crank angle diagrams for twelve "middle", "fast" and "slow" experimental cycles and output from the model at the reference condition associated with those of a motoring cycle and an absolute pressure record for one of the "middle" cycle. Good agreement can be seen between the "middle" cycles and model output during the compression stroke and for the combustion period up to the peak pressure position; after that differences occur; these are mainly associated with the effects of thermal shock (resulting in negative drift) on the dynamic pressure transducer. As discussed in Section 3.5.2, water cooling of the transducer was imperfect (because of space restrictions) and at the time the measurements were made, application of silicon grease to the transducer was not routinely adopted. The absolute transducer record of one of the "middle" cycle matches the modelled pressure, supporting the supposition that the measured experiment pressure levels were possible a little low in the expansion period.

The corresponding values of mean flame radius (derived from flame photography) versus crank angle for the twelve "middle", "slow" and "fast" cycles and the model are shown in Figure 7.6. The modelled results include application of the APF parameter. The agreement between the experimental and model results over the flame propagation period is considered good; although the modelled radius is slightly too low between 2 and $10^\circ aTDC$, when the recorded 2D flame imaging could be subject to 3D effect (with recorded flame radius in excess of the true mean value). The good fit at this reference condition is, of course, to be expected – as the model constants were tuned to match experiments at this condition. The test of the model is its ability to match other conditions with adjustment of the constants.

7.3.2 Sensitivity analysis of the combustion model

The turbulent burning velocity and burning rate expressions used in the combustion model [Equations (6.34), (6.4) and (6.5)] include three empirical parameters: laminar burning velocity, "rms" turbulent burning velocity and integral length scale. Data for these measurements are subject to uncertainty and, for the latter two, cyclic variation. To highlight the sensitivity of the model to the parameters, the effects of a $\pm 10\%$ variation in each parameter was considered at the "reference" condition.

In the combustion model, laminar burning velocity was used in both mass entrained and mass burned rates [Equations (6.34) and (6.4)]. Shown in Figure 7.7 are the cylinder pressure and mass fraction burned (based on instantaneous cylinder mass), unburned and burned gas temperatures, entrainment flame radius and turbulent burning velocity versus crank angle for $\pm 10\%$ change in laminar burning velocity at the "reference" condition. This change resulted in $\pm 10\%$ variation in peak pressure value with $\mp 1.5^\circ CA$ alteration in peak position [Figure 7.7(a)]; $\pm 15\ K$ and $\pm 25\ K$ in peak unburned and burned gas temperatures, respectively, with similar variation, $\mp 1.5^\circ CA$, in peak position for both [Figure 7.7(b)]. To express the effect of the change on entrainment flame radius, the crank angle duration for the achievement of 35 *mm* flame radius (when experimental flames usually began to hit the wall) was considered and turbulent burning velocity examined at that flame radius. The $\pm 10\%$ change in laminar burning velocity resulted in change of $\mp 1.5^\circ CA$ in crank angle

duration to achieve the radius (35 *mm*) and turbulent burning velocity alteration of about $\pm 8\%$ at that radius.

The diagrams obtained for the similar parameters with $\pm 10\%$ change in "rms" turbulent velocity and integral length scale are shown in Figure 7.8 and Figure 7.9, respectively. Change in "rms" turbulent velocity can only directly influence mass entrained rate (through turbulent burning velocity) while that in integral scale can affect both entrained and burned rates (main effect on the mass burned rate).

The $\pm 10\%$ change in "rms" turbulent velocity yielded $\pm 7\%$ variation in peak pressure value and $\pm 12\ K$ in peak unburned gas temperature with a $\mp 1.5^{\circ}\ CA$ alteration in peak position for both. The crank angle duration to achieve 35 *mm* flame radius varied $\mp 1.5^{\circ}\ CA$ and the corresponding turbulent burning velocity at the radius experienced $\pm 9\%$ change.

The $\pm 10\%$ change in integral length scale affected the peak pressure and peak unburned gas temperature. However, no significant change appeared in the developments of entrainment flame radius and burning velocity. The effect on peak pressure was $\mp 5\%$ with $\pm 1.0^{\circ}\ CA$ alteration in peak position. The change caused $\mp 7K$ change in peak unburned gas temperature associated with $\pm 0.5^{\circ}\ CA$ shift in the associated peak position.

7.3.3 Additional information from model

Set out in Figure 7.10 are the net mass flows (predicted by model) across the top land crevice (TLC) entrance and through the ring orifices at the reference condition. These are expressed as a percentage of the mass calculated to be contained in the cylinder at the time the piston crown just completely covers the exhaust port. The mass lost from cylinder between the time when the top of the piston and the upper piston-ring pass the exhaust port on the compression stroke is 2.4%; this value increases to 6.7% by ignition and reaches 19% at $23^{\circ}\ aTDC$ ($4^{\circ}\ CA$ after the peak pressure position). During expansion, the cylinder pressure drops below that in the TLC; resulting in flow back into the cylinder. By the time the top ring opens to the exhaust port

(position B'), ~6.5% of mass returns to the cylinder. Over the period between positions B' and A', the exhaust port is open to the TLC; within this period, strong flows occur from cylinder to the TLC and from the TLC to the exhaust due to a large pressure difference between cylinder and exhaust; this results in a 9.5% mass lost from cylinder in the period. Finally, 6.7% mass leaks through the bottom ring gap and the rest loses from crevices to the exhaust.

Definition of mass fraction burned (MFB) depends upon the definition of reference mass; this is particularly a problem when (as in this engine) there is significant mass loss. Three definitions of reference mass were considered based on: (i) total burned mass, (ii) cylinder mass at ignition timing and (iii) instantaneous cylinder mass. Shown in Figure 7.11 are the mass fractions burned against crank angle for these different reference masses. There are large differences between MFB based on cylinder mass at ignition timing and the other two; the difference is as much as ~0.15 at $60^\circ aTDC$. The lower values for definitions (ii) and (iii) are associated with incomplete combustion of the cylinder charge and cylinder mass exchange due to the crevice flow (blowby). Some unburned gas entrains into the flame front late, so there is insufficient time for it to burn, in addition to the cooling effect due to expansion; after peak pressure in the expansion period, some mass returns to the cylinder from crevices – this may be too cold to burn properly. The three definitions give identical results if blowby is ignored and all cylinder charge burns. It is apparent that mass fraction burned must be clearly defined for the case of a "leaky" engine.

Unburned and burned gas temperatures during combustion period are crucial parameters for the prediction of auto-ignition and exhaust gas emissions. Shown in Figure 7.12 are the modelled unburned and burned gas temperatures versus crank angle at the reference condition. Calculated unburned gas temperature increases from 572 K at ignition timing to a peak value of 726 K at $17^\circ aTDC$; with the increase due to compression associated with piston motion and combustion; after that it reduces to 430 K at $60^\circ aTDC$ because of expansion, heat transfer and relatively cold gas (350K) returning from the TLC. The computed burned gas temperature has a value of 2477 K at $18.5^\circ bTDC$ (just after ignition), increases to a peak value of 2634 K at $15^\circ aTDC$

and then decreases (due to expansion and heat transfer) to a value of 2080 K at $60^\circ aTDC$.

7.4 Validation at other conditions

With the blowby settings and model constants fixed identical to those at the "reference" condition, the code was run for different engine speeds and equivalence ratios. The kernel size at a fixed time from ignition was assumed the same as at the "reference" condition. The results are presented in the following sections.

7.4.1 Engine speed

- ***Low engine speed***

Shown in Figure 7.13 are cylinder pressure versus crank angle diagrams for six selected experimental cycles (two representative middle, fast and slow cycles) and a motoring cycle at a low engine speed (nominally, 750 *rpm*). Also shown are the associated absolute transducer record for a middle cycle and modelled result. Good agreement can be seen between the model and middle cycles until peak pressure; after that, modelled pressure is again above experimental. As before, this is thought to be associated with thermal drift of the dynamic transducer – since agreement with the absolute pressure record late in the cycle was again very good.

Shown in Figure 7.14 are the corresponding mean flame radii versus crank angle data for the six experimental and the modelled cycles. The model predicts greater flame radius in the early part of flame development. Because of lack of detailed information on kernel development, an identical kernel size (at defined time period elapsed from ignition) was used for all conditions modelled. Early flame development could be affected by change in ignition timing and engine speed, although later work by a colleague using close up Schlieren photography suggests that this is not so (Murad, 2003). Higher (entrainment) flame radius predicted by model suggests faster entrainment (Figure 7.14); however, the related burning rate is slower, such that the modelled cylinder pressure is very close to the experimental middle cycles (Figure 7.13); as a result, it could be argued that the model suggests greater flame brush

thickness than would pertain in the experiments at the low engine speed condition. The entrainment model used in this work adopts on two key equations. One of these is for entrained mass rate [Equation (6.1)], which directly influences mean (entrainment) flame radius rather than cylinder pressure. The other is for mass burning rate [Equation (6.4)], which directly influences cylinder pressure development. The effects of controlling parameters (such as u', u_l, α and l) are not similar for these two equations; therefore, even when predicted mean flame radii match the experimental values (using the assumptions made in the model) there is no guarantee of a similar match in cylinder pressure development and vice versa.

- ***High engine speed***

Set out in Figure 7.15 are cylinder pressure against crank angle diagrams for twelve selected cycles (four representative middle, fast and slow cycles), a motoring cycle and model output at a higher engine speed condition (2000 *rpm*). As previously, the absolute pressure record of a middle cycle has been included to demonstrate the magnitude of possible thermal drift in the dynamic transducer. The model output matches the fast cycles most closely; with peak cylinder pressure occurring $2^{\circ}CA$ earlier and 5 *bar* higher than for typical middle cycles.

Illustrated in Figure 7.16 are the corresponding mean flame radii against crank angle. Unlike modelled pressure (which aligned most closely with fast cycles), predicted flame radius was closer to those of the middle cycles. It should be noted that the 3D effect (discussed in Section 7.3.1) could be slightly more marked at the high engine speed condition, due to greater turbulence intensity.

7.4.2 Mixture strength

- ***Lean condition***

As outlined in Chapter 5, experimental data were also generated at a lean condition; with $\phi = 0.8$, ignition timing $31^{\circ}bTDC$ and a set engine speed of 1500 *rpm*. Set out in Figure 7.17 are cylinder pressure versus crank angle data output from the model and experimental information for nine cycles (three typical middle, fast and slow cases) at

this lean operating condition. Also set out in this figure are motoring cylinder pressure and absolute transducer records for one of the middle cycles. The model cylinder pressure lies close to the experimental middle cycles, with a peak value of 30.9 *bar* at $16^{\circ} aTDC$.

The film data at this condition were captured using a Kodak Ektapro camera with a framing rate of 4500 *fps*. However, there was no framing record to assist synchronisation with the pressure records with this camera; the first frame after ignition was assessed on the basis of visible spark light and hence synchronisation was subject to a maximum $\pm 2^{\circ} CA$ uncertainty at 1500 *rpm*. In addition, natural light emission was very weak at this lean condition early in flame development, even though a small quantity of sodium ethylate was dissolved in fuel to increase light emission (as Hynes, 1986). These effects may have resulted in the retarded mean experimental flame radii c.f. those predicted, particularly early in flame development, Figure 7.18. Nevertheless, the agreement is considered satisfactory given the possible uncertainties in the experimental data and the assumptions in the model.

- ***Rich condition***

Experimental data were also gathered for a rich condition, with $\phi = 1.1$, ignition timing at $18^{\circ} bTDC$ and a nominal engine speed of 1500 *rpm*. Shown in Figure 7.19 are model output and experimental cylinder pressure records, with nine selected experimental cycles (three representative middle, fast and slow cases). Once more, good agreement can be seen between the middle cycles and the model until the peak pressure position; as noted before, after this, the experimental data are subject to thermal drift error associated with transducer.

As in the "lean" case, film data were captured using the Kodak Ektapro camera; with resultant $\pm 2^{\circ} CA$ uncertainty in frame synchronisation with pressure recording at 1500 *rpm*. Set out in Figure 7.20 are the mean flame radii for the model and the nine experimental cycles. The predicted flame radii are within the range of experimental scatter.

7.4.3 Compression ratio

Using another disc-shaped head (with overhead optical access but no side windows) fitted to the LUPOE1 engine, "moderate" (10.2) and "high" (12.4) compression ratio (CR) conditions were created by adjusting the clearance height. Experimental simultaneous cylinder pressure and flame position data were captured at these compression ratios, with all other settings identical to those at the reference condition (Chapter 5). The film data for these conditions were captured using a Kodak Ektapro camera.

Jakubík (2002) attempted to measure "rms" turbulent velocity for the high compression ratio condition using LDV. However, due to the small clearance height at the TDC position, he experienced significant noise in his LDV signals (associated with reflected light) and was unable to obtain reliable data over the crank angle period of interest. Therefore, the "rms" turbulent velocities measured at 7.6 compression ratio were again adopted in the model for the "moderate" and "high" compression ratio computations.

- ***Moderate compression ratio***

Set out in Figure 7.21 is the cylinder pressure versus crank angle record generated by the model, nine representative fast, middle and slow experimental cycles together with a motoring cycle and associated absolute pressure record for one of the middle cycles at CR=10.2. Before and slightly after ignition, there is a good agreement between model prediction and the experimental data; thereafter, predicted pressure is somewhat too high (e.g. 13% greater than experimental peak value). The assumption of spatially uniform turbulence and the use of the turbulent intensity measured at low compression ratio may be invalid for the "moderate" (CR=10.2) compression ratio. It should be noted that the cylinder head used for the "moderate" and "high" compression ratios was equipped with a water-cooled dynamic transducer, giving little thermal drift.

The corresponding mean flame radii against crank angle for the experimental cycles and model are shown in Figure 7.22. Over whole propagation period, the radii

predicted by the model (as expected from pressure diagrams) were above those of the experimental cycles. Also, it should be noted that the synchronisation between experimental mean flame radius and crank angle position was subject to maximum $\pm 2^\circ CA$ error in the medium compression ratio (CR=10.2) condition.

- ***High compression ratio***

Similarly, shown in Figure 7.23, is the simulated cylinder pressure history together with those of nine selected experimental cycles at the high compression (CR=12.4) ratio condition. As at the "moderate" compression ratio, agreement is very close before TDC; however, after this, pressure is over predicted (with 24% greater peak pressure than experimental peak value). At this condition, the clearance height at TDC was only 4.6 *mm*; this may make the assumption of spatially uniform turbulent velocity invalid. The model prediction might have been subject to greater uncertainty in input laminar burning velocity at the high compression ratio conditions.

Illustrated in Figure 7.24 are mean flame radii for the model output and the nine selected cycles. Until $2^\circ bTDC$, the model prediction is within the scatter of the experimental cycles; thereafter, it is above the experiment, in accord with the pressure history.

As seen in Figure 7.24, the mean flame radius predicted by the model at any given crank angle is close to that noted in fast cycles; however, the corresponding predicted cylinder pressure is significantly higher, Figure 7.23. Reasons for such discrepancies, are as advanced in the discussion of the low engine speed case, Section 7.4.1.

Sensitivity analysis in Section 7.3.2 showed the combustion model to be sensitive to "rms" turbulent and laminar burning velocities. Although for the high compression ratio, Jakubík (2002) could not obtain reliable "rms" turbulent velocity data in the crank angle period of interest ($10^\circ bTDC$ - $20^\circ aTDC$), due to inadequate number of samples attainable (Section 2.3), he observed lower "rms" turbulent velocities than those with low compression ratio (CR=7.6) at the early crank angle positions for which he could obtain reliable data. To consider this effect, the "rms" turbulent velocities in the relevant period for combustion were estimated for the "moderate"

and "high" compression ratio conditions. For these estimations, the measured $u' - \theta$ diagram at 7.6 compression ratio was vertically shifted using an estimated difference for the reliable measurement region of crank angle at the "high" compression ratio. For the amount of shifting at the "moderate" compression ratio, a linear interpolation based on clearance height at TDC position was employed. These estimations were adopted in the model for revised computations of the "moderate" and "high" compression ratio conditions.

Set out in Figures 7.25, 7.26, 7.27 and 7.28 are the model output (with the estimated "rms" turbulent velocities) and experimental results for cylinder pressures and flame radii versus crank angle at the "moderate" and "high" compression ratios. The estimated "rms" velocities resulted in significantly reduced cylinder pressures predicted by the model; nevertheless, the model predictions still were higher (7% and ~9% greater peak pressure values than those of experiments at CR=10.2 and 12.4, respectively). This suggests that errors in measured "rms" turbulent velocity were not the only source of the greater pressure predictions.

At the time of data processing, lower cylinder pressures were initially obtained for these two higher compression ratio conditions. Then, the related dynamic transducer was calibrated against a highly accurate absolute transducer by creating dynamic pressure (0-15 *bar*) in a constant volume bomb. This calibration suggested that an ~24% increase in the linearity coefficient of the transducer was required over the pressure range. The pressure data shown were generated using this adjustment to the pressure data. However, the data are regarded as suspect and it is recommended that the quality of the collected pressure data at the "moderate" and "high" compression ratios be checked by repeating a number of firing tests using a well-calibrated transducer (time constraints prevented the current author from undertaking these additional tests).

7.5 Zimont model, Leeds K and KLe correlations

The predictions using the "Zimont" turbulent burning velocity expression were compared with those using the pre-existing Leeds ("*K*" and "*KLe*") turbulent burning

correlations available within LUSIE. This comparison was carried out for both homogeneous and radially stratified charge cases.

7.5.1 Homogeneous case

- ***Reference condition***

Shown in Figure 7.29(a) are cylinder pressure and mass fraction burned (based on instantaneous cylinder mass) in terms of crank angle using the Zimont Model, Leeds *K* and *KLe* expressions for u_t in LUSIE at the reference condition. The related entrainment flame radii and turbulent burning velocities versus crank angle are set out in Figures 7.29(b) and (c). In each case the u_t expressions were optimised to give good agreement with experiment at the reference conditions. This described for Zimont model, in Section 7.3. For the Leeds *K* and *KLe* correlations, it proved necessary to adopt multiplying factors of 1.3 and 1.78, respectively, to the values of u_t.

For the Zimont model and Leeds *KLe* correlation, the overall "shape" of the burning velocity versus crank angle plots were similar, as seen in Figure 7.29(c). The calculations using the Leeds *K* correlation exhibit lower turbulent burning velocity before $6^\circ bTDC$ and greater after that; the effect of this is reflected in cylinder pressure and flame radius developments, Figures 7.29(a) and (b). Nevertheless, optimised for this running condition, the three burning velocity expressions yield very similar cylinder pressures – with a maximum difference of 1.5 *bar* at any given crank angle over the combustion period and a peak pressure of ~34.2 *bar* at $18.5^\circ aTDC$' in each case.

Having optimised model output at the reference condition, the LUSIE code was run for each turbulent burning expression (without further adjustment/optimisation of the parameters of each expression) to explore their predictive capacity over the range of experimental conditions available for LUSIE. The output data at low engine speed (750 rpm), high engine speed (2000 rpm), rich ($\phi = 1.1$), lean ($\phi = 0.8$), "moderate" (10.2) and "high" (12.4) compression ratio conditions are shown in Figures 7.30 through 7.35.

- ***Varying engine speed***

The Leeds *KLe* correlation and the Zimont expression for u_t yielded very similar results at both 750 and 2000 *rpm*. With the Leeds *K* expression for u_t, modelled pressure crank angle diagrams gave reasonable agreement at both engine speeds (as for the intermediate reference speed), albeit with slightly slower pressure development in the early stages. This is more evident in the slower initial entrainment flame radius development curves. This is associated with under-prediction of u_t early in the combustion event. Pressure recovery late in the cycle is associated with compensating over prediction of u_t late in the cycle, Figures 7.30(c) and 7.31(c).

- ***Varying mixture strength***

With rich mixture ($\phi = 1.1$), the turbulent (entrainment) burning velocities computed using the *KLe* expression are slightly lower than those with Zimont model expression early in the cycle. Later in the combustion event, the *KLe* values of u_t are significantly above those from Zimont model. As a result, pressure development and entrainment of flame radius are somewhat over predicted using the *KLe* correlation.

As before, the Leeds K expression yields low early, and high late, u_t values. Overall, this results in better fit to the experimental pressure diagrams than with the *KLe* correlation – fits to observed flame radius are not good.

In comparison with the results at the "reference" condition, the lean mixture results show substantial differences between the Zimont and *KLe* expressions associated with a large variation in Lewis number for the isooctane-air mixture. In the case of the Leeds *K* correlation, this variation results in a shifting from one correlation graph to the other (Abdel-Gayed et al., 1987).

- **Varying compression ratio**

In both "moderate" and "high" compression ratio conditions, all the three expressions predict greater peak pressure than those of the experimental cycles. The Leeds *K* correlation results in early slower and faster later flame and pressure development;

whereas the outputs using the Leeds *KLe* correlation and Zimont model yielded results close to each other. Due to the lack of reliable LDV measurements for these conditions, "rms" turbulent velocities were "guessed" as described in Section 7.4.3.

7.5.2 Stratified charge case

The output generated using the Zimont model and the Leeds *K* and *KLe* correlations was also compared for the radially stratified case. For this comparison, parabolic stratification (considered more practicable and as defined in Sub-section 6.7.4(ii)) was selected.

Illustrated in Figure 7.36 are cylinder pressure and fuel mass fraction burned versus crank angle for the three burning velocity expressions. The *KLe* correlation results in faster burning, leading to a peak pressure value of 44.0 *bar* at 17.5° *aTDC* ; whereas the "Zimont" model and the *K* correlation produce results close to one another (with lower pressure value until 10.5° *aTDC* and slightly greater after that) with a peak pressure value of ~41.6 *bar* at 18.5° *aTDC* ; this can also be seen on fuel mass fraction burned (FMFB) diagrams. Shown in Figure 7.37 are the entrainment flame radii versus crank angle for the three expressions. The *KLe* output data show mostly greater values (with radii very close to those computed with the "Zimont" model until ~8° *bTDC*); the *K* correlation computations exhibit smaller radii until 7° *aTDC* , followed by slightly higher values than when applying the "Zimont" model.

Set out in Figure 7.38 are the predicted turbulent burning velocities and the estimated equivalence ratio at entrainment flame radius versus crank angle for the three expressions. Both *K* and *KLe* correlations result in discontinuous turbulent burning velocity curves. The highlighted horizontal and vertical help lines show that these discontinuities occur when the equivalence ratio at the entrainment flame radius is equal to one. When mixture quality varies from rich to lean, a substantial change occurs in Lewis number for the deficient reactant in isooctane-air mixture. This significant change results in considerable variation in the prediction of turbulent burning velocity by the *KLe* correlation, in which Lewis number is one of the key factors. In the case of Leeds *K* correlation, a switch from one chart to another is

involved, (Abdel-Gayed et al., 1987). Experiments using a fan-stirred bomb (Ormsby et al., 2003) have confirmed that such a discontinuities in the value of u_t with equivalence ratio at given u' is unrealistic.

7.6 Conclusions

A good level agreement was observed between LUSIE computations employing the "Zimont" model and experimental data for a range of equivalence ratio and engine speeds for which reliable "rms" turbulent velocities were available. For "moderate" and "high" compression ratios, the model predicted faster pressure development, even when "rms" turbulent velocities were adjusted to allow for uncertainty in the limited LDV data available. However, the measured cylinder pressure data were a little suspect for these high compression ratio cases.

Sensitivity analysis demonstrated that model computations are very sensitive to input laminar burning velocity and "rms" turbulent velocity. A $\pm 10\%$ change in laminar burning velocity, "rms" turbulent velocity and integral length scale resulted in ± 10, ± 7 and $\mp 5\%$ change in peak cylinder pressure at the "reference" condition, respectively.

For various engine speeds with a stoichiometric mixture, LUSIE computations using the Leeds *K* and *KLe* correlations yielded results close to those generated with the "Zimont" model. However, significant differences were observed at non-stoichiometric equivalence ratios. Under lean conditions, output generated using both *K* and *KLe* correlations suggested slower pressure development; for rich conditions, the *KLe* correlation resulted in faster development than observed experimentally. These differences seemed to be associated with Lewis number depending in the correlations; *Le* varied significantly from lean to rich condition for isooctane-air mixtures. Differences were also observed between the computed turbulent burning velocity development generated using the *K* correlation and those from the "Zimont" model and *KLe* correlation.

Application of the Leeds *K* and *KLe* correlations to the radially stratified charge case resulted in discontinuities in turbulent burning velocity as the equivalence ratio

reached stoichiometric; this was associated with a sharp change in the value of Lewis number going from rich to lean conditions.

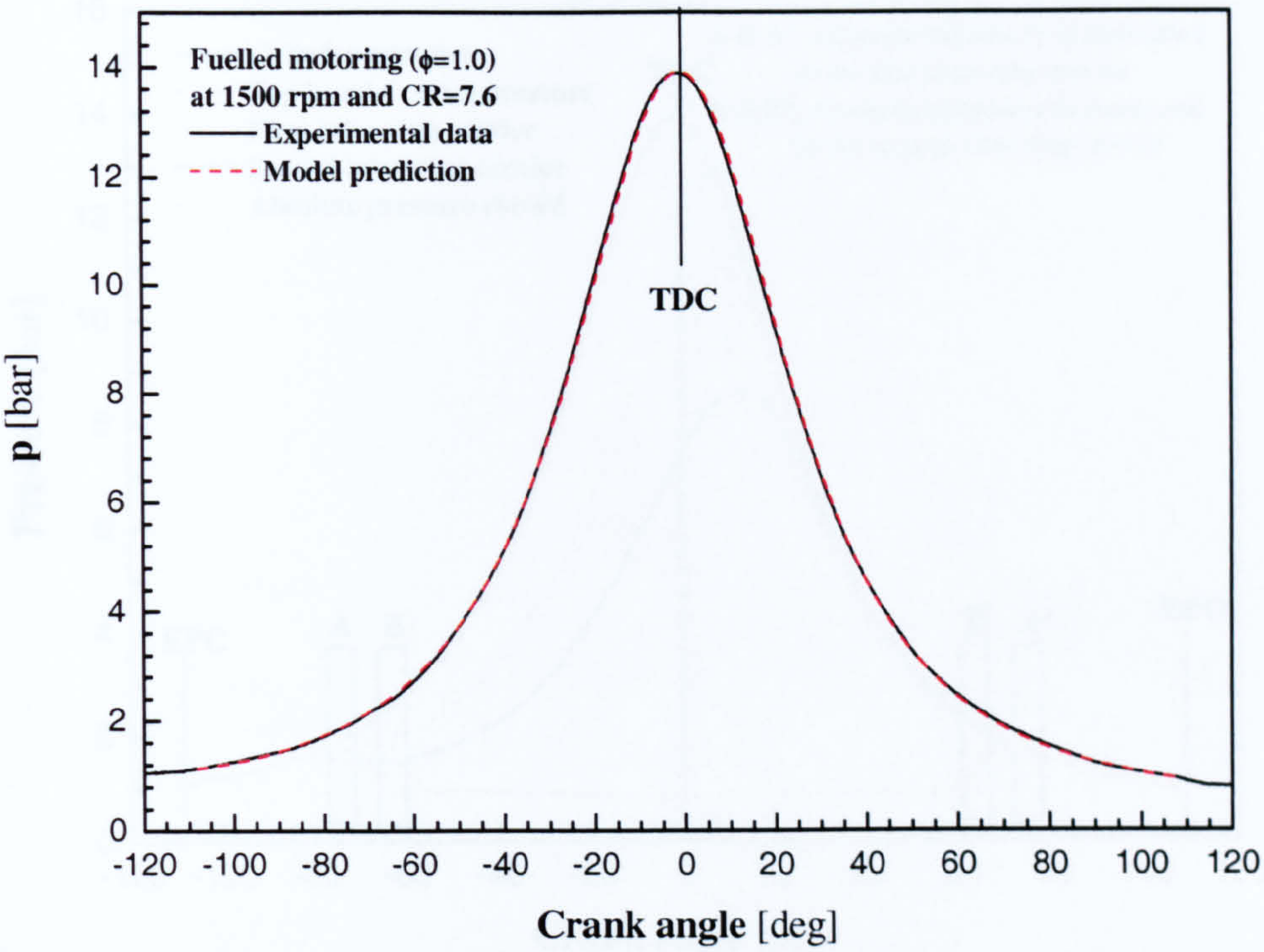

Figure 7.1 Cylinder pressure versus crank angle for the experimental data and model prediction in motoring condition.

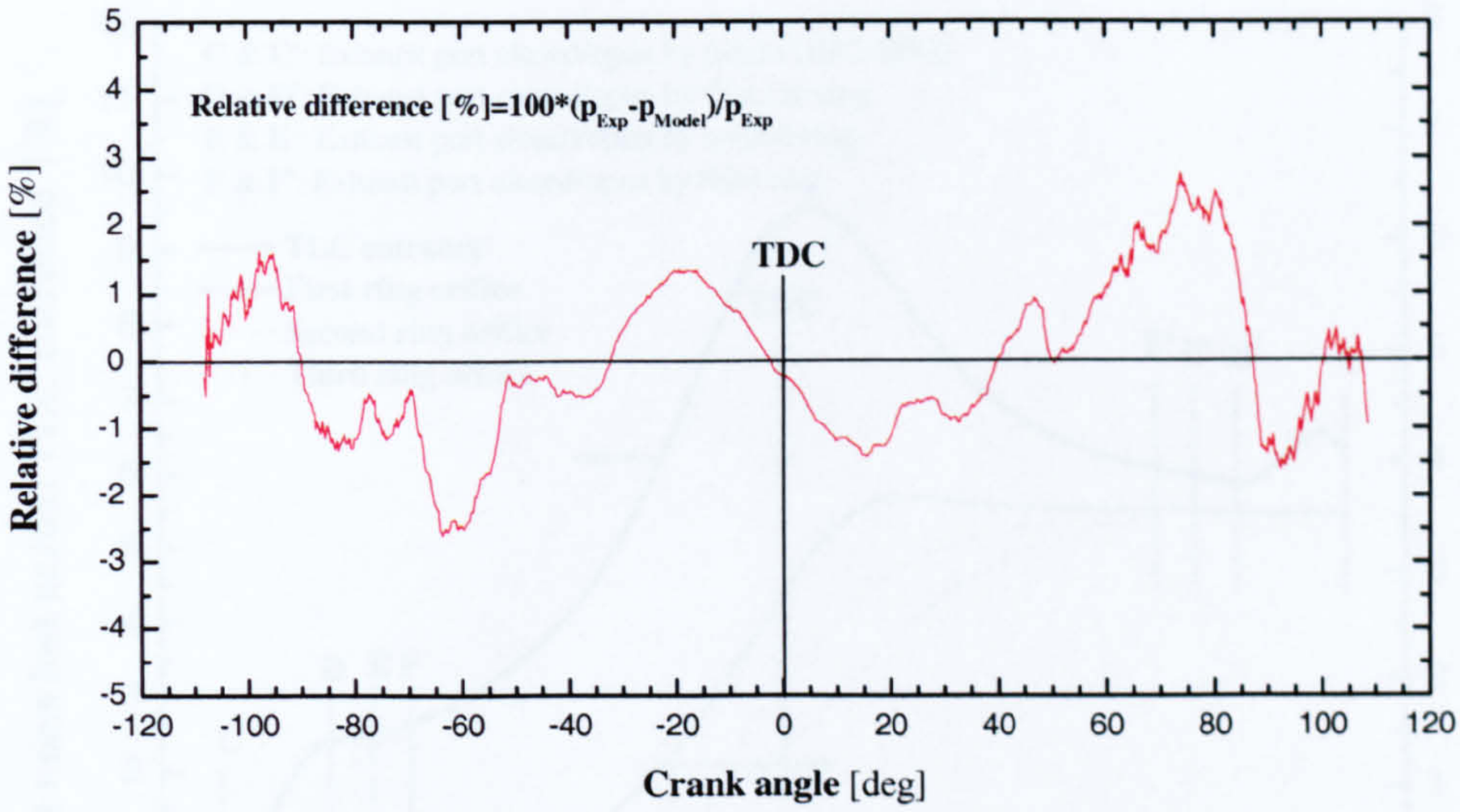

Figure 7.2 Relative differences between the experiment and model pressures versus crank angle in the motoring condition.

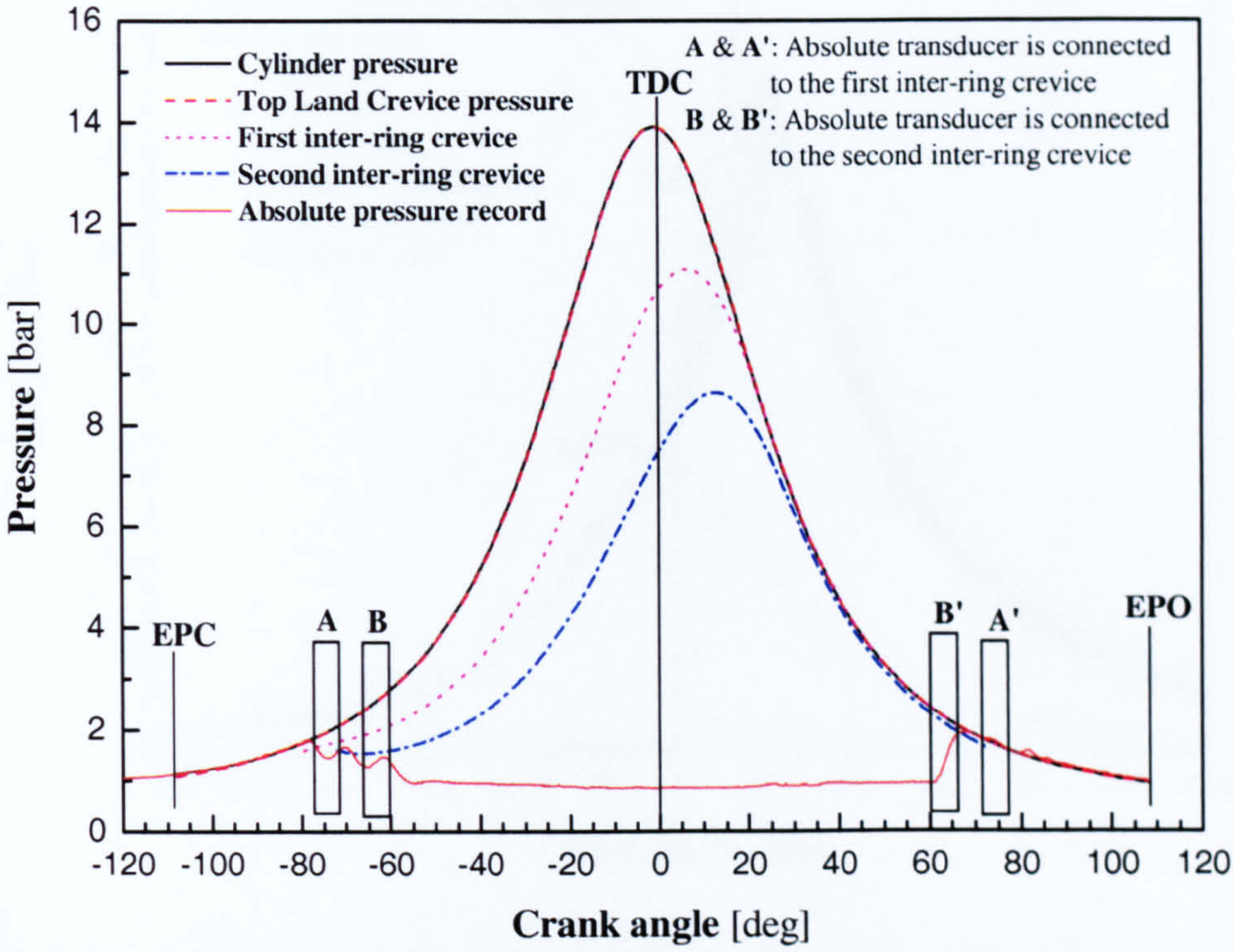

Figure 7.3 Predicted pressures of the cylinder, TLC, first and second inter-ring crevices associated with the absolute transducer record of a motoring cycle.

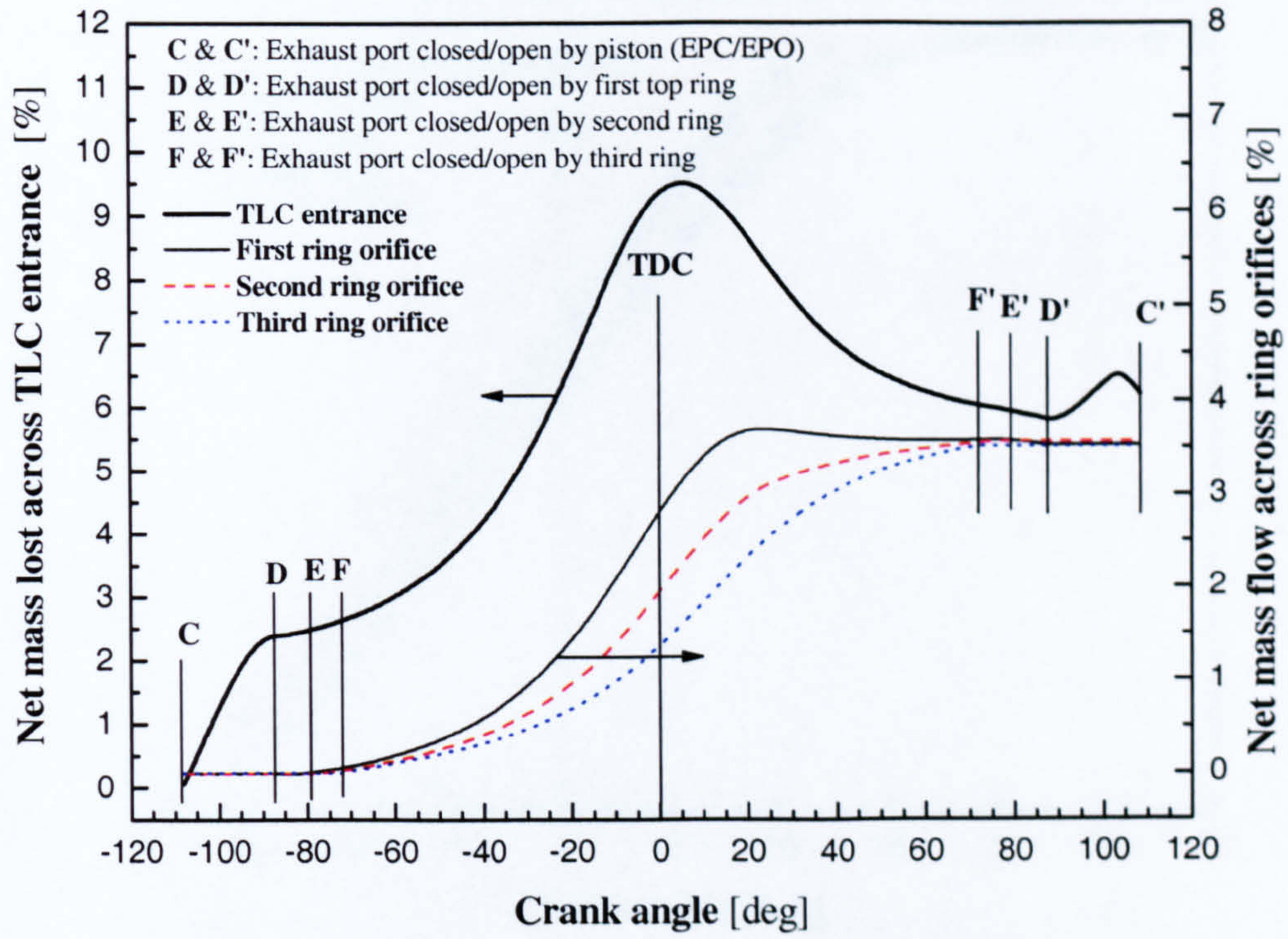

Figure 7.4 Net mass flow (based on the percent of cylinder mass at EPC) across the TLC entrance and ring orifices versus crank angle for the motoring condition.

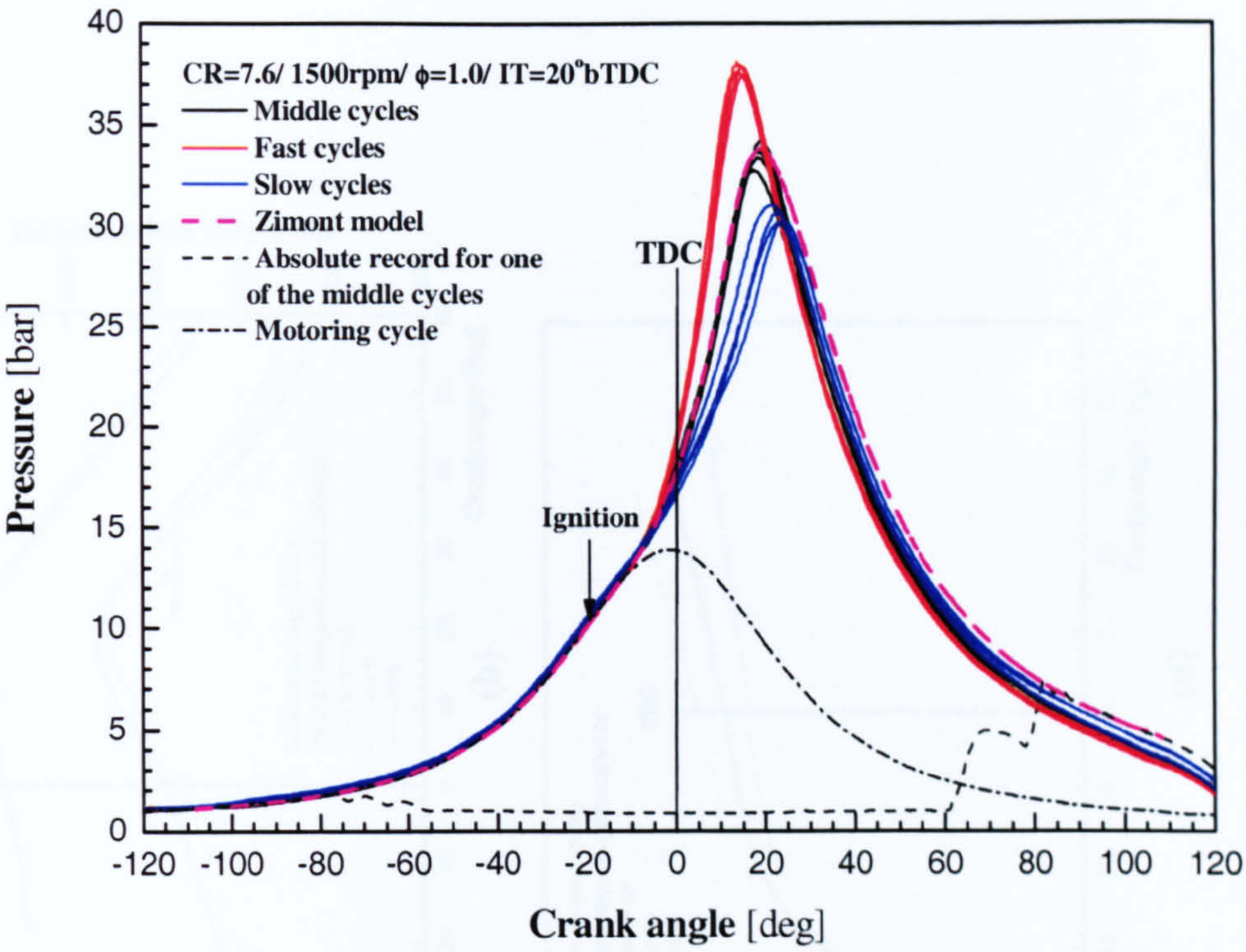

Figure 7.5 Cylinder pressure versus crank angle for twelve selected middle, fast and slow cycles and model at the reference condition associated with a motoring cycle and absolute pressure record for one of the middle cycles.

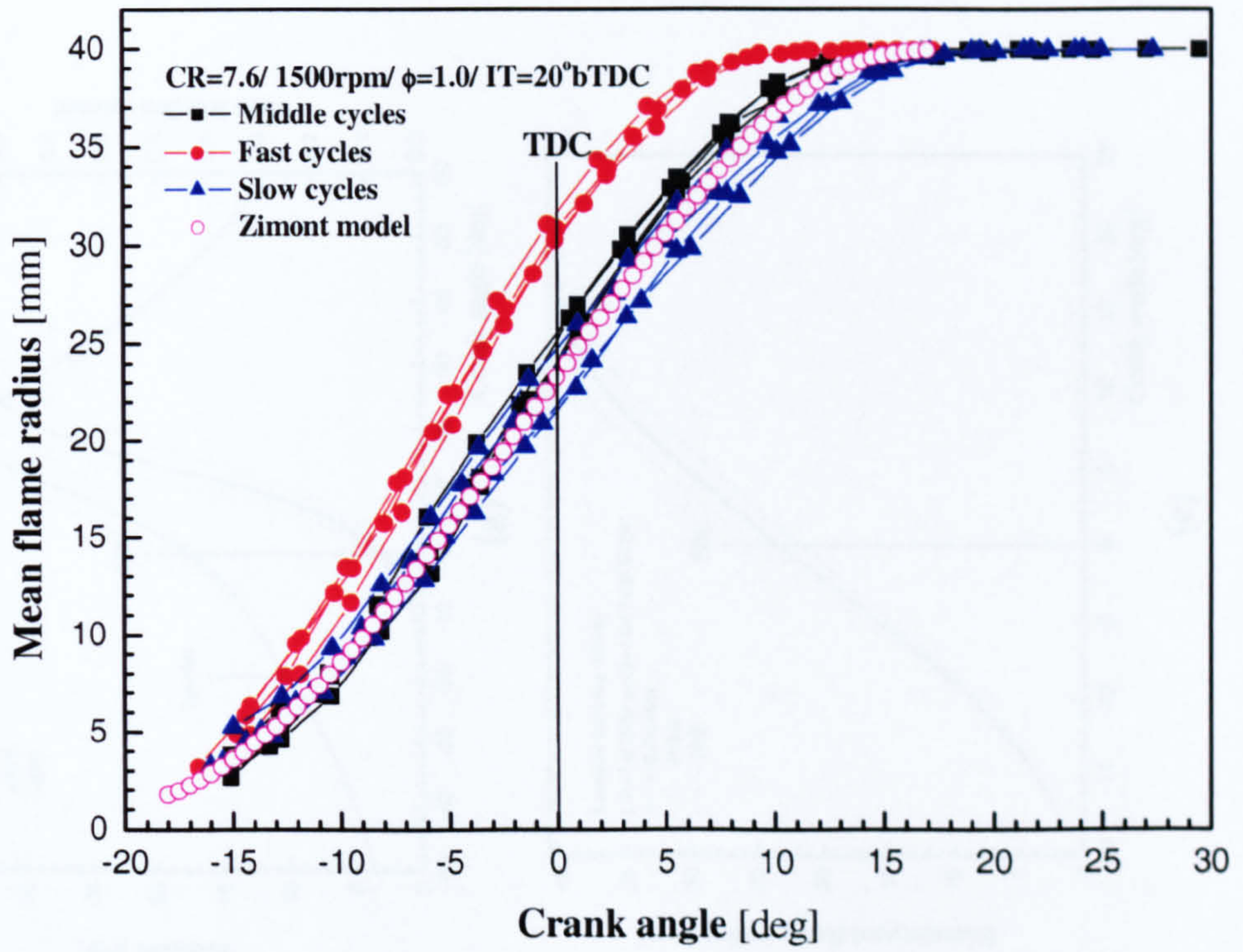

Figure 7.6 Mean flame radii of the twelve middle, fast and slow cycles and model versus crank angle at the reference condition.

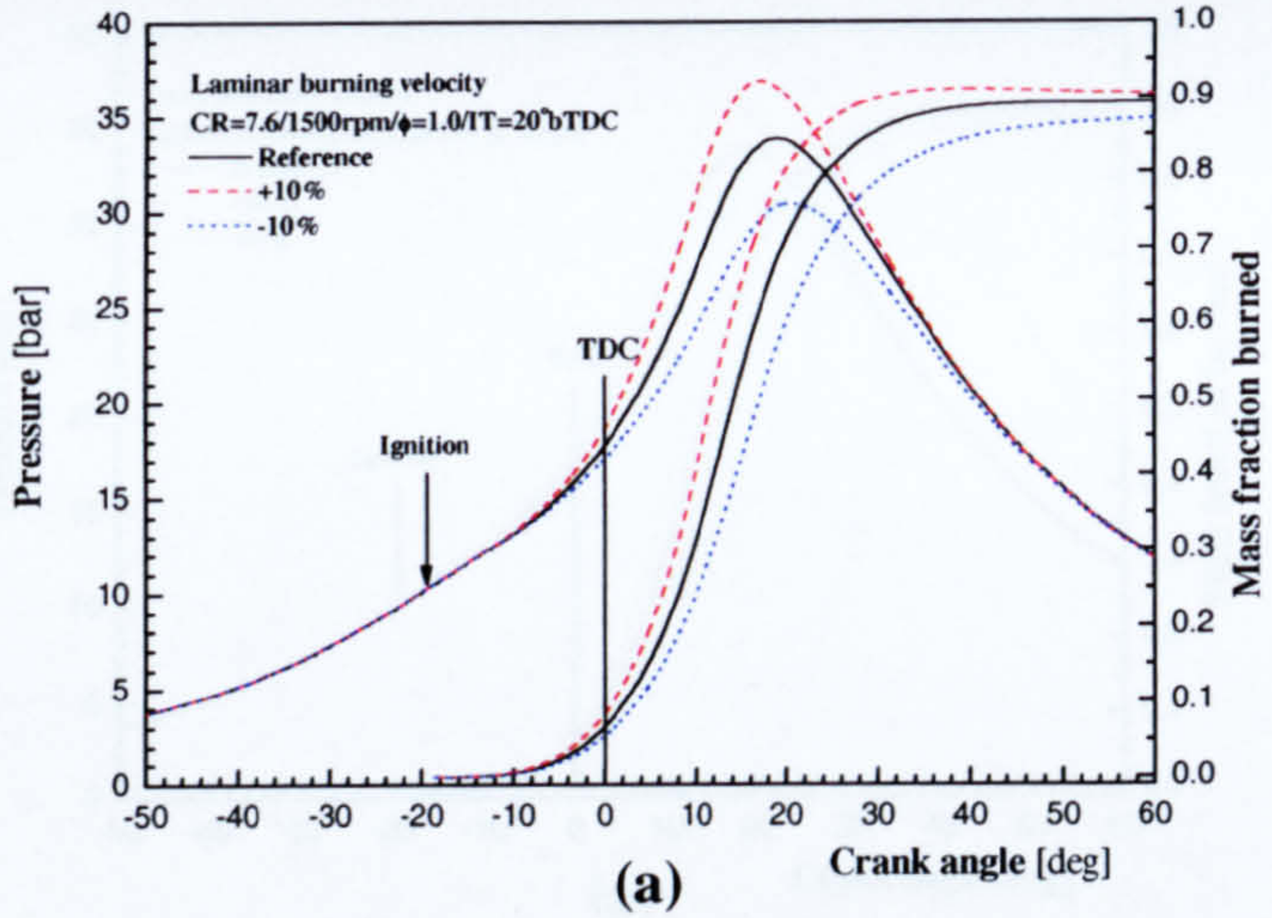

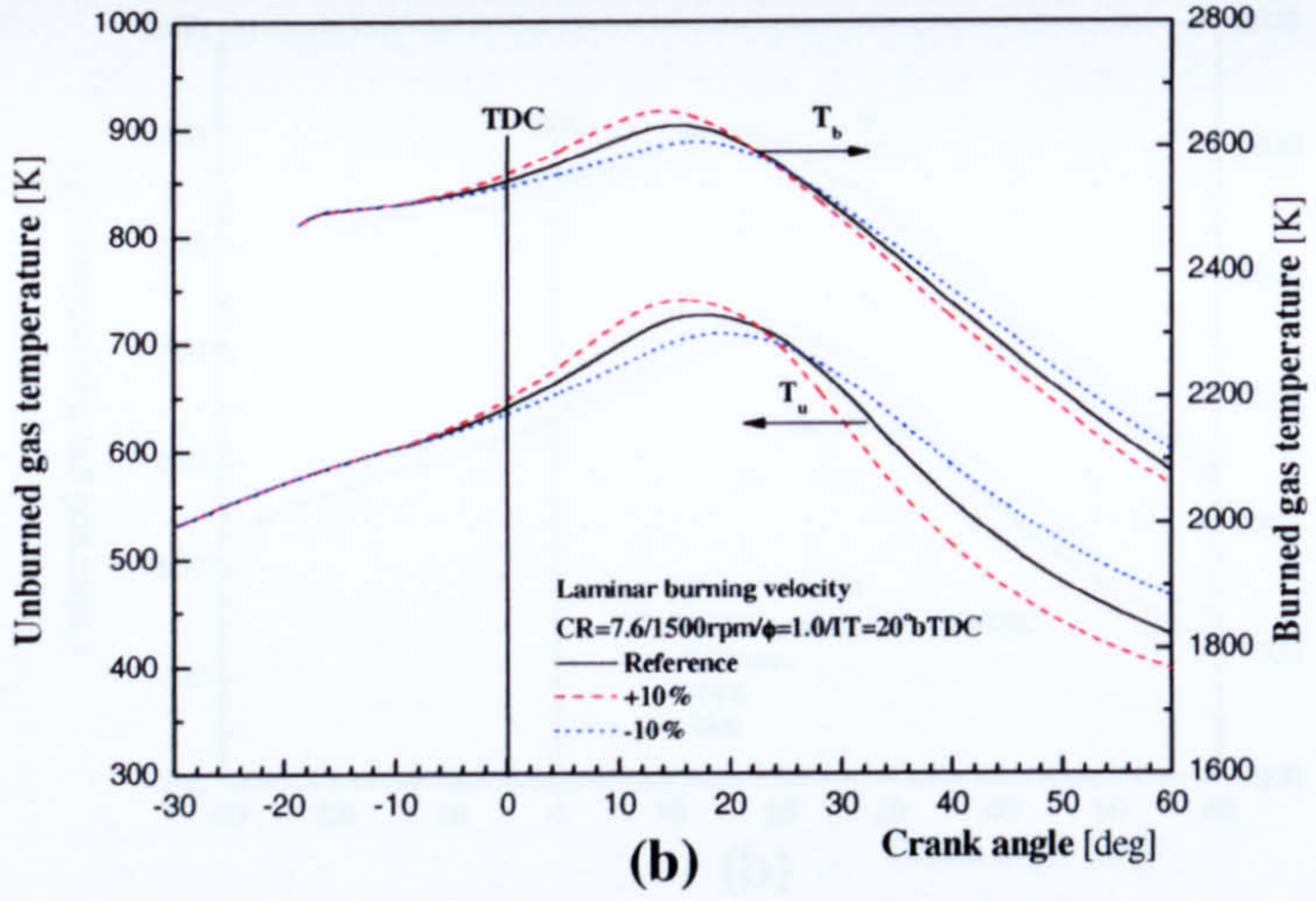

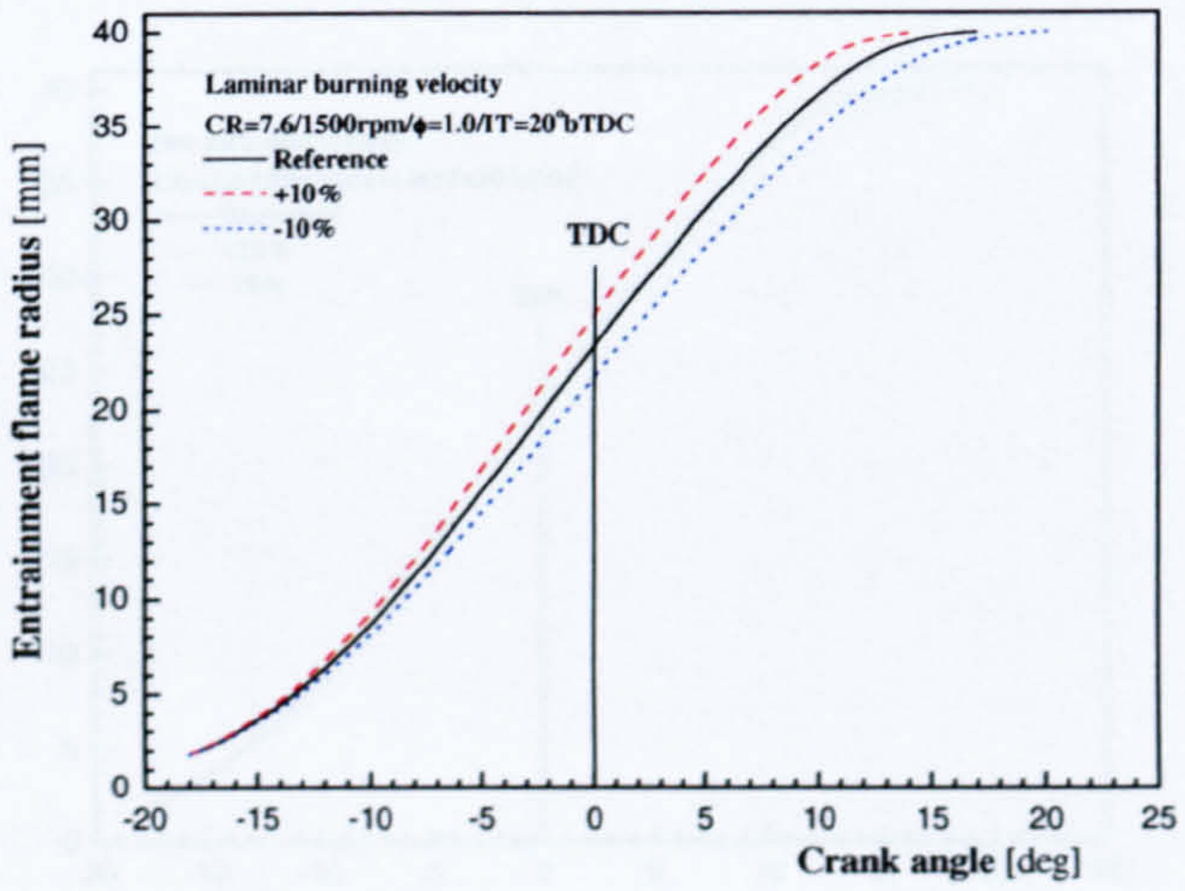

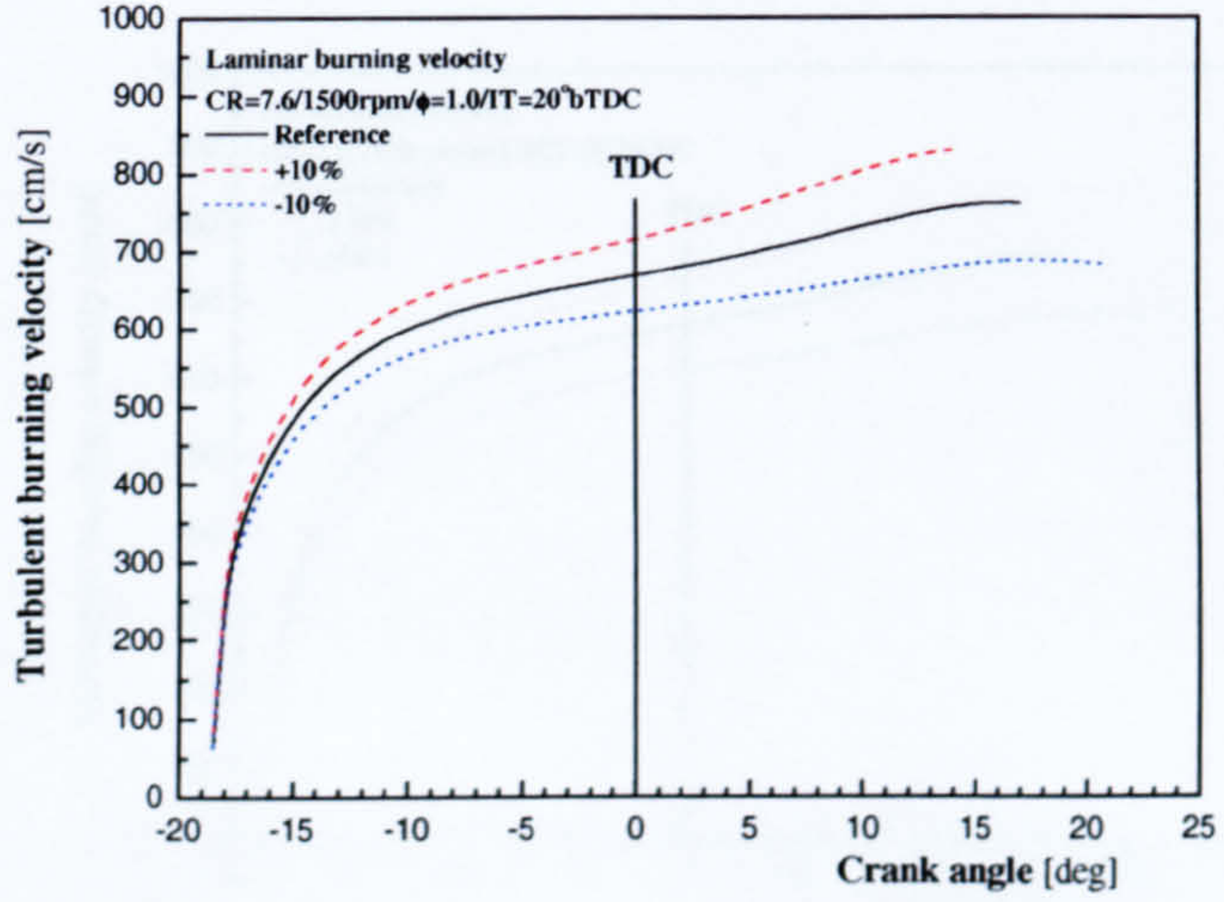

Figure 7.7 The effect of ±10% change in laminar burning velocity on **(a)** cylinder pressure and mass fraction burned, **(b)** unburned and burned gas temperatures, **(c)** entrainment flame radius and **(d)** turbulent burning velocity in the reference condition.

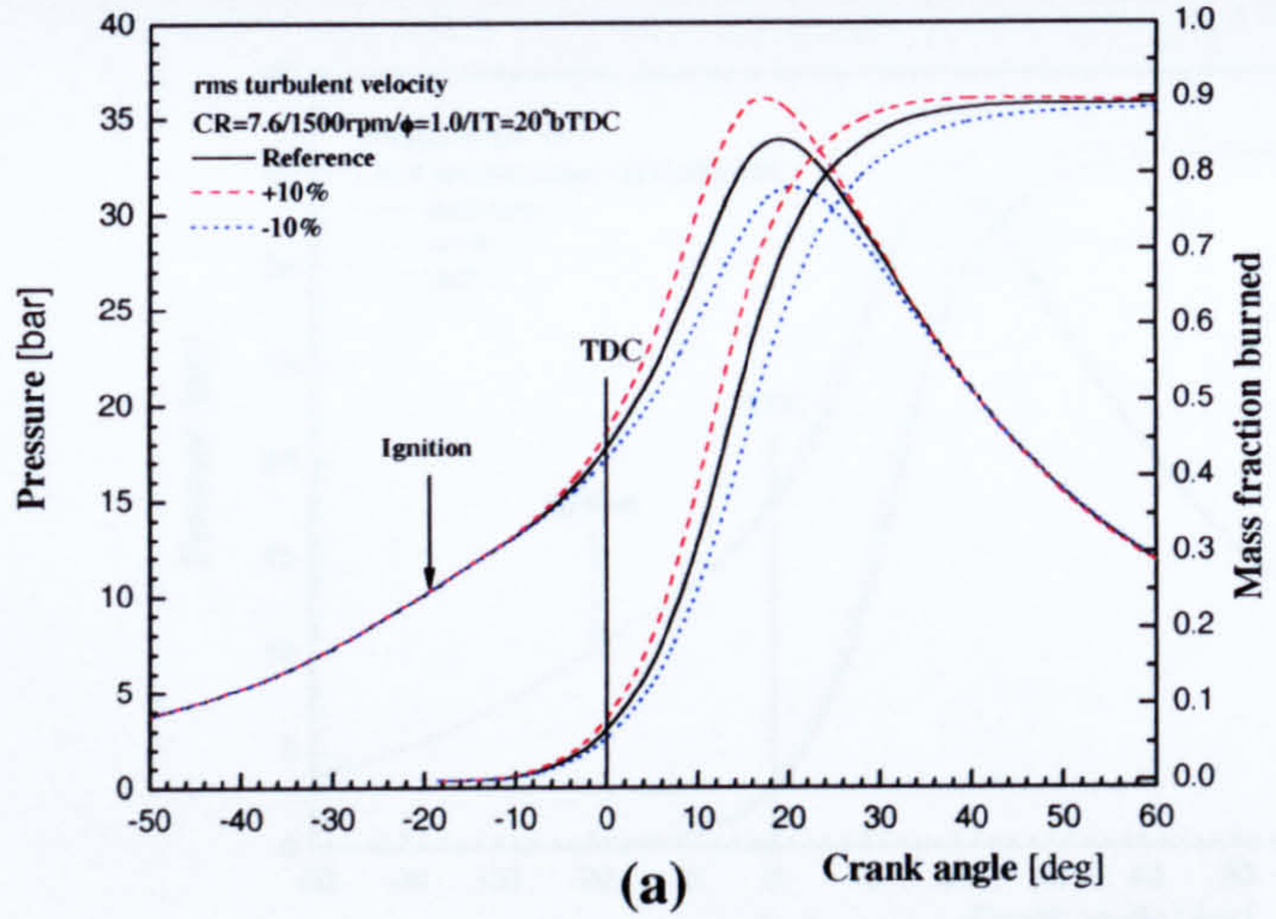

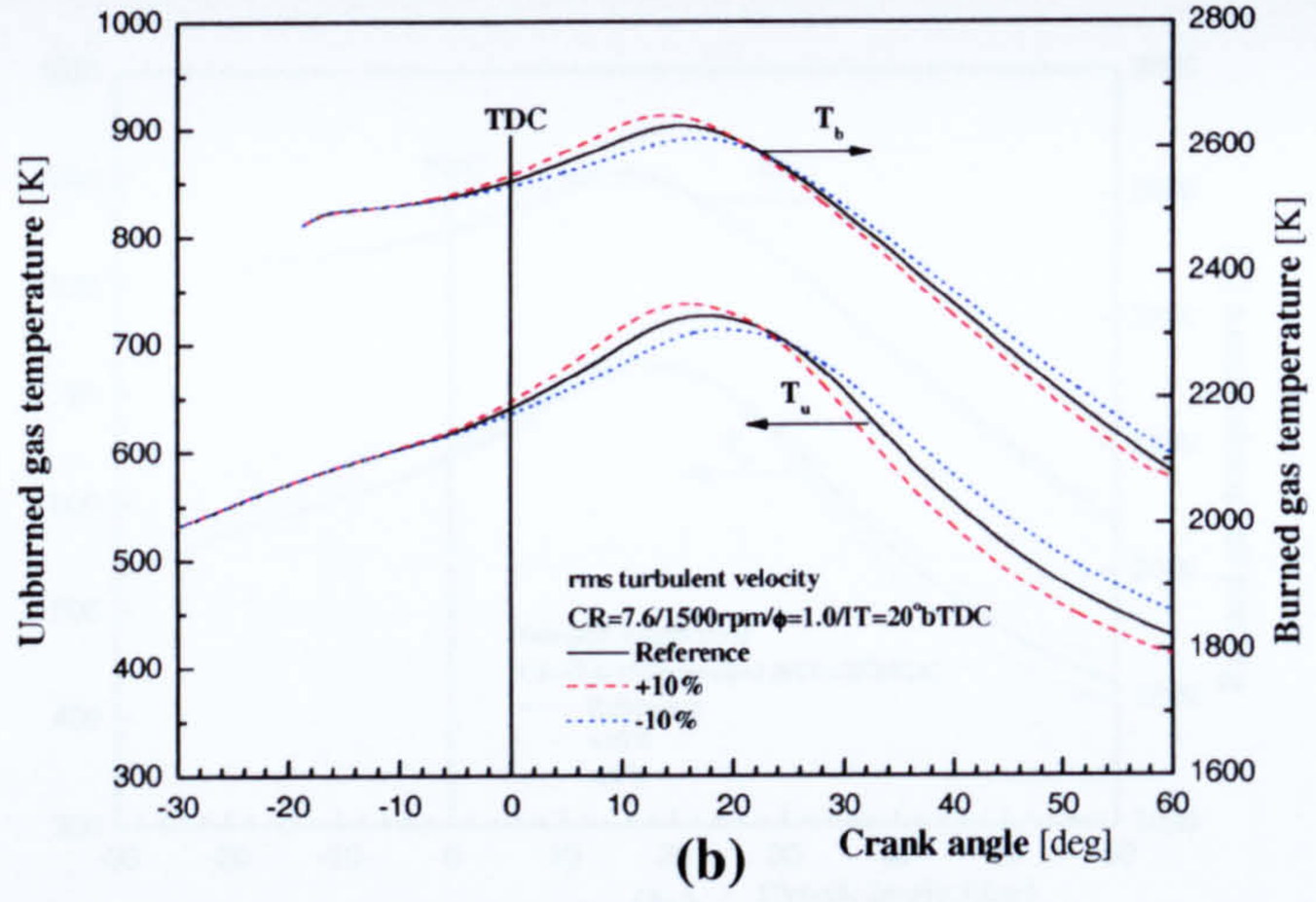

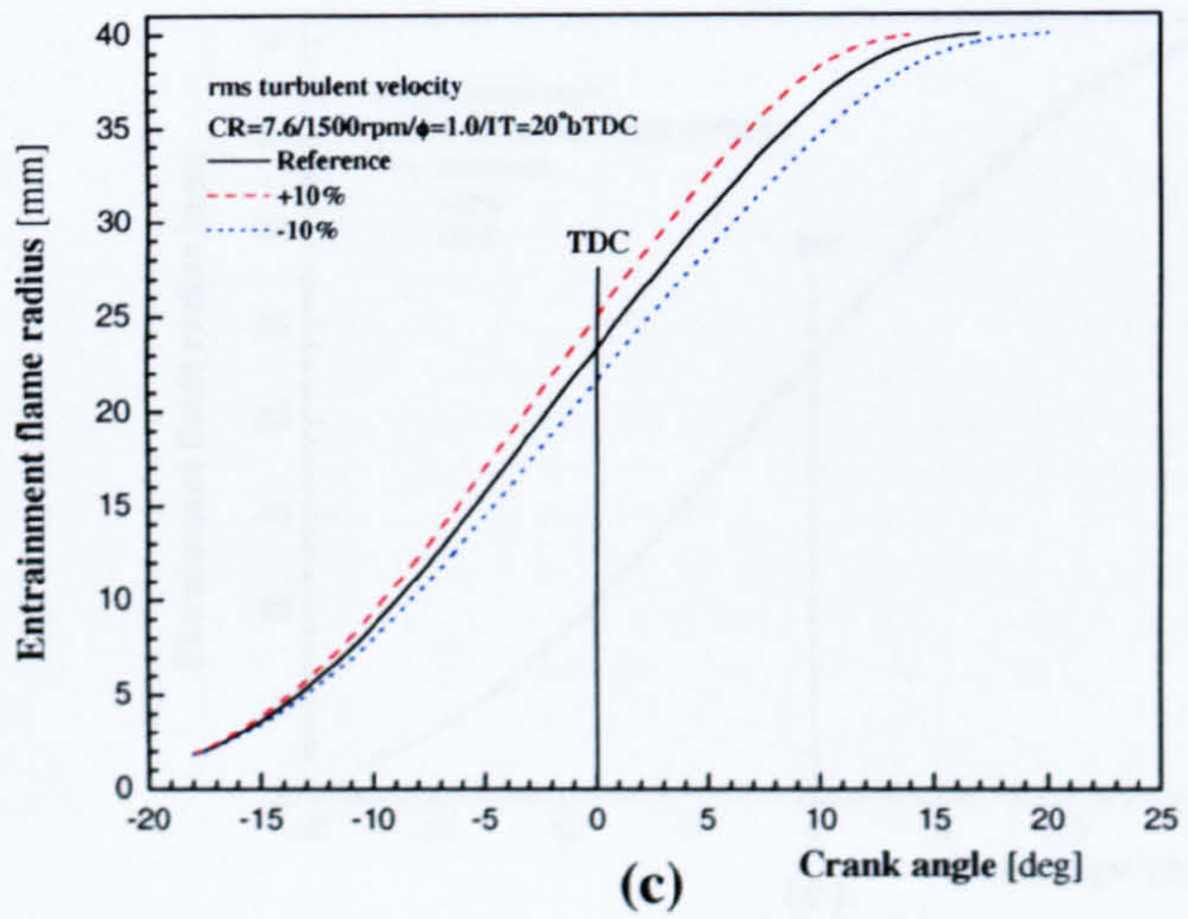

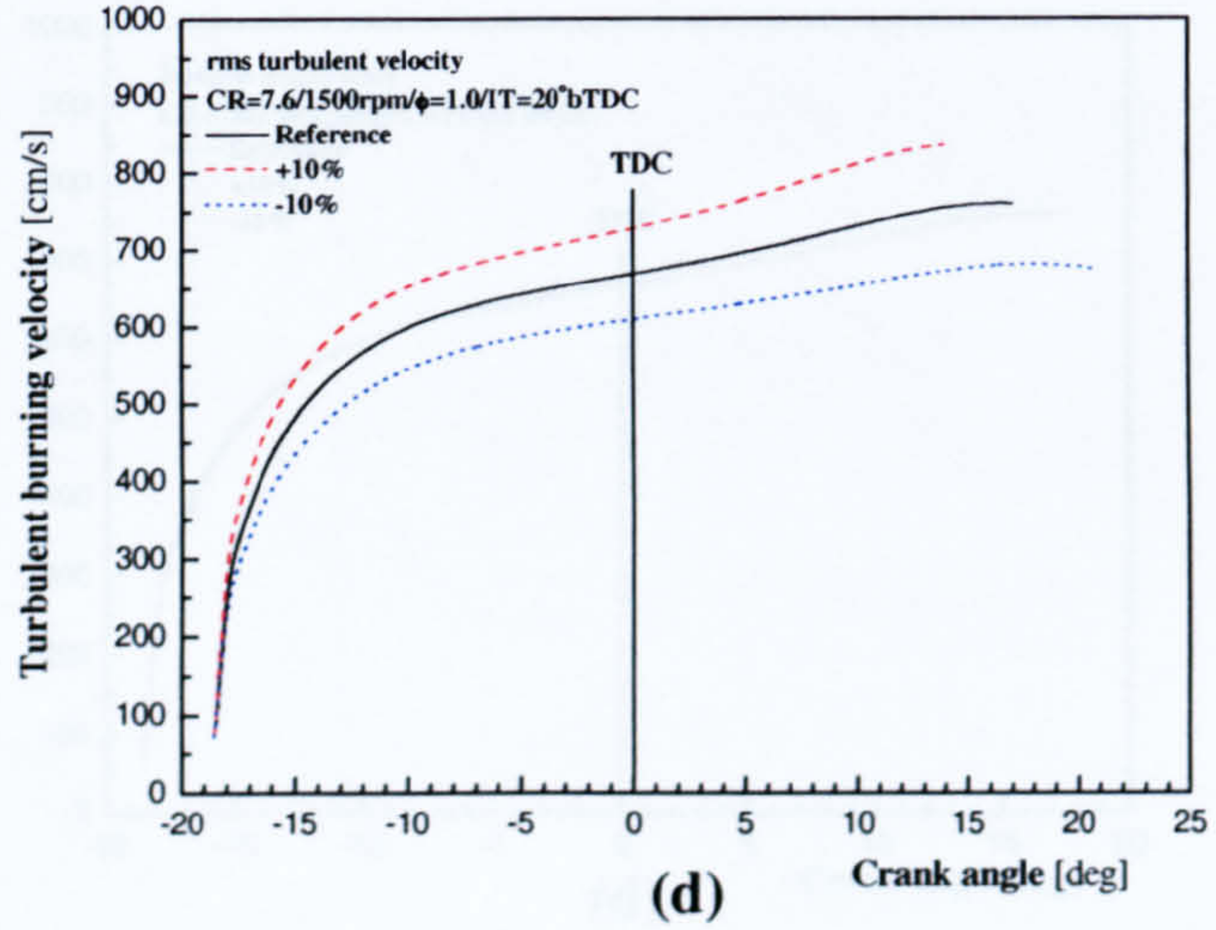

Figure 7.8 The effect of ±10% change in "rms" turbulent velocity on **(a)** cylinder pressure and mass fraction burned, **(b)** unburned and burned gas temperatures, **(c)** entrainment flame radius and **(d)** turbulent burning velocity in the reference condition.

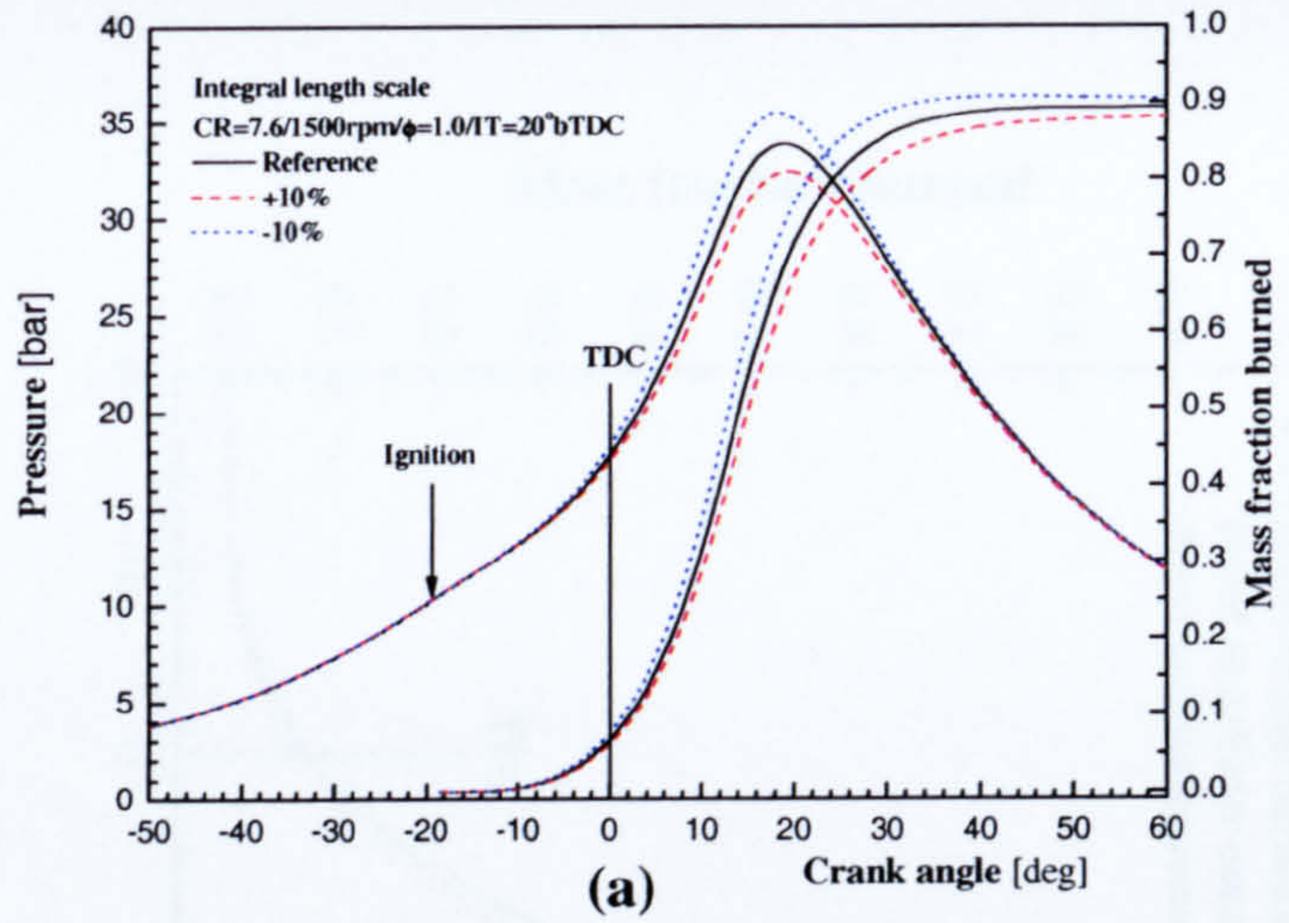

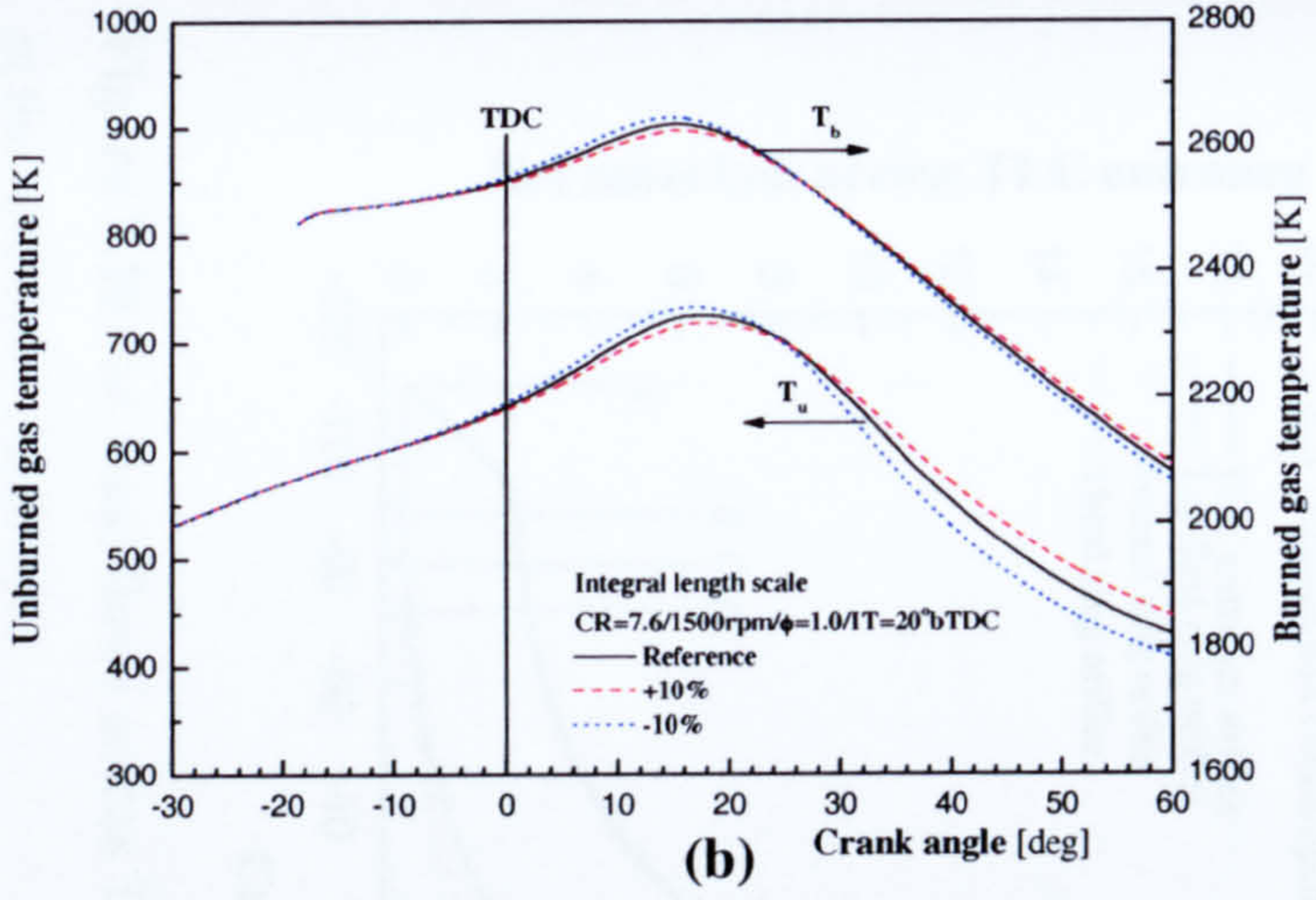

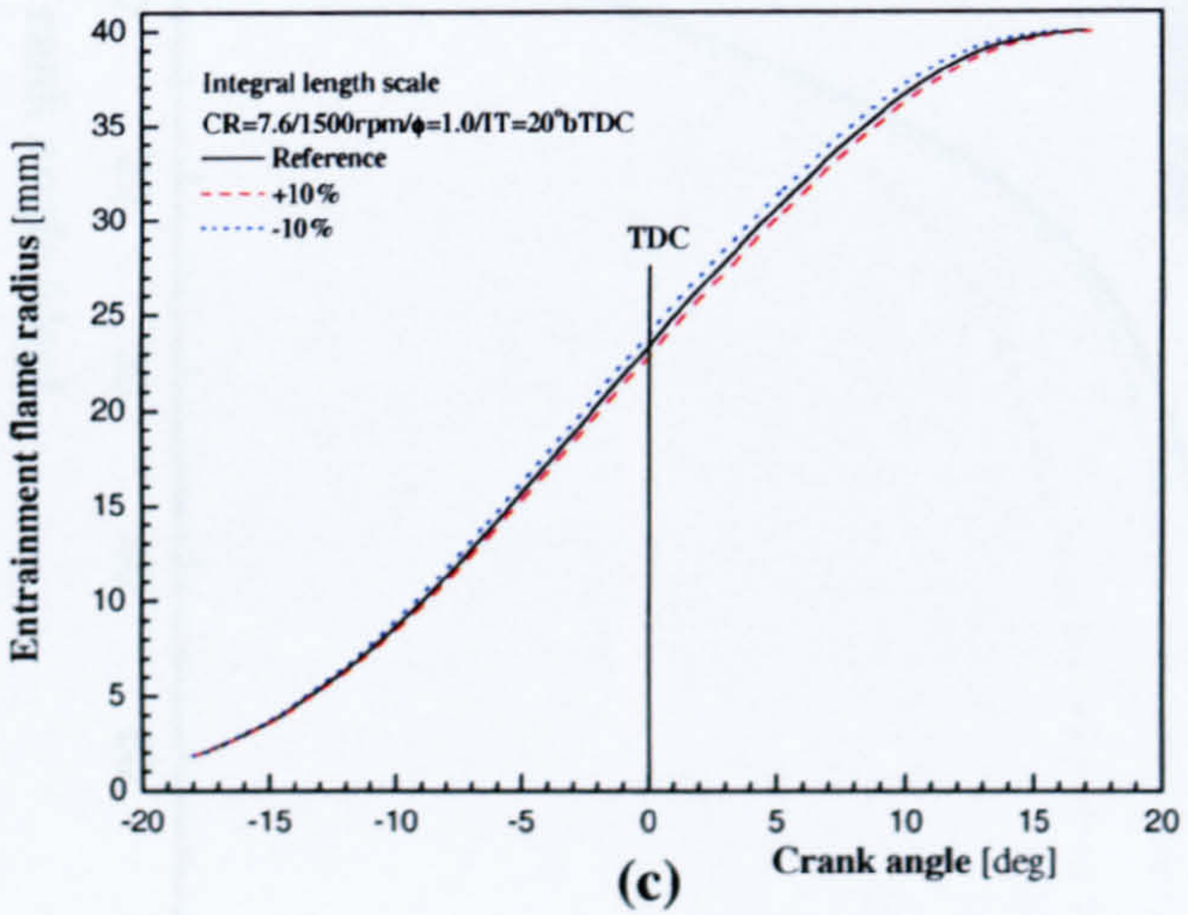

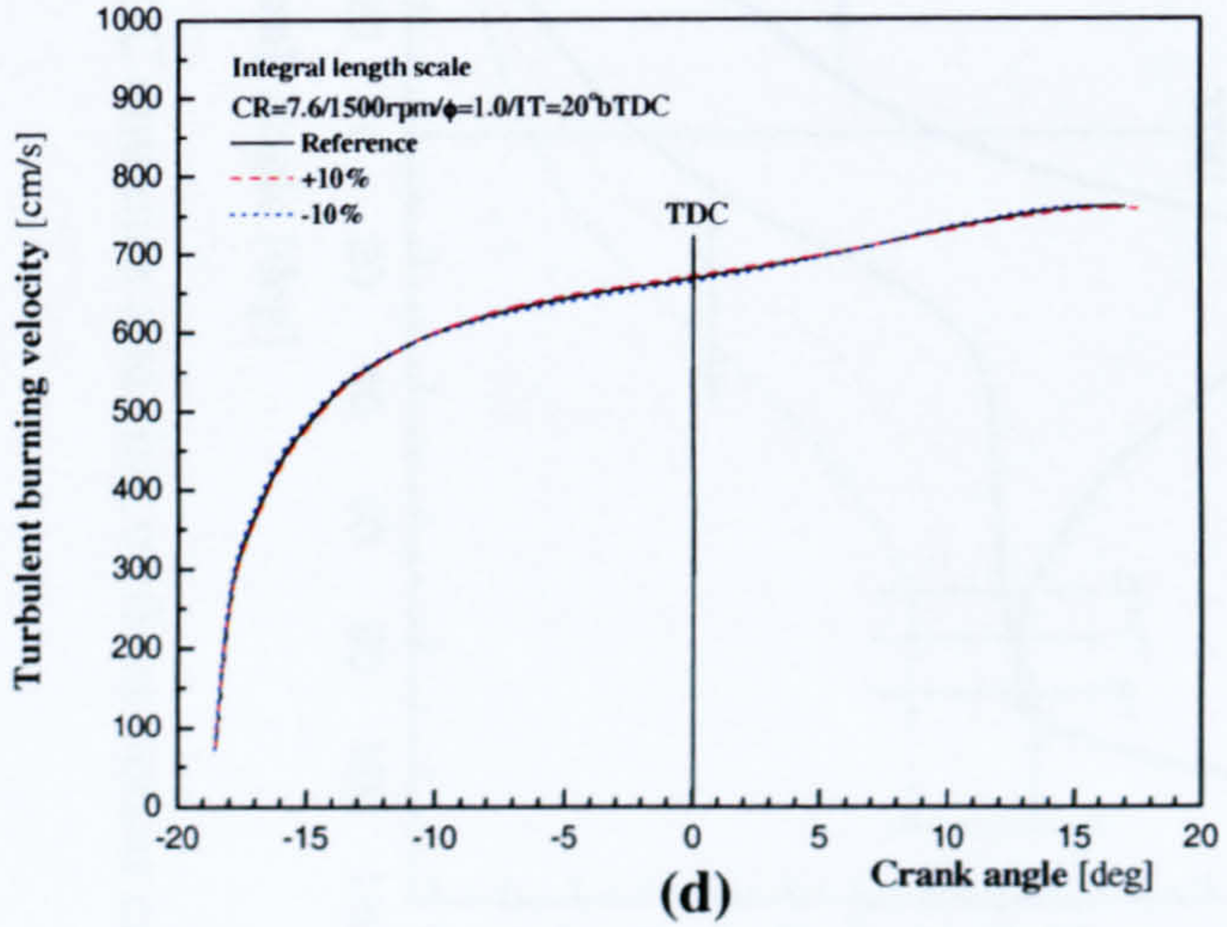

Figure 7.9 The effect of ±10% change in integral length scale on **(a)** cylinder pressure and mass fraction burned, **(b)** unburned and burned gas temperatures, **(c)** entrainment flame radius and **(d)** turbulent burning velocity in the reference condition.

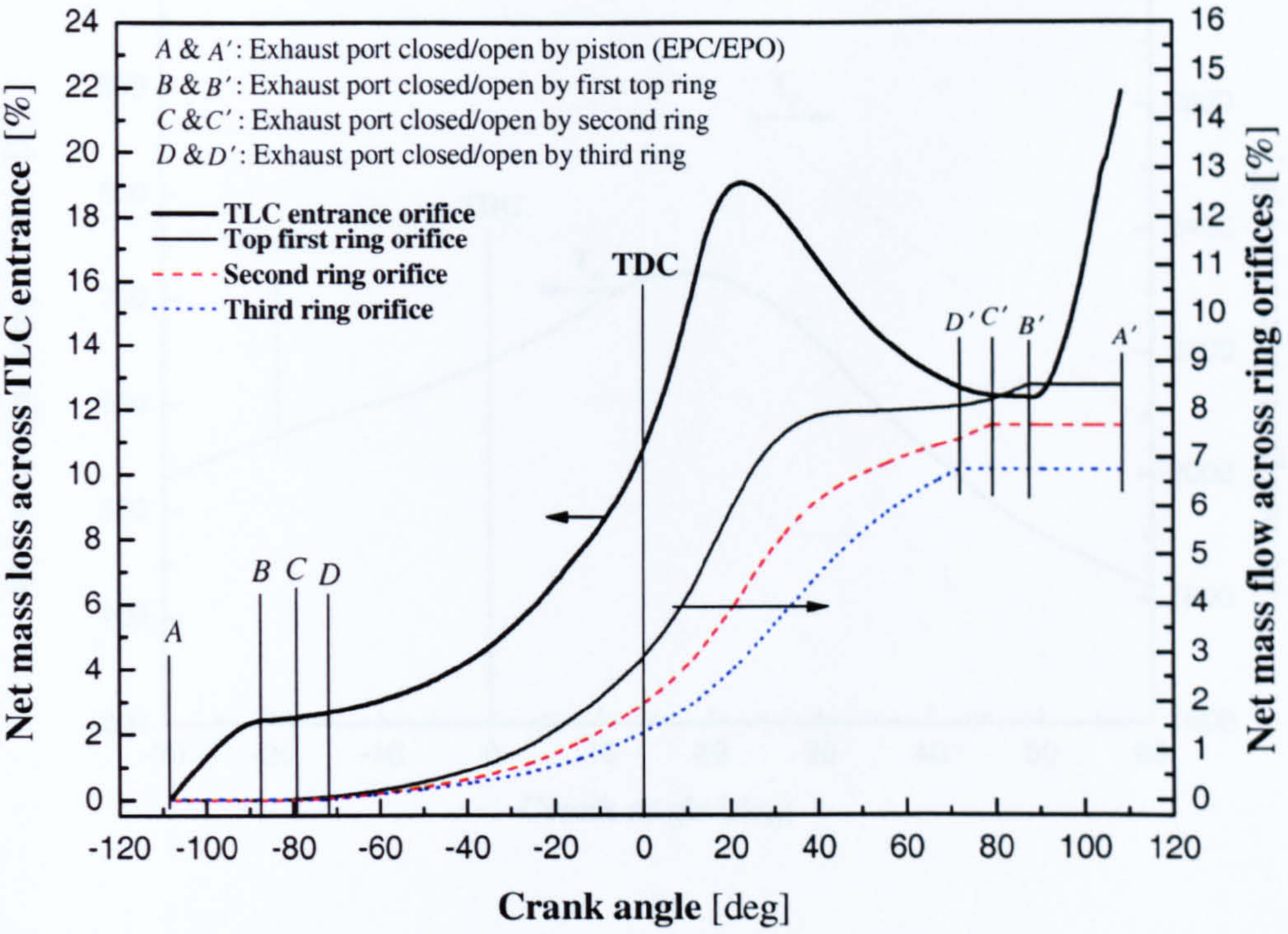

Figure 7.10 Net mass flows across TLC entrance and ring orifices versus crank angle at the reference condition.

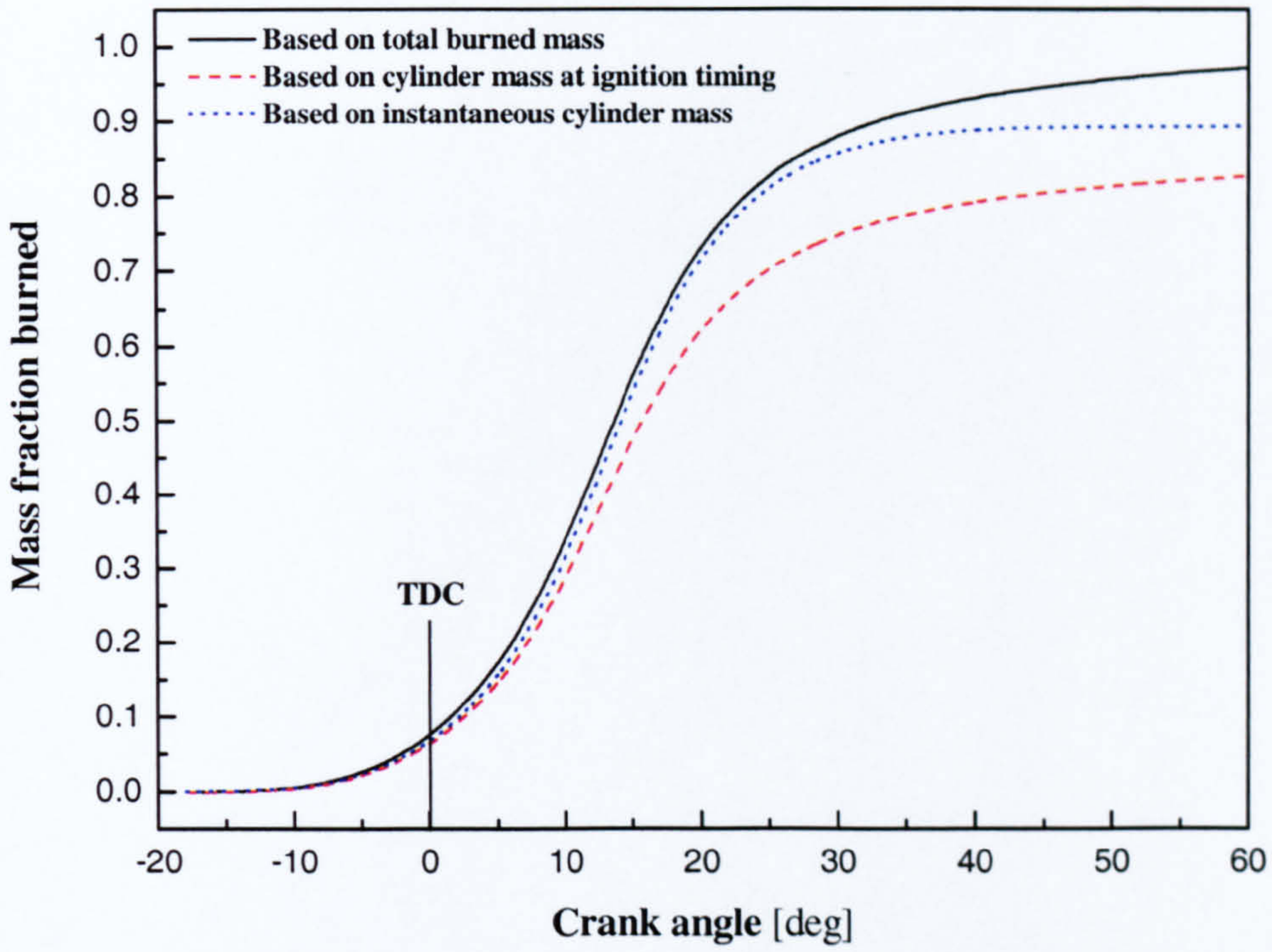

Figure 7.11 Mass fraction burned based on total burned mass, cylinder mass at ignition timing and instantaneous cylinder mass in terms of crank angle.

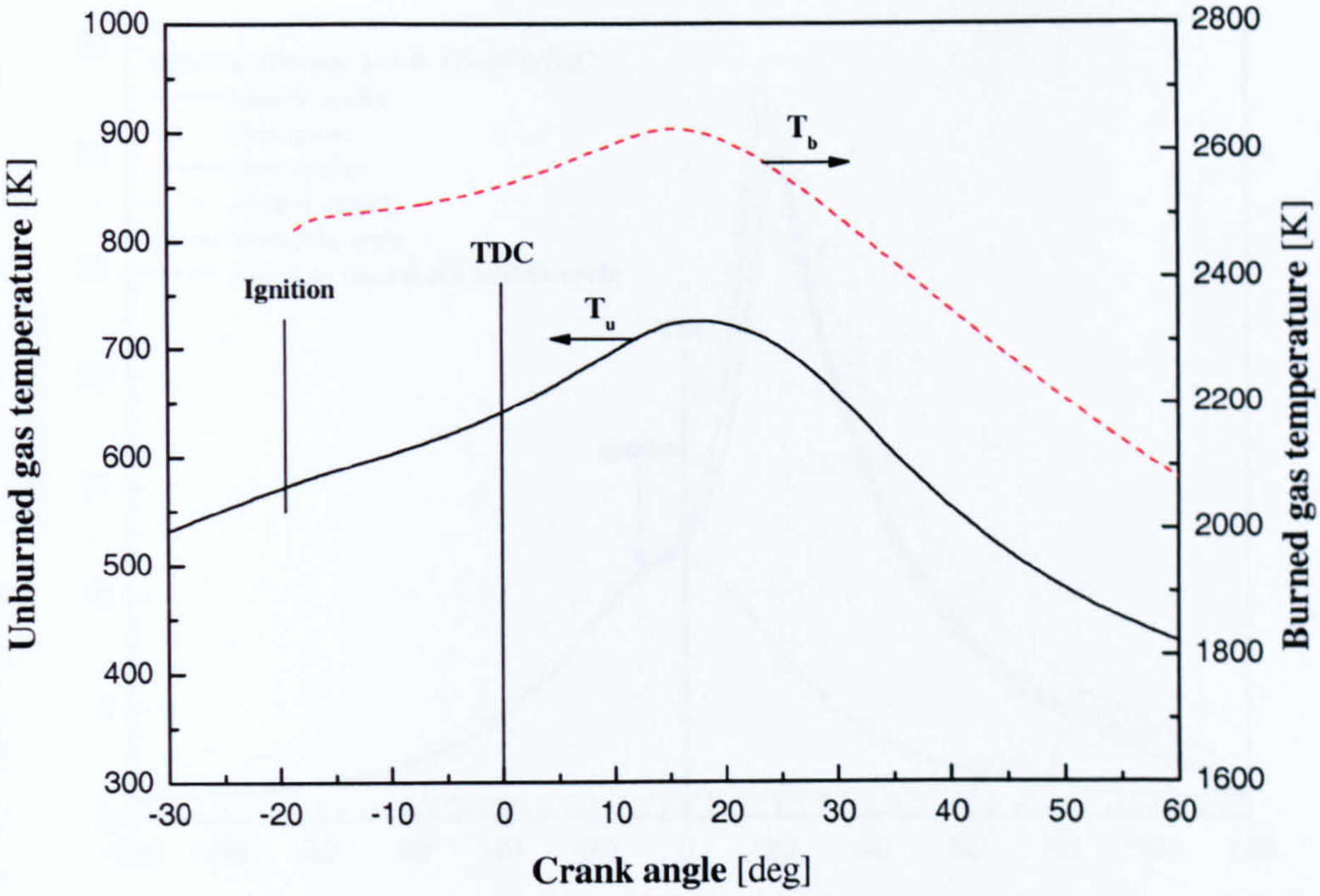

Figure 7.12 The predicted unburned and burned gas temperatures versus crank angle at the reference condition.

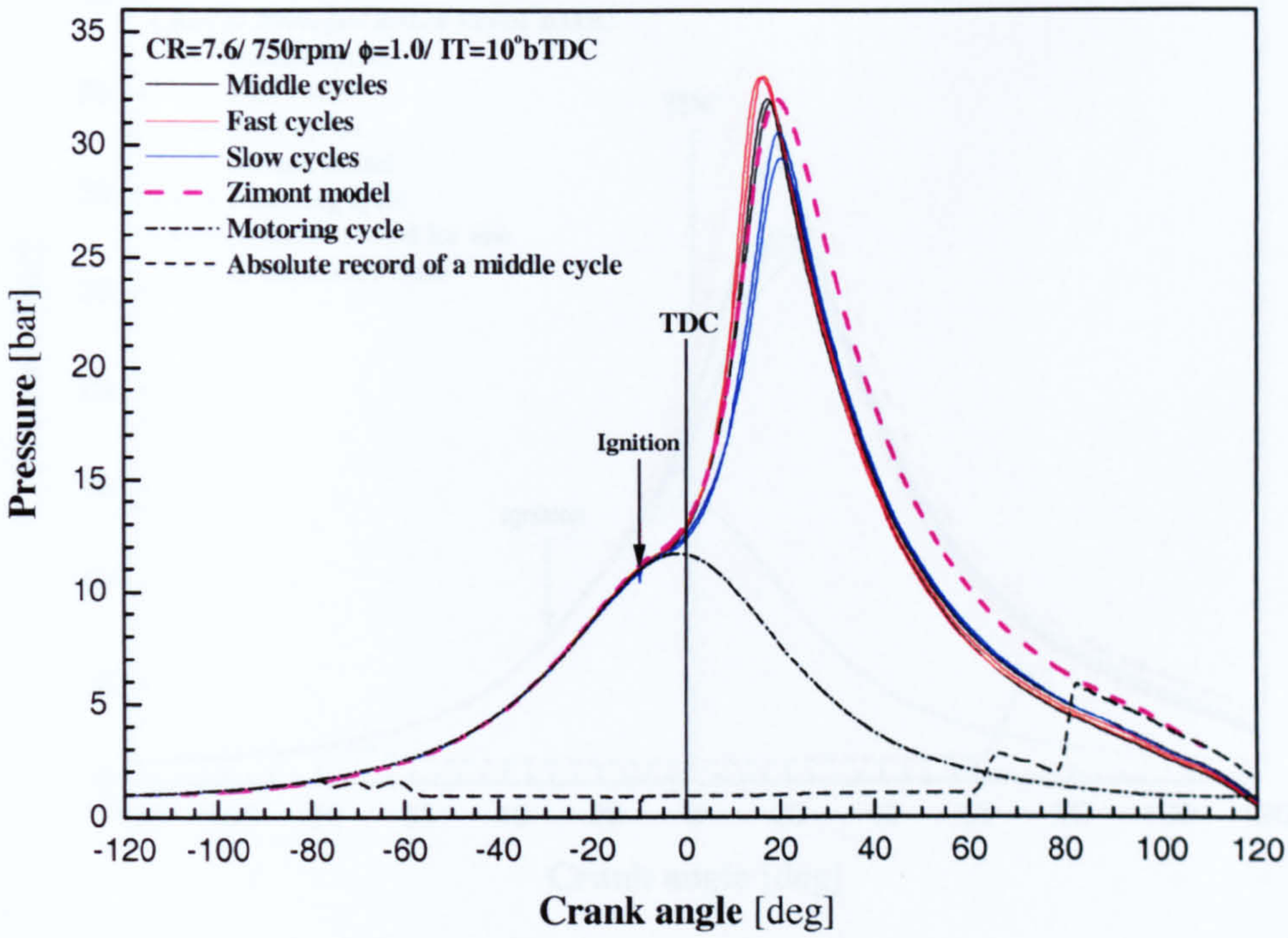

Figure 7.13 Cylinder pressure versus crank angle for six selected experimental cycles (middle, fast and slow) and model output associated with a motoring cycle and absolute transducer record of a middle cycle at the low engine speed condition.

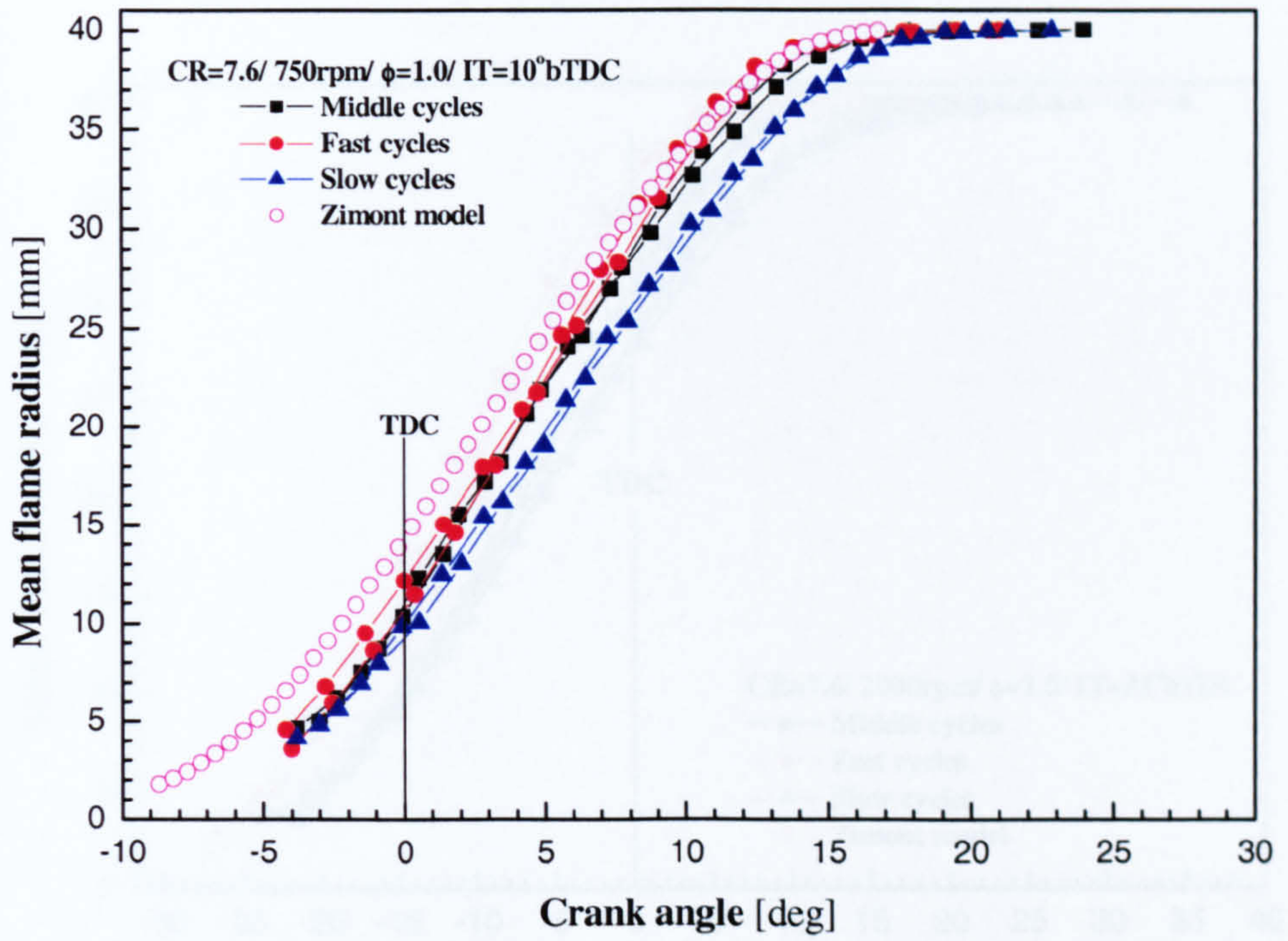

Figure 7.14 Mean flame radius versus crank angle for the six selected experimental cycles and the output of model at the low engine speed condition.

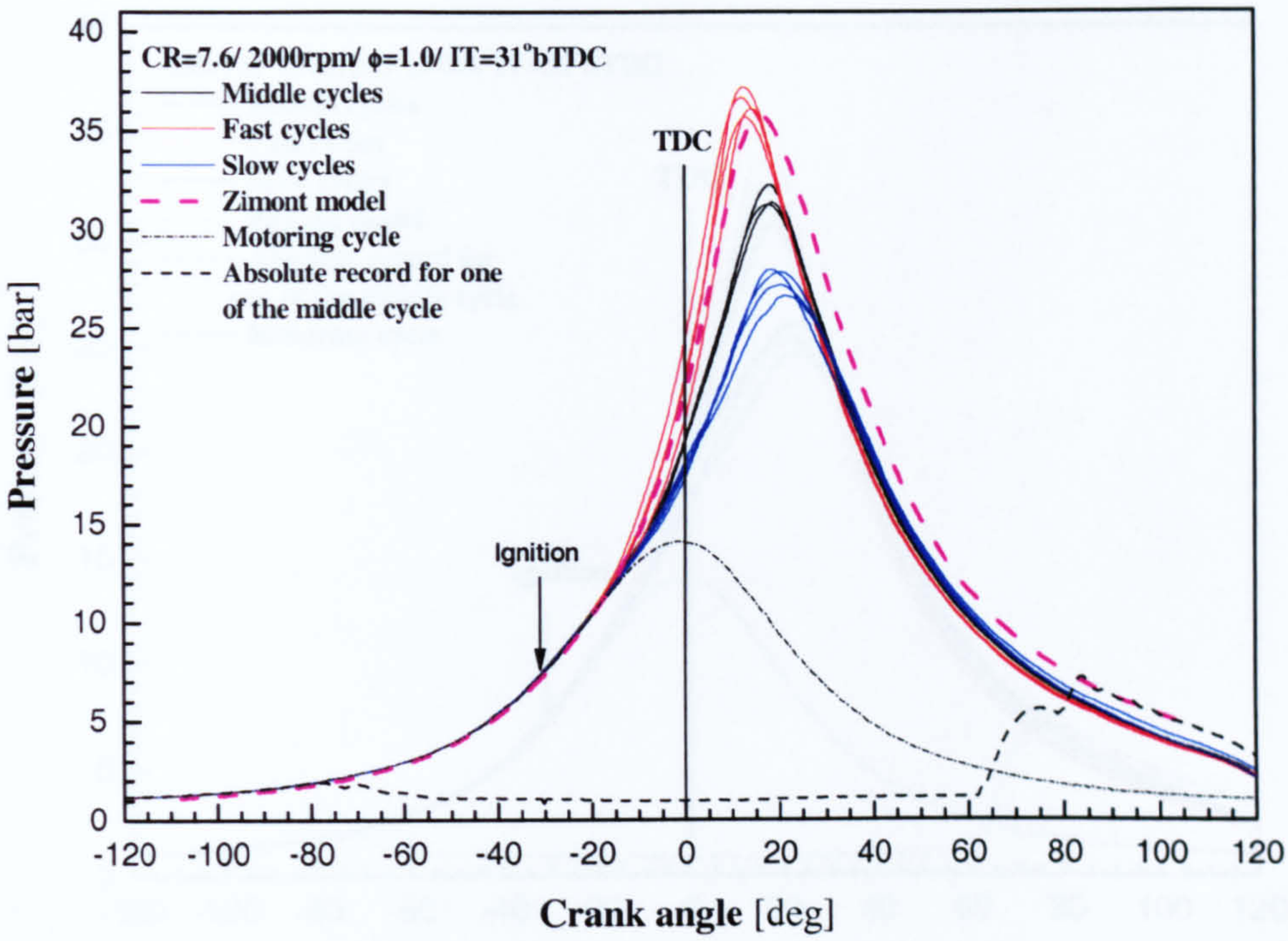

Figure 7.15 Cylinder pressure in terms of crank angle for the twelve selected cycles (middle, fast and slow) and the model at high engine speed condition associated with a motoring cycle and absolute pressure transducer record of a middle cycle.

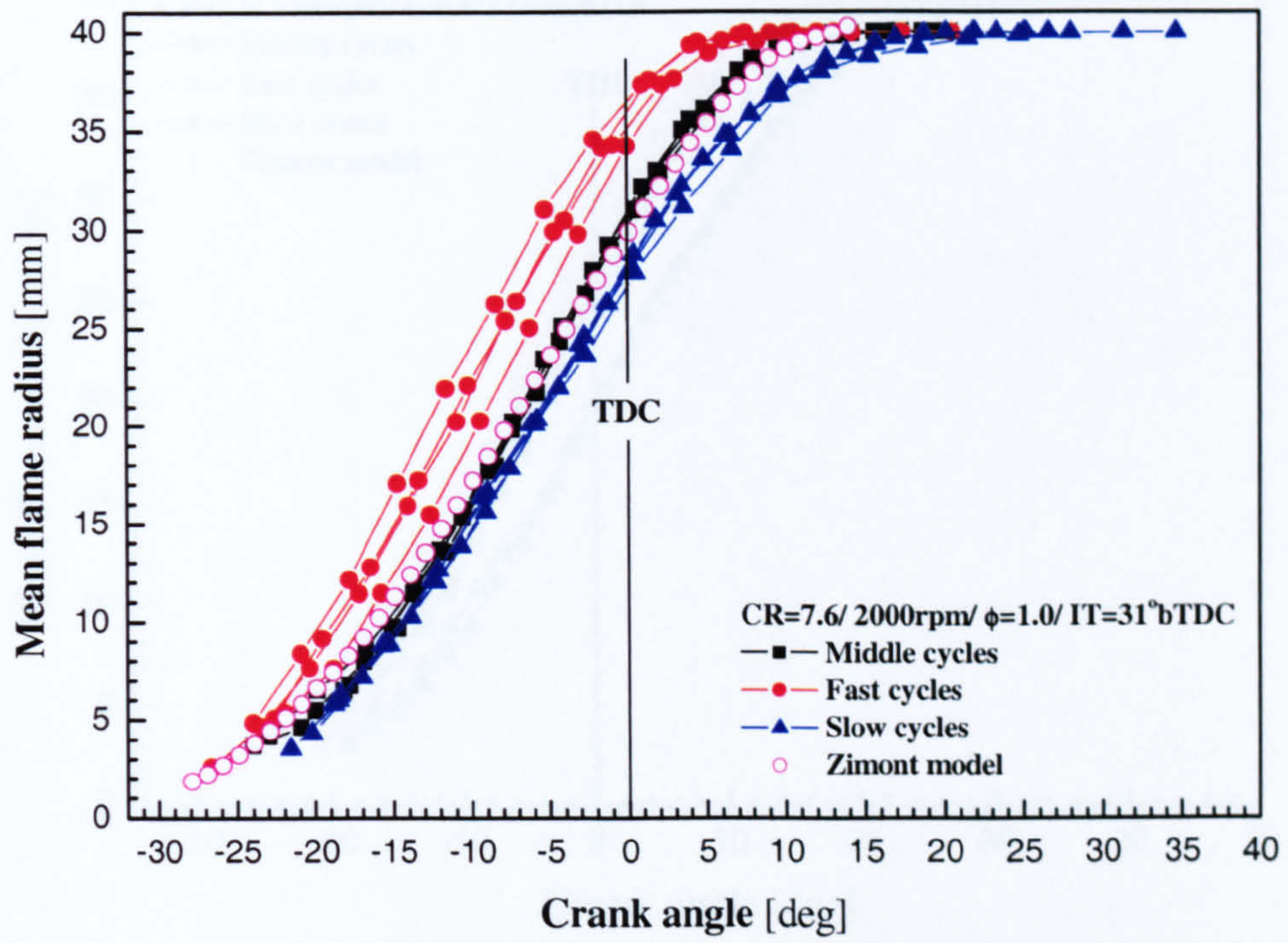

Figure 7.16 Mean flame radii of the twelve experimental cycles and model in terms of crank angle at the high engine speed condition.

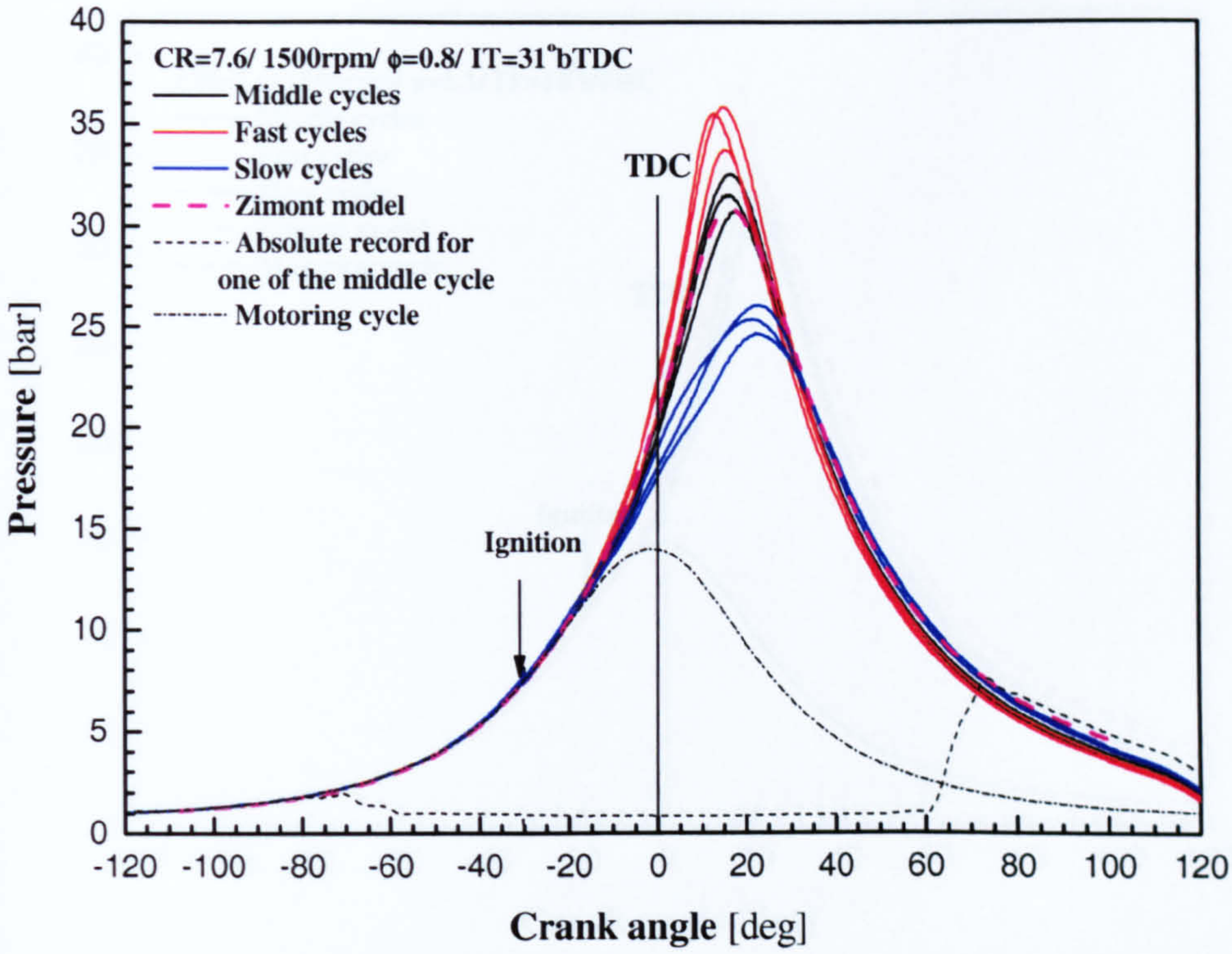

Figure 7.17 Cylinder pressure versus crank angle for nine selected experimental (middle, fast and slow), a motoring and modelled cycles associated with absolute transducer record for one of the middle cycles at lean condition.

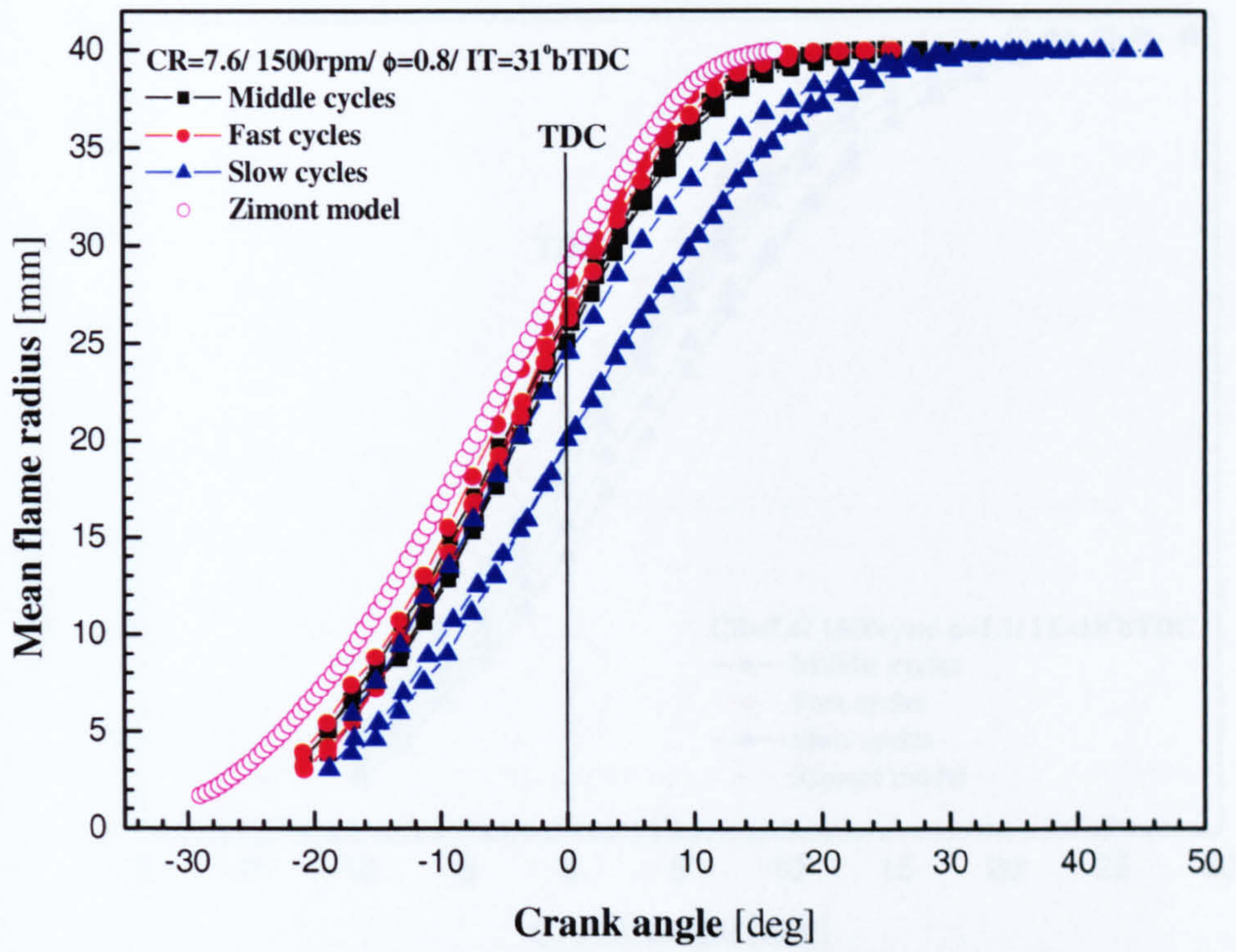

Figure 7.18 Mean flame radii of the nine selected experimental cycles (middle, fast and slow) and model at the lean condition.

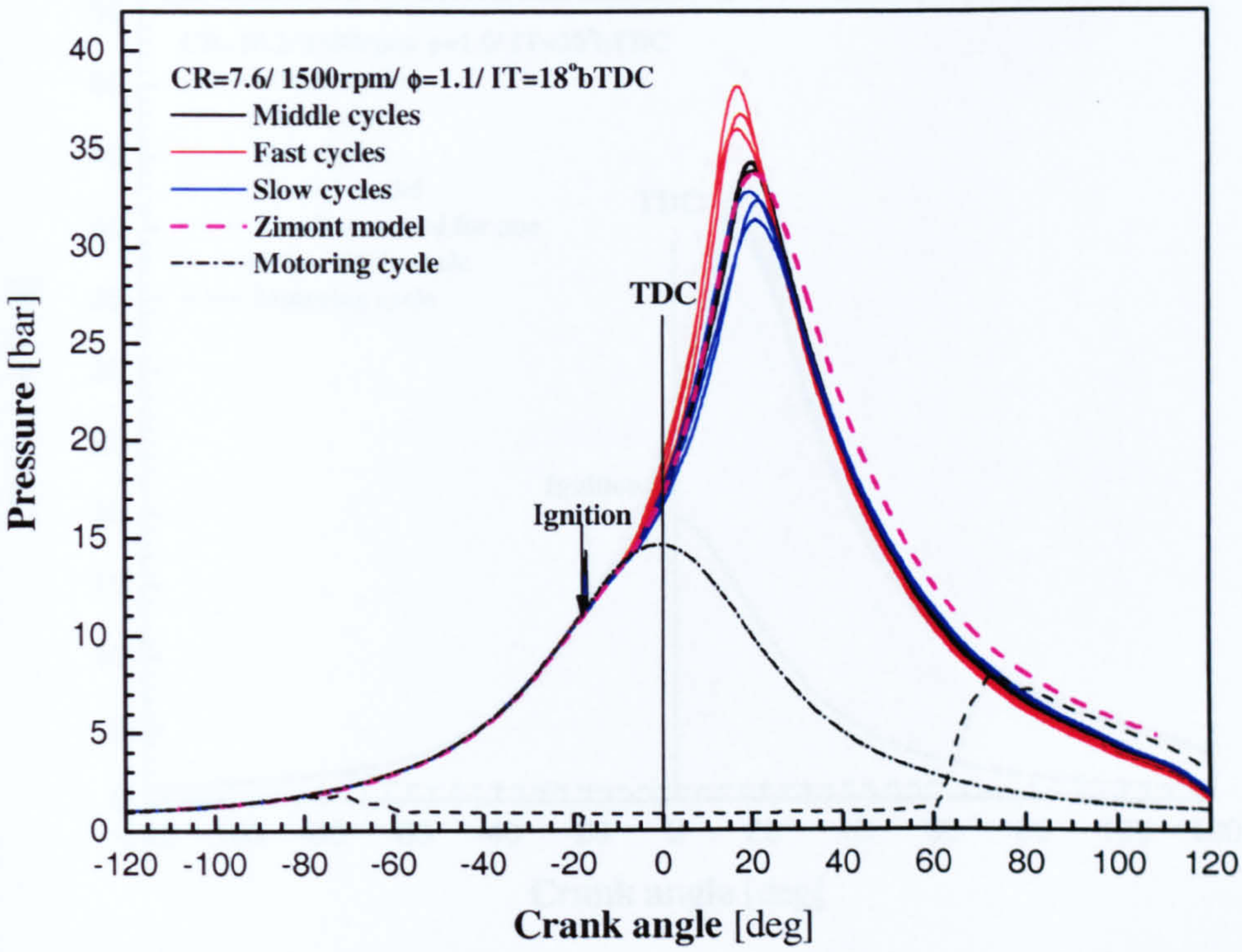

Figure 7.19 Cylinder pressure versus crank angle for nine selected experimental cycles (middle, fast and slow) and model output associated with a motoring cycle at rich condition.

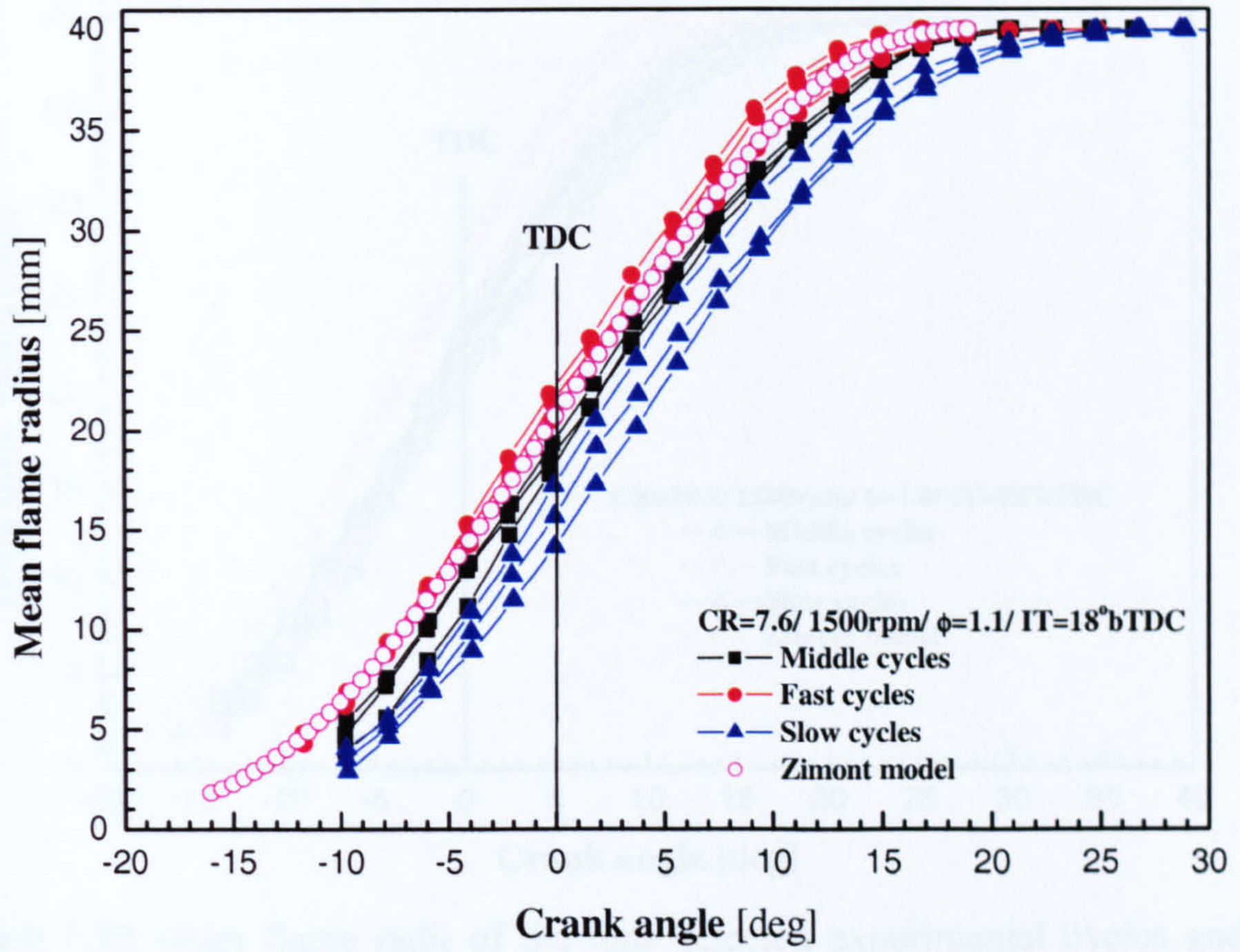

Figure 7.20 Mean flame radii of the nine selected experimental cycles (middle, fast and slow) and output by model at the rich condition.

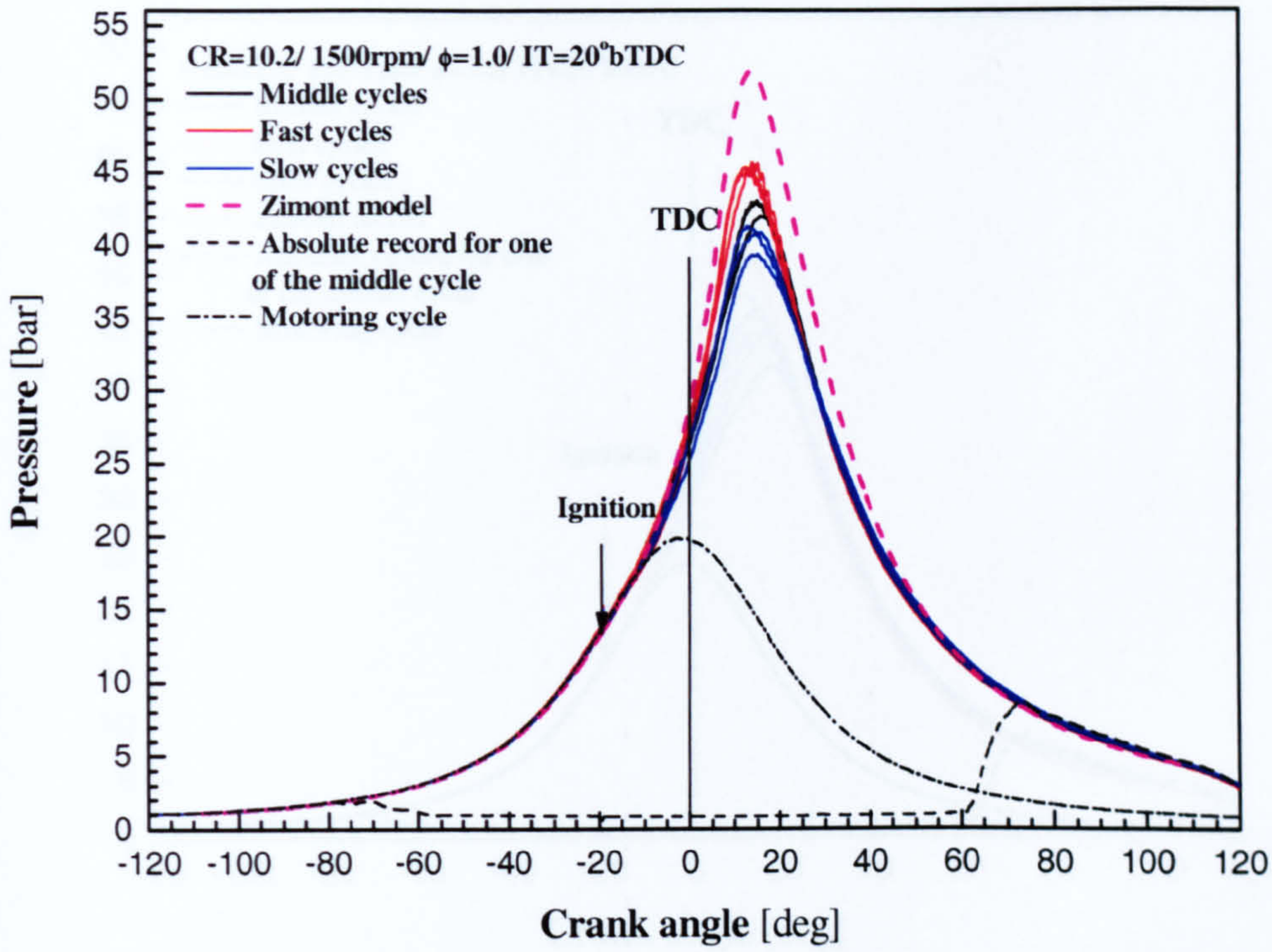

Figure 7.21 Cylinder pressure versus crank angle diagrams for nine selected experimental firing cycles (middle, fast and slow), a motoring cycle, absolute transducer record for one of the middle cycle and output from model (using "rms" measured at CR=7.6) at moderate compression ratio condition (CR=10.2).

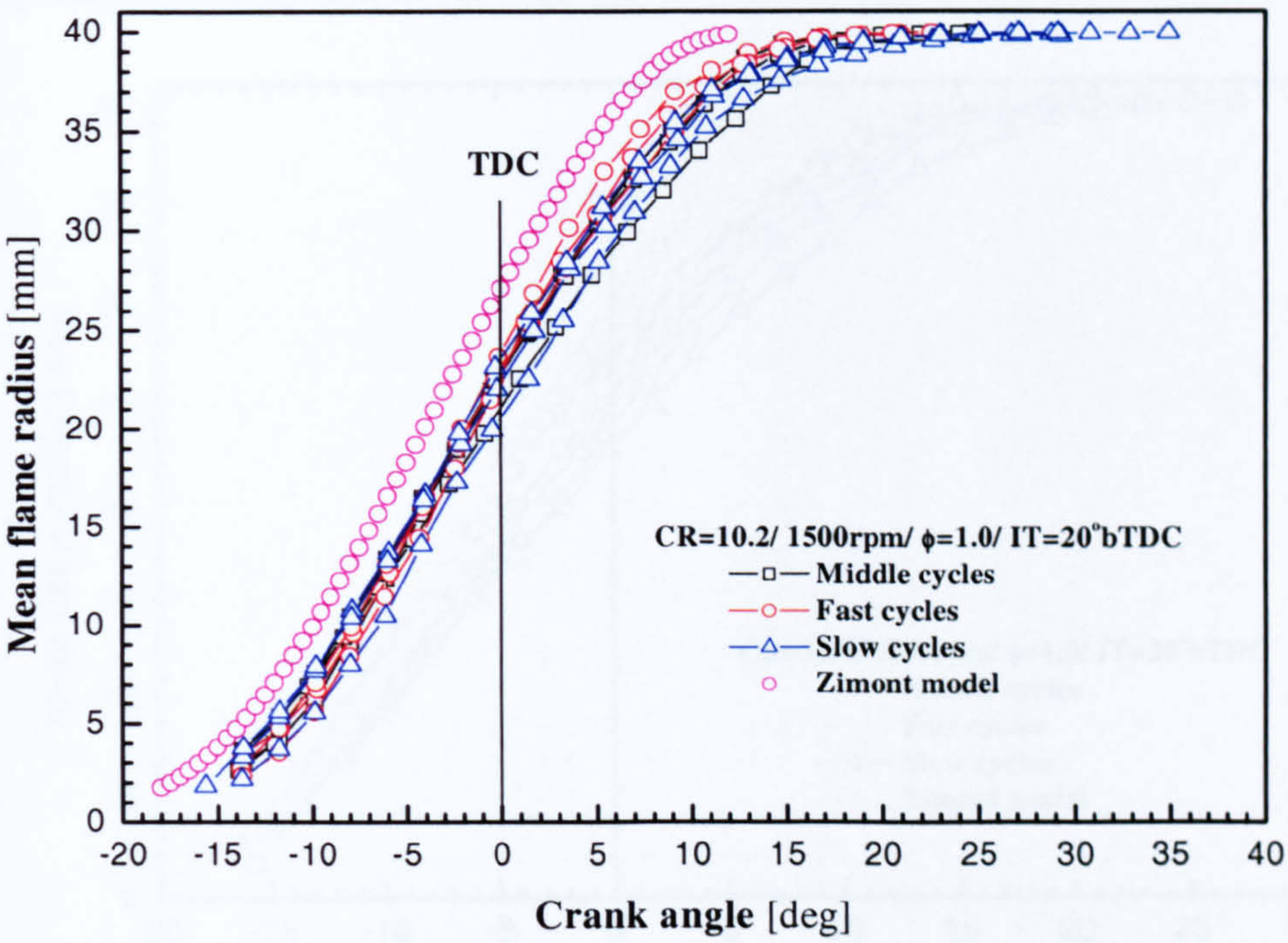

Figure 7.22 Mean flame radii of the nine selected experimental cycles and model (using "rms" measured at CR=7.6) at the moderate compression ratio (CR=10.2).

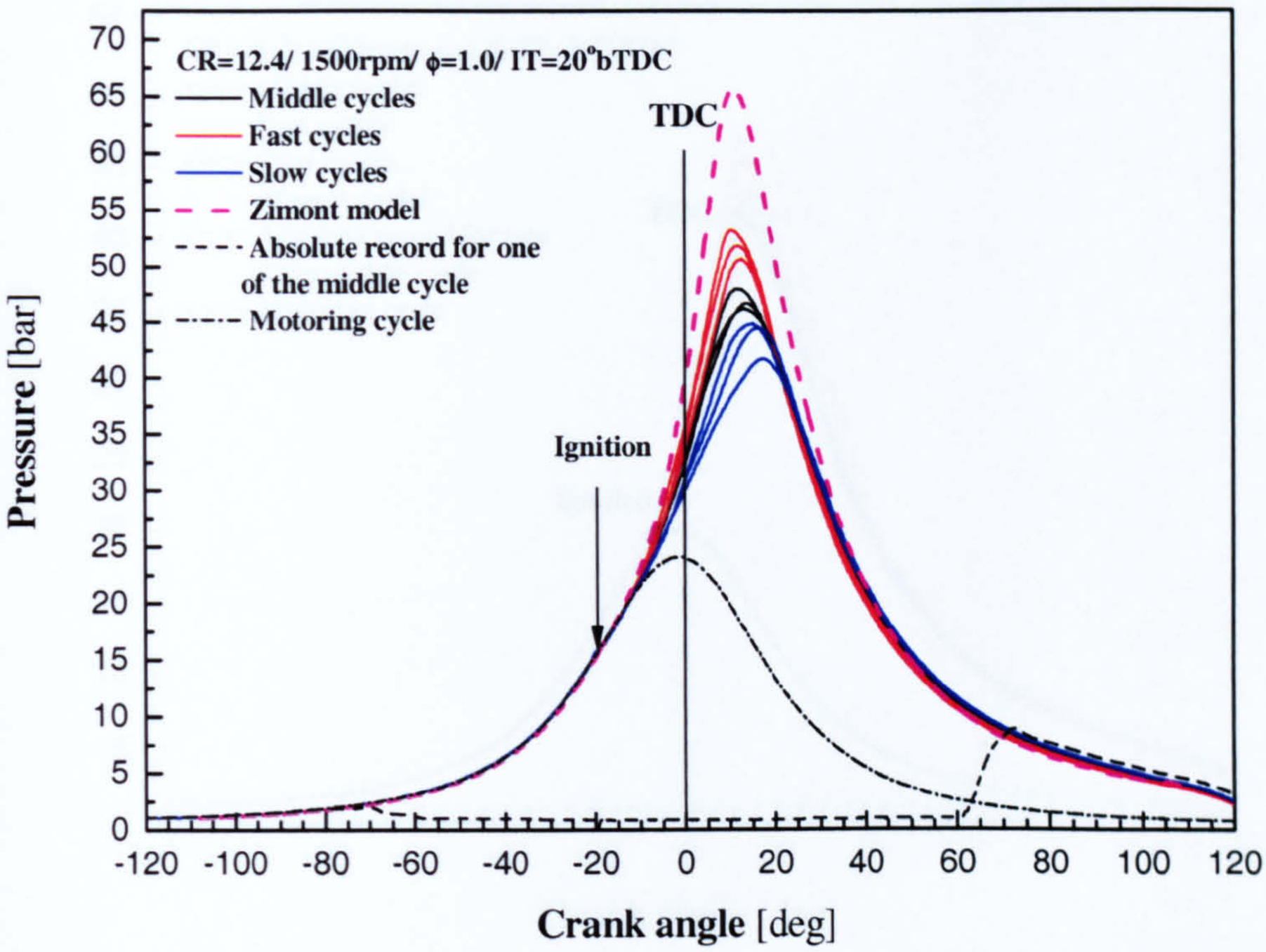

Figure 7.23 Cylinder pressure versus crank angle for model (using "rms" measured at CR=7.6) and nine selected experimental cycles (middle, fast and slow) associated with a motoring cycle and absolute record for one of the middle cycles at high compression ratio condition (CR=12.4).

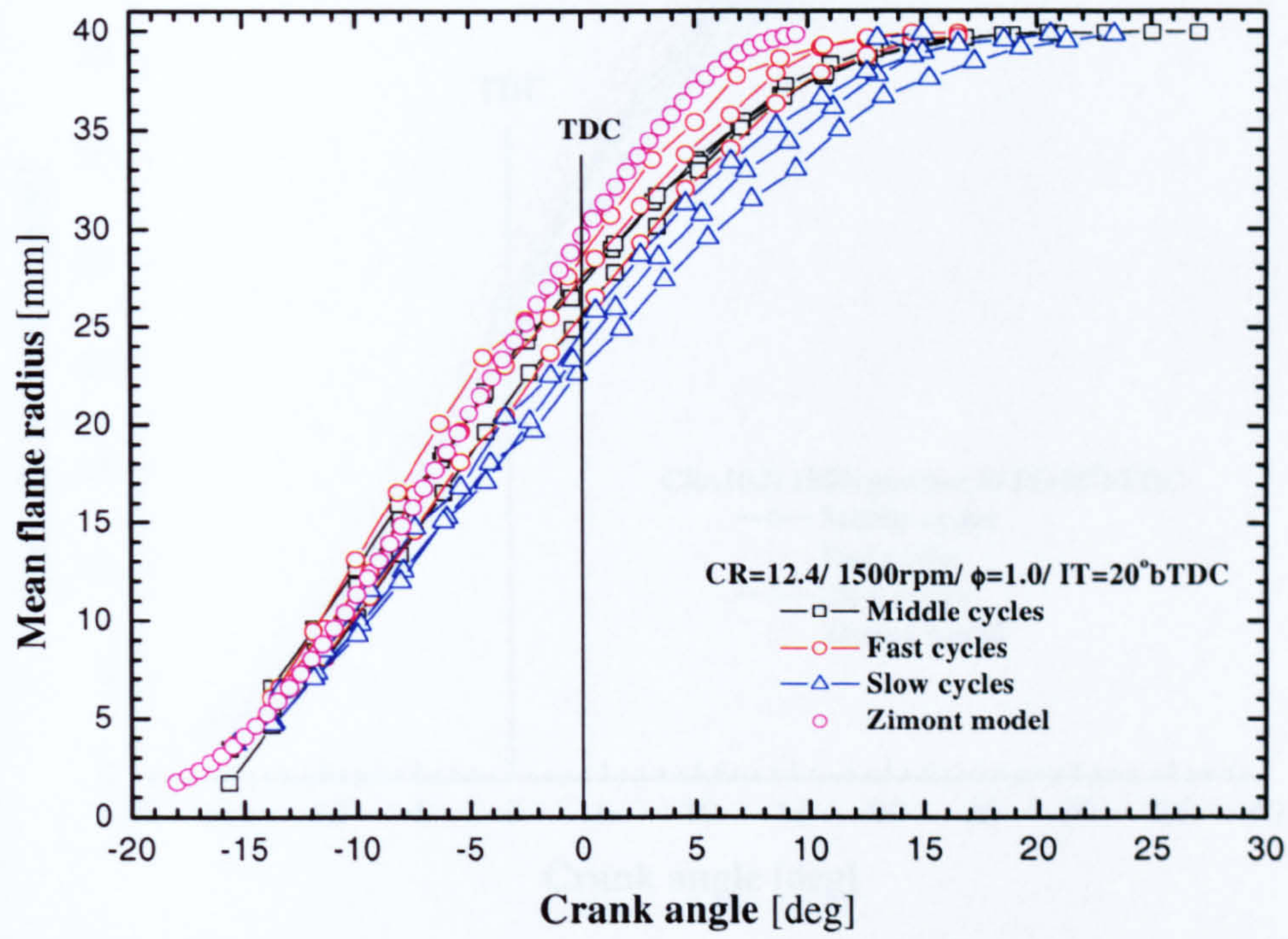

Figure 7.24 Mean flame radii of the nine selected experimental cycles and model (using "rms" measured at CR=7.6) at the moderate compression ratio (CR=12.4).

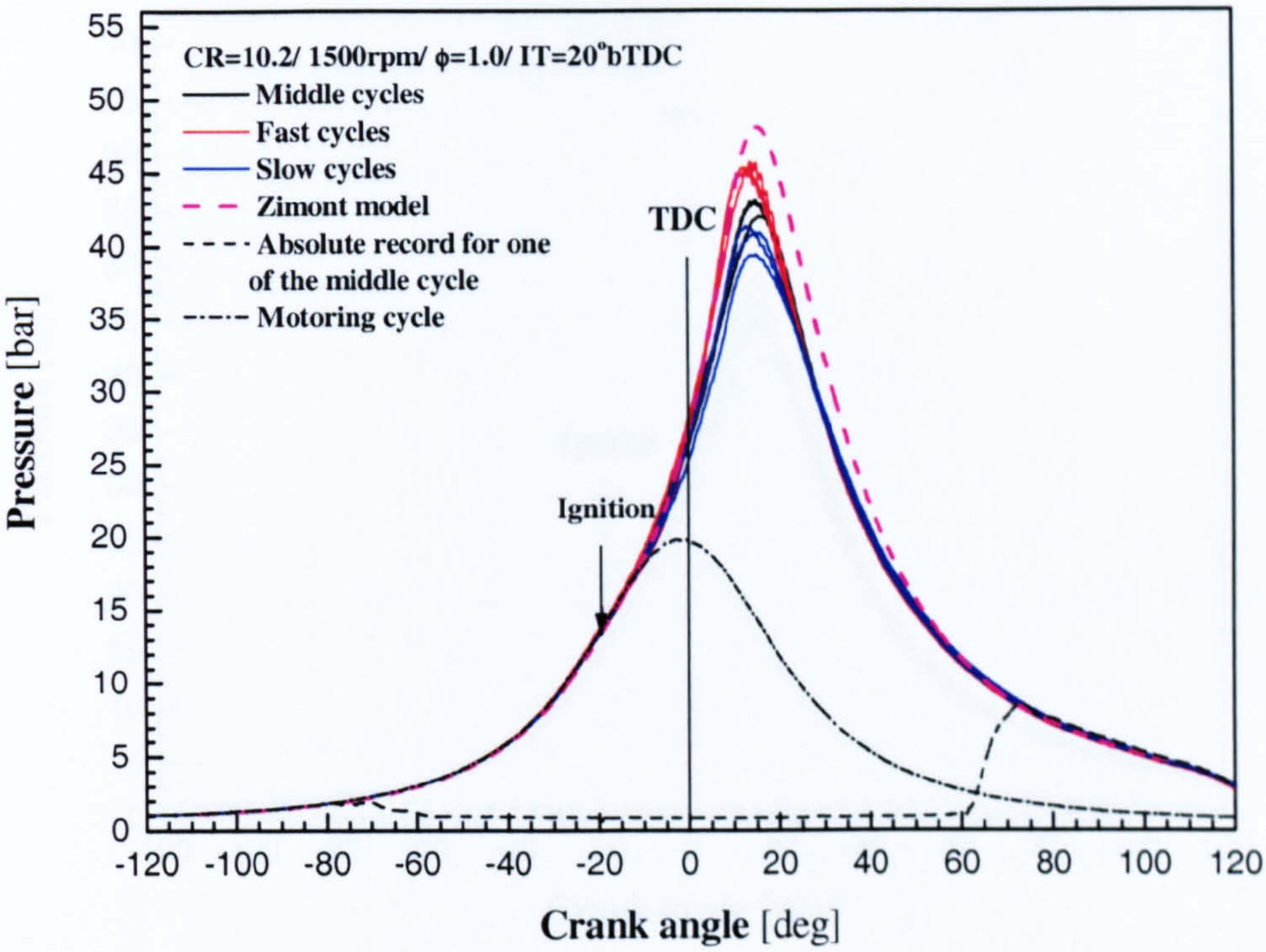

Figure 7.25 Cylinder pressure versus crank angle diagrams for the nine selected experimental firing cycles, a motoring cycle, absolute transducer record for one of the middle cycle and output from model using the estimated "rms" velocity at moderate compression ratio condition (CR=10.2).

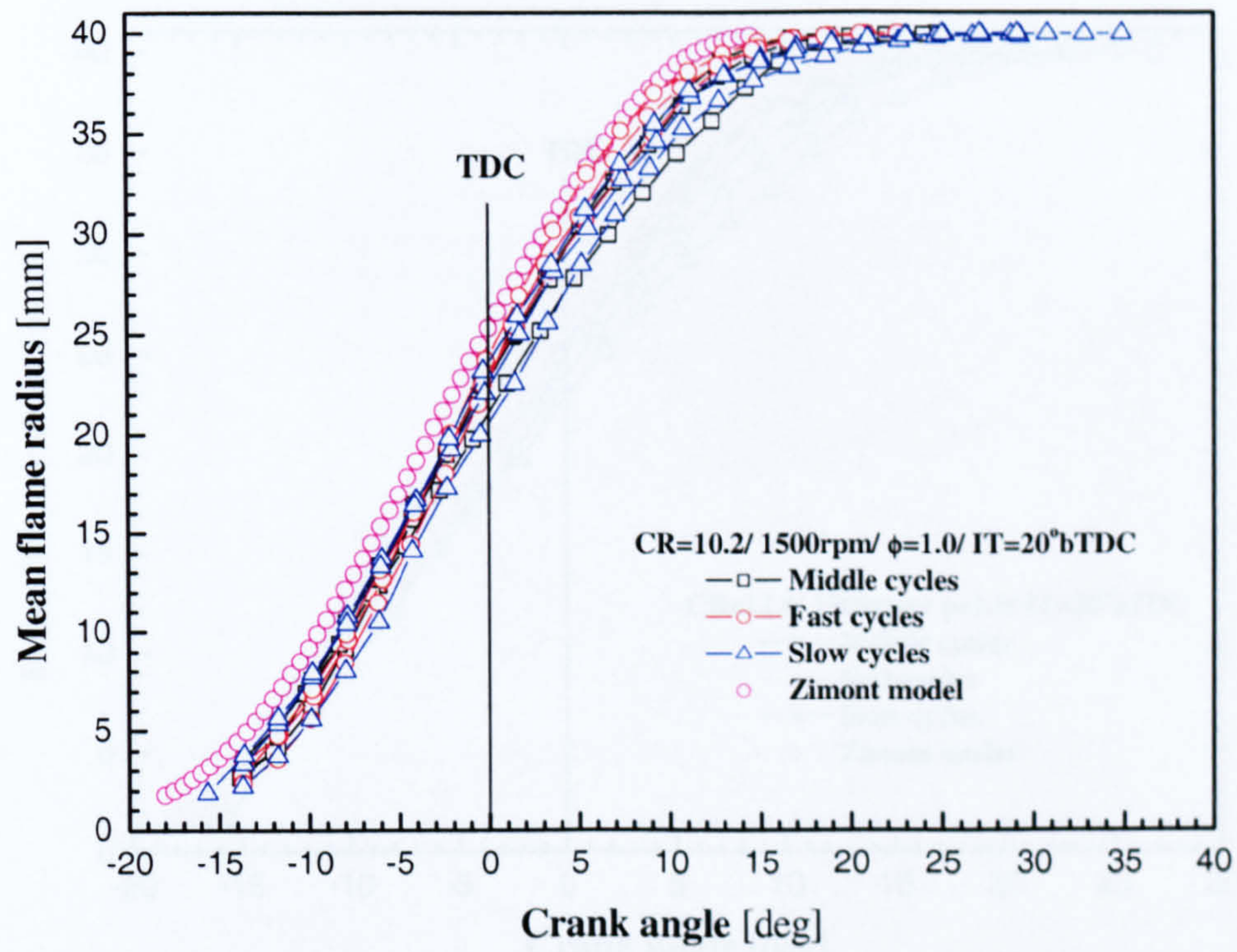

Figure 7.26 Mean flame radii of the nine selected experimental cycles and model using the estimated "rms" velocity at the moderate compression ratio (CR=10.2).

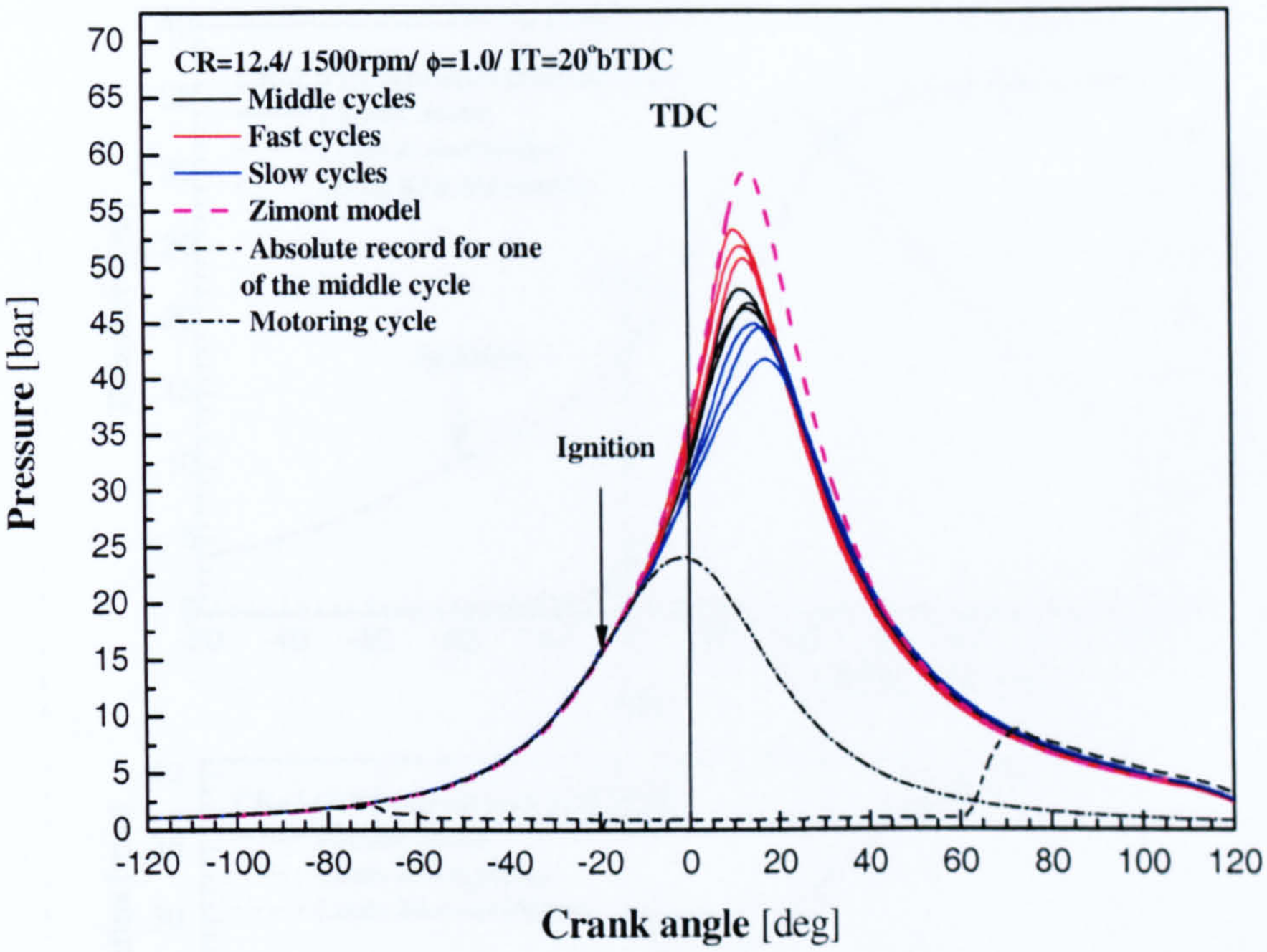

Figure 7.27 Cylinder pressure versus crank angle for model using the estimated "rms" velocity and nine selected experimental cycles (middle, fast and slow) associated with a motoring cycle and absolute record for one of the middle cycles at high compression ratio condition (CR=12.4).

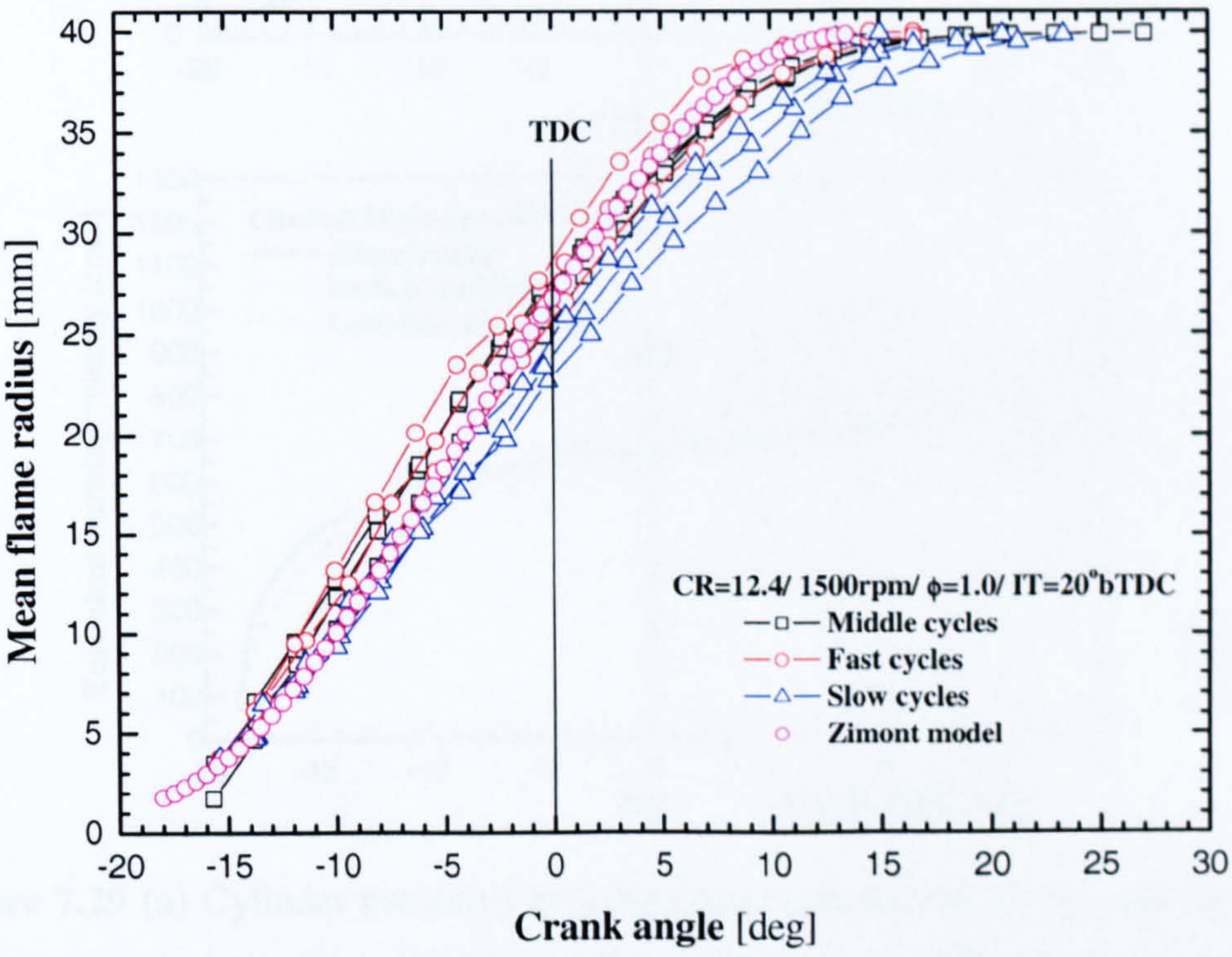

Figure 7.28 Mean flame radii of the nine selected experimental cycles and model using the estimated "rms" velocity at the moderate compression ratio (CR=12.4).

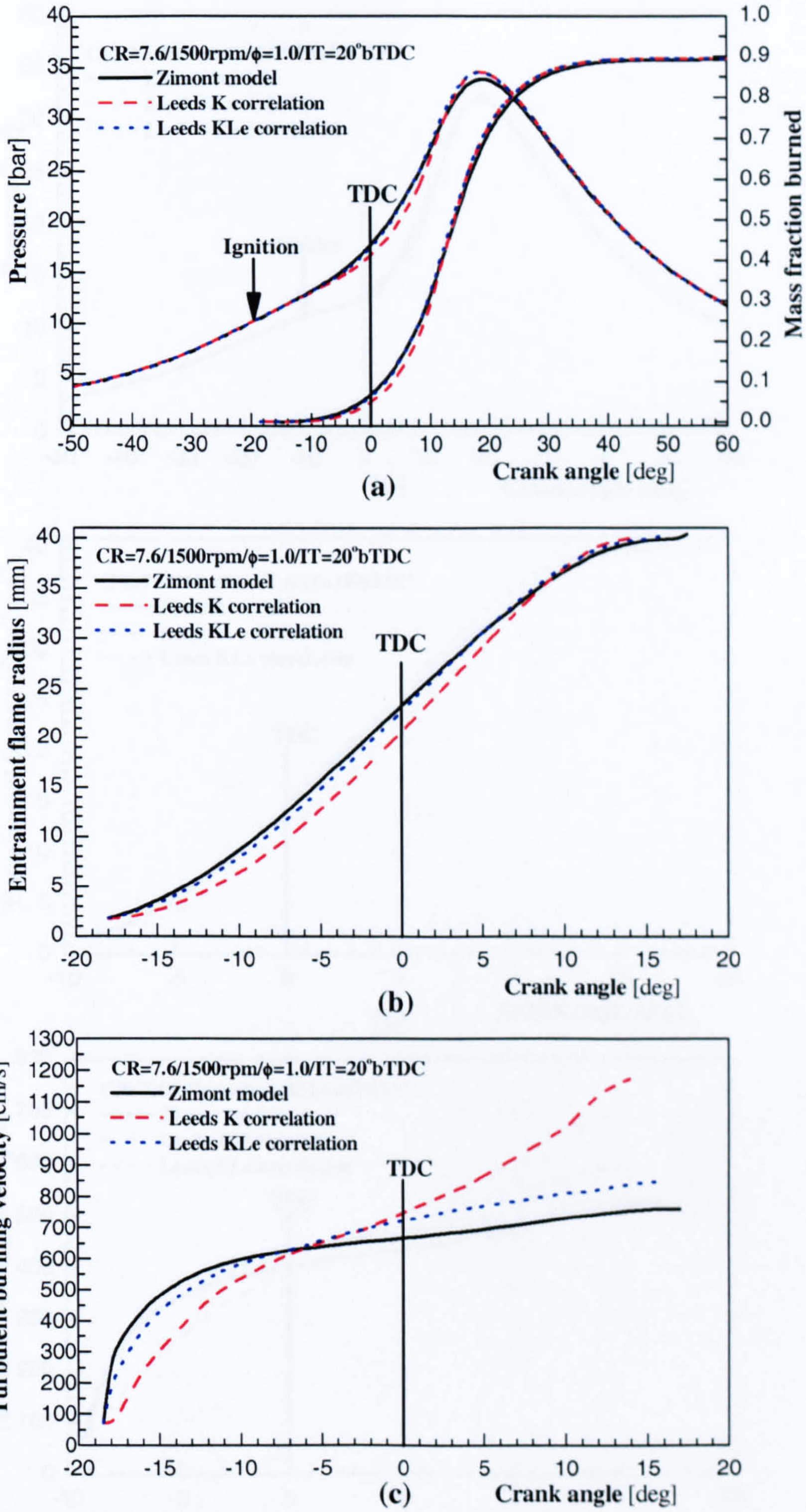

Figure 7.29 **(a)** Cylinder pressures and mass fractions burned **(b)** entrainment flame radii **(c)** turbulent burning velocities versus crank angle for Zimont model and Leeds *K* and *KLe* correlations at the reference condition.

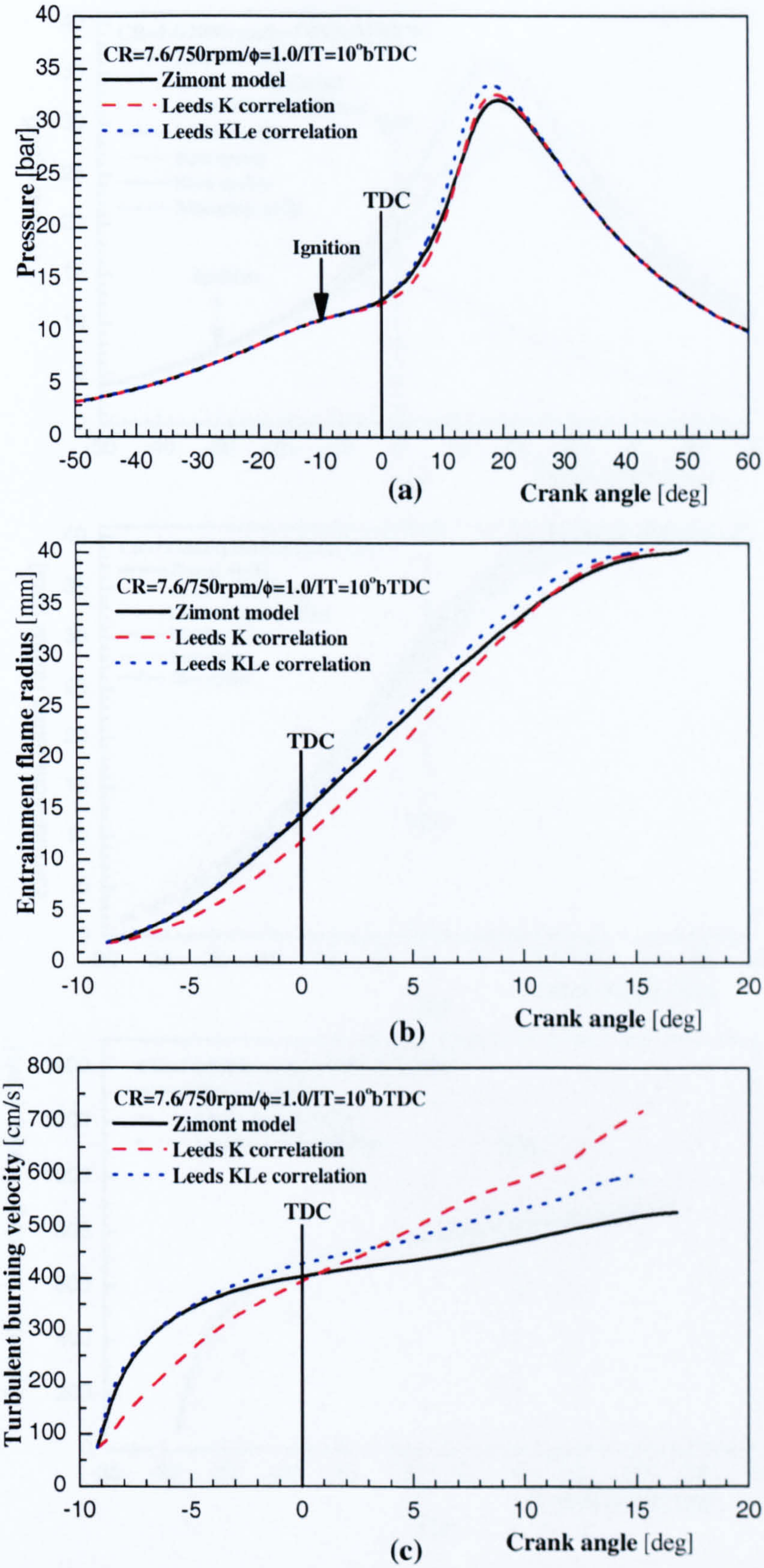

Figure 7.30 **(a)** Cylinder pressures **(b)** entrainment flame radii **(c)** turbulent burning velocities versus crank angle for Zimont model and Leeds *K* and *KLe* correlations at the low engine speed (750 *rpm*).

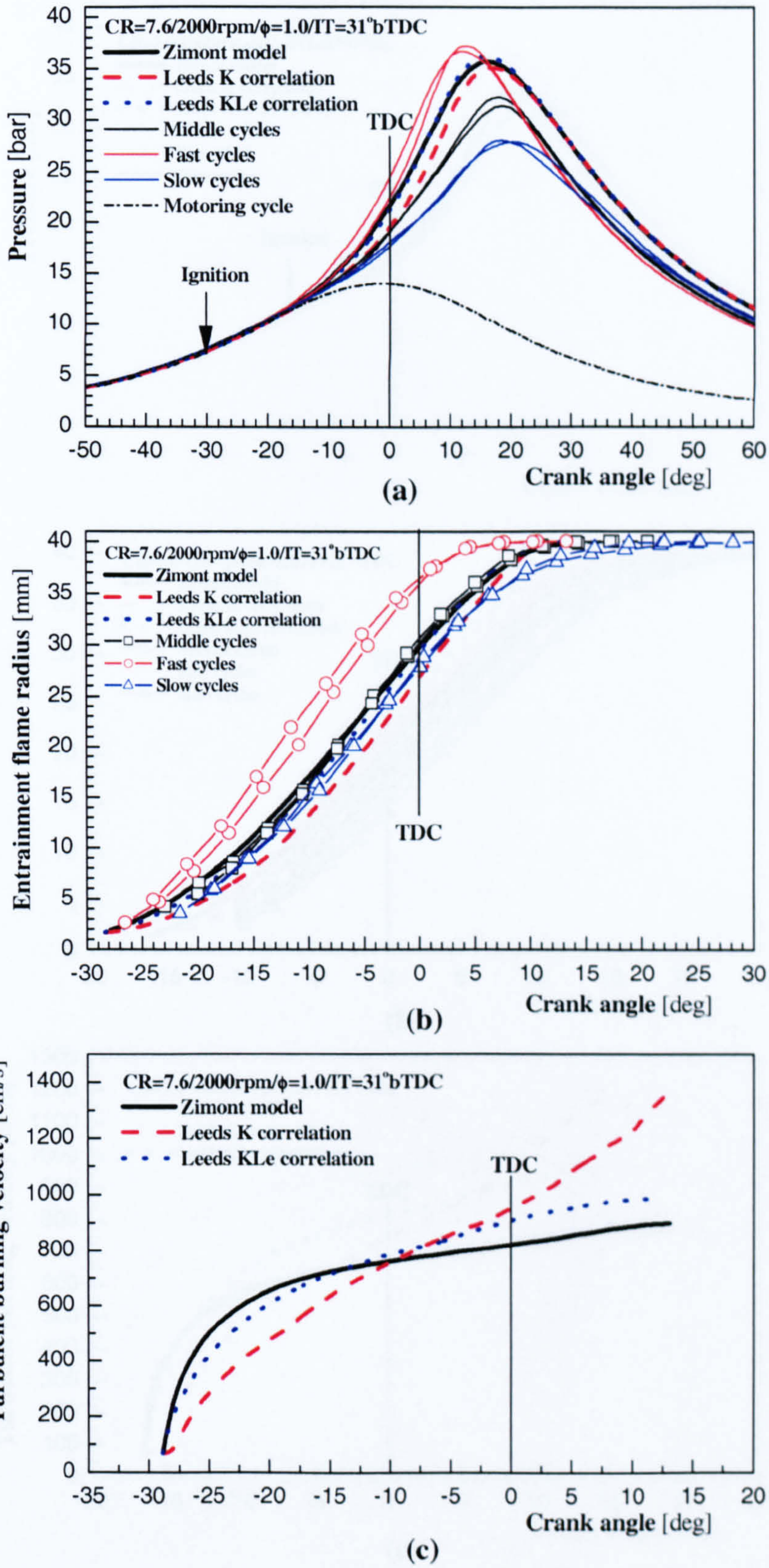

Figure 7.31 Experimental and model output **(a)** cylinder pressures and **(b)** entrainment flame radii, and **(c)** turbulent burning velocities versus crank angle for Zimont model and Leeds *K* and *KLe* correlations at the high engine speed (2000 *rpm*).

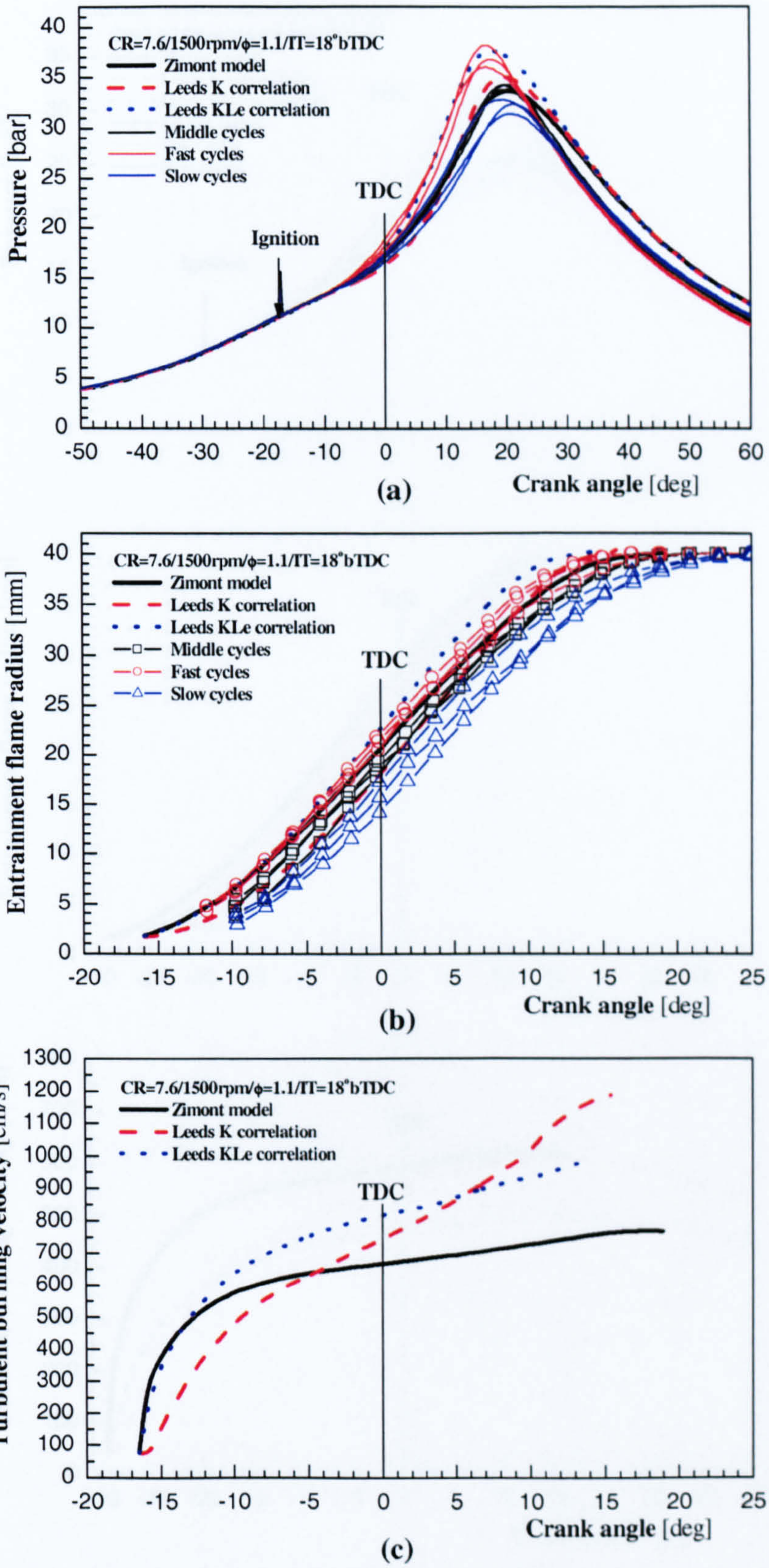

Figure 7.32 (a) Cylinder pressures, **(b)** entrainment flame radii and **(c)** turbulent burning velocities versus crank angle for Zimont model and Leeds *K* and *KLe* correlations at the rich condition ($\phi = 1.1$).

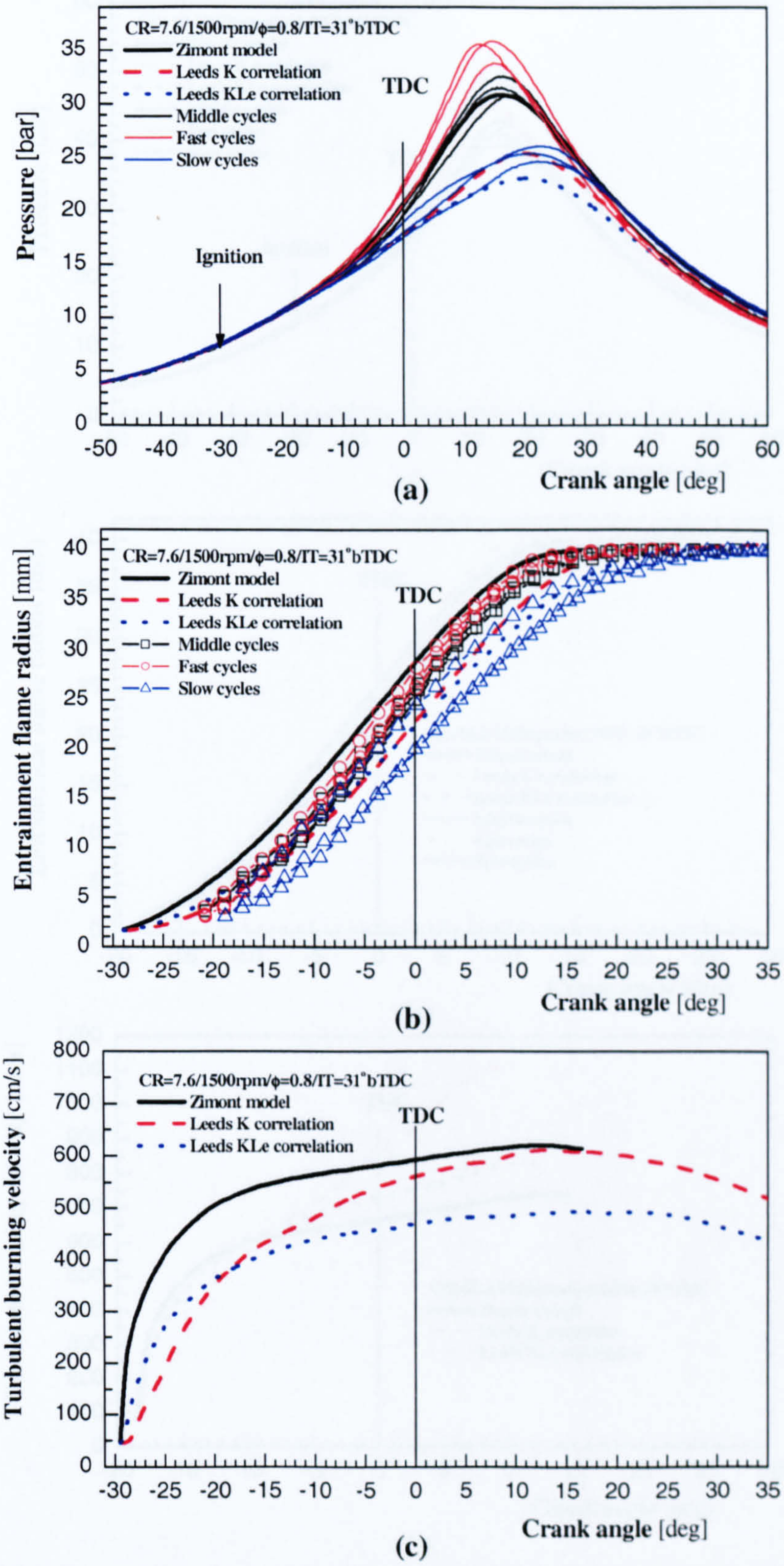

Figure 7.33 Experimental and model output **(a)** Cylinder pressures and **(b)** mean entrainment flame radii, and **(c)** turbulent burning velocities versus crank angle predicted by Zimont model, *K* and *KLe* correlations at the lean condition ($\phi = 0.8$).

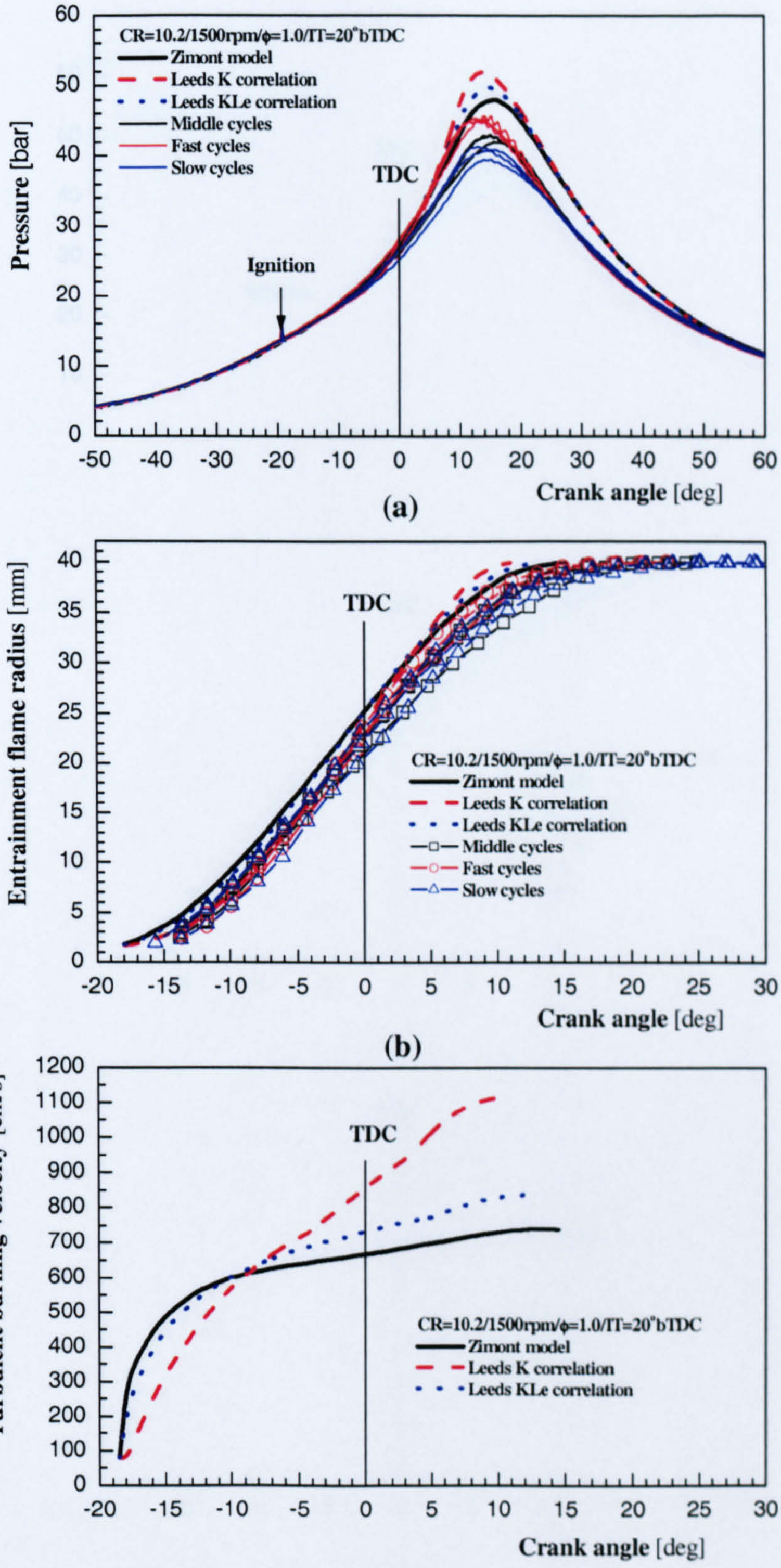

Figure 7.34 Experimental and model output (a) cylinder pressures and (b) mean entrainment flame radii, and (c) turbulent burning velocities versus crank angle predicted by Zimont model, *K* and *KLe* correlations in the "moderate" compression condition (CR=10.2).

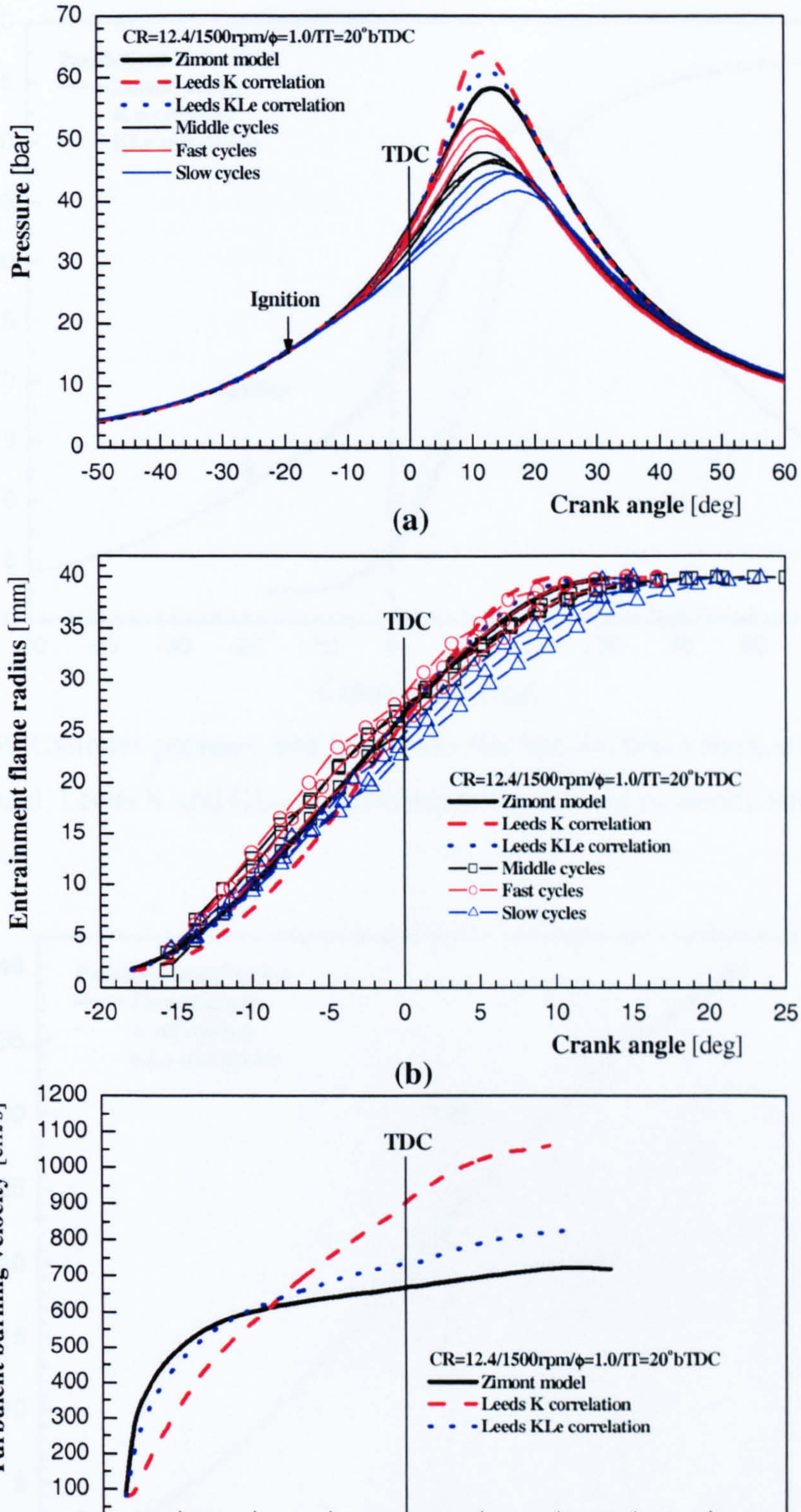

Figure 7.35 Experimental and model output **(a)** cylinder pressures and **(b)** mean entrainment flame radii, and **(c)** turbulent burning velocities versus crank angle predicted by Zimont model, *K* and *KLe* correlations in the "high" compression condition (CR=12.4).

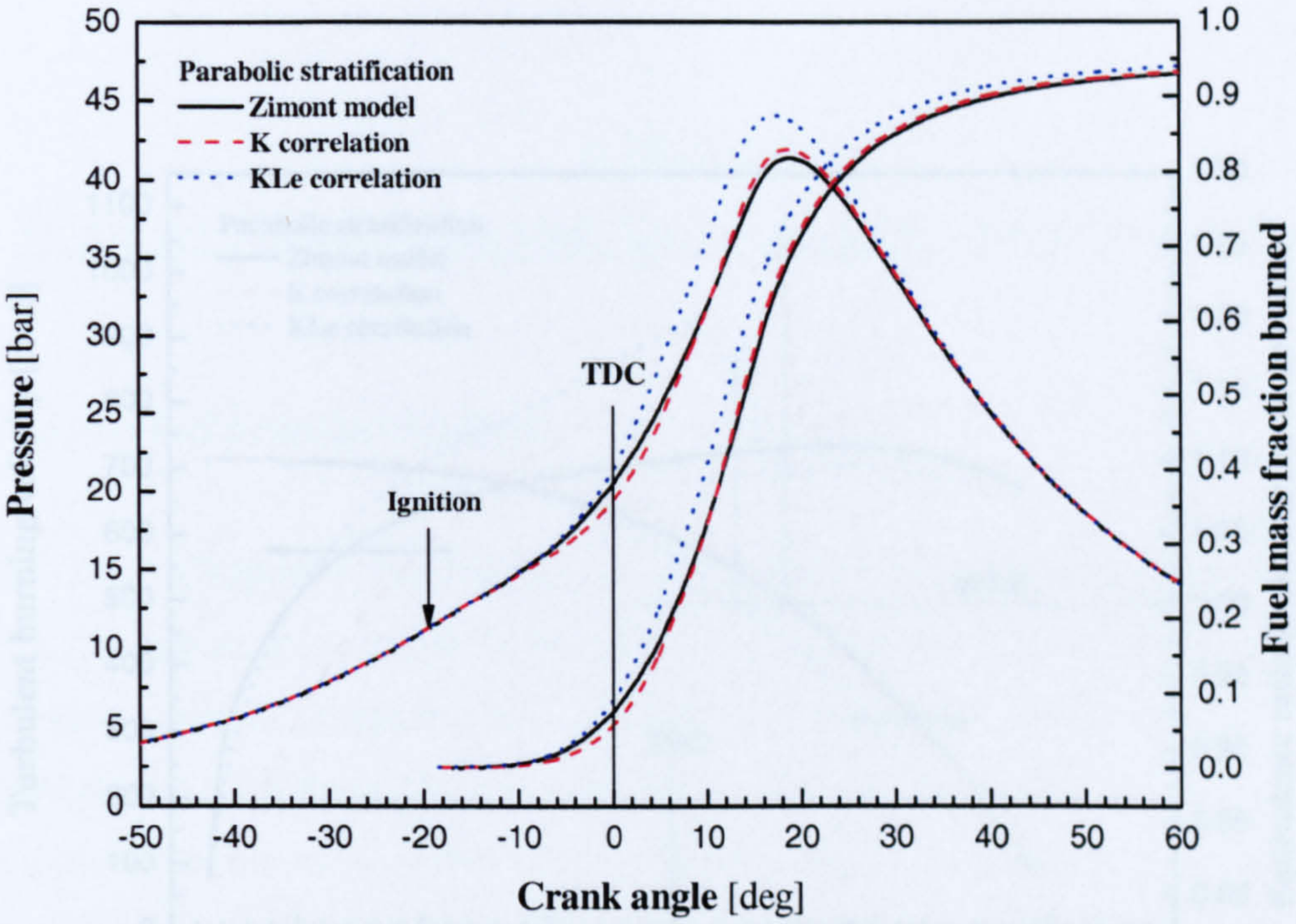

Figure 7.36 Cylinder pressure and fuel mass fraction burned versus crank angle for Zimont model, Leeds K and KLe correlations at the defined parabolic stratification.

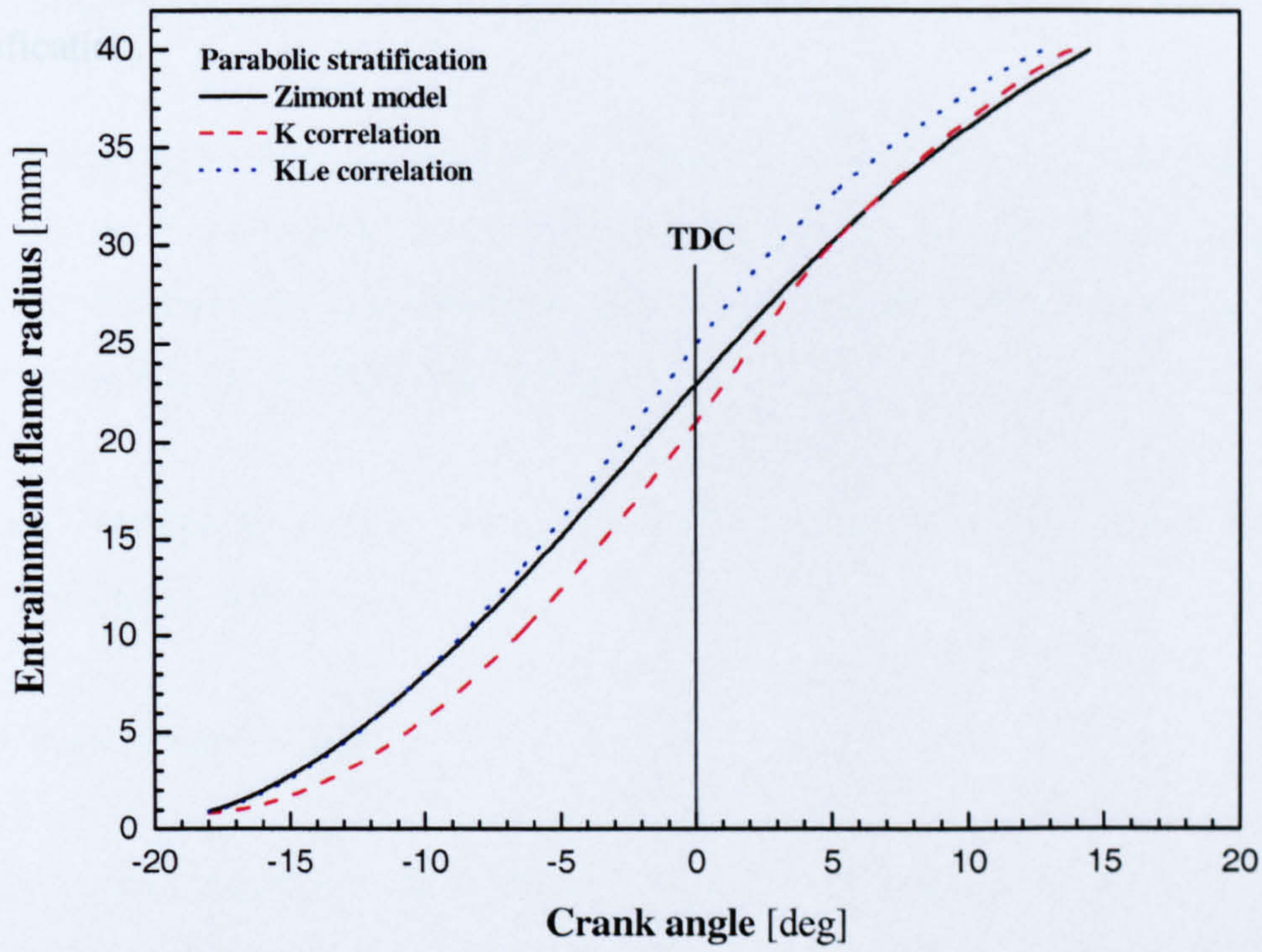

Figure 7.37 The predicted entrainment flame radius versus crank angle for the three expressions at the defined parabolic stratification.

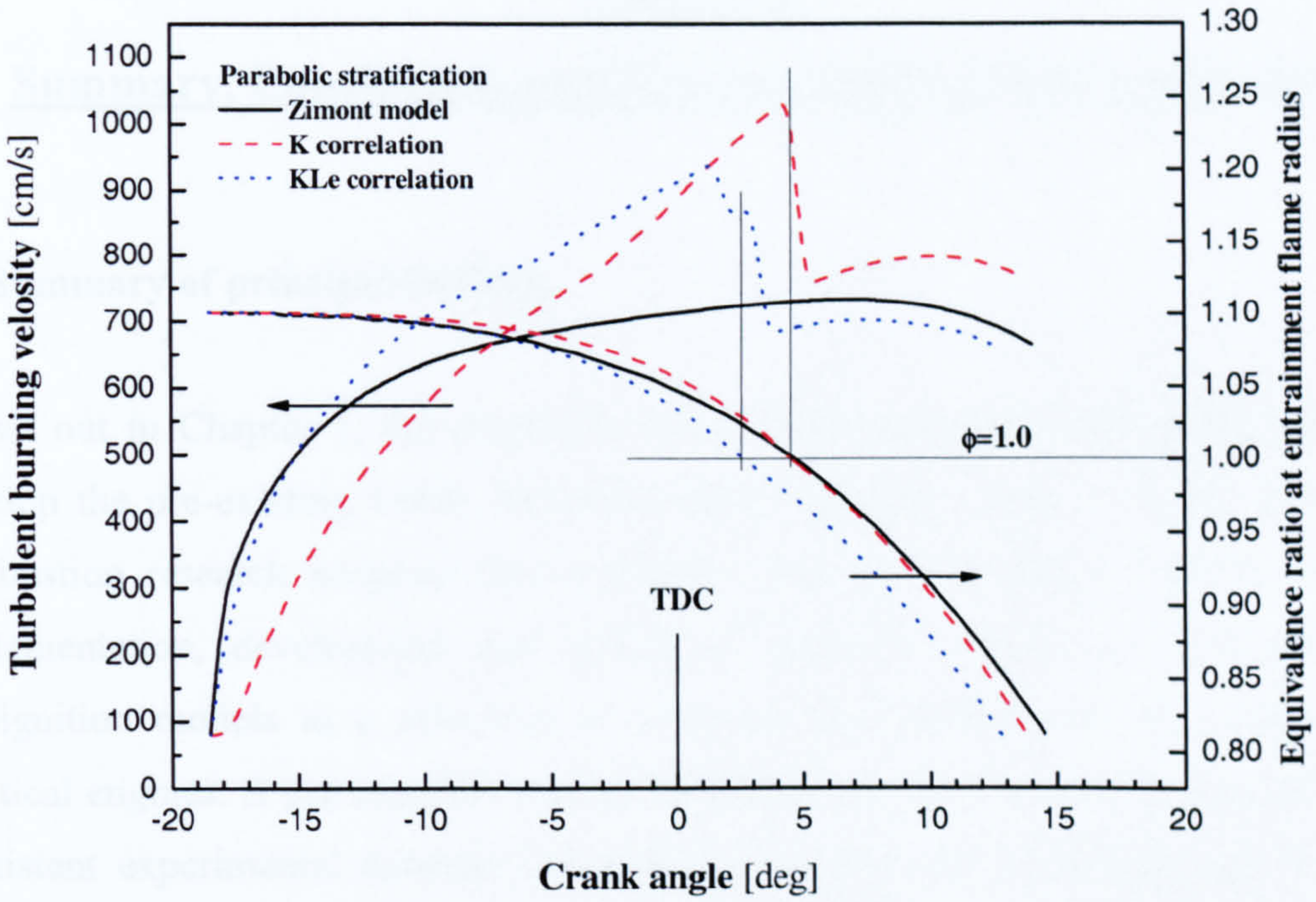

Figure 7.38 The predicted turbulent burning velocity and equivalence ratio at entrainment flame radius for the three expressions at the defined parabolic stratification.

Chapter 8

Summary, Conclusions and Recommendations for Future Work

8.1 Summary of principal findings

As set out in Chapter 1, the objectives of the work outlined in this thesis were to develop the pre-existing Leeds University Spark Ignition Engine (LUSIE) in-house combustion research program into a reliable, accurate and robust vehicle for the implementation, development and testing of turbulent entrainment and end gas autoignition models as a precursor to assessing the usefulness of such codes for practical engines. A pre-requisite was the establishment of an extensive, accurate and consistent experimental database for model calibration and validation; this in turn necessitated development of experimental equipment and data analysis techniques. Although generated principally for validation purposes, the experimental data yielded interesting findings in their own right.

The experimental findings (reported in Chapter 5) are summarised in Section 8.1.1 (below); the modifications to LUSIE code (outlined in Chapter 6) and comparisons between experimental and simulation data (considered in Chapter 7) are summarised in Sections 8.1.2 and 8.1.3, respectively.

General conclusions on the work are set out in Section 8.2 and recommendations for future study are made in Section 8.3.

8.1.1 Experimental study

In the current work, two principal parameters were adopted for model validation: temporal development of cylinder pressure and mean flame radius. In validation of turbulent entrainment thermodynamic models, these parameters implicitly allow examination of the entrained and burned mass rates [Equations (6.1) and (6.4)]. To

effect this, an extensive bank of data of simultaneous measurements of cylinder pressure and flame position at a number of operating conditions was required. To minimise complexity arising from 2D views of 3D flame development, the disc-shaped chamber variant of a full-bore overhead optical access engine (LUPOE1, Chapter 3) was utilised. This variant has previously been shown to yield an essentially zero mean velocity and relatively uniform level of "rms" turbulence throughout the chamber. To allow filming of a statistically significant number of cycles in the time available, flames were imaged using a digital video camera, capturing the light emitted from the flame ("natural light"). Later studies by a colleague (Murad, 2003) have shown mean flame radii determined by this technique to yield very similar values to those from Schlieren imaging. To minimise residual gas effects, data were captured with the engine operating in "skip-fire" mode.

A "reference" condition was defined (CR=7.6, n=1500 *rpm*, ϕ=1.0 and ignition timing 20° *bTDC*). At this condition, a library of earlier LDA (Atashkari, 1997), PTV (Cairns and Sheppard, 2000) and laser sheet Mie scatter imaging (Gillespie, 1998; Cairns, 2001) data were also available to model input and validation purposes. Using the test procedure described in Chapter 3, a large number of simultaneous cylinder pressure and flame imaging data were captured at different engine speeds (n=750, 1500 and 2000 *rpm*), equivalence ratios (ϕ=0.8, 1.0 and 1.1) and compression ratios (CR=7.6, 10.2 and 12.4).

Extensively revised methods were developed to process and analyse the vast pressure and film database. Greyscale flame pictures were converted to black and white images and a number of parameters were derived to characterise them; e.g. mean flame radius, flame centroid and a factor describing flame "circularity" (in terms of a flame "Shape Factor"). Good compatibility between cylinder pressures and mean flame radii for different cycles was observed when both sets of data were processed and synchronised on the basis of shaft encoder (external clock) signals. This time-base signal also proved useful in estimating engine speed variation within a cycle and from cycle to cycle.

Cyclic variation in both cylinder pressure development and flame features was observed. Analysis of the experimental data led to the following observations:

- The mean $p-\theta$ diagram derived from an ensemble average (arithmetic mean) over many firing cycles captured at the same operating condition resulted in a cycle unrepresentative of any individual real cycle, with a more smoothed curve around the peak pressure position. Although the mean $p-\theta$ reflects mean *imep*, it was considered inappropriate to use a mean $p-\theta$ diagram for validation of a combustion model due to its unreality for assessing simultaneous pressure and flame position in a single cycle. Therefore, a few "middle cycles" having peak pressure close to the mean peak pressures were adopted for validation purposes at the "reference" and other operating conditions.

- Analysis of cyclic variation at different engine speeds and different equivalence ratios revealed an increase in coefficient of variation (COV) with engine speed and reduction with equivalence ratio (ϕ=0.8-1.1).

- From analysis of the time-base shaft encoder signal, engine speed variation within a cycle was determined. This revealed a lower than time mean average engine speed over an important part of the combustion period. Similar engine speed variation was also observed in four stroke single (Ricardo E6) and multi-cylinder (VW 1.4 litre, "VWSE") SI engines.

- From processed experimental image data, "Shape Factors" characterising "circularity" of representative fast, middle and slow cycles at each engine operating condition were derived; no consistent correlation was observed between these Shape Factors and combustion development – distorted flames developed, on average, no faster or slower than relatively "circular" flames.

- An Active Perimeter Fraction (APF) was defined to characterise the effects of non-circular and convected flame growth on the mean surface area available for mixture entrainment in late flame developments. The relationship between APF and mean flame radius was remarkably consistent for cycles at different engine

speeds, equivalence ratios and compression ratios. This relationship proved very useful in later modelling studies.

8.1.2 Modelling studies

Extensive modifications have been made to the inherited version of LUSIE successively developed in Leeds by Hynes (1986), Langridge (1995), Merdjani (1996) and Cairns (2001). A number of deficiencies in the blowby sub-model, heat transfer and thermodynamic aspects were corrected. This was performed by modifying the existing routines or by writing completely new subroutines. Also, the "Zimont" model (based on Damköhler number) was incorporated into the code (Section 6.5.3) in addition to the pre-existing turbulent burning velocity expressions within LUSIE.

The combustion modelling was improved by including numerical solution of the "burn-up" equation, taking account of the observations of engine speed variation and flame approach to the wall (APF) from the experimental part of this study. In addition to these modifications, a new sub-model for flame development in radial stratified charge within a disc-shaped chamber was developed and incorporated into the LUSIE program. These improvements have been detailed in Sections 6.5.4-6.5.6.

The developed blowby model was set for hot, fuelled, motoring conditions, avoiding the complications associated with combustion and cyclic variation (Section 7.2). A high level of agreement was observed between the experimental data and model prediction over the period between EPC and EPO. The maximum relative difference between experimental and modelled cylinder pressure over the whole period was less than 3%, reducing to less than 1.5% between $50^{\circ} bTDC$ and $50^{\circ} aTDC$ (the relevant period for combustion).

The simulation code was first calibrated against experimental data for representative "middle" cycles recorded at the "reference" condition (Chapter 5). The "rms" turbulent velocity measured in the engine (Atashkari, 1997) and the average measured temperatures of the inlet charge, cylinder wall and head were input to the model. Other experimental data, such as engine speed variation within a cycle, actual ignition

timing and the variation of Active Perimeter Fraction with flame radius were also input to the model. Then, the model constants were tuned to achieve a good fit with both cylinder pressure and mean flame radius. For the "Zimont" turbulent burning velocity option of the code, the following were noted:

- The best level of agreement was found between experiment and model with A=0.86 (Equation (6.34)), vis-à-vis the value (0.4) used by Lipatnikov and Chomiak (1997) and k_τ=0.6 (Equation (6.5)). The revised value of A was within the range used in the literature (0.4-1).

- The blowby sub-model incorporated in the code predicted a maximum cylinder mass loss of 19% (based on cylinder mass at EPC timing) for firing and 9.5% for motoring cycles at the reference condition. During the period between exhaust port closure by piston crown and top ring, 2.4% mass loss was computed.

- Three mass fractions burned (MFB) were defined, on the basis of three reference masses: total burned mass, cylinder mass at ignition timing and instantaneous cylinder mass. Significant differences were observed between the three MFB's with a difference as great as ~15% at $60^\circ aTDC$. This highlights the need for clear definition of mass fraction burned in the case of such ported engines.

Sensitivity analysis of the combustion model to the empirical parameters used in the model expression was carried out at the "reference" condition. For this, $\pm 10\%$ changes in laminar burning velocity, "rms" turbulent velocity and integral length scale were considered:

- A $\pm 10\%$ change in laminar burning velocity yielded about $\pm 10\%$ variation in peak pressure value and $\pm 15\ K$ in peak unburned gas temperature. The peak positions for both were altered $\mp 1.5^\circ CA$. The effect of the change on entrainment flame radius was checked by the crank angle duration for the achievement of $35mm$ flame radius (when, in experiments, flame usually first touches the wall) and the corresponding value of turbulent burning velocity at that flame radius. For $\pm 10\%$ change in laminar burning velocity, the crank angle duration to reach

35*mm* flame radius changed $\mp 1.5^\circ CA$ and the corresponding turbulent burning velocity varied by about $\pm 8\%$ at that radius.

- A $\pm 10\%$ variation in "rms" turbulent velocity resulted in $\pm 7\%$ change in peak pressure value and $\pm 12\ K$ in peak unburned gas temperature. The related peak positions changed by $\mp 1.5^\circ CA$. The crank angle duration to achieve 35 *mm* flame radius varied by $\mp 1.5^\circ CA$ and the corresponding turbulent burning velocity at the radius was $\pm 9\%$ change.

- A change of $\pm 10\%$ in integral length scale resulted in $\mp 5\%$ variation in peak pressure value (with $\pm 1.0^\circ CA$ alteration in the related peak position) and $\mp 7\ K$ change in peak unburned gas temperature ($\pm 0.5^\circ CA$ shift in the associated peak position). The crank angle duration to achieve 35 *mm* flame radius changed by only $\pm 0.5^\circ CA$ and negligible change in turbulent burning velocity was observed at that radius.

The extension of the LUSIE code to radially stratified charge produced some interesting results. Two types of stratification (initial linear and parabolic distributions of equivalence ratio in terms of radius from the cylinder axis) were examined. Comparisons were made between the results for the stratified and equivalent homogeneous charges. Initially, the Zimont turbulent burning velocity expression was employed. The following observations obtained:

- Due to the effect of burned gas expansion, the initially linear variation in equivalence ratio was significantly distorted as combustion proceeded, such that over much of the flame propagation the mixture strength at the flame front was significantly higher than what one might have expected on the basis of the initial fuel/air distribution. Similarly, for the initially parabolic stratification, the burned gas expansion effect resulted in a non-parabolic distribution of equivalence ratio as propagation proceeded.

- In comparison with equivalent homogeneous mixture combustion, faster flame and pressure development were achieved for the stratified cases (in which the rich region was in the vicinity of spark and the lean region close to cylinder wall).

- When the Leeds K and KLe correlations were adopted in place of the Zimont expression for stratified combustion, a discontinuity in the value of turbulent burning velocity over propagation period occurred. This coincided with the point where the equivalence ratio of unburned gas at the flame front changed from rich to lean. This was associated with the significant change in Lewis number which occurs at the stoichiometric air-fuel ratio for most hydrocarbon fuels.

8.1.3 Model validation

Having calibrated the model (set its constants) at the "reference" condition, the model's "predictive" capability at different engine speeds, mixture strengths and compression ratios was examined. For this exercise the model constants set at the "reference" condition were fixed; only differences in relevant experimental measurements at each condition were changed. For moderate and high compression ratios (CR=10.2 and 12.4), the measured "rms" turbulent velocity at the low compression ratio (CR=7.6) was employed due to the lack of reliable "rms" measurements at the higher compression ratios. The following observations were made:

- Good agreement between experimental results (cylinder pressure and mean flame radius) and model output obtained at the different engine speeds.

- Similarly, good agreement was obtained between experimental results and model predictions for the range of equivalence ratios examined.

- For the moderate and high compression ratios, the model predicted higher peak pressure values than seen in experiments. The sensitivity analysis highlighted the significant effects of "rms" turbulent velocity and laminar burning velocity on combustion development. The lack of reliable LDV "rms" turbulent velocity

measurements at the higher compression ratios may account for the disparity between measured and predicted peak pressure values. Differences might also be related to uncertainty in the input values of laminar burning velocity. These were computed using Equations (6.25) and (6.26), incorporating the pressure and temperature correlations. The latter are greater at higher compression ratios.

The model was similarly calibrated at the "reference" condition with (successively) the Leeds *K* and *KLe* turbulent burning correlations in place of the Zimont model. Best agreement was obtained when the values obtained from these correlations were adjusted by factors of 1.3 and 1.78, respectively. The output from LUSIE was then compared with experimental data at other operating conditions, as before. A similar level of agreement to that obtained with the Zimont model was noted at the different engine speeds and for the rich engine condition. However, slower combustion development was predicted by both *K* and *KLe* expressions for lean conditions. This was considered to be associated with Lewis number effects. For the moderate and high compression ratio cases, simulations with both of the Leeds correlations resulted in higher peak pressure values than experiment; they were also slightly above those predicted using the "Zimont" model.

8.2 General conclusions and discussion

The engine combustion model validation data generated in the current study (particularly taken in conjunction with prior information on turbulence, flow and turbulent flame brush thickness development generated for the same engine) is considered to be possibly more consistent and wide ranging than any currently available in the open literature. A proper test of an engine model is, at least, its ability to predict both **in-cylinder pressure development** and **simultaneous flame position** through the combustion event. The current database provides this, from spark to cylinder wall, on a statistically significant basis – for a relatively wide range of conditions. In addition to use for validation of LUSIE in the current work, the data are being used at VW for validation of Ricardo's VECTIS CFD code. In due course, following publication, the complete database will be made available on the School's website for others wishing to validate/develop combustion models.

As discussed previously, although principally generated for model validation, a number of significant experimental findings interesting in their own right have emerged. Sufficient number of cycles have been analysed to demonstrate the fact that an ensemble averaged pressure record is not representative of any real cycle (given non-linear cyclic variation effects) and, as such, may be inappropriate for model validation. Indeed, a successful model may need to incorporate an element of cyclic variation (such as afforded by large eddy simulations in CFD); this may be particularly necessary for knock modelling since (in trace knock) it may be only fast burn cycles which suffer end gas autoignition.

The apparent lack of correlation between flame shape (here characterised by the "Shape Factor" parameter), initial flame kernel displacement and flame centroid trajectory and flame speed was surprising. The mixture preparation system and skip-fire mode operation of the LUPOE1 engine might be expected to minimise cyclic variation in mixture strength, residual concentration and unburned charge temperature. Subsequent experiments by a colleague (Murad, 2003) suggest that there is little cyclic variation in ignition energy for this engine. What then is the cause of the noted cyclic variation? The observed variations in initial flame "shape", initial kernel displacement and flame centroid trajectory must be related to the relatively large scale eddies (noting that the integral scale of turbulence is of the order 2 *mm*) present at the spark plug at the time of ignition. If the cyclic variation is not a function of the sizes of these large scale structures, is it possible that it is a function of the intensity/energy (rather than the scale) associated with these eddies (which may vary throughout the field at any instant, as well as from cycle to cycle)? To establish this, cycle-resolved, high resolution velocity measurements would be required.

The experimental finding of a near universal relationship between Active Perimeter Fraction (APF) and mean flame radius was significant for correct modelling of the final (approach to wall) phase of flame propagation in a disc-shaped combustion space. A truly spherical/cylindrical flame growth would yield a maximum mean flame surface area close to the wall. Flame "distortion" and movement result in much reduced surface area for flame propagation and hence reduced burn rate late in the combustion event. This will occur also (to a degree) in more complex combustion chamber geometries (e.g. pent-roof), although the lack of symmetrical approach to the

chamber walls inherent even for spherical flame development in such geometries may lead to the effect being less significant (at very least, there will be a different APF relationship with mean flame radius). This will be resolved in continuing studies in the full optical access idealised pent-roof variant of the LUPOE2 engine designed in the course of the current work.

The objective of developing LUSIE into a reliable "platform" for testing combustion/flame propagation models (as well as end gas autoignition models) has been achieved. To date, only "Zimont" and Leeds *K* and *KLe* turbulent burning velocity correlations have been tested; other expressions are currently being tested by colleagues and a *reverse* mode version of LUSIE (Leeds University Spark Ignition Engine Data Analysis, LUSIDA) has been coded to help develop alternative burning velocity expressions. The Zimont model generally proved the most effective of the models studied in simulating the LUPOE1-D engine; however, there were some queries relating to its performance at high compression ratios and the trend towards over prediction of peak pressure with increasing speed over the relatively limited range studied (750 – 2000 *rpm*, a factor of 2.7) puts an unresolved question mark against its performance at the higher engine speeds experienced by production engines.

The ported nature of the LUPOE1 engine, together with the relatively large top land crevice height (associated with piston crown mirror attachment), necessitated careful consideration of top land crevice and inter-ring flows in the current study. These problems are somewhat less severe in a modern four stroke, poppet valve production engine, where blowby losses are much less significant (~1% cylinder charge mass). Nevertheless, even in such engines the mass of unburned mixture flow from cylinder into the top land crevice at peak cylinder pressure can amount to as much as 8% (Heywood, 1988). Since a normally propagating flame cannot penetrate into this crevice, this mixture is unavailable for combustion at that time; although much of it will return to the combustion chamber, mix and burn later in the expansion stroke, it will have a significant effect on modelled pressure development in an engine. This phenomenon is often neglected in thermodynamic (and CFD) engine models. Hence, when incorporated into codes such as WAVE, this feature of LUSIE developed in the current study will enhance modelling of normal four stroke engines in due course.

Do thermodynamic engine models with turbulent entrainment burn models have a future? The "Zimont" sub-model in LUSIE yielded reasonably good fits to experimental data (over the range of conditions tested) for the disc-shaped combustion chamber of the LUPOE1 ported research engine, without adjustment of model constants. It would have been possible, of course, to obtain even better fits to each condition using an empirical Wiebe function burn rate – however, the Wiebe function control constants would have been different (and difficult or impossible to fix in advance of the experiments) in each case. Whether or not the entrainment model can perform equally well for real engines (of complex shape with strong bulk flows and turbulence and mixture inhomogeneity) is not yet resolved.

The spherical flame (centred on the spark plug) approximation proved satisfactory for the disc-shaped combustion space in the LUPOE1 engine (particularly when due allowance was made for the Active Perimeter Fraction late in the combustion event). In the more complex real engines referred to above, the spherical flame approximation may not apply. Preliminary observations in the pent roof variant of the revised LUPOE2 engine suggest that the spherical flame approximation may also be applicable in this engine, although a degree of movement in the flame centroid was apparent (particularly early in combustion) which it may prove necessary to incorporate into the model. It would be possible to successively apply LUSIE's GEOM routine to the trajectory of the flame centre if this locus was known (e.g. cold flow CFD computations). Similarly, it would be possible to adopt spatial and temporal variation in "rms" turbulent velocity and integral scale into LUSIE from such CFD computations. However, it is arguable that the resultant loss of simplicity of the thermodynamic model would remove its principal advantage over CFD codes. As suggested in the Introduction, perhaps it should be accepted that turbulent entrainment thermodynamic models will not be accurately predictive and that they should be used to predict trends in engine performance and to indicate operating conditions where potential combustion problems might be encountered. In this vein, the simplified stratified charge modelling presented in Chapter 6 may be adequate to indicate trends expected under the more complex conditions of real GDI engines.

8.3 Recommendations for future work

Arising from the current study, a number of recommendations for future work are made:

- The present work has highlighted deficiencies in the Leeds *K* and *KLe* correlations when applied within LUSIE. The results with the Zimont formulation for turbulent burning velocity (u_t) show promise. Nevertheless, the established LUSIE platform should be used to test all expressions for u_t available in the technical literature against the LUPOE1 database. In using expressions for u_t, care should be taken to ensure that they relate to entrainment turbulent burning velocity (u_{te}), usually derived from natural light or Schlieren photography, rather than the turbulent burning velocity based on mean reaction front (u_{tr}), derived from pressure record and/or laser sheet imaging (Gillespie et al., 2000; Bradley and co-workers, 2003).

- Relating to the above, and in the interest of simplicity, the performance of a two-zone (burned and unburned) thermodynamic model employing u_{tr} should be explored. Such a model would need carefully to consider a suitable procedure for flame approach to cylinder walls – which will disturb the relationship between the mean flame front and turbulent flame brush thickness.

- Recently, colleagues have re-established three and two-zone reverse mode (LUSIEDA) variants of the revised version of LUSIE, developed by the current author, for the analysis of engine in-cylinder pressure and mean flame radius data. This can be used to generate instantaneous values of u_{te} and u_{tr} through the combustion phase in engine cycles. The resultant information should be used to develop improved expressions/correlations for u_t for subsequent use in the LUSIE code.

- The LUSIE platform developed in the current study should also be used to test alternative autoignition/knock models available in the literature; further LUPOE1 experiments should be conducted under knocking conditions to provide a suitable validation database for these autoignition/knock subroutines.

- In improving and correcting LUSIE, the pre-existing simple NO_x and CO emissions routines have been neglected. These routines should be restored/improved (possibly adding UHC routines) and appropriate experimental validation data collected.

- With the LUPOE2 engine, the task of acquiring experimental validation data for the radially stratified model should be re-attempted. If it proves impossible to assess stratification via seed density variation in laser sheet Mie imaging, doped fuel planar laser induced fluorescence (PLIF) might be considered.

- Modelling has been shown to be extremely sensitive to the value of "rms" turbulent velocity (u') adopted. Measured values of u' are ensemble averaged over a finite crank angle window over many cycles – in order to obtain a statistically meaningful number of data "counts". Hence the value of u' includes variations due to cyclic variation in flow/ turbulence as well as velocity fluctuations at a point in a given cycle. Particle Image Velocimetery (PIV) offers a 2-D snapshot of the velocity field affecting the combustion at an instant in the combustion process. Recent improvements in PIV afford better spatial resolution (allowing imaging of smaller scale vortices) and a degree of temporal resolution in a particular combustion event. The technique should be re-applied to the LUPOE engines.

- The work has also highlighted the sensitivity to values of laminar burning velocity (u_l). The data for u_l used in the current work (Metghalchi and Keck, 1982) is considered to remain the best available for u_l for engine fuels at elevated temperature and pressure. However, the data have quite large error bands and have been questioned in recent years due to lack of consideration of flame stretch and cellularity effects (Bradley et al., 1998; Gillespie et al., 2000). In addition, recent work (Ormsby et al., 2003) has cast doubt on the universality of normalising u_t with u_l; certainly for rich mixtures encountered in stratified charge engines. Further fundamental study of laminar and turbulent burning (and measurement and assessment of the u_l and u_t concepts) is recommended.

References

Abdel-Gayed, R.G., Al-Khishali, K.J. and Bradley, D. (1984) *Turbulent Burning Velocities and Flame Straining in Explosions.*; Proc. R. Soc. Lond. A **391,** 393-414.

Abdel-Gayed, R.G., Bradley, D. and Lawes, M. (1987) *Turbulent burning velocities: a general correlation in terms of straining rates.*; Proc. R. Soc. Lond. A **414**, 389-413.

Abdel-Salam, H. A. (1992) *Modelling and Experimental Validation of Turbulent Flame Propagation in Spark Ignition Engines.;* PhD Thesis, El-Mansoura University, Egypt (in association with Department of Mechanical Engineering, University of Leeds).

Abdi Aghdam, E. (2000) *Computational and Experimental Study of Flame Propagation in Radial Stratified Charge SI Engines.*; PhD Transfer Report, Department of Mechanical Engineering, University of Leeds.

Abdi Aghdam, E. (2003) *Analysis of Cylinder Pressure and Flame and Flame Development in S.I. Engines.*; Technical Report, School of Mechanical Engineering, University of Leeds.

Al-Mamar, F.N.A.A. (1983) *Combustion in a Dual Chamber Spark Ignition Engine.*; PhD Thesis, Leeds University, Department of Mechanical Engineering.

Al-Fakhri, Y. and Raine, R.R. (2000) *Application of a New Technique for the Evaluation of Cycle-by-Cycle Variation of Completeness of Combustion to Changes of Compression Ratio.*; SAE paper 2000-01-1213.

Anderson, R.W., Yang, J., Brehob, D.D., Vallance, J.K. and Whiteaker, R.M. (1996) *Understanding the Thermodynamics of Direct Injection Spark Ignition (DISI) Combustion Systems: An Analytical and Experimental Investigation.*; SAE Paper 962018.

Annand, W. J. D. (1963) *Heat Transfer in the Cylinder of Reciprocating Internal Combustion Engines;* Proc. Instn. Mech. Engrs Vol.177, 36, pp. 973-990.

Arcoumanis, C., Bae, C.S. and Hu, Z. (1994) *Flow and Combustion in a Four-Valve Spark-Ignition Optical Engine.*; SAE paper 940475.

Arcoumanis, C., Gold, M. R., Whitelaw, J. H. and Xu, H. M. (1996) *Local Charge Stratification in Spark-Ignition Engines.;* Instn. Mech. Engrs S433/006.

Arsie, I., Pianese, C. and Rizzo, G. (1998) *Models for the Prediction of Performance and Emissions in a Spark Ignition Engine – A Sequentially Structured Approach.*; SAE paper 980779.

Atashkari, K. (1997) *Experimental Study of Flow and Turbulence in a V-flame Burner and a SI Engine.*; PhD thesis, Department of Mech. Eng., University of Leeds.

Ball, J.K., Raine, R.R. and Stone, C.R. (1998) *Combustion analysis and cycle-by cycle variations in spark ignition engine combustion Part2: a new parameter for completeness of combustion and its use in modelling cycle-by-cycle variations in combustion.*; Proc. Instn Mch. Engrs, Vol 212, Part D, pp. 507-523.

Beretta, G.P., Rashidi, M. and Keck, J.C. (1983) *Turbulent Flame Propagation and Combustion in spark Ignition Engines.*; Combustion and Flame, Vol. 52, pp. 217-245.

Bianco, Y., Cheng, W.C., and Heywood, J.B. (1991) *The Effect of Initial Flame Kernel Conditions on Flame Development in SI Engines.*; SAE paper 912402.

Biagioli, F. and Zimont, V.L. (2002) *Gasdynamics Modeling of Countergradient Transport in Open and Impinging Turbulent Premixed Flames.*; Proceeding of the Combustion Institute, Vol. 29, pp 2087-2095.

Blizard, N.C. and Keck, J.C. (1974) *Experimental and Theoretical Investigation of Turbulent Burning Model for Internal Combustion Engines.;* SAE paper 740191.

Borman, G. and Nishiwaki, K. (1987) *Internal Combustion Engine Heat Transfer.*; Prog. Energy Combust. Sci., Vol. 13, pp.1-46.

Bradley, D., Haq, M.Z., Hicks, R.A., Kitagawa, T., Lawes, M., Sheppard, C.G.W. and Woolley, R. (2003) *Turbulent burning velocity, burned gas distribution, and associated flame surface definition.*; Combustion and Flame, **113**, pp 415-430.

Bradley, D., Hicks, R. A., Lawes, M., Sheppard, C.G.W. and Woolley, R. (1998) *The Measurement of Laminar Burning Velocities and Markstein Numbers for Iso-octane–Air and Iso-octane–n-Heptane–Air Mixtures at Elevated Temperatures and Pressures in an Explosion Bomb.;* Combustion and Flame **115**, pp. 126-144.

Bradley, D., Hynes, J., Lawes, M. and Sheppard, C.G.W. (1988) *Limitations to Turbulence-Enhanced Burning Rates in Lean Burn Engines.*; Proc. Instn. Mech. Engrs. Lond., C46/88, pp. 17-24.

Bradley, D., Lau, A. K. C. and Lawes, M. (1992) *Flame Stretch Rate as a Determinant of Turbulent Burning Velocity.;* Phil. Trans. R. Soc. Lond. A **338**, pp 359-387.

Bradley, D., Lawes, M. and Sheppard, C.G.W. (2000) *Combustion and the thermodynamic performance of spark ignition engines.*; Proc Instn Mech Engrs, Vol 214, Part C, pp 257-268.

Brehob, D.D. and Newman, C.E. (1992) *Monte Carlo Simulation of Cycle by Cycle Variability.*; SAE paper 922165.

Brunt, M.F.J., Rai, H. and Emtage, A.L. (1998) *The Calculation of Heat Release Energy from Engine Cylinder Pressure.*; SAE paper 981052.

Buran, D. (1998) *Turbulent Flame Propagation in a Methane Fuelled Spark Ignition Engine.*; PhD Thesis, Department of Mechanical Engineering, University of Leeds.

Butler, G.R. (1999) *The Effects of Swirl on Combustion in Spark Ignition Engines.*; PhD Thesis, Department of Mechanical Engineering, University of Leeds.

Cairns, A. (2001) *Turbulent Flame Development in a Spark Ignition Engine.*; PhD Thesis, Department of Mechanical Engineering, University of Leeds.

Cairns, A. and Sheppard, C.G.W. (2000) *Cyclically Resolved Simultaneous Flame and Flow Imaging in a SI Engine.;* SAE Paper 2000-01-2832.

Chen, C. and Veshagh, A. (1992) *A Refinement of Flame Propagation Combustion Model for Spark-Ignition Engines.;* SAE Paper 920679.

Chen, K.S. and Chen, S. (1993) *Engine Diagnostics by Dynamic Shaft Measurement: A Progress Report,;* SAE Paper 932412.

Chow, A. and Wyszynski, M.L. (1999) *Thermodynamic modelling of complete engine systems – a review.*; Proc. Instn Mech Engrs, Vol. 213, Part D.

Chun, K.M. and Heywood, J.B. (1987) *Estimating Heat-Release and Mass-of-Mixture Burned from Spark-Ignition Engine Pressure Data.*; Combust. Sci. and Tech. Vol. 54 pp. 133-143.

Dare, T. and Yagi, S. (1974) *Research and Development of the Honda CVCC Engine.*; SAE paper 740605.

Damköhler, G. (1940) *The Effect of Turbulence on Flame Velocity in Gas Mixtures.*; Z. Elektrochemie Angewandte Phys. Chem. Vol 46.

Desoky, A.R.A.A. (1981) *An Experimental and Theoretical Study of the Combustion Process in a Divided Chamber Spark Ignition Engine.*; PhD Thesis, Leeds University Department of Mechanical Engineering.

Dugger, G. and Graab, D. (1952) *Flame Velocities of Hydrocarbon-Oxygen-Nitrogen Mixtures.*; Fourth Symposium (International) on combustion.

Fraser, R.A., Felton, P.G., Bracco, F.V. and Santavicca, D.A. (1986) *Preliminary Turbulent Length Scale Measurements in a Motored Internal Combustion Engine.;* SAE paper 860021.

Fujimoto, M., Nishida, K., Hiroyasu, H. and Tabata, M. (1995) *Influence of Mixture Stratification Pattern on Combustion Characteristics in a Constant-Volume Combustion Chamber.;* SAE paper 952412.

Furuhama, S. and Tada, T. (1961a) *On the Flow of Gas Through the Piston-Rings (1st Report, The Discharge Coefficient and Temperature of Leakage Gas).;* Bulletin of JSME, Vol.4, No.16, pp 684-690.

Furuhama, S. and Tada, T. (1961b) *On the Flow of Gas Through the Piston-Rings (2nd Report, The Character of Gas Leakage).;* Bulletin of JSME, Vol.4, No.16, pp 691-698.

Gatowski, J.A., Balles, E.N., Chun, K.M., Nelson, F.E., Ekchian, J.A., and Heywood, J.B. (1984) *Heat Release Analysis from Pressure Data.*; SAE paper 841359, SAE Trans., Vol. 93.

Gere, J. M. and Timoshenko, S. P. (1985) *Mechanics of Materials.;* PWS Publishers, p747.

Gibbs, G.J. and Calcote, H.F. (1959) *Effect of Molecular Structure on Burning Velocity.*; J. Chem. Eng. Data, 4.

Gillespie, L. (1998) *Imaging and Analysis of Turbulent Flame Development in Spark-Ignition Engines.;* PhD Thesis, Department of Mechanical Engineering, University of Leeds.

Gillespie, L., Lawes, M., Sheppard, C. G. W. and Woolley, R. (2000) *Aspects of Laminar and Turbulent Burning Velocity Relevant to SI Engines.;* SAE paper 2000-01-0192.

Groff, E.G. and Matekunas, F.A. (1980) *The Nature of Turbulent Flame Propagation in a Homogeneous Spark Ignited Engine.*; SAE paper 800133.

Guezennec, Y.G. and Hamama, W. (1999) *Two Heat Release Analysis of Combustion Data and Calibration of Heat Transfer Correlation in an I.C. Engine.*; SAE paper 1999-01-0218.

Gülder, O.L. (1982) *Laminar Burning Velocities of Methanol, Ethanol and Isooctane-Air Mixtures.;* 19th Symposium (International) on Combustion, The Combustion Institute, Pittsburgh, p. 275.

Gülder, O.L. (1990) *'Turbulent Premixed Flame Propagation Models for Different Combustion Regimes.'*, Twenty-Third Symposium (International) on Combustion pp 743-750.

Gyan, Ph., Ginoux, St., Champoussin, J.C. and Guezenec, Y. (2000) *Crank Angle Based Torque Estimation: Mechanistic/Stochastic,; SAE Paper 2000-01-0559.*

Hall, M. J. and Bracco, F. V. (1987) *A study of Velocities and Turbulence Intensities Measured in Firing and Motored Engines.;* SAE paper 870453.

Hamid, M.N. (1986) *Fundamental Turbulent Combustion Problems Related to Gasoline Engines.*; PhD Thesis, Leeds University, Department of Mechanical Engineering.

Hayakawa, M., Takada, S., Yonesige, K., Nagaoka, M. and Takeda, K. (2002) *Fuel Spray Simulation of Slit Nozzle Injector for Direct-Injection Gasoline Engine.*; SAE paper 2002-01-1135.

Heimel, S. and Weast, R.C. (1957) *Effect of Initial Mixture Temperature on the Burning Velocity of Benzene-Air, n-Heptane-Air and Iso-octane-Air Mixtures.*; Sixth Symposium (International) on Combustion.

Heywood, J. B. (1988) *Internal Combustion Engine Fundamentals.;* McGraw-Hill.

Hicks, R.A. (1994) *Turbulent Flame Structure and Autoignition in Spark Ignition Engines.*; PhD Thesis, Department of Mechanical Engineering, University of Leeds.

Hill, P.G. (1988) *Cyclic Variation and Turbulence Structure in Spark-Ignition Engines.*; Combustion and Flame, 72,pp.73-89.

Ho, S.Y. and Kuo, T.-W. (1997) *A Hydrocarbon Autoignition Model for Knocking Combustion in SI Engines.;* SAE Paper 971672.

Hynes, J. (1986) *Turbulence Effects on Combustion in Spark Ignition Engines.;* PhD Thesis, Department of Mechanical Engineering, University of Leeds.

Ipp, W., Egermann, J., Wagner, V. and Leipertz, A. (2000) *Visualization of the Qualitative Fuel Distribution and Mixture Formation Inside a Transparent GDI Engine with 2D Mie and LIEF Techniques and Comparison to Quantitative Measurements of the Air/Fuel Ratio with 1D Raman Spectroscopy.*; SAE paper 2000-01-1793.

Itoh, T., Iiyama, A., Muranaka, S. and Takagi, Y. (1998) *Combustion Characteristics of a Direct-Injection Stratified Charge S. I. Engine.;* JSAE Review, Vol. 19, n3, (July 1998), pp. 217-222.

Jakubík, T (2002) *Engine LDA Technique Progress Report.*; The University of Leeds, School of Mechanical Engineering.

James, E.H. (1987) *Laminar Burning Velocities of Iso-Octane-Air Mixtures –A Literature Review.*; SAE paper 870170.

Jensen, T.K. and Schramm, J. (2000) *A Three-Zone Heat Release Model for Combustion Analysis in a Natural Gas SI Engine –Effects of Crevices and Cyclic Variations on UHC Emissions.*; SAE paper 2000-01-2802.

Keck, J.C., Heywood, J.B. and Noske, G. (1987) *Early Flame Development and Burning Rates in Spark Ignition Engines and Their Cyclic Variability.*; SAE paper 870164.

Kern, Y.K. and Je, H.B. (1996) *Tumble Flow and Turbulence Characteristics in a Small Four-Valve Engine.*; SAE paper 960265.

Kido, H., Wakuri, Y. and Nakashima, K. (1983) *Experiments and a Correlation of Turbulent Burning Velocities.*; Proceedings of ASME-JSME Thermal Engineering Joint Conference, Vol. 4, 183-190.

Kim, B., Kaneko, M., Mitani, M., Ikeda, Y. and Nakajima, T. (2002) *In-cylinder Turbulence Measurements with a Spark Plug-in Fiber LDV.*; Kobe University, Japan, http://in3.dem.ist.utl.pt/lxlaser2002/papers/Paper_38_3.pdf.

Koike, M., Saito, A., Tomoda, T. and Yamamoto, Y. (2000) *Research and Development of a New Direct Injection Gasoline Engine.*; SAE paper 2000-01-0530.

König, G. (1993) *Autoignition and Knock Aerodynamics in Engine Combustion.*; PhD Thesis, Department of Mechanical Engineering, University of Leeds.

Krieger, R.B. and Borman, G.L. (1966) *The Computation of Apparent Heat Release for Internal Combustion Engine.*; ASME 66-W/DGP-4.

Kume, T., Iwamoto, Y., Iida, K., Murakami, M., Akishino, K. and Ando, H. (1996) *Combustion Control Technologies for Direct Injection SI engines.*; SAE paper 960600.

Kuratle, R.H. and Märki, B. (1992) *Influencing Parameters and Error Sources During Indication on Internal Combustion Engines.*; SAE Paper 920233.

Kuwahara, K., Watanabe, T., Takemura, J., Omori, S., Kume, T. and Ando, H. (1994) *Optimization of In-Cylinder Flow and Mixing for a Center-Spark Four-Valve Engine Employing the Concept of Barrel-Stratification.;* SAE paper 940986.

Lancaster, D.R, Krieger, R.B, Sorenson, S.C. and Hull, W.L. (1976) *Effects of Turbulence on Spark Ignition Engine Combustion.*; SAE paper 760160.

Langridge, S. (1995) *Imaging and Thermodynamic Analysis of Autoignition and Knock in S.I. Engines.*; PhD Thesis, Department of Mechanical Engineering, University of Leeds.

Lee, A.P. (1995) *The Effects of Bulk Motions and Turbulence on Combustion in S.I. Engines.*; PhD Thesis, Department of Mechanical Engineering, University of Leeds.

Lewis, B., and Von Elbe, G. (1987) *Combustion, Flames and Explosions of Gases.*; (third edition) Academic Press Inc.

Lipatnikov, A. N. and Chomiak, J. (1997) *A simple Model of Unsteady Turbulent Flame Propagation.;* SAE paper 972993.

Lipatnikov, A. N. and Chomiak, J. (2002) *Turbulent Flame Speed and Thickness: Phenomenology, Evaluation, and Application in Multi-Dimensional Simulations.;* Progress in Energy and Combustion Science, 28, 1-74.

Liu, R.L., Liu, W., Wu, L.Q. and Zhao, C.L. (1999) *LDV Measurements of velocities and Turbulence Intensities in a Production SI Engine Under Motored and Firing Conditions.*; SAE paper 1999-01-0955.

Mahmud, Z. A. (1999) *End Gas Autoignition and Knock in Spark Ignition Engines.;* PhD Thesis, Department of Mechanical Engineering, University of Leeds.

Mann, K.R.C., Ting, D. S-K and Henshaw, P.F. (2000) *A Semi-Empirical Model of Spark-Ignited Turbulent Flame Growth.*; SAE paper 2000-01-0201.

Matekunas, F.A. (1983) *Modes and Measures of Cyclic Combustion Variability.*; SAE paper 830337.

Merdjani, S. (1996) *Leeds University Spark Ignition Engine Computer Model.* Version 6.1, User Manual.

Merdjani, S. and Sheppard, C.G.W. (1993) *Gasoline Engine Cycle Simulation Using the Leeds Turbulent Burning Velocity Correlations.;* SAE paper 932640.

Metghalchi, M. and Keck, J.C. (1982) *Burning Velocities of Mixtures of Air with Methanol, Isooctane, and Indolene at High Pressure and Temperature.;* Combustion and Flame **48**, pp 191-210.

Meyer, J. , Schreiber, M., Haug, M., Siemers, A. and Schulpin, H.J. (1994) *Quantitative Fuel Distribution in a Spark Ignition Engine, Measurement and Observation Analysis of Combustion in Engines.;* IMech E-Seminar.

Morel, T. and Keribar, R. (1985) *A Model for Predicting Spatially and Time Resolved Convective Heat Transfer in Bowl-in-Piston Combustion Chambers.*; SAE paper 850204.

Moriyoshi, Y., Morikawa, H., Kamimoto, T. and Hayashi, T. (1996) *Combustion Enhancement of Very Lean Premixture Part in Stratified Charge Conditions.*; SAE paper 962087.

Müller, U. C., Bollig, M. and Peters, N. (1997) *Approximations for Burning Velocities and Markstein Numbers for Lean Hydrocarbon and Methanol Flames.;* Combustion and Flame, **108**, pp. 349-356.

Murad, A. (2003) PhD Thesis in progress, Department of Mechanical Engineering, University of Leeds.

Namazian, M. and Heywood, J. B. (1982) *Flow in the Piston-Cylinder-Ring Crevices of a Spark-Ignition Engine: Effect on Hydrocarbon Emissions, Efficiency and Power.;* SAE Paper 820088.

Ohsuga, M., Shiraishi, T., Nogi, T., Nakayama, Y. and Sukegawa, Y. (1997) *Mixture Preparation for Direct-Injection SI Engines.*; SAE paper 970542.

Ormsby, M., Sheppard, C.G.W. and Woolley, R. (2003) *The Influence of Fuel Air Ratio on the Turbulent Burning Velocity of Iso-octane Air Flames.*; Fourth International Seminar of Fire and Explosion Hazards, Londonderry, UK.

Ozdor, N., Dulger, M. and Sher, E. (1994) *Cyclic Variability in Spark Ignition Engines A Literature Survey.*; SAE paper 940987.

Pajot, O. and Mounaïm-Rousselle, C. (2000) *Instantaneous Flow Field Effects on the Flame Kernel in S.I. Engine by Simultaneous Optical Diagnostics.*; SAE paper 2000-01-1796.

Pan, J. (1994) *End-Gas Autoignition Modes and Spark-Ignition Engine Knock Severity.;* PhD Thesis, Department of Mechanical Engineering, University of Leeds.

Pischinger, S. and Heywood, J.B. (1990) *How Heat Losses to the Spark Plug Affect Flame Kernel Development in an SI-Engine.*; SAE paper 900021.

Prothero, A. (1969) *Computing with Thermochemical Data.*; Combustion and Flame Vol. 13, pp 399-408.

Ramos, J. I. (1989) *Internal Combustion Engine Modelling.;* Hemisphere Publishing Corporation.

Randolph, A.L. (1990) *Cylinder-Pressure-Transducer Mounting Techniques to Maximize Data Accuracy.*; SAE Paper 900171.

Rassweiler, G.M. and Withrow, L. (1938) *Motion Pictures of Engine Flames Correlated with Pressure Cards.*; SAE Trans., Vol. 83, pp. 184-204. Reissued as SAE paper 800131, 1980.

Reid, M. and Douglas, R. (1994) *Quasi-Dimensional Modelling of Combustion in a Two-Stroke Cycle Spark Ignition Engine.*; SAE paper 941680.

Reynolds, W.C. (1980) *Modelling of fluid motion in engines- An introductory overview.*; in J.N. Mattavi and C.A. Amann (eds.), Combustion Modelling in Reciprocating Engine, pp 69-124, Plenum Press.

Ricardo, H.R. and Hempson, J.G.G. (1968) *The High –Speed Internal-Combustion Engine.*; 5th Edition, London, Blackie.

Ruddy, B. L., Dowson, D. and Economou, P. N. (1981) *The Prediction of Gas Pressures Within the Ring Packs of Large Bore Diesel Engines.;* J. Mech. Eng. Science, Vol. 23, No. 6, pp 295-304.

Ryan, T.W. and Lestz (1980) *The Laminar Burning Velocity of Isooctane, N-Heptane, Methanol, Methane, and Propane at Elevated Temperature and Pressures in the Presence of Diluent.*; SAE paper 800103.

Shapiro, A. H. (1953) *The Dynamics and Thermodynamics of Compressible Fluid Flow.:* the Ronald Press Company, New York, Vol. 1.

Shen, H., Hinze, P.C., and Heywood, J.B. (1996) *A Study of Cycle-to-Cycle Variations in SI Engines Using a Modified Quasi-Dimensional Model.*; SAE paper 961187.

Stone, R. (1991) *Introduction to internal combustion engines.*; 2nd Edition, Macmillan.

Stroud, K.A. and Dexter, J.B. (2001) *Engineering Mathematics.*; 5th Edition, PALGRAE.

Tabaczynski, R.J. (1983) *Turbulence Measurements and Modelling in Reciprocating Engines – an Overview.*; I. Mech. E., Paper No. C51/83.

Tabata, M., Kataoka, M., Fujimoto, M. and Noh, Y. (1995) *In-Cylinder Fuel Distribution, Flow Field, and Combustion Characteristics of a Mixture Injected SI Engine.;* SAE paper 950104.

Taraza D. (2001) *Quantifying Relationship Between Crankshaft's Speed Variation and Gas Pressure Torque.;* SAE Paper 2001-01-1007.

Taraza D. (2002) *Accuracy Limits of IMEP Determination from Crankshaft Speed Measurements.;* SAE Paper 2002-01-0331.

Tennekes, H. and Lumley, J.L. (1972) *A First Course in Turbulence.*; MIT Press.

Tindal, A. (1997) *Autoignition and Knock in Spark Ignition Engines.*; PhD Thesis, Dep. of Mech. Eng., University of Leeds.

Ting, D. S-K. and Checkel, M. D. (1997) *The Importance of Turbulence Intensity, Eddy Size and Flame Size in Spark Ignited, Premixed Flame Growth.* Technical Note, Proc. Inst. Mech. Engrs., Vol. 211, Part D, pp.83-86.

Ting, D.S-K., Checkel, M.D. and Johnson, B. (1995) *The Importance of High-Frequency, Small-Eddy Turbulence in Spark Ignited, Premixed Engine Combustion.*; SAE paper 952409.

Ting, L.L. and Mayer, J.E. (1974) *Piston Ring Lubrication and Cylinder Bore Wear Analysis.;* Part 1 – Theory, Journal of Lubrication Technology, pp 305-314.

Wahiduzzaman, S., Morel, T. and Sheard, S. (1993) *Comparison of Measured and Predicted Combustion Characteristics of a Four-Valve S.I. Engine.*; SAE paper 930613.

Witze, P.O., Hall, M.J. and Bennett, M.J. (1990) *Cycle-Resolved Measurements of Flame Kernel Growth and Motion Correlated with Combustion Duration.*; SAE paper 900023.

Woschni, G. (1967) *A Universally Applicable Equation for the Instantaneous Heat Transfer Coefficient in the Internal Combustion Engine;* SAE Paper 670931.

Wyszynski, L.P., Stone, C.R. and Kalghatgi, G.T. (2002) *The Volumetric Efficiency of Direct and Port Injection Gasoline Engines with Different Fuels.*; SAE Paper 2002-01-0839.

Zaho, H., Calnan, P., Ladommatos, N. and Ma, T. (1999) *Development of an Engine Simulation Program and Its Application to Stratified Charge SI Engines.;* Int. J. of Vehicle Design, Vol. 22, pp. 159-194.

Zhao, F., Lai, M.C. and Harrington, D.L. (1999) *Automotive spark-ignition direct-injection gasoline engines.*; Progress in Energy and Combustion Science, 25, pp 437-562.

Zhao, H., Yang, X., Zhou, L. and Liu, S. (1996) *An Investigation of a New Type Direct-Injection Stratified Charge Combustion System for Gasoline Engines.;* SAE paper 961150.

Zimont, V.L. (1979) *Theory of Turbulent Combustion of a Homogeneous Fuel Mixture at High Reynolds Number.*; Combustion, Explosions, and Shock Waves. Vol.15, 305-311.

Zimont, V.L. and Lipatnikov, A.N. (1995) *A Numerical Model of Premixed Turbulent Combustion.*; Chemical Physics Reports 14, pp 993-1025.